SWCC AND CLAY MINERALOGY BASED MODELS FOR REALISTIC SIMULATION OF SWELL BEHAVIOR OF EXPANSIVE SOILS

by

ARAVIND PEDARLA

Presented to the Faculty of the Graduate School of
The University of Texas at Arlington in Partial Fulfillment
of the Requirements for the Degree of

DOCTOR OF PHILOSOPHY

THE UNIVERSITY OF TEXAS AT ARLINGTON

May 2013

ACKNOWLEDGEMENTS

The efforts of many have led to the successful completion of this dissertation and made my time at the University of Texas at Arlington a fruitful one. I would like express my deepest gratitude to my professor, Dr. Anand J. Puppala, for his excellent guidance and enthusiastic encouragement throughout this research study. His dedication and immeasurable effort towards the field of Geotechnical Engineering always inspire me. In addition, his support, patience and most of all his friendship throughout this research are truly cherished. I would also like to convey my gratitude to Dr. Laureano R. Hoyos for his suggestions, guidance and friendship through the research. I also would like to extend my gratitude to Dr. Dong Jun Seo, Dr. Shih-ho Chao and Dr. Chein-Pai Han for accepting to be on the examination committee. I would also like to thank these committee members for introducing me to various fields of study and my interactions during course works. I am grateful for the research assistantship granted by NSF under Grant no. 1031214. I would like to acknowledge Dr. Sandra Houston, Dr. Claudia Zapata, Daniel Rosenbalm and Elham Bani Hashem, from Arizona State University for their excellent co-operations throughout the research. I would like to thank Dr. Sai K Vanapalli, University of Ottawa, for his constant support and guidance throughout this research.

Appreciations are broadened to all the members of Department of Civil Engineering staff, Ms. Ginny Bowers, Ms. Sarah, Ms. Ava Chapman, Ms. Christiana, Mr. Lewis Crowe, and Mr. Paul Shover for their unconditional help in various aspects during my course of study at UTA. I would like to thank Dr. Bhaskar Chittoori, Dr. Thornchaya Wejrungsikul and Dr. Srinivas Prabakar for their advice and help during the course of this study. I like to extend my sincere appreciations to my colleagues Nagasreenivasu Talluri, Minh Le, Tejo Vikas, Ranjan Rout, Vijay

Ganne, Pinit Ruttanaporamakul, Ahmed Gailey, Justin Thomey, Chatuphat Savigamin, Jeffrey Phillip, Matthew Kammerdiener, Carlos Esparza, Lisandro Murua, Raja Yenigalla, Anil Raavi, Priya Lad, Ujwal Kumar, Sadikshya Poudel, Rathna Mothkuri, Spoorthi Reballi and Praveen Vanga for their sincere supports, encouragement and contribution in laboratory and field studies of this research work. The value of their friendship will never be forgotten.

I would like to express my deepest gratitude for all the inspiration from my first teacher; my mother Madhavi Pedarla. My heartfelt thanks to my father, Mohan Chand Pedarla who all along trusted and believed in my goals and my brother, Akhilesh Pedarla who is always there to share my joy. I am grateful for your never ending love, support and encouragement.

Finally, I would like to express my heartfelt regards to my beloved wife, Preethi Suriamoorthy. Her support, encouragement, patience and unwavering love were undeniably the bedrock upon which the past few years of my life have been built, in this unstable and expansive soil dominant world…

April 18th, 2013

ABSTRACT

SWCC AND CLAY MINERALOGY BASED MODELS FOR REALISTIC SIMULATION

OF SWELL BEHAVIOR OF EXPANSIVE SOILS

Aravind Pedarla

The University of Texas at Arlington, 2013

Supervising Professor: Dr. Anand J Puppala

Predicting the volume change behavior of expansive soils has been a major challenge to the engineers in the past few years, due to the intricate coupling effects caused by different soil composition related mineralogy and pore void distribution to unsaturated soil property related parameters toward soil swelling. Hence, the main objective of this research is to develop models for realistic simulation of expansive soil behavior by accounting for inherent composition and unsaturated soil properties. In order to accomplish this research, eight natural expansive clays have been sampled from different active expansive soil regions across the United States. Basic soil classification and mineralogy studies were performed on these soils to identify the type of expansive clays and approximate mineralogy. The swell behavior of these clays is then studied by using different testing methods on soils compacted at different initial dry density conditions. A novel 3-D swell test apparatus was introduced to measure the volumetric strains

of these soils under confining pressures. These test results are utilized for the development and validation of swell prediction models.

Different soil composition parameters like clay mineralogy, soil-suction relationship and pore distribution are studied using advanced techniques. These techniques include the determination of clay mineralogy from chemical properties of soil, soil water relationship (i.e. soil water characteristic curve) from pressure plate and filter paper techniques and pore distribution studies from mercury intrusion porosimetry technique and X-ray computed tomography tests. Once the soil composition parameters are determined, analysis of test results was performed to identify the variation of composition parameters with soil type.

Based on the soil composition test results three soil swell prediction models have been formulated in the current research. The first model was based on diffused double layer theory of clay minerals present in the soil. The second model termed as MHC model was based on two swell governing parameters which constitutes the effects of soil matric suction, void ratio change and clay mineralogy. The final model was based on the ratio of total surface area measured from clay mineralogy and mercury intrusion porosimetry. All the models showed reliable predictions of swell movements of soils that matched well with the measured test results.

TABLE OF CONTENTS

LIST OF ILLUSTRATIONS

Figure Page

LIST OF TABLES

CHAPTER 1

INTRODUCTION

1.1 Expansive soils

Expansive soils have been found in different topographical zones around the world. These soils are formed from the weathering of rocks over time and have a microstructure which absorbs moisture between their mineral layers and undergo volume changes. These volumetric changes cause swell and shrinkage movements in soils, which in turn will inflict severe damage to structures built above them (Nelson and Miller, 1992). These soils typically exhibit moderate to high plasticity, low to moderate strength and high swell and shrinkage characteristics (Holtz and Gibbs 1956).

Problems associated with differential movements from swell, can be expected for all the structures built on these soils, including residential building foundations, retaining walls, slopes and pavements. Swell pressures contribute to heave movements and lifting of structures in both lateral and vertical directions, inducing at least some damage to structures for a majority of expansive soil sites.

Generally expansive soils are characterized based on soil index parameters. Since, soils encompass a wide spectrum of particulate materials and were difficult to generalize the expansive soil behavior based on these individual parameters. It is imperative to better understand the swelling behavior and the factors affecting it. Henceforth, the actual parameters governing the swell/shrink behavior are identified and studied in this research.

Mineralogy which is one of the fundamental parameter governing the swell shrink behavior of any expansive clay has been explored in this research. The large cation exchange

capacities and specific surface area of minerals like Montmorillonite, allow the clay to absorb more moisture content than non-expansive minerals like Kaolinite.

Soil suction relationship plays a crucial role in the volume change behavior of clays. Most natural problematic soils are in an unsaturated state and the moisture varies with seasonal conditions. The soil water characteristic curve (SWCC) of a soil reveals the variation of suction in the soil with moisture content. More recent studies have shown that the engineering behavior of these expansive soils can be better interpreted if the influence of matric suction is taken into account (Alonso et al. 1999).

Pore distribution is the next governing parameter responsible for swell behavior, since the hydraulic conductivity and the soil water absorption characteristics are mainly dependent on the pore distribution (Mitchell and Soga, 2005). Mercury intrusion porosimetry (MIP) is a technique where a non wetting liquid like mercury is forced to enter and exit the pores of the soil specimen (Washburn, 1921). This test reveals the different pore sizes present in the soil and also the volume of the constituent pores. X-ray computed tomography (XCT) technique identifies the inner structure of a solid mass like soil specimen. This information reveals about the pores network distribution in a soil specimen. Both the techniques provide insight in to the internal structure of the soil specimens and were used in the current research.

Most expansive soil problems emanate from poor characterization and swell property interpretation methods, which do not account for soil variations and unsaturated soil mechanics principles as discussed (Nelson and Miller, 1992, Al Rawas et al., 2005, Puppala et al, 2012) Hence, there is a strong and a basic research need to better understand fundamental factors affecting expansive soil movements within the context of unsaturated soil mechanics principles, which would lead to sound characterization and better design methodologies.

1.2 Research Objectives

To accomplish the proposed research work, the following specific objectives will be addressed:

1. Study and select various soil compositional and environmental variables that are responsible for the expansive behavior;

2. Conduct experimental investigations on eight natural expansive clays having different clay mineralogy and variable degree of swell potential. This results in the study of soils having a wide spectrum of clay mineralogy and fabric.

3. To evaluate the impacts of clay mineralogy, initial moisture content, overburden stress, and density on swell related volume change behavior of these soils.

4. Study their SWCC and develop a fundamental linking of SWCC and volume change trends for expansive soils in terms of clay mineralogy, pore distribution and specific surface area using advanced digital image analysis

5. Develop formulations based on the SWCC models and incorporating clay mineralogy, pore void and specific surface areas of soils to better interpret swell characteristics of expansive soils.

6. Demonstrate the usefulness of prediction models based on modern unsaturated soil principles for better simulation of heave behavior of expansive soils.

The final positive outcome of the proposed research will be the development of analytical and numerical approaches for the prediction of the volume change properties and responses of expansive soils using clay mineralogy and unsaturated soil mechanics principles. These methods will result in improved characterization tools for evaluating expansive soil swell potentials and thereby develop better design methodologies for civil infrastructure resting on or made of expansive soils

Figure 1.1 below presents the current research experimental design flowchart. After the modeling framework is established with the help of advanced soil parameters, the predictions are validated with the help of standard swell properties obtained from these soils.

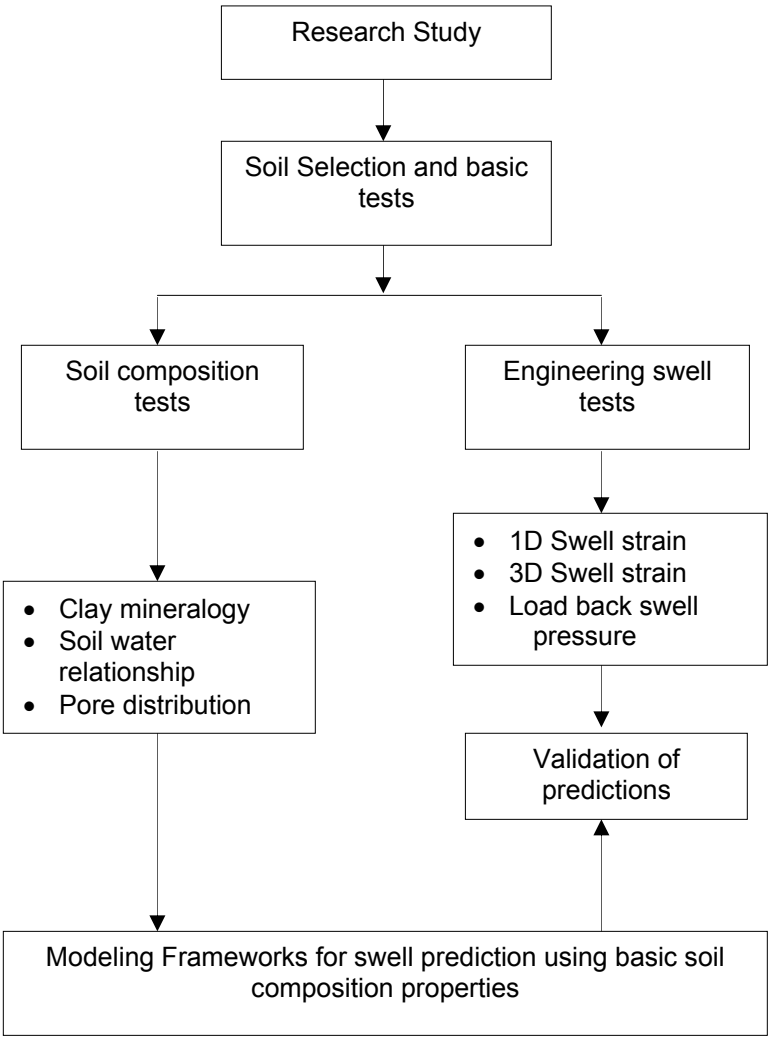

Figure 1.1: Experimental design for the current study

1.3 Organization and dissertation

Chapter 1 provides an introduction and background history explaining the significance of the project, research objectives, and dissertation organization to provide a framework of the current research.

Chapter 2 presents the literature review on expansive soil behaviors, properties and the current swell prediction models. Different factors responsible for the swell/shrink behavior of expansive clays were studied in detail. Previous studies conducted on all the major factors identified responsible for expansive behavior were highlighted in this chapter.

Chapter 3 covers the selection of test soil and basic soil classification. The experimental program includes basic soil properties tests, chemical and mineralogy tests, and engineering tests on the soils from these locations. Laboratory testing designed to determine the properties relating to volume change behavior of expansive soil samples were also presented. A novel 3-D swell strain test apparatus is introduced in this chapter to study the swell strain behavior under overburden pressure. A summary of the laboratory procedures, equipments used and methods were clearly explained in this chapter.

Chapter 4 summarizes the swelling behavior exhibited by each of the clays. The 1-D swell strain, 3-D swell strain and load back swell pressure test results were presented. Also, variation of swell behavior with changes in dry density and overburden confining pressure conditions were studied and presented.

Chapter 5 covers the soil suction relationships obtained for all the clays. Measurement of soil water characteristic curve (SWCC) was made using techniques like axis translation and filter paper methods. Analysis of SWCC and identification of the parameters involved in the swell behavior were also covered in this chapter. This Chapter describes with the pore size distribution measurements and evaluations using Mercury Intrusion Porosimetry (MIP) and X-ray Computed Tomography (XCT) methods. Details of the pore network in the soil specimen was revealed and presented in this chapter. Variations of pores of the soils before and after soil swelling were identified with the help of XCT studies. Analysis of the pore network for clays was also presented in this chapter.

Chapter 6 presents the formulation of three swell behavior models based on soil composition parameters like clay mineralogy, soil suction behavior and total surface are. The validations of these models are validated by comparing their prediction results with the measured swell data of the present soils.

Chapter 7 presents the summary and conclusions obtained from analysis and future recommendations.

CHAPTER 2

LITERATURE REVIEW

2.1 Expansive soils

Soils that exhibit swell shrink characteristic when subjected to moisture fluctuations are termed as expansive soils. These expansive soils are found in abundance in semi-arid regions of tropical and temperate climatic zones, where annual evapo-transpiration is more than the precipitation (Jones and Holtz, 1973). These soils are quite unstable and often avoided as a construction material.

The behavior of these fine grained soils is better understood with their type of constituent mineralogy and the pore size distribution. Other factors including stress history and current state of stress conditions will also influence the soil swell behavior patterns. The factors influencing the shrink-swell potential of a subgrade can be categorized into three different groups: soil characteristics (clay mineral, plasticity and pore connectivity), environmental factors (climate, groundwater, vegetation, soil suction, dry density and drainage) and the state of stresses (Nelson and Miller 1992).

The first part of this chapter deals with problems caused to the structures built on expansive soils based on the current design standards. Currently, the Index properties of expansive soils are used to correlate their expansive behavior. Hence a brief review of all the correlations and techniques based on index properties were presented in this chapter. The factors responsible for the swell shrink behavior were identified and the previous studies conducted on them are presented in this chapter. It was found in literature that, mineralogy plays a vital role in governing the behavior of these clays. A brief review of studies conducted

on mineralogy and their influence on soil behavior are presented in this chapter. Behavior of expansive soils with moisture content has been studied by many researchers for the past few decades. The soil water characteristic curve is identified as one of the fundamental parameters governing the behavior of expansive soils. Measurement techniques such as Filter paper method, axis translation technique using Tempe method were discussed. Literature on different volume change correlations based on soil suction parameter is presented. Research conducted with novel techniques like Mercury Intrusion Porosimetry (MIP) and X-ray Computed Tomography to reveal the internal pore structure of a soil specimen was also presented. Details on these studies and their applications on soils to analyze the pores were discussed in the later parts of this chapter.

2.1.1 Problems caused by expansive soils

Though expansive soils in natural conditions are not suitable for urban infrastructure construction, the growth in population in the last decade and the associated urbanization led to construction in areas encompassing with expansive soils (Williams 2003). As a result, expansive soils-related damages to engineering structures have increased exponentially and in the United States alone, these damage costs were estimated ranging from $2 to $9 billion annually (Jones and Jones 1987). Prior to Katrina disaster, it can be noted that the damage from swelling soils annually causes a greater economic loss than the damage caused by floods, hurricanes, tornadoes, and earthquakes (Jones and Holtz, 1973). Figure 2.1 shows the distribution of highly expansive soils over The United States.

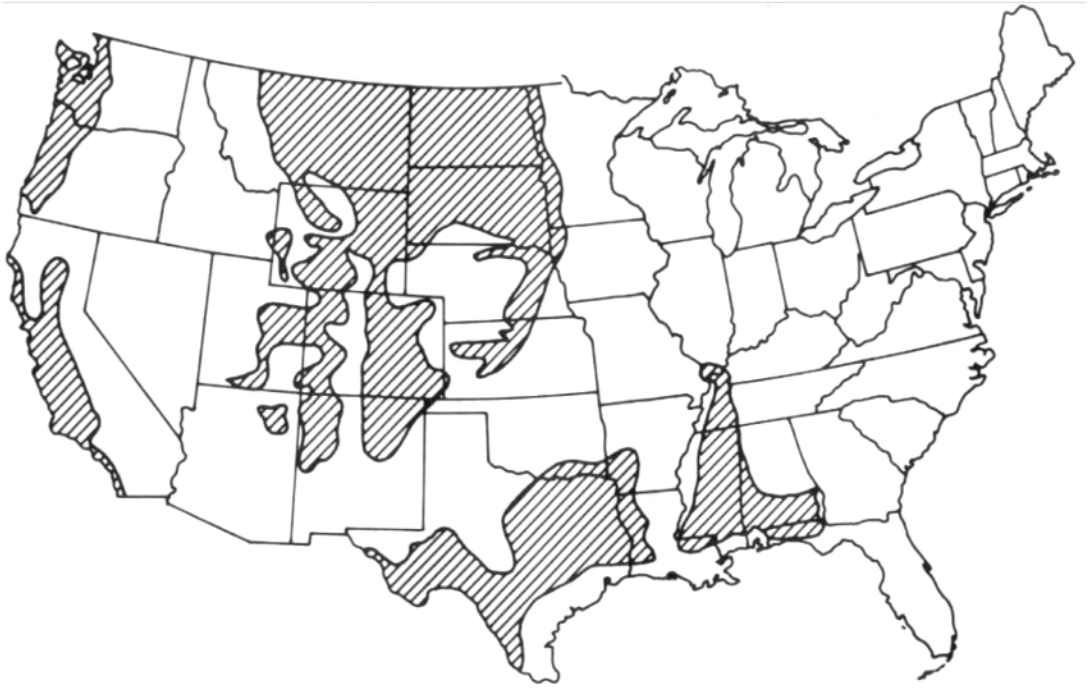

Figure 2.1: Distribution of expansive soils over The United States (Chen, 1988)

The subsoil problems in these regions are mainly attributed to volumetric swell and shrink related changes during long dry periods and subsequent periodic rains for short duration (Chen 1988, Bowles 1996, and Nelson and Miller 1992). This volume change and/or cyclic swell shrink behavior of expansive soils cause severe distress to engineering structures including foundations and pavement infrastructure. Some examples of engineering failures associated with expansive soil behavior are detailed below.

2.1.1.1 Building foundation failures

Al Rawas et al (2005) conducted a study on the potential problems associated with expansive soils on foundations in the Arabian Gulf. Figure 2.2 and Figure 2.3 shows the distress caused to the building by swell shrink characteristic of expansive soils. Authors investigated the mineralogical composition of expansive soils and rocks from different sites in northern Oman using the X-ray diffraction (XRD) technique.

The presence of Smectite clay mineral in the soil has been identified in this research as the factor responsible for foundation failures in the buildings. They also indicated the presence of Illite, Palygorskite, and Kaolinite clay minerals in the samples but in relatively small quantities.

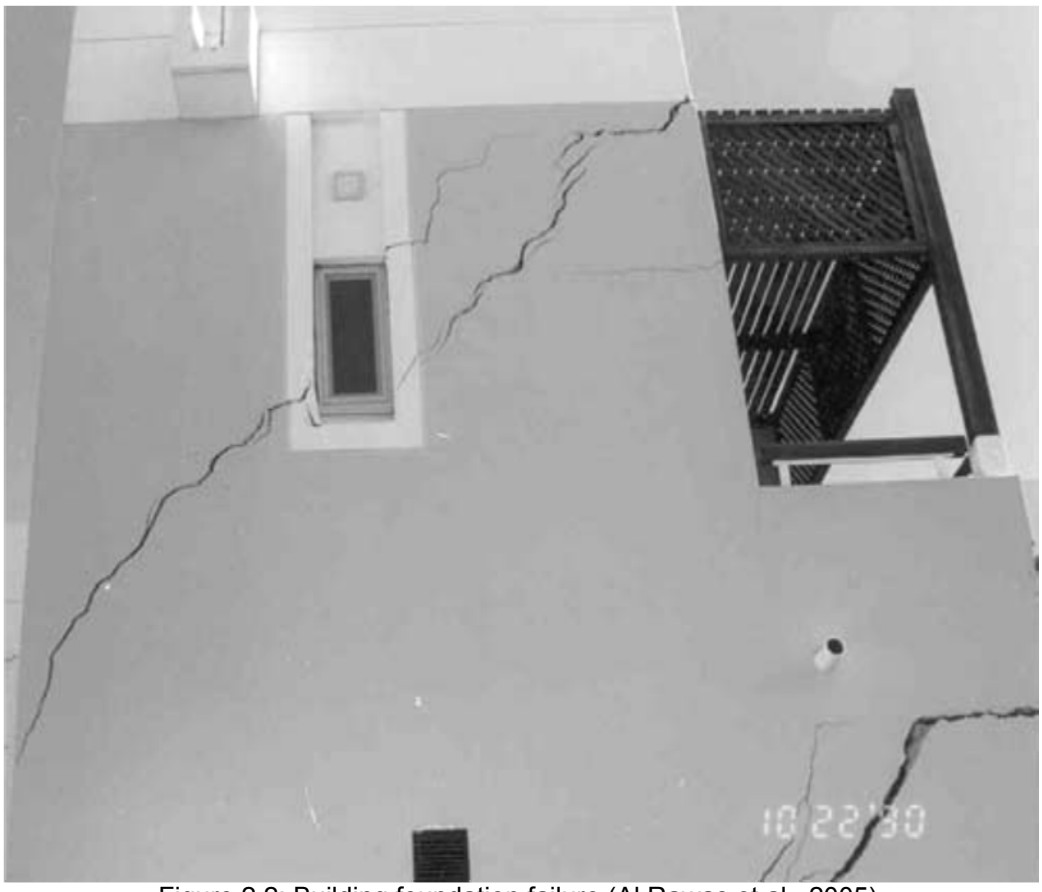

Figure 2.2: Building foundation failure (Al Rawas et al., 2005)

It was suggested that the principal mechanism of swelling was related to the presence of Smectite clay minerals. A secondary mechanism for swelling was observed due to over-consolidation and the presence of gypsum.

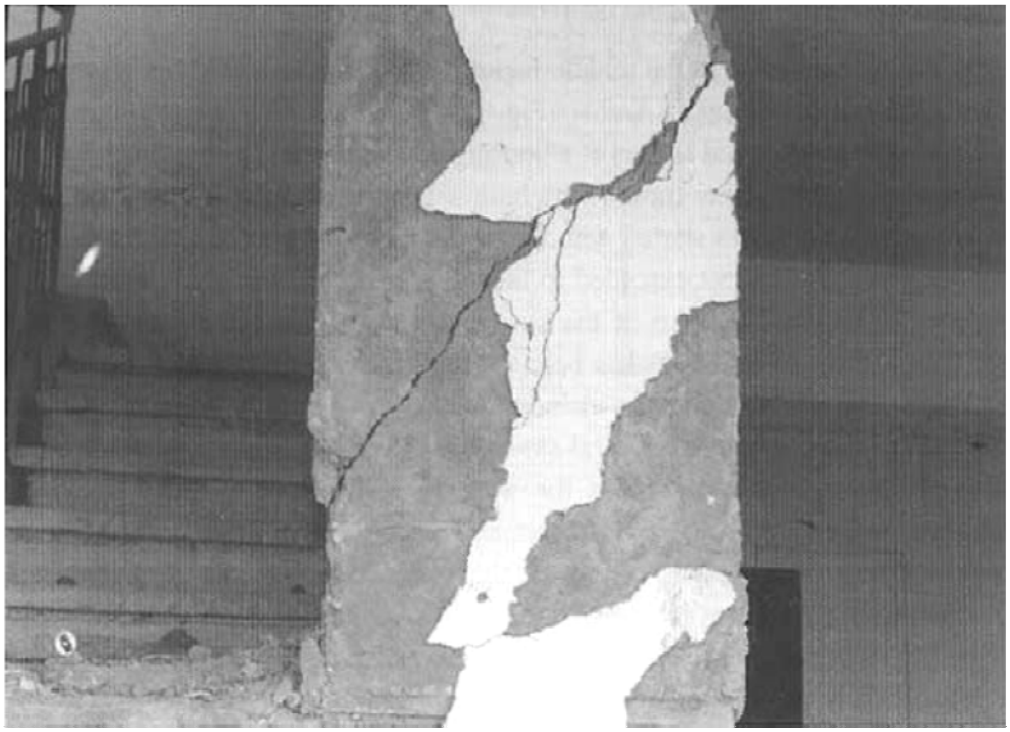

Figure 2.3: Column failure (Al Rawas et al., 2005)

2.1.1.2 Slope failures

McCleskey et al. (2008) reported slope failures occurred at Grapevine Dam in the state of Texas, USA. This dam is built on expansive soil and is subjected to desiccation cracks during seasonal changes. During a rainfall event, water infiltrates into the soil through the desiccation cracks. Infiltration increases pore water pressure which leads to reduction of shear strength triggering failure (Rahardjo et al. 2001, Cho and Lee, 2002). The shrinkage cracks formed due to desiccation during dry season get filled up during precipitation and the water exerts hydrostatic pressure resulting in sliding of slope from the crack which is responsible for an increase of width of shrinkage crack. Figure 2.4 (a) and (b) shows the failures caused by moisture infiltration in to the desiccation cracks. Failures associated with expansive soils are quite detrimental and clearly shows the extent of damage in these corresponding sections.

(a)

(b)

Figure 2.4 (a) & (b): Failures at slope triggered by dessication cracks of expansive soils (McCleskey et al. (2008)

2.1.1.3 Pavement failures

Damages sustained by pavements on expansive soils include distortion and cracking in all directions. In addition, bumps caused due to heave can increase the roughness of pavements and result in poor riding comfort. Differential soil movements may induce large changes in moments and shear forces in the pavement structures. If not accounted for these in the original design, both rigid concrete and asphaltic pavements may experience severe distress in the forms of high roughness and cracking in both the longitudinal and transverse directions as shown in Figure 2.5.

Figure 2.5: Pavement failure (Al Rawas et al., 2005)

Overall, the magnitudes and extent of damages to pavement structures can be extensive, and it is often necessary to repair these pavements, thus increasing the pavement repair costs. Puppala et al. (2012) conducted studies on pavements constructed on expansive soils. Lime stabilization techniques utilized to mitigate the expansive behavior of these soils were successful. Below shown Figure 2.6 is a pavement distress caused by swell shrink characteristic of expansive soils.

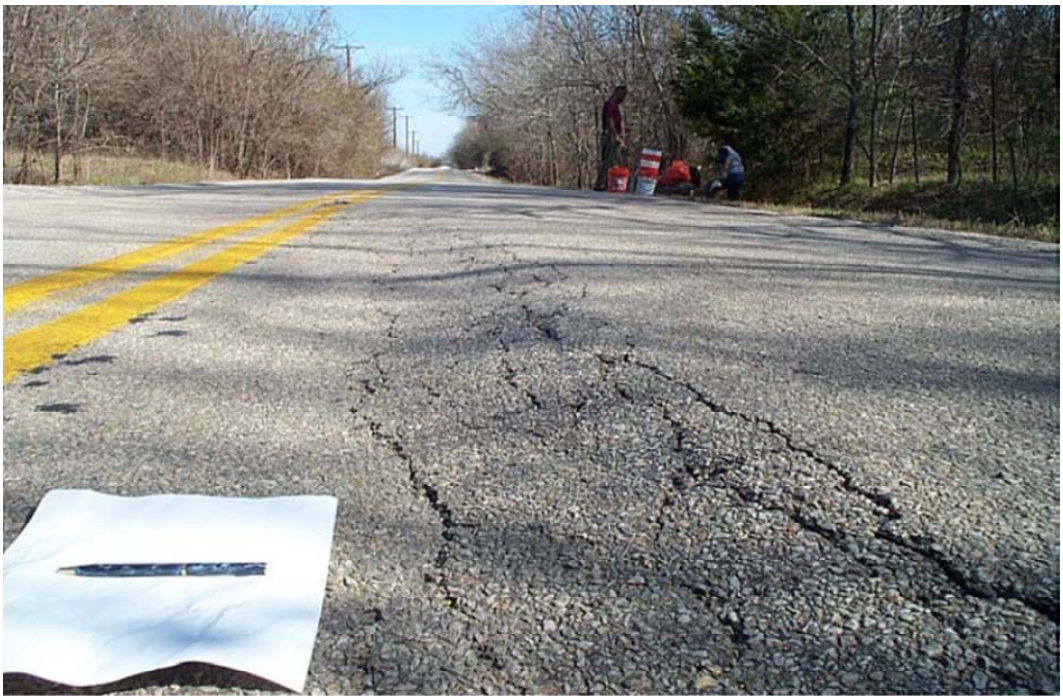

Figure 2.6: Pavement distress caused by swell shrink phenomenon (Puppala et al, 2012)

2.2 Identification of swell behavior

Swell properties such as swell strain and swell pressure of expansive soils are dependent on natural moisture content variation, dry density, and plasticity index, temperature and humidity conditions and overburden pressure conditions (Puppala et al., 2004). Because of the influence of these factors, several expansive soil characterization methods were developed in the literature. These methods are mainly based on plasticity based soil properties, and empirical correlations using activity and compaction properties.

2.2.1 Swell prediction correlations:

In some cases, the contractors and researchers might not have the resources and time to conduct the swell experiments to determine the soil potential. In this case, correlations which are formulated and standardized by many researchers are available. Empirical methods get the swelling potential of any clay from the parameters like void ratio, moisture content, liquid limit and activity. But, these correlations often are based on basic soil parameters and do not

represent the actual swell potential of the soil. Below given are some of the methods widely followed for the prediction of swell potential.

The activity chart proposed by Van Der Merwe (1964), was frequently used by many researchers and contractors to assess the expansiveness of clays as shown in Figure 2.7 below.

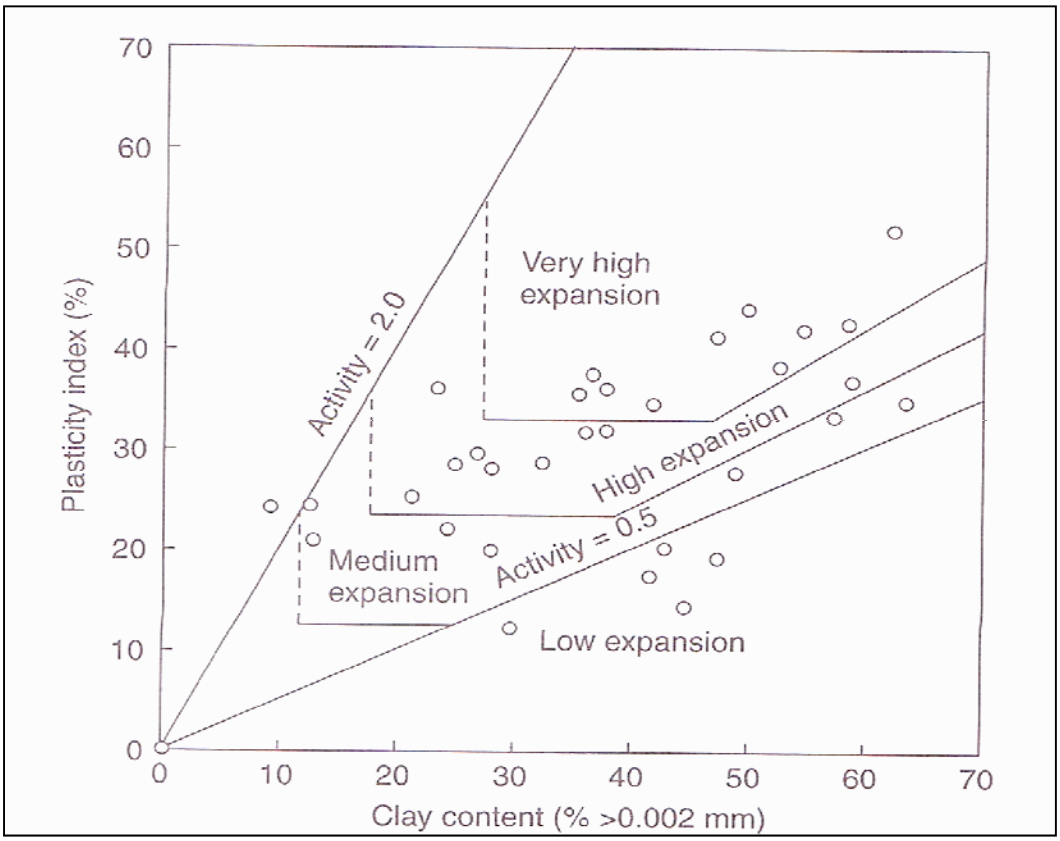

Figure 2.7: Activity chart for estimation of the degree of expansiveness (Van Der Merwe, 1964)

Chen (1965) developed a correlation using percent finer than No.200 Sieve, liquid limit and standard penetration test blow counts to predict the expansion potential of any clay. Table 2.1 shown below represents the expansive soil classification based on the above stated parameters.

Table 2.1: Expansive soil classification by Chen (1965)

% Passing No.200 Sieve	Liquid Limit (%)	SPT (Blows/ft)	Expansion (% Total volume change)	Degree of expansion
>95	>60	>30	>10	Very High
60-95	40-60	20-30	3-10	High
30-60	30-40	10-20	1-5	Medium
<30	<30	<10	<1	Low

The building research establishment (BRE) located in the United Kingdom, suggested that the plasticity index as an indication to volume change potential in a soil (Anon, 1979). Table 2.2 shown below represents the classification of expansive soils followed by BRE.

Table 2.2: Soil activity related to swell (Anon, 1979)

Plasticity Index (%)	Potential for volume change
> 35	Very high
22-48	High
12-32	Medium
< 18	Low

Several researchers have used Index parameters as a governing tool to identify the swell behavior of expansive soils. Table 2.3 below shows some of the correlations and models developed by researchers for the prediction of swell pressure. Several researchers used initial parameters of the soil like moisture content, density, clay content etc for the swell prediction correlations.

Table 2.3: Correlations for swell pressure prediction
(Nagaraj et al., 1985 and Mowafy et al., 1985a)

Reference	Correlations	Remarks
El-Ramli (1965)	$P_s = 0.5\gamma_d l w_s$	Does not consider initial water content
Komornik and David (1969)	$\log P_s = 2[132 + 0.0208LL + 0.000665\gamma - 0.0269w_n]$	Insensitive to dry density
Dedier (1973)	$\log P_s = 2.55\frac{\gamma_d}{\gamma_w} - 1.705$ $\log P_s = 0.0294C - 1.923$	Does not consider initial water content
Vijayavergiya and Ghazzaly (1973)	$\log P_s = \frac{1}{2}(0.4LL - w_n - 0.4)$ $\log P_s = \frac{1}{19.5}(\gamma_d + 0.65LL - 139.5)$	Correlations developed based on 270 test results of undisturbed natural soils at shallow depth.
Rabba (1975)	For sandy clay: $\log P_s = 2.17(\gamma_d + 0.084C) - 3.91$ For silty clay: $\log P_s = 2.5(\gamma_d + 0.006C) - 4$	Use of equations limited to an initial water content of 8%
Johnson and Stroman (1976)	PI ≥ 40 $S_p = 23.82 + 0.7346PI - 0.1458H - 1.7w_0 + 0.0025PI \times w_0 - 0.00884PI \times H$ PI ≤ 40 $S_p = -9.18 + 1.5546PI + 0.0842H + 0.1w_0 - 0.0432PI \times w_0 - 0.01215PI \times H$	For 1 psi surcharge pressure to saturation
McKeen (1980)	$S_p = -100\gamma_h \log\frac{\tau_f}{\tau_0}$	The γ_h is found from a chart using CEC, PI, and percent clay.
Mowafy and Bauer (1985a)	$\log 10.2P_s = 1.366(10.2\gamma_d) + 0.008954C - 0.02179w_h - 2.84$	For soils from Nasr city, a satellite city of Cairo, Egypt
Nagaraj and Murthy (1985)	$P_s(kPa) = 2492 - 12811.3\frac{e_0}{e_L}/(5.52 - l_0)$ $\frac{e_0}{e_L} = 1.122 - (0.2343 - \rho)\log P_c - \rho \log P$	These three equations have three unknowns in Ps, Pc and _ and the solutions could be obtained by iteration process.

P_s = swell pressure (kg/cm^2);

γ_d = dry density (g/cm^3);

w_s = shrinkage limit (%);

LL = liquid limit (%);

w_n = natural water content (%);

SI = shrinkage index;

S_r = degree of saturation of specimen before start of test;

w* = water content at Sr = 100%;

C = clay content (%);

γ_w = density of water (g/cm3);

P = overburden effective pressure;

e_0/e_L= generalized initial state of soil;

ρ = slope of the line joining the present state to preconsolidation pressure;

S_p = percent swell (%);

PI = plasticity index (%);

W_0 = initial water content (%);

H = depth of soil (ft)

As presented above, many researchers followed that the swell behavior of clays was mainly dependent on a single index parameter, the Plasticity Index (PI). However the determination of plasticity is performed on remolded soil. Hence, the above methods are highly unreliable as they do not consider the influence of soil texture, moisture content, soil suction or pore structure, which are important factors in relation to volume change potential of expansive soils. The present research tries to perform a comprehensive study the parameters responsible for the volume change behavior.

2.2.2 Laboratory measurements

Laboratory studies were conducted on natural and remolded specimens to determine the swell potential of a soil. Swell potential for a soil is determined by tests like 1 dimensional (1D) swell test and swell pressure tests. Below presented are some of the tests conducted by the researchers for soil swell potential determination. Due to the limitation of these tests, difficulties arise in the accurate characterization of expansive soils.

2.2.2.1 1 D Swell strains

In conventional engineering practice, majority of laboratory swell tests are conducted in Oedometer type apparatus with low seating pressures. Holtz and Gibbs (1956) and Lambe and Whitman (1959) were the first to report the use of consolidometers for heave prediction in case of swelling clays. ASTM D 4546-08 explains three alternate methods for the determination of swell pressure. The free swell of the test specimen is achieved when the specimen reaches an equilibrium state with no further swell. Figure 2.8 shows the typical variation of swell deformation of clay with logarithmic of time.

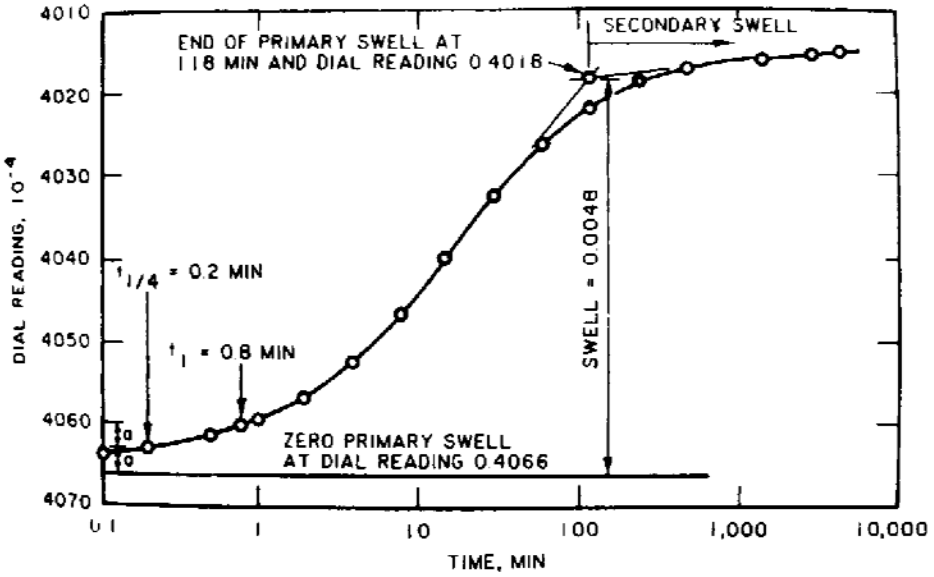

Figure 2.8: Time-swell curve for clay (ASTM D4546)

2.2.2.2 3-D Swell strains

In a study conducted by Punthutaecha et al. (2006), A three-dimensional free swell test did not only provide a reasonable representation of the soil maximum volumetric swell potential but also yielded reliable and repeatable test results (Punthutaecha et al., 2006). This test was conducted to investigate the maximum vertical, radial and volumetric swell potentials. In the testing, a specimen of 4 in. diameter and 6 in. height was placed between two porous stones at the top and bottom, covered by a rubber membrane, fully inundated with water at both ends and monitored for the vertical and radial swell movement until there was no further significant swell (Figure 2.9). The radial swell movement was simply measured by using Pi tape at the times of recording. Test results were expressed as the percentage of swell strain versus time.

Figure 2.9: Three dimensional free swell test setup (Punthutaecha et al., 2006)

However, all the swell measurements are made at no confinement. The present research targets to study the swell strains of clay specimens under different confinements.

2.2.2.3 Swell Pressure

Swell pressure come in to picture when a soil mass is restricted to free swell. The amount of swell pressure exhibited by a particular soil depends on its factors contributing to swell. Swell pressures contribute to heave movements and lifting of structures in both lateral and vertical directions, inducing at least some damage to structures for a majority of expansive soil sites.

The swell pressure of expansive soils is commonly determined by the load required to apply on to the specimen to bring it back to its initial state under fully soaked conditions (load back method). The surcharge loads added to the soil specimen so that the specimen reaches its initial height is determined. The swell pressure value is estimated from the information of surcharge loads and sample dimensions. There are different test methods that can be used to measure swell pressures, details of the test procedures are given in ASTM D 4546.

Seed et al. (1961) stated that small changes in volume during testing procedure produce a noticeable decrease in the measured value. It was found by Kassif et al. (1965) that the consolidometer based test had become widely accepted for evaluating swelling soils and predicting the heave that may be encountered during and after construction.

Fredlund (1969) conducted swell tests on soft compressible soils to measure compliance of the Oedometer apparatus. It was concluded, that a number of procedural factors affect the swell results obtained from a standard Oedometer. Figure 2.10 presents the typical variation of void ratio with swell pressure for a clay specimen from a swell pressure test.

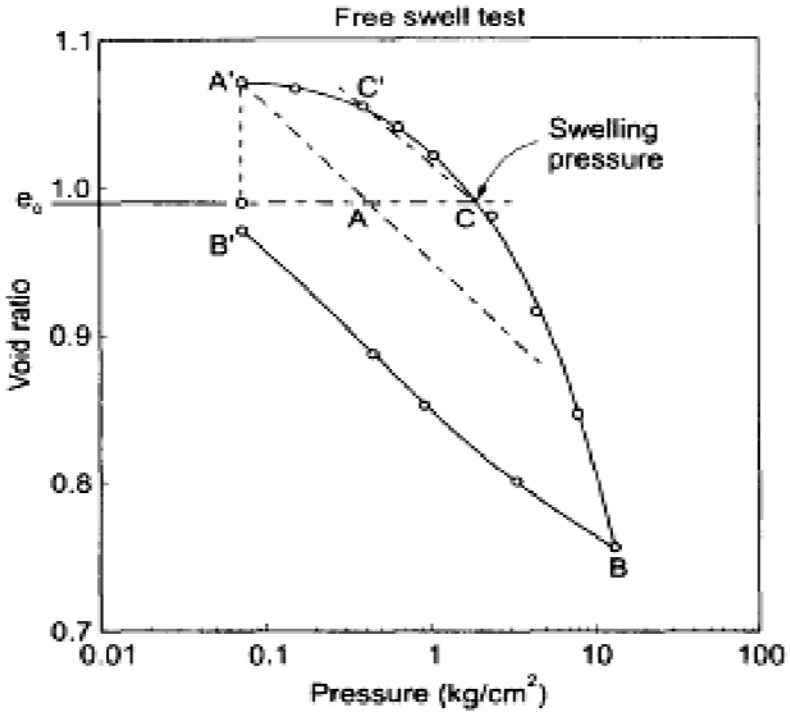

Figure 2.10: Void ratio versus swell pressure of a clay (Fredlund, 1969)

Fredlund (1969) also measured the compressibility of different elements like compressibility of filter paper, porous disks and appliance corrections, which are responsible for the inaccurate measurement of swell behavior. The light frame consolidometer was tested in this study for apparatus compressibility and friction. When subjected to pressure a slight deformation was observed as shown in Figure 2.11.

Other factors like the compressibility of porous stones and filter paper were also studied in the present research. Correction factors for all the types of procedural elements responsible for the inaccurate swell prediction were presented. Figure 2.12 presents the variation of swell pressures from the corrected or actual swell pressures exhibited by the clay specimens at different depths. There appears to be considerable difference between the measured and corrected swell pressure values. Hence, the current research considers all these procedural errors in the measurement of swell pressure of a clay specimen.

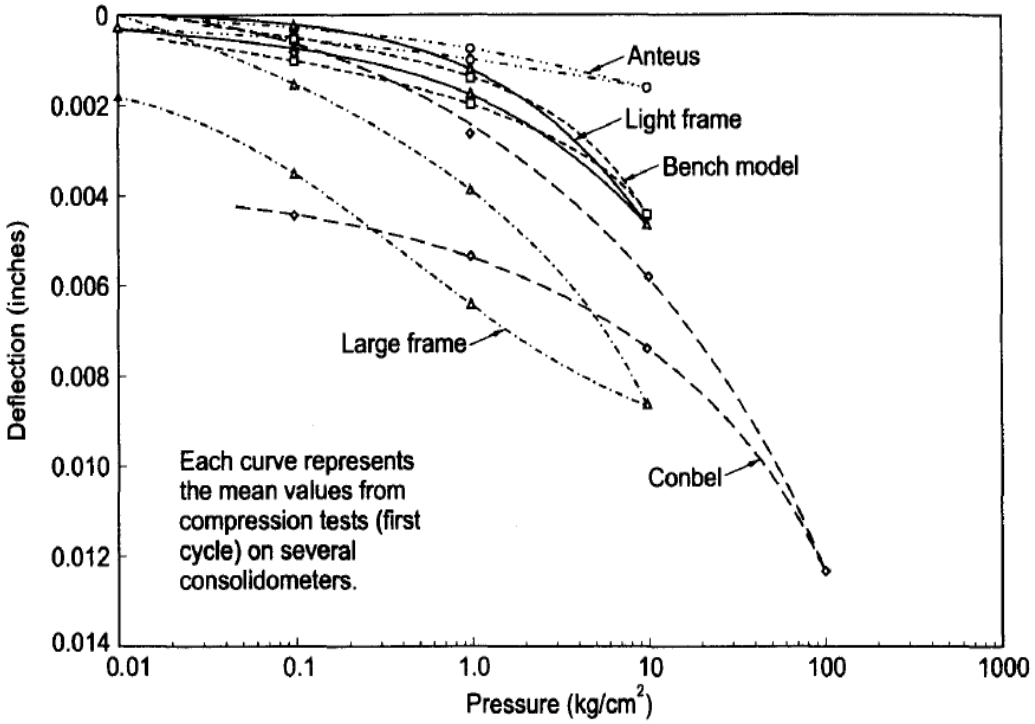

Figure 2.11: Light frame consolidometer deflection with pressure (Fredlund, 1969)

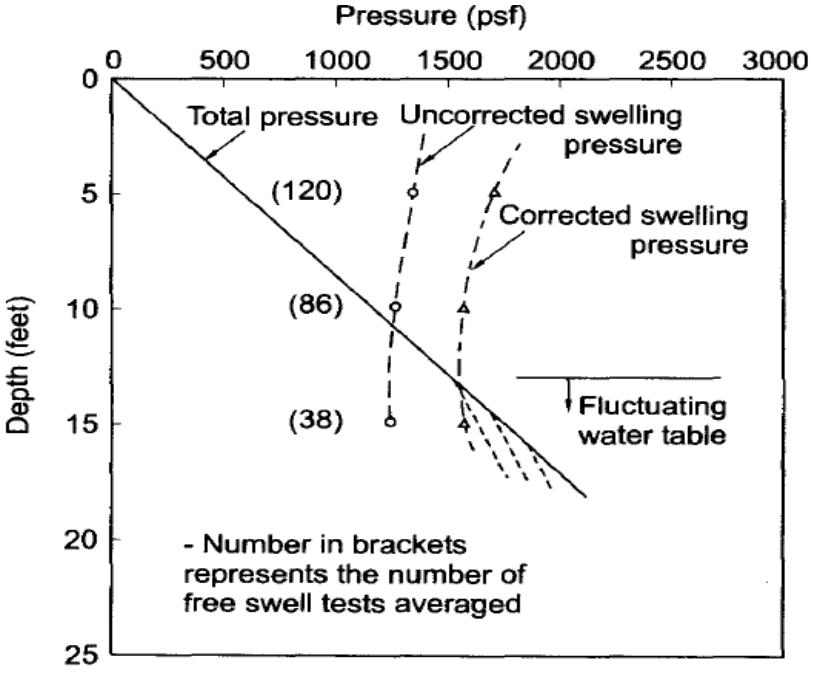

Figure 2.12: Difference between corrected and uncorrected swell pressure (Fredlund, 1969)

2.2.2.4 Lateral Swell pressure

Damage to structures caused by lateral swell pressures is well documented. Kassif, Zeitlen and Komornik (1961) discussed field observations of damage to pipelines buried in expansive clays. They found inequalities in the lateral and vertical swelling behavior resulted in very large stresses on the pipelines. Total lateral pressure, acting on a retaining structure which is built within expansive soil, consists of lateral earth pressure, surcharge pressure and lateral swell pressure. During swelling, clay exhibits anisotropic behavior, and the lateral swell pressure may exceed the vertical pressure.

In a research conducted by Ofer and Komornik (1983), two instruments for the determination of lateral swell pressure have been designed and tested. Both instruments showed similar test results under same test conditions. Based on the test results, It was concluded that a change in moisture content from maximum density resulted in a decrease in lateral swell pressure. Also, it shows that the compaction and sampling methods showed no effect on the lateral swell pressure.

Wattanasanticharoen (2004) devised a novel swell pressure set up to measure both vertical and lateral pressures of a soil specimen. The pressure regulator is used to apply the lateral pressure to the soil as shown in Figure 2.14. A K_0 value of 0.5 was used in the present research. The sample is allowed to swell in the vertical direction, henceforth the vertical axis is the minor principal stress and the lateral is the major principal stress. Below shown Figures 2.13 and 2.14 shows the swell test apparatus used by Wattanasanthicharoen (2004).

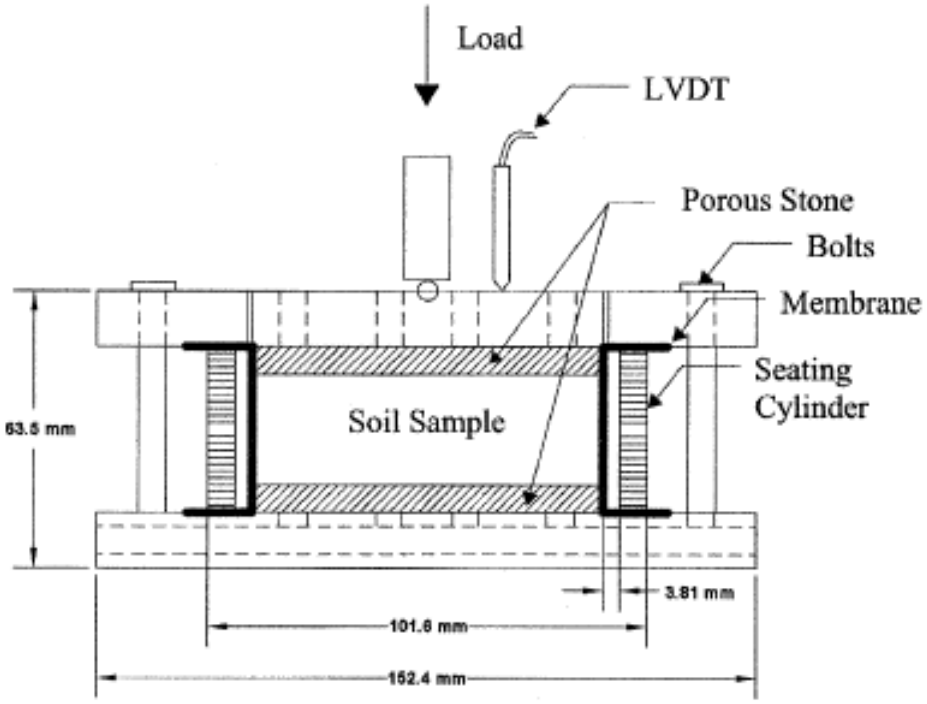

Figure 2.13: Modified Swell Pressure Setup (Wattanasanthicharoen, 2004)

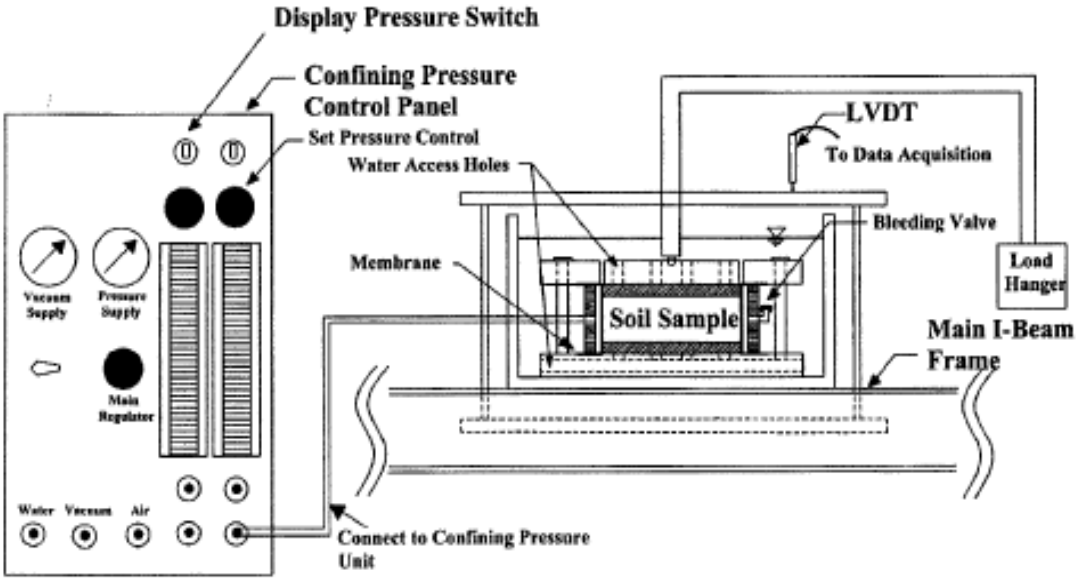

Figure 2.14: Lateral swell pressure test setup (Wattanasanthicharoen, 2004)

The sample was inundated with water after the initial stresses were applied to the soil specimen. The swell readings were monitored using dial gauges positioned on top of the setup.

Avsar et al. (2009) conducted a comprehensive swell pressure study on the Ankara clay to determine the swelling parameters for both vertical and lateral directions. The ratio between the swell pressures in lateral and vertical directions was found to be 0.34 to 0.98. Micro structural investigations performed on the clay revealed that the clay minerals were aligned horizontally. Vertical swell is defined as swell perpendicular to sheeting direction, which explains why the vertical swell pressure is more than the lateral.

The thin wall oedometer used for the determination of lateral and vertical swell pressures by Avsar et al (2009) is as shown in Figure 2.15 below.

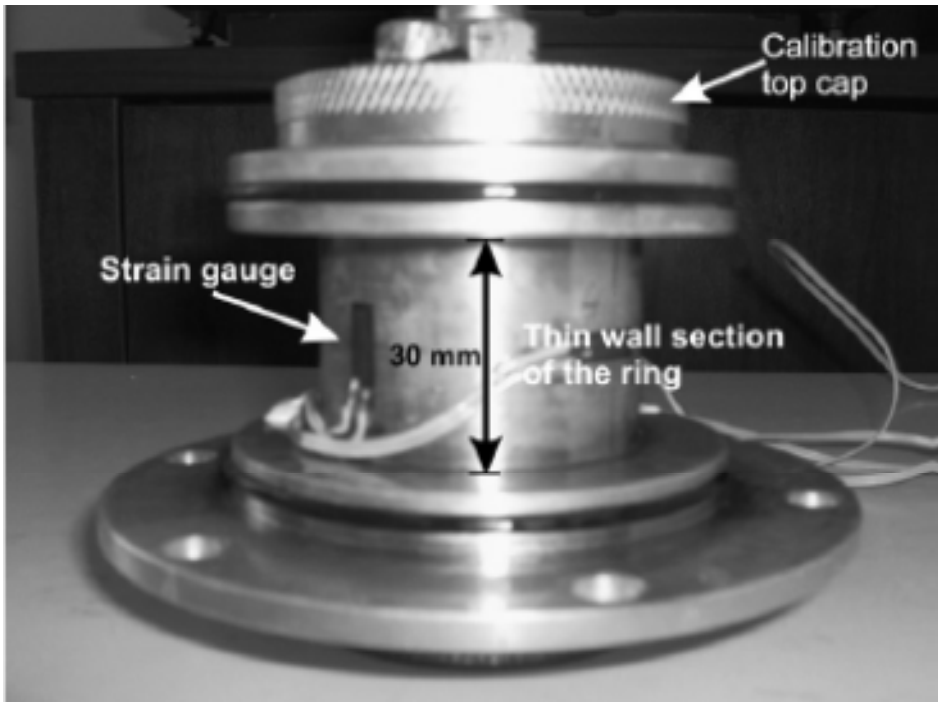

Figure 2.15: Thin wall oedometer ring (Avsar et al.,2009)

Figure 2.16 shows the variation of horizontal and vertical swell pressures measured by the thin wall oedometer.

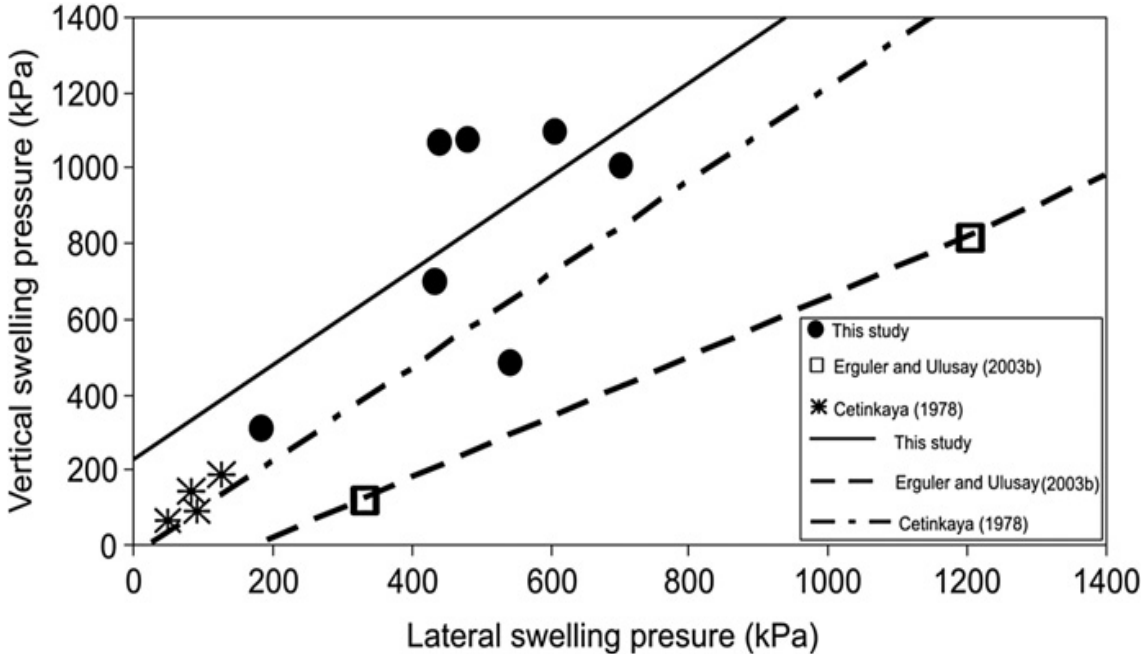

Figure 2.16: Lateral swell pressure versus vertical swell pressure of Ankara clay (Avsar et al, 2009)

Problems associated with differential movements from swell, can be expected for lightly loaded structures, including residential building foundations constructed on expansive soils. These infrastructure failures explain the need for better swell related characterization and determination of swell properties of expansive subsoil and backfills.

This chapter also discusses a comprehensive study on the major factors influencing the swell potential. The following sections presents the previous studies conducted on these factors.

2.3 Clay Mineralogy

Mineralogy of a soil controls its size, shape, physical and chemical properties. Based on the mineralogy, the particle size of soil varies from very large cobbles and gravel to very fine silts and clays (Mitchell and Soga, 2005). The common clay minerals usually found in soils are Kaolinite, Illite and Montmorillonite. Kaolinite is a common phyllosilicate mineral in subgrades and is most abundant in soils of warm moist climates. In nature clayey soils exists with different

clay mineral compositions which in turn show variation in these soils with respect to how they behave.

Clay minerals in soils belong to a family known as phyllosilicates or layered silicates. Clay minerals occur in small particle sizes and their unit cells ordinarily have a residual negative charge. The different clay mineral groups are characterized by the stacking arrangements of alumina and silica sheets (Mitchell and Soga, 2005). Clay minerals contain continuous two-dimensional tetrahedral sheets of composition Si_2O_5, Al_2O_5 and Be_2O_5. The tetrahedral sheets are linked in the unit structure to octahedral sheets, or to groups of coordinated cations, or individual cations (Bailey, 1980). Figure 2.17 presents different types of minerals and their structures.

The bonds between layers are weak, allowing water and other molecules to enter between the layers causing expansion (Grim, 1953). These minerals are in small size and are concentrated in the fine clay fraction of soils. The alkaline environment and lack of leaching favor the formation of Montmorillonite (Smectite group) minerals in the soils (Abduljauwad, 1993). Some soils exhibit same characteristics but different mineralogical contents which in turn lead to behavior differences (Teresa et.al 2004).

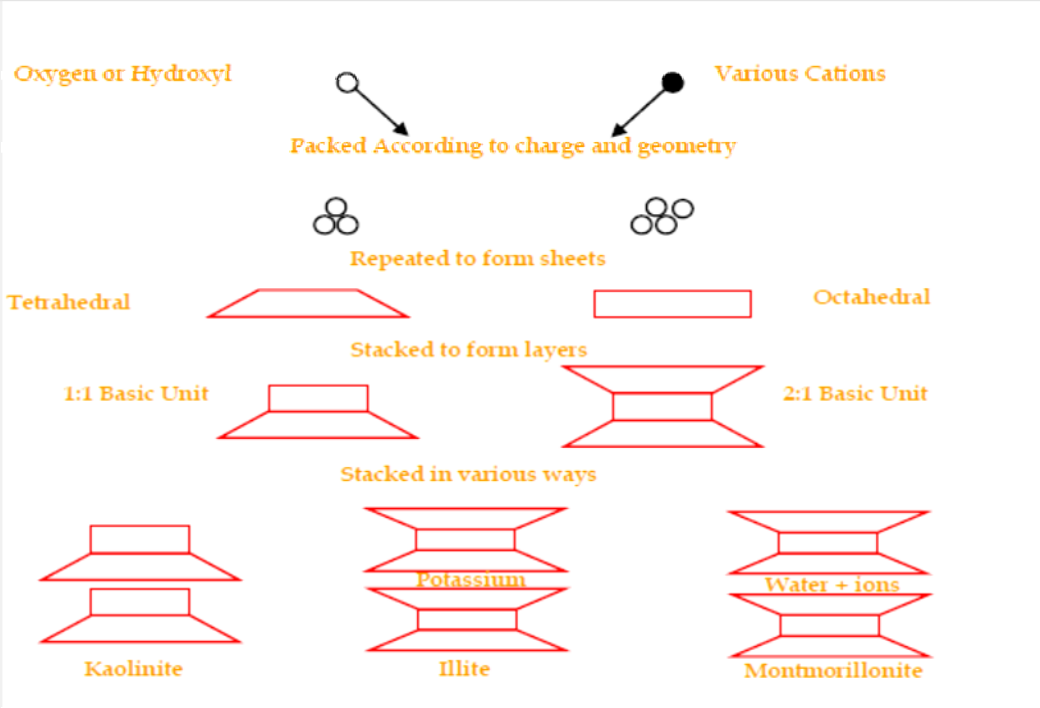

Figure 2.17: Figure showing the mineral structures of dominant clay minerals (Chittoori, 2008)

The identification of any clay mineral is indirectly detected by tests such as cation exchange capacity (CEC), specific surface area (SSA) and total potassium (TP). CEC is the quantity of exchangeable cations required to balance the negative charge on the clay particle surfaces. CEC is expressed in milliequivalents per 100 gms of dry soil. High values of CEC indicate a high surface activity, which is possible by the presence of highly active minerals like Montmorillonite. Henceforth, Quantification of the clay minerals was obtained with the help of properties such as CEC, SSA and TP is more reliable. In a research conducted by Chittoori and Puppala (2011) the soil mineral percentages were identified based on the measurement of these properties. Measurements were later used to develop ANN models to quantify and identify the dominant clay minerals in the fine fraction of the soil. Details of the identification methods are explained clearly in the next chapter.

2.3.1 Montmorillonite

Montmorillonite is a member belonging to the Smectite group which includes other dioctahedral minerals such as Beidellite, and Nontronite, and the trioctahedral minerals Hectorite (Li-rich), Saponite (Mg-rich), and Sauconite (Zn-rich). Smectites commonly result from the weathering of basic rocks. Smectites are known for their capacity to absorb large quantities of water and decrease the strength of the soil. The negative charge of Smectites and their expansive nature cause them to be extremely reactive in soil environments. The basic structural unit is a layer consisting of two inward-pointing tetrahedral sheets with a central alumina octahedral sheet. Because of the small particle size and interlayer expansion, Montmorillonite has high specific surface area values ranging from 600 m2/g to 800 m2/g. The range of CEC values for smectites is given by Borchardt (1989) as 47 to 162 meq/g. The structure of mineral Montmorillonite is as shown in Figure 2.18.

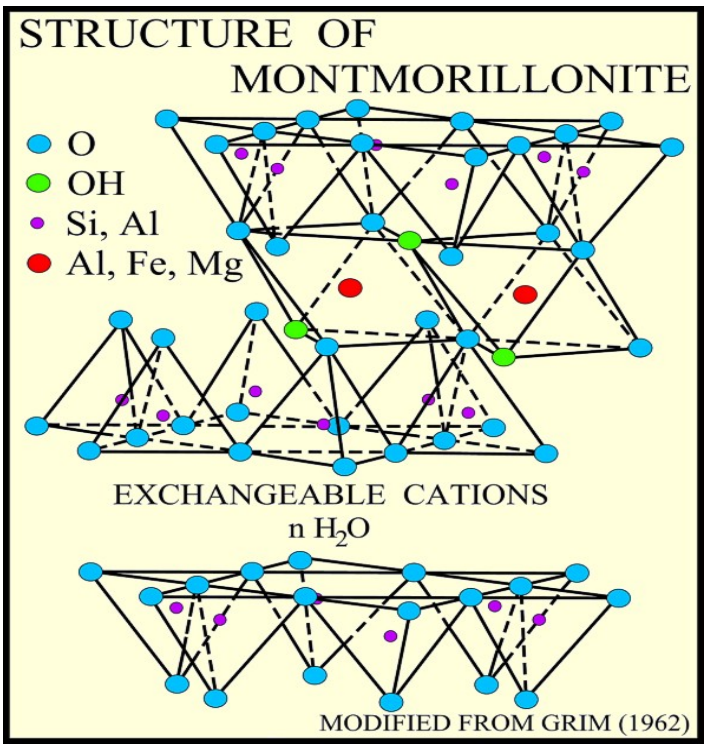

Figure 2.18: Structure of mineral Montmorillonite
(Source: http://pubs.usgs.gov/of/2001/of01-041/htmldocs/clays/smc.htm)

The scanning electron micrograph (SEM) of mineral Montmoillonite is shown in Figure 2.19 below.

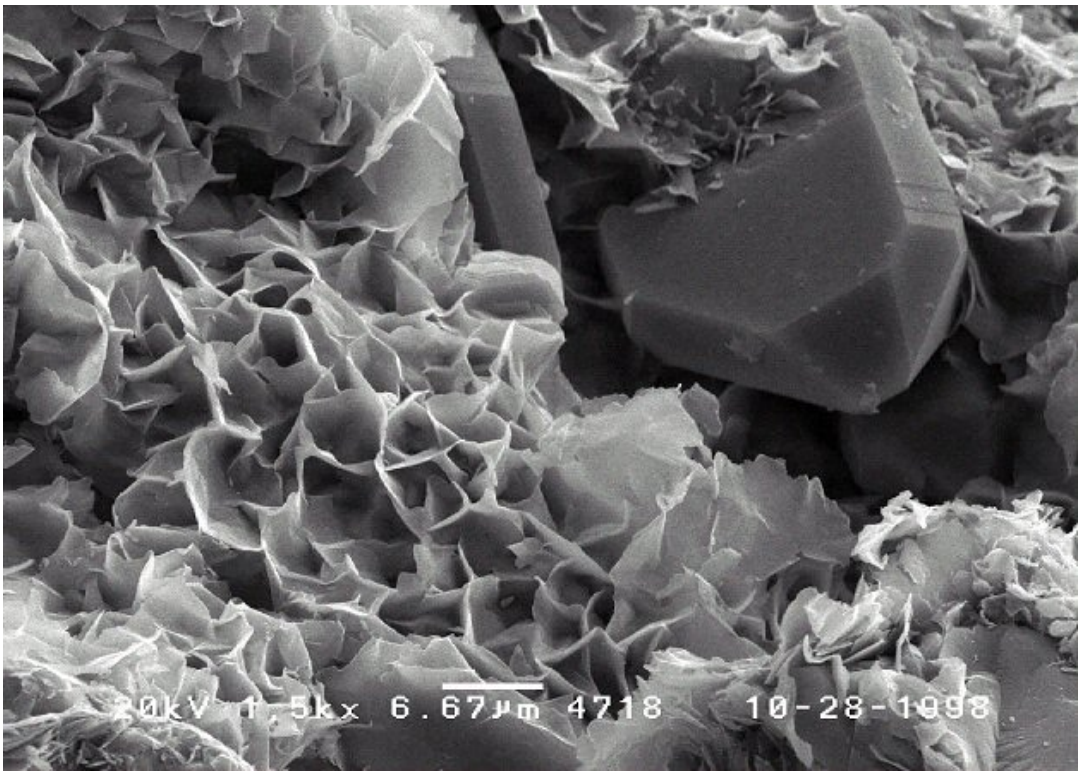

Figure 2.19: SEM picture of Mineral Montmorillonite
(Source: http://webmineral.com/specimens/picshow.php?id=1285&target=Montmorillonite)

The expansive behavior of the clays is mainly attributed due to the water absorption characteristic of highly expansive minerals like Montmorillonite (MM) (Mitchell and Soga, 2005).

Mollins et al. (1996) conducted one dimensional swell tests and hydraulic conductivity on compacted Na-bentonite mixtures. This study also presented an approach to determine the hydraulic conductivity of sand/bentonite mixture from basic parameters like bentonite content, sand porosity, tortuosity and vertical effective stress conditions.

2.3.2 Illite

Illite is essentially a group name for non-expanding, clay-sized, di-octahedral, mica minerals. It is structurally similar to muscovite in that its basic unit is a layer composed of two

inward-pointing silica tetragonal sheets with a central octahedral sheet. Figure 2.20 shows the mineral structure and scanning electron micrograph or SEM photograph of the mineral Illite. The weaker interlayer forces caused by fewer interlayer cations in Illite also allow for more variability in the manner of stacking (Grim, 1962).

Illites are the dominant clay minerals in argillaceous rocks and are formed by the weathering of silicates (primarily feldspar), through the alteration of other clay minerals, and during the degradation of muscovite.

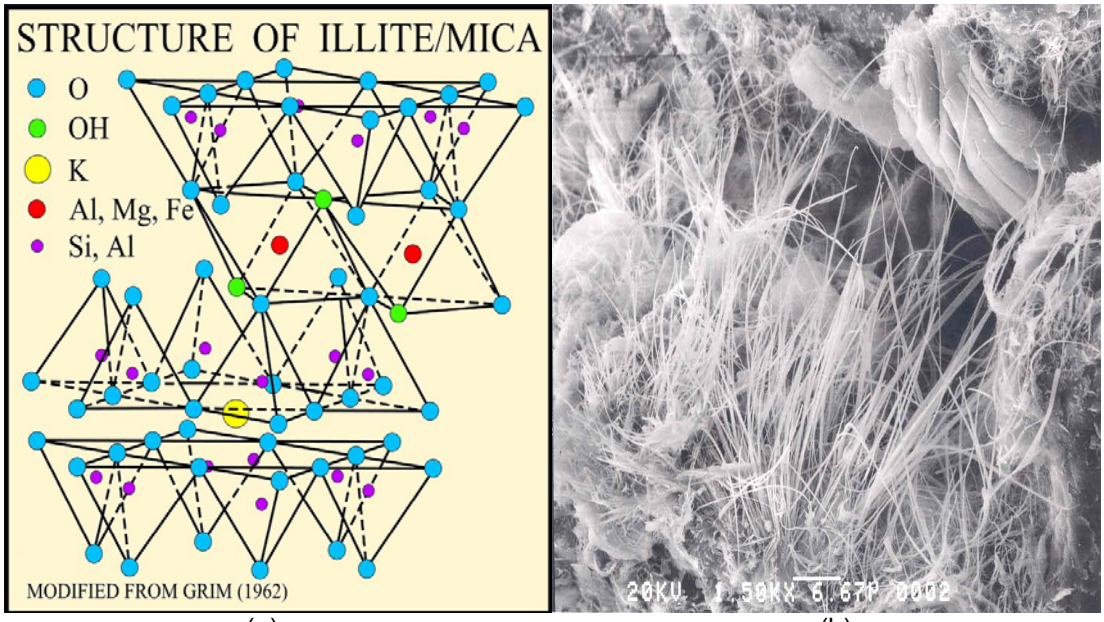

(a) (b)

Figure 2.20 : (a) Structure and (b) SEM of mineral Illite
(source: http://en.wikipedia.org/wiki/File:Illstruc.jpg)

Formation of Illite is generally favored by alkaline conditions and by high concentrations of Al and K. The number of inter particle contacts is less in micas and hence, the cohesive forces between the crystallites are weak (Thompson & Ukrainczyk, 2002). The degree to which Illite crystals contact adjacent grains is a function of soil water content as well as particle size, shape and flexibility.

2.3.3 Kaolinite

Kaolinite is a common phyllosilicate mineral in subgrades; it is most abundant in soils of warm moist climates (Mitchell and Soga, 2005). Kaolinite's structure is composed of alternate silicate sheets (Si2O5) and aluminum oxide/hydroxide sheets ($Al_2(OH)_4$) called gibbsite sheets. The silicate and gibbsite layers are tightly bonded together with only weak bonding existing between these silicate/gibbsite paired layers (called s-g layers) (Mitchell and Soga, 2005). The weak bonds between these s-g layers cause the cleavage and softness of this mineral. The structure is very similar to the Serpentine Group and at times the two groups are combined into a Kaolinite-serpentine Group (Figure 2.21). These minerals are also called as 1:1 minerals. Kaolinite shares the same chemistry as the minerals Halloysite, dickite and nacrite. The four minerals are polymorphs; meaning they have the same chemistry, but different structures. All four minerals form from the weathering of aluminum rich silicate minerals such as feldspars. Kaolinite is by far the most common clay mineral found in any clay (Mitchell and Soga, 2005).

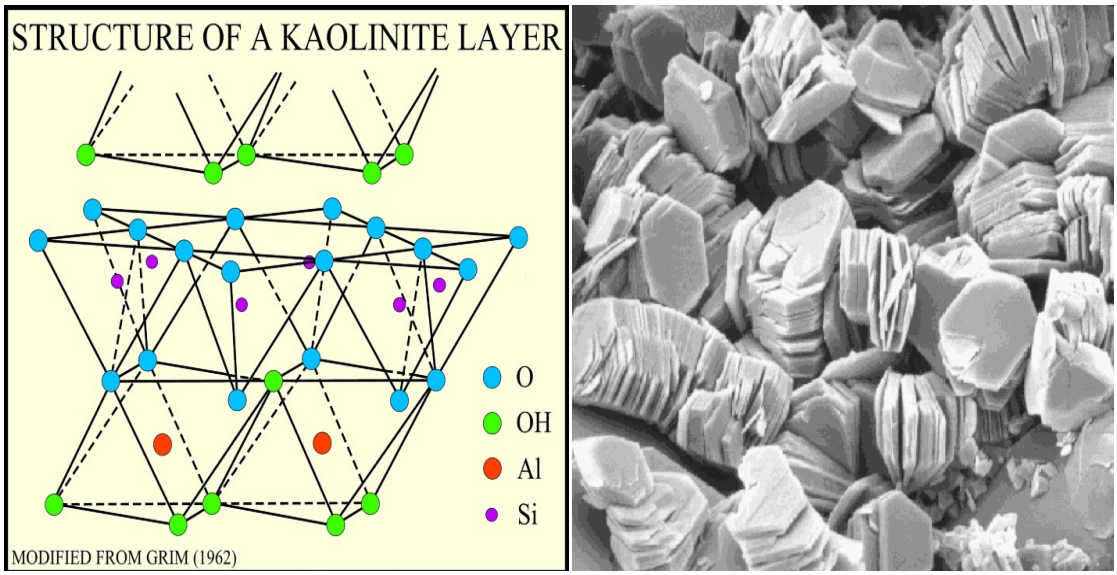

(a) (b)

Figure 2.21 : (a) Structure and (b) SEM picture of mineral Kaolinte
(Source: http://www.uni-kiel.de/anorg/lagaly/group/jose/Kaolinite.gif)

2.4 Soil suction relationships and unsaturated heave prediction methodologies

2.4.1 Introduction to soil-suction relationship

The variation of water or moisture affinity for a soil is better represented by soil water characteristic curves (SWCC). The soil water characteristic curve (SWCC) defines the relationship between the water content and suction for a soil. The shape of the SWCC curve depends on the soil type, density, soil state, pore size distribution, presence of salt concentrations, temperature, etc.

Total suction is divided into two components, matric suction and solute suction or osmotic suction. Matric suction is calculated in terms of difference in water and air pressures, and the radius of the curvature and the osmotic suction reflects the effect of dissolved salts in the pore fluid. The suction corresponding to the sudden drop in the curve is referred to as air entry value (ψa) as shown in Figure 2.22.

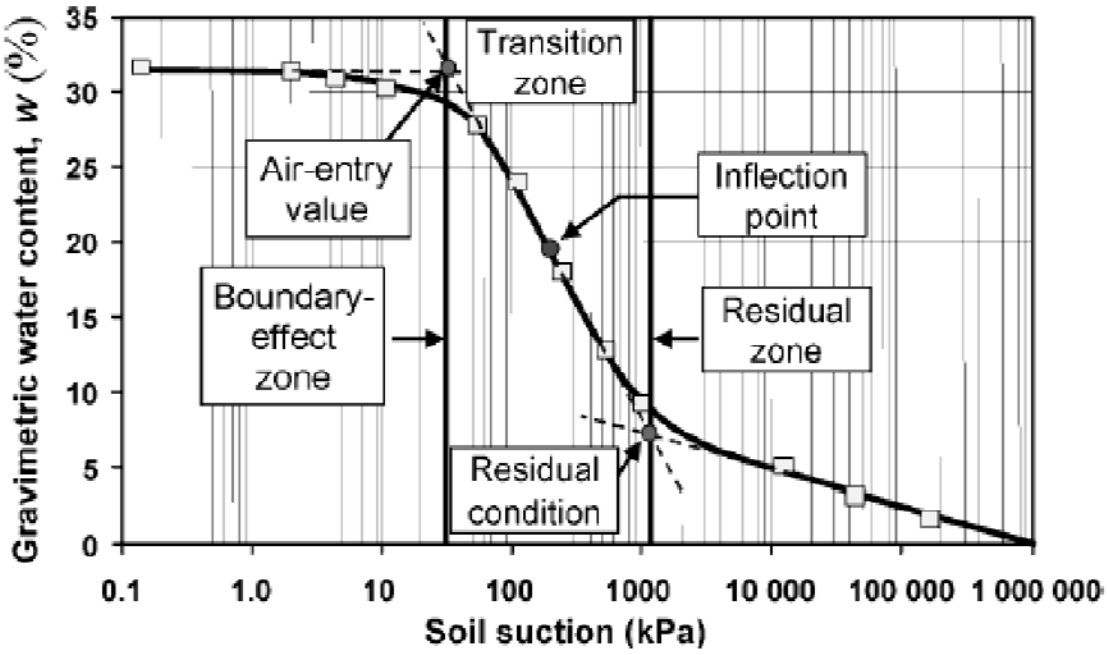

Figure 2.22: Soil water characteristic curve (Fredlund and Houston, 2009)

The water content corresponding to the bend in the curve at low degrees of saturation is known as the residual water content (Θr). Both these parameters define the shape of the curve along with the type of soil. Soils with more micro pores have high ψa. Soils with very large

pore sizes exhibit greater changes in water content with low suction levels. (Fredlund and Rahardjo 1993). This clearly explains that the shape and characteristics of the SWCC are greatly influenced by the pore size distribution of the soil. As a result, the SWCC is hysteric; that is, for a given water content, higher suctions exist for desorption (drying) than sorption (wetting) as shown in Figure 2.23. Hysteresis is caused by size differences between the primary pores and the interconnecting pore throats, changes in the contact angle during wetting and drying, and trapped air (Fredlund and Rahardjo 1993). Hence, due to hysteresis effects, desorption and sorption curves do not coincide. Different laboratory methods, such as pressure plate apparatus, psychrometer method, dew point potentiometer and filter paper technique are available to measure components of total suction, matric suction, and osmotic suction to develop the SWCC relationship.

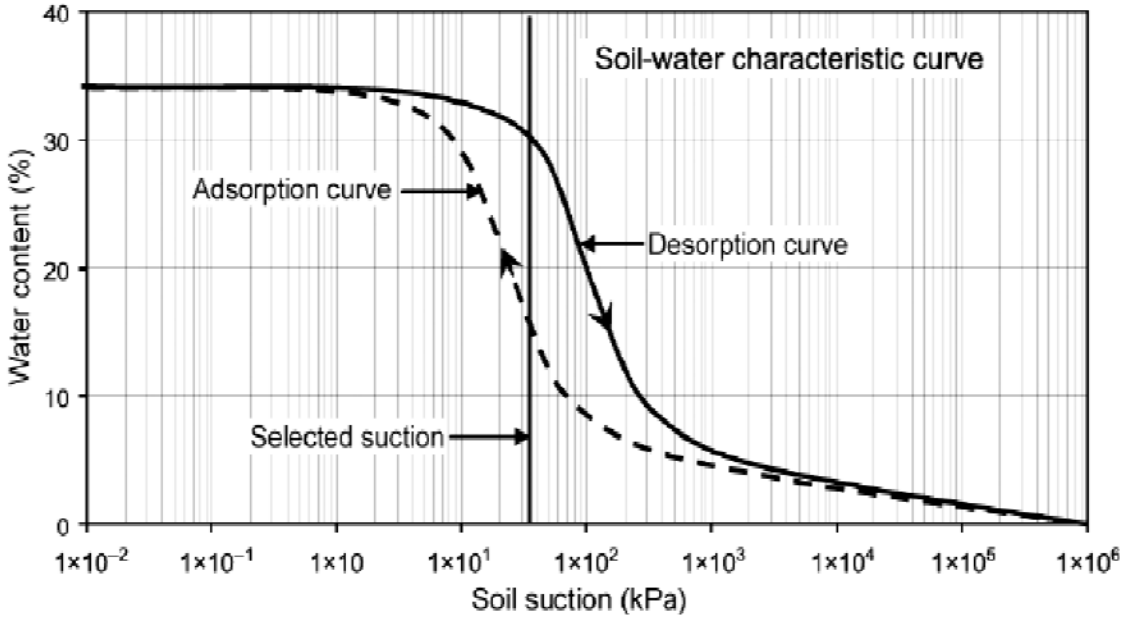

Figure 2.23: Adsorption and desorption curves (Fredlund and Houston, 2009)

2.4.2 Measurement of SWCC:

There are many methods for the determination of SWCC of a soil. All the methods have a common equilibration time where the soils matric suction comes to equilibrium to the

measuring media. Below given are some of the measurement techniques commonly used by researchers and engineers alike.

2.4.2.1 Filter paper method

The filter paper technique is based on the principle that the relative humidity inside the container will be controlled by the soil water content and suction. The filter paper will absorb moisture until it comes into equilibrium with the relative humidity inside the container for non-contact technique and soil water content for contact technique. After equilibrium has been reached between the filer paper, and the relative humidity in the container, the suction in the filter paper is measured from its absorbed moisture content. The humidity in non-contact case is influenced by both the osmotic and matric components of the soil suction (Fredlund and Rahardjo, 1993). This technique is used to measure both total and matric suction for a soil specimen.

Ash-free filter papers exhibit a consistent and predictable relationship between water content and suction (Nelson and Miller, 1992). Agricultural scientists were the first to use filter papers as indirect soil suction sensors. Filter paper method has been used routinely by the Water Resources Division of the U.S. Geological Survey (USGS) for many years (Nelson and Miller, 1992). The filter paper method can be used over a wide range of suctions up to approximately 150,000 psi. It has been used for a number of investigations of soil water relationships and it has been found to produce good results in field studies (Snethen and Johnson, 1980).

On the other hand, the equilibrium water content of the filter paper corresponds to the matric suction of the soil when the paper is placed in contact with the water in the soil (Fredlund and Rahardjo, 1993). Therefore, the same calibration curve is used for both the matric and total suction measurements (

Figure **2.24**).

Standard quantitative filter papers have a bilinear relationship between suction and water content. Calibrations have been determined for different papers, but the most commonly used paper is the Whatman 42, Schleicher and Schnell, No. 589, White Ribbon type, or its equivalent. The filter paper is by far the best measurement technique for the measurement of soil suction. The filter paper method was used as a calibration standard for all suction measurement devices.

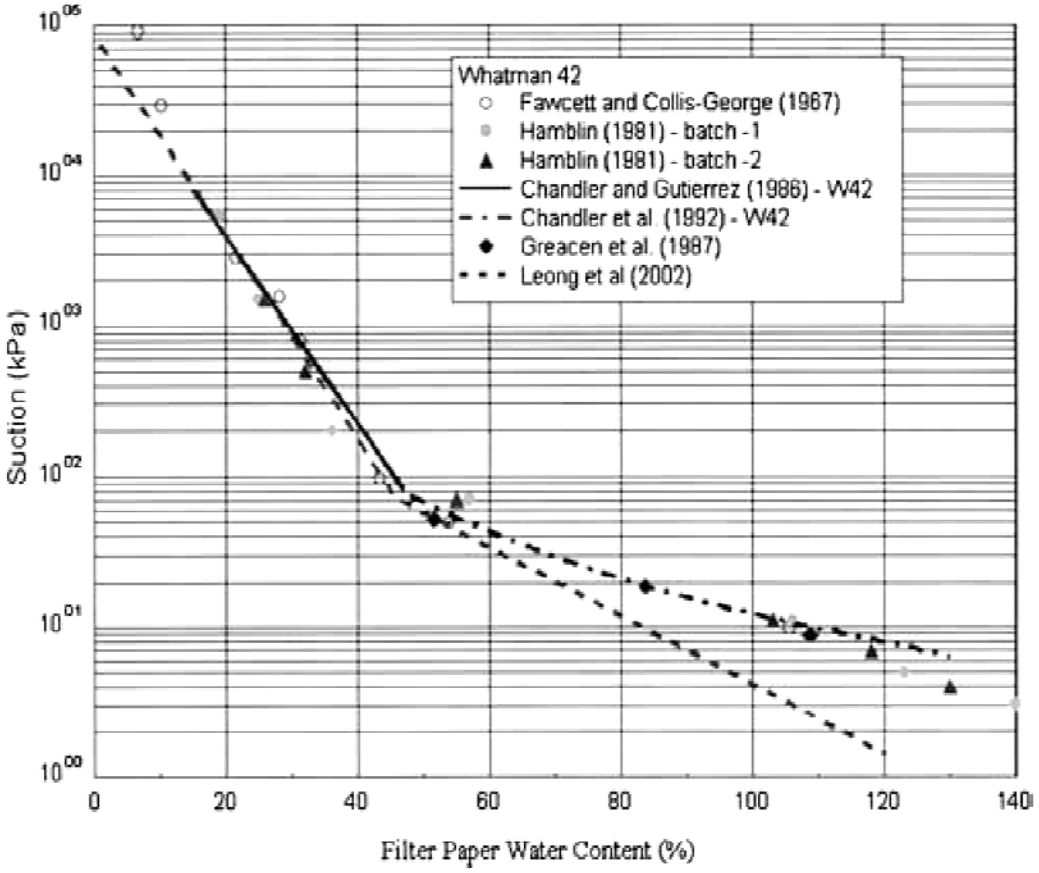

Figure 2.24: Calibration curve for Whatman 42 filter paper (Marinho and Oliveira, 2006)

2.4.2.2 Pressure cell apparatus:

Hilf (1956) proposed the technique called the Axis Translation, where the air pressure applied on to the soil specimen converted to the matric suction at equilibrium with the help of a

Air Entry disk. In the apparatus designed by Hilf, a saturated high air entry probe was inserted into the soil. The soil suction would draw water into the soil through the porous stone, where the water flow was monitored with the help of a null indicator. Air pressure increment was regulated when there is no more moisture flow into the soil. Figure 2.25 show the apparatus and measurement technique by Hilf. After Hilf, many other researchers conducted investigations where a modified pressure plate apparatus was used in measuring soil suction (Olson and Langfelder 1965, Fredlund 1989)

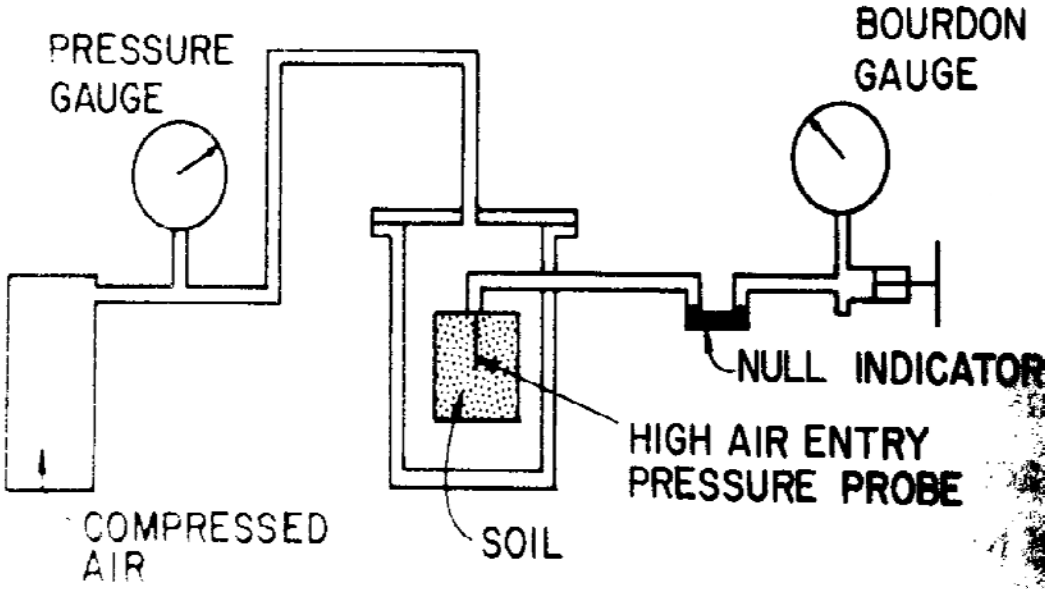

Figure 2.25: Hilf's apparatus for measuring soil suction (Hilf, 1956)

Lins and Schanz (2004) conducted soil suction studies on sand using the pressure cell apparatus. Figure 2.26 shows the wetting and drying curves of the sand obtained from this apparatus. The SWCC for sands was divided into three zones, the saturated zone, transition zone and residual zone.

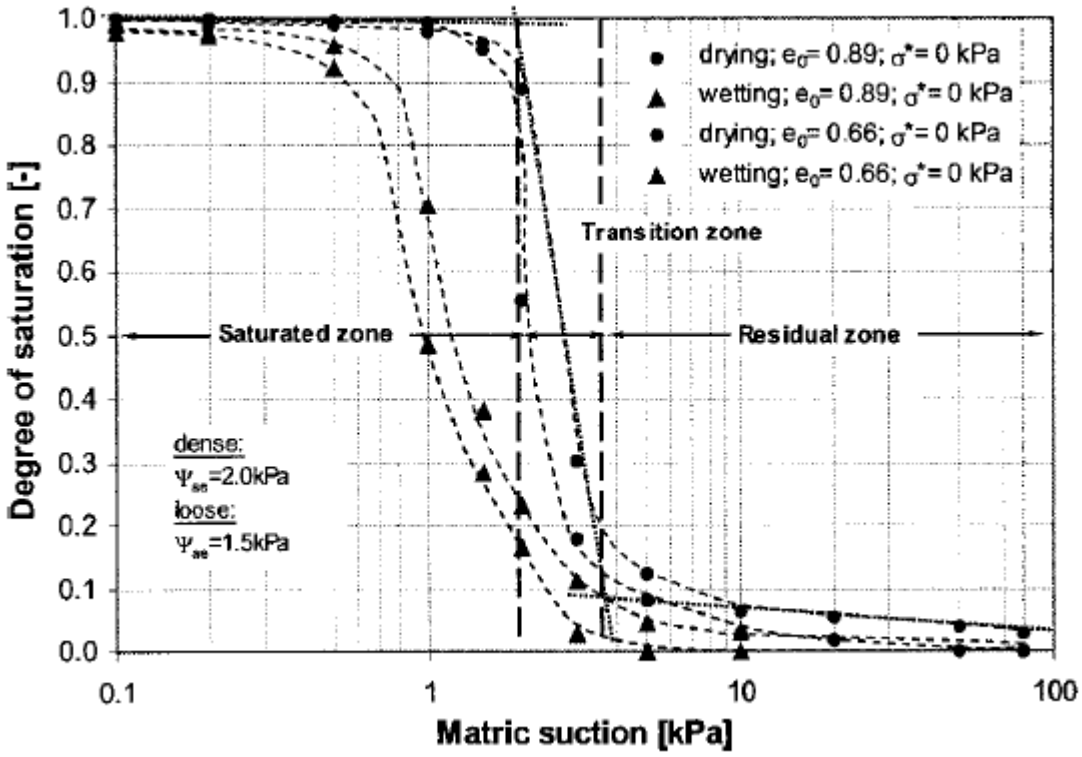

Figure 2.26: Drying and wetting curves for sand using pressure cell apparatus (Lins and Schanz, 2004)

The primary components of the modern pressure cell apparatus are a steel pressure vessel and a saturated High Air Entry (HAE) ceramic plate. As shown in Figure 2.25, the water reservoir is vented to the atmosphere through the two outflow tube located on the sides of the apparatus, thus allowing the air pressure in the vessel and the water to atmospheric. In general, specimens are initially saturated and placed on the high air entry value ceramic disk so that proper contact between the soil and disk is achieved. Air pressure in the vessel is then increased to some desired level while pore water is allowed to drain from the specimens in pursuit of equilibrium.

The outflow of water is monitored until it ceases. Then the water content of one or more of the specimen is measured from the outflow tubes, thus generating one point on the soil-water characteristic curve. Subsequent increments in air pressure are applied to generate addition points on the curve using the other specimen.

Fredlund (2006) conducted a study on the usefulness of pressure cell apparatus with volume changes as shown in Figure 2.27 and came up with the following conclusions. The ranges of suctions that can be applied are limited to 1500 kPa. The independent application of total stresses to the soil using the vertical loading arm is possible with this apparatus. Also, measurement of both water volume change and overall volume change of the specimen was easy. It was stated that the measured water collected from the specimen must be corrected for the diffused air volume.

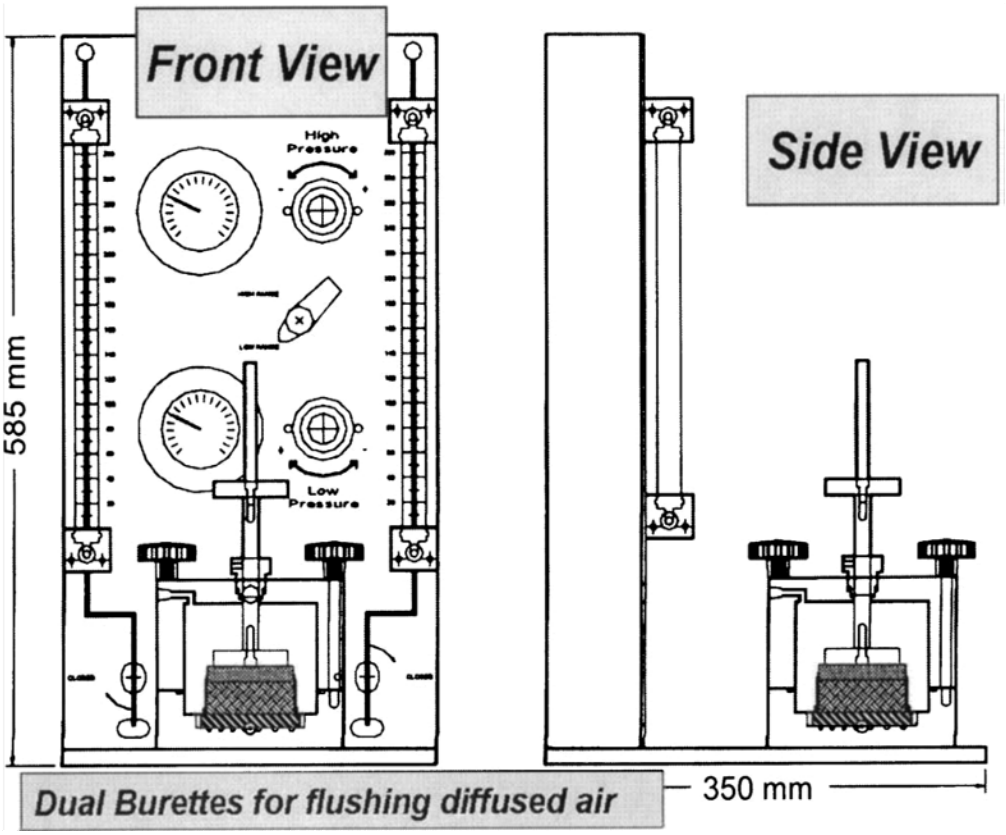

Figure 2.27: Pressure cell apparatus for the measurement of volume mass relationship (Fredlund, 2006)

2.4.2.3 Dew point potentiometer

The WP4C measures water potential by determining the relative humidity of the air above a sample in a closed chamber, using the principle of chilled-mirror technique (ASTM D 6836; Leong et al., 2003; Thakur and Singh, 2005). The WP4 consists of a sealed block

chamber in which the soil sample can be placed in a 15 cc sampling cup. The block chamber consists of a mirror; an optical sensor which is used to detect the dew formation on the mirror; a temperature sensor which measures the dew point temperature of the air; a thermopile to measure the temperature of the sample; and a fan, which enhances the equilibration of the sample with the chamber environment (Thakur and Singh, 2005)

Thakur et al. (2006), used Dewpoint Potentiameter to measure suction for two soils. The study showed that Van Genuchten (1980) fitting function is valid only under 20 MPa, whereas Brooks and Corey (1964) and Fredlund and Xing (1994) fitting functions showed good validity for high ranges of suction. Figure 2.28 shows the SWCC obtained from experimental data along with standard fitted models. The WP4 device also showed a good repeatability in the test results (Thakur et al, 2006).

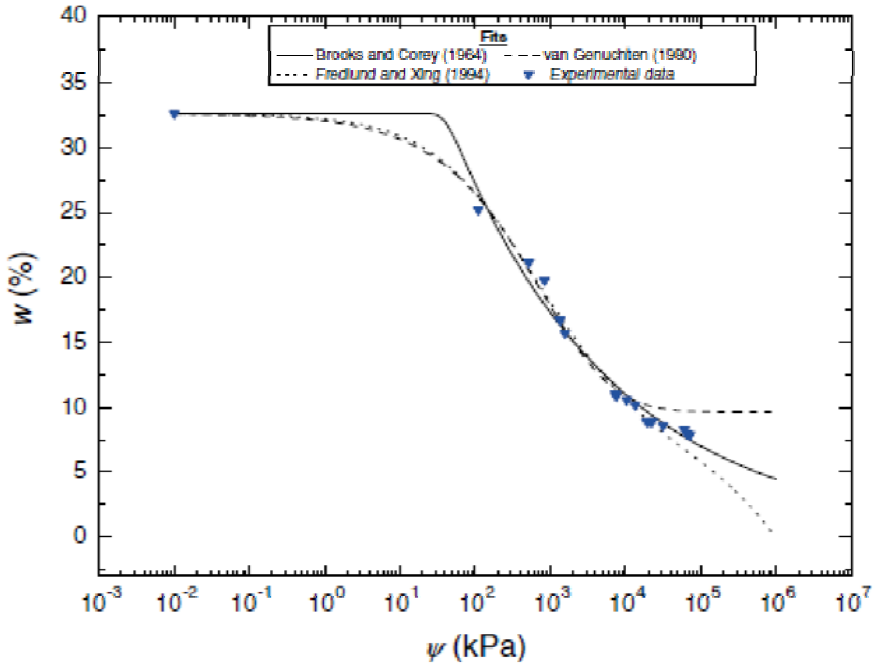

Figure 2.28: SWCC obtained from WP4 and compared with standard fits (Thakur et al, 2006)

In another research conducted by Petry and Jiang (2007) used the WP4 device for quick and cost effective measurement of SWCC. Soil suction parameters were used in this

research to predict the volume change behavior of 3 expansive clays. It was concluded that the WP4 Potentiameter provided measurements on the more conservative side. Figure 2.29 shows the filter paper method measurements (red) versus the WP4C measurements (black). This method of measurement is highly recommended due to the time and cost effective when compared to standard filter paper method.

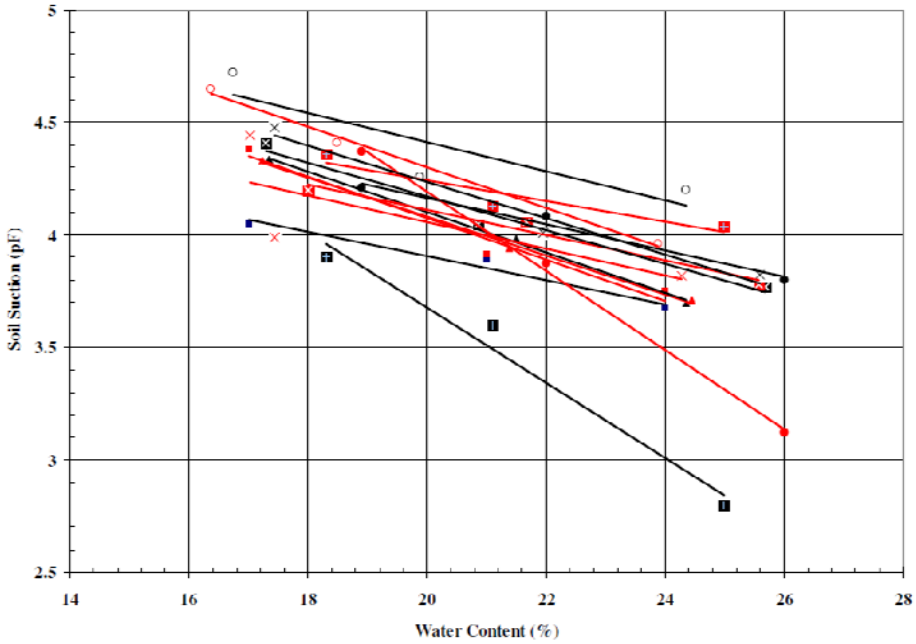

Figure 2.29: Filter paper method vs WP4C measurement (Petry and Jiang,2007)

2.4.2.4 Measurement Methods overview

Psychrometers are less sensitive in the low suction ranges and require frequent recalibration as they are sensitive to temperature of surrounding. Filter paper measurements are difficult to automate while the tensiometers function well in the low suction range but require daily maintenance. Pressure plate apparatus or Tempe cell are restricted to measure matric suction only of a certain range due to the High Air Entry value disks. Thermal conductivity sensors are used for a lower suction range and need regular calibration.

A list of suction measurement methods, the component of soil suction measured, valid ranges, and constraints associated with these methods are presented in Table 2.4. As reflected in the table, each method has its own limitations.

Table 2.4: Total and Matric suction determination methods (Rahardjo and Leong 2006, Lu and Likos 2004)

Device	Suction type	Range (kPa)	Constraint
Tensiometer	Matric	0 to 90	Daily maintenance, low range
Thermister Psychrometers	Total	100 to 10,000	Poor sensitivity in low suction range
Transistor Psychrometers	Total	200 to 18,000	Affected by environmental conditions
Thermocouple Psychrometers	Total	100 to 7,500	Sensitivity deteriorates with time
Thermal conductivity sensors	Matric	0 to 6000	Sensitivity deteriorates with time
Filter Paper (non-contact)	Total	400 to 30,000	Sensitive to equilibration time
Filter Paper (Contact)	Matric	0 to 100,000	Automation is difficult
Dewpoint Potentiameter	Total	100 to 100,000	Require regular calibration
Pressure Plate	Matric	0 to 1500	Long equilibration time for clays

2.4.3 *Interpretation of SWCC:*

Several soil suction measurement devices have been used for establishing the SWCC. The determination of SWCC is often time consuming and strenuous depending on the type of soil. Many researchers have also attempted to model and interpret the swccs measured and the three most established SWCC models are given in Table 2.5.

Table 2.5: Widely used SWCC models used in literature (Lu and Likos, 2004)

	Model	Parameters
Brooks and Corey (1966)	$\theta = \left(\frac{\psi_a}{\psi}\right)^{\lambda}$ where $\psi \geq \psi_a$	ψ_a – air entry suction λ – pore size distribution index
Van Genuchten (1980)	$\theta = \left(\frac{1}{(1+(a\psi)^n)}\right)^m$	a, n and m – soil parameters $m = 1 - \frac{1}{n}$
Fredlund and Xing (1994)	$\theta = \theta_r + \frac{\theta_s - \theta_r}{\left(\ln\left(e + \left(\frac{\psi}{a}\right)^n\right)\right)^m}$	a_1, n_1 and m_1 – soil parameters Θ_s – saturated water content Θ_r – residual water content

2.4.4 *Unsaturated Volume change relationships*

Many researchers have proposed vertical movement prediction models for expansive soils and a few of them are those developed by researchers like Fredlund and Morgenstern (1976), Snethen (1979), etc. In this research, revisit of these models and their predictions of heave movements of soils based on laboratory tests are presented. Other evaluations are attempted with heave movements in real subgrades, which are already obtained in this study.

Budge et al. (1966) used one-dimensional consolidometer test to determine the swell characteristics of an expansive subgrade soil. This method was specifically applied to stiff and fissured clay shale subgrades. In their research, new sampling equipment that contained a series of liners was designed to enable the test specimens remain confined in linear rings. These specimens were used in the swell potential determination.

In a research conducted by Fredlund and Morgenstern (1976), the volume change constitutive relations for expansive soils are proposed from a semi empirical model. Two

equations were proposed for volume change, Eq. 1 is used for deformation of soil structure and a Eq. 2 for the volume of water present in the soil.

$$\epsilon = \frac{1}{v} * \frac{\partial v}{\partial(\sigma - u_a)} * d(\sigma - u_a) + \frac{1}{v} * \frac{\partial v}{\partial(u_a - u_w)} * d(u_a - u_w) \quad (1)$$

$$\theta_w = \frac{1}{v} * \frac{\partial v}{\partial(\sigma - u_a)} * d(\sigma - u_a) + \frac{1}{v} * \frac{\partial v}{\partial(u_a - u_w)} * d(u_a - u_w) \quad (2)$$

Where ∂v is the differential change in volume, σ is the vertical pressure, u_a is the pore air pressure and u_w is pore water pressure.

These constitutive equations were validated using the measured volume changes by the swell apparatus. Tests were performed on Regina Clay and compacted Kaolin clay. However compacted Kaolin clay showed relatively poor correlation between the predicted and measured volume changes. In this research, Lack of measurement of total volume change is observed as the air and water pressures are uncontrollable in the soil. The comparison between the predicted volume change and measured volume change are shown in Figure 2.30.

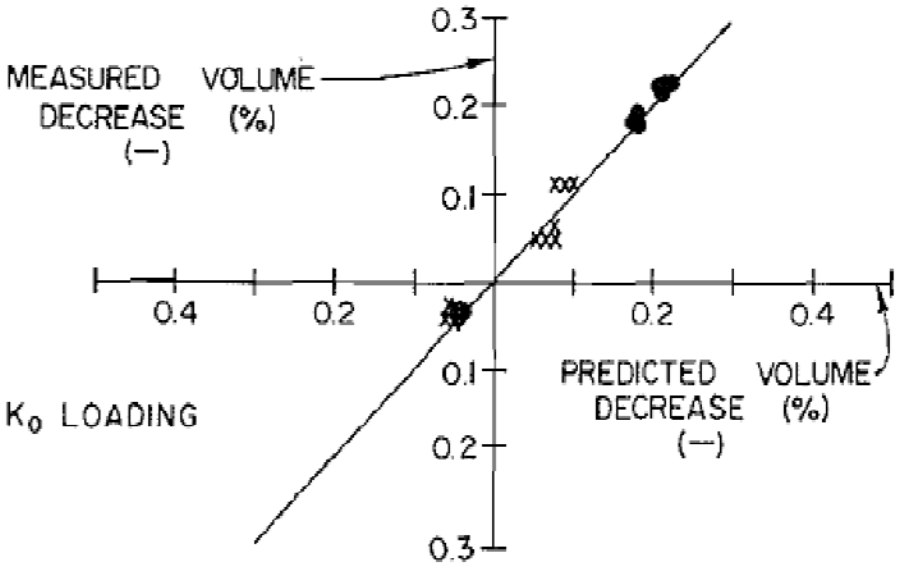

Figure 2.30: Predicted and measured volume change from Fredlund and Morgenstern (1976)

Snethen (1979) reported the following model, i.e Eq. 3 to estimate the vertical swell movement of an expansive soil. This model requires the use of soil matric suction as one of the parameters.

$$\frac{\Delta H}{H} = \frac{C_r\left[(A - Bw_o) - log\left(\tau_{mf} + \alpha\sigma_f\right)\right]}{1 + e_o} \quad (3)$$

Where

ΔH = vertical movement (ft.)

H = thickness of the layer (ft.)

e_o = initial void ratio

A, B = constants from matric suction vs water content relationship

w_o = initial moisture content (%)

τ_{mf} = final matric suction (kPa)

α = compressibility factor (slope of specific volume_*f* = final applied pressure (kPa)

C_r = suction index shown in Eq. 4 below

$$C_r = \frac{\alpha G_s}{100B} \quad (4)$$

B = slope of matric suction versus water content curve

Gs = specific gravity of soil.

The United States Army Engineers Waterways Experimental Station (USAEWES) came up with a classification of swell potential based on liquid limit, plastic limit and initial suction (O'Neill and Poorymoayed, 1980). Soil suction in the present study was measured using psychrometer. Table 2.6 presents the classification of swell potential based on these parameters.

Table 2.6: USAEWE classification of swell potential (O'Neill and Poorymoayed, 1980)

Liquid Limit	Plastic Limit	Initial suction (kPa)	Potential Swell (%)	Classification
< 50	<25	<145	<0.5	Low
50-60	25-35	145-385	0.5-1.5	Marginal
>60	>35	>385	>1.5	High

Berniner et al (1997) conducted suction controlled experiments on Bloom clay. The authors tried to validate the interpretive model developed by Alonso et al (1990), and to build a database of unsaturated clay thermo-mechanical parameters. The authors used a relative humidity apparatus for controlling the suction measurements in the oedometer. Swell pressure tests were conducted with oedometers under suction control. Vertical pressure was determined by keeping the sample deformation to zero. It was found that the swell pressure increases, reaches a maximum value and then decreases to and equilibrium due to relaxation effect. The relationship between suction and swell pressure is as shown in Figure 2.31. The swell pressures close to saturation remain in same range for different initial vertical stresses. It was also found that the suction controlled hydro mechanical tests validate the swelling collapse behavior model given by Alonso et al (1990).

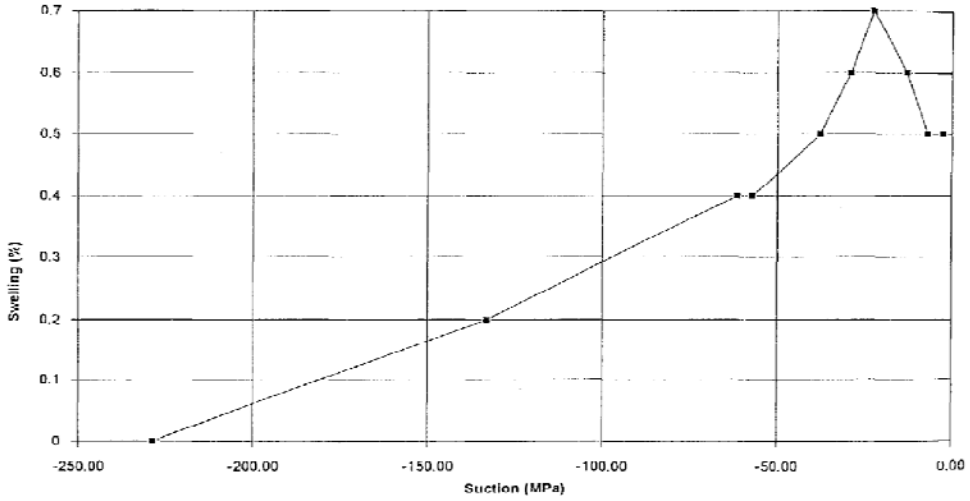

Figure 2.31: Soil suction and swelling variance for the bloom clay (Bernier et al, 1997)

Delage et al. (1998) studied the hydro mechanical behavior of highly compacted unsaturated clays. The variation of swelling properties with water retention for the clay under controlled suction was presented in this research. The dominant role played by the microstructural saturated level which is strongly affected by the physico-chemical interactions between water and the active clay mineral. The volume change with matric suction is shown in Figure 2.32.

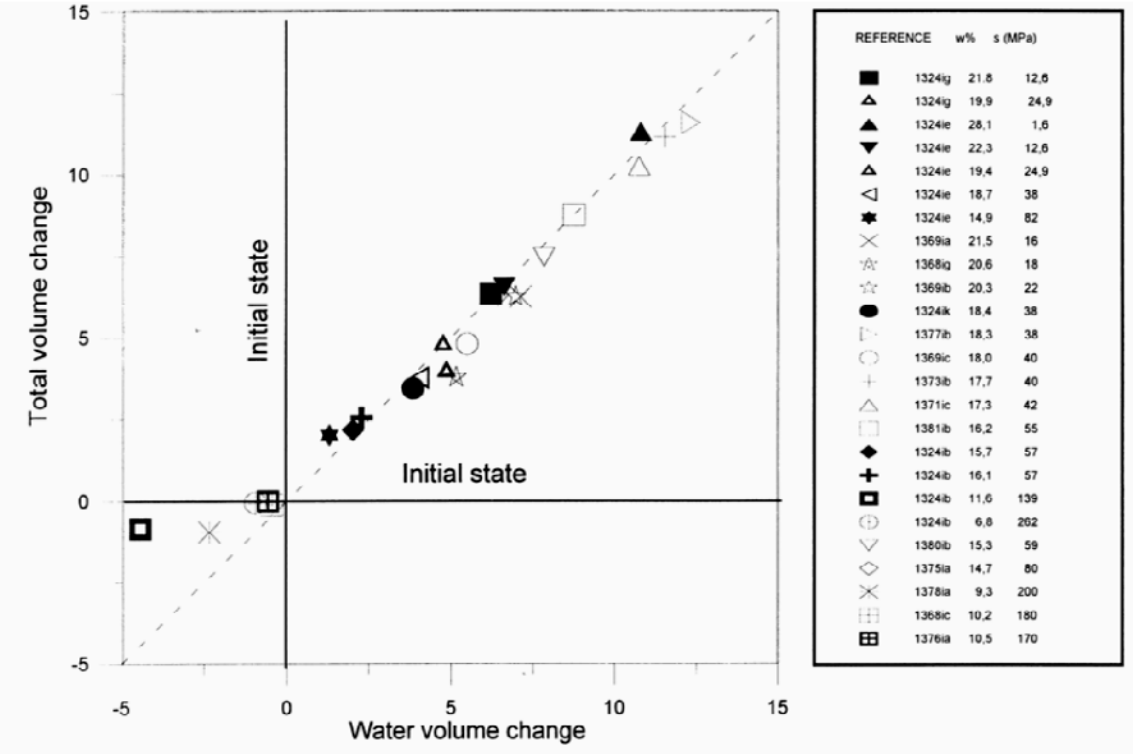

Figure 2.32: Volume change and suction variation (Delage et al.,1998)

Alonso et al. (1999) formulated a mathematical model to determine the behavior of expansive unsaturated clays. Two levels of structure, one at micro level and another at macro level were considered. It was found that the strain is dependent on the stress-suction path, accumulation of expansion strain during suction cycles at low confining stress, accumulation of compression strain, strain fatigue during wetting-drying cycles, macropore invasion by expanded microstructure.

Hussein (2001) derived a constitutive model to represent the visco-plastic behavior of an expansive soil upon wetting and drying. The model takes into account the current stress, water content and clay content as well as environmental factors. The time-dependent deformation and stress changes are associated with pore-water migration as well as the swelling and viscous nature of the material. Also it was concluded that the magnitudes of percent swell pressure are also influenced by other factors such as the following:

1. Compositional factors, which include the type and amount of clay mineral present in the soil as well as the pore fluid characteristics. Environmental factors, such as initial moisture content, initial density, initial degree of saturation, initial soil structure, stress history, availability and composition of ambient water and temperature

2. Procedural factors in laboratory testing like size and shape of soil sample, degree of disturbance and testing procedure and techniques used.

3. Climate, depth of active zone, location and thickness of the expansive soil layer, applied loads (weight of structure and soil overburden), vegetation, site topography, surface drainage and confinement.

In a research conducted by Saiyouri et al. (2004), compacted samples were hydrated by subjecting them to different suction pressures in a range between 0.14 psi (1 kPa) and 14,503 psi (100 MPa) and at each equilibrium state, the volume change (swelling) and water content (hydration) were measured. It was concluded that the differences in clay swelling are mainly due to the nature of the saturating cations (Na or Ca). This change in behavior seems to be a consequence of the very different texture between the clays as observed in other clays. It was also shown that swelling is essentially a subdivision of quasi-crystals and not a homogenous increase of interlayer distances. Quasi-crystal size, in relation to surface area, mainly determines the swelling properties. It was noted that, compaction also played an important role in restricting the swell behavior.

Alonso et al. (2005) used vapor equilibrium technique to study the features controlling soil behavior at different suction levels. Alonso et al. (2005) conducted studies on sand-bentonite mixtures and predicted the swelling behavior using an elasto plastic constitutive model, which uses a double structure approach. There is a reasonably good agreement between the model predictions and the volumetric deformations measured during the application of different suction cycles as shown in Figure 2.33.

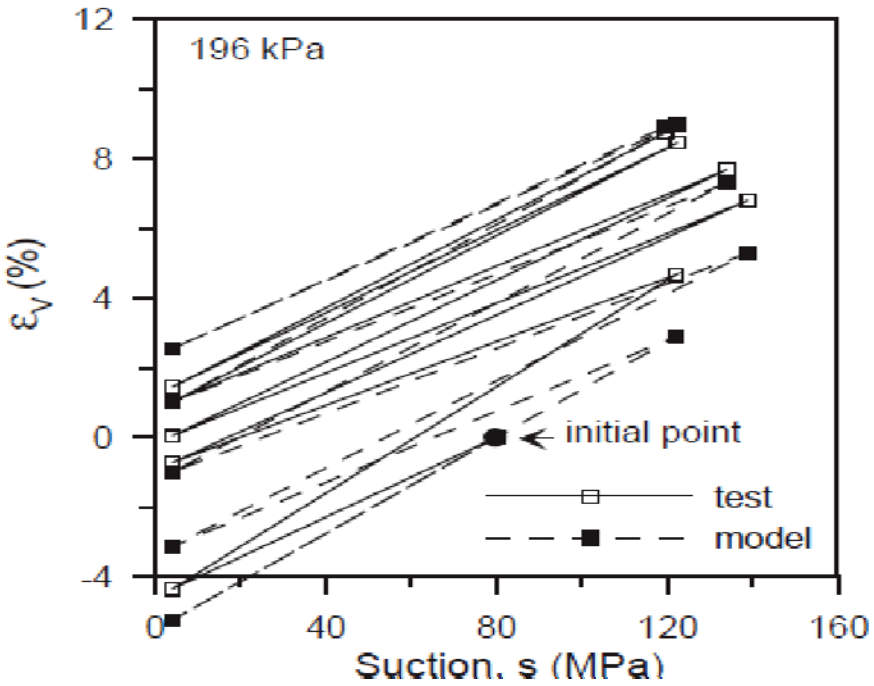

Figure 2.33: Volume change with suction (Alsonso, 2005)

It was found that the collapse tendency is compensated for by the expansion of the swelling microstructure, and the vertical stress reduces to maintain the constant volume condition from the yield point.

Yusuf and Erol (2007) used Na-bentonite to study the dependency of soil suction on water content, dry density and mineral content. Soil suction was correlated to the soil properties, namely, water content, plasticity index, dry density, cation exchange capacity and specific surface area using multiple regression analyses.

A linear relationship was established between the logarithm soil suction and the swell pressure. It was also found that an experimental relationship which would directly relate the initial soil suction to the swell pressure can be established. In order to investigate soil suction versus swell pressure behavior, the results of standard constant volume swell tests (ASTM, 1990) were used. Samples with initial water contents of 10, 15, 20, and 25% and having initial dry densities of 1.5, 1.6, 1.7, and 1.8 g/cm^3 in conventional oedometer cells, were tested and the results show a linear relationship between log suction and swell pressure as shown in Figure 2.34.

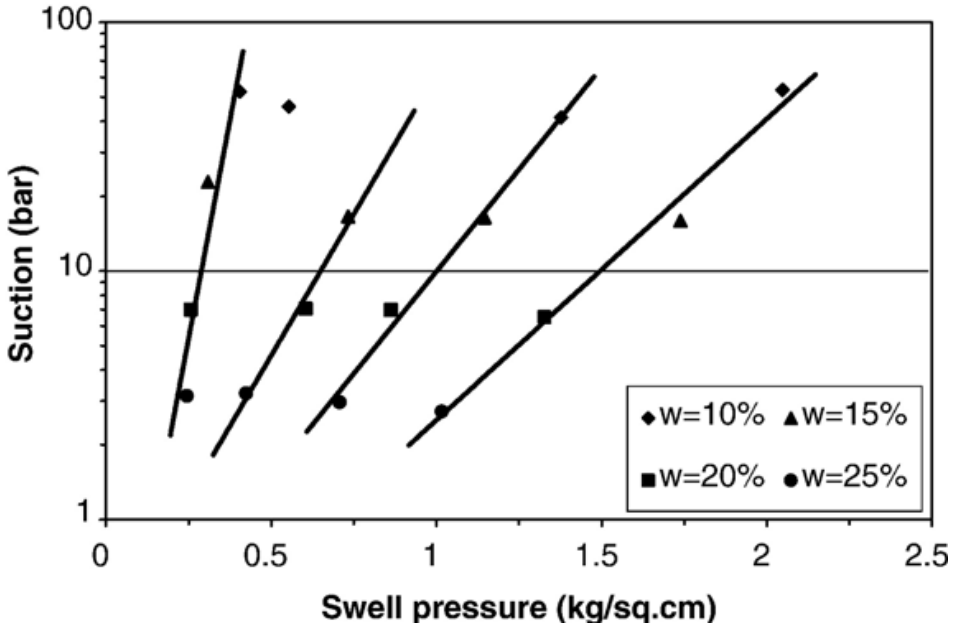

Figure 2.34: Swell pressure versus soil suction for clay mixture (Yusuf and Erol 2007)

Results confirmed the influence of mineralogical composition as a controlling factor governing the slope of the line for log suction versus swell pressure. Two swell pressure prediction models are developed by Yusuf and Erol (2007), using the previous experimental data. Below shown Eqns. 5 and 6 represent the swell pressure prediction models.

For 0 < Ps < 100 kPa

$$P_s = -3.72 + 0.0111\, I_p + 2.077\, \rho_{dry} + 0.244\, \log s \quad (5)$$

For 100 < Ps < 350 kPa

$$P_s = -16.31 + 0.0330\, I_p + 8.253\, \rho_{dry} + 0.829\, \log s \quad (6)$$

Where P_s is the swell pressure, I_v is index property, s is soil suction and ρ_{dry} is the soil dry density.

Below shown Figure 2.35 presents the predicted and measured values from the above equations. Both the equations showed very high coefficients of determinations.

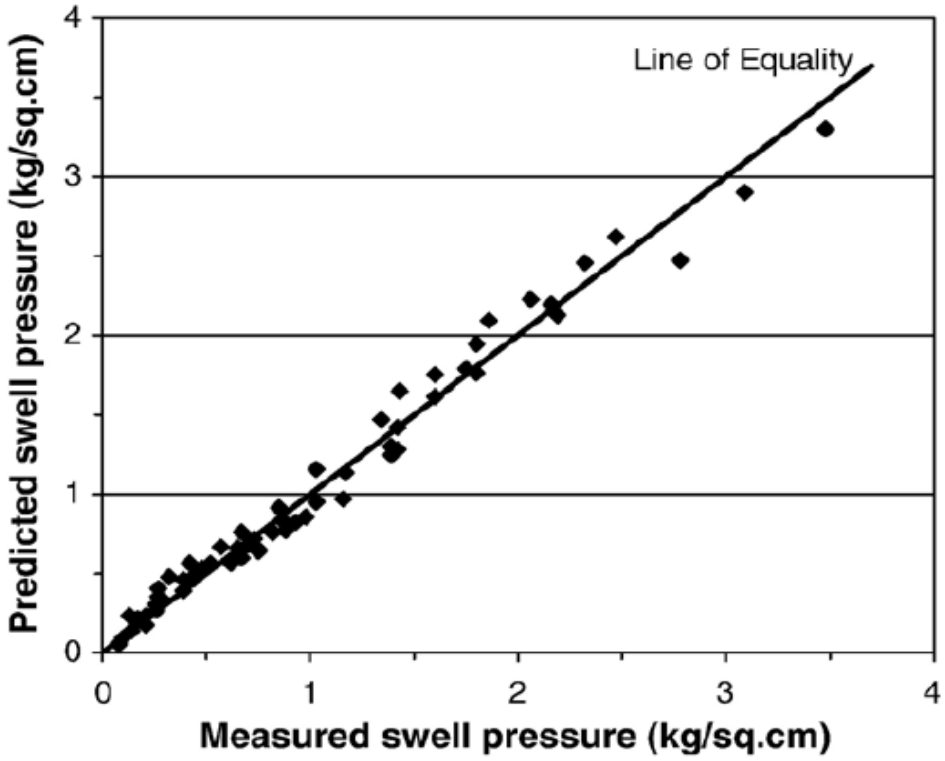

Figure 2.35: Predicted and measured swell pressures (Yusuf and Erol, 2007)

Zhan et al (2007) studied both natural and remolded specimens to determine the complex soil water interaction in unsaturated expansive clay. It was found that the natural soil specimens exhibited lower swelling than the compacted specimen. The less swell potential of the natural

specimens may be attributable to both its over-consolidation nature and secondary structures. It was also found that the stiffness of soil skeleton with respect to a change in external stress is generally lower than that with respect to change in matric suction.

Within the suction range considered, the relationship between swell strain and initial suction appears to be bilinear on a linear scale. The inflection points for the compacted and natural specimens correspond to an initial suction of 200 and 100 kPa, respectively. Figure 2.36 and Figure 2.37 present the one dimensional swell and swell pressure of expansive clay specimens with change in initial matric suction.

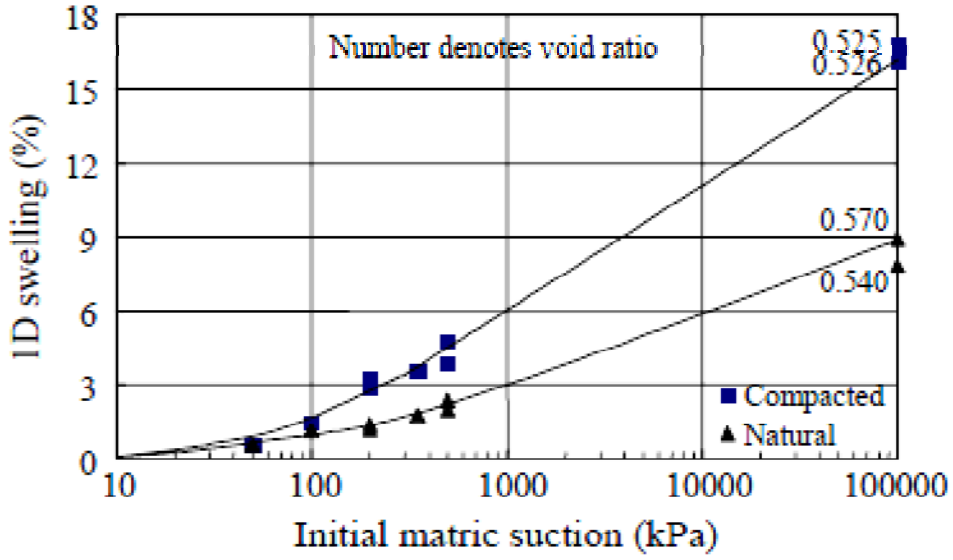

Figure 2.36: 1 D free swell for natural and compacted specimens (Zhan et al, 2007)

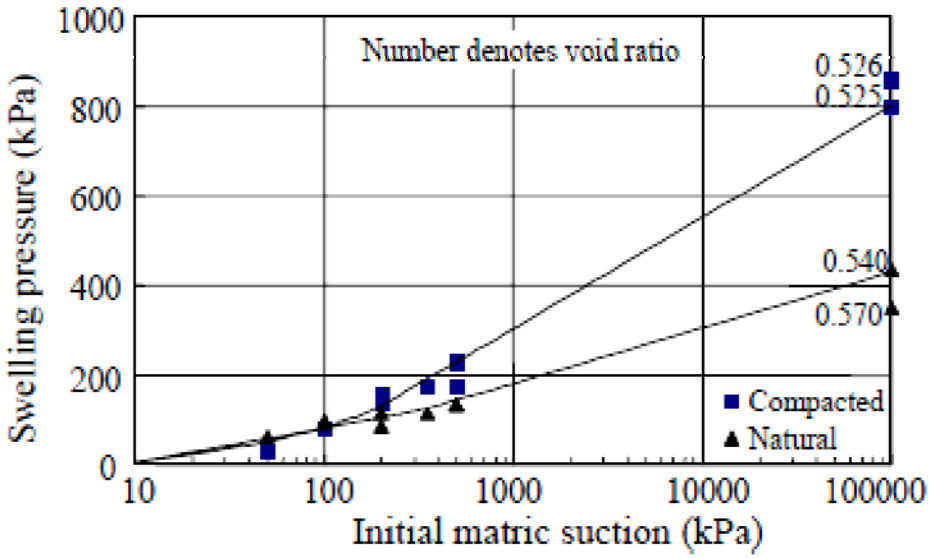

Figure 2.37:Swell pressure for natural and compacted specimens (Zhan et al, 2007)

Agus et al. (2010) studied compacted sand-bentonite mixtures to understand the suction concept in expansive soils. It was found that suction depends primarily on the water content and the bentonite content of the mixture. Below shown Figure 2.38 shows the vapor equilibrium apparatus used by Agus et al. (2010)

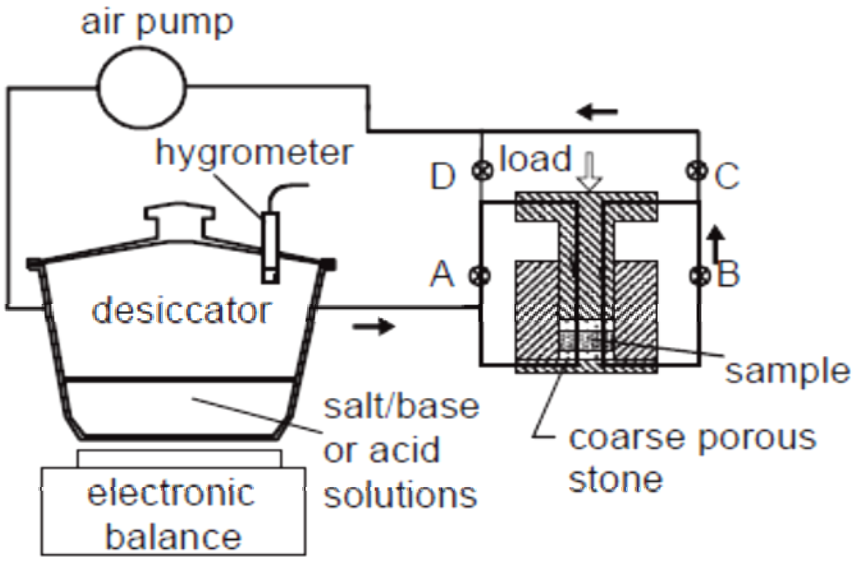

Figure 2.38: Vapour equilibrium technique setup (Agus et al., 2010)

Cyclic controlled suction tests were performed on bentonite sand mixtures. Clearly, the soil tends towards an elastic (reversible) state. This trend is better appreciated if the volumetric strains either in expansion or compression are plotted as the number of cycle's increases. Also, a technique to derive the micro-structural parameters and to interpret the mechanical interaction between both structural levels has been proposed in this research. Figure 2.39 shows the swelling and shrinkage behavior of bentonite sand mixtures with suction cycles.

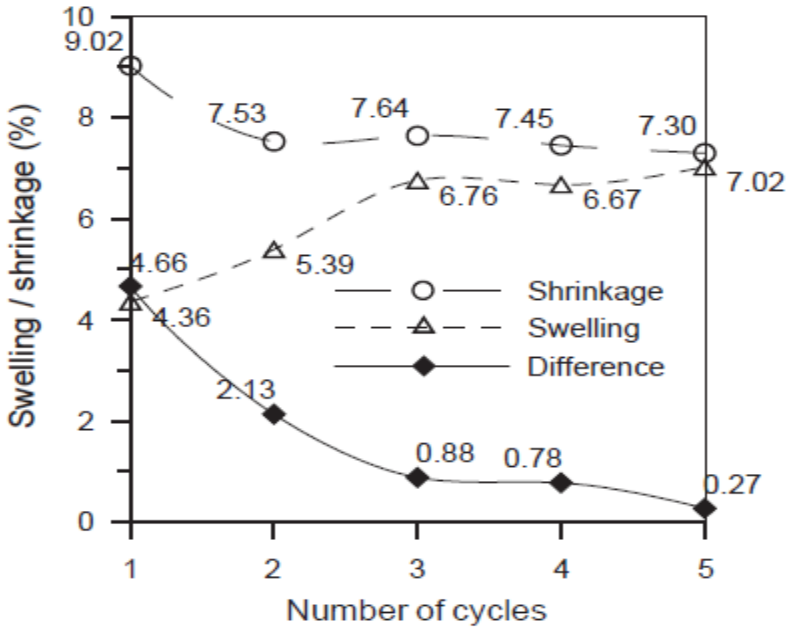

Figure 2.39: Swelling and shrinking with suction cycles (Alonso et al., 2005)

Habib and Karube (2011) conducted a study to determine the swell pressure behavior of expansive soils in both vertical and lateral directions under controlled suction. The test apparatus is as shown in the figure. It was found that both vertical and lateral pressure increase as suction decreases and reach a peak value simultaneously followed by decrease. Figure 2.40 shows the apparatus used by Habib and Karube (2011) for the determination of swell pressure of expansive soils.

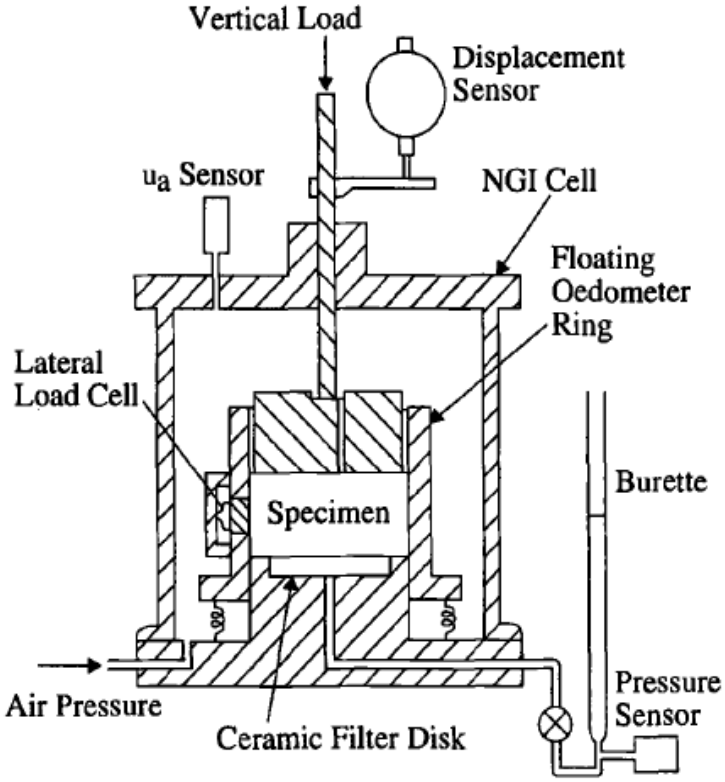

Figure 2.40: Modified oedometer for measuring lateral swell pressure (Habib and Karube 2011)

The vertical pressure from the soil specimen is measured by the displacement sensor mounted on top of the specimen. Lateral swell pressure is monitored by the load cell connected to the sides as shown above.

Lateral confinement prevents stress relief accompanied by premature expansion during the transfer of the sample into the consolidometer. The samples were loaded and unloaded in single increments to determine the expansion characteristics. The portion of total heave resulting from moisture increase was obtained in a similar swell test in which the soil was given free access to water while it was under full overburden pressure. Figure 2.41 shows the plot of vertical and lateral swell pressure variation with loading and unloading sequences.

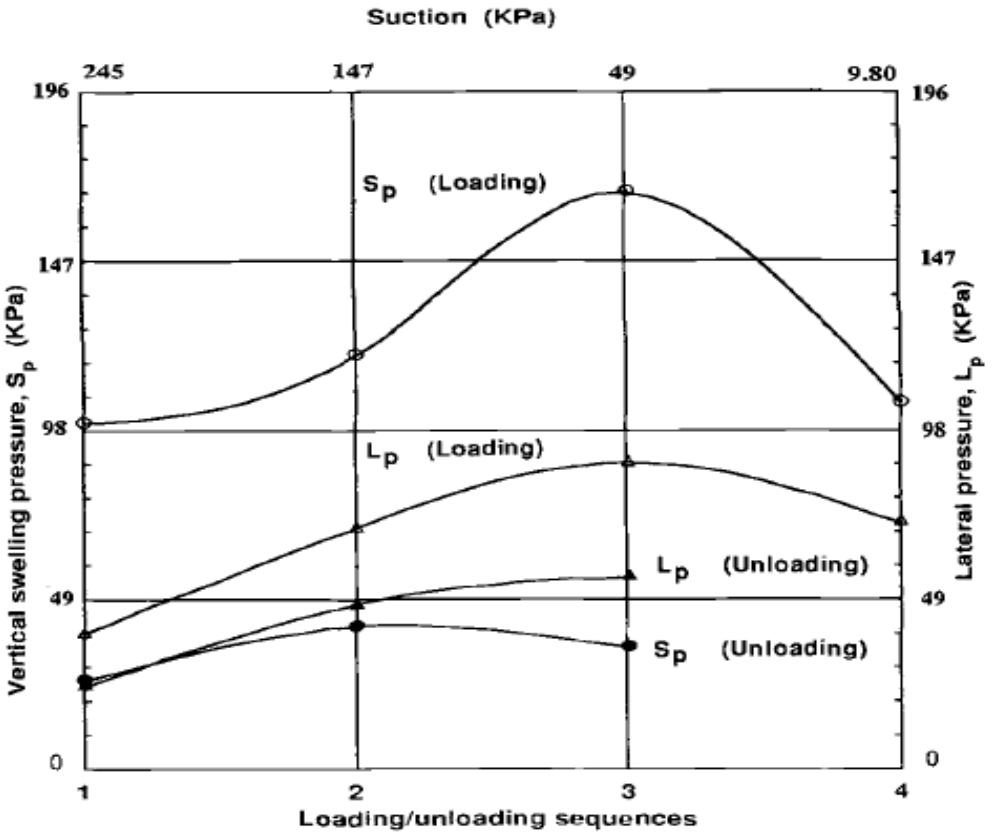

Figure 2.41: Vertical and lateral swell pressure behavior under different loadings (Habib and Karube 2011)

2.5 Pore Size Distribution

Surficial measurements of a mass are possible with techniques like Scanning electron microscope (SEM). The measurement of internal pore structure of a solid mass is the main challenge for the researchers in the past decade. These measurements are possible with the help of techniques like Mercury Intrusion Porosimetry (MIP) and X-ray Computed Tomography (XCT). Details of these techniques are presented in the following.

2.5.1 Mercury Intrusion Porosimetry Technique

The grain size distribution of a soil is easy to measure in the geotechnical laboratory using a stack of sequentially smaller screens and sieves, a shaker, and a scale. On the other hand, determination of the pore size distribution of a soil has traditionally been a difficult task for soil scientists and engineers.

Mercury intrusion method is a new technique used to measure the pore size and distribution of the soil. Because of the mercury impermeability to soil, the mercury-injecting pressure is required to overcome the capillary resistance which prompts mercury to outflow from the capillary. The greater the aperture diameter, the capillary resistance will be smaller and the lower the required pressure for intrusion. As long as the amount of mercury sent into specimen at various pressure points are measured, their pore scale distributions and porosity can be easily obtained based on the theory of cylindrical pore model (Washburn, 1921). The basic theory for this technique is presented as Eq. 7.

$$p' \times r = -2 \times \sigma \times \cos(\alpha) \tag{7}$$

where p′ is the mercury-injecting pressure, r is the pore radius, σ is the surface tension coefficient of the mercury, and α is the wetting angle of mercury on the material. σ is 0.485 N/m and α is 130

Simms and Yanful (2004), conducted pore size distribution studies on fine grained soils to predict the SWCC. The predicted SWCC from Pore size distribution under predicted the SWCC. These predictions were improved by incorporating a simple pore-shrinkage model that assumes pores as elastic cylinders.

Figure 2.42 shows the experimental results and the soil water characteristic curve predicted from the pore size distribution.

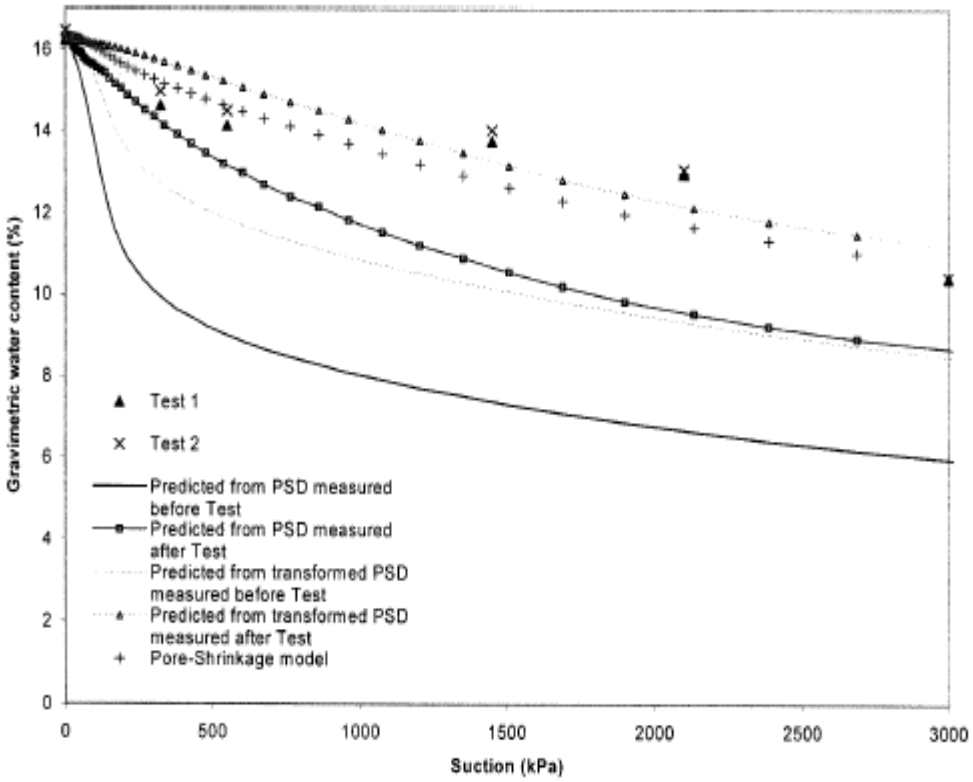

Figure 2.42: Predicted and measured SWCC of a glacial till (Simms and Yanful, 2004)

The study conducted by Rao and Revanasiddappa (2005) examined the influence of the microfabric on the matrix suction of residual soils by referencing the matrix suction of undisturbed residual soil specimens to their remolded state. It was found that pore fabric plays a vital role in governing the soil behavior.

It was also found that, the matrix suctions of the undisturbed and remolded residual soil specimens are greatly influenced by the relative abundance of the inter-aggregate porosity and intra-aggregate porosity. Figure 2.43 shows the pore radius distribution curves for two soils obtained from MIP.

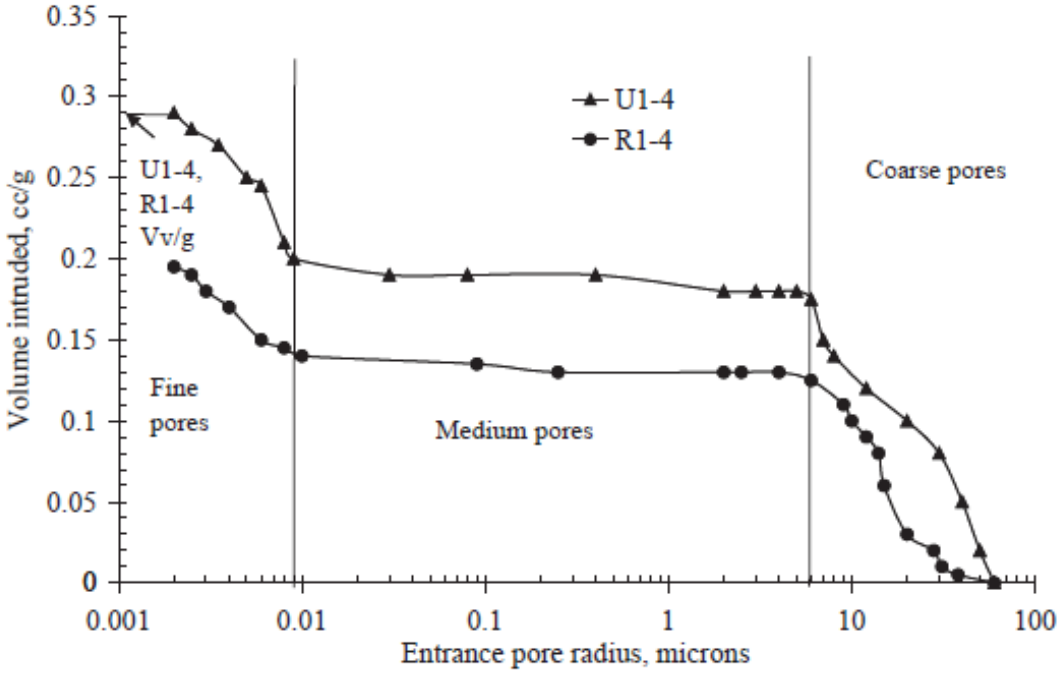

Figure 2.43: Distribution of pores of different radii (Rao and Revanasiddappa, 2005)

As shown in the above figure, the variation of pore radius with volume intrusion gives an idea of the pore volume intruded at that particular radius. This experiment reveals the different pore radii and the volume of pores associated with a soil mass.

It was concluded from results that the matric suction of a soil specimen is influenced by the relative abundance of inter aggregate porosity suggested by the MIP results. It was also concluded that the micro fabric plays an important role in determining the matrix suction of undistributed and remolded soils.

Soto and Vilar (2006) evaluated a model for the prediction of soil water retention curve based on fractal geometry. The fractal geometry model is based on the combined effect of pores size distribution and grain size distribution. This model showed a good fitting with experimental data and was able to reproduce SWCC using one fractal dimension for a whole span of soil suction. Figure 2.44 shows the measured SWCC and the predicted SWCC obtained from MIP.

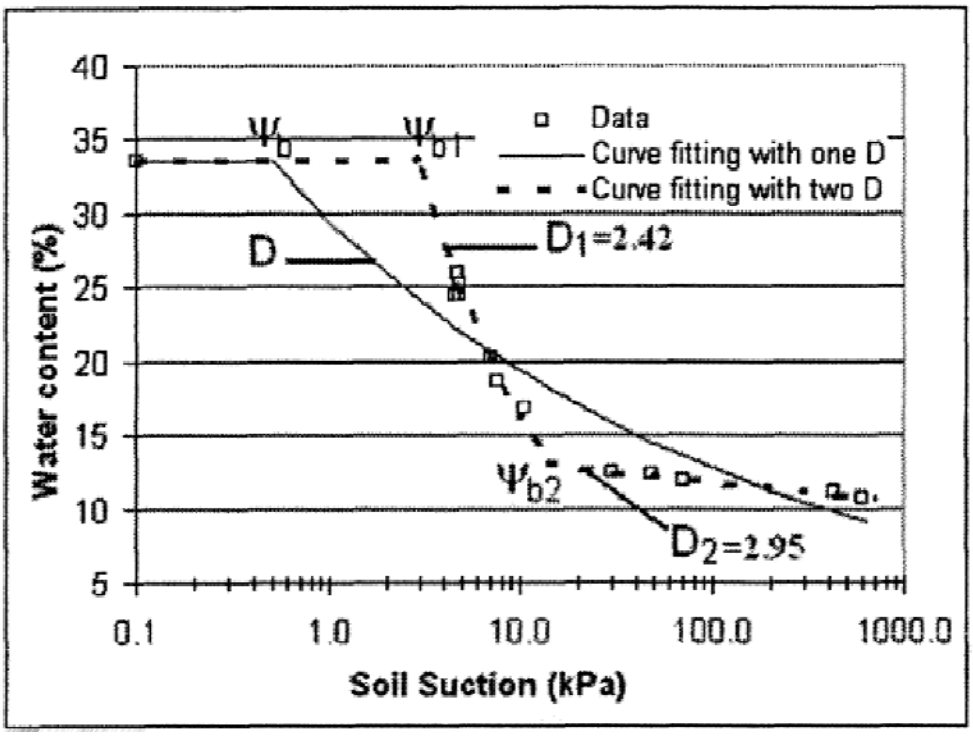

Figure 2.44: Predicted and measured SWCC (Soto and Vilar, 2006)

Ferber et al. (2009) conducted research on micro structural interpretation of swelling tests performed on four clays. The results showed that swelling of clays leads to a micropores increase and a macropores decrease. In addition, it was found out that micropores volume increase is not affected by the initial dry densities, whereas the macropores volume increase. The analysis of these data with different parameters, such as void ratio or air void ratio, showed a linear relationship between the air void ratio before swelling and the void ratio after swelling. MIP tests results suggested that the coupled influence of water content and dry density is related to the microstructure changes of the clay. Figure 2.45 below shows the variation of MIP curve for the clay before and after swelling.

Delage (2010) investigated the micro-macro relationships of granular soils with the help of scanning electron microscope and mercury intrusion porosimetry. It was concluded that a

simple micro–macro model developed under this framework provided reliable results in terms of compression behavior of a soil.

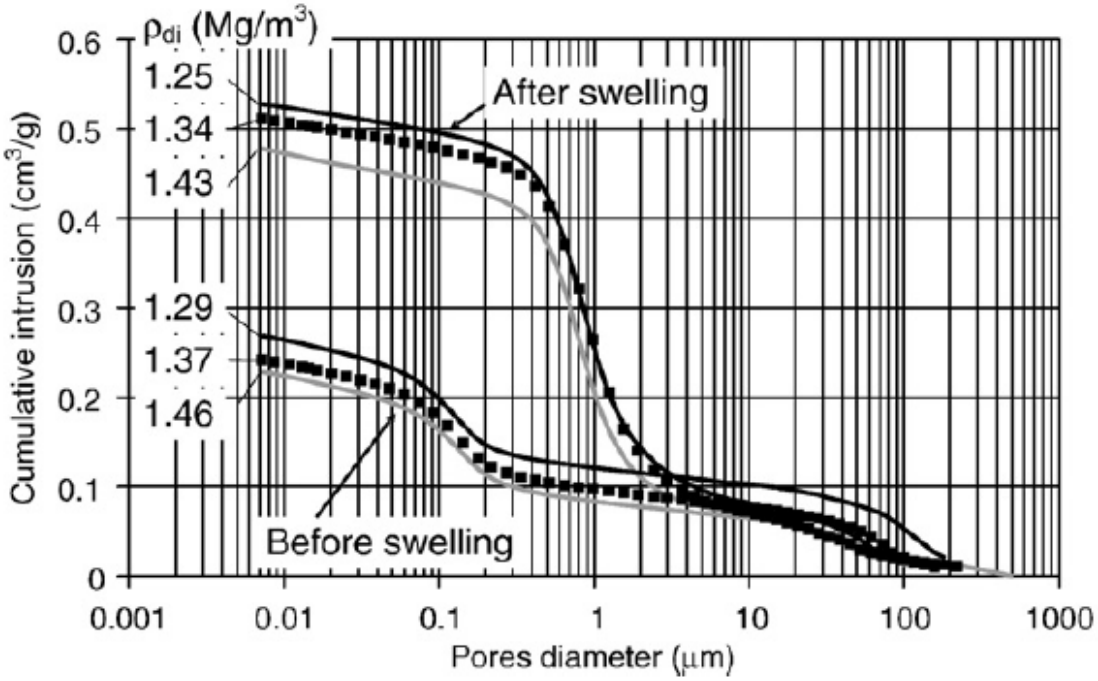

Figure 2.45: MIP tests performed on clay before and after swelling (Ferber et al, 2009)

In a study conducted by Ferreiro and Vazquez (2010), the potential of multifractal parameters obtained from mercury injection porosimetry (MIP) between two soils with contrasting structure stability was observed. Mercury intrusion analysis showed that the pore networks of the two soils were modified at the 0–2 cm layer. In the loamy soil after 260-mm cumulative rainfall, pore volume decreased mainly in the 10–2 μm diameter size. In the silty loam after 140 mm rainfall the change was an increase in the 2–0.2 μm pore size range, even if a smaller loss in the 10–2 μm class also occurred.

In a research conducted by Verges et al. (2011), internal structure and fabric of sedimentary rocks were studied using MIP technique. 3D imaging technologies like computed tomography was used to construct and evaluate virtual representation of internal pore distribution. The two limiting factors of the experiment are the resolution of the images in relation

to the pores size and the segmentation process. A good approximation is achieved using numerical method for pores with large diameter than voxel size. The effective porosity is computed as the percentage of reachable pores. The pore interconnectivity measured the ratio between the effective porosity and the global porosity. The variation of pore radius with differential volume and relative volume obtained from MIP were plotted in Figure 2.46.

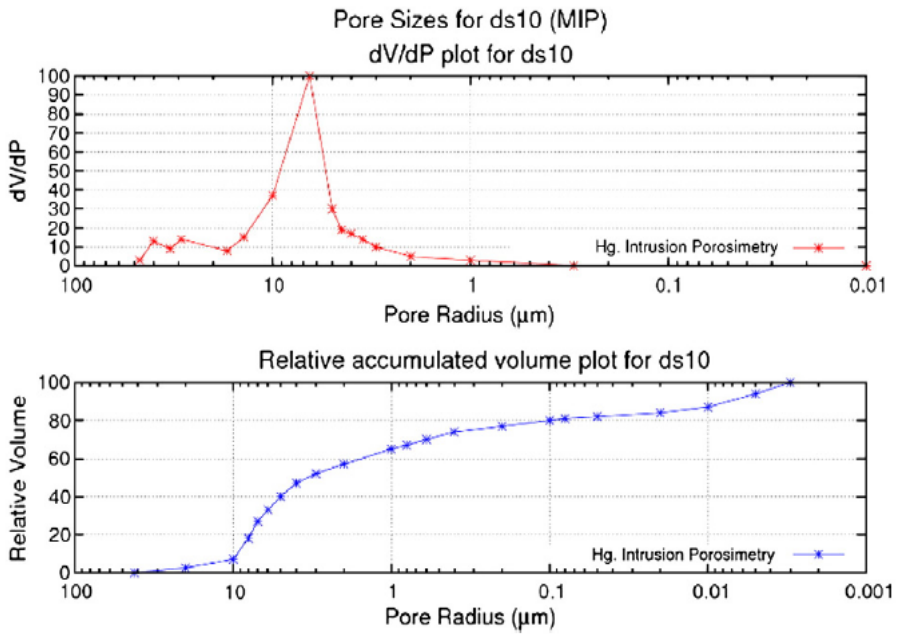

Figure 2.46: Pore size distribution analysis showing plots of differential intrusion volume and relative volume with radius (Verges et al., 2011)

Scanning electron microscope and mercury intrusion analyzer were used in a study conducted by Hui et al (2011), to study the pore size distribution characteristics of silt. From the pore size distribution analysis it was found that the micro pore distribution curve is steep indicating the largest number of particles. It was concluded that mercury intrusion method was an effective means to study the pores. The intrusion extrusion curve obtained from the MIP was plotted in Figure 2.47.

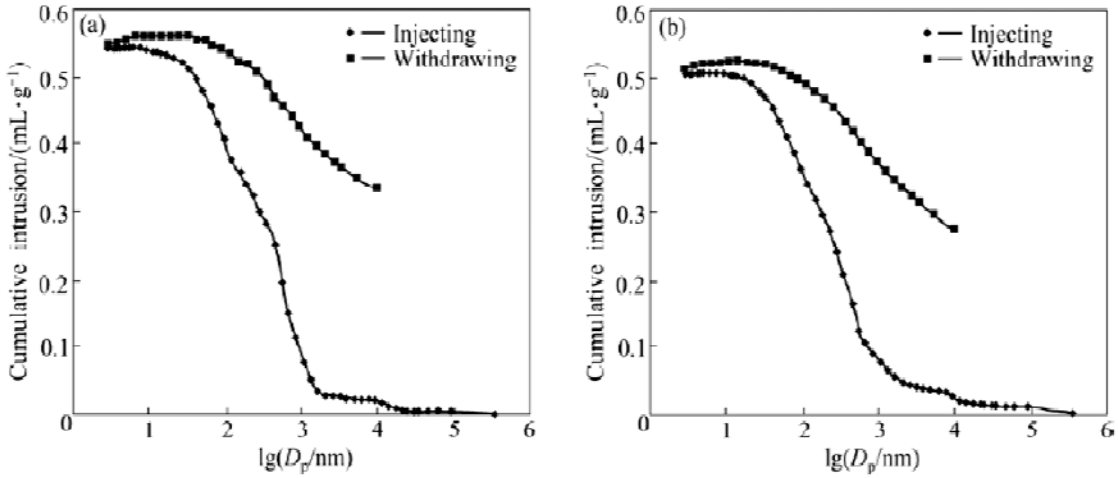

(a) (b)

Figure 2.47: Pore diameter vs cumulative intrusion of mercury of a soil at two different consolidation pressures (a) 0 and (b) 1600 kPa (Hui et al, 2011)

Above shown are MIP curves obtained at two consolidation pressures. It was observed that there is a decrease in cumulative intrusion when the consolidation pressure increased. Also, it was found that the post consolidation stage produces more tiny pores and more bound water which results in lower permeability. Figure 2.48 shows the pore analysis conducted by Hui et al (2011) using MIP and SEM studies.

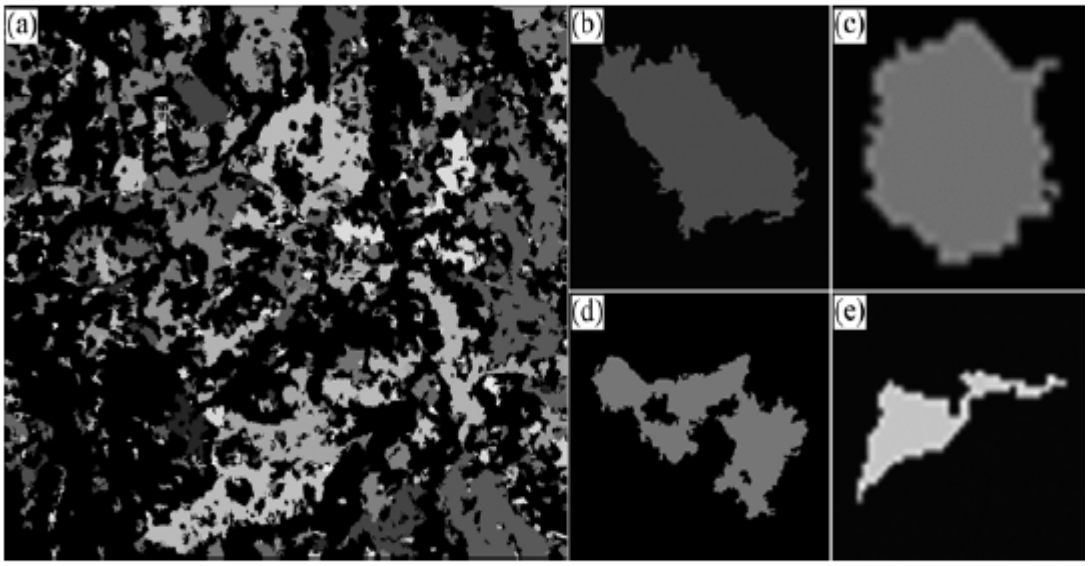

Figure 2.48: (a) (b) (c) (d) (e): Pore analysis by Hui et al (2011)

Cui and Tang (2011) studied the microstructure of sub soil layers under the building loads in the centrifuge model by the scanning electron microscopy and the mercury intrusion porosimetry (MIP). The pore structure of each soil layer was studied by MIP, and the pore distribution of each soil layer was studied by the fractal theory. It was also found that flocculation and honeycomb-flocculation are the main structures found in clays.

Below shown Figure 2.49 is the Intrusion-extrusion curve for the clay sample obtained from the Mercury Intrusion Porosimetry (MIP) technique. Figure 2.50 (a) and (b) presents the variation of pore diameter with total pore volume and intrusion pressure respectively.

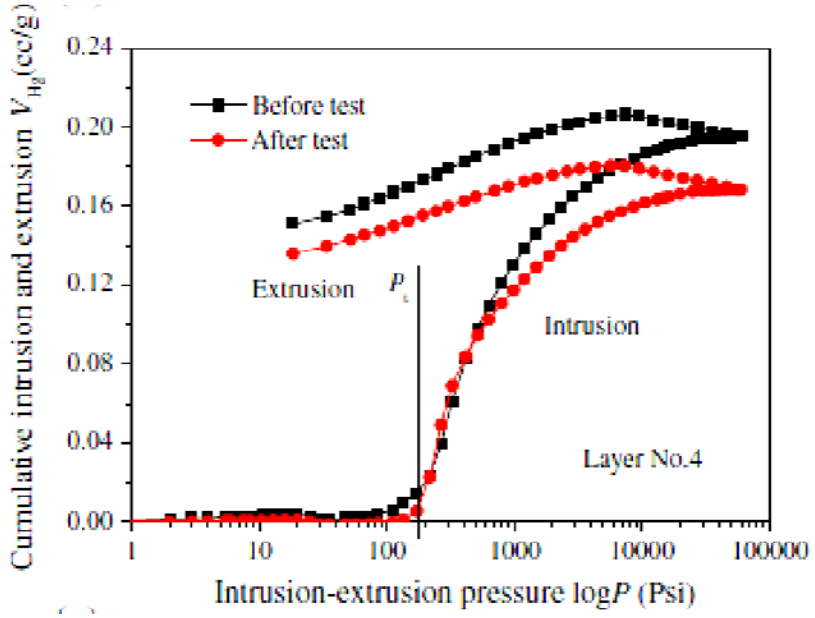

Figure 2.49: Intrusion extrusion curve for soil using MIP (Cui and Tang, 2011)

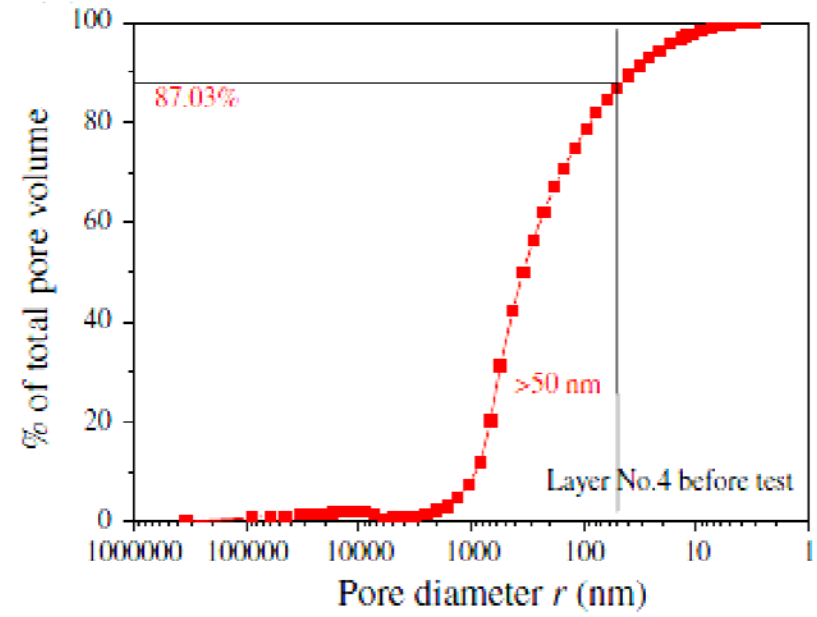

(a)

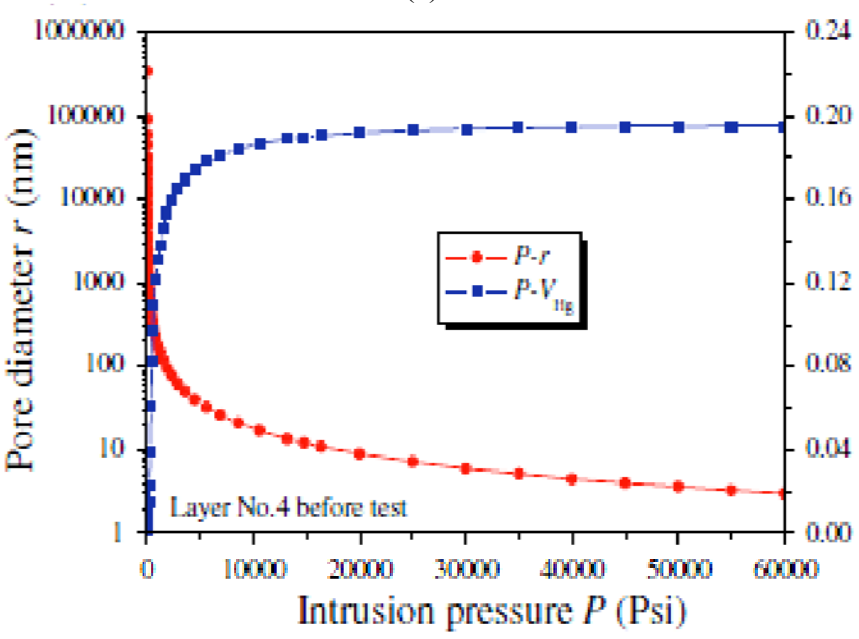

(b)

Figure 2.50: (a) Pore diameter vs pore volume and (b) Intrusion pressure vs pore diameter (Cui and Tang, 2011)

The micro and macro mechanisms of land subsidence caused by building group were analyzed. It was concluded that the engineering behavior of soils are controlled by the state of microstructure to a great extent.

2.5.2 X-ray Computed Tomography Technique

In geotechnical engineering research, Computed Tomography (CT) has been used to observe localized deformations and shear bands in specimens undergoing triaxial compression, void ratio evolution inside shear bands, and characterization of failure in soils (Desrues et al. 1996; Otani et al. 2000; Alshibli et al. 2000). In a recent application, Matsuhima et al. (2006) used CT to visualize and quantify the motion of individual particles inside a triaxially compressed specimen. Alramahi and Alshibli (2006) studied the application of computed tomography (CT) in the field of geotechnical engineering. They found out the several factors like geometry of material, beam hardening and partial volume affect the quality of images. They recommended considering all the above factors for successful quantitative CT analysis. Figure 2.51 shows the CT scan images obtained on soil specimens.

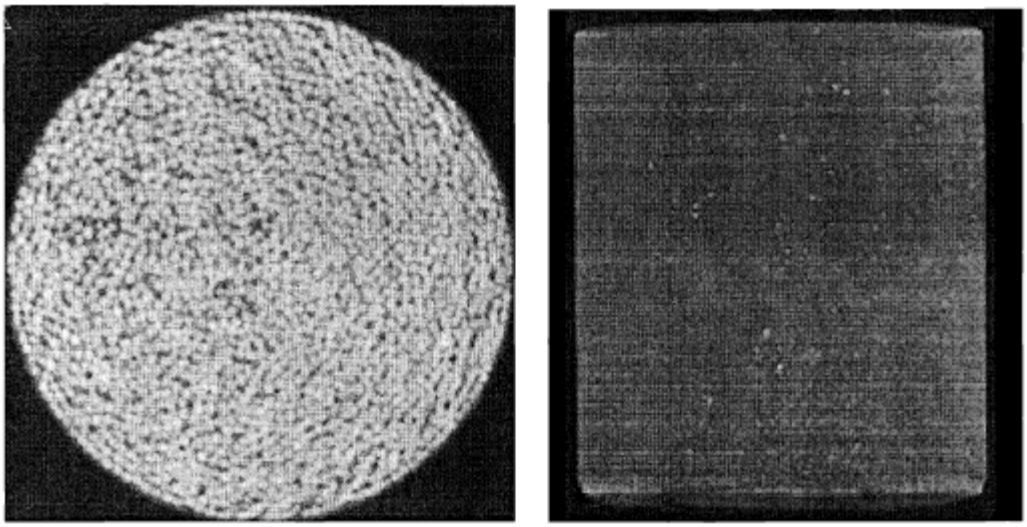

Figure 2.51: CT slice of a triaxial specimen (Alramahi and Alshibli (2006)

Mokwa and Nielsen (2006) studied the micro properties of soils using digital images produced by X-ray tomography technique. It was concluded that x ray tomography was a viable means for nondestructive study of pore characteristics and pore size distributions for soils. Also, the CT scan approach provided a comparatively accurate grain size distribution curve for five coarse grained soils.

Torrance et al (2007) studied internal structure of intact natural silt loam soil cores using X-ray tomography technique. Improvements to the conventional CT scanner were made for this particular study as the samples need to be in frozen condition throughout the scanning time. The changes in structure and redistribution of water to form ice lenses in saturated samples were observed. The soil samples were subjected to rapid freezing with access to water at the base. Ice lenses of less than 1mm thickness are detected during the procedure. Figure 2.52 presents the side and top view of the silty loam cores collected for the research.

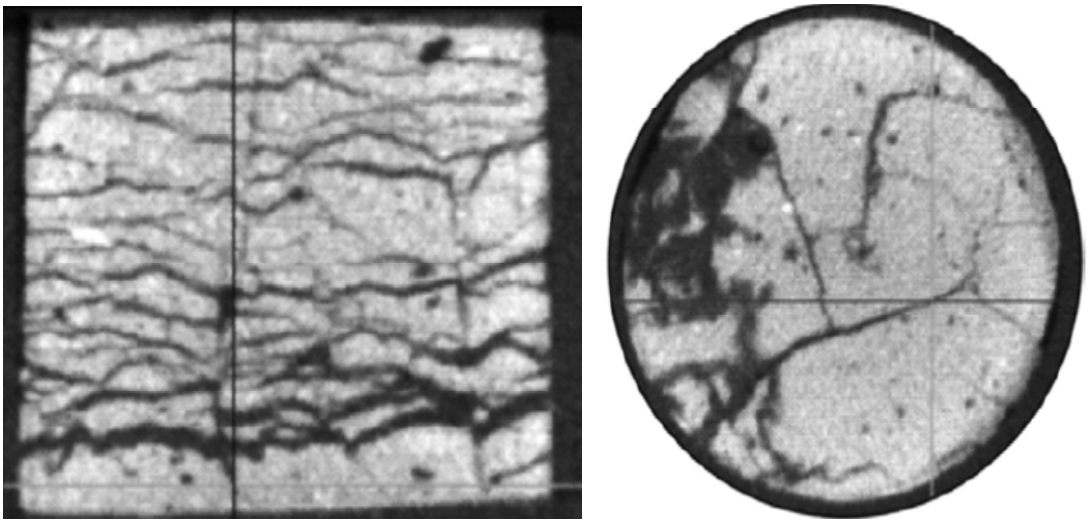

(a) (b)

Figure 2.52:(a) and (b) Showing the side and top view of the silty loam core samples (Torrance et al, 2007)

It was concluded that CT scanning was successful in differentiating the ice lenses within the frozen soil samples.

In a research conducted by Sander et al. (2008) the cracking patterns for soil at different depths were studied with the help of computed tomography (CT). Aggregated matrix structures were found in the subsoil of both samples and horizontal cracks were identified. The X-ray scanning results together with water contents and particle densities at different depths allow calculating the vertical mean bulk density distribution in the soil mass. Figure 2.53 below shows the CT scan images collected from the soil at different depths.

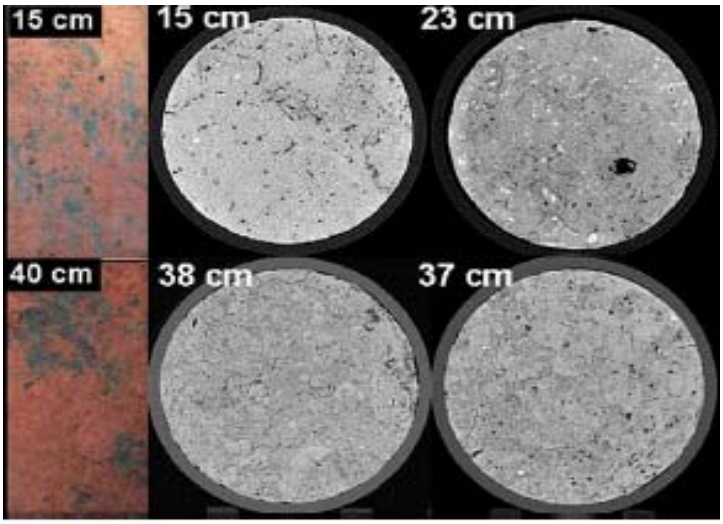

Figure 2.53: Horizontal CT images of samples collected from two depths (15 and 40 cm)

Tippkoter et al. (2009) conducted micro X-ray tomography on soil specimens to study the soil water in relation to pores and soil matrix. The application of micro-focus computerized tomography using X-ray tubes allowed the visualization of both soil matrix and soil water with higher resolutions.

Water films in pores of undisturbed soil are clearly detected in mCT-generated micrographs, but were questionable especially with respect to the thickness of the water films and the protuberances of these films. It was observed that the effects of adhesion and cohesion caused by nanoparticles are responsible for water films in the range of some micrometres in

macropores. Figure 2.54 presents the 2D and 3D images collected by Tippkotter using X-ray tomography technique.

Image analysis of water films detected in the images revealed a presence of 42% moisture condition. The authors recommended a further investigation on the pore analysis and determination of moisture content from X ray CT scan images. Figure 2.55 shows the pore analysis conducted on thin soil sections by Tippkotter, 2005.

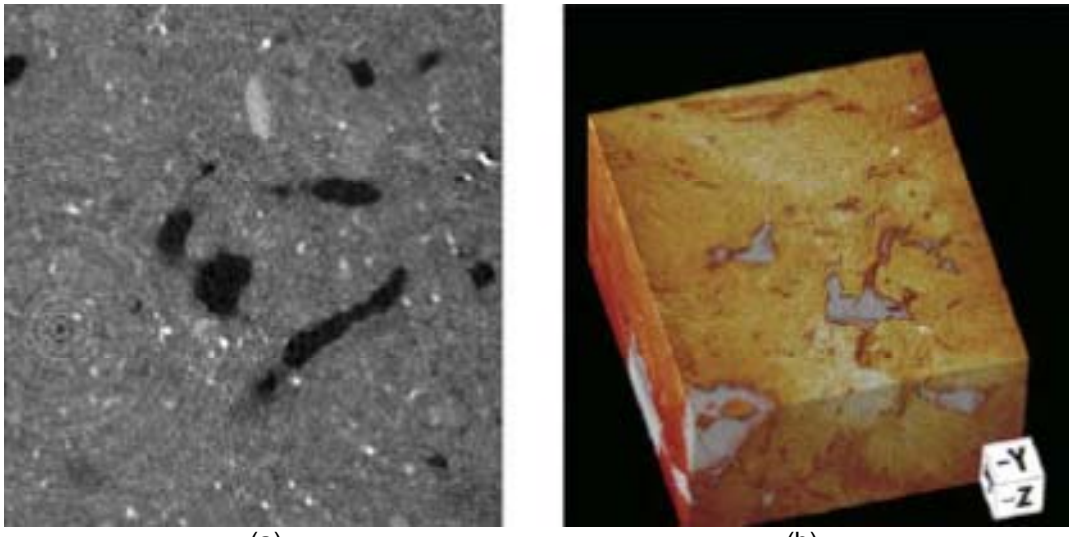

(a) (b)

Figure 2.54: (a) 2D and (b) 3D images of soil specimens (Tippkotter, 2009)

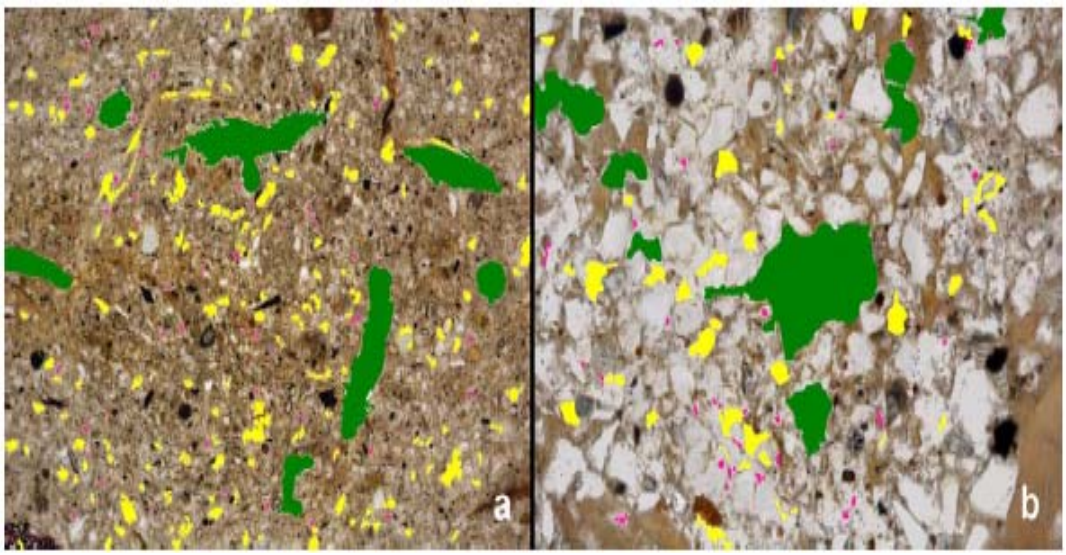

(a) (b)

Figure 2.55: (a) and (b) showing pore analysis of thin soil sections (Tippkotter, 2009)

In a research conducted by Luo et.al (2008), two soils with contrasting textures and structures from two land uses (row crop and pasture) were investigated using X-ray tomography.

After reconstruction, characteristics of macropore networks were quantified, including continuous macroporosity change along depth, macropore size distribution, network density, surface area, length density, length distribution, mean hydraulic radius, tortuosity, inclination (angle), and connectivity.

Figure 2.56 below shows the X-ray Tomography equipment used by Luo et al (2008) for pore image acquisition.

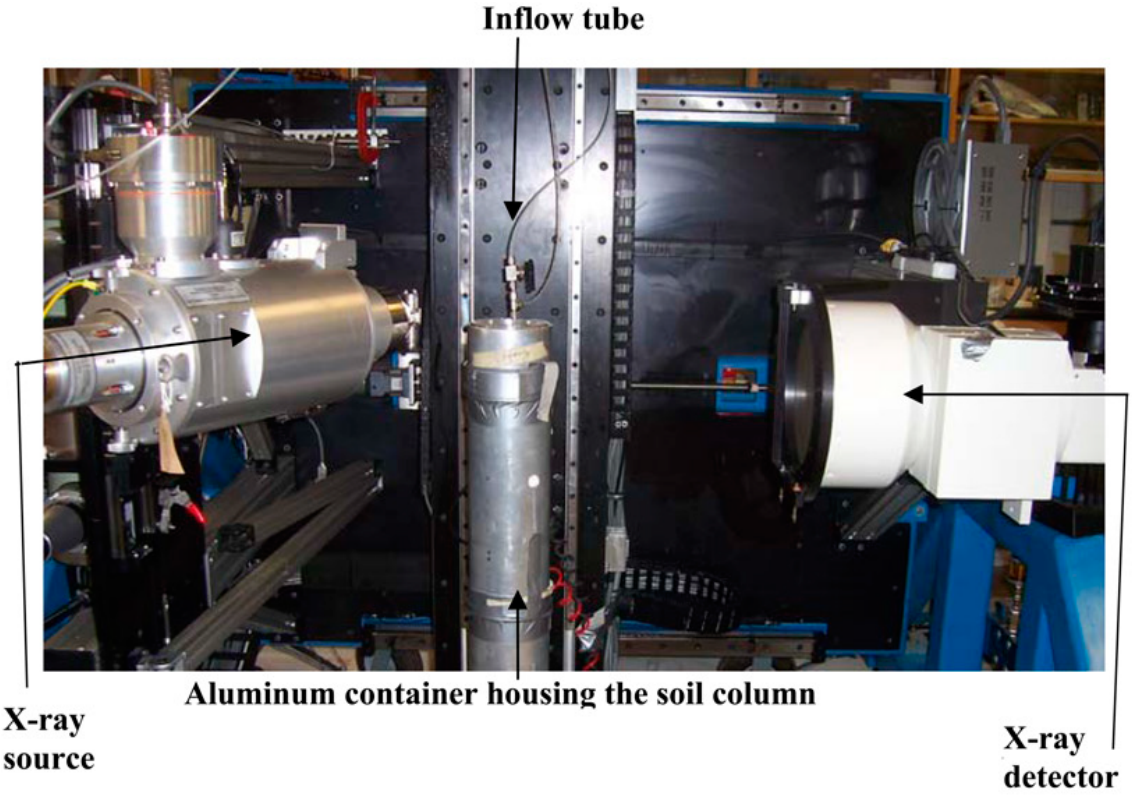

Figure 2.56: X-ray Computed Tomography apparatus used by Luo et.al (2008)

The approach they developed provided an improved quantification of complex 3-D macropore networks. It was found that physical, chemical, and biological impacts of macropores

will be enhanced with an increase in macro-porosity, surface area, size, network density, length density, connectivity, and decrease in vertical angle and tortuosity. In this study, 3-D macro-pore characteristics are be linked to soil functional properties to better understand soil processes and related management practices.

High-resolution industrial CT has allowed reconstruction, visualization, and quantification of soil structure and solute transport in a relatively large intact soil column. This study illustrated the complex nature of flow dynamics of air and water in a structured soil mass. Figure 2.57 shows the image analysis approach used by Luo et al. (2010).

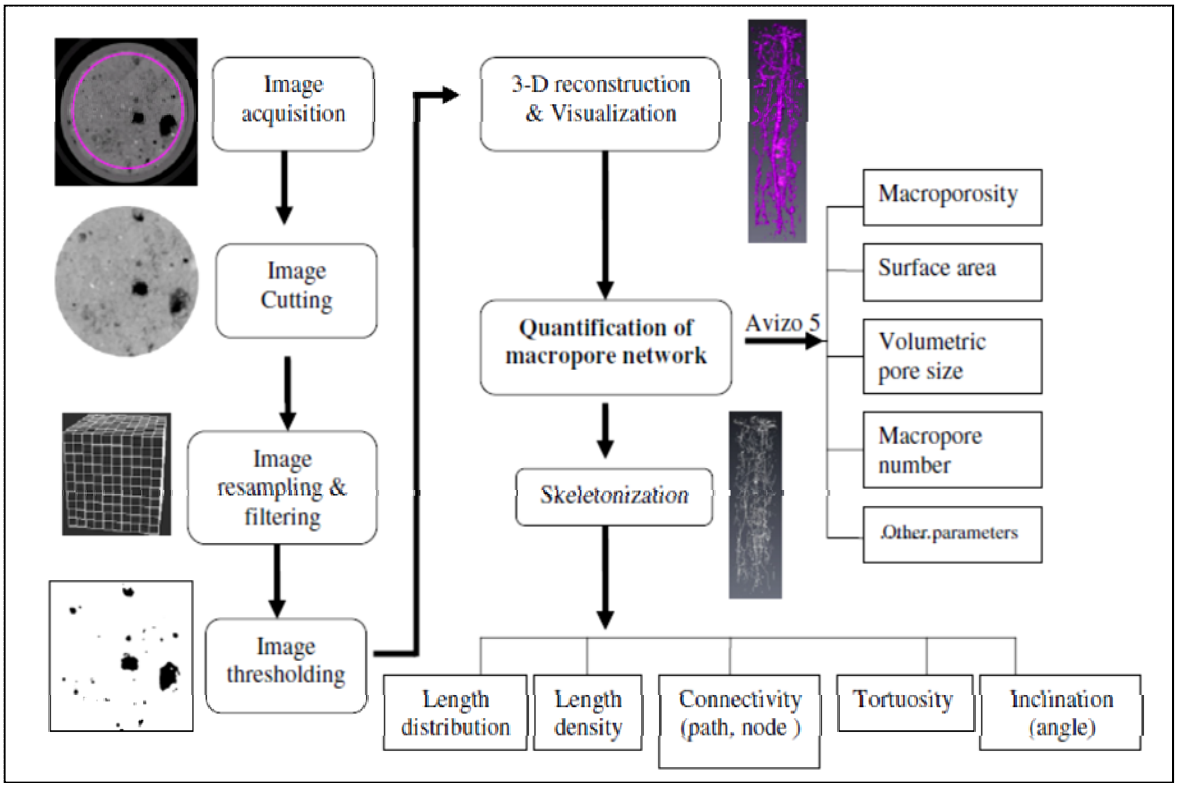

Figure 2.57: Approach developed by Luo et al. (2010) for improved quantification

The non continuity of macro-pores in the soil structure resulted in a restricted flow and transport due to air entrapment or hydrologic discontinuities. This research led to a new way of modeling a predicting flow dynamics in soil structure.

Pires et al. (2010) studied the effects of wetting drying cycles with the help of X-ray computed tomography. Parameters like soil porosity and pore size distribution, water movement through soils and effects of agricultural management systems on soil structure were studied in this research. Figure 2.58 presents the variation of particle density for the soil image acquired by X ray computed tomography technique.

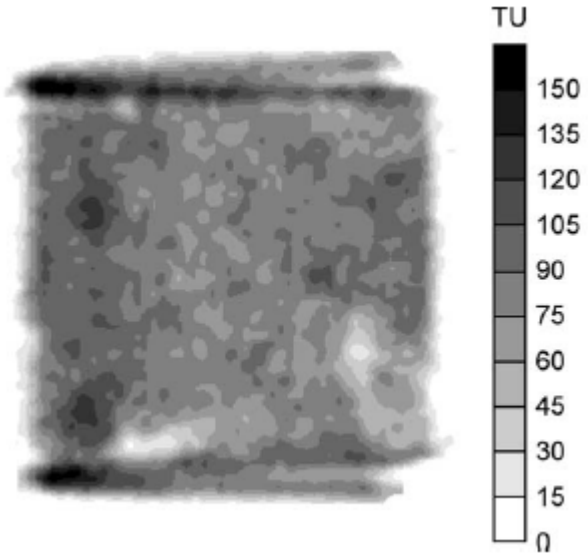

Figure 2.58: Density of particles from Tomographic analysis (Pires et al., 2010)

It was concluded that the use of the X-ray tomography in soil science would certainly lead to new applications of CT that would bring new developments related to soil structure, like more realistic studies on tortuosity, connectivity, shape, size and pore distribution.

Rezanezhad et.al (2010) conducted tomography analysis on the parameters affecting the hydraulic conductivity of peats. It was found that the hydraulic properties of unsaturated peat are controlled by the peat structure and air-filled pore size and geometric distribution as well as the physical properties of peat materials. Figure 2.59 shown below presents the image analysis conducted by Rezanezhad et al. (2010).

.

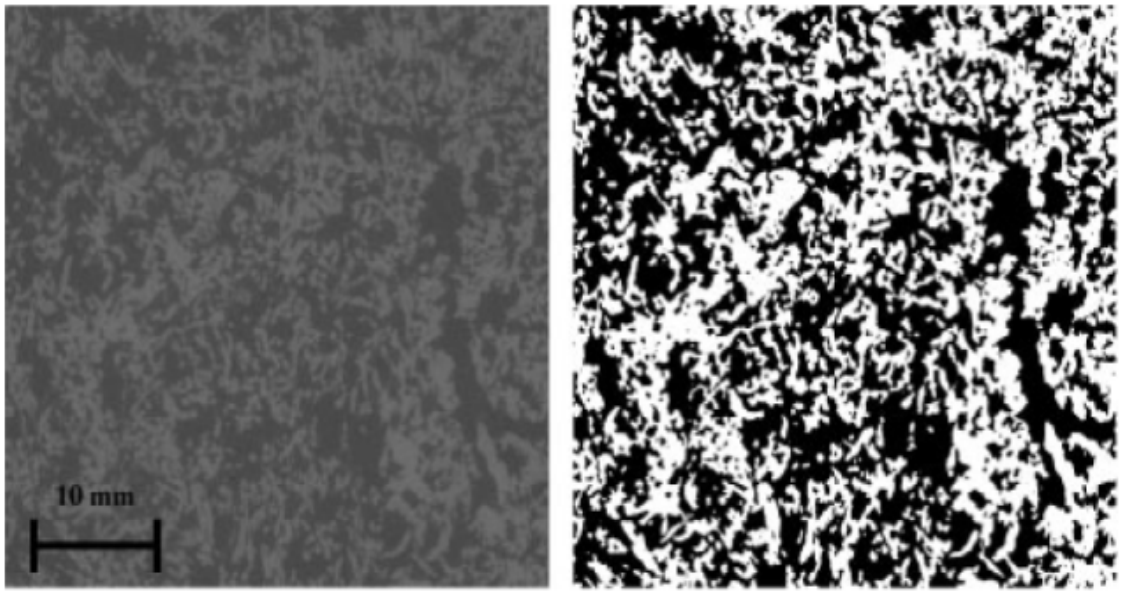

(a) (b)

Figure 2.59: (a) and (b) Image analysis conducted by Rezanezhad et al. (2010)

Three-dimensional CT digital image analysis of peat samples showed that the pore structure and configuration of peat soils are very complex and contains many variables in its physical and hydraulic properties at different depths. Quantified 3-D CT data indicated that at the constant pressure head, there are significantly more distinct, yet volumetrically smaller air-filled pores with increased depth. It was also concluded that the pore structure has a major impact on the unsaturated hydraulic conductivity of a soil.

As discussed above Verges et al. (2011) conducted experiments to study the pore analysis using Mercury intrusion porosimetry. Also, they used micro-CT scanned data sets to map the pore distribution in the soil. Below shown Figure 2.60 shows the 3-D image and 2-D image along with pore network processing.

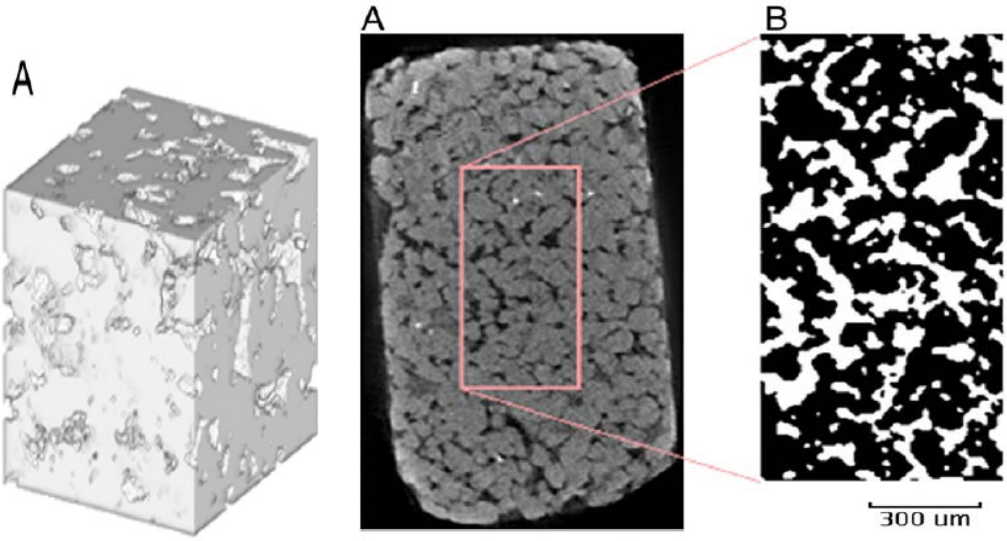

(a) (b) (c)

Figure 2.60: (a) (b) and (c): Pore analysis by Verges et al. (2011)

The current study has two limiting factors, which are the resolution of the images in relation to the pores size and the segmentation process. The observed porosity of the samples when measured via MIP can only predict smaller diameter pores where as, for pores of larger diameter; the numerical method has shown a good approximation of the results.

The Mercury Intrusion Porosimetry (MIP) and X-ray Computed Tomography (XCT) are utilized in the current study for the determination of pore size distribution and network connectivity in the soil mass.

2.6 Summary

In this chapter, an attempt has been made to review the past researches performed on expansive soils. Previous studies on the damages related to expansive soils and the factors responsible were studied. Current laboratory testing and correlations from index properties to identify the swell behavior of soils were identified in this chapter. Mineralogical studies and the role of each mineral in shaping the behavior of a soil are addressed. Also, the role of moisture content and the effects of soil suction on the swelling behavior of clays are studied. The

correlations which include the suction parameter in the volume change behavior were identified in this chapter.

Past studies conducted using techniques like mercury intrusion porosimetry and X-ray computed tomography to study the internal pore structure and distribution, have been addressed in this chapter. These techniques are unique in their own way to determine the soil internal properties which are responsible for the swell behavior. However, each of these parameters are equally or partially responsible for the swell behavior of expansive soils. In the present research unification of all these factors responsible for swell behavior are identified and used in accurate swell predictions.

In the next chapter, soil selection and basic soil classification results are provided. Methodology of all the engineering tests along with their principles is provided in the coming chapter.

CHAPTER 3

METHODOLOGY

3.1 Introduction

The present research targets to study the factors responsible for the swell shrink behavior of expansive clays. Hence 8 different clays from different geological formations have been selected for this study. The laboratory testing program was designed to determine the properties relating to volume change behavior of expansive soil samples taken from these sites, which are Anthem, Burleson, Colorado, Grayson, Keller, Oklahoma, San Antonio and San Diego. These soils were selected based on their diversified soil mineral characteristics and topographical conditions as shown in Figure 3.1.

The basic soil properties, chemical and mineralogy tests were performed in the experimental program. Basic soil test results of the eight soils collected are presented along with their soil classification details. Also, minerals dominant in each of these expansive clays were identified and presented in this chapter. Engineering tests were conducted on the soils and different test procedures were followed for the determination of swell and soil composition properties. Test procedures for the determination of 1-D free swell strain and swell pressures are presented. A novel 3-D swell strain apparatus designed at The University of Texas at Arlington was used for measuring the swell potential of a soil specimen under different confinement conditions and details of this device are presented in this chapter.

The soil water characteristic curves which represent the behavior of a soil with moisture were obtained by using Pressure Cell and Filter paper test methods. Details of the test procedures and working principles are given in this chapter.

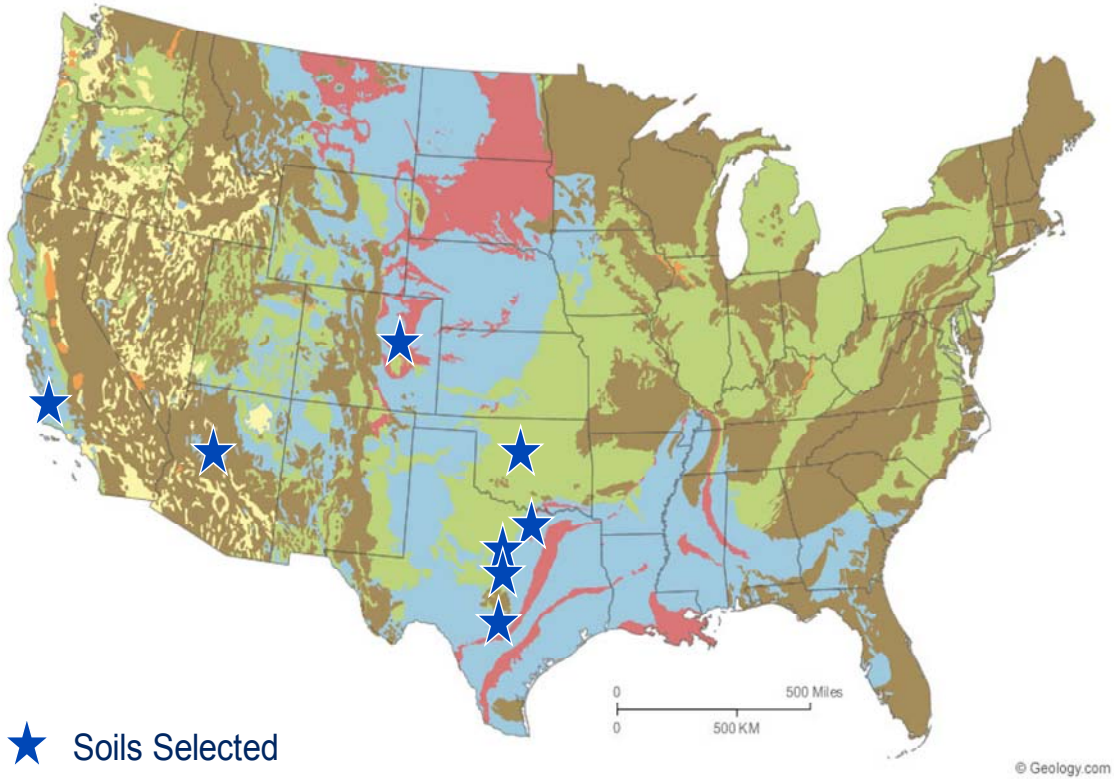

Figure 3.1: Soils selected from different geological formations for the current research

The study of the pores present in the soil mass which are responsible for the expansive soil behavior is a major focus area in the present research. Techniques like Mercury Intrusion Porosimetry (MIP) and X-ray Computed Tomography (XCT) which deal with the internal pore distribution and pore structure are detailed along with their working principles in this chapter.

Flow chart as shown in Figure 3.2 represents the research methodology followed in the present research. The final objective of this research is to formulate a model based on soil composition properties. After the formulation stage, the model is tested for its validity based on the soil swelling behavior measured from engineering tests as shown in the flowchart below.

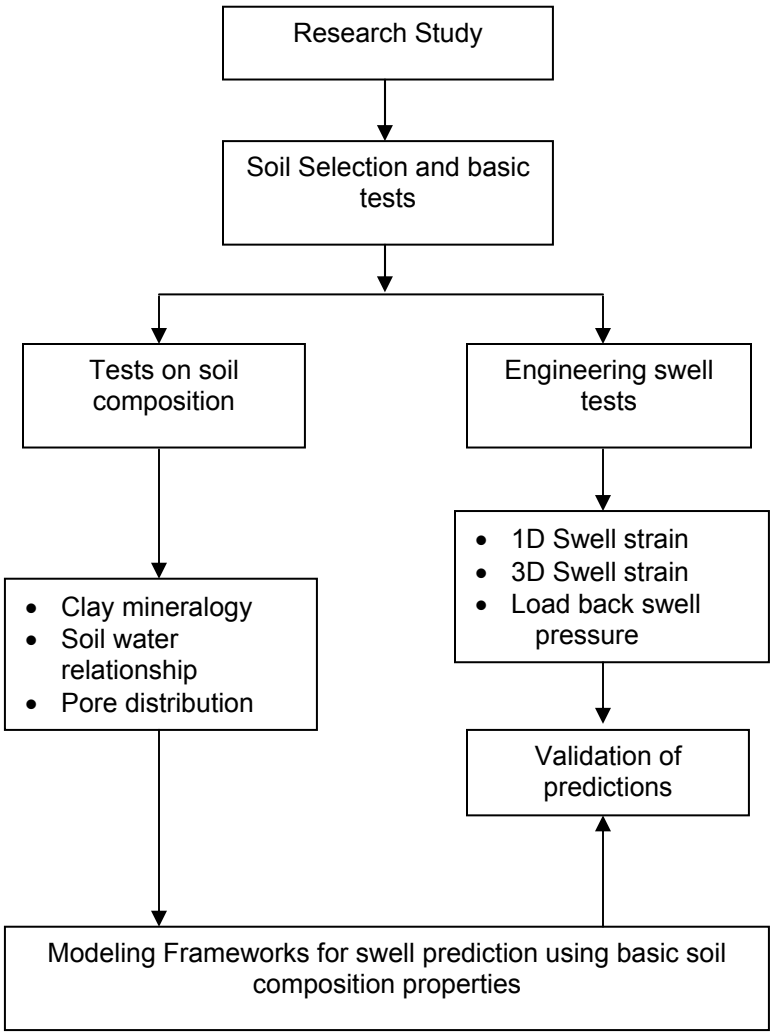

Figure 3.2: Research methodology

A summary of the laboratory procedures, equipment used and results obtained are presented in this chapter.

3.2 Basic Laboratory Tests

Tests were conducted in order to measure the basic soil properties as needed in the geotechnical investigations. The tests performed consist of specific gravity test, sieve analysis, hydrometer test, Atterberg limits, and Standard Proctor tests. Descriptions and procedures of the tests are presented below.

3.2.1 Specific Gravity, Sieve Analysis and Hydrometer tests

Specific gravity (G_s) is defined as the ratio of the mass of a given volume of solid or liquid to the mass of an equal volume of water, of testing materials was determined as per TxDOT procedure Tex-108-E. The distribution of the grain sizes in test materials was determined using TxDOT procedure Tex-110-E. This method was followed to determine the amount of soils finer than the No. 200 sieve opening. Finer particle size analysis was performed using hydrometer tests.

3.2.2 Atterberg Limits

Atterberg limit tests reveal properties related to consistency of the soil. These include liquid limit (LL), plastic limit (PL) and shrinkage limit (SL) and these are essential to correlate the shrink-swell potential of the soils with their respective plasticity indices. Upon addition of water the state of soil proceeds from dry, semisolid, plastic and finally to liquid states. The water content at the boundaries of these states are known as shrinkage (SL), plastic (PL) and liquid (LL) limits, respectively (Lambe and Whitman 2000). Therefore, the LL is measured as the water content at which the soil flows and the PL is determined as the water content at which the soil starts crumbling when rolled into a 1/8-inch diameter thread.

The numerical difference between LL and PL values is known as plasticity index (PI) and this index characterizes the plasticity nature of the soil. Representative soil samples from each location are tested following the procedure from Tex-104-E and Tex-105-E. The water content of the samples during tests is measured using oven drying method.

3.2.3 Standard Compaction Tests

In order to determine the compaction moisture content and dry unit weight relationships of the soils in the present research program, it is necessary to conduct standard Proctor compaction tests on soils to establish compaction relationships. The optimum moisture content of the soil is the water content at which the soils are compacted to a maximum dry unit weight condition. Standard Proctor test method using Tex-114-E procedure was followed. In this

research the soil specimens are prepared and tested at two density conditions maximum dry density (MDD) and 95% MDD condition. It should be noted here that dry density is used in the notation system that is representative of dry unit weight condition.

The soil samples collected from different sites and locations were oven dried for a period of 24 hours. Once dried the soil samples were crushed and pulverized. Pulverized soil samples were then tested for Proctor compaction and other basic soil tests.

3.2.4 Basic laboratory test results

The eight soils collected were tested for basic soil classification, specific gravity (G_s) and Atterberg limits and the results are shown in Table 3.1. The plasticity index (PI) value for the Grayson soil is the highest whereas least plasticity properties are exhibited by Keller soil.

The soils were tested for wet sieve analysis passing through No.200 and the passing finer soil was used for Hydrometer analysis. Figure 3.3 to 3.10 present the gradation curves for all the soils obtained from sieve analysis and hydrometer tests.

Table 3.1: Atterberg limits, Specific Gravity and USCS Classification

Soil	Liquid Limit	Plasticity Index (PI)	Specific Gravity Gs	USCS classification
Anthem	48	27	2.72	CL
Burleson	55	37	2.72	CH
Colorado	63	42	2.70	CH
Grayson	75	49	2.73	CH
Keller	25	11	2.70	CL
Oklahoma	41	21	2.80	CL
San Antonio	67	43	2.79	CH
San Diego	42	28	2.72	CL

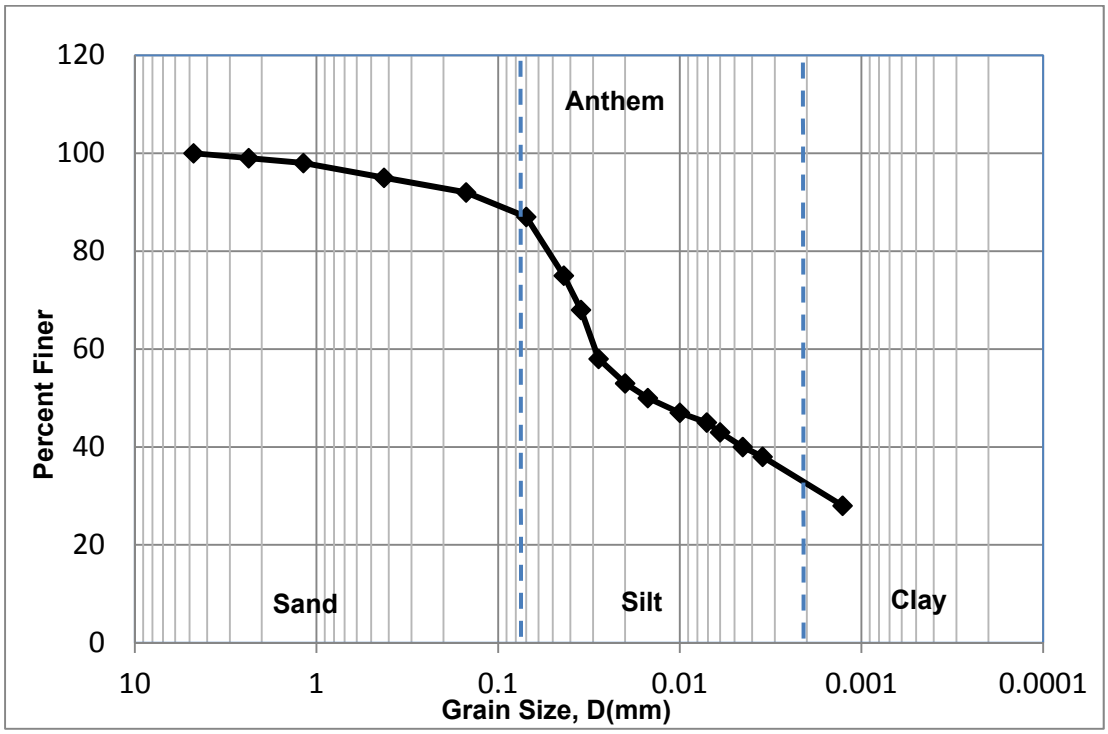

Figure 3.3: Gradation curve for Anthem Soil

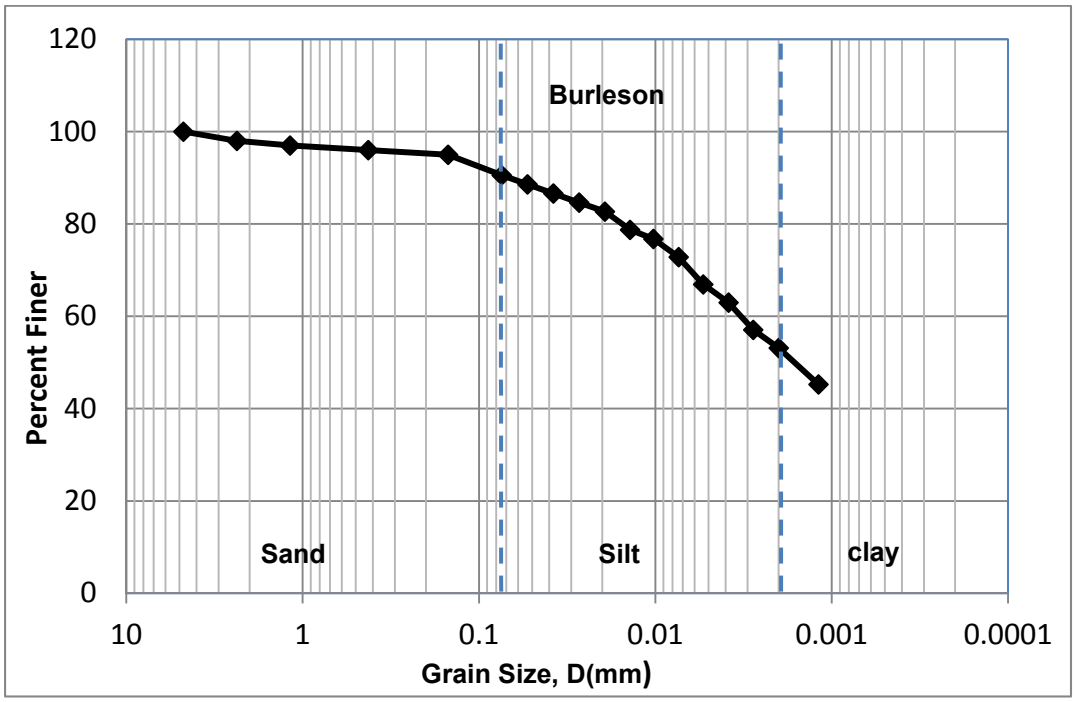

Figure 3.4: Gradation curve for Burleson Soil

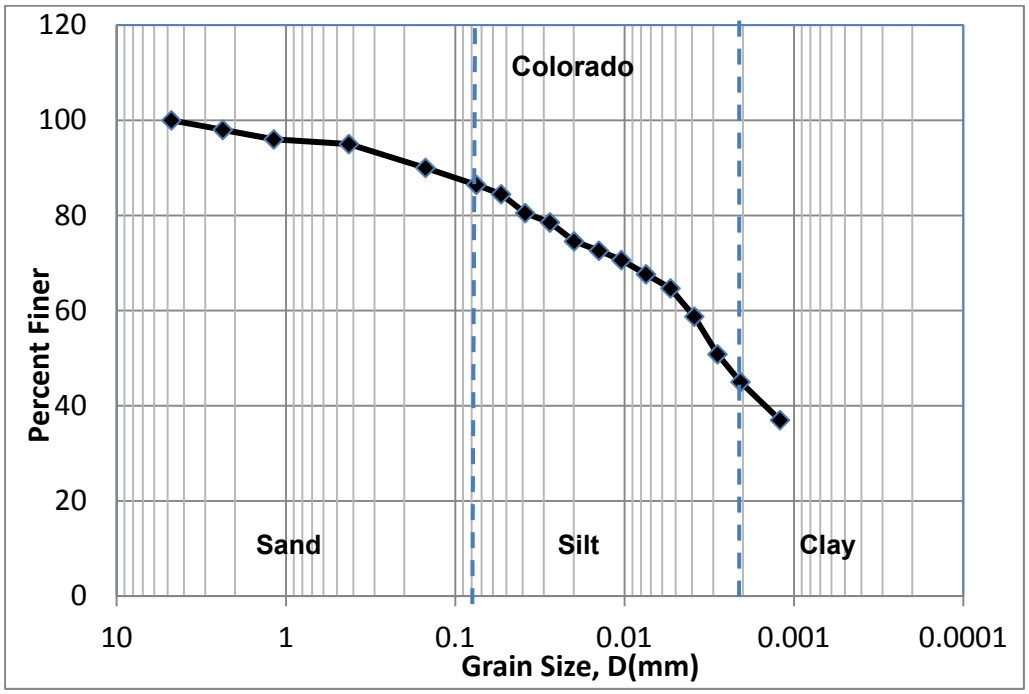

Figure 3.5: Gradation curve for Colorado Soil

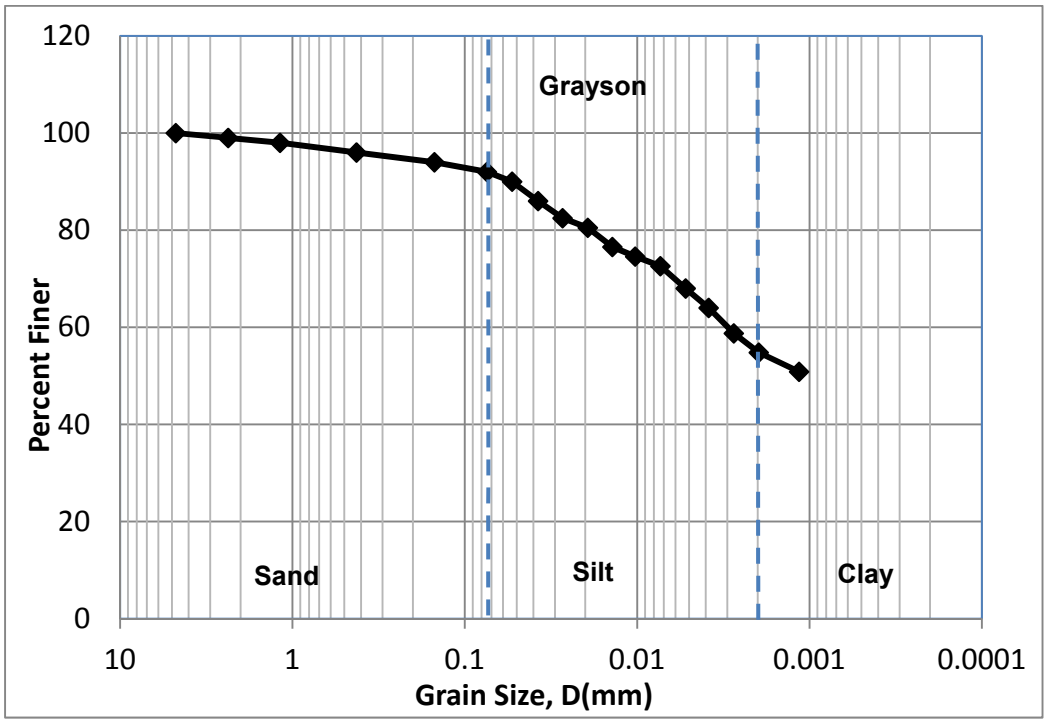

Figure 3.6: Gradation curve for Grayson Soil

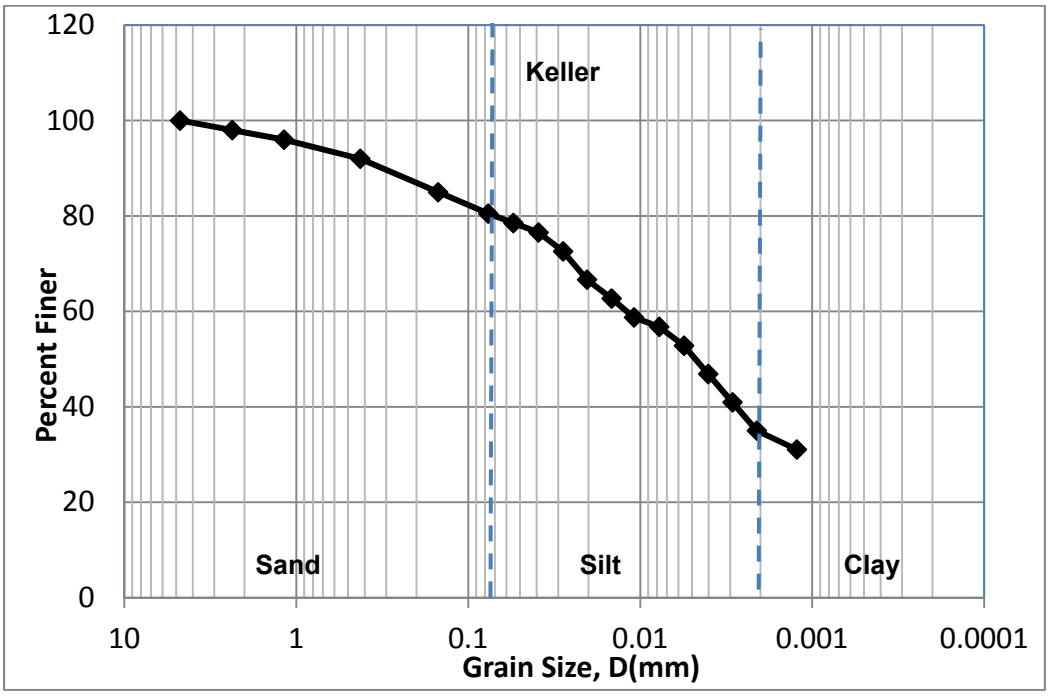

Figure 3.7: Gradation curve for Keller Soil

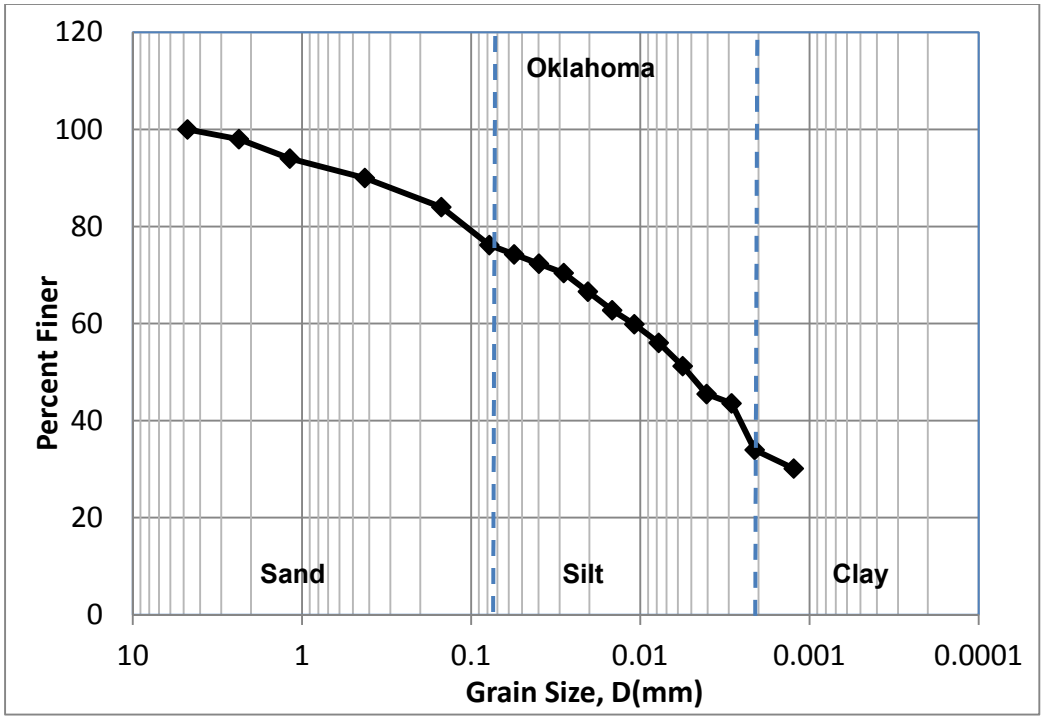

Figure 3.8: Gradation curve for Oklahoma Soil

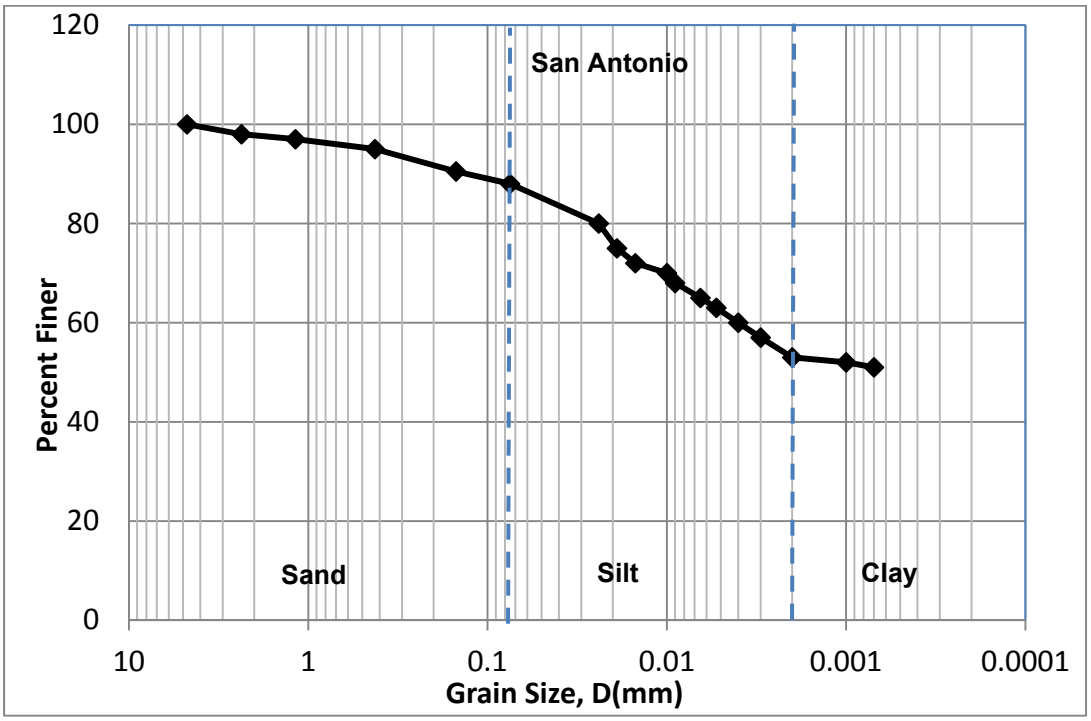

Figure 3.9: Gradation curve for San Antonio Soil

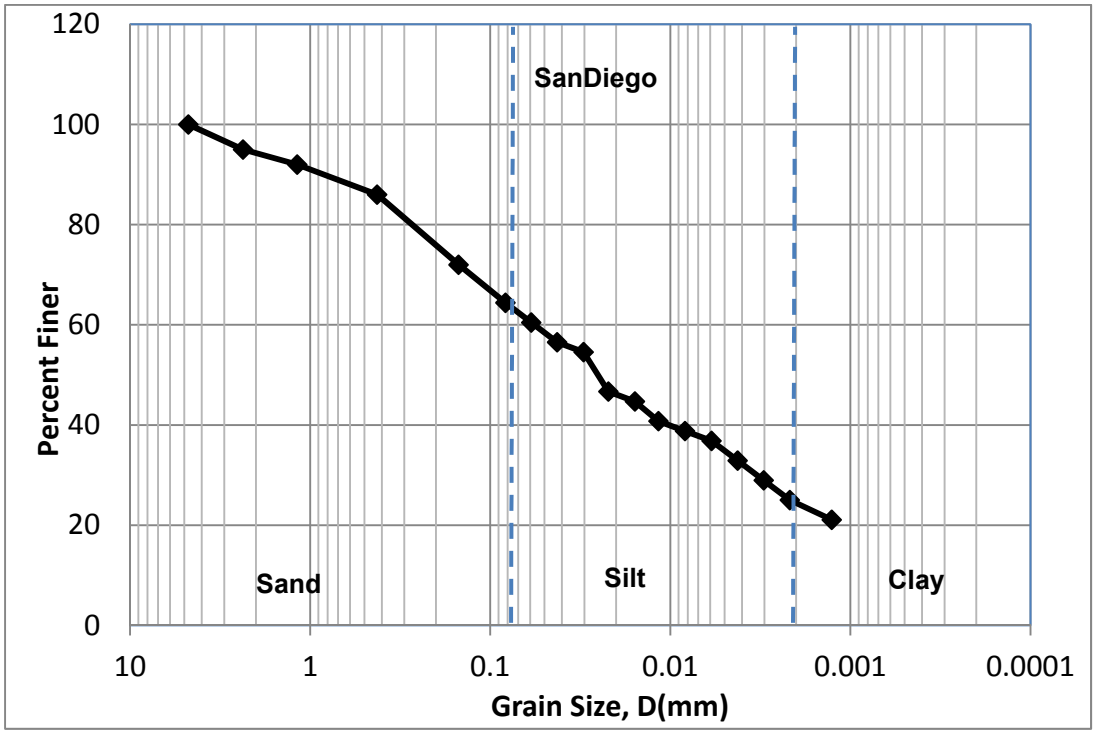

Figure 3.10: Gradation curve for San Diego Soil

The summary of the gradation analysis are given in Table 3.2 below.

Table 3.2: Summary of gradation test on all soils

Soil	Gradation			
	% Gravel	% Sand	% Silt	% Clay
Anthem	0	14	54	32
Burleson	0	10	38	52
Colorado	0	15	39	46
Grayson	0	8	37	55
Keller	0	20	46	34
Oklahoma	0	22	48	30
San Antonio	0	14	34	52
San Diego	0	38	39	23

Standard proctor compaction tests were performed on all eight soil specimens. Table 3.3 below shows the maximum dry density (MDD) and Optimum moisture content (OMC) for all the eight soils.

Table 3.3: Standard Proctor compaction results

Soil	MDD (kg/m^3)	OMC	95% MDD (kg/m^3)
Anthem	1720	18	1633
Burleson	1633	19	1522
Colorado	1649	19	1566
Grayson	1457	24	1385
Keller	1890	14	1795
Oklahoma	1593	24	1513
San Antonio	1608	22	1528
San Diego	1736	17	1649

3.3 Chemical and Mineralogical Tests

3.3.1 Determination of soluble sulfates content

The soluble sulfate in the soil is known for the cause of soil heaving when stabilized with calcium based stabilizers. In the present research, The Modified University of Texas Method (2002) formulated by Puppala et al. (2002) which is based on gravimetric procedure was used for measuring the amount of soluble sulfates in this research. Further details on the sulfate gravimetric method can be found in Wattanasanticharoen (2004). The soluble sulfates determined for all the 8 soils are presented in Table 3.4.

3.3.2 Cation Exchange Capacity (CEC)

CEC of a soil can be defined as the capacity or the ability of the soil to exchange free cations that are available in the exchange locations. One of the earliest methods proposed by Chapman (1965) is the most commonly used method in the field and this method had been selected for the current research. Cation exchange capacity (CEC) can be used to determine the mineral composition of the soil specimen with a high CEC value indicating a high amount of expansiveness due to the presence of the clay mineral Montmorillonite where as a low CEC indicates the presence of non-expansive clay minerals such as Kaolinite and Illite. The method involves addition of a saturating solution and then removal of the adsorbed cations using an extracting solution. Procedural steps of this method are presented in Figure 3.11. The saturating solution used here is ammonium acetate (NH_4OAc) at pH 7. This solution is added to prepared soil specimen (preparation involves treating for organics with 30% hydrogen peroxide (H_2O_2) and set aside for 16 hrs after shaking for half hour, to ensure that all the exchange locations are occupied by the ammonium ion ($NH4^+$).

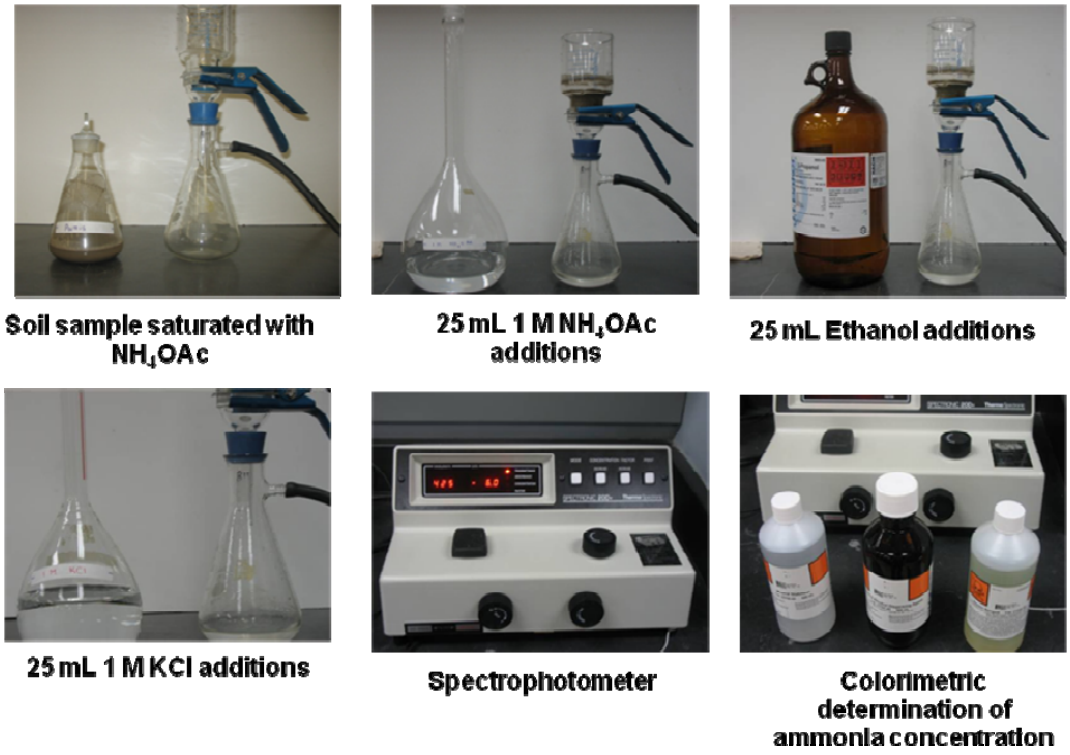

Figure 3.11: Showing the testing of Cation Exchange Capacity (CEC)

Then the solution is filtered through a Buchner funnel and washed with 4 different 25 mL additions of NH_4OAc. This step is to bring out all the cations from the soil sample solution that has been replaced by ammonium ion. Excess NH_4OAc removed by the addition 8 different 10 mL additions of 2-propanol. Now, all the cation places are replaced by the ammonium ion and excess ammonium is also removed. The CEC of the soil sample can be obtained if we can measure the amount of ammonium ions by taking them out. This is done by washing the sample with 8 different 25 mL additions of 1M potassium chloride (KCl) solution. Though potassium ion (K^+) has similar electro negativity it has higher molecular weight and has the ability to substitute the $NH4^+$ ion.

The concentration the $NH4^+$ in the KCl extract gives the CEC of the soil. The detailed step by step procedure of how the test is conducted is given in Chittoori (2009). The CEC measured for all soils are presented in Table 3.4.

3.3.3 Total Potassium (TP)

Illite is the only clay mineral to have potassium in its structure (Mitchell & Soga, 2005). Hence measuring the amount of potassium ion in the soil gives a direct indication of the presence of the mineral Illite. The test procedure formulated by Knudsen et al. (1984) was followed to obtain the amount of total potassium present in the soil. The method involves a double acid digestion technique developed by Jackson (1958) which uses two acids (Hydrofluoric acid and Perchloric acid) to break the mineral structure of the soil and extract the potassium ions from the structure. Once the potassium is extracted, its concentration in the solution can be obtained with the help of a spectrophotometer or any other suitable device.

Procedural steps of this method are presented in Figure 3.12. The test starts by taking 0.1 gm of soil in a teflon digestion vessel. The original method recommends the use of platinum vessels as the hydrofluoric acid used has the ability to dissolve silica and glass is 90% silica.

However the usage of platinum vessel was not possible due to cost constraints hence other possible alternatives were looked at and teflon vessel was found to have resistance to the acids that are being used in the current test procedure (Hydrofluoric acid).

Teflon vessel was selected due to its high temperature tolerance (200^{o}C). Hence, 5 mL of hydrofluoric acid and 0.5 ml of perchloric acid are added to the 0.1 gm of the soil sample. The TP measured for all the 8 soils in the present research study were presented in Table 3.4

Weigh 0.1000 gm of the soil sample

Add 5 ml of Hydrofluoric acid

Add Hydrofluoric acid and perchloric acid

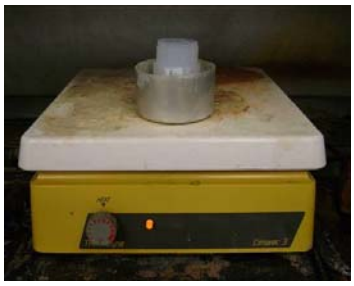

Heating the sample on a hot plate

6N HCl

Colorimetric determination of Total Potassium

Figure 3.12: Testing procedure for Total potassium (TP)

Hydrofluoric acid dissolves the silicate mineral structure and releases the interlayer cations, perchloric acid is used as an oxidizing agent to oxidize the organic matter in the soil sample. Then the vessel is placed on hot plate and heated to 200^{o}C and then cooled and another addition of HF and $HClO_4$ is made and reheated on the hot plate. Now the sample is added until it is dry, the process is repeated to make sure all the interlayer cations are released and then finally 6N HCl is added and the amount of potassium in this solution is obtained by using a spectrophotometer. Procedural steps followed for the determination of total potassium are detailed in Chittoori (2009).

3.3.4 Specific Surface Area (SSA)

Specific surface area or SSA of a soil sample is the total surface area contained in a unit mass of soil. This property of the soil is primarily dependent on the particle size of the soil.

Soils with smaller particle size have higher specific surface areas. It should be noted here that a soil with high specific surface area has high water holding capacity and greater swell potential. The most commonly used method in the field of agronomy is the adsorption of ethylene glycol monoethyl ether (EGME) (Carter et al., 1986).

This involves saturating prepared soil specimens, equilibrating them in vacuum over a calcium chloride – EGME ($CaCl_2$-EGME) solvate, and weighing to find the point when equilibrium is reached. Specific surface is then determined from the mass of retained EGME in comparison to the amount retained by pure montmorillonite clay, which is assumed to have a surface area of 810 m^2/g (Carter et al., 1986).

Test procedure typically takes two days to complete. This method was fully evaluated for geotechnical usage by Cerato and Lutenegger (2002) and concluded that the method is applicable to a wide range of mineralogies and is capable of determining specific surface area ranging from 15 to 800 m^2/g. They also indicated that the procedure gives reliable results. A detailed procedure for the determination of SSA by EGME method that has been followed are detailed in Chittoori (2009). Details of the procedural steps of this method are presented in Figure 3.13.

The SSA measured for all the 8 soils in the present research study were presented in Table 3.4. Chittoori (2009) presented an artificial neural network model to determine the percentage minerals present in clay from properties like CEC, TP and SSA.Table 3.5 shows the percentages of each mineral present in the clays.

Dried soil sample

Addition of 3 mL of EGME

Desiccator containing $CaCl_2$

Desiccator containing $CaCl_2$-EGME Solvate over $CaCl_2$

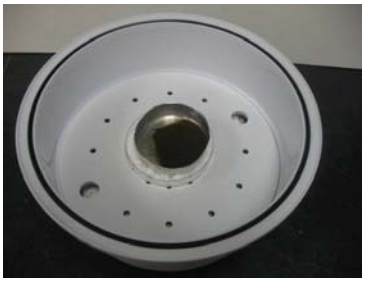

EGME mixed soil sample placed in the desiccator placed

Apply vacuum to the desiccator

Figure 3.13: Testing procedure for Specific Surface Area (SSA)

Based on the methodology for quantification of minearls proposed by Chittoori and Puppala (2011), minerals are quantified in the present test soils and these results are presented in Table 3.4 and Table 3.5.

Table 3.4: Mineralogical tests performed on the soils

Soil	CEC (meq/100g)	TP	SSA (m^2/g)
Anthem	71.7	1.46	118.5
Burleson	100.1	1.17	132.4
Colorado	91.6	2.10	185.0
Grayson	116.1	1.43	223.0
Keller	60.0	1.10	115.0
Oklahoma	63.3	4.20	76.3
San Antonio	97.4	1.85	192.4
San Diego	87.2	1.51	92.6

Table 3.5: Showing the mineralogical properties of the clays

Soil	Soluble Sulfates (ppm)	% Montmorillonite	% Illite	% Kaolinite
Anthem	2082	25.2	24.4	50.4
Burleson	1835	33.7	19.6	46.7
Colorado	280	35.7	35.0	29.3
Grayson	13861	43.3	24.0	32.7
Keller	963	21.9	18.4	59.7
Oklahoma	19281	19.7	70.0	10.3
San Antonio	6791	37.8	30.9	31.3
San Diego	152	26.9	25.3	47.8

3.4 Engineering tests

Engineering tests in this research were used to study the swell behavior and pore void composition of the eight selected soils. Tests like one dimensional swell strain, swell pressure and 3 dimensional swell strains under confinements were studied to understand the swell behavior of the test soils. Determination of soil water characteristic curve (SWCC) which is the fundamental soil inherent composition property was also studied. Techniques like filter paper, pressure cell and potentiometer were discussed along with their working principles. Determination of soil porosity and the pore networks are characterized using techniques like Mercury Intrusion Porosimetry (MIP) and X-ray computed Tomography (XCT). Details of their working principles and test procedures followed are presented in the coming sections.

3.4.1 Soil sample preparation

A static compactor, as suggested in the AASHTO T-307 for preparing fine-grained soil specimens, was used in the present research. With this method, specimens with targeted moisture and density levels can be prepared in a short time. A comprehensive study was carried out by Wanyan et al. (2008) to develop a process for static compaction of clays in one layer with small variation in density. Compaction process that was recommended in that study

was used here for the preparation of soil specimens. The specimens were prepared at a low strain rate to maintain uniform density throughout its height. The specimen preparation procedure was presented in Figure 3.14. After compaction, the soil sample was transferred to the desired test equipment for further engineering tests. Specimens of 2.54 cm (1 inch) height and 6.35 cm (2.5 inches) in diameter were prepared and used for the one dimensional swell and swell pressure testing. Samples having sizes of 10.16 cm (4 inches) in height and 5.08 cm (2 inches) in diameter were used for the 3-D Swell strain testing.

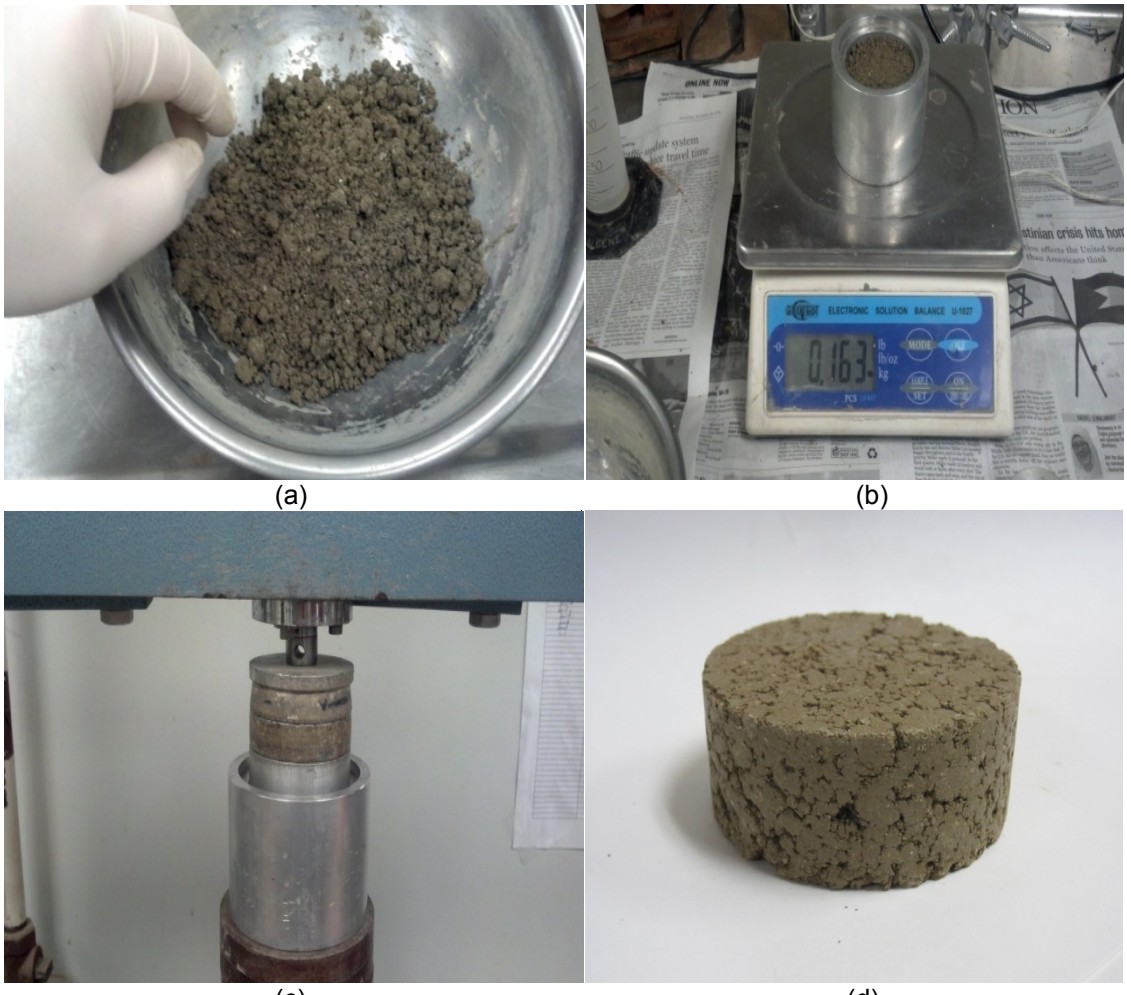

(a) (b)

(c) (d)

Figure 3.14: Sample preparation procedure (a) soil mixture (b) placing soil in to the mould (c) static compaction (d) prepared soil specimen

3.4.2 One Dimensional Swell

ASTM D 4546 covers the determination of free swell of a compacted or intact clay sample. One dimensional swell strain for the soil specimens were performed on a conventional consolidometer setup. The soil samples obtained from the above compaction procedure were placed in the consolidometer. Filter papers were then placed both on top and bottom of the soil specimen. A token load of 7 kPa or 1 psi was applied on the soil specimen prior to the start of testing. Once proper seating loading was placed and the dial gauges were positioned in place to monitor vertical soil deformation, the soil specimen was subjected to moisture inundation which resulted soil swelling with time. The time versus swell induced soil deformation by the soil specimen was recorded and these results are used to estimate 1-D swell strains.

3.4.3 Swell pressure test

The load back swell pressure test was conducted as per ASTM D-4546 and is defined as the magnitude of pressure required to bring back the soil specimen to initial condition in vertical direction. An initial token load of 7 kPa (1psi) is applied on to the soil specimen for proper contact between the load frame and soil specimen. The test set up for the present study is shown in Figure 3.15.

Two porous stones were placed at the top and bottom of the specimens. A dial gauge was used to monitor changes in specimen's movement. The specimens were fully soaked in the standard consolidation setup. Once the specimen reaches a saturated swelling point, loads were added in order to bring back the soil to its original position. The total load applied to the specimen to bring back to its original position was then used to calculate its swell pressure. Appliance correction factors as studied in literature were applied to each of the swell pressure tests for the determination of actual swell pressure. This test is commonly used to determine maximum swell pressure of the soil specimen.

Figure 3.15: 1-D swell and load back swell pressure test setup

3.4.4 3-D swell strain apparatus:

The determination of vertical swell strains for soils under different overburden seating pressures has been studied by many researchers. The main challenge is the determination of the lateral swell strains exhibited by the soil specimen when confined in all the three dimensions. The main objective of this test is to simulate the swell strains of a soil mass present at a particular overburden depth. Figure 3.16 shows the 3-D swell strain apparatus designed at the University of Texas at Arlington and used in the present research.

The soil specimen of 10.16 cm (4 inches) in height and 5.08 cm (2 inches) in diameter was encased in the acrylic chamber. De-aired water was then used as a medium of confinement in this test. A latex membrane was used to restrict the water from the chamber from entering the soil specimen. Soil specimens used in this test have a h/d ratio of 2. Hence, all the soil specimens used were of 10.16 cm (4 inches) in height and 5.08 cm (2 inches) in diameter.

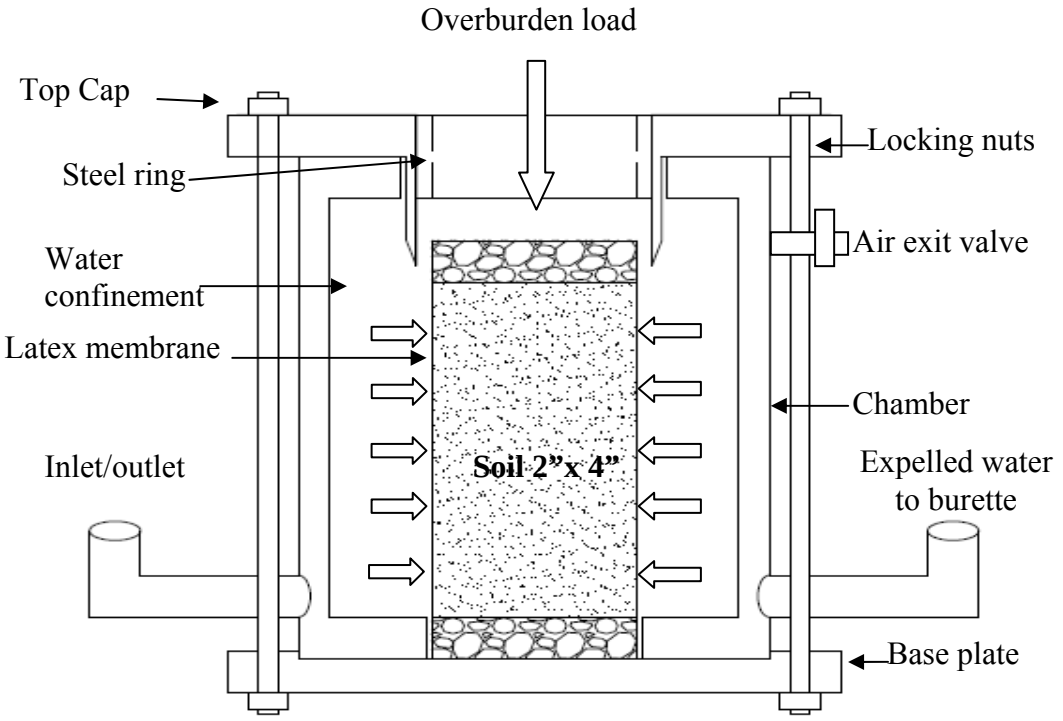

Figure 3.16: 3-D Swell strain test setup designed at UTA

The inlet/outlet valves on either side of the test apparatus were connected to a conventional pressure regulator with volume change measurement apparatus. The main challenge in this apparatus is the separation between horizontal and lateral pressure application. This is achieved with the help of a steel metallic ring as shown in Figure 3.17 (a) and (c).

An inner grove was made to the steel ring to house an O-ring (Figure 3.17 (b)). This O-ring acts as a moisture barrier for the porous disk which was attached to the soil specimen. The steel ring slides into the top cap and interlocks the soil specimen to slide freely over the outer ring.

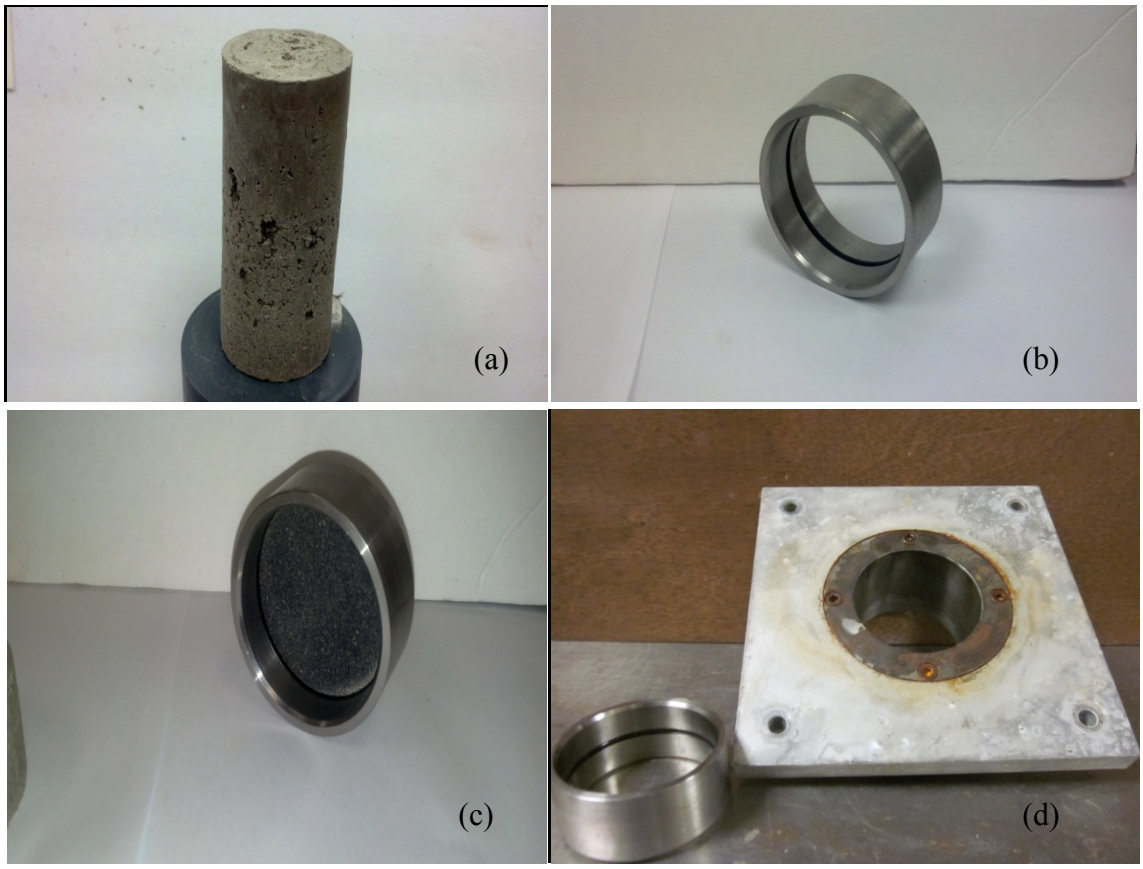

Figure 3.17: Pictures showing (a) compacted soil specimen (2” x 4”) (b) steel ring (c) Steel ring with porous disk attached (d) Top cap with steel ring

The soil specimen as shown above was placed inside the pressure chamber surrounded by a latex membrane. Porous disks are placed at the top and bottom of the soil specimen. The top porous disk was attached to the steel ring. This steel ring slides in to the top cap and locks the joint. This lock prevents the horizontal or lateral confinement from interfering with the vertical surcharge. Hence both the confinements are achieved independently.

In the present research, uniform confinement was applied to the soil specimens both in horizontal and vertical directions. Once the top cap is fastened to the bottom plate with the help of nuts, the chamber was connected to the inlet and outlet valves present on both sides to the pressure regulator. The chamber is then filled with the de-aired water. Any excessive air bubbles present in the chamber were removed with the help of air exit valve present at the side

of the chamber. The vertical pressure was then applied to the specimen with dial gauge arrangement as shown in Figure 3.18 (b).

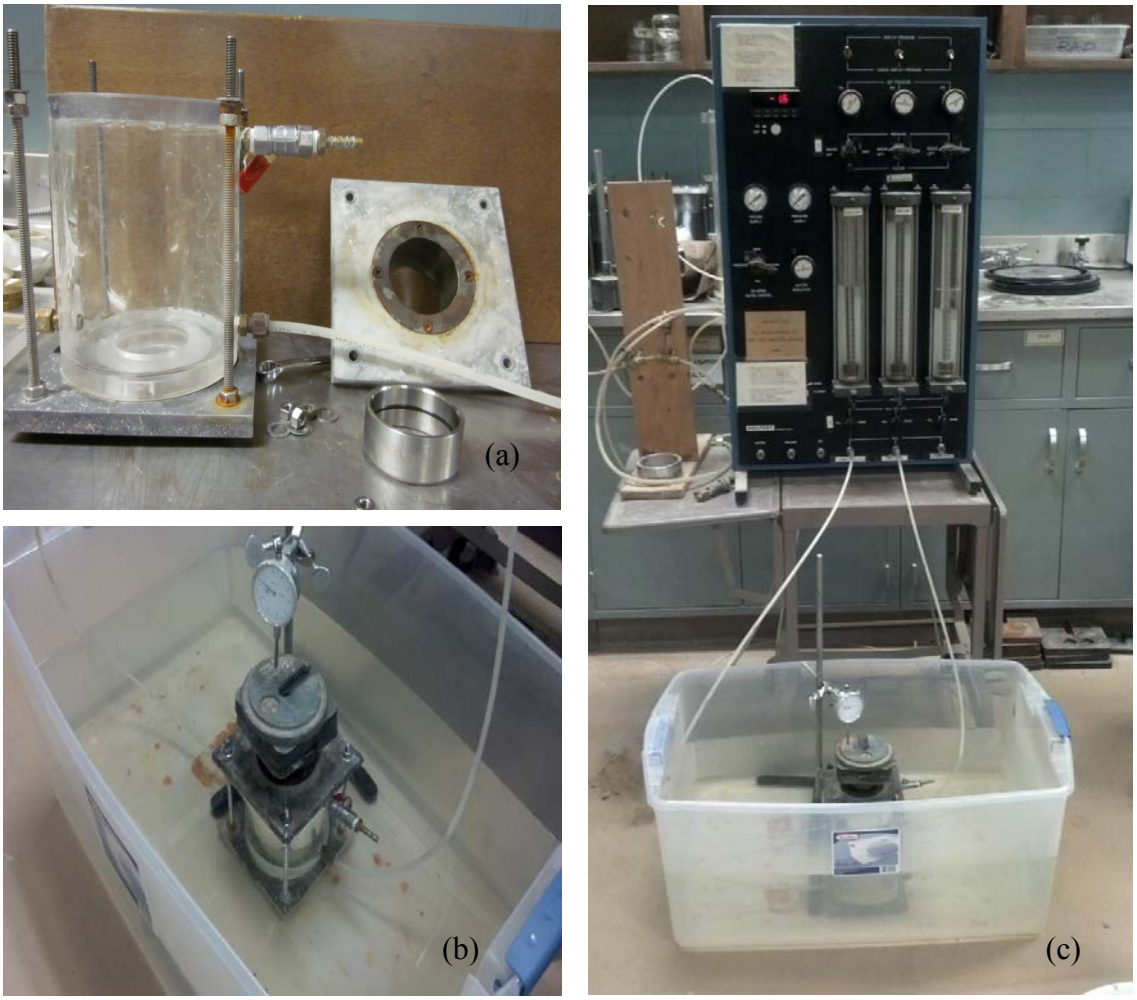

Figure 3.18: Showing (a) components of the setup (b) dial gauge arrangement to measure vertical movement (c) Test apparatus

Once proper application of pressure was achieved and no leaks are found within the membrane, the tub was inundated with water and the sample was allowed to saturate and undergo heaving.

Soil specimen was allowed to saturate under confinement for a period of 24 hours. Confinement levels of 7 kPa (1 psi), 50 kPa (7.25 psi), and 100 kPa (14.5 psi) were applied on

to each specimen for the whole saturation periods. Vertical strain measurements were recorded with the help of a dial gauge and horizontal strains were calculated as shown below.

The change in volume of water in the chamber is directly correlated to the areal change for the soil specimen.

During the volume change the height of the chamber remains constant; hence the total volume change is related to the areal change in the chamber. The areal change in the soil specimen is due to the change in outer diameter of the specimen from swelling. The radial strain in the horizontal direction is thus calculated from the observed volume change in the apparatus.

The absorption of water in the acrylic material was observed in many research studies. Calibration of the chamber is an essential part of the measurement of radial swell strains. Hence, a steel bar of the similar dimensions as soil specimen is placed in the chamber and tested at two confinements 50 kPa (7.25 psi), and 100 kPa (14.5 psi)) for a period of 3 days. Figure 3.19 shows the change in radial strain observed from the chamber.

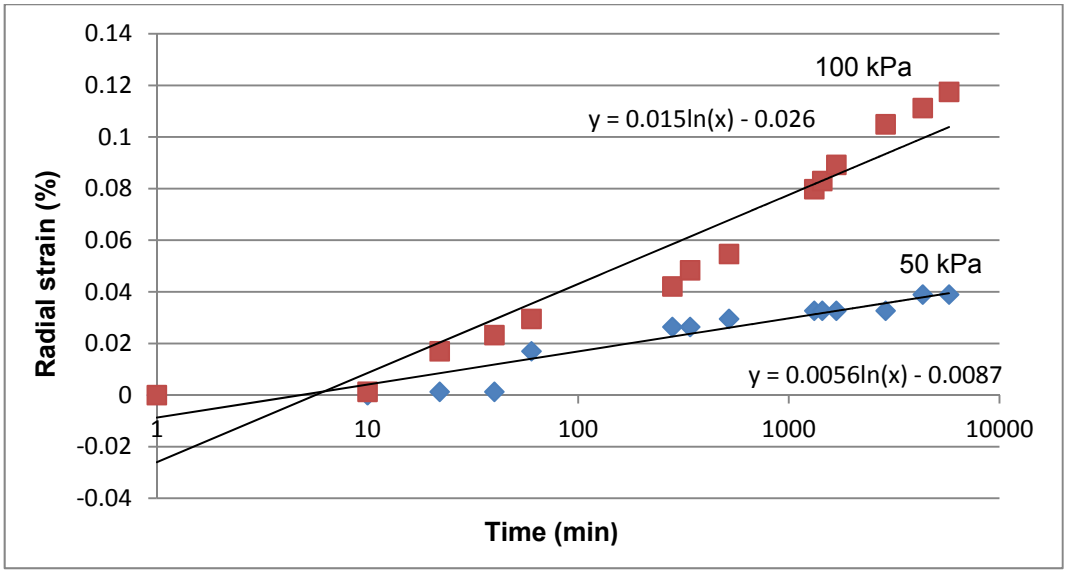

Figure 3.19: Correction factor for diffusion of water in acrylic chamber

The following correction was applied to the readings of radial strain to get the exact radial strain experienced by the soil specimen at these confinements. The final swell strains

obtained for the soil specimens under different confinement levels are presented in the next chapter.

3.5 Soil suction studies

The soil water characteristic curve (SWCC) is one of the fundamental behavior of a soil that correlate soil matric suction with moisture content property. There are different methods to determine the SWCCs of a given soil. In the present research three methods have been extensively used to determine the SWCCs of all test soils. They are presented in the following sections.

3.5.1 Filter paper method

The ASTM Filter Paper Method (ASTM D5928-94 - Standard Test Method for Measurement of Soil Suction) determines the matrix suction of the undisturbed and remolded specimens in the unsaturated state. Filter paper method is based on the assumption that the filter paper will come to equilibrium with a soil having a specific suction. This equilibrium state can be obtained with vapor moisture exchange or liquid exchange. When a dry filter paper is placed in direct contact with the soil specimen then liquid exchange occurs between the filter paper and soil specimen. The recorded moisture of the filter paper is the matric or solute suction for a soil specimen. Similarly when a dry filter paper is suspended above a soil specimen without contact, the moisture transfer between the soil and filter paper occur thorough vapor exchange. This measured moisture content in the filter paper corresponds to 'total suction' of the soil.

The water content of the filter paper corresponds to a suction value given in the filter paper calibration curve designed by researchers. The same calibration curve is used to obtain total and matric suction for any soil. The filter paper method is used to measure a wide range of suctions. This method has been utilized in the current research to get the suction over higher ranges.

The filter papers used in the current research are as specified by ASTM E832. Figure 3.20 presents the Whatman No.42 filter papers used in the current research and the calibration chart for these filter papers for the determination of matric suction.

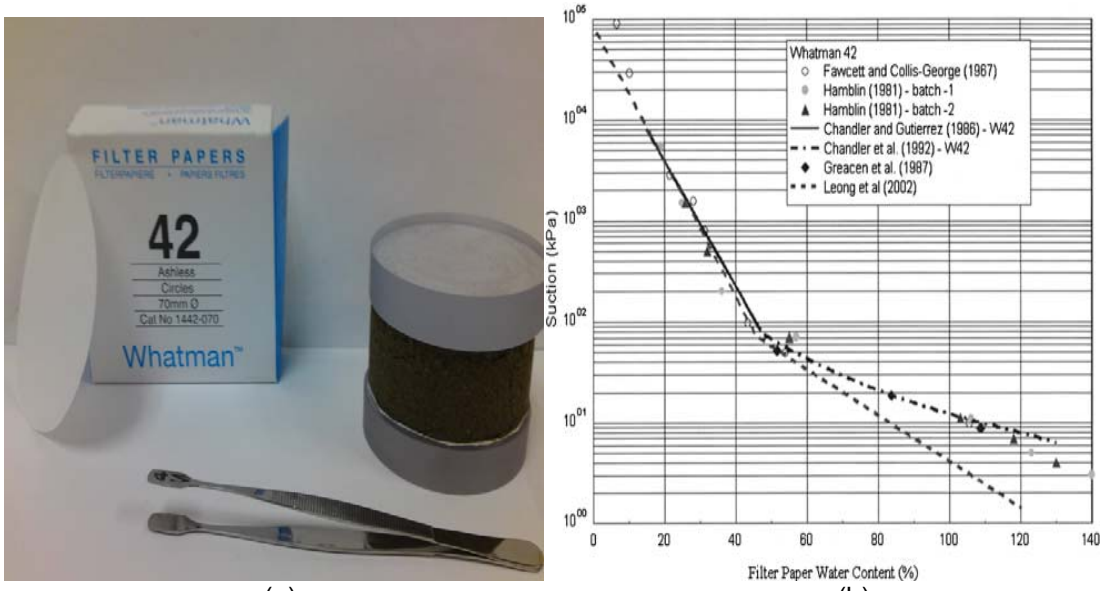

(a) (b)

Figure 3.20: (a) Filter paper technique and (b) calibration chart for Whatman No 42 filter paper

3.5.2 Pressure cell apparatus

The pressure cell apparatus uses axis translation technique to measure the matric suction of a soil specimen. This is achieved with the help of a High Air Entry value disk (HAE). This disk acts as an interface between the unsaturated soil and pore water and allows only water to pass through. Hence, the volume of water expelled from the soil sample was collected through the disk in to the burette columns. The flow of water through the HAE disk was monitored for a period of time. Air pressure of a known value was applied until the sample reached an equilibrium stage and then shifts to the next pressure application. This can be identified by lack of change in height of water in the burettes. Figure 3.21 presents the pressure cell apparatus utilized in the current research.

The maximum matric suction that can be maintained across the HAE disk is called its air entry value. In the current research the HAE disks have an entry value of 5 bars.

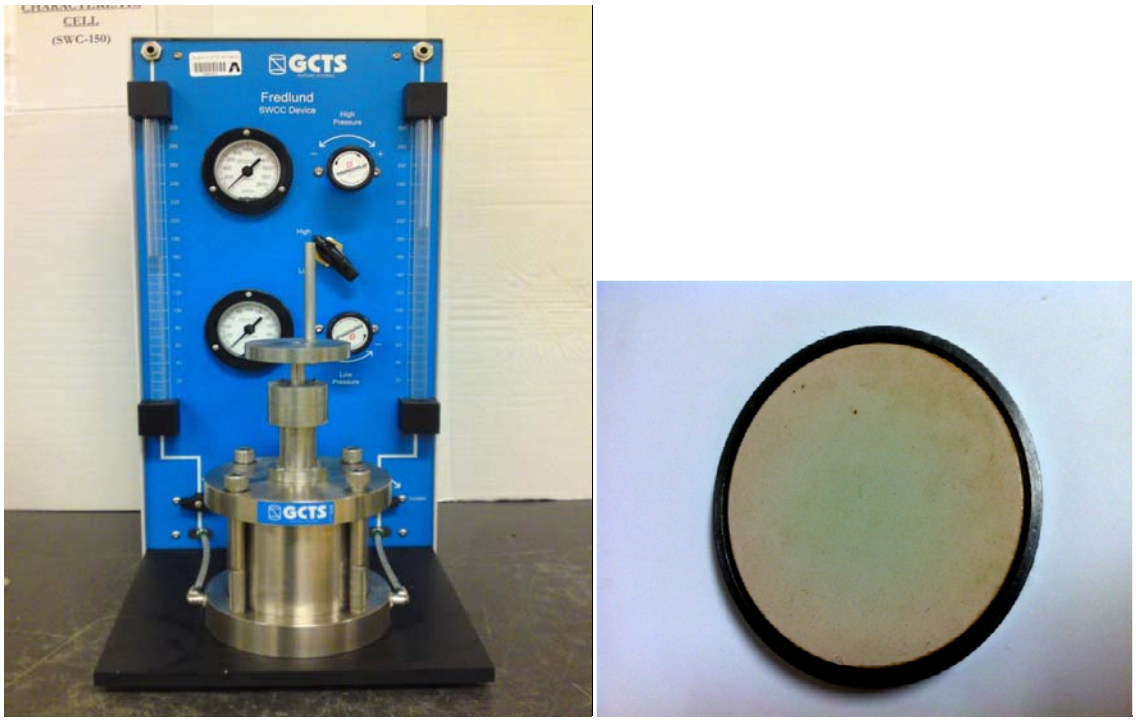

(a) (b)

Figure 3.21: (a) Pressure cell apparatus and (b) high air entry value disk (HAE)

3.5.3 WP4C Dewpoint potentiometer

The WP4 measures water potential by chilled mirror dewpoint technique which is determining the relative humidity of the air above a sample in a closed chamber. At equilibrium, relative humidity measured is in direct relationship to the water potential.

The soil sample was cut in to thin sections and placed in the container shown below. The container was cleaned on the top to make sure no soil particles come in contact with the relative humidity sensor. Once the steel cup is placed in the potentiometer, the sensor locks the top of the cup to measure the relative humidity of the air present at the top of the soil specimen. After equilibrium was achieved the potentiometer displays the total matric suction of the soil specimen. This device has been used in the present research to determine the total suction levels for soil specimens at high suction ranges. Figure 3.22 presents the WP4C potentiometer apparatus utilized in the current research.

Figure 3.22: WP4C dewpoint potentiameter

3.6 Pore studies

Porosity of a soil specimen is important in understanding the formation, structure, and voids. The porosity of a material influences its physical properties and, subsequently, soil behavior in its surrounding environment. The adsorption, permeability, strength, density, and many other factors are also influenced by the porosity of the material or a soil. Two methods are presented here to identify and measure the pore network present in a given soil specimen.

3.6.1 Mercury intrusion porosimetery (MIP)

Mercury intrusion porosimetry or MIP is based on the premise that a non-wetting liquid (contact angle greater than 90) will intrude capillaries (pores of a solid) under external pressure. Since mercury does not wet most substances and will not spontaneously penetrate pores by capillary action, it must be forced into the pores by the application of external pressure. The required equilibrated pressure is inversely proportional to the size of the pores, only slight

pressure being required to intrude mercury into large macro-pores, whereas much greater pressures are required to force mercury into small pores.

The Equation (1) developed by Washburn (1921) is used to calculate equivalent pore radii from the applied pressure on to the mercury.

$$r = \frac{-2\gamma \cos\theta}{p} \quad (1)$$

Where θ is the contact angle between the mercury and the surface of the soil tested, r is pore radii, p is pressure applied and γ is the surface tension of mercury.

The MIP equipment consists of a penetrometer where the soil sample is seated. Trimmed soil mass of less than 5 gms is placed in the penetrometer after the soil sample is freeze dried. Freeze drying is a process of removing the moisture content of the soil specimen without disturbing its internal pore structure. This method has been proved effective by Acar and Olivieri (1990) and hence was used in the current research. The freeze-dried specimen was surrounded by Mercury in the sample tube and hence pressurized in small increments.

The analyses were performed in two stages, corresponding to the different pressure ranges, a low pressure phase (below atmospheric pressure), which corresponds to pore diameters ranging from approximately 9 to 200 μm and a high pressure phase (above atmospheric pressure), which corresponds to pore diameters ranging from 7 nm to 9 μm.

The volume of mercury entering the specimen after each increment was automatically recorded. Each pressure increment forced mercury into the accessible soil pores of a diameter larger than or equal to that calculated by the Washburn (1921) equation for the given pressure. The device is very sensitive and can detect a change in mercury volume of under 0.1μL. The intrusion volume increases slowly in the beginning. But when the intrusion pressure reaches a certain value (that is threshold value Pt), the intrusion volume increases quickly. Figure 3.23 (a) and (b) presents the standard MIP test equipment utilized for the current research.

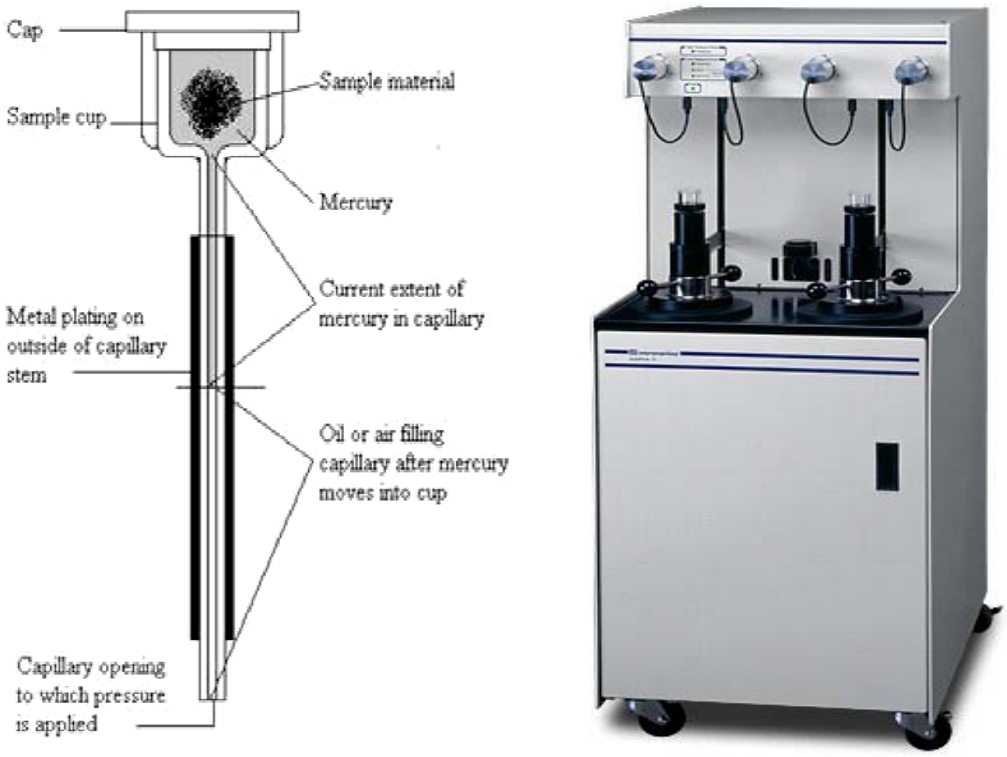

(a) (b)

Figure 3.23: (a) Penetrometer and (b) MIP equipment

The ink-bottle effect exists in the intrusion stage. The extrusion curve does not coincide with the intrusion curve due to the retention of mercury in the pores of soil specimen during the mercury extraction phase.

3.6.2 X-ray Computed Tomography (XCT)

CT is a non-destructive, non-invasive technique used to investigate the pores and internal structure of a solid mass, and is based on the principle of the attenuation of an electromagnetic wave beam that is focused on the object.

The characteristic of an absorbing material to scatter or absorb a photon is called the attenuation coefficient. A material with high density will attenuate more x-rays than a low-density material; therefore, two materials of different densities will appear differently in an X-ray image. X-ray computed tomography (XCT) is an imaging technique in which an object is placed

between an X-ray source and a detector, and the object is rotated while the X-ray passes through it, collecting information about its internal structure. As the X-ray beam passes through an object, some photons are either scattered with some loss of energy, or completely absorbed in a photoelectric interaction. The digital image created during the CT process provides an internal cross-section of the specimen in which different materials can be distinguished. Below Figure 3.24 shows the X-ray computed tomography principle.

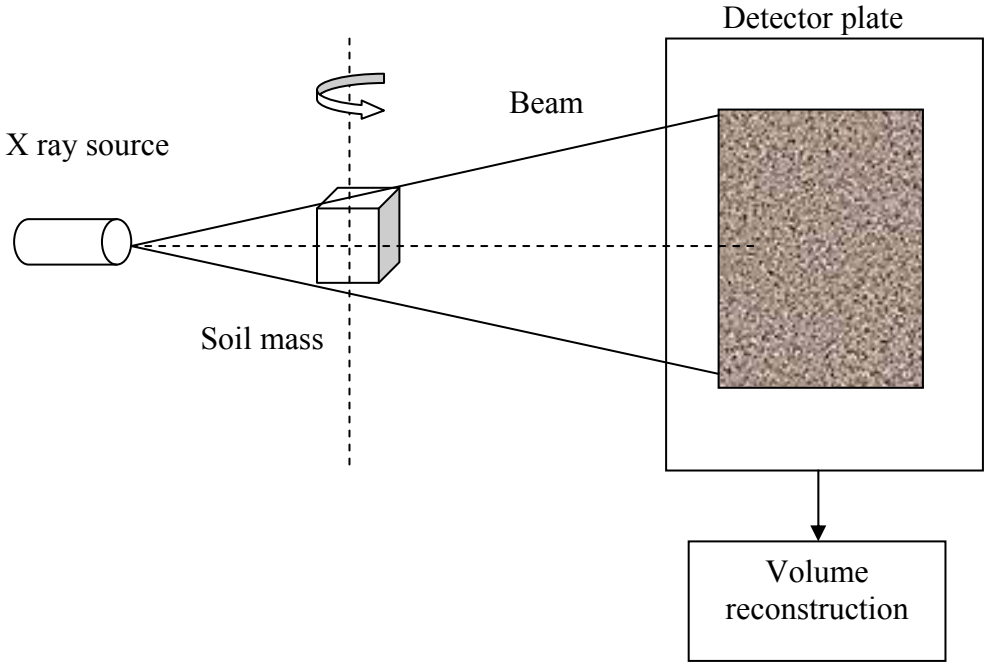

Figure 3.24: X-ray computed tomography principle

Image reconstruction involves an overlaying procedure in which individual X-ray images are aligned and stacked on top of each other to form a graphical two-dimensional image of the object. This image provides a cross-sectional view of the object as if it had been cut through the plane at the scan location. CT equipment is capable of performing scans at increments as small as 1/8 degree of rotation. For this study, 1/4 degree rotation increments were used with a full 360-degree rotation of the soil samples relative to the X-ray, resulting in 1,440 X-ray scans per image.

A representative soil specimen of 1 cm in height, width and depth were sliced from compacted soil specimens as shown in Figure 3.25 (a). Once sliced the specimens, the specimens were oven dried or saturated depending on the requirement for computed tomography scan. The soil specimen has to be seated steady in the CT chamber, if any changes in the initial position occur, the CT scan will be blurred. Hence, proper care needs to be taken when placing the specimen in the chamber.

(a)

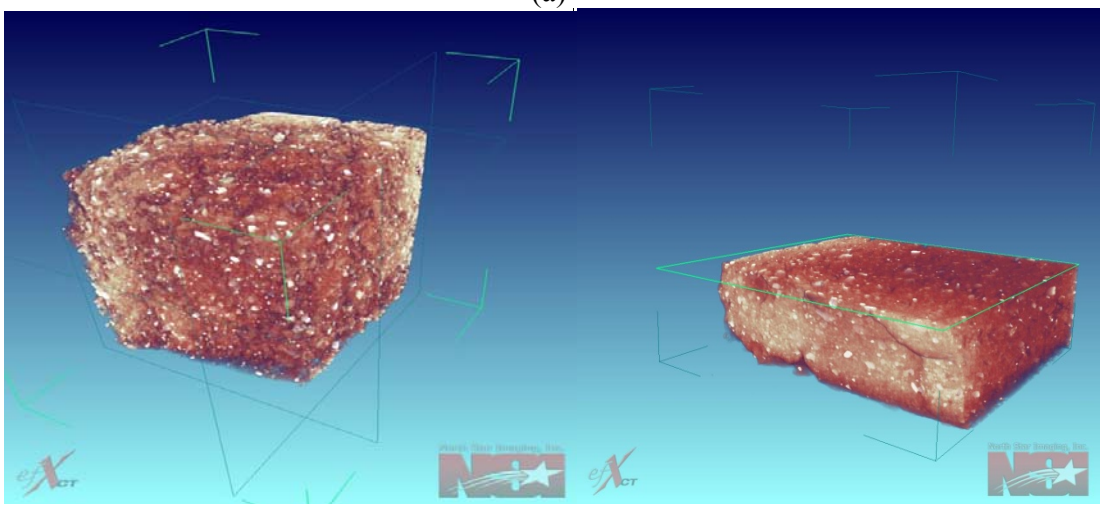

(b) (c)

Figure 3.25: (a) Soil specimens prepared for Tomography testing (b) CT Scan of a compacted specimen (c) Sliced CT Scan for 2-D pore identification

Figure 3.26 presents the X-ray computed tomography equipment used for the current research.

Figure 3.26: X-ray tomography equipment used at UTA

The main challenge lies with the scanning of a saturated expansive clay specimen. The sample loses moisture and undergoes shrinking process once removed from saturation. Hence, a new technique was followed to keep the soil specimen from shrinking while performing a CT scan. The saturated soil specimens were transferred to a freezer and then allowed to freeze for one day. Once frozen the soil specimens were immediately transferred to the XCT equipment. A plastic membrane arrangement was placed around the soil specimen in order to restrict moisture transfer from soil specimen. After the placement, a one hour CT scan was performed on saturated soil specimens followed by image reconstruction.

3.7 Summary

Basic soil classification and other geotechnical testing performed on the eight expansive soils are presented in this chapter. Chemical analysis to determine the mineral content of expansive clays is presented along with their procedures. Details of the test results and the variation of pore network with moisture content in clays are studied in Chapter 5.

The present chapter details the different techniques that are used to determine the soil swell and composition properties. Swell behavior of compacted soil specimens was determined using different swell measurement procedures like 1-D vertical swell strain, swell pressures and novel 3-D swell strain tests. The details and working of each test procedure are discussed in this chapter. Determination of soil moisture relationships were developed using suction measurement techniques. Advanced techniques like mercury intrusion porosimetry and X-ray computed tomography which are used to study the pore space and distribution are discussed in detail along with their working principles.

The next chapter deals with the test results obtained from different swell measurement test procedures.

CHAPTER 4

SWELL BEHAVIOR OF EXPANSIVE SOILS

4.1 Introduction

Expansive soils are characterized based on their swell and shrink behaviors exhibited. Many laboratory tests have been used in the characterization of expansive soils. The differences between test procedures vary with the type of confinement applied on the soil specimen, the swelling process and the monitoring of strains. The one dimensional consolidometer has been widely accepted method for testing swelling potential of soils (Holtz and Gibbs, 1956). In the current research, one dimensional vertical swell strains as well as load back swell pressures were measured in a conventional consolidometer setup. A novel 3-dimensional swell strain measurement apparatus was used for the measurement of swell strains in all directions. Details of the working principles and techniques are given in Chapter 3. Swell strain results exhibited by all the eight soils are presented in this Chapter.

4.2 Measured Swell Behavior

4.2.1 Anthem Soil

Anthem soil was collected from the state of Arizona. Based on the USCS soil classification system the soil was classified as a low plasticity clay (CL). The swelling behavior of Anthem soil is presented in the following.

4.2.1.1 1-D Swell strain and Load-back swell pressures

Figure 4.1 shown below presents the 1-D swell strains exhibited by Anthem soil specimen at two different compaction dry densities, maximum dry density (MDD) and 95% of maximum dry density (95% MDD).

The specimens exhibited a maximum swell of 5.8% at maximum dry density (MDD) condition and 4.5% swell at 95% MDD condition. The soil specimens reached 95% saturation level at the end of the test.

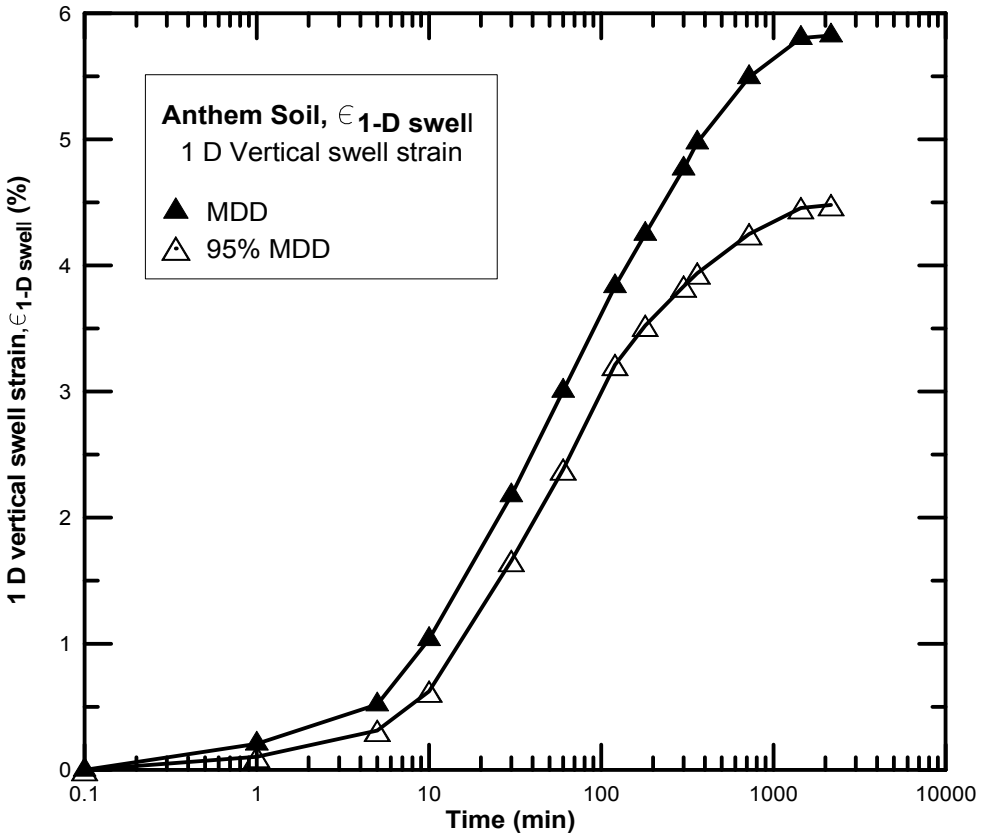

Figure 4.1: One dimensional swell strains for Anthem soil

Figures 4.2 and 4.3 present the load-back swell pressures exhibited by Anthem soil at two different densities. Soil specimens compacted at 95% MDD and MDD condition exhibited swell pressures of 94.2 kPa (13.6 psi) and 134.6 kPa (19.6 psi), respectively. The particle and mineral density was very high in case of MDD condition which was the main factor contributing for higher swelling behavior.

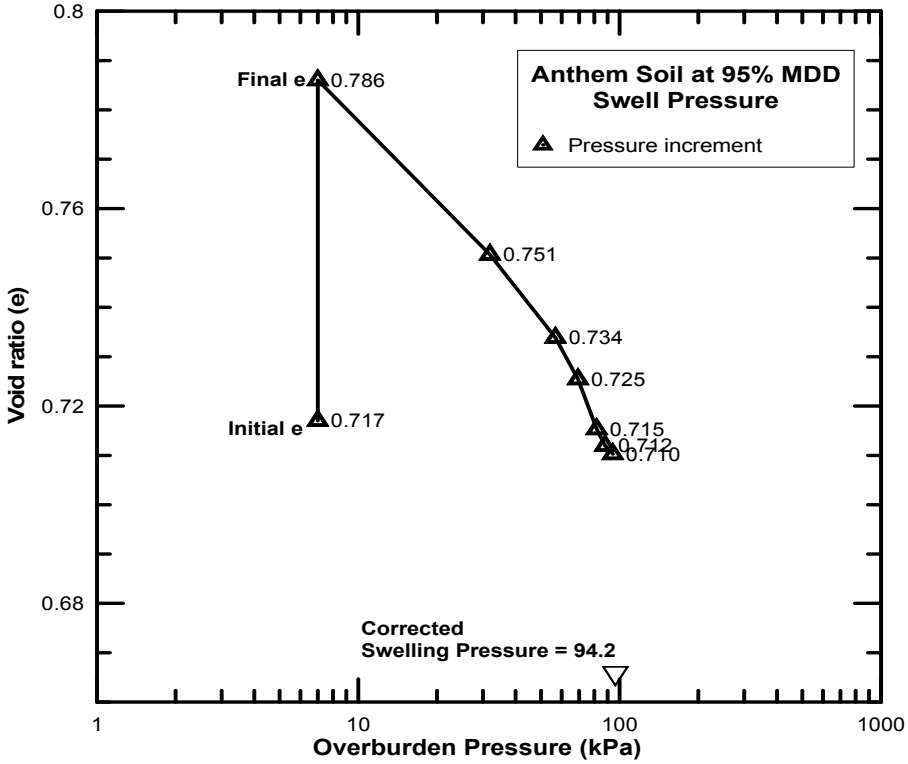

Figure 4.2: Load-back swell pressure test on Anthem soil at 95% MDD

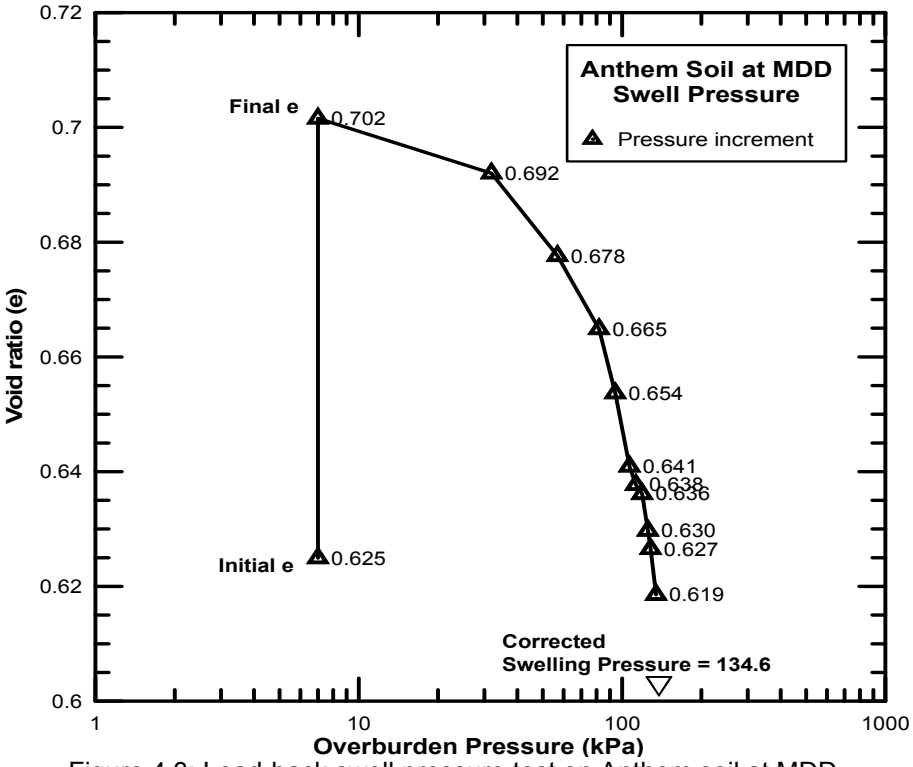

Figure 4.3: Load-back swell pressure test on Anthem soil at MDD

4.2.1.2 3-D swell strains

Soil specimens of 50.8 mm (2 in.) diameter and 101.6 mm (4 in.) height were compacted at 95% MDD and were tested for 3-D volumetric swell strains. Figure 4.4 presents the 3-D vertical swell strains exhibited by Anthem soil specimen at 3 different confinement levels. The specimen showed a maximum vertical strain of 3% at 7 kPa (1 psi) confinement whereas; it showed 1.7% strain at 100 kPa (14.5 psi) confinement. Similarly, Figure 4.5 shows the radial swell strain exhibited by the same soil specimen at different confinements. The specimen exhibited a maximum radial swell strain of 0.89% at 7 kPa (1 psi) confinement and least radial strain of 0.56% at 100 kPa (14.5 psi) confinement.

The total volumetric strain is calculated from the summation of vertical swell strain and twice radial swell strain and is presented in Figure 4.6. The specimen showed maximum volumetric swell strains of 4.9% at 7 kPa (1 psi), 4.3% at 50 kPa (7.25 psi) and 3% at 100 kPa (14.5 psi) confinement levels.

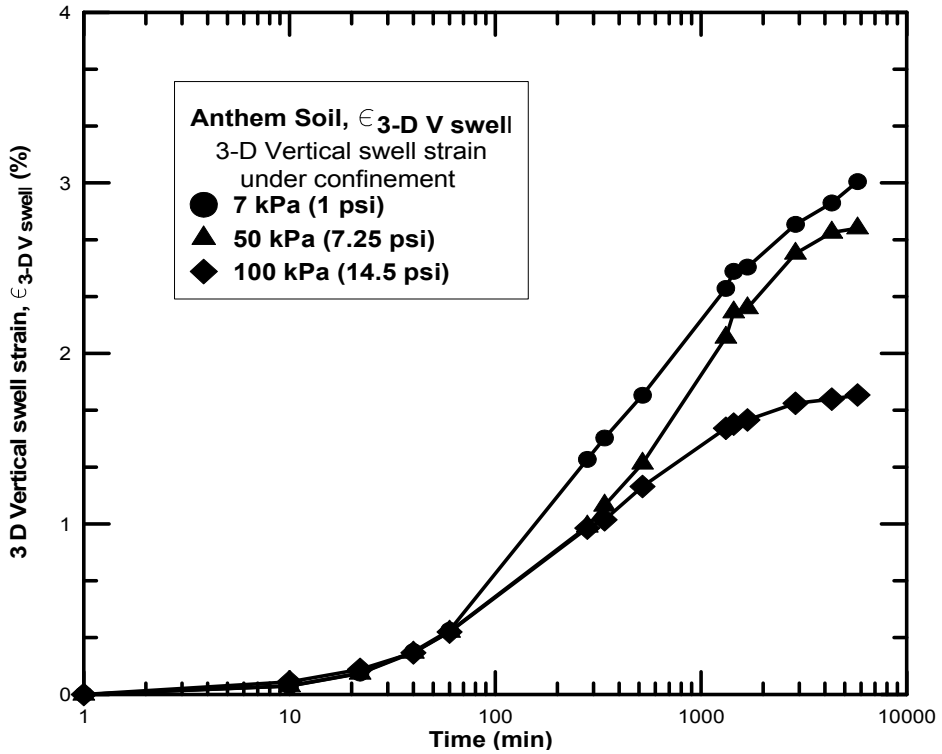

Figure 4.4: Vertical swell strain exhibited by Anthem soil at different confinements

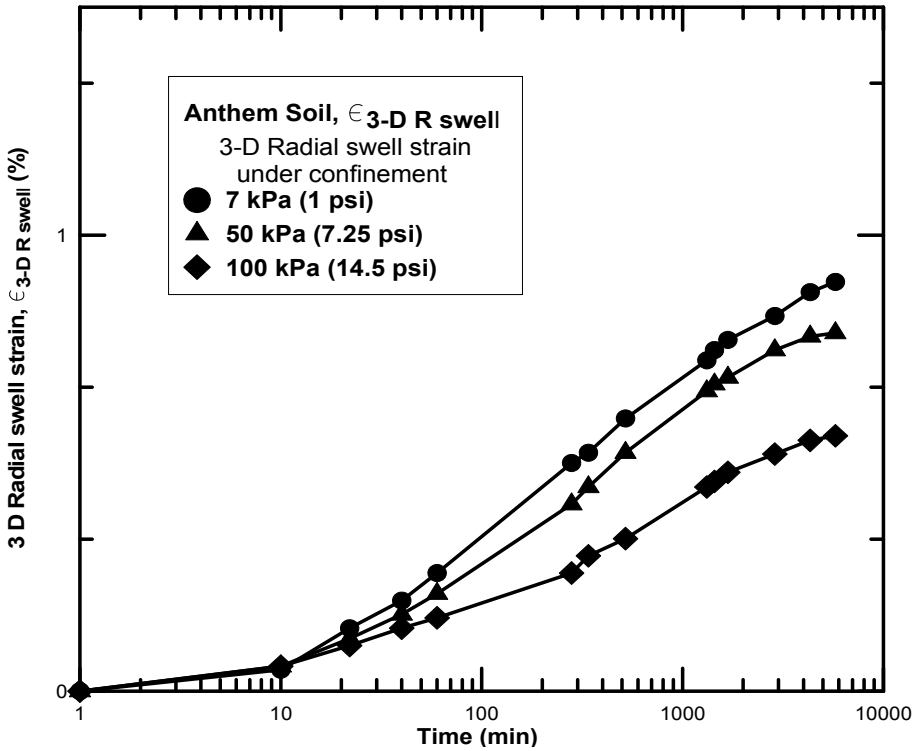

Figure 4.5: Radial swell strain exhibited by Anthem soil at different confinements

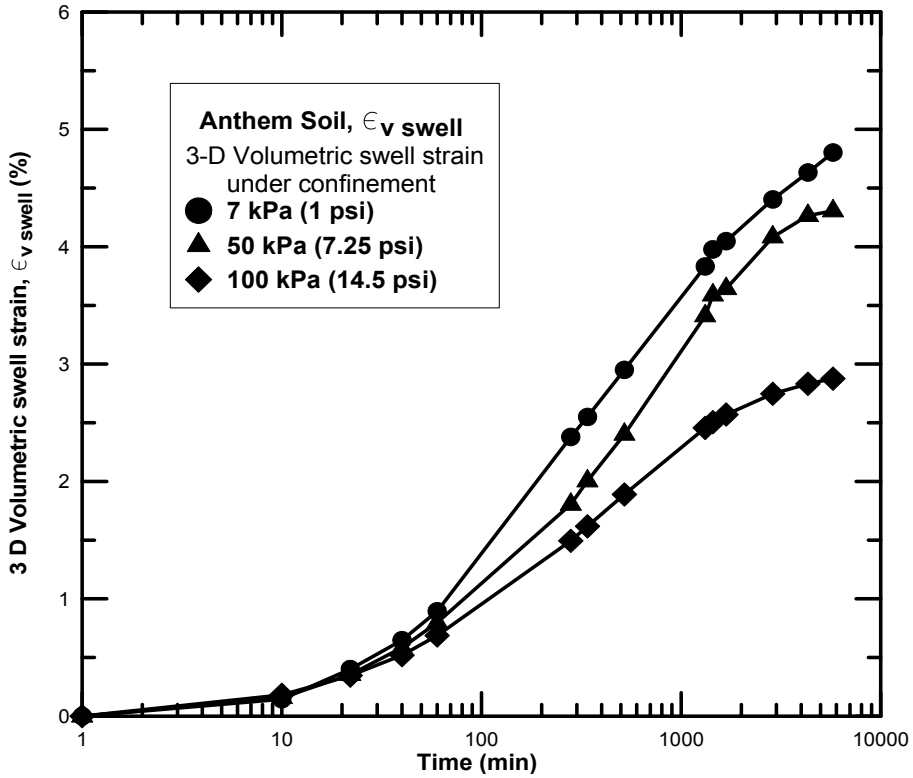

Figure 4.6: Volumetric swell strain exhibited by Anthem soil at different confinements

4.2.2 Burleson Soil

Burleson soil was collected from the state of Texas. Based on the USCS soil classification system the soil was classified as a high plasticity clay (CH). The swelling behavior of Anthem soil is presented in the following.

4.2.2.1 1-D Swell strain and Load-back swell pressures

Figure 4.7 shown below presents the 1-D swell strains exhibited by Burleson soil specimen at two different compaction dry densities, maximum dry density (MDD) and 95% of maximum dry density (95% MDD) condition. The specimens exhibited a maximum swell of 8.8% at maximum dry density (MDD) and 5.8% swell at 95% MDD. The soil specimens reached 98% saturation levels at the end of the test.

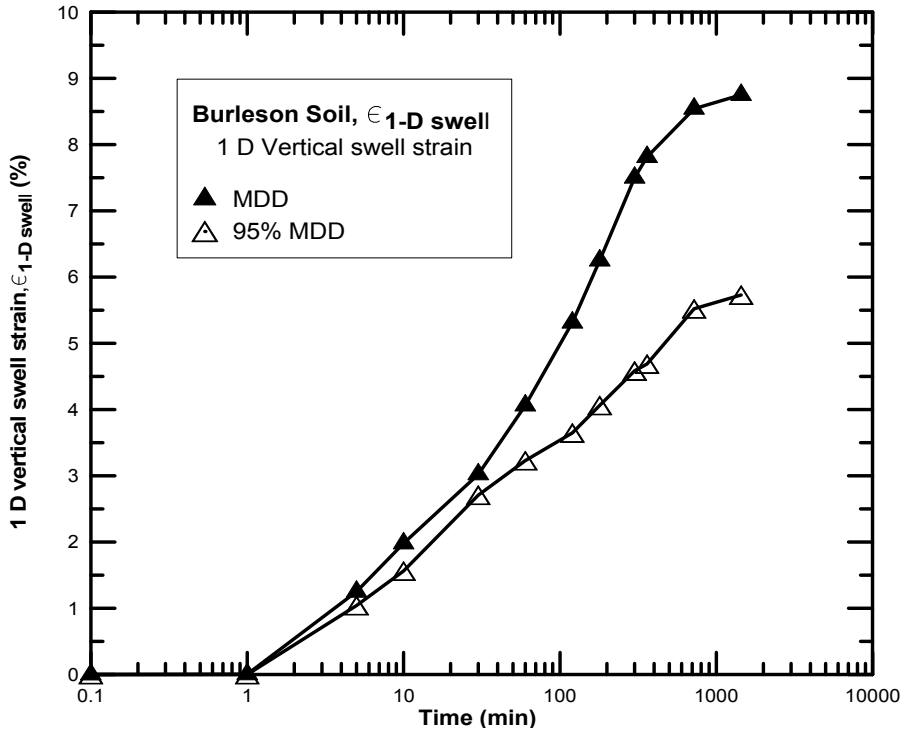

Figure 4.7: One dimensional swell strains for Burleson soil

Figures 4.8 and 4.9 present the load back swell pressures obtained from Burleson soil at two different densities. Soil specimen at 95% MDD exhibited a swell pressure of 112.8 kPa (16.4 psi) and 183.4 kPa (26.7 psi) at MDD condition. The particle and mineral density was very high in case of MDD condition which resulted in higher swelling behavior.

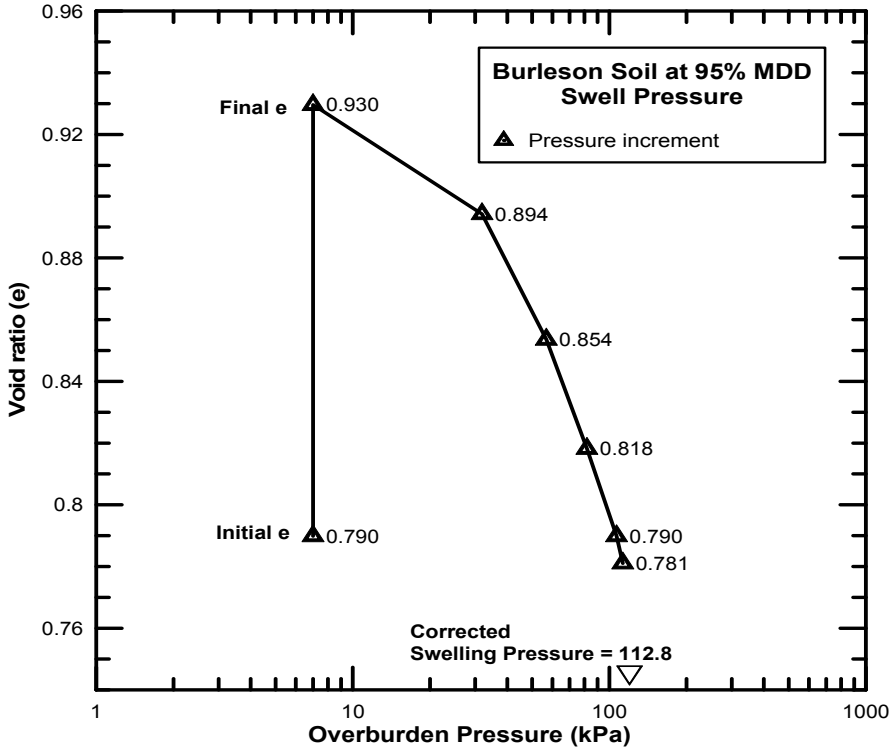

Figure 4.8: Load-back swell pressure test on Burleson soil at 95% MDD

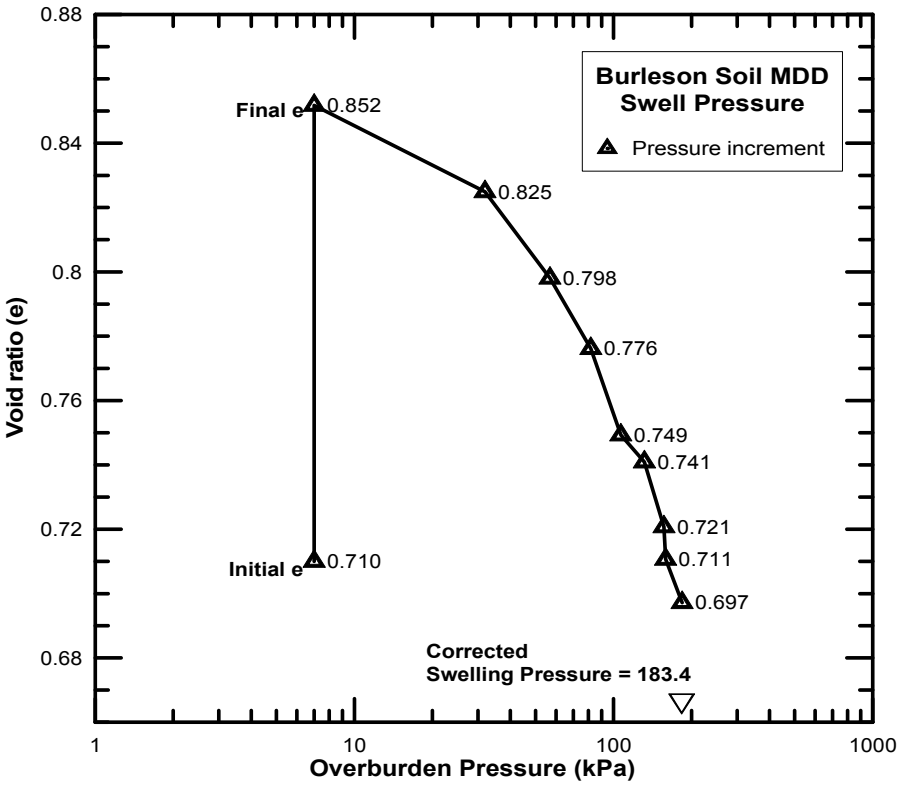

Figure 4.9: Load-back swell pressure test on Burleson soil at MDD

4.2.2.2 3-D swell strains

Soil specimens of 50.8 mm (2 in.) diameter and 101.6 mm (4 in.) height were compacted at 95% MDD and were tested for 3 D volumetric swell strains. Figure 4.10 presents the 3-D vertical swell strains exhibited by Burleson soil specimen at 3 different confinement levels. The specimen showed a maximum vertical strain of 5.8% at 7 kPa (1 psi) confinement whereas; it showed 3% strain at 100 kPa (14.5 psi) confinement. Similarly, Figure 4.11 shows the radial swell strain exhibited by the soil specimen at different confinements. The specimen exhibited a maximum radial swell strain of 1.12% at 7 kPa (1 psi) confinement level and least radial strain of 0.8% at 7 kPa (14.5 psi) confinement.

The total volumetric strain is calculated from the summation of vertical and twice radial strain is presented in Figure 4.12. The specimen showed maximum volumetric swell strains of 8% at 7 kPa (1 psi), 6.45% at 50 kPa (7.25 psi) and 4.69% at 100 kPa (14.5 psi) confinement levels.

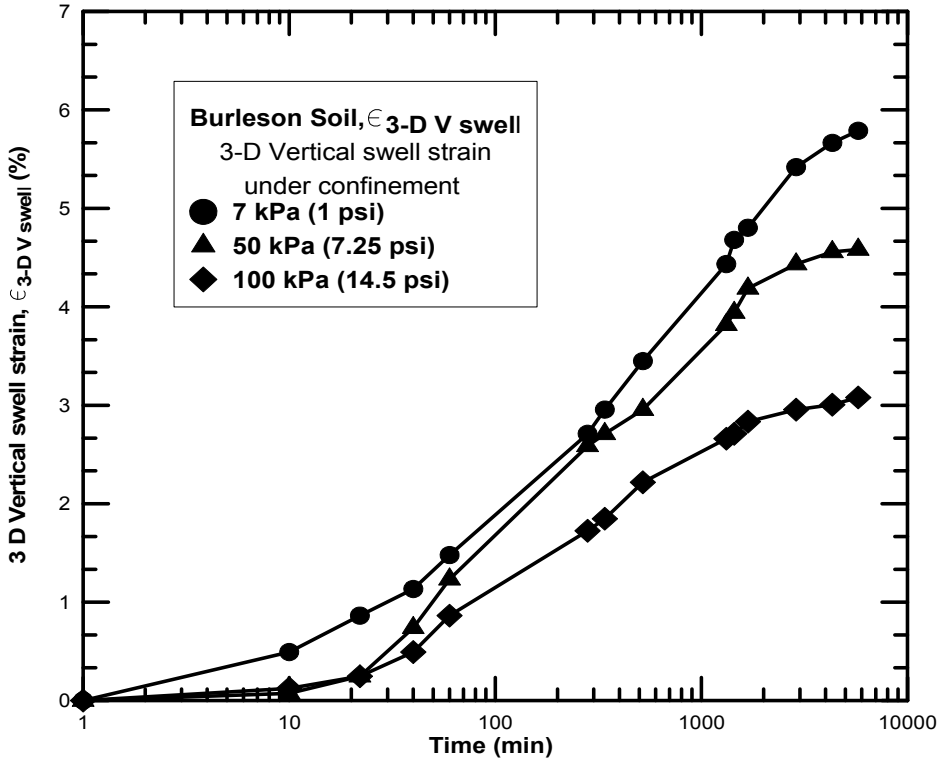

Figure 4.10: Vertical swell strain exhibited by Burleson soil at different confinements

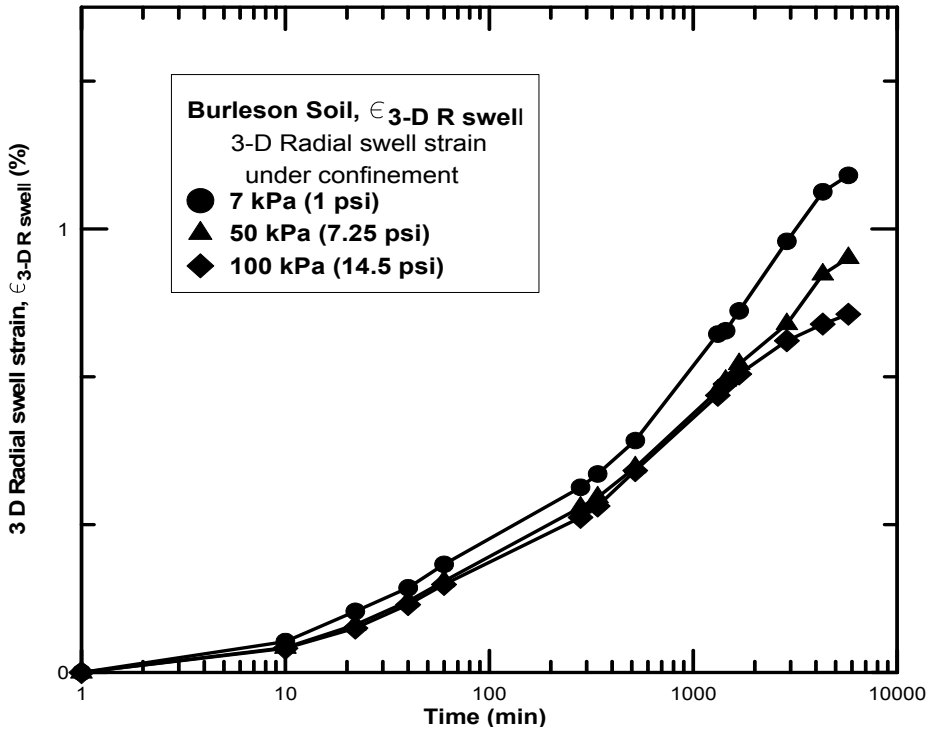

Figure 4.11: Radial swell strain exhibited by Burleson soil at different confinements

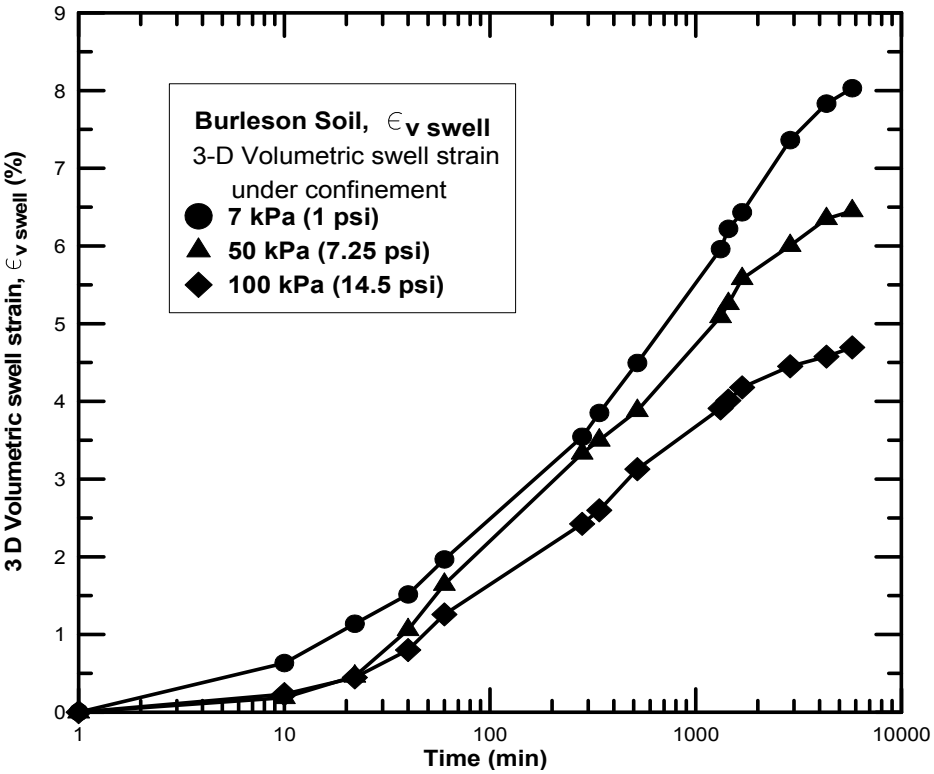

Figure 4.12: Volumetric swell strain exhibited by Burleson soil at different confinements

4.2.3 Colorado Soil

Colorado soil was collected from the state of Colorado. Based on the USCS soil classification system the soil was classified as a high plasticity clay (CH). The swelling behavior of Colorado soil is presented in the following.

4.2.3.1 1-D Swell strain and Load-back swell pressures

Figure 4.13 shown below presents the 1-D swell strains exhibited by Colorado soil specimen at two different compaction dry densities, maximum dry density (MDD) and 95% of maximum dry density (95% MDD). The specimen exhibited a maximum swell of 12% at maximum dry density (MDD) and 8.2% swell at 95% MDD.

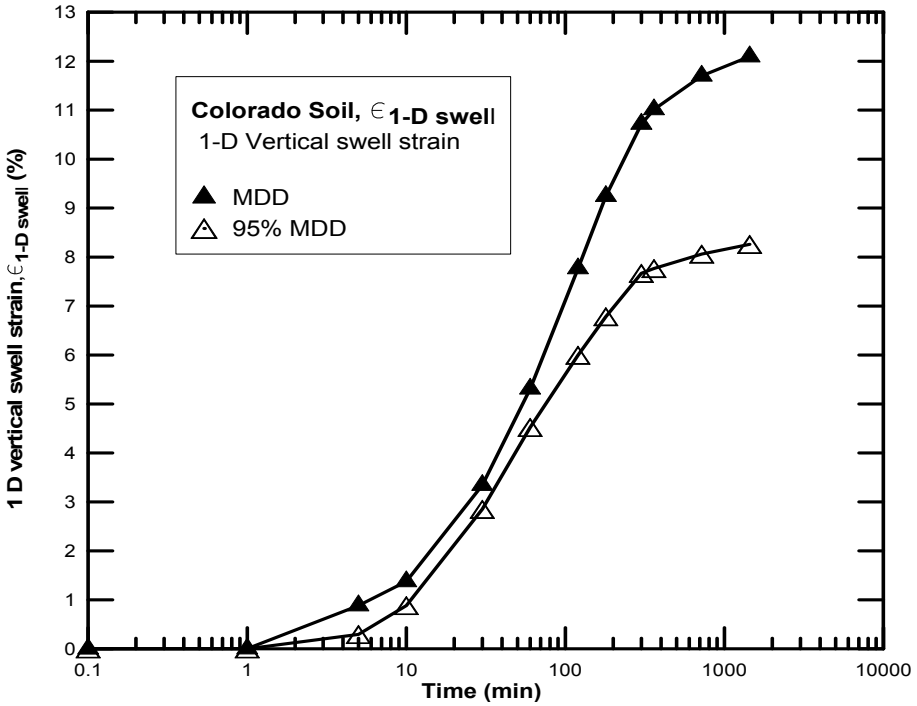

Figure 4.13: One dimensional swell strains for Colorado soil

Figures 4.14 and 4.15 present the load-back swell pressures obtained from Colorado soil at two different densities. Soil specimen at 95% MDD exhibited a swell pressure of 137.7 kPa (20 psi) and 194 kPa (28 psi) at MDD condition. The particle and mineral density was very high in case of MDD condition which resulted in higher swelling behavior.

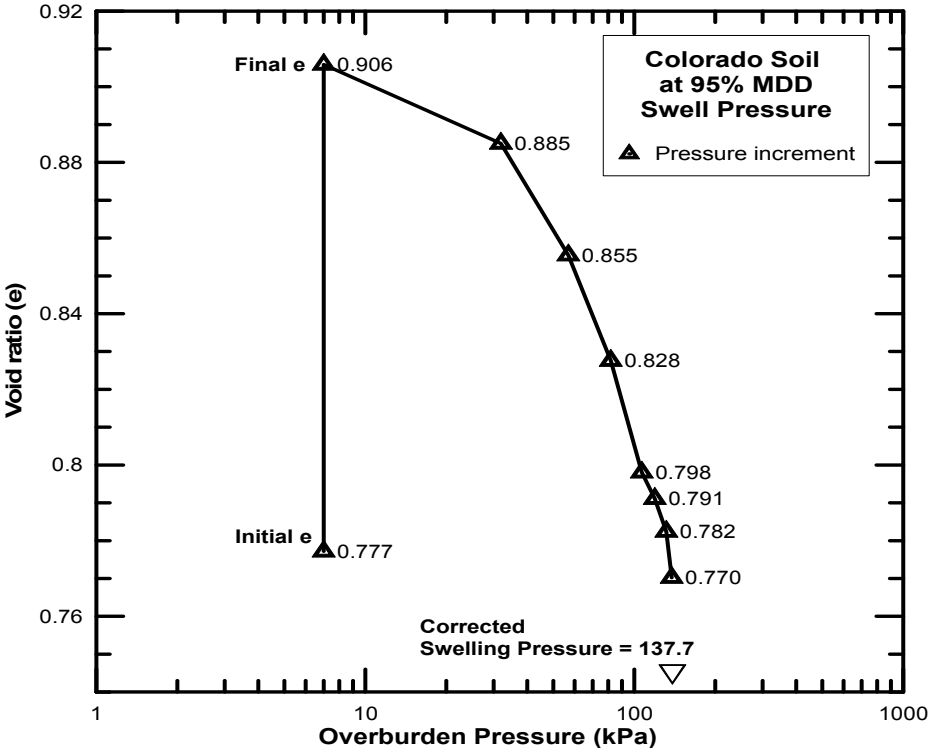

Figure 4.14: Load-back swell pressure test on Colorado soil at 95% MDD

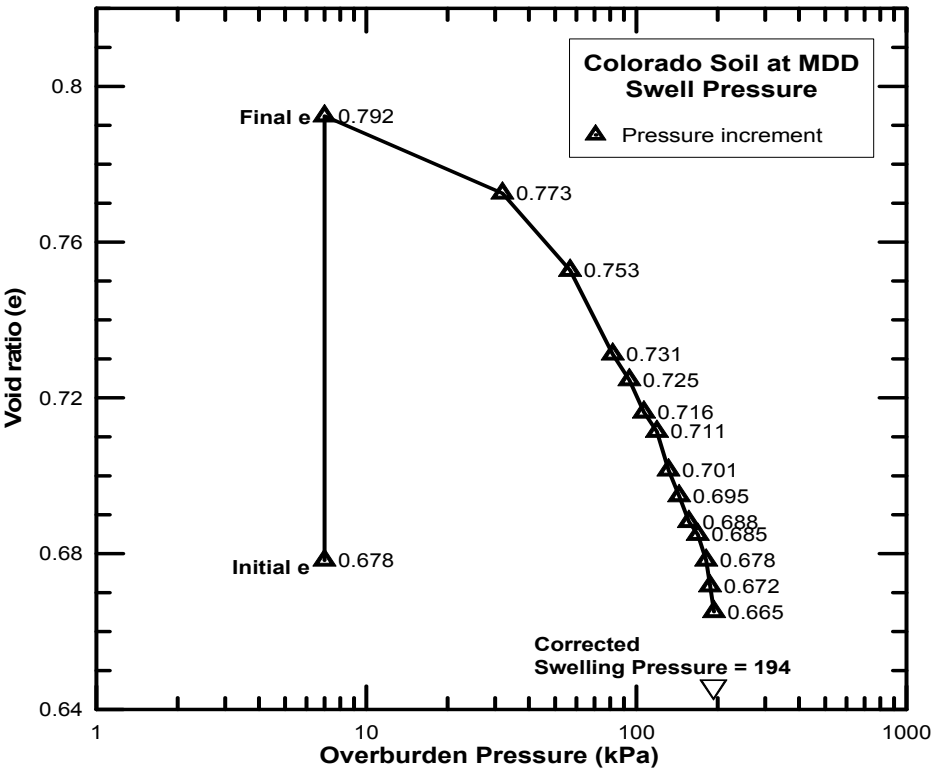

Figure 4.15: Load-back swell pressure test on Colorado soil at MDD

4.2.3.2 3-D swell strains

Soil specimens of 50.8 mm (2 in.) diameter and 101.6 mm (4 in.) height were compacted at 95% MDD and were tested for 3-D volumetric swell strains. Figure 4.16 presents the 3-D vertical swell strains exhibited by Colorado soil specimen at 3 different confinement levels. The specimen showed a maximum vertical strain of 6.8% at 7 kPa (1 psi) confinement whereas; it showed 4.4% strain at 100 kPa (14.5 psi) confinement. Similarly, Figure 4.17 shows the radial swell strain exhibited by the soil specimen at different confinements. The specimen exhibited a maximum radial swell strain of 1.23% at 7 kPa (1 psi) confinement and least radial strain of 0.95% at 100 kPa (14.5 psi) confinement.

The total volumetric strain is calculated from the summation of vertical and twice radial strain is presented in Figure 4.18. The specimen showed maximum volumetric swell strains of 9.3% at 7 kPa (1 psi), 7.5% at 50 kPa (7.25 psi) and 6.3% at 7 kPa (14.5 psi) confinement.

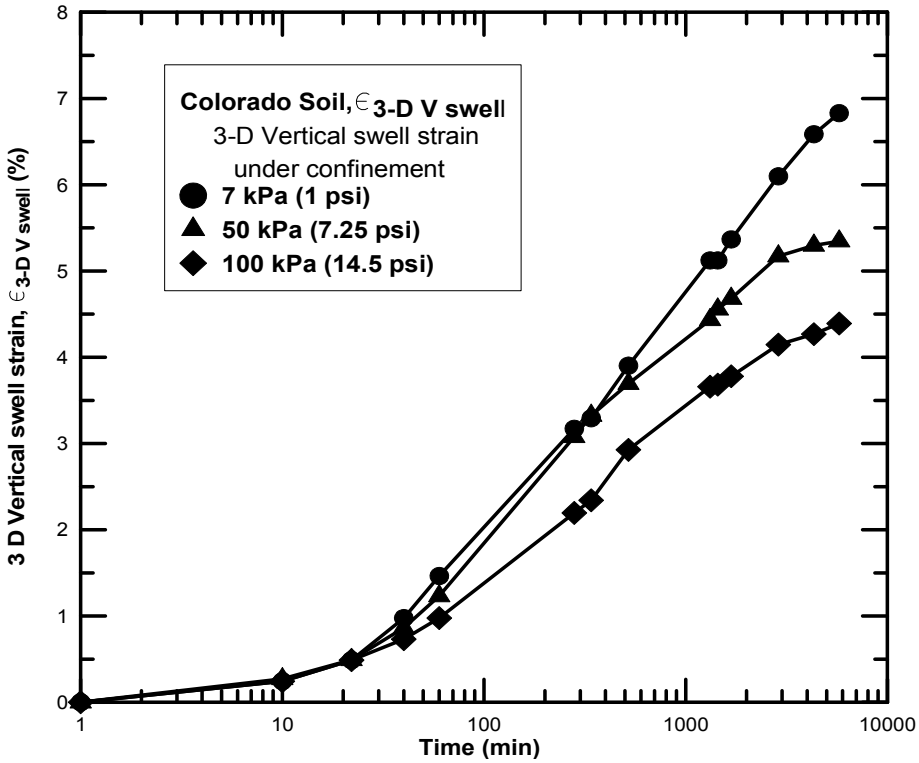

Figure 4.16: Vertical swell strain exhibited by Colorado soil at different confinements

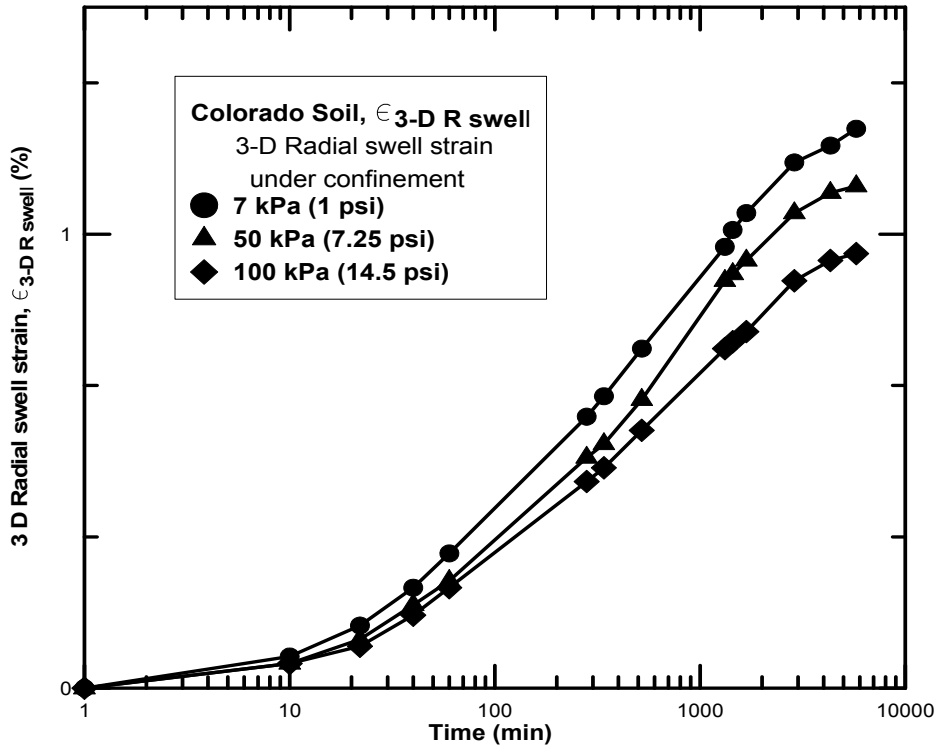

Figure 4.17: Radial swell strain exhibited by Colorado soil at different confinements

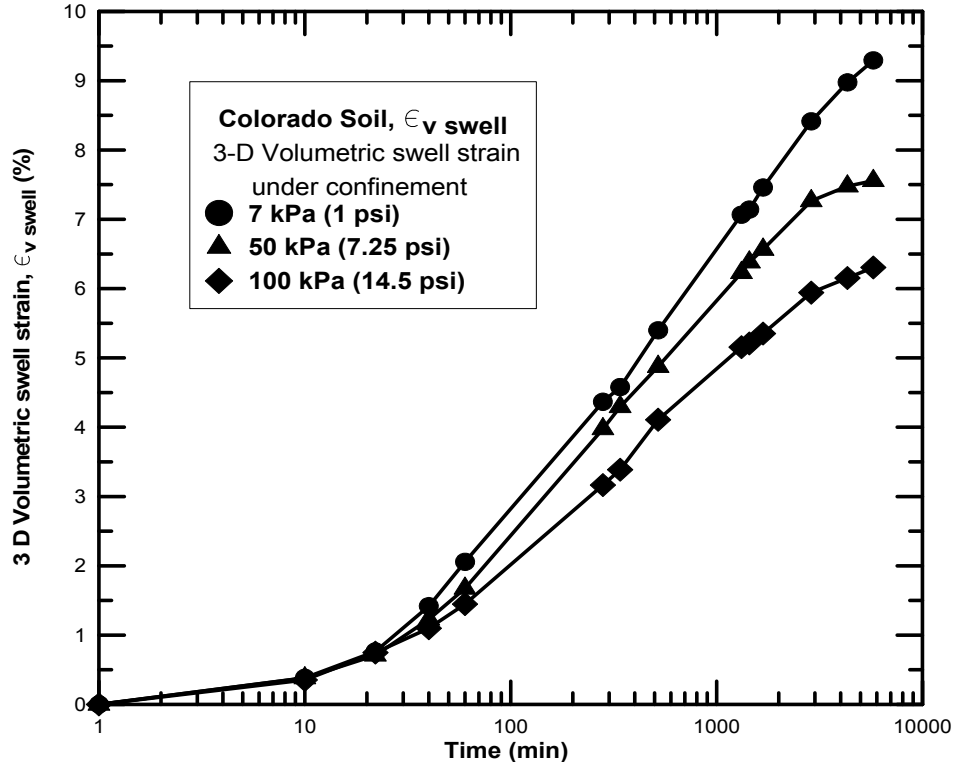

Figure 4.18: Volumetric swell strain exhibited by Colorado soil at different confinements

4.2.4 Grayson Soil

Grayson soil was collected from the state of Texas. Based on the USCS soil classification system the soil was classified as a high plasticity clay (CH). The swelling behavior of Grayson soil is presented in the following.

4.2.4.1 1-D Swell strain and Load-back swell pressures

Figure 4.19 shown below presents the 1-D swell strains exhibited by Grayson soil specimen at two different compaction dry densities, maximum dry density (MDD) and 95% of maximum dry density (95% MDD). The specimen exhibited a maximum swell of 14.2% at maximum dry density (MDD) and 9.8% swell at 95% MDD. The soil specimens reached 98% saturation levels at the end of the test.

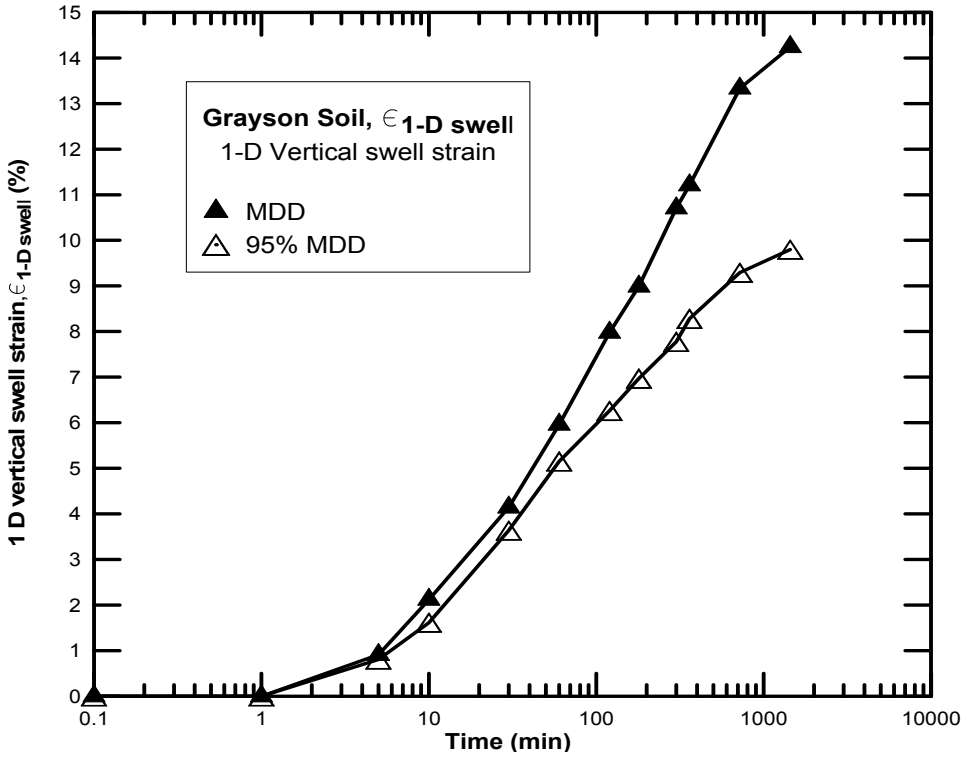

Figure 4.19: One dimensional swell strains for Grayson soil

Figures 4.20 and 4.21 present the load-back swell pressures obtained from Grayson soil at two different densities.

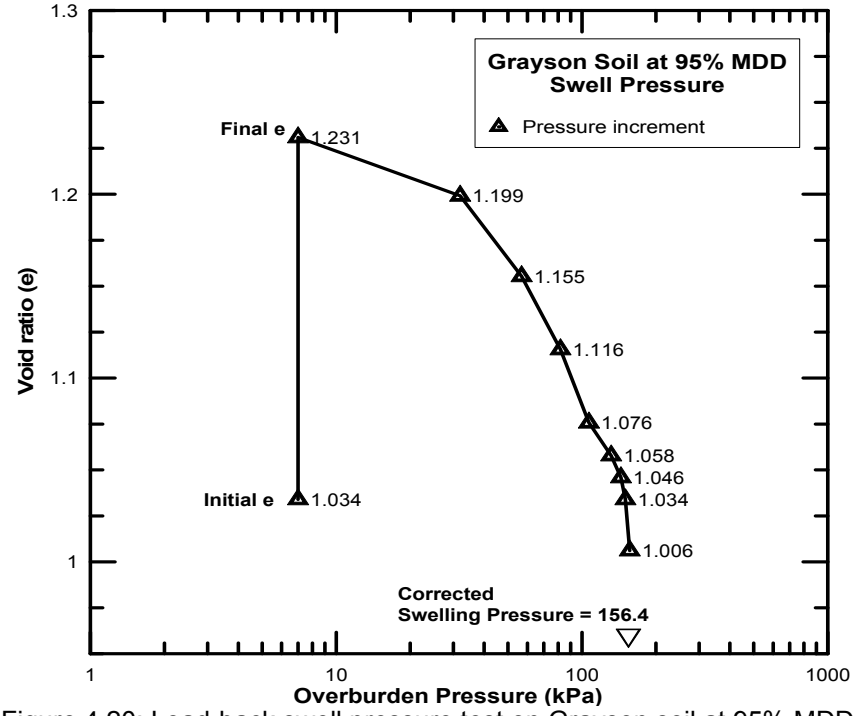

Figure 4.20: Load-back swell pressure test on Grayson soil at 95% MDD

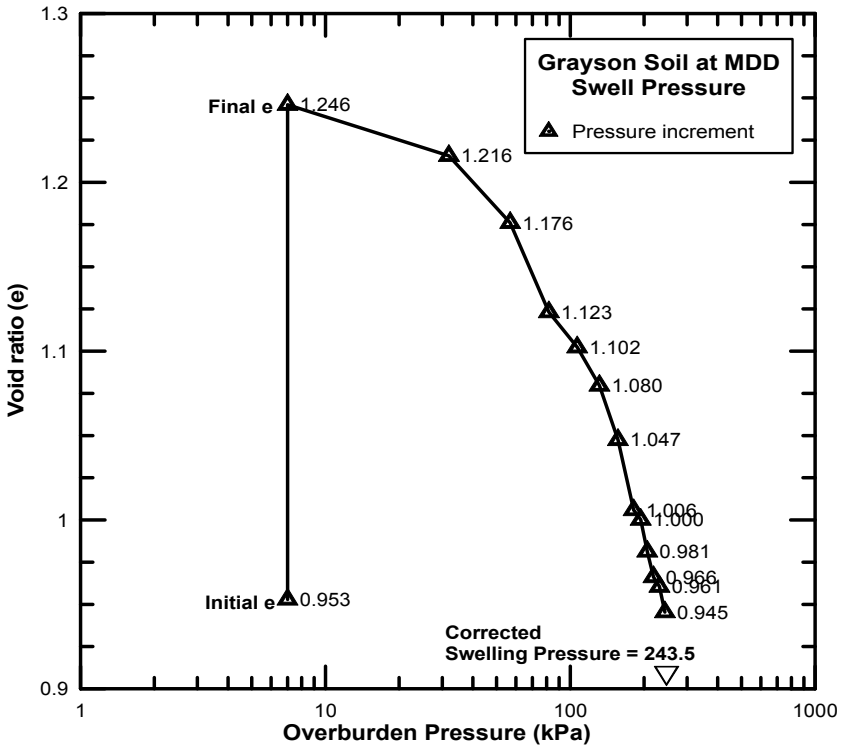

Figure 4.21: Load-back swell pressure test on Grayson soil at MDD

Soil specimen at 95% MDD exhibited a swell pressure of 156 kPa (22.7 psi) and 243.5 kPa (35.3 psi) at MDD condition. The particle and mineral density was very high in case of MDD condition which resulted in higher swelling behavior.

4.2.4.2 3-D swell strains

Soil specimens of 50.8 mm (2 in.) diameter and 101.6 mm (4 in.) height were compacted at 95% MDD and were tested for 3-D volumetric swell strains. Figure 4.22 presents the 3-D vertical swell strains exhibited by Grayson soil specimen at 3 different confinement levels. The specimen showed a maximum vertical strain of 9.1% at 7 kPa (1 psi) confinement whereas; it showed 5.6% strain at 100 kPa (14.5 psi) confinement. Similarly, Figure 4.23 shows the radial swell strain exhibited by the soil specimen at different confinements. The specimen exhibited a maximum radial swell strain of 1.27% at 7 kPa (1 psi) confinement and least radial strain of 1.03% at 100 kPa (14.5 psi) confinement.

The total volumetric strain is calculated from the summation of vertical and twice radial strain is presented in Figure 4.24. The specimen showed maximum volumetric swell strains of 11.65% at 7 kPa (1 psi), 8.76% at 50 kPa (7.25 psi) and 7.67% at 100 kPa (14.5 psi) confinement levels.

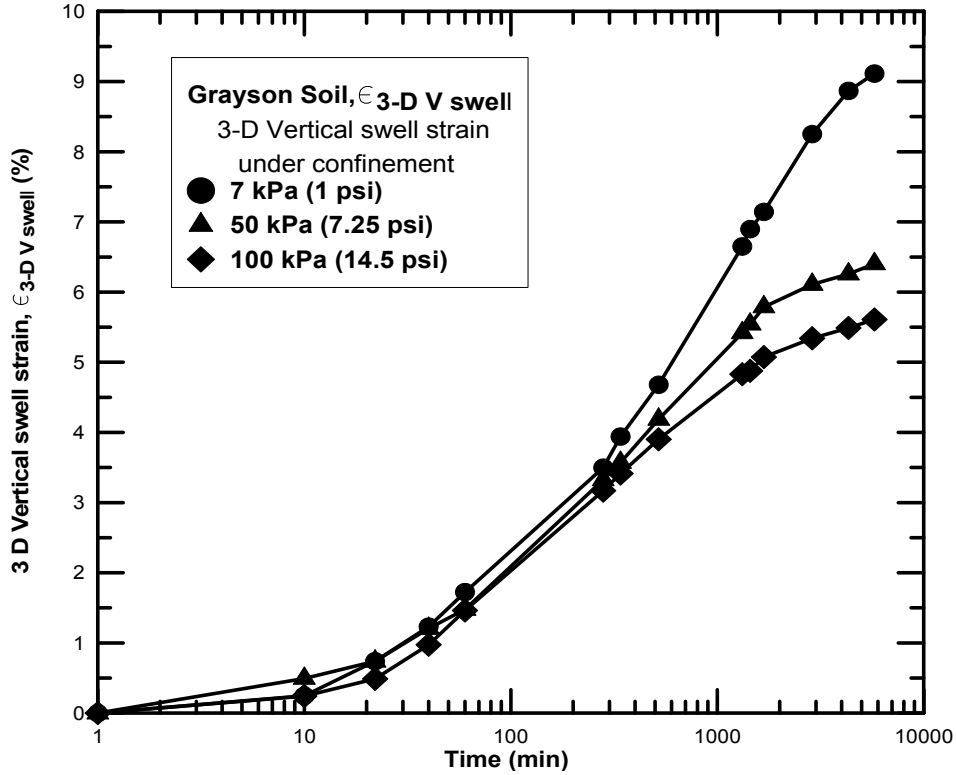

Figure 4.22: Vertical swell strain exhibited by Grayson soil at different confinements

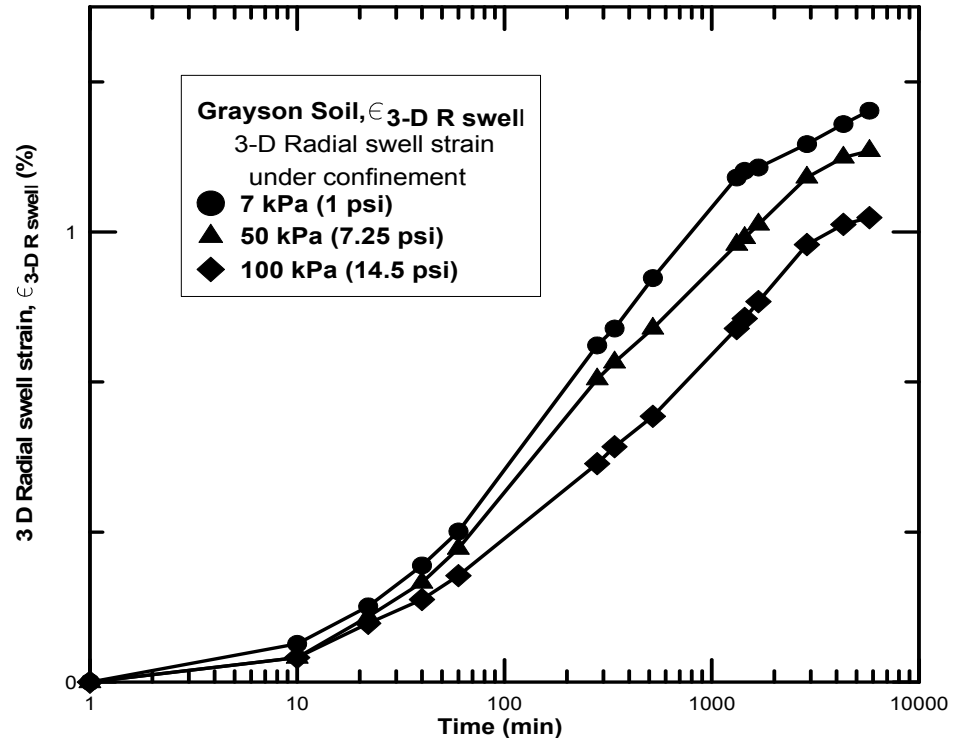

Figure 4.23: Radial swell strain exhibited by Grayson soil at different confinements

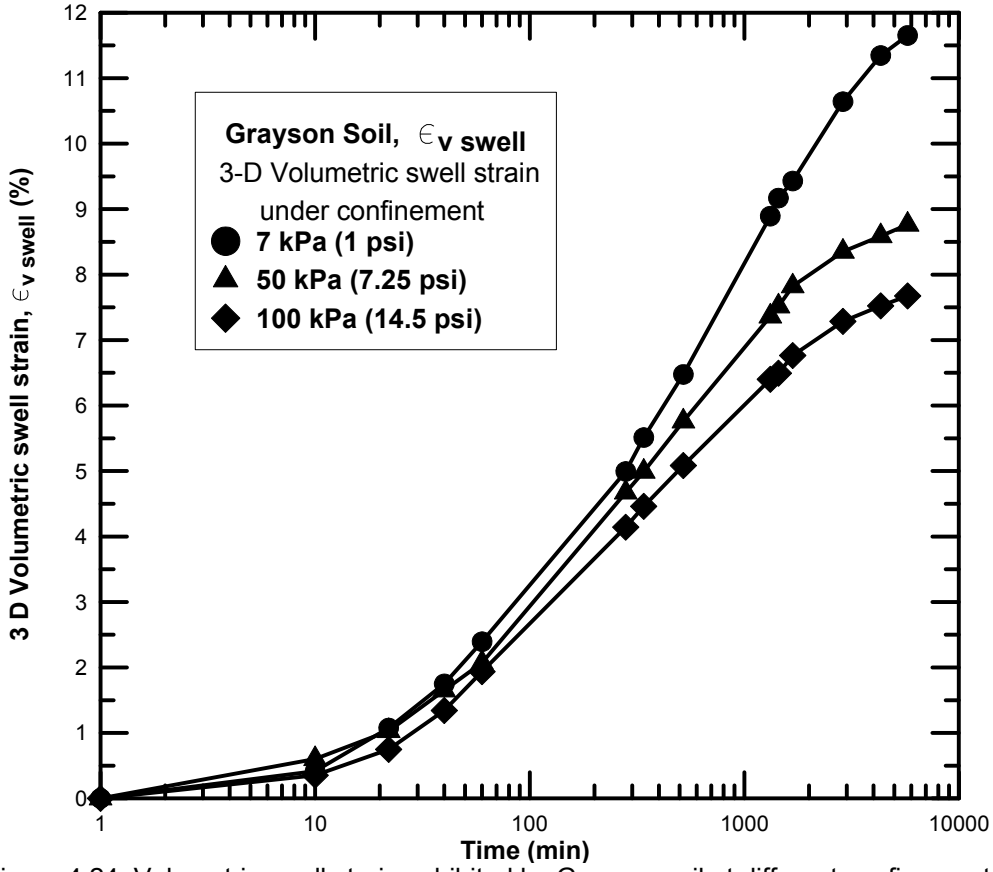

Figure 4.24: Volumetric swell strain exhibited by Grayson soil at different confinements

4.2.5 Keller Soil

Keller soil was collected from the state of Texas. Based on the USCS soil classification system the soil was classified as a low plasticity clay (CL). The swelling behavior of Keller soil is presented in the following.

4.2.5.1 1-D Swell strain and Load-back swell pressures

Figure 4.25 shown below presents the 1-D swell strains exhibited by Keller soil specimen at two different compaction dry densities, maximum dry density (MDD) and 95% of maximum dry density (95% MDD). The specimen exhibited a maximum swell of 7.9% at maximum dry density (MDD) and 5.6% swell at 95% MDD.

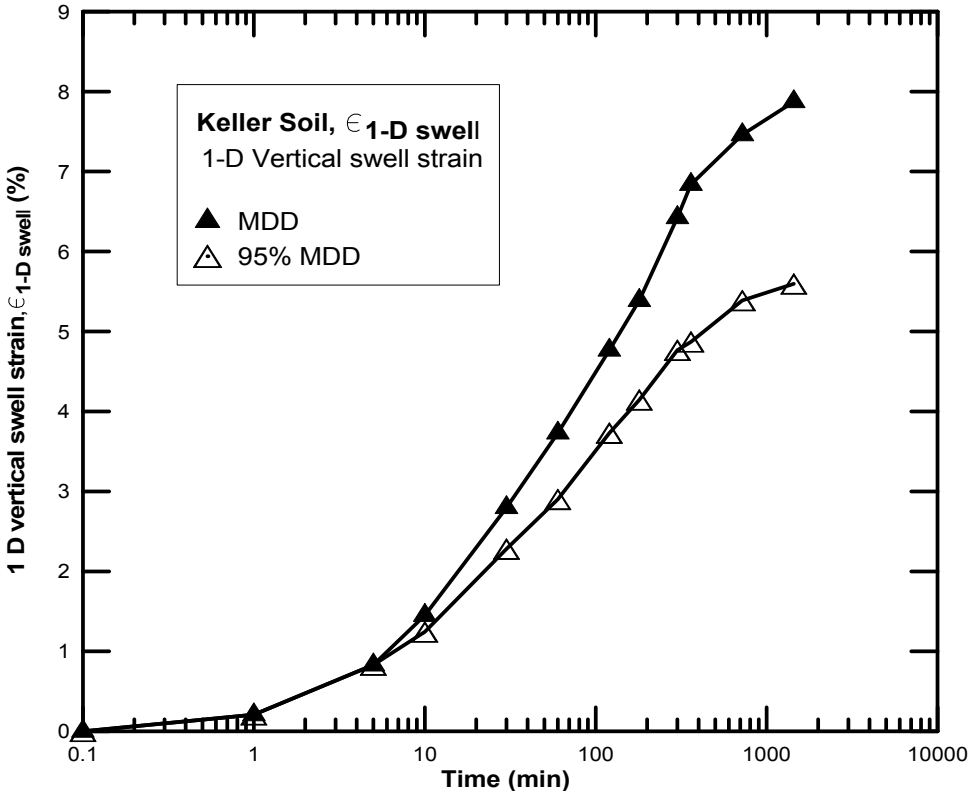

Figure 4.25: One dimensional swell strains for Keller soil

Figures 4.26 and 4.27 present the load-back swell pressures obtained from Keller soil at two different densities. Soil specimen at 95% MDD exhibited a swell pressure of 98 kPa (14.2 psi) and 137.7 kPa (20 psi) at MDD condition. The particle and mineral density was very high in case of MDD condition which resulted in higher swelling behavior.

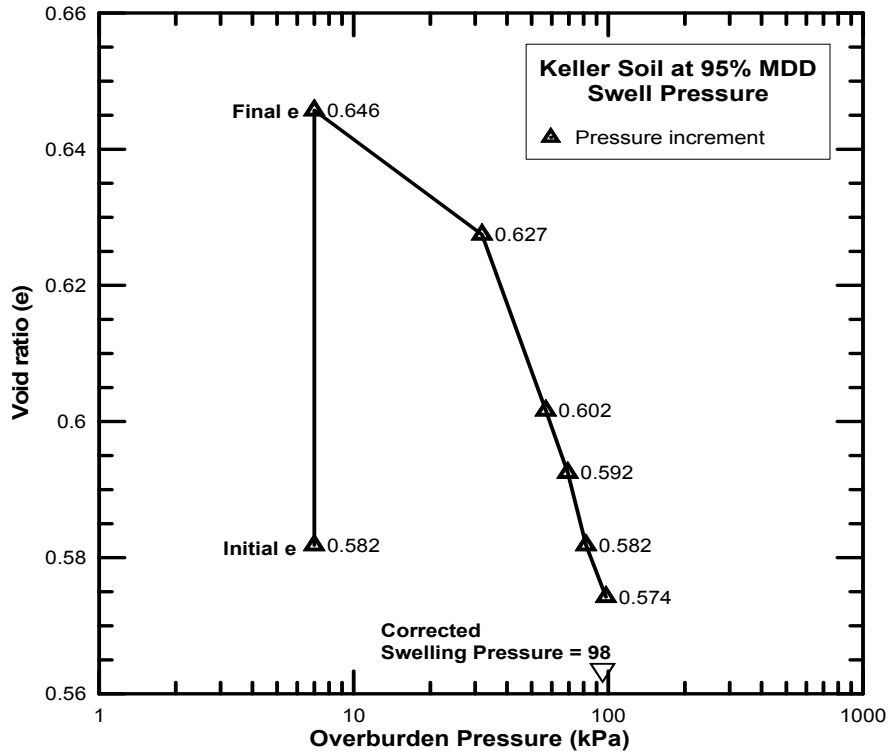

Figure 4.26: Load-back swell pressure test on Keller soil at 95% MDD

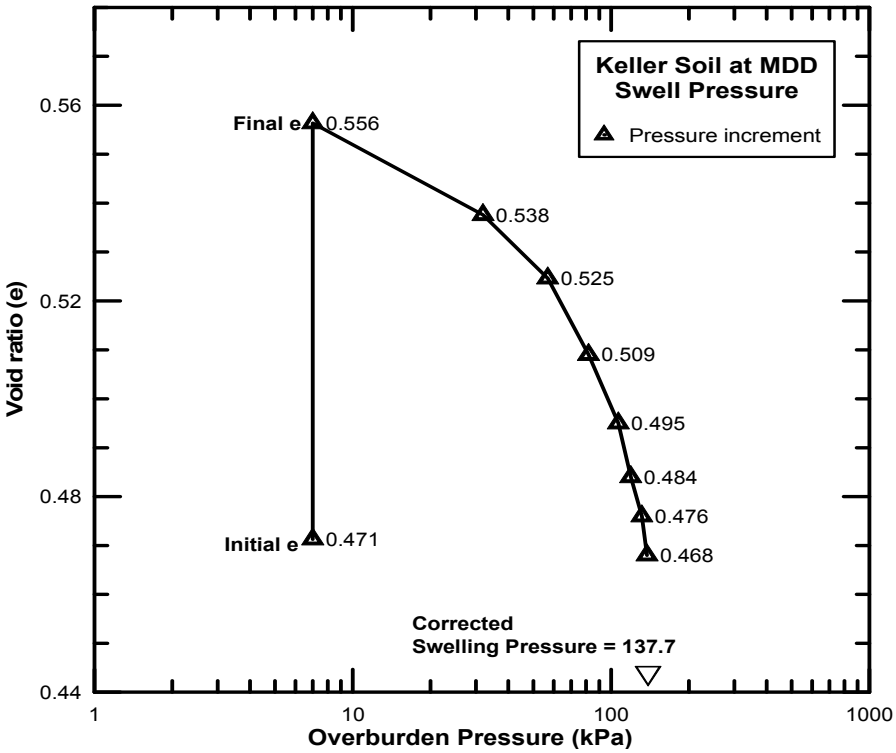

Figure 4.27: Load-back swell pressure test on Keller soil at MDD

4.2.5.1 3-D swell strains

Soil specimens of 50.8 mm (2 in.) diameter and 101.6 mm (4 in.) height were compacted at 95% MDD and were tested for 3-D volumetric swell strains. Figure 4.28 presents the 3 D vertical swell strains exhibited by Keller soil specimen at 3 different confinement levels. The specimen showed a maximum vertical strain of 4.7% at 7 kPa (1 psi) confinement whereas; it showed 2% strain at 100 kPa (14.5 psi) confinement. Similarly, Figure 4.29 shows the radial swell strain exhibited by the soil specimen at different confinements. The specimen exhibited a maximum radial swell strain of 1.04% at 7 kPa (1 psi) confinement and least radial strain of 0.82% at 100 kPa (14.5 psi) confinement.

The total volumetric strain is calculated from the summation of vertical and twice radial strain is presented in Figure 4.30. The specimen showed maximum volumetric swell strains of 6.85% at 7 kPa (1 psi), 5.73% at 50 kPa (7.25 psi) and 3.71% at 100 kPa (14.5 psi) confinement levels.

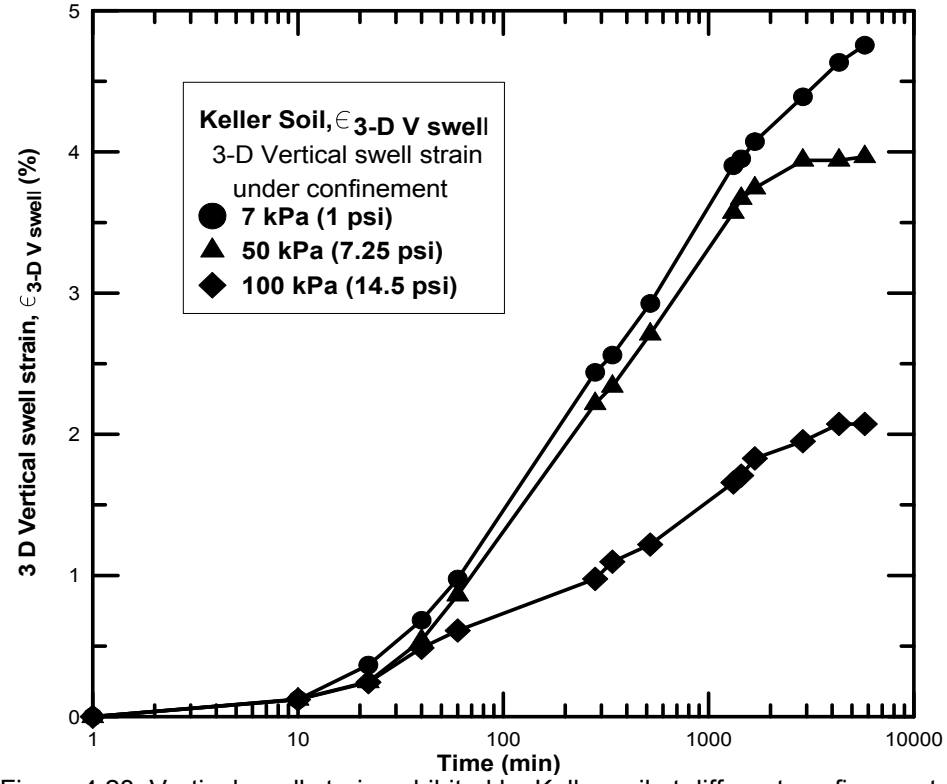

Figure 4.28: Vertical swell strain exhibited by Keller soil at different confinements

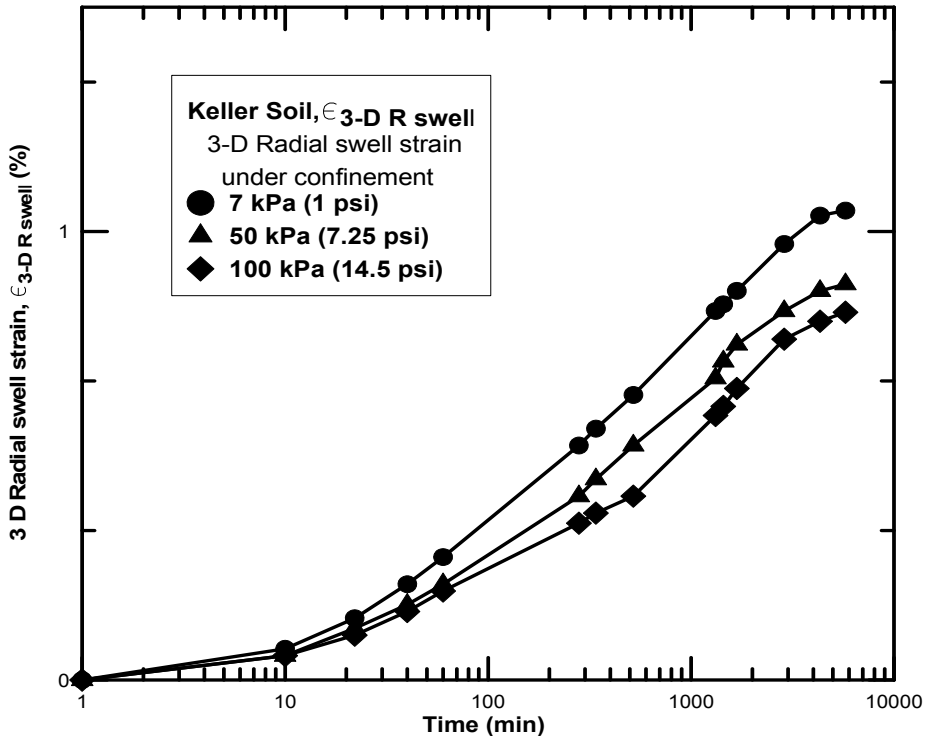

Figure 4.29: Radial swell strain exhibited by Keller soil at different confinements

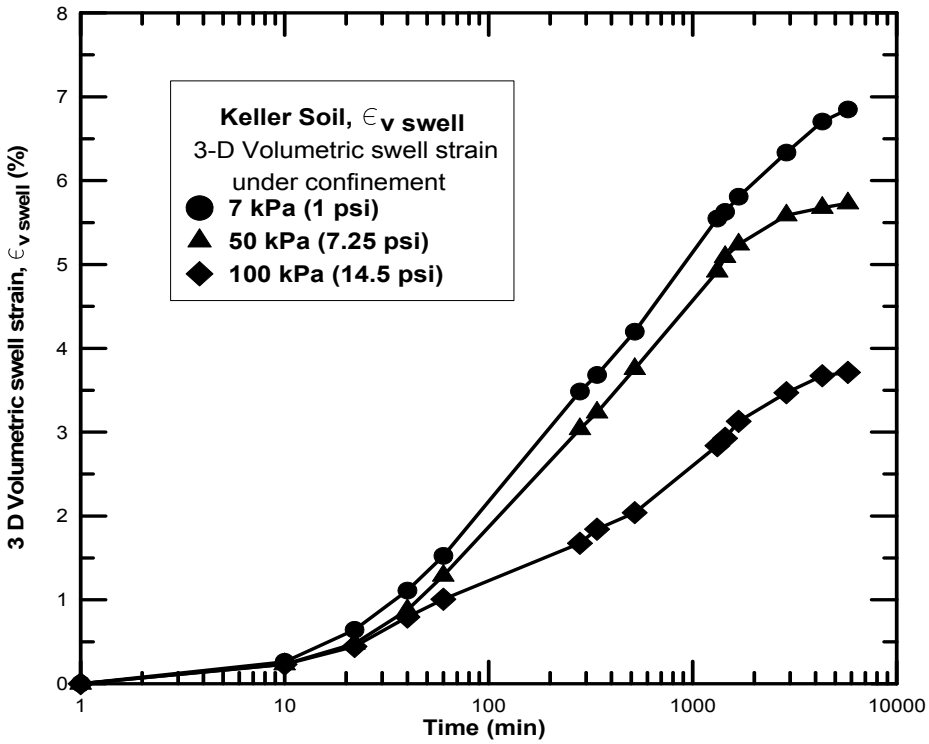

Figure 4.30: Volumetric swell strain exhibited by Keller soil at different confinements

4.2.6 Oklahoma Soil

Oklahoma soil was collected from the state of Oklahoma. Based on the USCS soil classification system the soil was classified as a low plasticity clay (CL). The swelling behavior of Oklahoma soil is presented in the following.

4.2.6.1 1-D Swell strain and Load-back swell pressures

Figure 4.31 shown below presents the 1-D swell strains exhibited by Oklahoma soil specimen at two different compaction dry densities, maximum dry density (MDD) and 95% of maximum dry density (95% MDD). The Oklahoma specimen exhibited a maximum swell of 4.8% at maximum dry density (MDD) and 3.8% swell at 95% MDD.

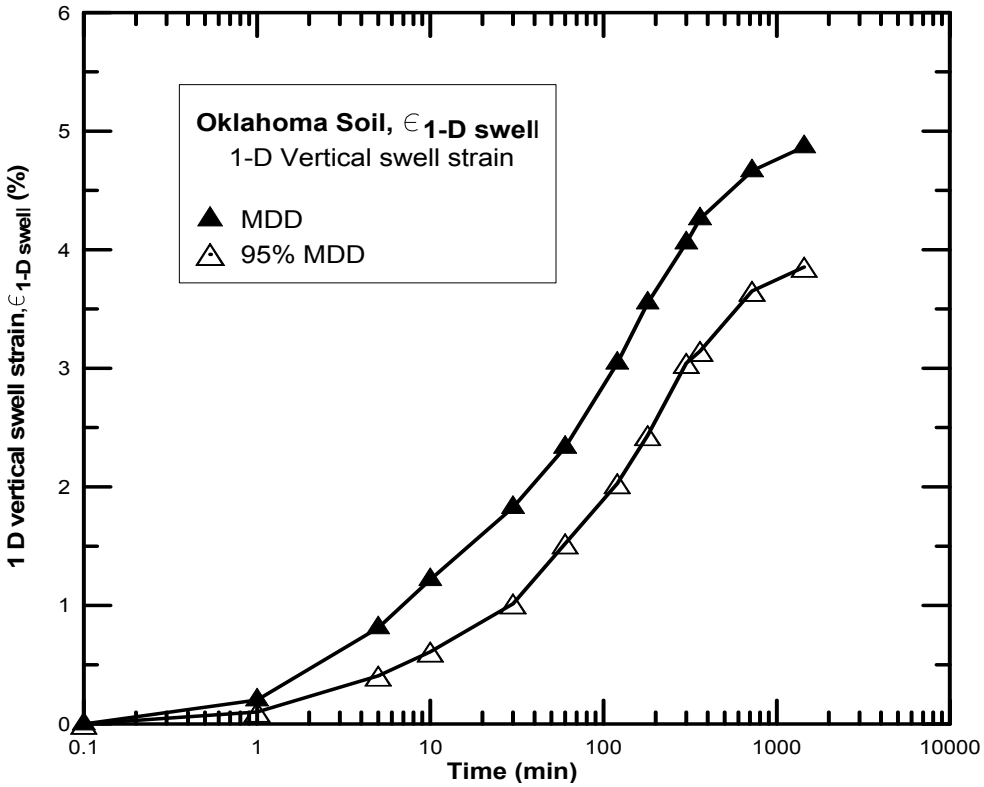

Figure 4.31: One dimensional swell strains for Oklahoma soil

Figures 4.32 and 4.33 present the load back swell pressures obtained from Oklahoma soil at two different densities. Soil specimen at 95% MDD exhibited a swell pressure of 63 kPa (9.1 psi) and 106.6 kPa (15.5 psi) at MDD condition. The particle and mineral density was very high in case of MDD condition which resulted in higher swelling behavior.

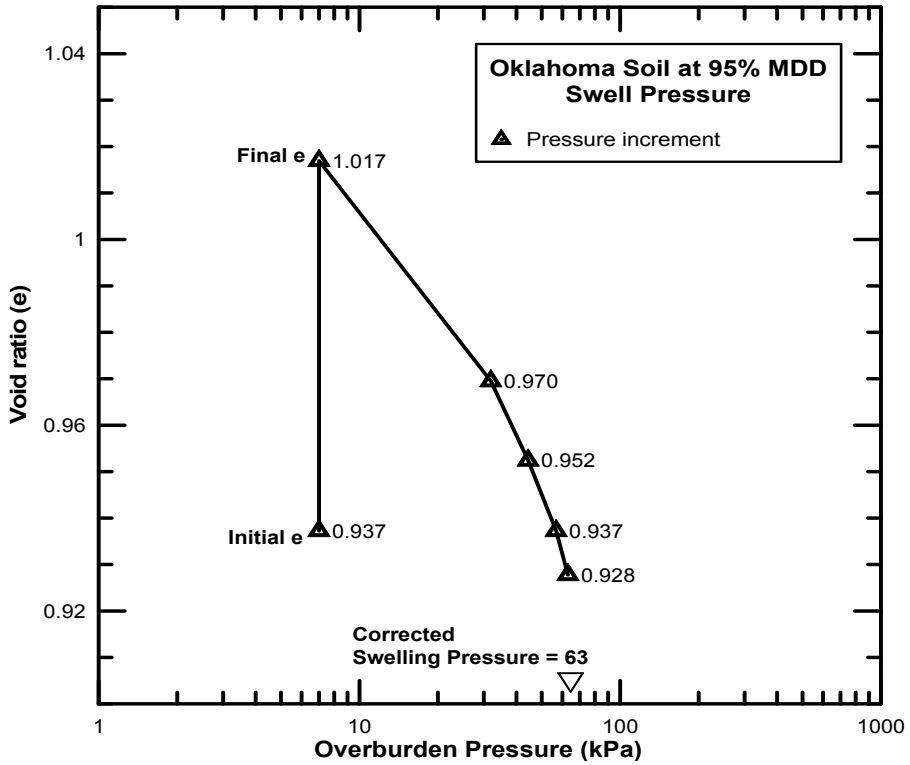

Figure 4.32: Load-back swell pressure test on Oklahoma soil at 95% MDD

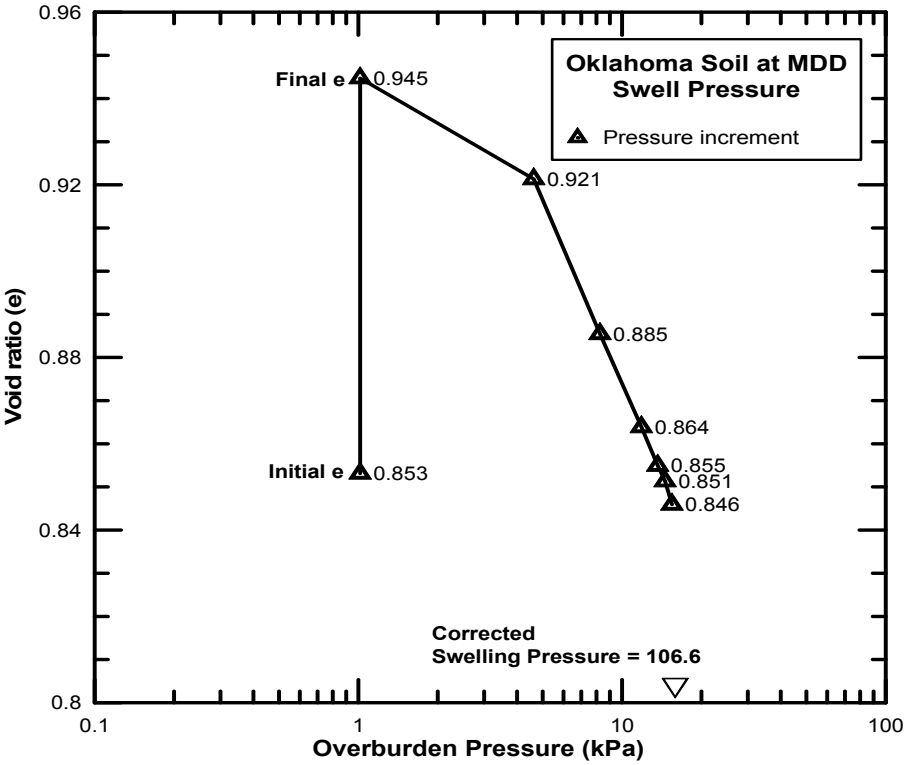

Figure 4.33: Load-back swell pressure test on Oklahoma soil at MDD

4.2.6.2 3-D swell strains

Soil specimens of 50.8 mm (2 in.) diameter and 101.6 mm (4 in.) height were compacted at 95% MDD and were tested for 3-D volumetric swell strains. Figure 4.34 presents the 3-D vertical swell strains exhibited by Oklahoma soil specimen at 3 different confinement levels. The specimen showed a maximum vertical strain of 3.2% at 7 kPa (1 psi) confinement whereas; it showed 1.63% strain at 100 kPa (14.5 psi) confinement. Similarly, Figure 4.35 shows the radial swell strain exhibited by the soil specimen at different confinements. The specimen exhibited a maximum radial swell strain of 0.91% at 7 kPa (1 psi) confinement and least radial strain of 0.53% at 100 kPa (14.5 psi) confinement.

The total volumetric strain is calculated from the summation of vertical and twice radial strain is presented in Figure 4.36. The specimen showed maximum volumetric swell strains of 5% at 7 kPa (1 psi), 3.7% at 50 kPa (7.25 psi) and 2.7% at 100 kPa (14.5 psi) confinement levels.

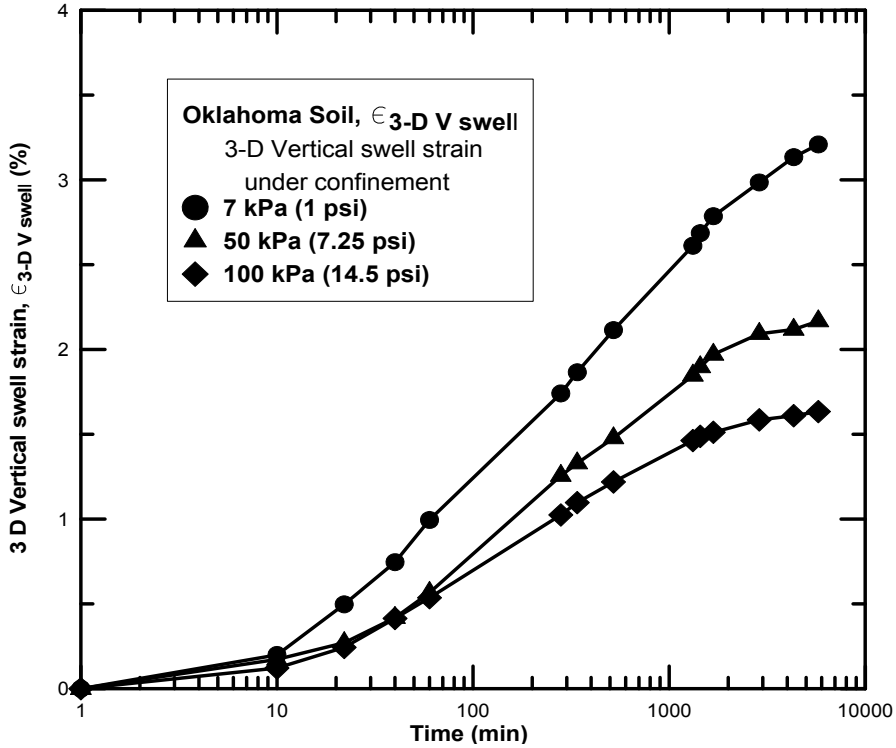

Figure 4.34: Vertical swell strain exhibited by Oklahoma soil at different confinements

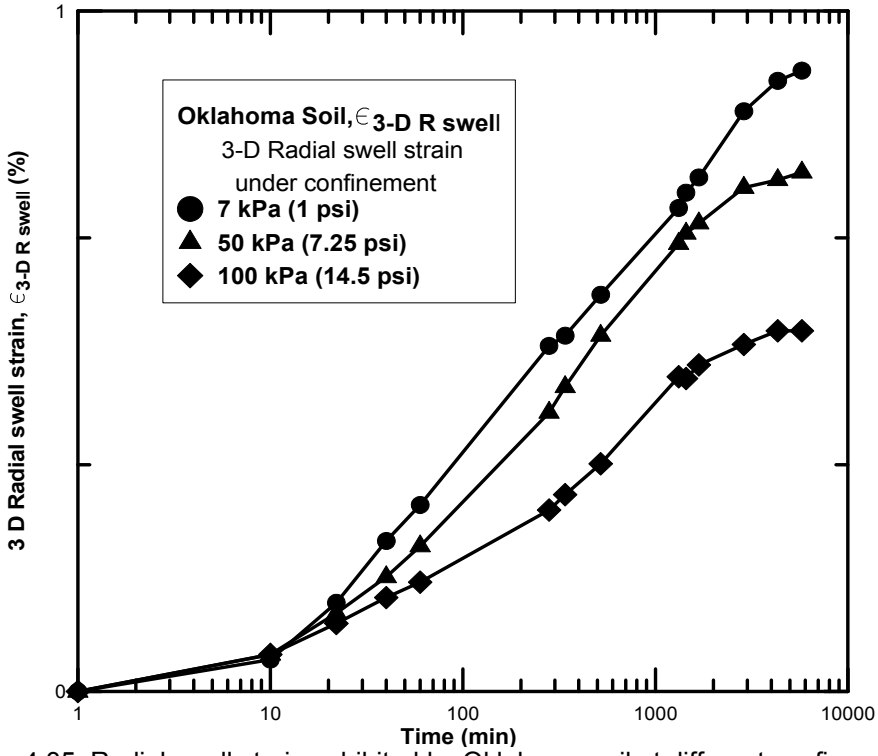

Figure 4.35: Radial swell strain exhibited by Oklahoma soil at different confinements

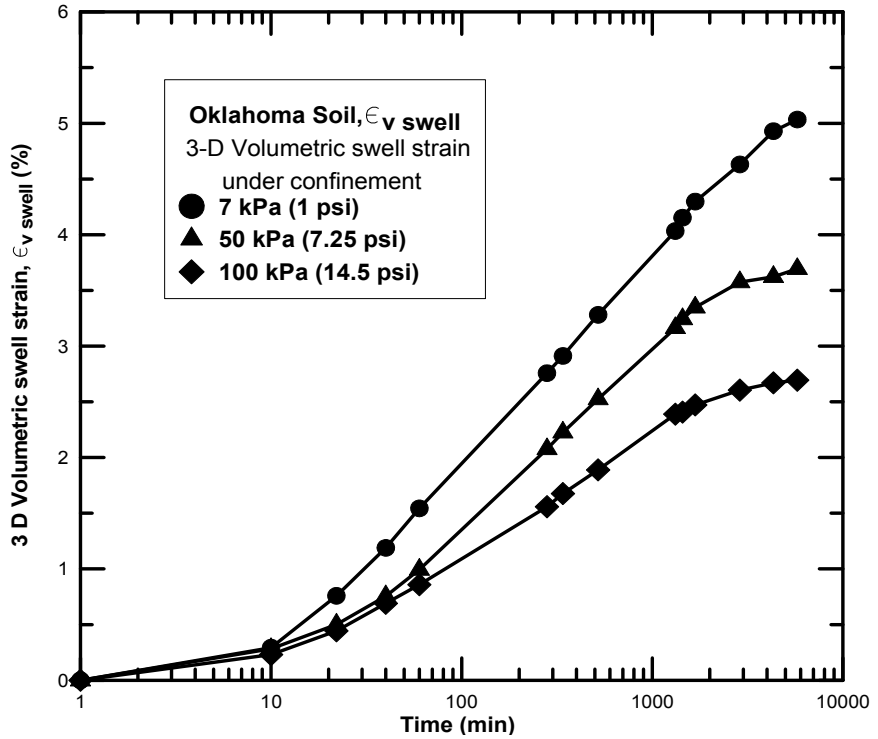

Figure 4.36: Volumetric swell strain exhibited by Oklahoma soil at different confinements

4.2.7 San Antonio Soil

San Antonio soil was collected from the state of Texas. Based on the USCS soil classification system the soil was classified as a high plasticity clay (CH). The swelling behavior of San Antonio soil is presented in the following.

4.2.7.1 1-D Swell strain and Load-back swell pressures

Figure 4.37 shown below presents the 1-D swell strains exhibited by San Antonio soil specimen at two different compaction dry densities, maximum dry density (MDD) and 95% of maximum dry density (95% MDD). The specimen exhibited a maximum swell of 10.2% at maximum dry density (MDD) and 7.3% swell at 95% MDD.

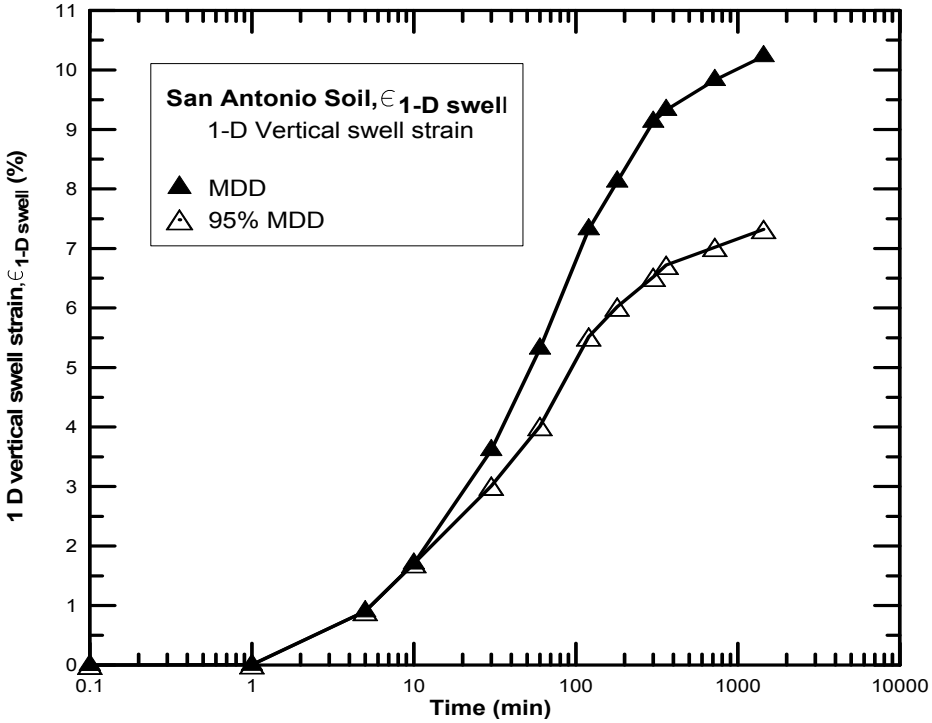

Figure 4.37: One dimensional swell strains for San Antonio soil

Figures 4.38 and 4.39 present the load back swell pressures obtained from San Antonio soil at two different densities. Soil specimen at 95% MDD exhibited a swell pressure of 137.7 kPa (20 psi) and 231.1 kPa (33.5 psi) at MDD condition. The particle and mineral density was very high in case of MDD condition which resulted in higher swelling behavior.

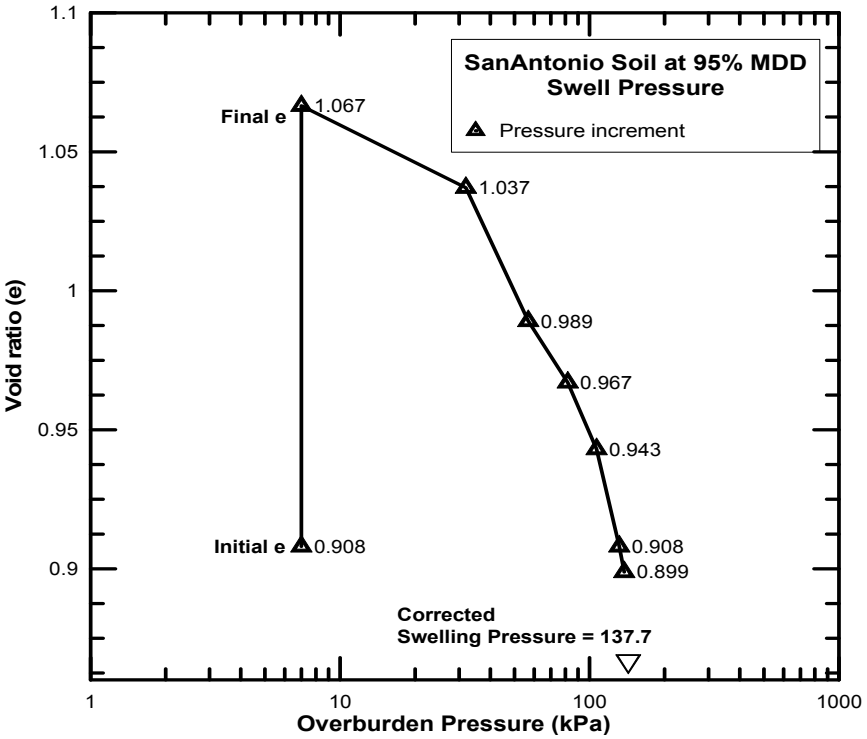

Figure 4.38: Load-back swell pressure test on San Antonio soil at 95% MDD

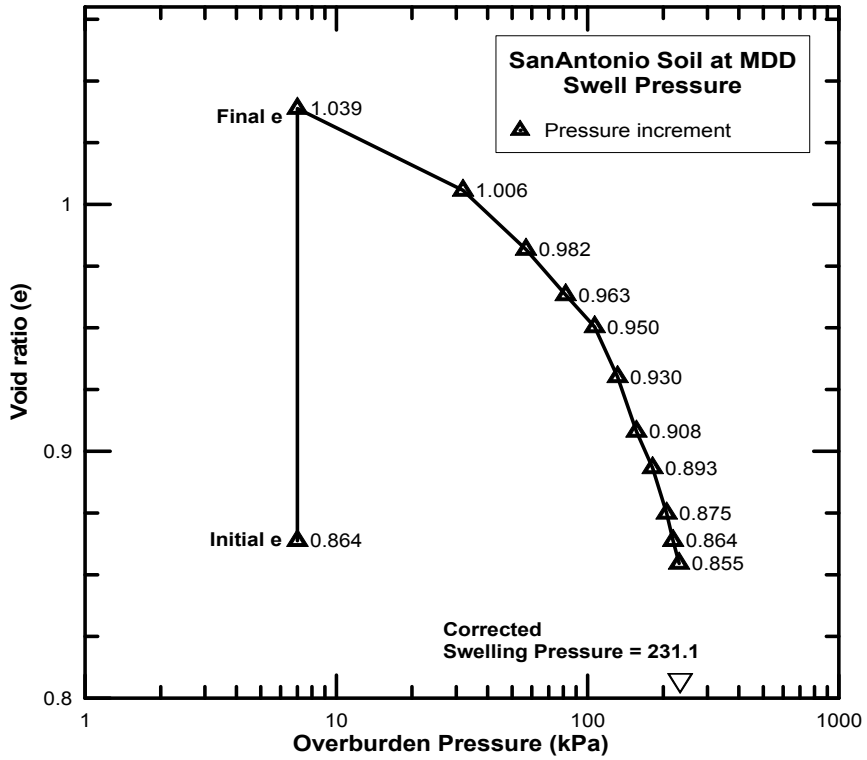

Figure 4.39: Load-back swell pressure test on San Antonio soil at MDD

4.2.7.2 3-D swell strains

Soil specimens of 50.8 mm (2 in.) diameter and 101.6 mm (4 in.) height were compacted at 95% MDD and were tested for 3-D volumetric swell strains. Figure 4.40 presents the 3 D vertical swell strains exhibited by San Antonio soil specimen at 3 different confinement levels. The specimen showed a maximum vertical strain of 6.7% at 7 kPa (1 psi) confinement whereas; it showed 3.83% strain at 100 kPa (14.5 psi) confinement. Similarly, Figure 4.41 shows the radial swell strain exhibited by the soil specimen at different confinements. The specimen exhibited a maximum radial swell strain of 1.2% at 7 kPa (1 psi) confinement and least radial strain of 0.95% at 100 kPa (14.5 psi) confinement.

The total volumetric strain is calculated from the summation of vertical and twice radial strain is presented in Figure 4.42. The specimen showed maximum volumetric swell strains of 9.13% at 7 kPa (1 psi), 7.4% at 50 kPa (7.25 psi) and 5.7% at 100 kPa (14.5 psi) confinement levels.

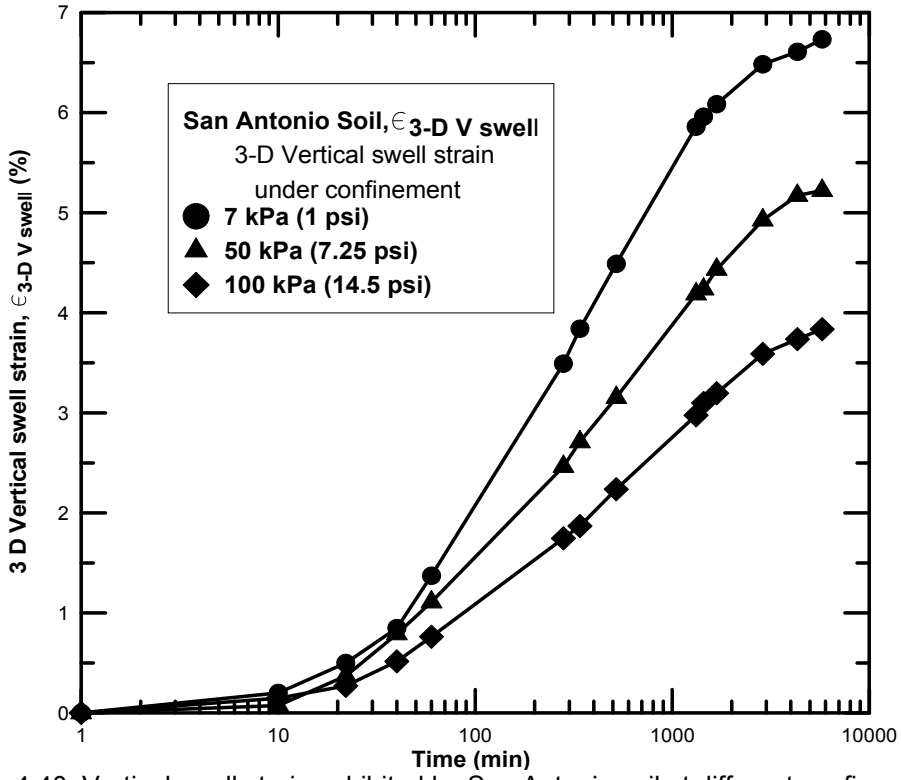

Figure 4.40: Vertical swell strain exhibited by San Antonio soil at different confinements

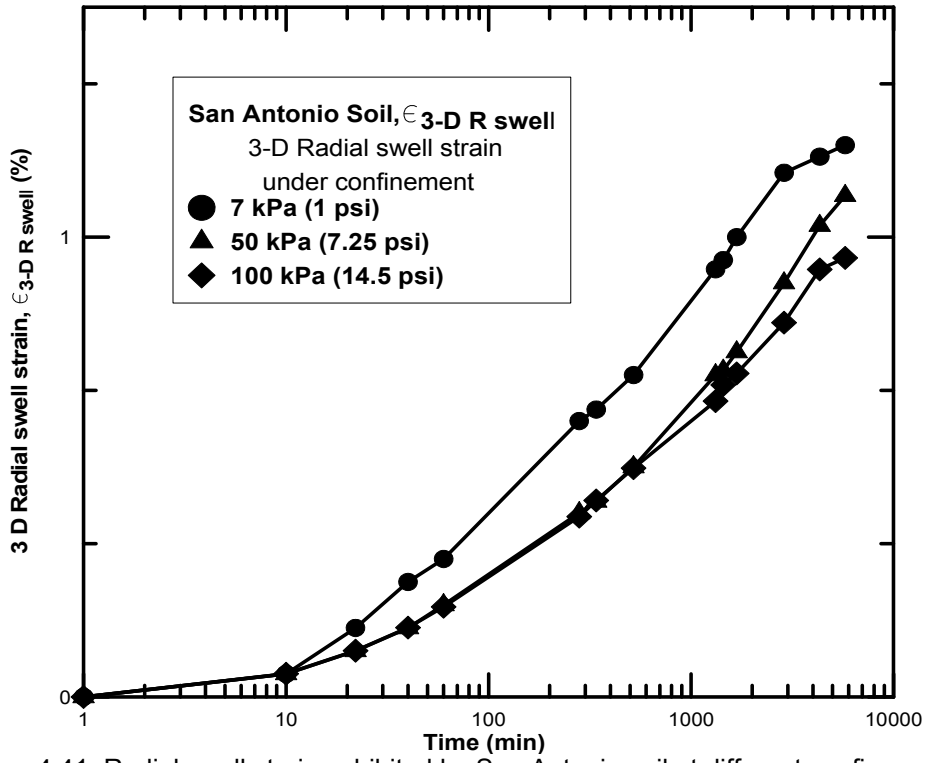

Figure 4.41: Radial swell strain exhibited by San Antonio soil at different confinements

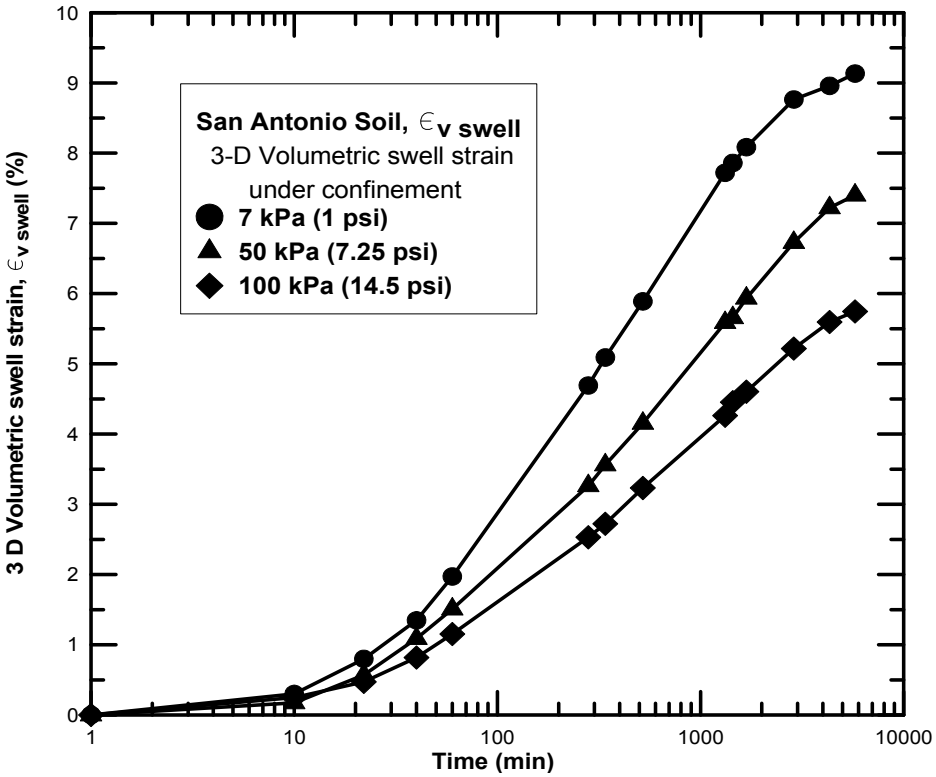

Figure 4.42: Volumetric swell strain exhibited by San Antonio soil at different confinements

4.2.8 San Diego Soil

San Diego soil was collected from the state of California. Based on the USCS soil classification system the soil was classified as a low plasticity clay (CL). The swelling behavior of San Diego soil is presented in the following.

4.2.8.1 1-D Swell strain and Load-back swell pressures

Figure 4.43 shown below presents the 1-D swell strains exhibited by San Diego soil specimen at two different compaction dry densities, maximum dry density (MDD) and 95% of maximum dry density (95% MDD). The specimen exhibited a maximum swell of 4.35% at maximum dry density (MDD) and 3.41% swell at 95% MDD.

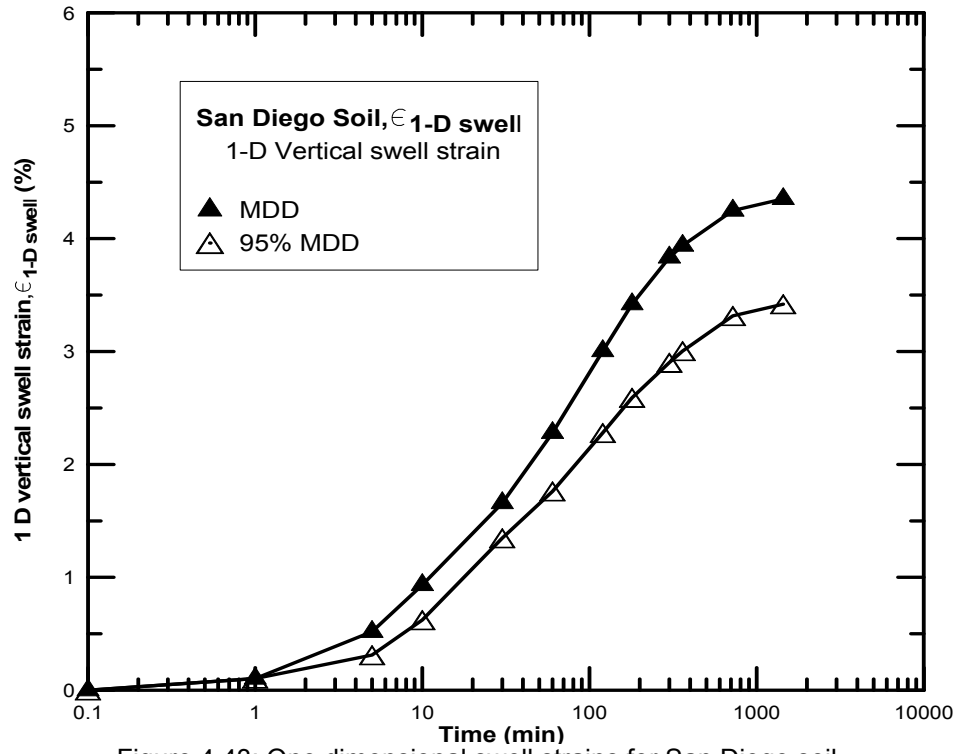

Figure 4.43: One dimensional swell strains for San Diego soil

Figures 4.44 and 4.45 present the load back swell pressures obtained from San Diego soil at two different densities. Soil specimen at 95% MDD exhibited a swell pressure of 50.5 kPa (7.3 psi) and 75.5 kPa (10.9 psi) at MDD condition. The particle and mineral density was very high in case of MDD condition which resulted in higher swelling behavior.

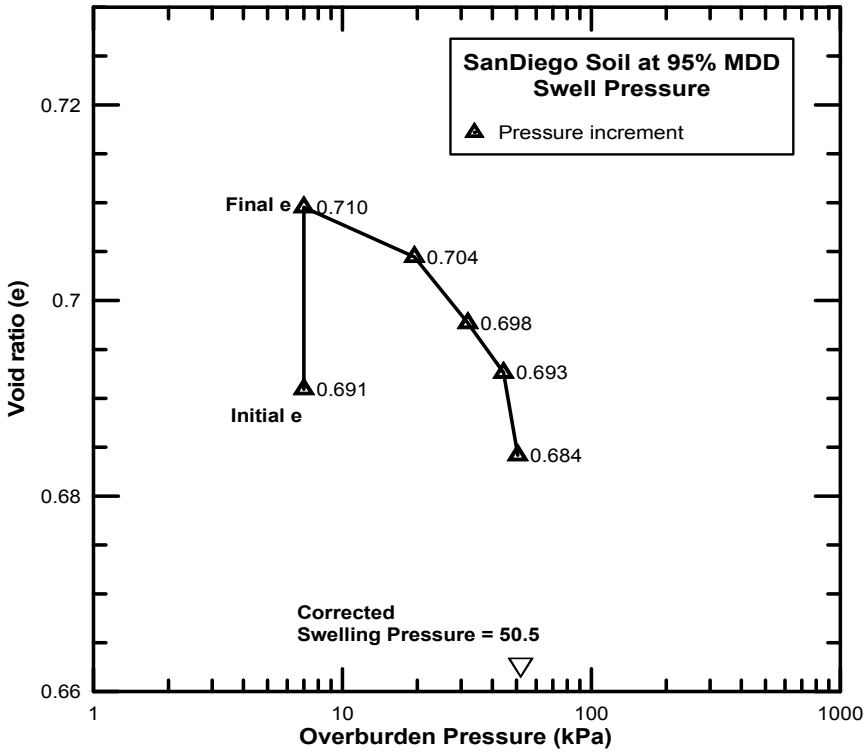

Figure 4.44: Load-back swell pressure test on San Diego soil at MDD

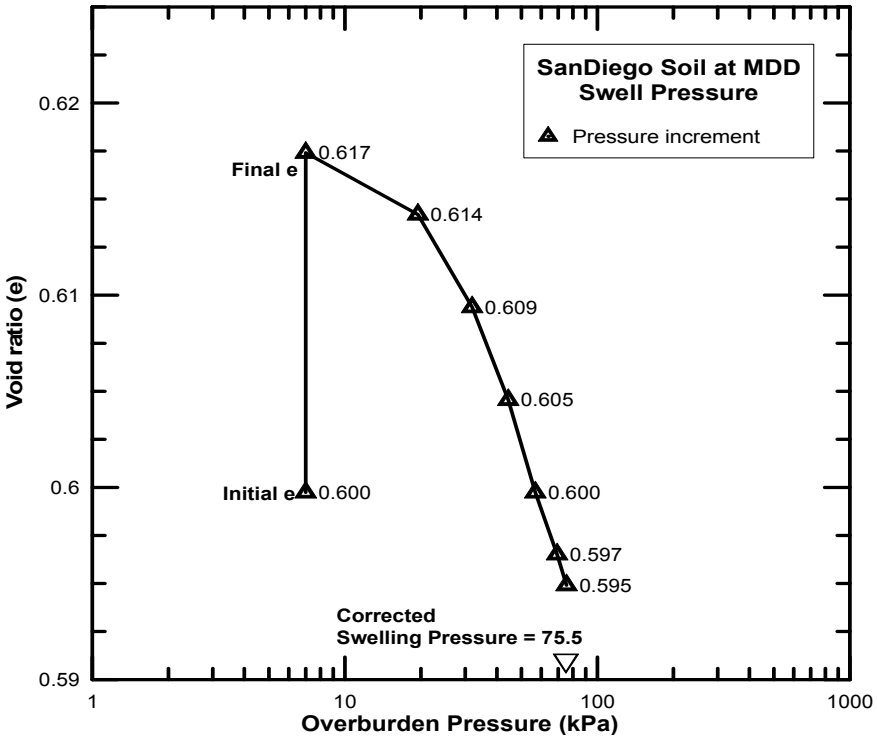

Figure 4.45: Load-back swell pressure test on San Diego soil at MDD

4.2.8.2 3-D swell strains

Soil specimens of 50.8 mm (2 in.) diameter and 101.6 mm (4 in.) height were compacted at 95% MDD and were tested for 3-D volumetric swell strains. Figure 4.46 presents the 3 D vertical swell strains exhibited by San Diego soil specimen at 3 different confinement levels. The specimen showed a maximum vertical strain of 2.95% at 7 kPa (1 psi) confinement whereas; it showed 1.17% strain at 50 kPa (14.5 psi) confinement. Similarly, Figure 4.47 shows the radial swell strain exhibited by the soil specimen at different confinements. The specimen exhibited a maximum radial swell strain of 0.78% at 7 kPa (1 psi) confinement and least radial strain of 0.48% at 100 kPa (14.5 psi) confinement.

The total volumetric strain is calculated from the summation of vertical and twice radial strain is presented in Figure 4.48. The specimen showed maximum volumetric swell strains of 4.5% at 7 kPa (1 psi), 3.4% at 50 kPa (7.25 psi) and 2.1% at 100 kPa (14.5 psi) confinement.

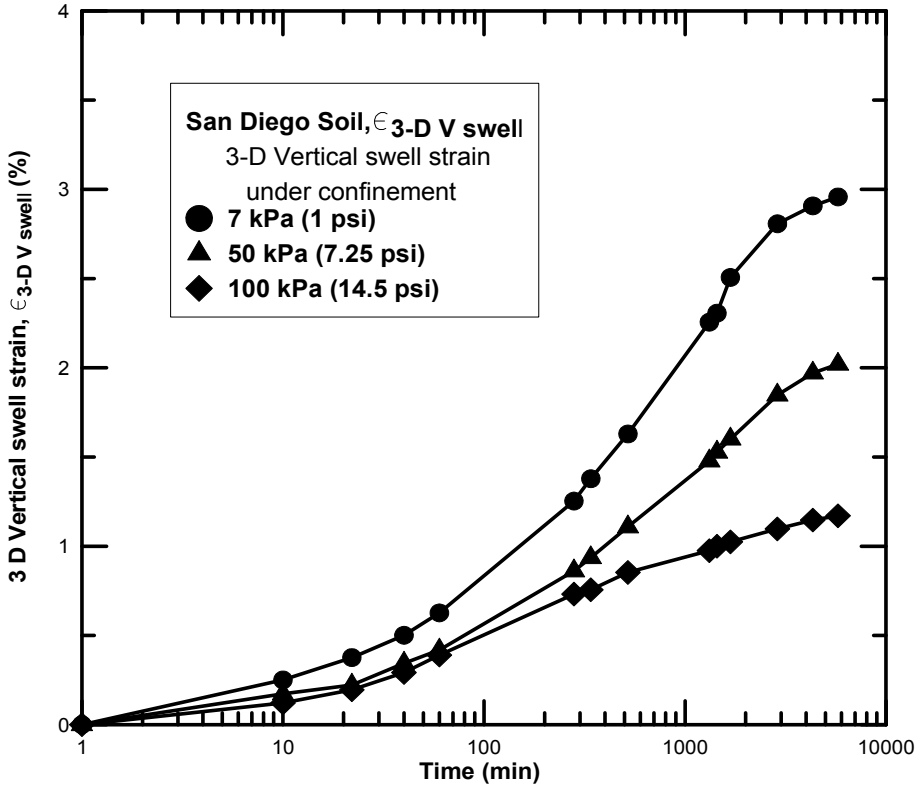

Figure 4.46: Vertical swell strain exhibited by San Diego soil at different confinements

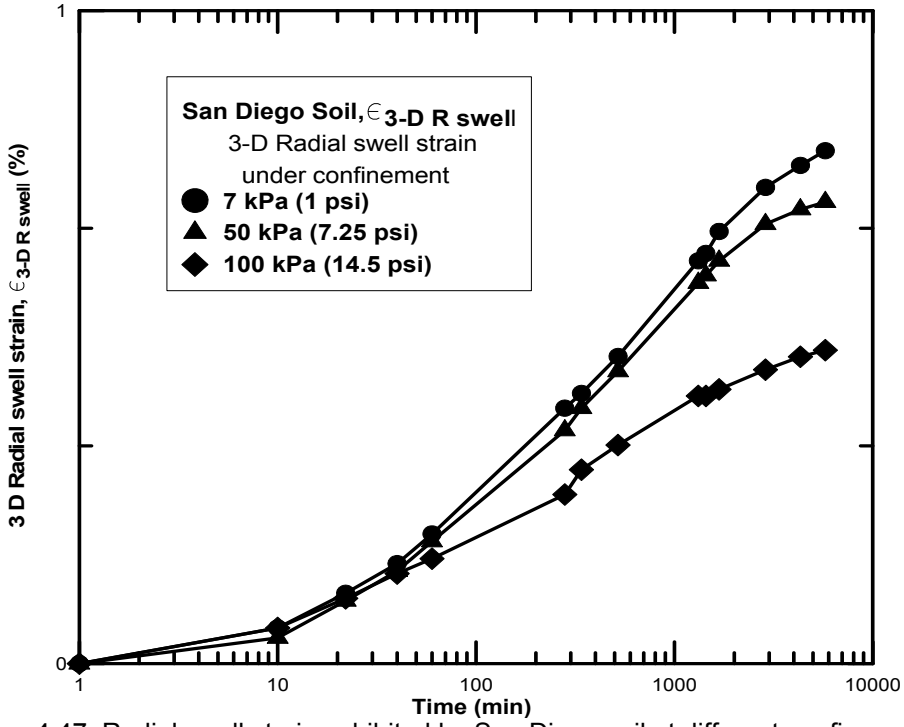

Figure 4.47: Radial swell strain exhibited by San Diego soil at different confinements

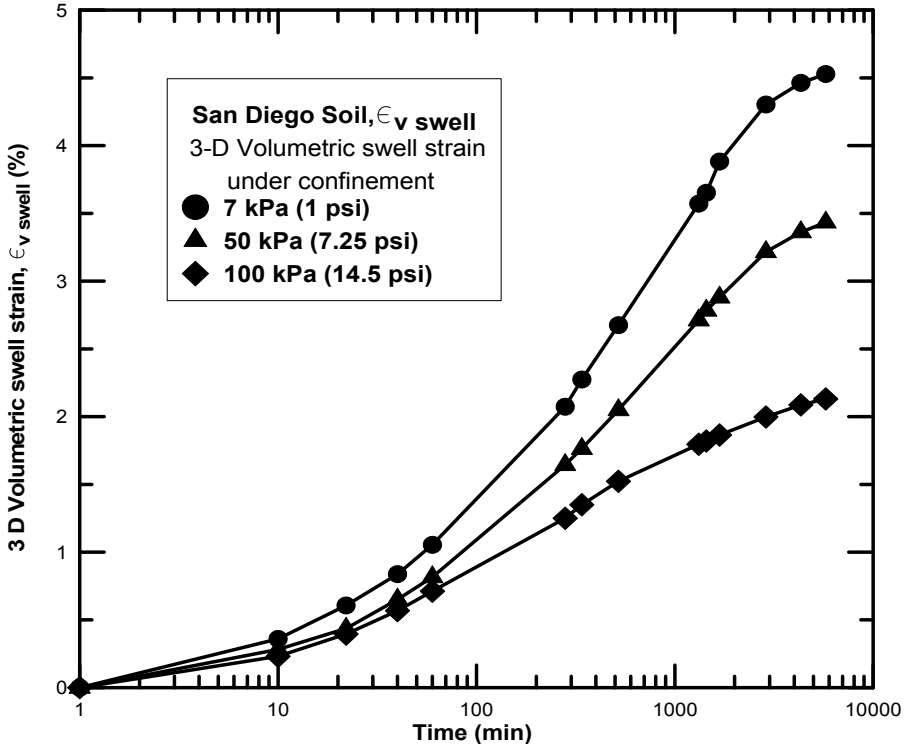

Figure 4.48: Volumetric swell strain exhibited by San Diego soil at different confinements

4.3 Summary

Test results showed that the soil exhibiting the maximum swell strains was Grayson soil and the one exhibiting the least swell strains was San Diego soil. The soils presented in Table 4.1 are in the order of their maximum swell strains exhibited in the present swell testing. Clay mineralogy plays an important role in governing the swell behavior of expansive clays. The soils exhibiting maximum swell strains (Grayson) also showed a higher swell pressure due to the presence of high amounts of Montmorillonite content present in this soil when compared to the same of the remaining soils. Soils compacted at maximum dry density (MDD) condition showed higher swell strains and swell pressures due to the presence of more soil and mineral content than at 95% MDD. Table 4.1 below presents the 1-D swell strains and load back swell pressure result summary for all the selected soils.

Table 4.1: Summary of the 1-D swell strains and swell pressure test results

Ranking		1-D Swell strain (%)		Swell Pressure (kPa)	
Soil	PI	MDD	95% MDD	MDD	95% MDD
Grayson	50	14.2	9.8	243.5	156.4
Colorado	42	12.0	8.2	194.0	137.7
San Antonio	43	10.2	7.3	231.1	137.7
Burleson	37	8.8	5.5	183.4	112.8
Keller	11	7.9	5.6	137.7	98.0
Anthem	27	5.8	4.5	134.6	94.2
Oklahoma	21	4.8	3.8	106.6	63.0
San Diego	28	4.4	3.4	75.5	50.5

Grayson clay exhibited the maximum swell strains at both MDD and 95% MDD condition. The soil also exhibited a maximum swell pressure of 35 psi at MDD condition and

22.7 psi at 95% MDD condition. San Diego soil showed the least swell strains and swell pressures at MDD and 95% MDD conditions.

All the clays were tested for 3-D swell strains with the help of the novel apparatus detailed in Chapter 3. The remolded clay specimens of 2" diameter and 4" height are allowed to saturate at confinement levels of 7kPa (1 psi), 50 kPa (7.25) and 100 kPa (14.5 psi). The swell strains exhibited by the soil specimens were measured and the summaries of test results are presented in Table 4.2. Grayson soil exhibited maximum vertical, radial and volumetric strains under all confinements, while San Diego exhibited the least strains.

At least confinement levels (7 kPa) all the soils underwent maximum swell strains in both vertical and radial directions. The swell strains reduced considerably as the confinement levels increased for all the clays.

Table 4.2: Summary of the 3-D swell strain test results

Ranking	Vertical strains (%)			Radial Strains (%)			Volumetric Strains (%)		
Soil	σ = 7 kPa	σ = 50 kPa	σ = 100 kPa	σ = 7 kPa	σ = 50 kPa	σ = 100 kPa	σ = 7 kPa	σ = 50 kPa	σ = 100 kPa
Grayson	9.11	6.40	5.60	1.26	1.18	1.03	11.65	8.76	7.67
Colorado	6.82	5.34	4.39	1.23	1.10	0.95	9.29	7.55	6.30
San Antonio	6.73	5.22	3.83	1.20	1.09	0.95	9.13	7.40	5.74
Burleson	5.78	4.58	3.07	1.12	0.93	0.80	8.03	6.45	4.69
Keller	4.75	3.96	2.07	1.04	0.88	0.82	6.84	5.73	3.71
Anthem	3.00	2.70	1.75	0.89	0.78	0.56	4.80	4.30	2.87
Oklahoma	3.20	2.16	1.63	0.91	0.76	0.53	5.03	3.69	2.69
San Diego	2.95	2.01	1.17	0.78	0.70	0.48	4.52	3.43	2.13

Where σ = 3-D confinement pressure

4.3.1 Influence of Mineral Montmorillonite on swell behavior

Montmorillonite plays an important role in governing the swell behavior. The presence of this mineral in large percentages allows the clay to have higher swelling/shrinking capabilities. Figure 4.49 shown below presents the variation of 1 Dimensional swell with Montmorillonite content. From the test results on eight expansive clays it was observed that, with an increase in Montmorillonite content the soils exhibited more 1-D swell strains. Polynomial fitting models were plotted both for MDD and 95% MDD condition. These fitting models were based on the test soils and show a coefficient of determination (R^2) around 0.8. These models can be used to predict the one dimensional swell strains from the pre-determined mineral Montmorillonite content in a soil.

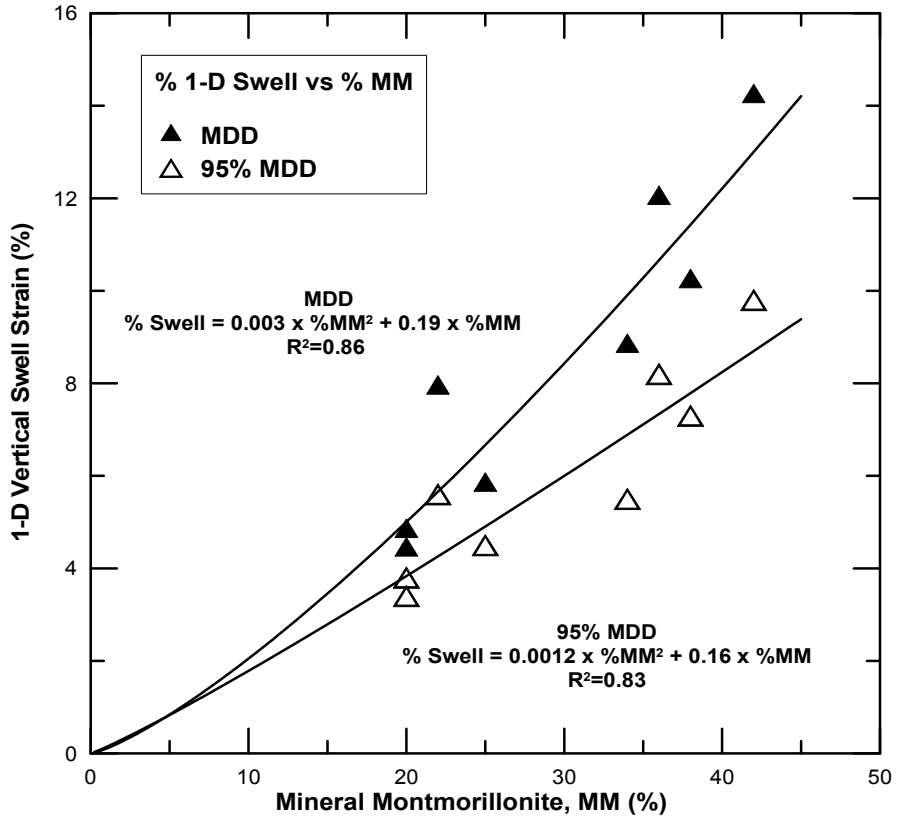

Figure 4.49: Variation of 1-D Vertical Swell with Montmorillonite content for expansive clays

Figure 4.50 shown below presents the variation of swell pressures of expansive clays with percent Montmorillonite content in a soil. The load back swell pressure tests were

conducted on soil specimens compacted at MDD and 95% MDD. From the test results it was observed that, with an increase in Montmorillonite content the soils exhibited more swell pressures.

Polynomial fits were plotted both for MDD and 95% MDD conditions. These fitting models were based on 8 soils and are show a coefficient of determination (R^2) around 0.9. These models are used to predict the one dimensional swell strains from the pre-determined mineral Montmorillonite content in a soil.

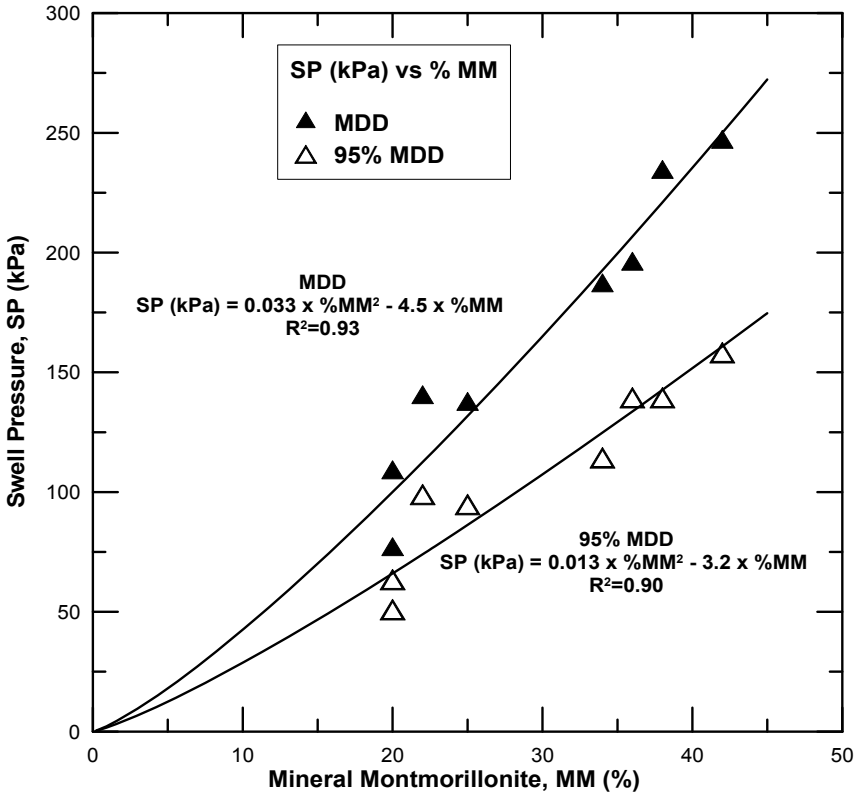

Figure 4.50: Variation of swell pressures with Montmorillonite content for expansive clays

The volumetric swell strains at three confinement pressures (1, 7.25 and 14.5 psi, respectively) are presented and the corresponding fitting models for all the test results of eight soils are presented. With an increase in confinement pressure, the volumetric swell strains have decreased. From the test results it was observed that, with an increase in Montmorillonite content the soils exhibited a higher volumetric swell strains. The polynomial models presented

here have a coefficient of determination value around 0.9 and hence these models are appropriate for the determination of volumetric swell strains under different confinement pressures and pre-determined Montmorillonite contents. The variation of volumetric swell strains with Montmorillonite content is shown in Figure 4.51 below.

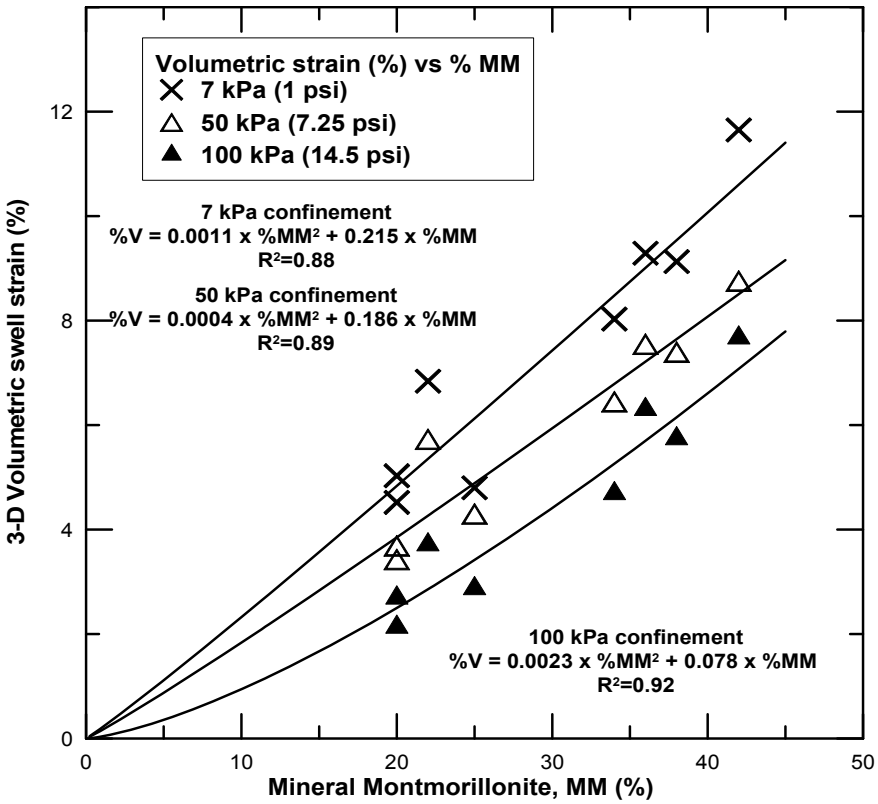

Figure 4.51: Variation of volumetric strains under confinement with Montmorillonite content

The test results of swell strains and swell pressure values exhibited by the soils under different loading and confinement conditions are discussed in this chapter. Also, the variation of swell behavior with clay mineral content was studied and presented. The next chapter deals with the soil composition properties like soil-water relationship and pore distribution. The soil composition test results obtained from the various tests on the expansive clays are presented and discussed in the next Chapter.

CHAPTER 5

SOIL COMPOSITION TEST RESULTS

5.1 Introduction

The behavior of any expansive soil is dependent on its inherent properties such as clay mineralogy, relationship with moisture content, and pore void distribution. The mineralogy of clay governs the micro parameters like specific surface area and cation exchange capacity which influences the swell shrink behavior of soils (Mitchell and Soga, 2005).

The next important factor governing the swell behavior is the relationship with compaction moisture content. This is well understood with the help of a soil water characteristic curve (SWCC) which describes the variation of soil suction with volumetric moisture content. Fredlund et al. (1980) detailed that the soil water characteristic for a soil has a unique relationship with a given soil and is dependent on the compaction density and grain distribution. In the present chapter, the SWCC for all the eight soils collected were measured and presented along with the commonly used curve fitting models like Van Genuchten (1980) and Fredlund and Xing (1994).

Pore size distribution plays an important role in the hydraulic conductivity behavior of the clay specimen, which in turn affects the swelling process. This internal distribution of pores in the soil specimen was studied by Mercury Intrusion Porosimetry (MIP) technique. The presence of pores of different sizes are determined and classified to different levels based on the MIP test results. X-ray Tomography technique which was used to scan and reconstruct a solid mass helps in the identification of internal structure of a soil specimen. The pore connectivity and the variation of void ratio with change in density and moisture content are

studied with the help of this laboratory technique. This chapter presents the soil composition test results on all the eight soils obtained from different parts of The United States.

5.2 Soil suction studies

The determination of soil water characteristic curve (SWCC) is possible with laboratory measurement techniques like the filter paper, pressure plate and potentiometer methods as previously discussed in Chapter 3. The variation of volumetric moisture content of the soil specimens with corresponding changes in soil matric suction is recorded as a SWCC. Soils were subjected to these tests at two compaction dry density conditions, one at MDD condition and other at 95% MDD condition.

5.2.1 Anthem Soil SWCC

Compacted Anthem soil specimen was subjected to SWCC studies at 95% MDD and OMC condition. The variation of volumetric moisture content with matric suction for Anthem soil specimen is shown in Figure 5.1.

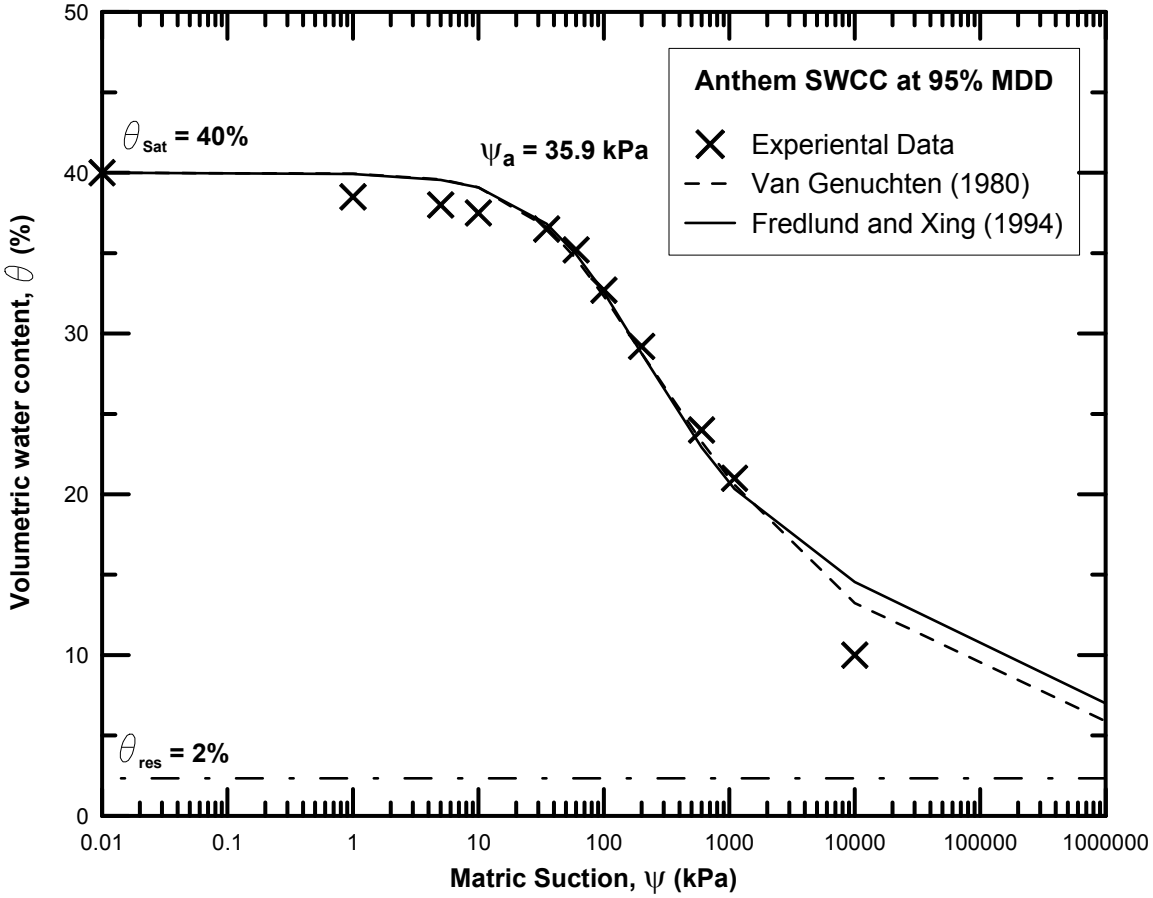

Figure 5.1: Soil water characteristic curve of Anthem soil

Anthem soil being characterized as a low plasticity clay has exhibited maximum saturated volumetric moisture content (θ_{sat}) of 40%. The soil exhibited a high air entry value (ψ_a) of 35.9 kPa (5.2 psi). The residual moisture content (θ_{res}) retained within Anthem soil is 2%. Two most commonly used fitting models Van Genuchten (1980) and Fredlund and Xing (1994) were used to fit and model the experimental data. Parameters obtained for Van Genuchten curve fitting model on Anthem soil are a=0.02, n=1.23 and m=0.186 and similar parameters are also obtained for Fredlund and Xing curve fitting model on the same Anthem soil test results. These model constants are: a_1=75, n_1=1.1 and m_1=0.6.

5.2.2 Burleson Soil SWCC

Burleson soil which was high plasticity clay and this material was compacted at 95% MDD and OMC condition and was then tested for SWCC. The variation of volumetric moisture content with matric suction for Burleson soil specimen is shown in Figure 5.2.

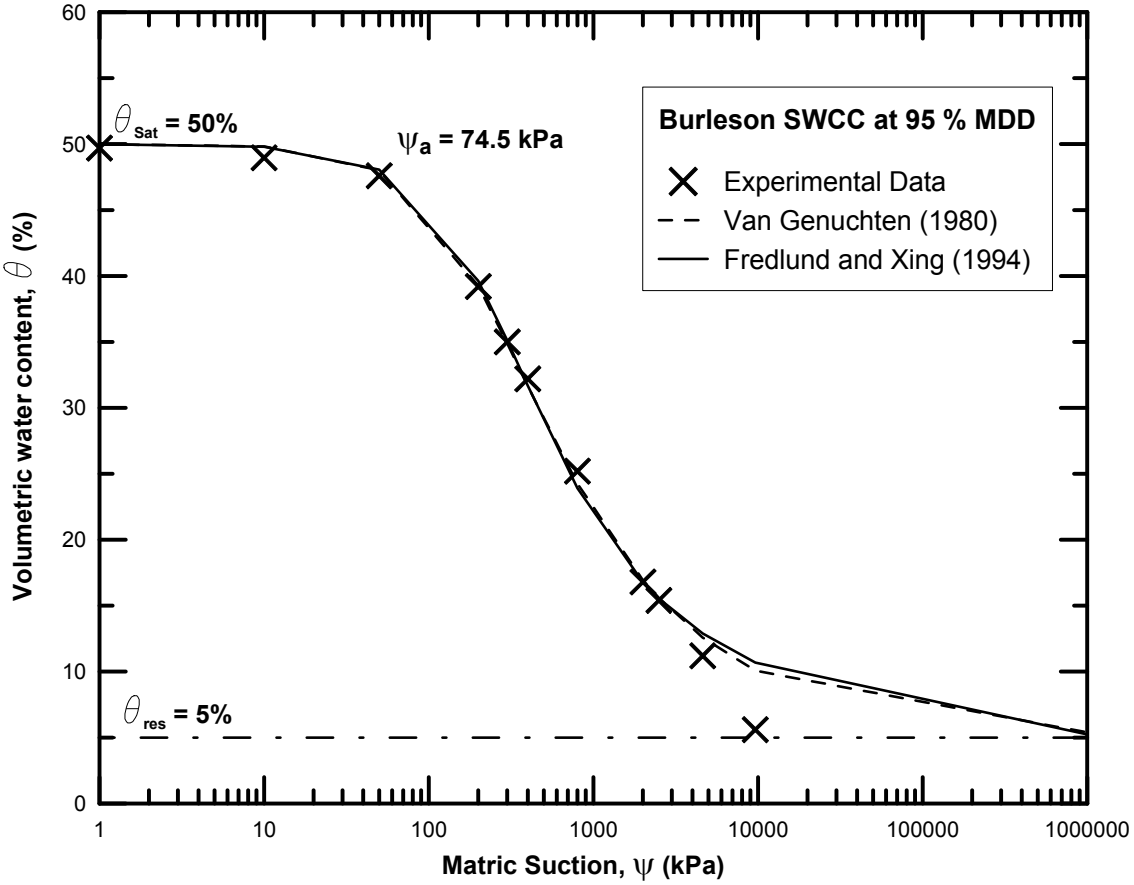

Figure 5.2: Soil water characteristic curve of Burleson soil

Burleson soil absorbed a maximum saturated volumetric moisture content (θ_{sat}) of 50% and showed an air entry value (ψ_a) of 74.5 kPa (10.8 psi). The residual moisture content retained in the specimen (θ_{res}) was 5%. Two models, Van Genuchten (1980) and Fredlund and Xing (1994) were used to fit the experimental data. Parameters obtained for Van Genuchten curve fitting model on Burleson soil are: a=0.0055, n=1.55 and m=0.35 and similar parameters are also obtained for Fredlund and Xing curve fitting model on Burleson soil. These are: a_1=210, n_1=1.45 and m_1=0.9.

5.2.3 Colorado Soil SWCC

Colorado soil specimen compacted at its 95% MDD and OMC condition was then tested for SWCC. The variation of volumetric moisture content with matric suction for Colorado soil specimen is shown in Figure 5.3.

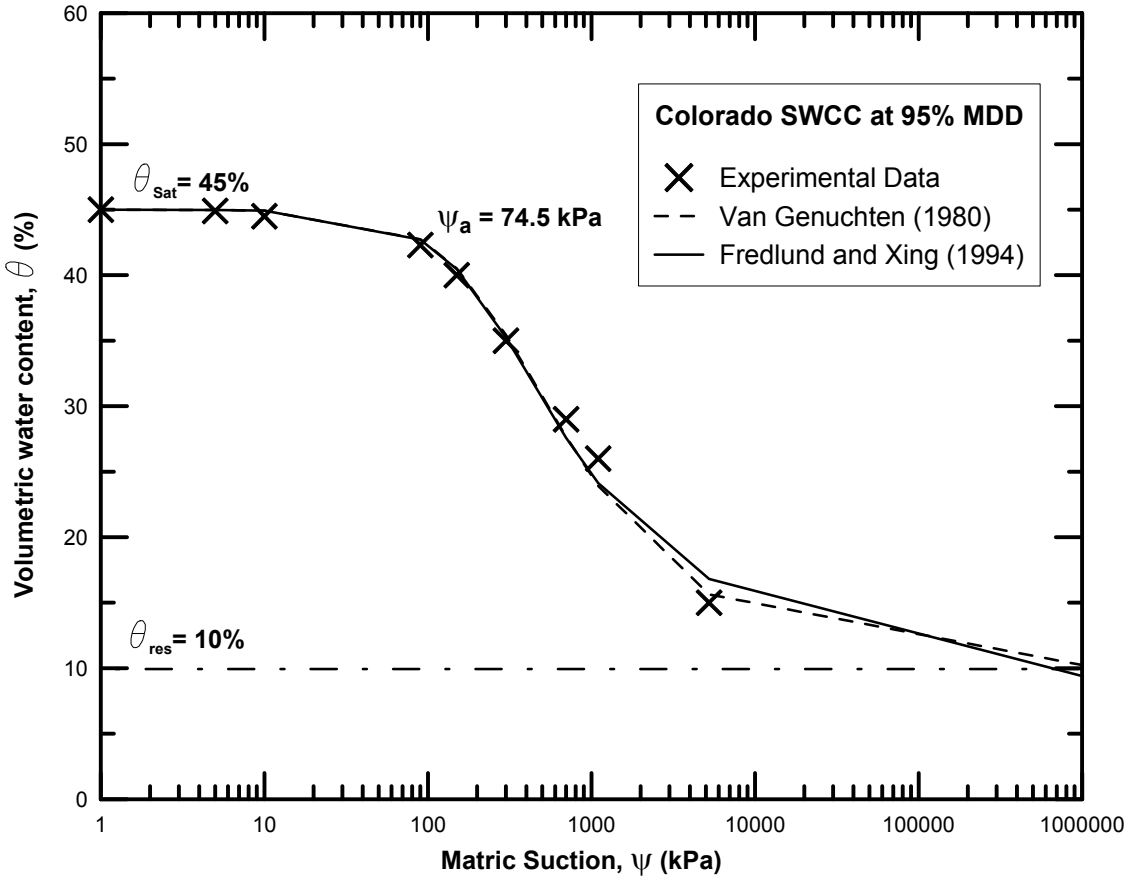

Figure 5.3: Soil water characteristic curve of Colorado soil

Colorado soil being a high plasticity clay had absorbed a maximum saturated volumetric moisture content (θ_{sat}) of 45%. The soil exhibited a high air entry value (ψ_a) of 74.5 kPa (10.8 psi). The residual moisture content (θ_{res}) retained within Colorado soil specimen is 10%. Van Genuchten (1980) and Fredlund and Xing (1994) models are used to fit the experimental data. Parameters obtained for Van Genuchten curve fitting model on Colorado soil are: a=0.004, n=1.6 and m=0.375 and Similar parameters are also obtained for Fredlund and

Xing curve fitting model on Colorado soil. The model constants of Fredlund & Xing model are: a_1=210, n_1=1.6 and m_1=0.6.

5.2.4 Grayson Soil SWCC

The compacted Grayson soil specimen was tested for SWCC at its 95% MDD and OMC condition. The variation of volumetric moisture content with matric suction for Grayson soil specimen is given in Figure 5.4.

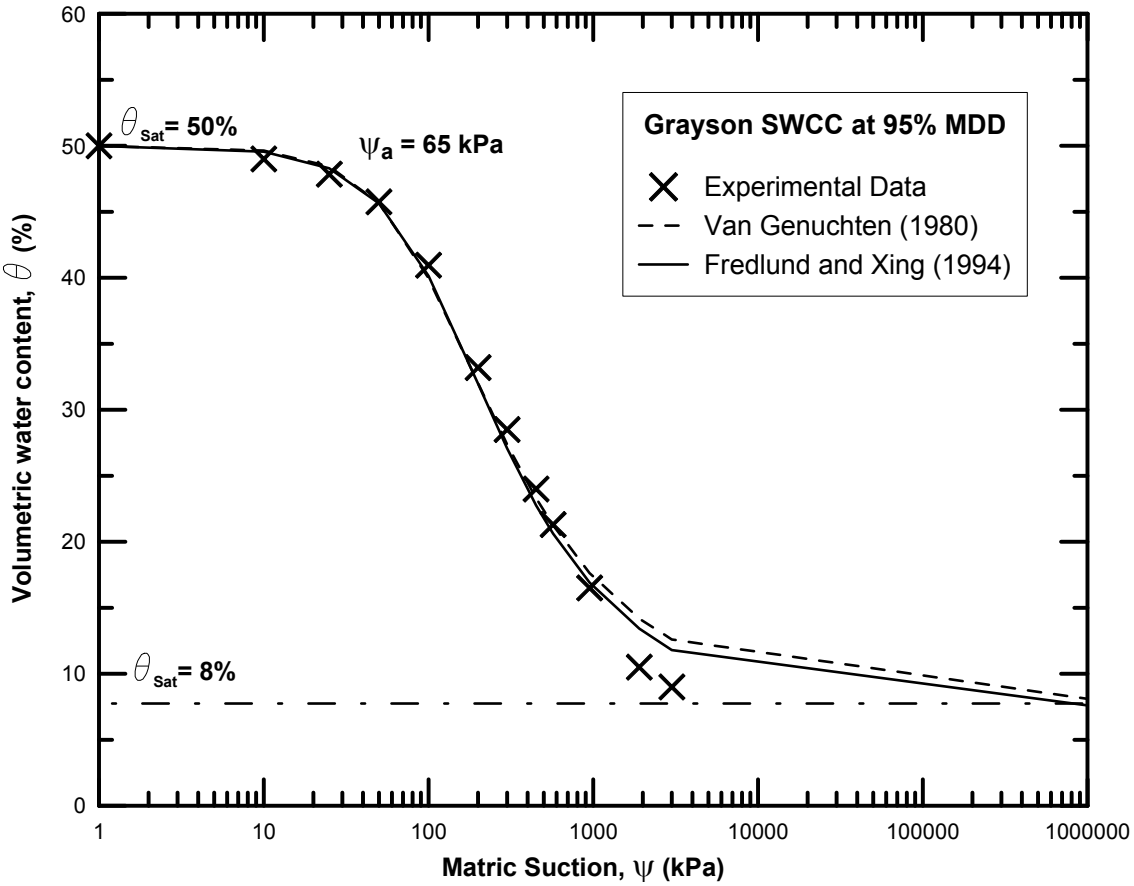

Figure 5.4: Soil water characteristic curve of Grayson soil

Grayson soil is a high plasticity clay and it absorbed a maximum saturated volumetric moisture content (θ_{sat}) of 50% and retained a residual moisture content (θ_{res}) of 8%. The soil showed an air entry value (ψ_a) of 65 kPa (9.4 psi). Models like Van Genuchten (1980) and Fredlund and Xing (1994) are used to simulate the experimental data. Parameters obtained for Van Genuchten curve fitting model on Grayson soil are: a=0.01, n=1.65 and m=0.39 and similar

parameters are also obtained for Fredlund and Xing curve fitting model on Grayson soil. These are: a_1=110, n_1=1.5 and m_1=0.9.

5.2.5 Keller Soil SWCC

Keller soil specimen compacted at its 95% MDD and OMC condition was then tested for SWCC. The variation of volumetric moisture content with matric suction for Keller soil specimen is shown in Figure 5.5.

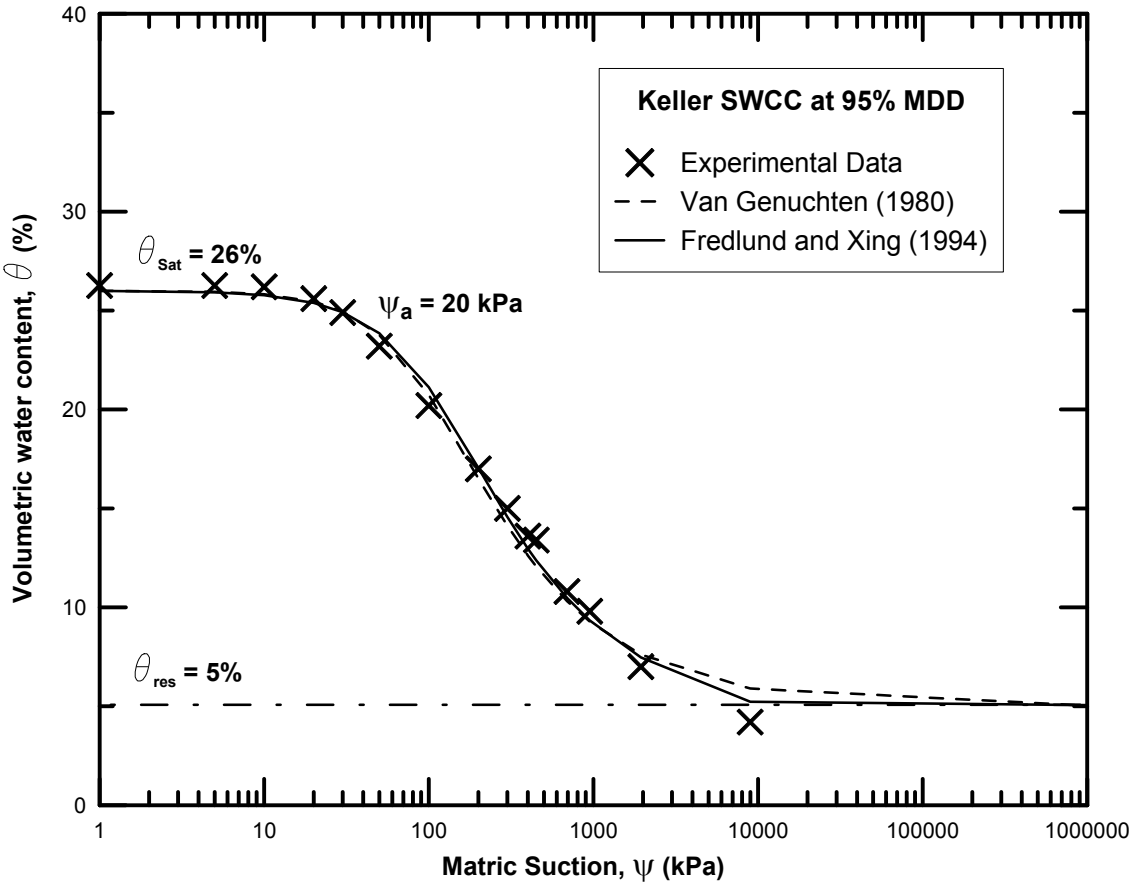

Figure 5.5: Soil water characteristic curve of Keller soil

Keller soil being low plasticity clay absorbed a maximum saturated volumetric moisture content (θ_{sat}) of 26%. The soil exhibited a high air entry value (ψ_a) of 20 kPa (2.9 psi) and a residual moisture content (θ_{res}) of 5%. Models like Van Genuchten (1980) and Fredlund and Xing (1994) were used to fit the experimental data. Parameters obtained for Van Genuchten curve fitting model on Keller soil are: a=0.01, n=1.7 and m=0.41 and similar parameters are also

obtained for Fredlund and Xing curve fitting model on Keller soil. They are: a_1=110, n_1=1.5 and m_1=0.85.

5.2.6 Oklahoma Soil SWCC

Compacted Oklahoma soil specimen was tested for SWCC at its 95% MDD and OMC condition. The variation of volumetric moisture content with matric suction for Oklahoma soil specimen is shown in Figure 5.6.

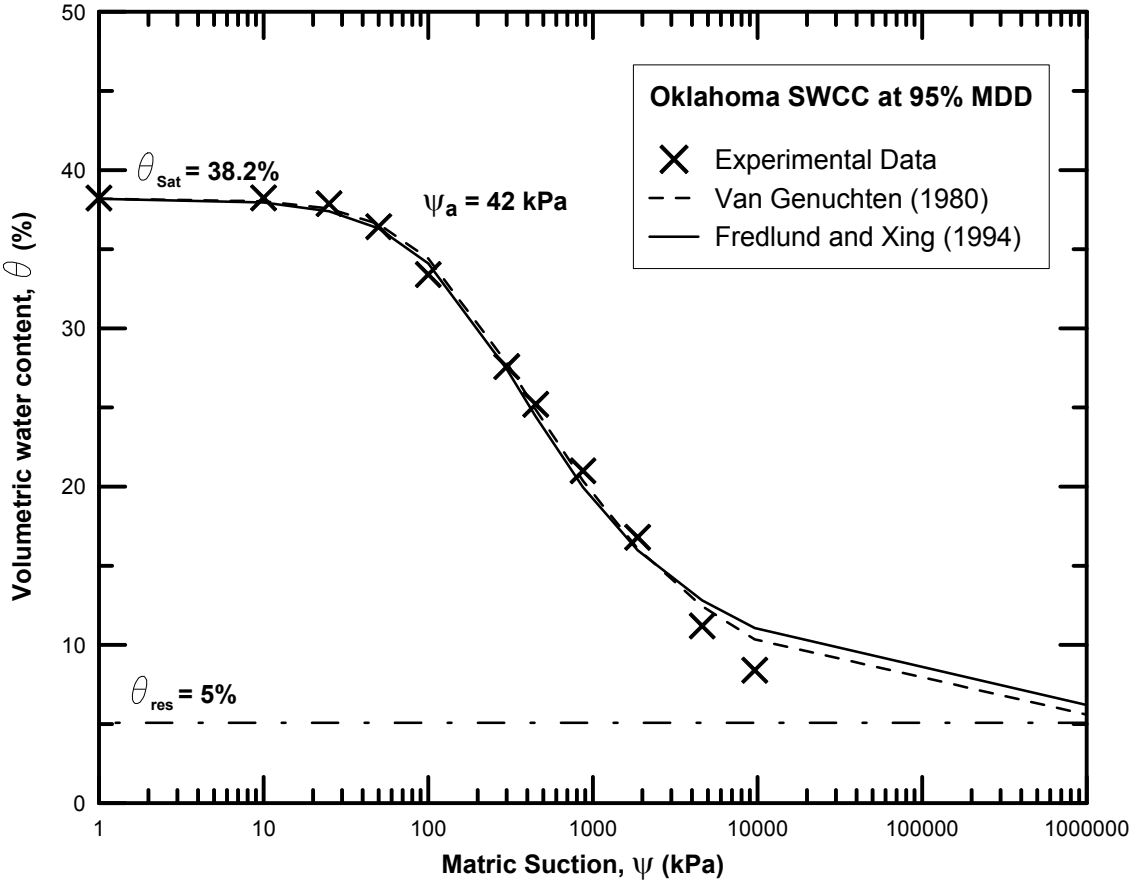

Figure 5.6: Soil water characteristic curve of Oklahoma soil

Oklahoma soil being a low plasticity clay absorbed a maximum saturated volumetric moisture content (θ_{sat}) of 38.2% and retained a residual moisture content (θ_{res}) of 5%. The specimen exhibited an air entry value (ψ_a) of 42 kPa (6 psi). Commonly used fitting models Van Genuchten (1980) and Fredlund and Xing (1994) were used to fit the experimental data. Parameters obtained for Van Genuchten curve fitting model on Oklahoma soil are: a=0.006,

n=1.45 and m=0.31 and similar parameters are also obtained for Fredlund and Xing curve fitting model on Oklahoma soil. They are: a_1=175, n_1=1.3 and m_1=0.75.

5.2.7 San Antonio Soil SWCC

The variation of volumetric moisture content with matric suction for San Antonio soil specimen is shown in Figure 5.7. The compacted soil specimen was tested for SWCC at its 95% MDD and OMC condition.

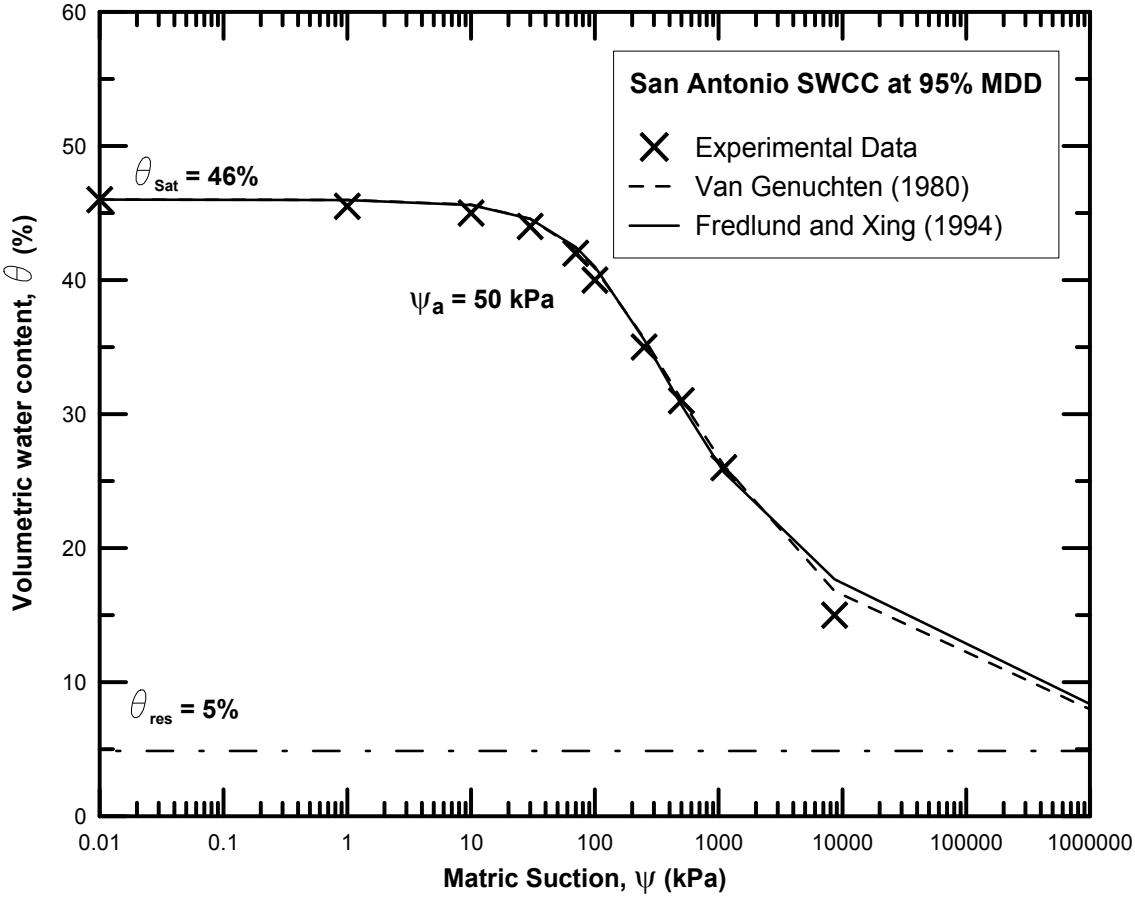

Figure 5.7: Soil water characteristic curve of San Antonio soil

San Antonio soil was characterized as a high plasticity clay and it exhibited a maximum saturated volumetric moisture content (θ_{sat}) of 46% and retained a residual moisture content (θ_{res}) of 5%. The soil exhibited a high air entry value (ψ_a) of 50 kPa (7.25 psi). Models like Van Genuchten (1980) and Fredlund and Xing (1994) were used to fit the experimental data. Parameters obtained for Van Genuchten curve fitting model on San Antonio soil are a=0.0085,

n=1.29 and m=0.22 and similar parameters are also obtained for Fredlund and Xing curve fitting model on San Antonio soil. The model constants from Fredlund and Xing model are: a_1=145, n_1=1.2 and m_1=0.6.

5.2.8 San Diego Soil SWCC

Compacted San Diego soil specimen was tested for SWCC at its 95% MDD and OMC condition. The variation of volumetric moisture content with matric suction for San Diego soil specimen is shown in Figure 5.8.

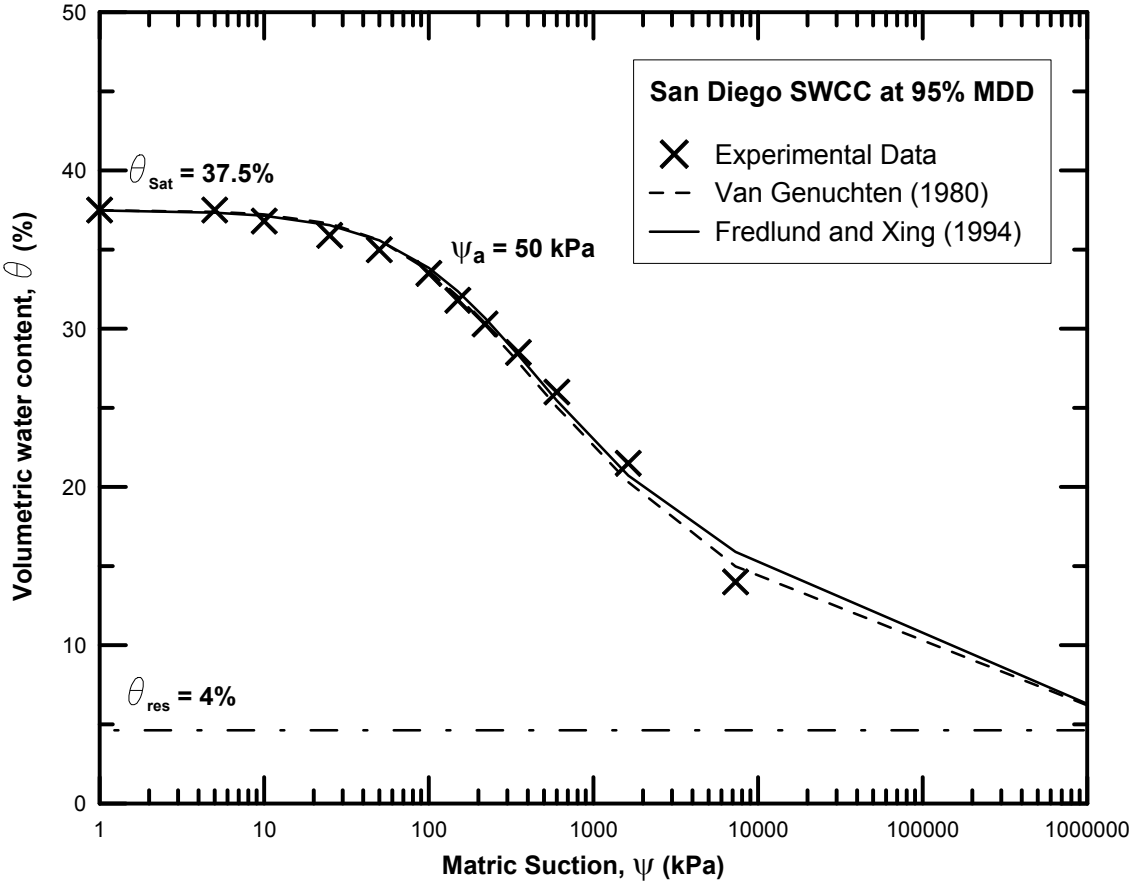

Figure 5.8: Soil water characteristic curve of San Diego soil

San Diego soil which was a low plasticity clay absorbed a maximum saturated volumetric moisture content (θ_{sat}) of 37.5% and retained a residual moisture content (θ_{res}) of 4%. The air entry value (ψ_a) for San Diego soil specimen was 50 kPa (7.25 psi). Van Genuchten (1980) and Fredlund and Xing (1994) were used to fit the experimental data. Parameters

obtained for Van Genuchten curve fitting model on San Diego soil are a=0.008, n=1.29 and m=0.22 and Similar parameters are also obtained for Fredlund and Xing curve fitting model on San Diego soil. They are: a_1=170, n_1=1.1 and m_1=0.6. The air entry value, saturated water content (θ_{sat}) and residual moisture content (θ_{res}) for each soil will be the influential parameters that explain the soil swell behavior and are utilized in the modeling analyses attempted in the next Chapter.

Unique soil suction parameters obtained from the measured soil water characteristic curves are presented in Table 5.1.

Table 5.1: Soil suction parameters obtained from measured SWCCs

Soil	Saturated volumetric moisture content (θ_{sat})(%)	Residual volumetric moisture content (θ_{res})(%)	Air entry value (ψ_a) (kPa)
Anthem	40.0	2	35.9
Burleson	50.0	5	74.5
Colorado	45.0	10	74.5
Grayson	50.1	8	65.0
Keller	26.0	5	20.0
Oklahoma	38.2	5	42.0
San Antonio	46.0	5	50.0
San Diego	37.5	4	50.0

The experimental SWCC data obtained from the laboratory measurements were plotted against the commonly used curve fitting models.

Table 5.2 presents the curve fitting parameters obtained from the Van Genuchten (1980) and Fredlund and Xing (1994) models plotted against all the eight soils. The coefficient

of determination (R^2) for all the models are greater than or equal to 0.97. These models have proven to be reliable in modeling the soil water characteristic curves of present soils.

The variations of curve fitting parameters are studied in detail in the following sections.

Table 5.2: Curve fitting parameters for SWCC models

Soil	Van Genuchten Model (1980)				Fredlund and Xing Model (1994)			
	A	n	m	R^2	a_1	n_1	m_1	R^2
Anthem	0.020	1.23	0.18	0.98	75	1.10	0.60	0.99
Burleson	0.005	1.55	0.35	0.98	210	1.45	0.90	0.99
Colorado	0.004	1.60	0.37	0.97	210	1.60	0.60	0.98
Grayson	0.010	1.65	0.39	0.98	110	1.50	0.90	0.99
Keller	0.010	1.70	0.41	0.98	110	1.50	0.85	0.98
Oklahoma	0.006	1.45	0.31	0.98	175	1.30	0.75	0.98
San Antonio	0.008	1.29	0.22	0.98	145	1.20	0.60	0.98
San Diego	0.008	1.29	0.22	0.98	170	1.10	0.60	0.98

Figure 5.9 presents the variation of parameter ‘a’ from Van Genuchten fitting model with percent amount of clay fraction and percentage of mineral Montmorillonite in a given soil.

From the figure presented below, the variation of ‘a’ parameter did not show a consistent trend with change in percent clay fraction or percent mineral Montmorillonite. The highest value of 0.012 for Van Genuchten’s ‘a’ parameter was obtained for Anthem soil.

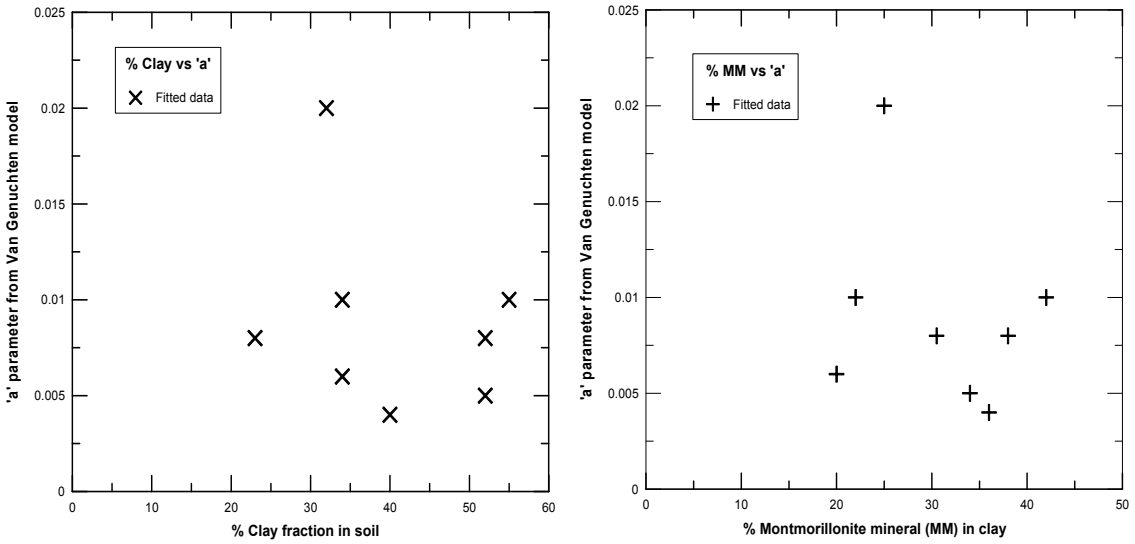

Figure 5.9: Variation of 'a' parameter with change in clay fraction and mineral Montmorillonite

Similarly, Figure 5.10 presents the variation of parameter ‘n’ from Van Genuchten fitting model with change in clay fraction and percentage mineral Montmorillonite.

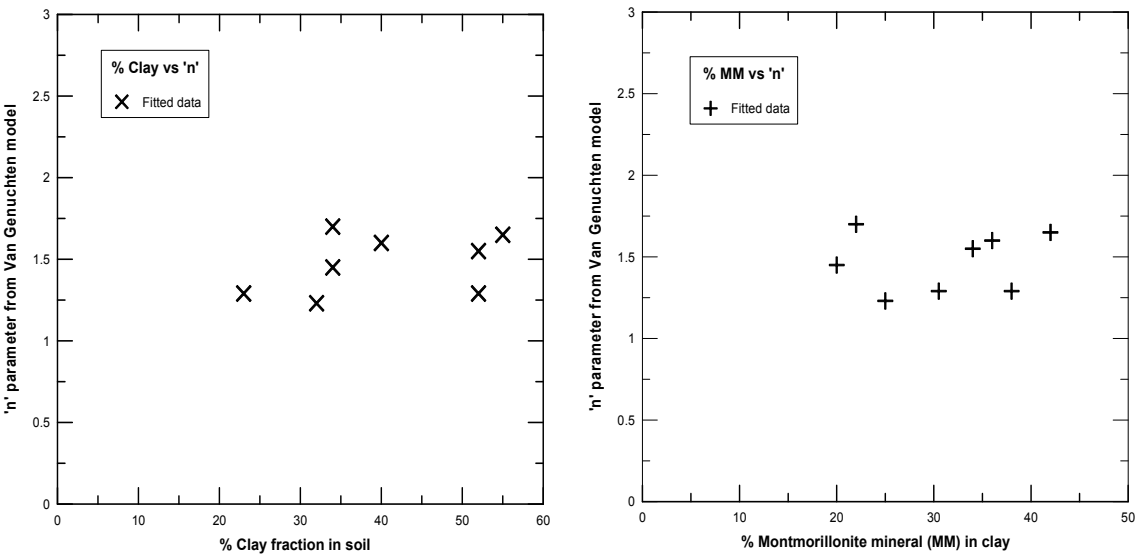

Figure 5.10: Variation of 'n' parameter with change in clay fraction and mineral Montmorillonite

Since it was observed that there was not much variation within test results for the SWCC model parameters with soil composition properties, it could be concluded that the ‘n’ parameter from Van Genuchten model was not affected by clay fraction or mineral

Montmorillonite. Figure 5.11 presents the variation of parameter ‘m’ from Van Genuchten fitting model with change in clay fraction and percentage mineral Montmorillonite.

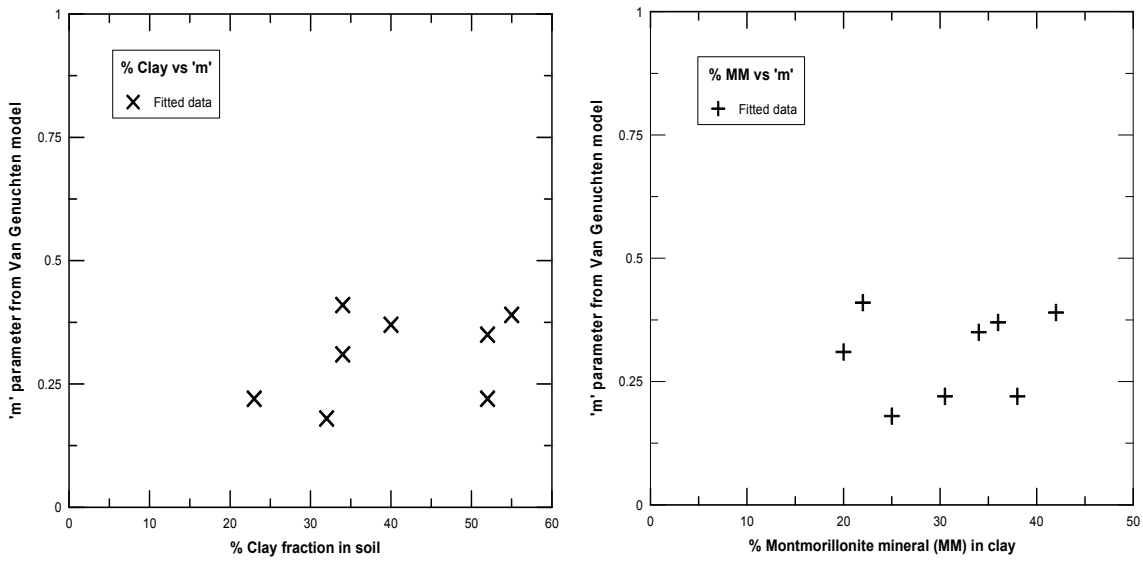

Figure 5.11: Variation of 'm' parameter with change in clay fraction and mineral Montmorillonite

It was found that there was not much variation with test results. Hence, it could be concluded that the ‘n’ parameter from Van Genuchten model was not affected by clay fraction or mineral Montmorillonite. Similar results were plotted against Fredlund and Xing fitting models. Figure 5.12 presents the variation of parameter ‘a_1’ from Fredlund and Xing fitting model with change in clay fraction and percentage mineral Montmorillonite.

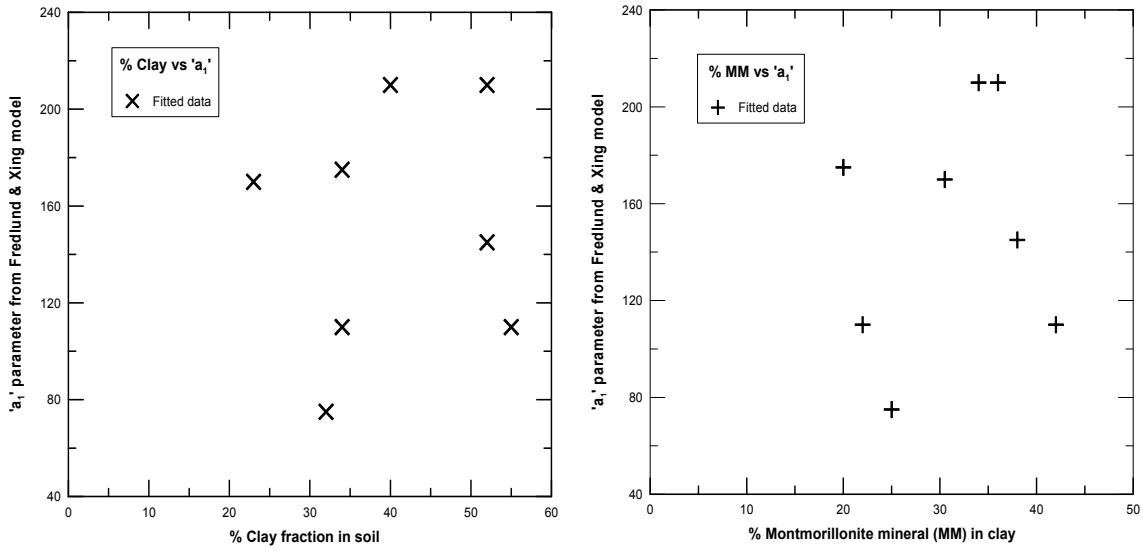

Figure 5.12: Variation of 'a_1' parameter with change in clay fraction and mineral Montmorillonite

From the above figure, the variation of 'a_1' parameter did not show a consistent trend with change in clay fraction or mineral Montmorillonite. A highest value of 210 for a_1 parameter from Fredlund and Xing model was obtained for Anthem and Burleson soils. Similarly, Figure 5.13 presents the variation of parameter 'n_1' from Fredlund and Xing fitting model.

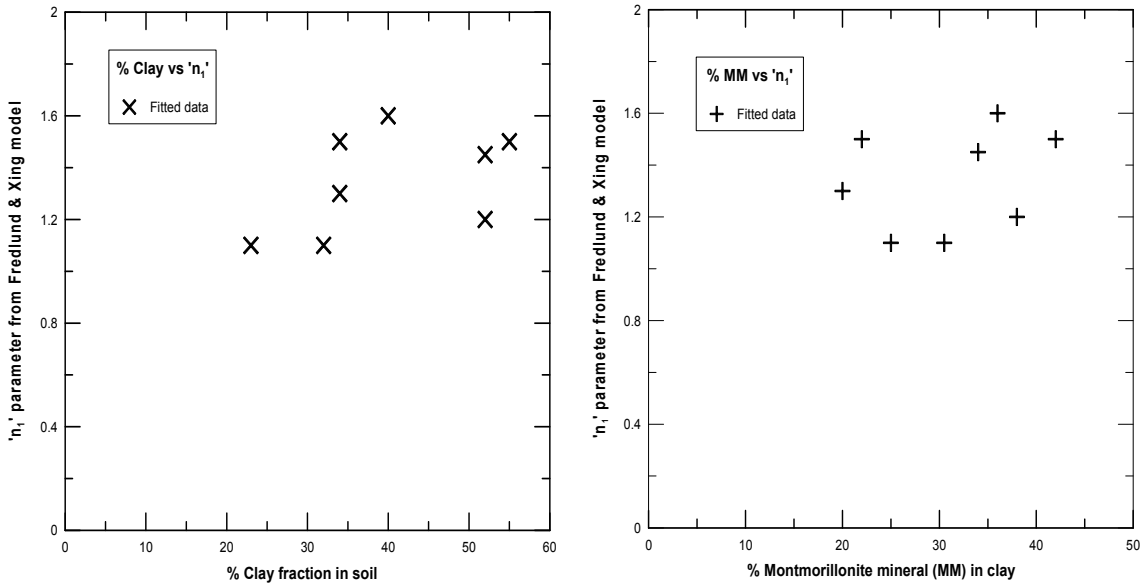

Figure 5.13: Variation of 'n_1' parameter with change in clay fraction and mineral Montmorillonite

Figure 5.14 presents the variation of parameter 'a_1' from Fredlund and Xing fitting model with change in clay fraction and percentage mineral Montmorillonite.

Though there does not exist a definite trend with SWCC model attributes with clay fraction or mineral Montmorillonite, one should note that the SWCC is a complete representation of a soil entire composition. This indirectly explains that more than one soil parameter or one clay mineral type are needed to correlate the model constants.

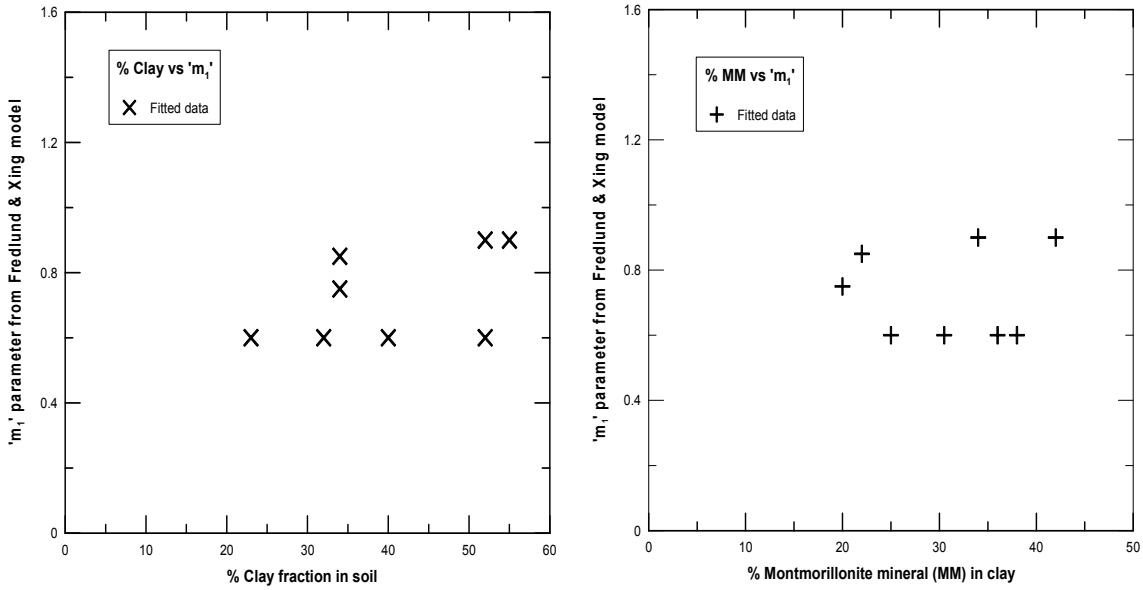

Figure 5.14: Variation of 'm_1' parameter with change in clay fraction and mineral Montmorillonite

For the Van Genuchten fitting model, the 'a' parameter did not show a consistent trend with expansive property of a soil. Anthem soil has the highest 'a' parameter from Van Genuchten model whereas Colorado soil has the least value. Parameters 'n' and 'm' from Van Genuchten model were highest for Keller soil. For the Fredlund and Xing fitting model, 'a_1' parameter was highest for Burleson and Colorado soils. Similarly 'n_1' parameter was highest for Colorado soil and least for Anthem and San Diego soils. Similarly 'm_1' parameter was highest for Burleson and Grayson soils.

From the above plots, it was concluded that the fitting parameters from both the models did not show a consistent trend in variation with expansive behavior of soils. Parameters n, m,

n_1, m_1 did not exhibit any variation with change in clay fraction or percent mineral Montmorillonite. This could be due to the dependency of SWCC on grain size distribution, rather than the degree of expansion of a soil or the presence of one type of clay mineral. Also, the soils tested for expansive behavior belong to low to high plastic soil types and this means the composition details do not vary considerably for the soils and hence it is difficult to draw conclusive trend when comparing soil parameters with the corresponding model constants. Future analyses will be needed in the future to develop trends with more than one soil composition related parameter.

5.3 Pore studies using Mercury Intrusion Porosimetry

The measurement of internal pore structure and distribution is essential to study the water conductivity behavior in a soil specimen. The pore size distribution in a soil mass can be evaluated with the help of Mercury Intrusion Porosimetry technique (MIP) as discussed in the Chapter 3. The variation of dry density of a soil specimen influences the internal pore structure and pore size distribution. Hence, soil specimens were tested at two compaction dry density conditions, i.e. at maximum dry density (MDD) condition and at 95% maximum dry density (95% MDD) condition.

From the previous literature, it was understood that pores ranging below 0.02 micro meters (μm) are classified as micro pores. Pores ranging from 0.02 μm to 12 μm comes under medium pores and pores larger than 12 μm are classified as macro pores. This classification system was used in the current research for proper pore identification. Two soil specimens from the same clay were tested for pore distribution and the test results showed similar behavior. The mercury intrusion porosimetry test yielded good repeatability of test results. The pore size distribution for all the eight soils at different dry density conditions are presented in the following sections.

5.3.1 Anthem soil pore distribution

The mercury intrusion/extrusion curves of Anthem clay obtained from MIP technique at two compaction densities are shown in Figure 5.15. Anthem soil which is classified as a low plasticity clay showed a cumulative pore volume of 0.165 ml/g at 95% MDD and 0.15 ml/g at MDD, respectively. Figure 5.16 shows the variation of pore diameter with total pore volume. The 95% MDD specimen showed higher macro pore volume of 32% where at MDD it showed 28%. The specimen exhibited 50% medium pores at 95% MDD and 54% at MDD conditions.

Both the specimens showed equal volume of micro pores. This shows that the micro pore volume is independent of compaction dry density for this particular clay.

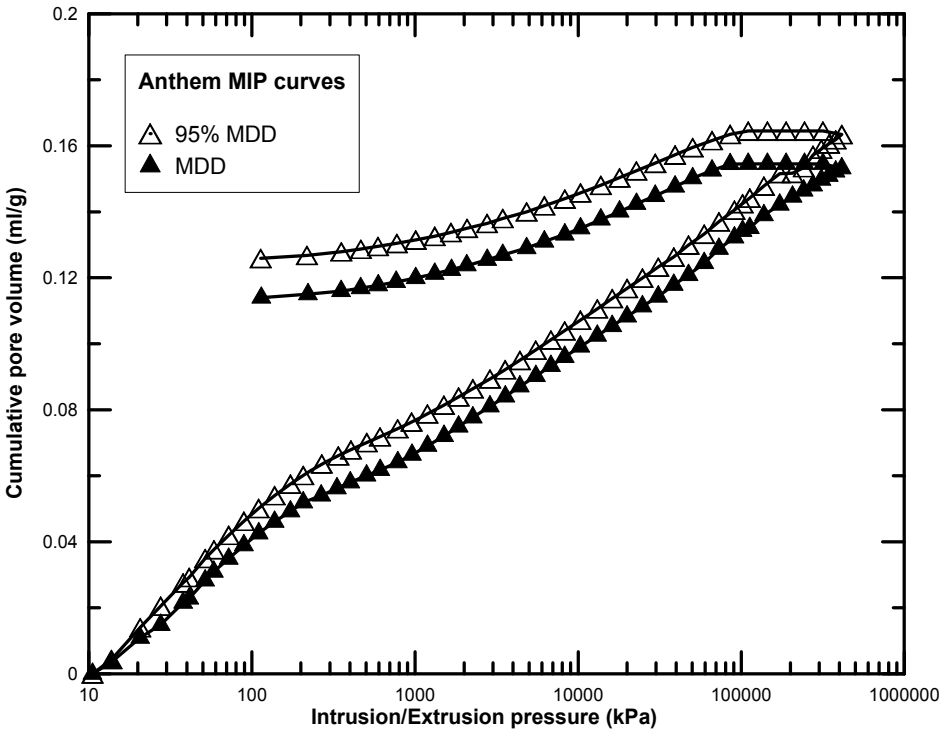

Figure 5.15: Intrusion/Extrusion curves for Anthem soil at MDD and 95% MDD

It was evident that the soil specimen carries more pore volume at 95% MDD condition than at MDD condition. The hysteresis observed between the intrusion and extrusion curves is due to the retention of mercury in the soil pores. The soil specimen exhibited a difference of

0.063ml/g at 95% MDD and 0.07ml/g at MDD, respectively. This reveals that the specimen retained higher volume of mercury at MDD condition.

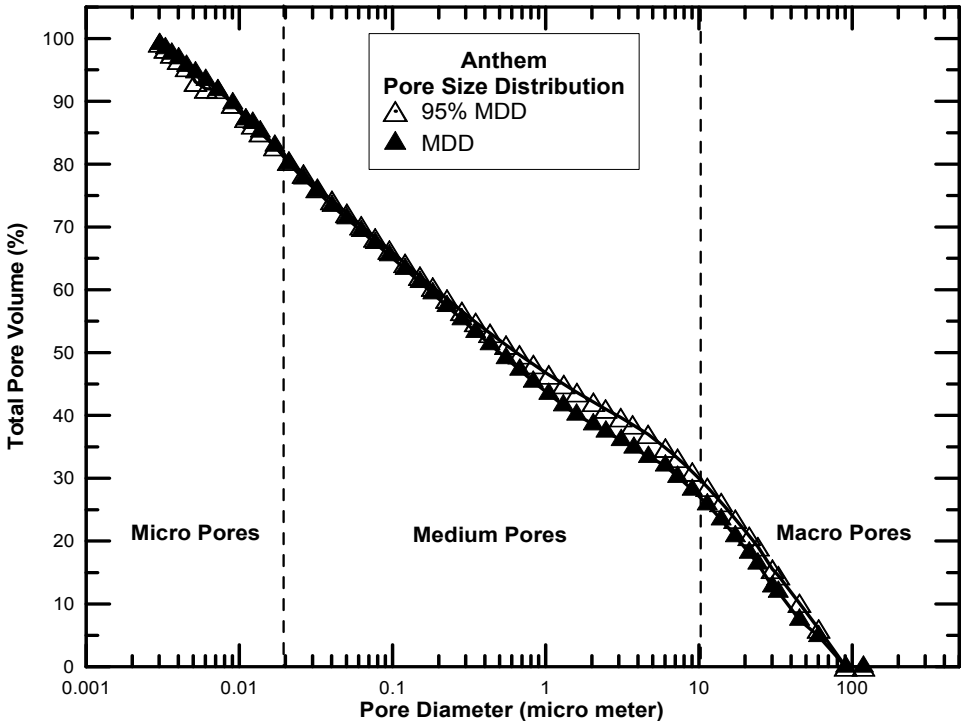

Figure 5.16: Pore size distribution for Anthem soil at MDD and 95% MDD

5.3.2 Burleson soil pore distribution

The mercury intrusion/extrusion curves of Burleson clay obtained at two compaction densities are shown in Figure 5.17. Burleson soil which is classified as a high plasticity clay showed a cumulative pore volume of 0.185 ml/g at 95% MDD and 0.15 ml/g at MDD, respectively. It was evident that the soil specimen carries more pore volume at 95% MDD condition than at MDD condition. Similar behavior was identified in Anthem soil.

The soil specimen exhibited a hysteresis difference of 0.07 ml/g at 95% MDD and 0.08 ml/g at MDD, respectively. This states that the specimen retained higher volume of mercury at MDD condition. Figure 5.18 shows the variation of pore diameter with total pore volume. The 95% MDD specimen exhibited a macro pore volume of 30% where at MDD condition it was 23%. The specimen exhibited 55% medium pores at 95% MDD and 59% at MDD conditions. The specimen showed a micro pore volume of 15% at 95% MDD and 18% at MDD condition.

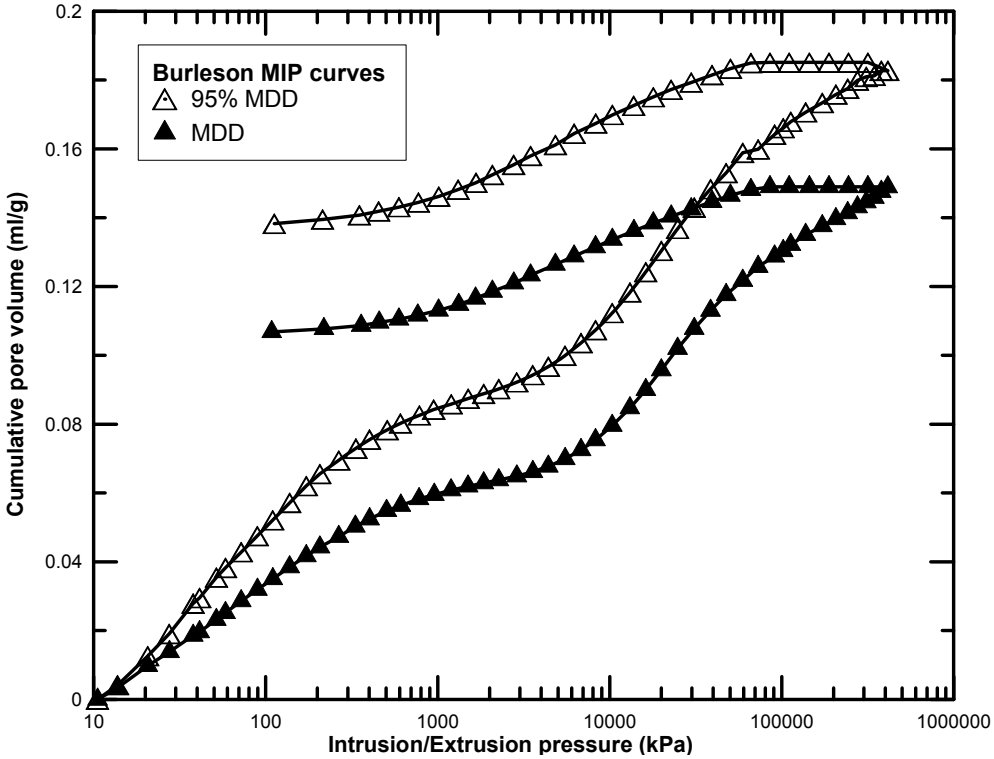

Figure 5.17: Intrusion/Extrusion curves for Burleson soil at MDD and 95% MDD

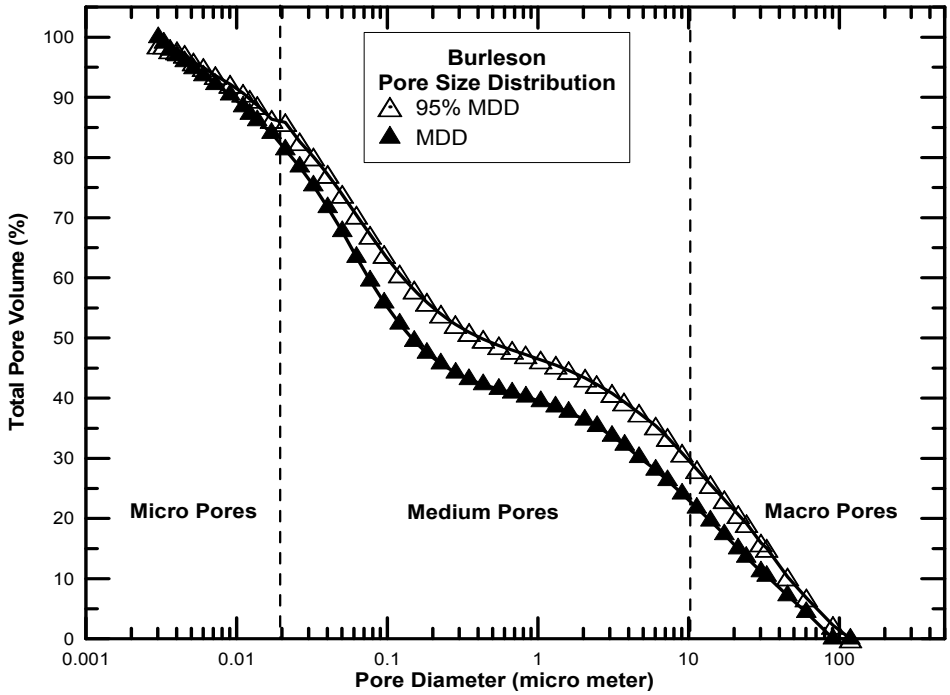

Figure 5.18: Pore size distribution for Burleson soil at MDD and 95% MDD

5.3.3 Colorado soil pore distribution

The mercury intrusion/extrusion curves of Colorado clay obtained at two compaction densities are shown in Figure 5.19. Colorado soil which is classified as a high plasticity clay showed a cumulative pore volume of 0.23 ml/g at 95% MDD and 0.18 ml/g at MDD, respectively. It was evident that the soil specimen carries more pore volume at 95% MDD condition than at MDD condition and similar behavior was identified in Burleson and Anthem soils. The hysteresis observed between the intrusion and extrusion curves is due to the retention of mercury in the soil pores. The soil specimen exhibited a hysteresis difference of 0.08 ml/g at 95% MDD and 0.1 ml/g at MDD, respectively. This states that the specimen retained higher volume of mercury at MDD condition. Figure 5.20 shows the variation of pore diameter with total pore volume. The 95% MDD specimen exhibited a macro pore volume of 40% where at MDD condition it was 20%. The specimen exhibited 50% medium pores at 95% MDD and 68% at MDD conditions. The specimen showed a low micro pore volume of 10% at 95% MDD and 12% at MDD condition.

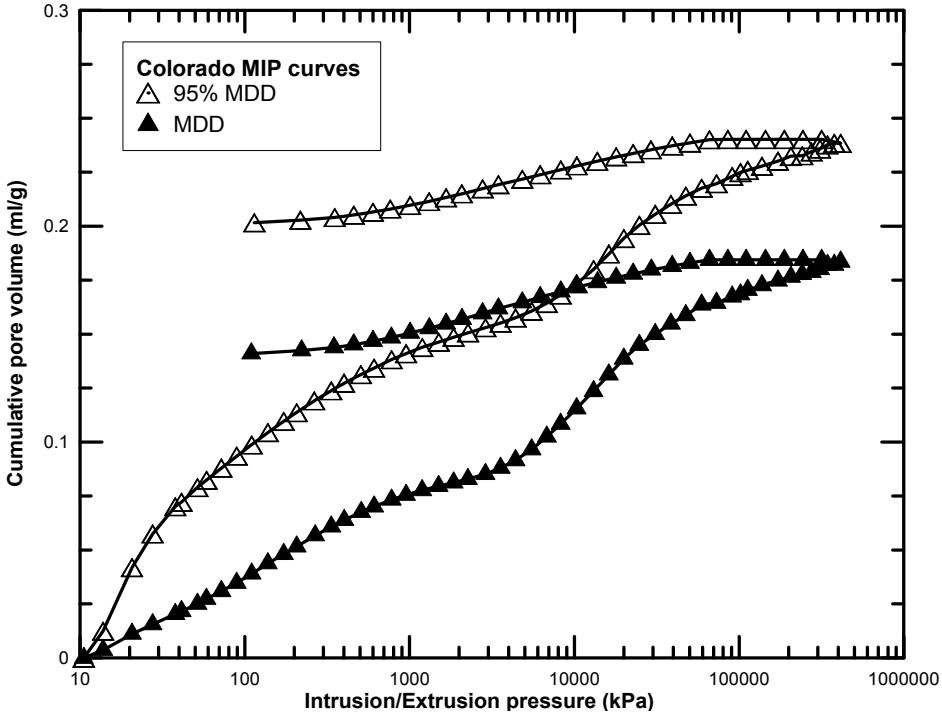

Figure 5.19: Intrusion/Extrusion curves for Colorado soil at MDD and 95% MDD

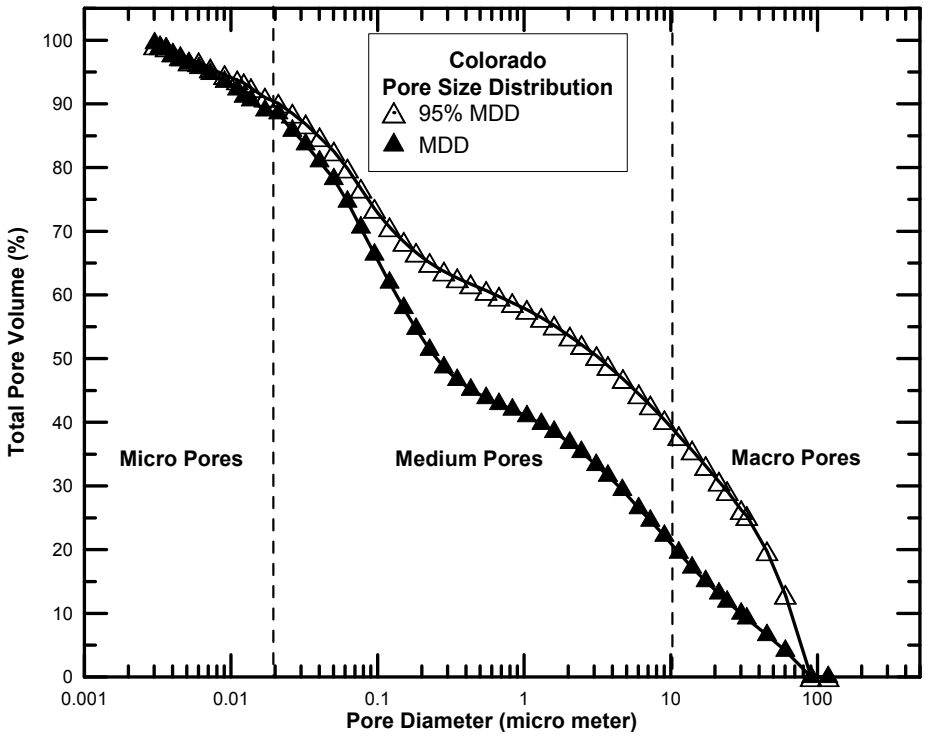

Figure 5.20: Pore size distribution for Colorado soil at MDD and 95% MDD

5.3.4 Grayson soil pore distribution

The mercury intrusion/extrusion curves of Grayson soil obtained at two compaction densities are shown in Figure 5.21. Grayson soil which was classified as a high plasticity clay showed a cumulative pore volume of 0.25 ml/g at 95% MDD and 0.18 ml/g at MDD, respectively. The soil specimen carried more pore volume at 95% MDD condition than at MDD condition. The soil specimen exhibited a hysteresis difference of 0.08 ml/g at 95% MDD and 0.1 ml/g at MDD, respectively. This states that the specimen retained higher volume of mercury at MDD condition. Figure 5.22 shows the variation of pore diameter with total pore volume. The 95% MDD specimen exhibited a macro pore volume of 40% where at MDD condition it was 27%. The specimen exhibited 37% medium pores at 95% MDD and 43% at MDD conditions. The specimen showed a high micro pore volume of 23% at 95% MDD and 30% at MDD condition.

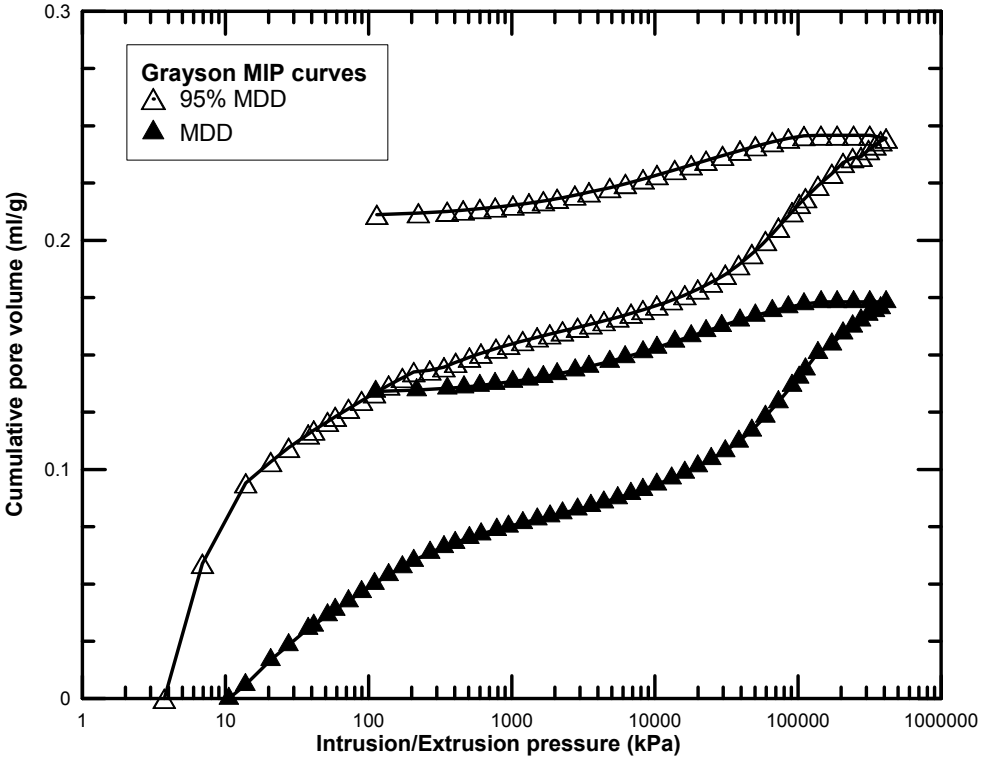

Figure 5.21: Intrusion/Extrusion curves for Grayson soil at MDD and 95% MDD

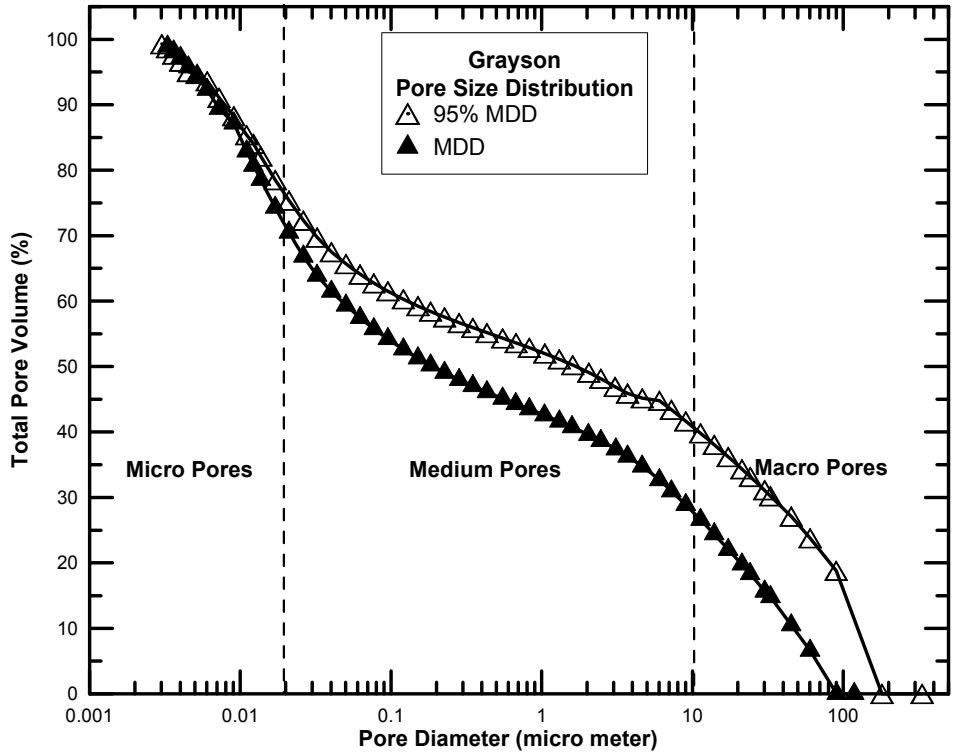

Figure 5.22: Pore size distribution for Grayson soil at MDD and 95% MDD

5.3.5 Keller soil pore distribution

The mercury intrusion/extrusion curves of Keller soil obtained at two compaction densities are shown in Figure 5.23. Keller soil which is classified as a low plasticity clay showed a cumulative pore volume of 0.125 ml/g at 95% MDD and 0.105 ml/g at MDD, respectively. It was evident that all the above soils carried more pore volume at 95% MDD condition than at MDD condition and the same reflects here. The hysteresis observed between the intrusion and extrusion curves is due to the retention of mercury in the soil pores. The soil specimen exhibited a hysteresis difference of 0.06 ml/g at 95% MDD and 0.065 ml/g at MDD, respectively. This specimen retained a little higher volume of mercury at MDD condition. Figure 5.24 shows the variation of pore diameter with total pore volume. The 95% MDD specimen exhibited a macro pore volume of 32% where at MDD condition it was 23%. The specimen exhibited 48% medium pores at 95% MDD and 52% at MDD conditions. The specimen showed a high micro pore volume of 20% at 95% MDD and 25% at MDD condition.

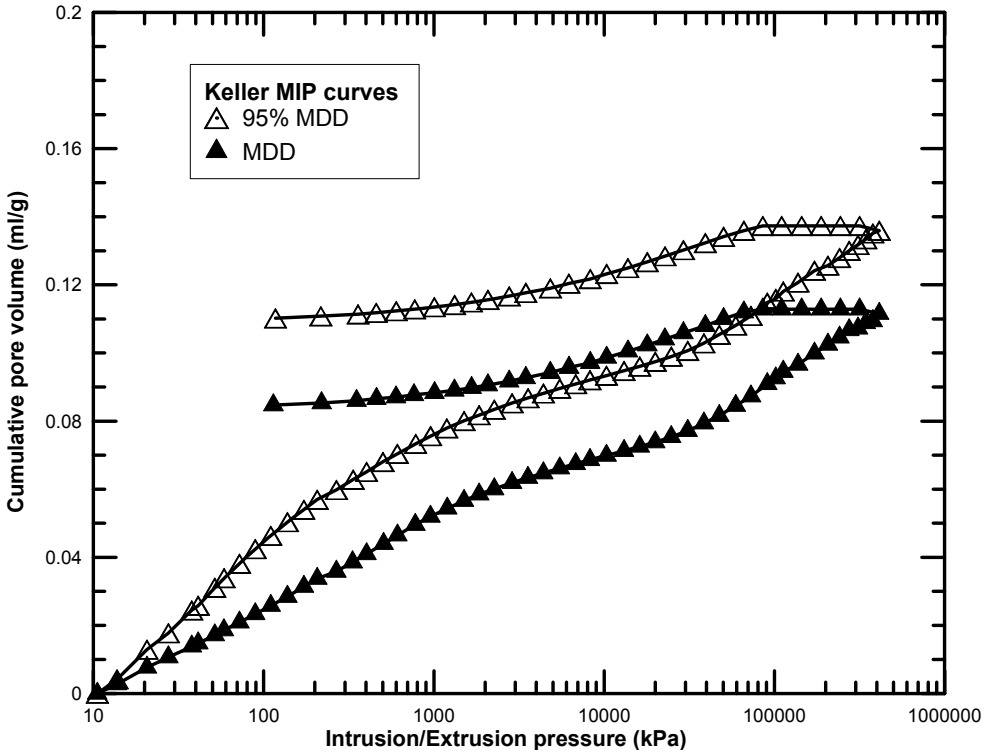

Figure 5.23: Intrusion/Extrusion curves for Keller soil at MDD and 95% MDD

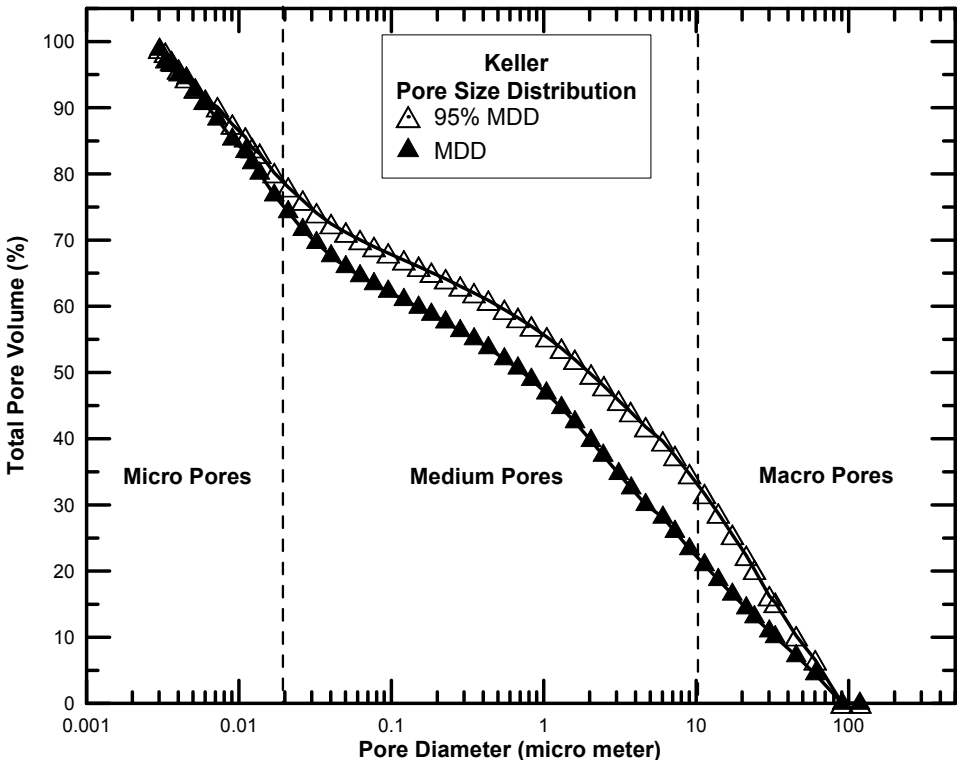

Figure 5.24: Pore size distribution for Keller soil at MDD and 95% MDD

5.3.6 Oklahoma pore distribution

The mercury intrusion/extrusion curves of Keller clay obtained at two compaction densities are shown in Figure 5.25. Oklahoma soil which is classified as a low plasticity clay showed a cumulative pore volume of 0.21 ml/g at 95% MDD and 0.18 ml/g at MDD, respectively. The soil specimen carried more pore volume at 95% MDD condition than at MDD condition. The soil specimen exhibited a hysteresis difference of 0.06 ml/g at 95% MDD and 0.07 ml/g at MDD, respectively. This specimen retained a little higher volume of mercury at MDD condition. Figure 5.26 shows the variation of pore diameter with total pore volume. The 95% MDD specimen exhibited a macro pore volume of 24% where at MDD condition it was 10%. The specimen exhibited 54% medium pores at 95% MDD and 66% at MDD conditions. The specimen showed a high micro pore volume of 26% at 95% MDD and 24% at MDD condition.

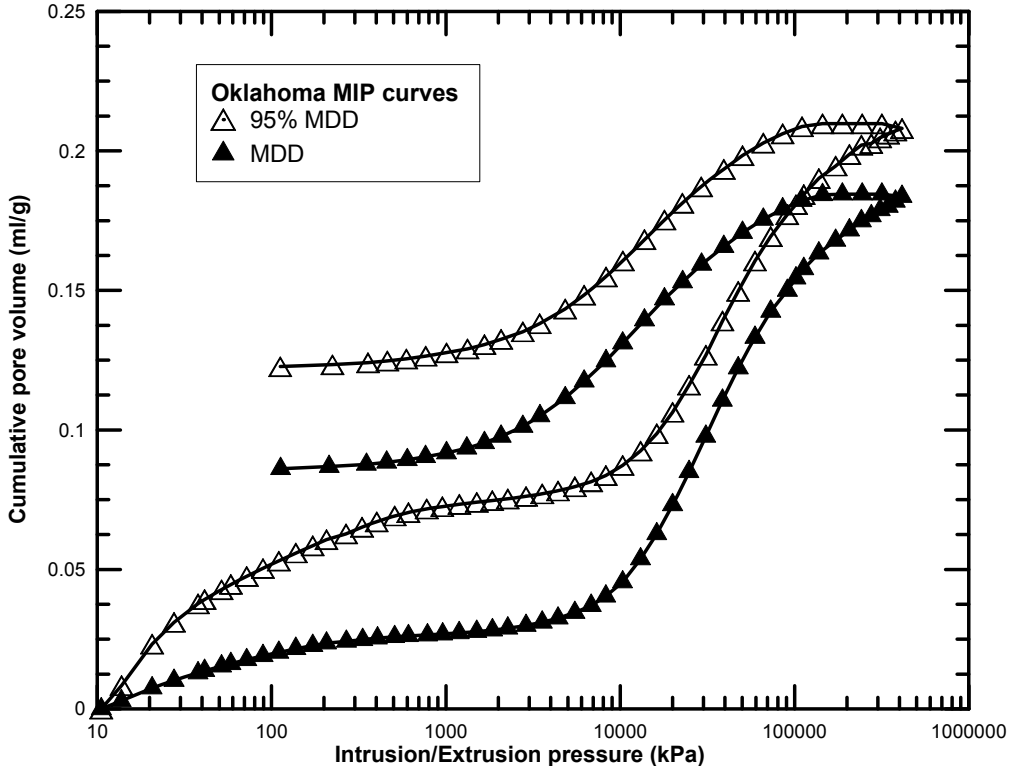

Figure 5.25: Intrusion/Extrusion curves for Oklahoma soil at MDD and 95% MDD

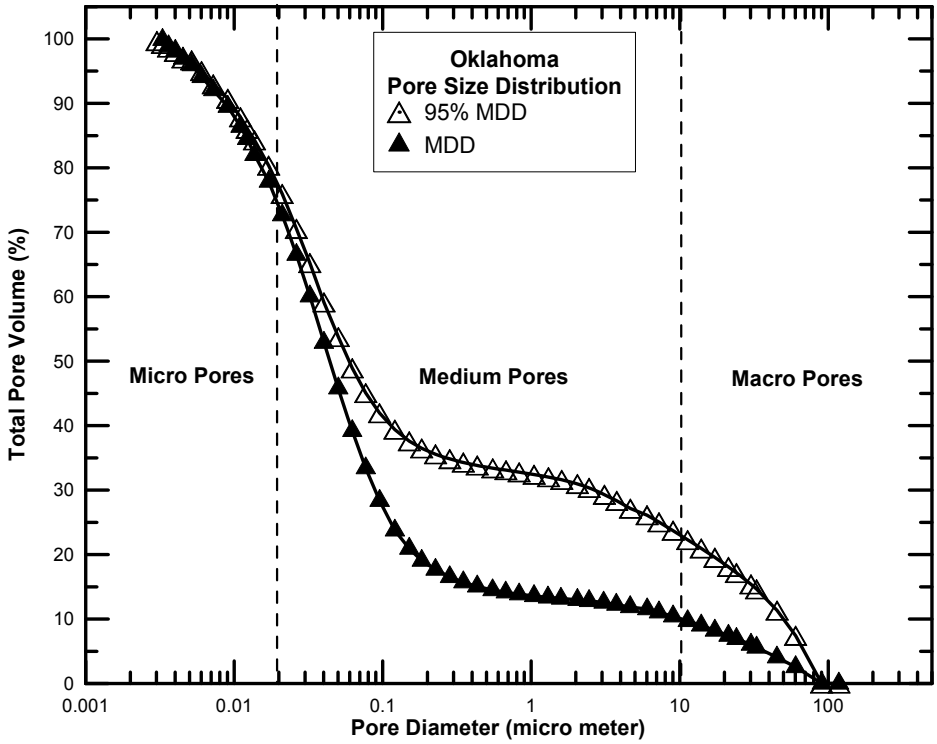

Figure 5.26: Pore size distribution for Oklahoma soil at MDD and 95% MDD

5.3.7 San Antonio soil pore distribution

The mercury intrusion/extrusion curves of San Antonio soil at two compaction densities are shown in Figure 5.27. San Antonio soil which is classified as a high plasticity clay showed a cumulative pore volume of 0.16 ml/g at 95% MDD and 0.125 ml/g at MDD condition, respectively. It was evident that the soil specimen carries more pore volume at 95% MDD condition than at MDD condition. The hysteresis observed between the intrusion and extrusion curves is due to the retention of mercury in the soil pores. The soil specimen exhibited a hysteresis difference of 0.065 ml/g at 95% MDD and 0.07 ml/g at MDD, respectively. This specimen retained a little higher volume of mercury at MDD condition. Figure 5.28 shows the variation of pore diameter with total pore volume. The 95% MDD specimen exhibited a macro pore volume of 27% where at MDD condition it was 15%. The specimen exhibited 53% medium pores at 95% MDD and 58% at MDD conditions. The specimen showed a high micro pore volume of 20% at 95% MDD and 27% at MDD condition.

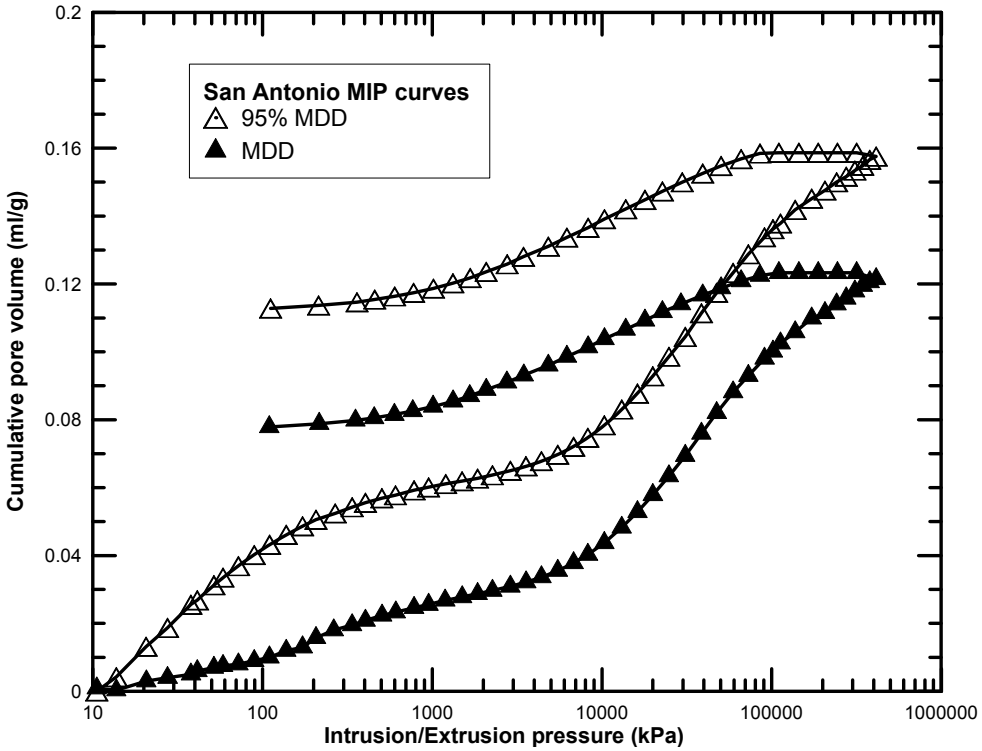

Figure 5.27: Intrusion/Extrusion curves for San Antonio soil at MDD and 95% MDD

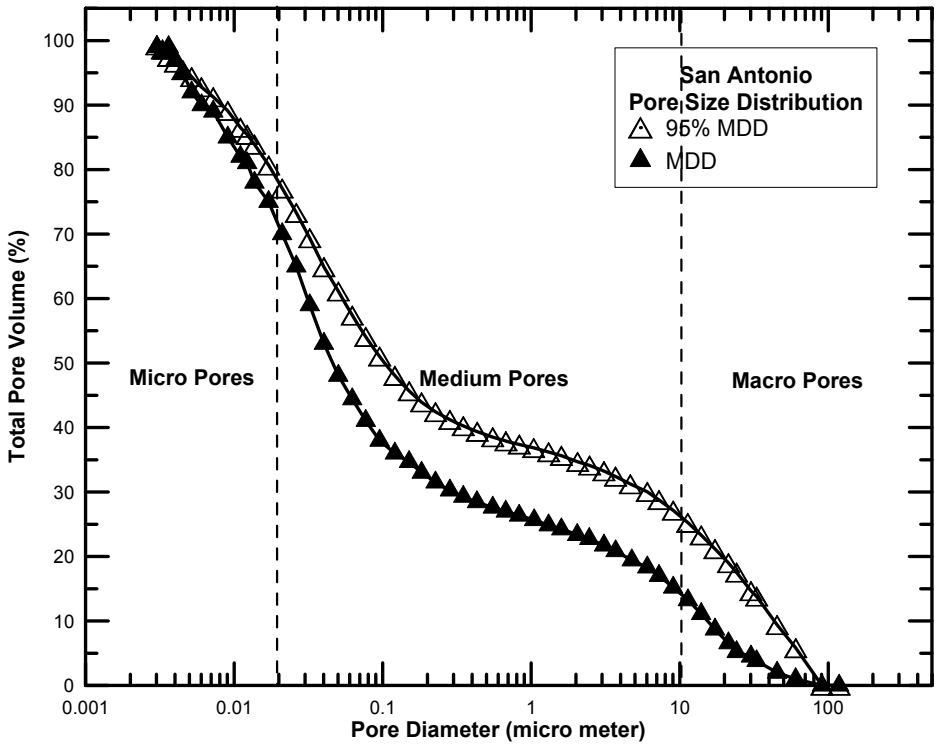

Figure 5.28: Pore size distribution for San Antonio soil at MDD and 95% MDD

5.3.8 San Diego pore distribution

The mercury intrusion/extrusion curves of San Diego clay obtained from MIP technique at two compaction densities are shown in Figure 5.29. San Diego soil which is classified as a low plasticity clay showed a cumulative pore volume of 0.165 ml/g at 95% MDD and 0.125 ml/g at MDD, respectively. It was evident that the soil specimen carries more pore volume at 95% MDD condition than at MDD condition. The hysteresis observed between the intrusion and extrusion curves is due to the retention of mercury in the soil pores. The soil specimen exhibited a hysteresis difference of 0.065 ml/g at 95% MDD and 0.07 ml/g at MDD, respectively. This specimen retained a little higher volume of mercury at MDD condition. Figure 5.30 shows the variation of pore diameter with total pore volume. Both the specimens exhibited a high macro pore volume of 47% and 40% at 95% MDD and MDD condition, respectively. The specimen exhibited 46% medium pores at 95% MDD and 50% at MDD conditions. The specimen showed a low micro pore volume of 7% at 95% MDD and 10% at MDD condition.

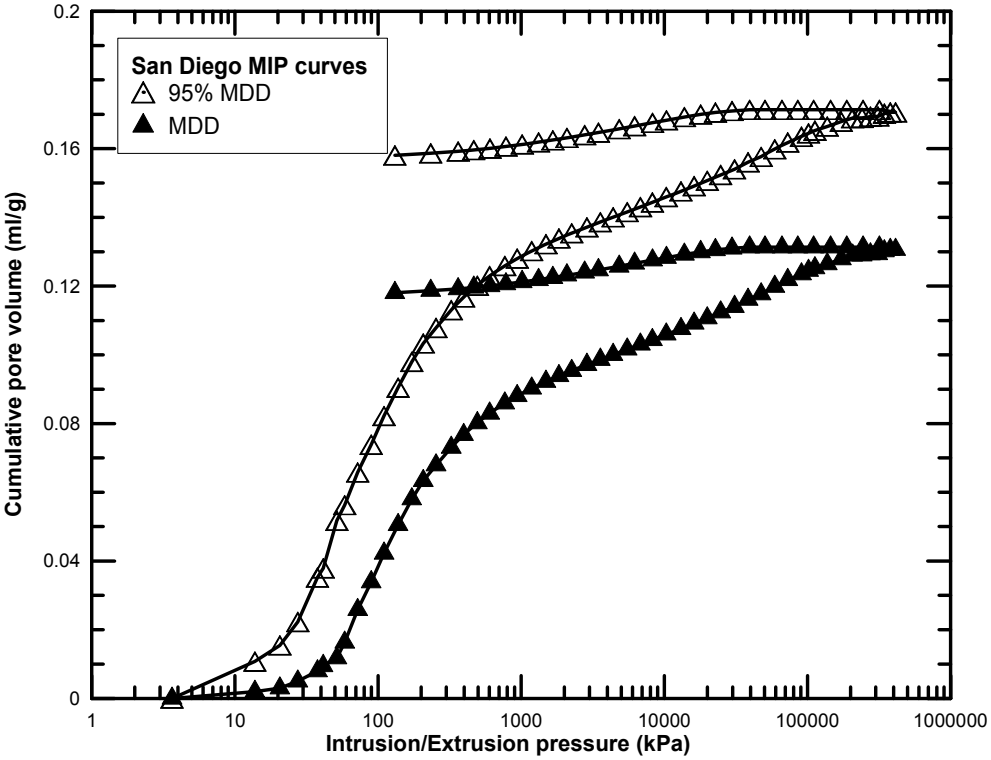

Figure 5.29: Intrusion/Extrusion curves for San Diego soil at MDD and 95% MDD

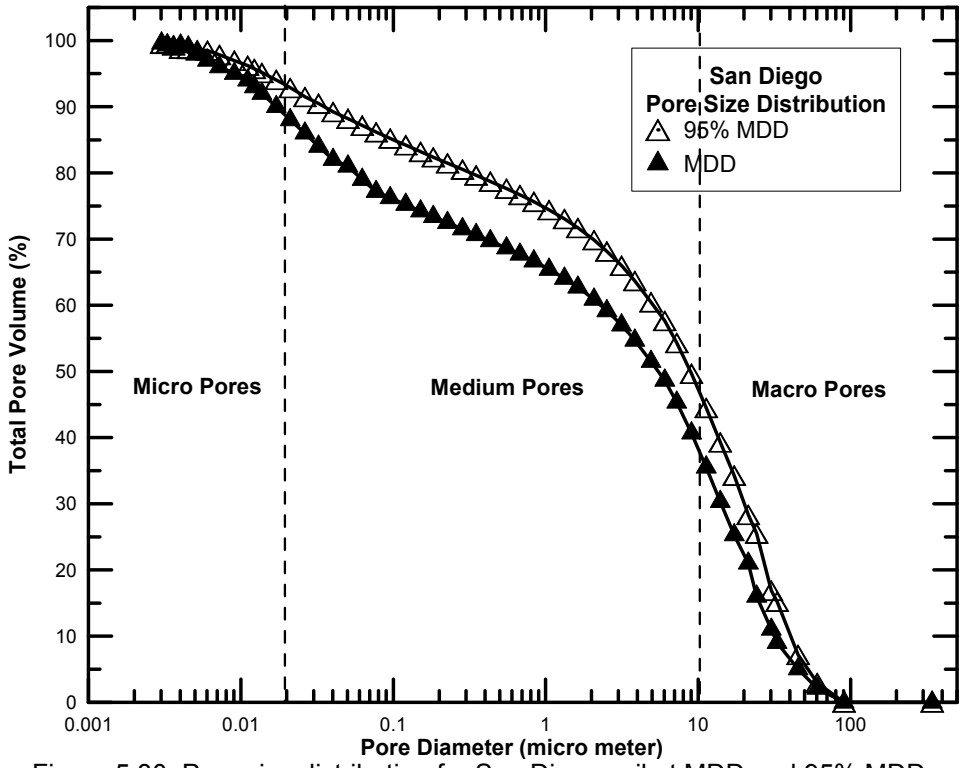

Figure 5.30: Pore size distribution for San Diego soil at MDD and 95% MDD

The intrusion extrusion curve from MIP test revealed the volume of mercury intruded in to the pores of the soil specimen and the volume of mercury retained in the specimen after the test. The variation of different pore sizes for all the eight soils was identified and presented with the help of MIP technique. The dependency of total volume of mercury induced and pore size variation on the compaction density of the specimen was monitored.

From the above discussions, it was found that the variation of density and moisture content of soils had a major influence on the pore distribution of the soil specimen. The volume of micro pores is found to be more in specimens compacted at MDD than at 95% MDD. Similarly macro pore volume is found to be higher in the case of 95% MDD condition than at MDD condition. The high compaction level at MDD condition packs the soil particles together thereby increasing the micro pore volume and decreasing the macro pore volume when compared to 95% MDD condition. The size and volumes of pores present in the soil specimen as determined by the MIP method are presented in Table 5.3.

Table 5.3: Pore size distribution results obtained from MIP test

Soil	Cumulative volume of mercury intrusion (ml/g)		Micro pores (%)		Medium pores (%)		Macro pores (%)	
	95% MDD	MDD	95% MDD	MDD	95% MDD	MDD	95% MDD	MDD
Anthem	0.16	0.15	18	18	50	54	32	28
Burleson	0.18	0.15	15	18	55	59	30	23
Colorado	0.23	0.18	10	12	50	68	40	20
Grayson	0.25	0.18	23	30	37	43	40	27
Keller	0.13	0.10	20	25	48	52	32	23
Oklahoma	0.21	0.18	26	24	54	66	24	10
San Antonio	0.16	0.12	20	27	53	58	27	15
San Diego	0.16	0.12	7	10	46	50	47	40

5.4 X-ray Computed Tomography results

X-ray computed tomography (XCT) is a scanning technique utilized to monitor 3-Dimensional internal pore structure of a solid mass. X-rays are passed through the soil specimen in all directions and the attenuating parameter, which helps in revealing the internal structure of the soil specimen, was monitored. Image reconstruction software helps us in creating the true 3-D image of the scanned soil specimen from the attenuating parameter. Working principles of this computed tomography were detailed in Chapter 3.

A 1 cm^3 soil specimen was cut from the statically compacted soil. Tomography scanning was performed on soil specimens at different initial conditions and the test results are presented in the coming sections for all the eight soils. Figure 5.31 gives a graphical presentation of the slicing of scanned 3-D soil image.

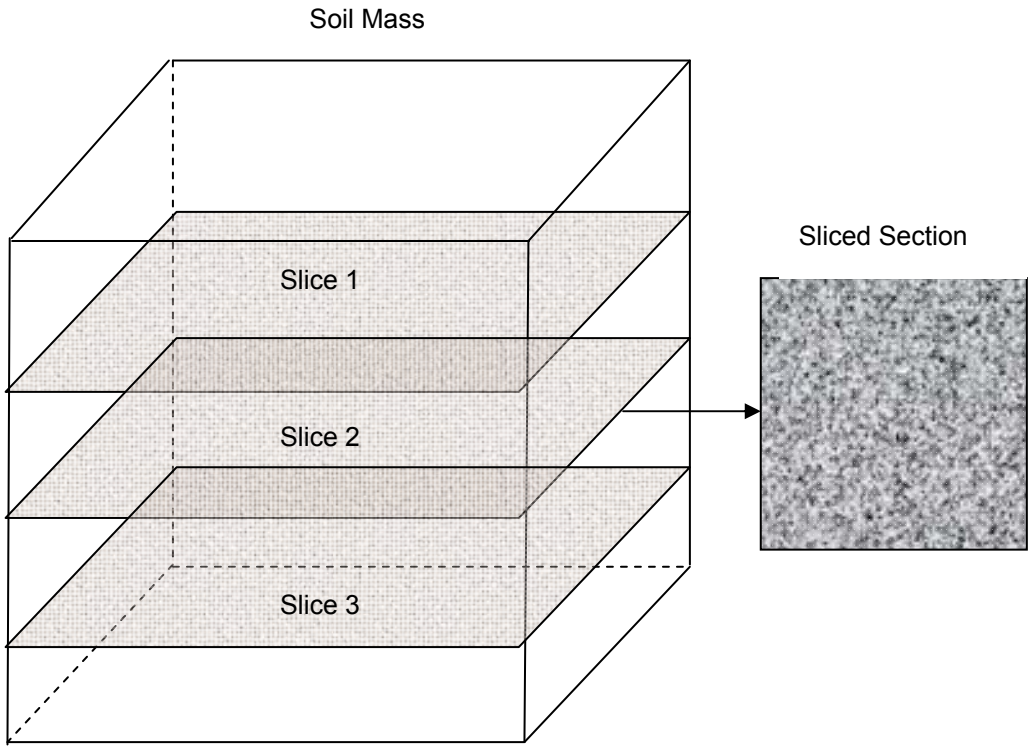

Figure 5.31: Showing the slicing of soil mass for void ratio computation

Once sliced, the image was processed with the help of MATLAB software and the details of image processing results are presented in the later sections.

The sliced images from XCT were studied for pore network and void ratio. To determine the void ratio of a soil specimen, the numbers of black and white pixels in a picture are counted with the help of image processing software. In the current research, MATLAB software was used for this purpose. The 3-D soil mass was sliced at different levels and the average of the computed void ratio was determined and presented in the following sections.

Once the program was executed, the software ask for the details of the input file. The scanned images of the soil specimens from Tomography were then used as input files for the software. Once the program completes the analysis, the final window displays the number of black pixels and the number of white/colored pixels in a given image. This helps us in the determination of compaction void ratio at a 2-D level scanned picture. The void ratios of all the soil specimens are calculated and the results are presented in the following sections. The software is coded with the following MATLAB code as shown in Figure 5.32.

```
close all

clear all

clc

[Fn,Pn,FilterIndex]=uigetfile('*.*');

Pa = strcat(Pn,Fn);

if Fn==0

  h = errordlg('Please pick a file');

  break

end

A = imread(Pa); % read the image if the image is in another folder then use A =

imread('C:/Computer.../AnthemDRY .bmp')

            imshow(A)

%given image is 8 bit image

% the native format of image is .bmp. So convert it into gray scale image for further processing

% gray scale has 256 colors(8 bit: 2^8 = 256) (black =0 and white=255)

K = rgb2gray(A);

figure;

imhist(K) % plots histogram to give overall distribution of colors

            Threshold=20;

Num_of_whites1=numel(find(K>Threshold));

Num_of_black1=numel(find(K==0));

V_ratio=Num_of_whites1/Num_of_black1;
```

Figure 5.32: MATLAB image processing code for the calculation of void ratio of individual slices

The histogram in Figure 5.33 represents the intensity of white and black pixels present in the slice. The division or boundary between the black and white pixels is represented by the threshold value. This value is obtained by back calculating the void ratio results with known values from weight volume relationships. The output of the final void ratio for the particular target image is presented in the workspace tab as shown in Figure 5.33.

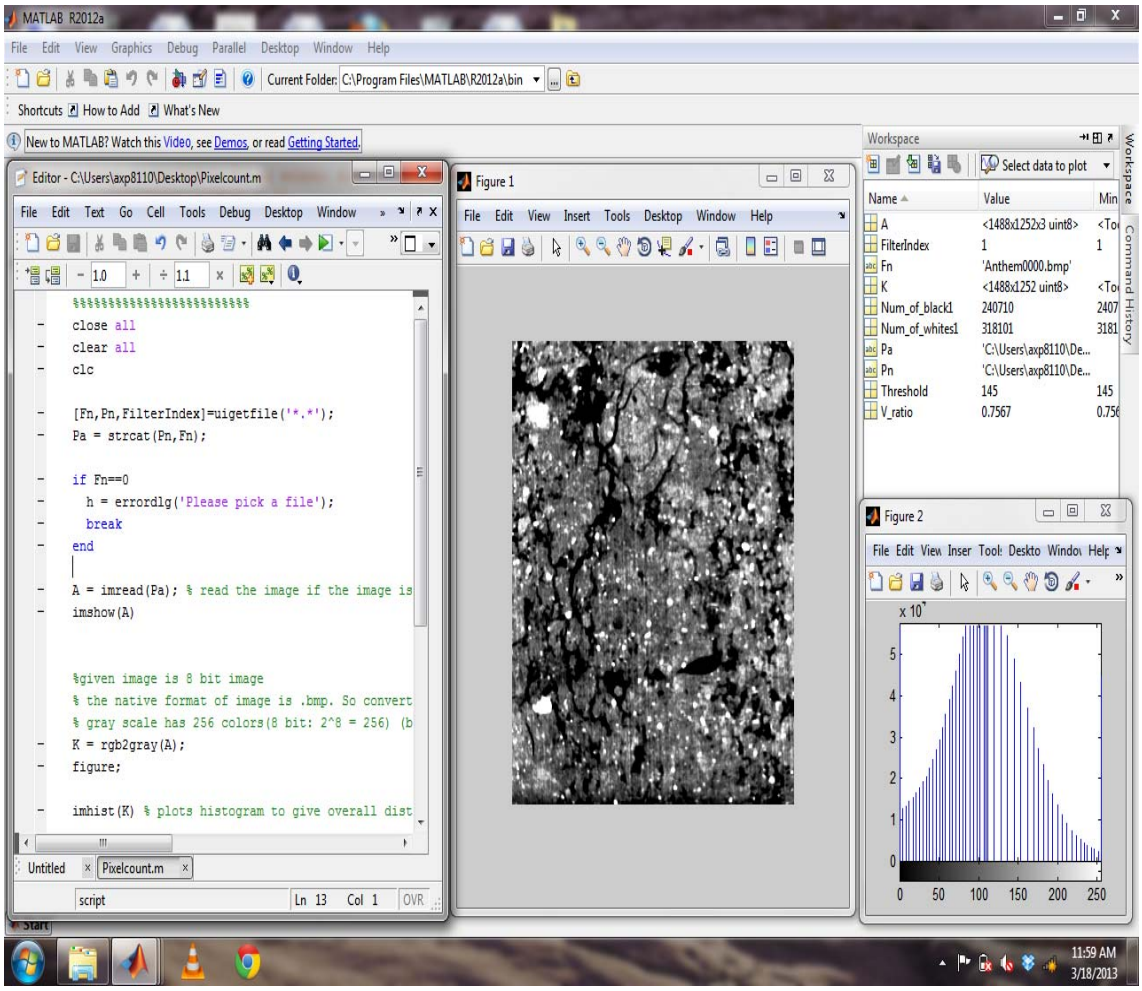

Figure 5.33: Snapshot of the MATLAB program for void ratio calculation

The cut soil specimens were oven dried for a period of 24 hours before scanning for X-ray tomography. A dry scan was performed on the soil specimen by allowing the specimen in an oven dry for a period of 24 hours and then subjecting it to X-ray tomography scan. After scanning, the same specimen was allowed to saturate for a period of 24 hours. Once the

saturation process ends, the sample was allowed to freeze for a period of 24 hours. Since, the saturated sample is highly unstable and tends to lose moisture; the freezing process allows the sample to be stable during the scanning process.

The reconstruction software allows the user to rotate or slice the specimen to investigate the internal pore structure of the specimen. Replicate samples from different specimens are tested under similar conditions and the slices showed good repeatability of test data using XCT method. The soil specimen was sliced at 3 to 4 levels and the average void ratio for the particular specimen is presented as the end result.

The CT scan test results for all the eight expansive soils are studied and the variation of their void ratio is presented in the following sections.

5.4.1 Anthem soil CT scan

The reconstructed Anthem soil CT scan image at 95% MDD is presented in Figure 5.34. The 3-D image shows the packing and arrangement of particles of different sizes. The high density particles are represented by white color and low density particles with darker color. Once sliced to a desired level, a snapshot of the element was taken for further analysis which describes with MATLAB programming for the determination of compaction void ratio. The specimen was compacted at two density conditions, 95% MDD and MDD.

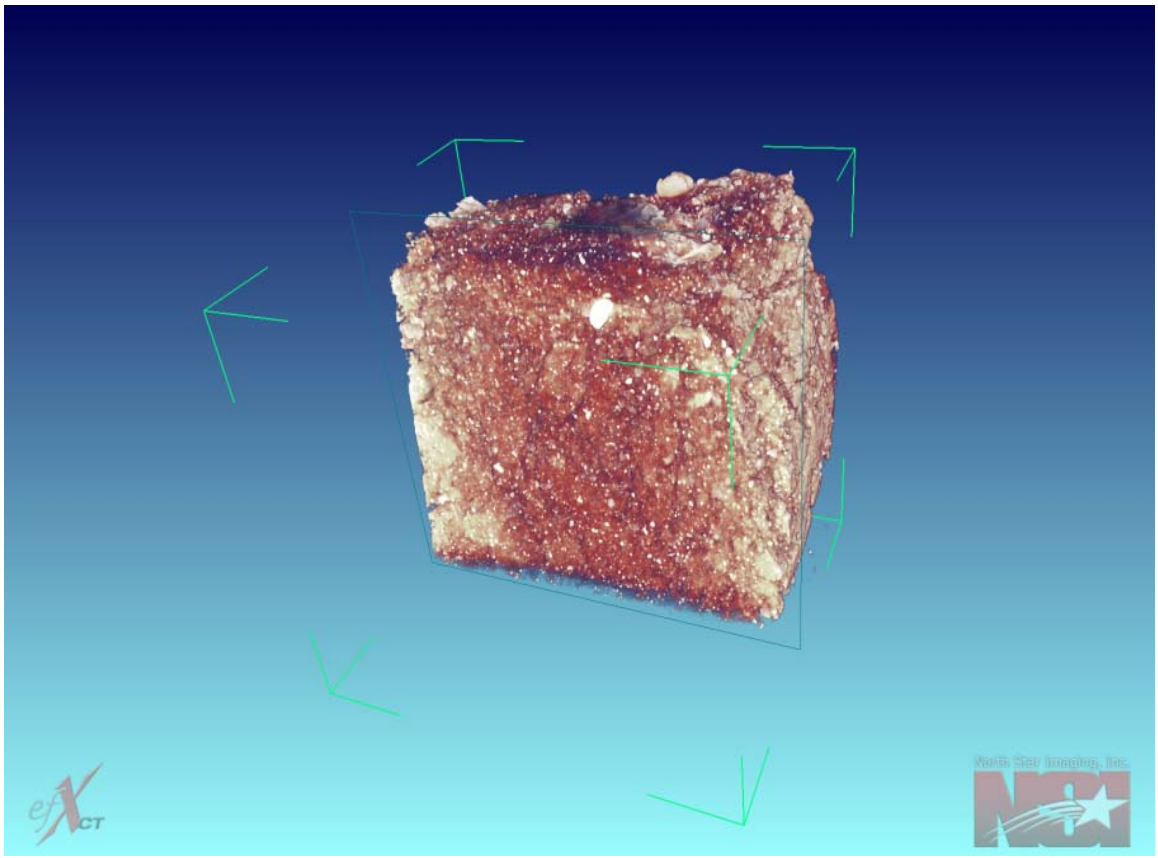

Figure 5.34: Reconstructed Anthem Soil specimen from XCT technique

Figure 5.35 shows the variation of particle arrangement in the soil mass with change in density from 95% MDD to MDD. The void ratio of the mass is calculated using MATLAB image processing program as presented in the previous sections. For the Anthem soil the void ratio varied from 0.71 at 95% MDD condition to 0.61 at MDD condition. Figure 5.36 shows the snapshot of the MATLAB image processed output for Anthem soil. The soil specimen is sliced at three portions to study the variation of void space. Table 5.4 shows the determination of average void ratio of Anthem soil specimen at different conditions.

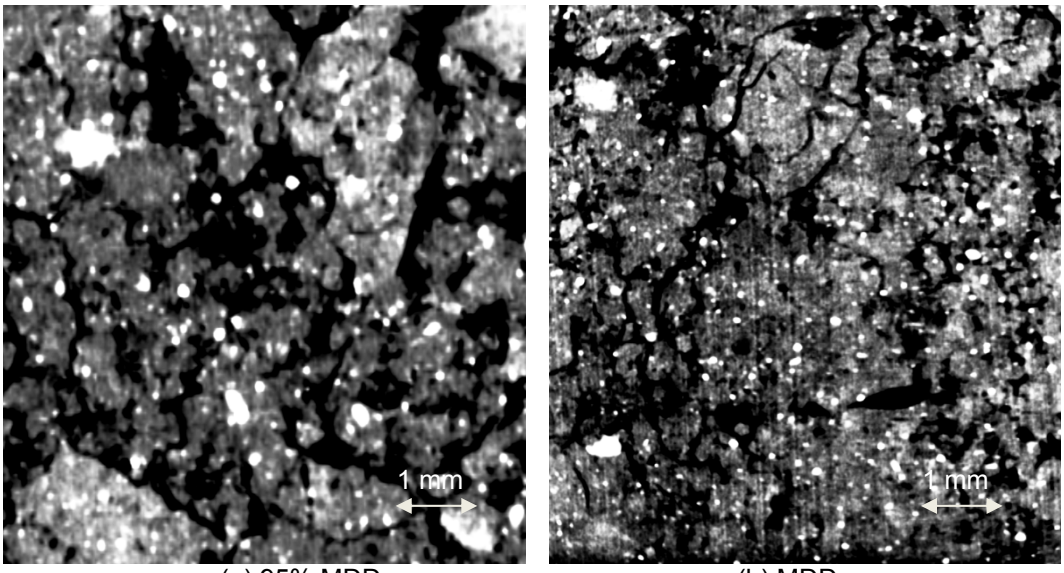

(a) 95% MDD (b) MDD

Figure 5.35: (a), (b) XCT Scanned images on Anthem soil at different densities

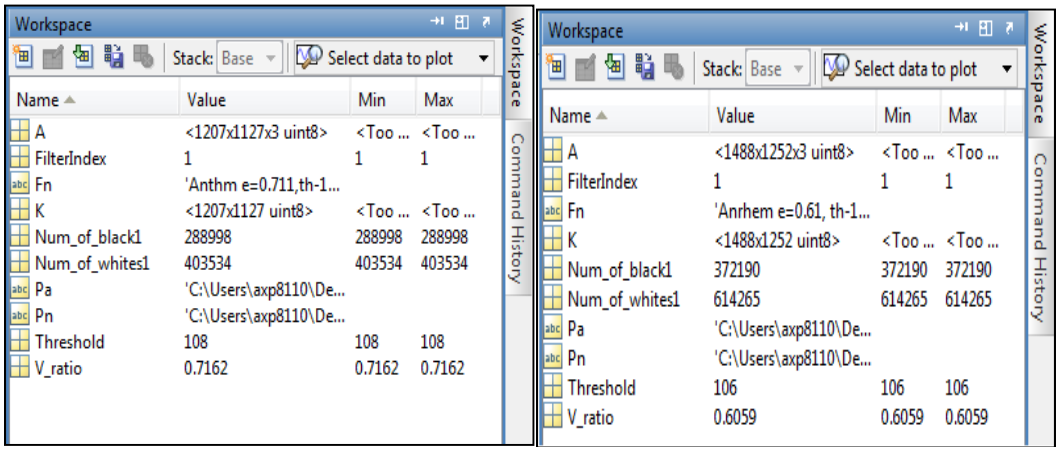

(a) 95% MDD Void ratio, e=0.716 (b) MDD Void ratio, e=0.605

Figure 5.36: Snapshot of the MATLAB workspace showing the void ratio output

Table 5.4: Average void ratio determination for Anthem soil

Slices	Void ratio		
	95% MDD	MDD	95% MDD at saturation
Slice 1	0.716	0.605	0.344
Slice 2	0.710	0.612	0.339
Slice 3	0.703	0.612	0.336
Average	0.71	0.61	0.34

Anthem soil specimen compacted at 95% MDD was used for monitoring the variation of void ratio with saturation. Figure 5.37 shows the variation of pore structure and void ratio with saturation of the specimen. For the Anthem soil, the void ratio decreased from 0.71 at dry side to 0.34 at saturation. Figure 5.38 shows the snapshot of the MATLAB image processed output for Anthem soil.

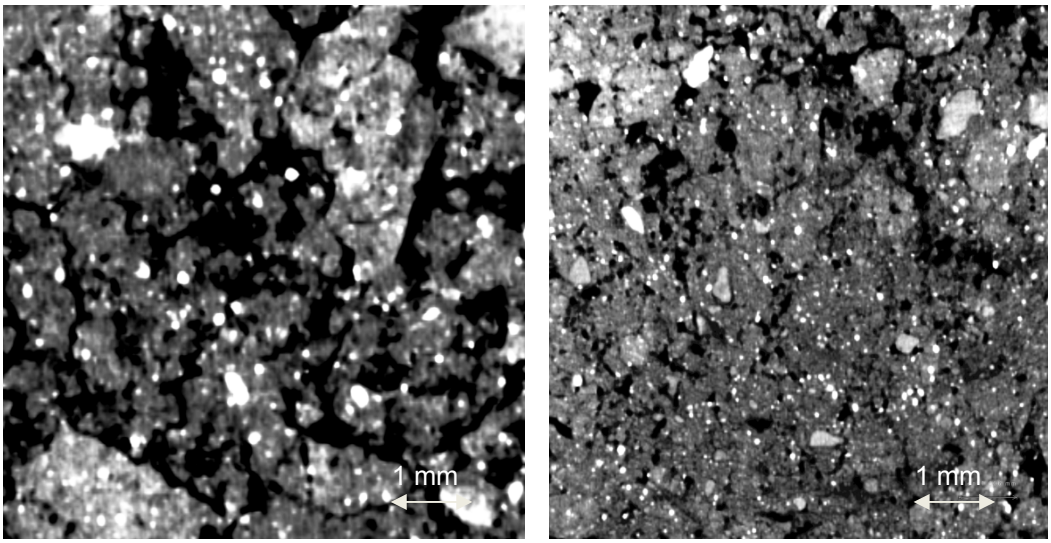

(a) Dry specimen (b) Saturated specimen

Figure 5.37: XCT Scanned images on Anthem soil at 95% MDD; (a), (b) dry and saturated conditions

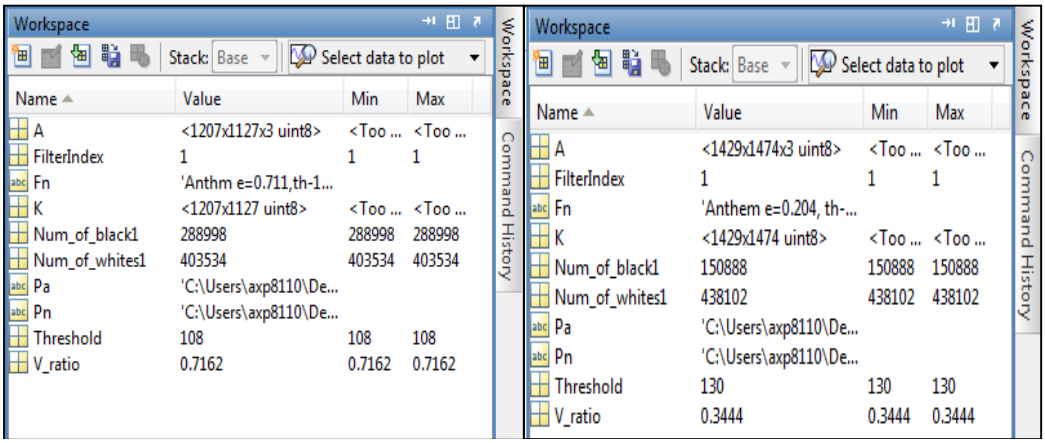

(a) Void ratio at dry e=0.716 (b) Void ratio at saturation e=0.344

Figure 5.38: (a), (b) Snapshot of the MATLAB workspace showing the void ratio output

5.4.2 Burleson soil CT scan

The reconstructed Burleson soil CT scan image at 95% MDD is presented in Figure 5.39. The 3-D image shows the packing and arrangement of particles of different sizes. The high density particles are represented by white color and low density particles with darker color.

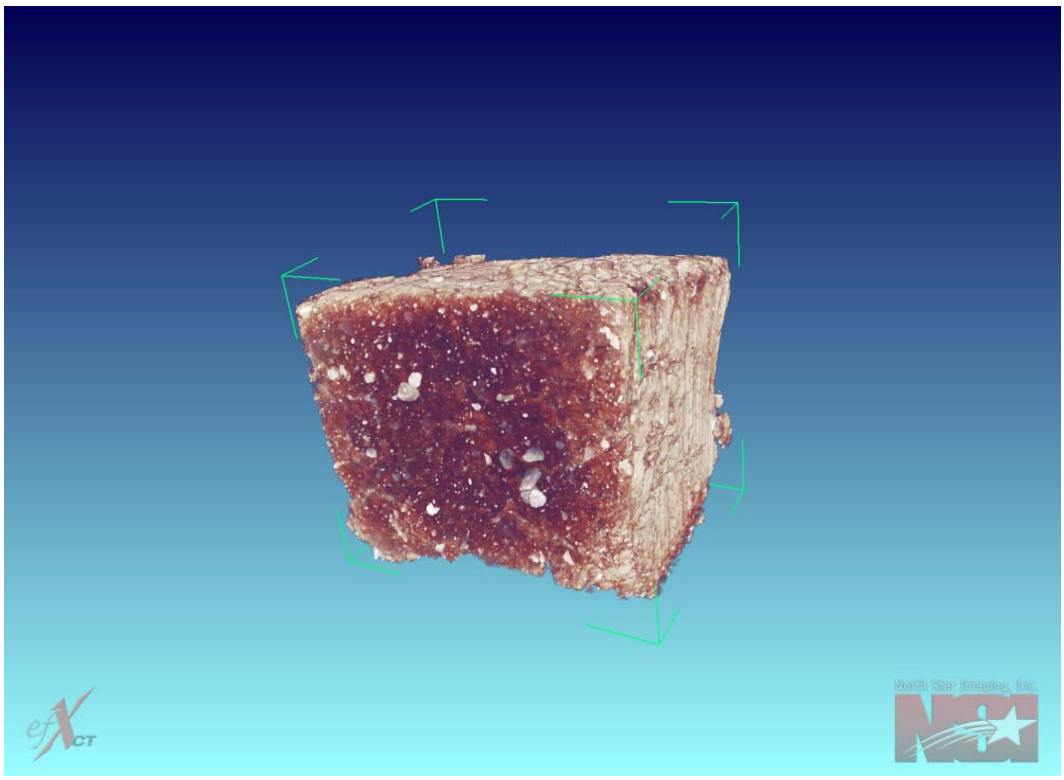

Figure 5.39: Reconstructed Burleson Soil specimen from XCT technique

Burleson soil specimen was compacted at two density conditions, 95% MDD and MDD. The cut samples are oven dried for a period of 24 hours before scanning for X-ray tomography. Figure 5.40 shows the variation of particle arrangement in the soil mass with change in density from 95% MDD to MDD condition. The void ratio of the mass is calculated using MATLAB image processing program as presented in the previous sections. For the Burleson soil the void ratio varied from 0.79 at 95% MDD to 0.69 at MDD condition. Figure 5.41 shows the snapshot of the MATLAB image processed output for Burleson soil.

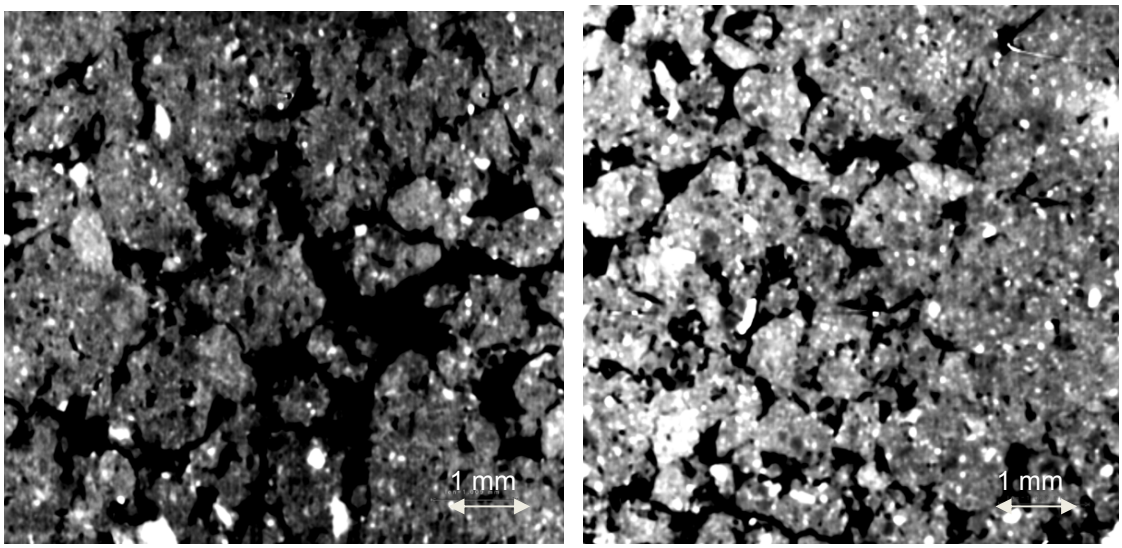

(a) 95% MDD e=0.79 (b) MDD e=0.69

Figure 5.40: (a), (b) XCT Scanned images on Burleson soil of different densities

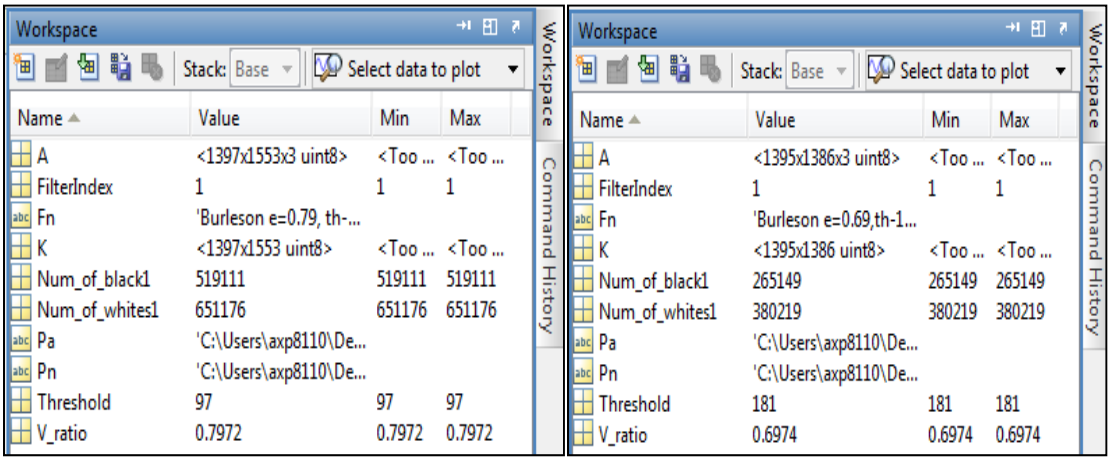

(a) 95% MDD Void ratio, e=0.797 (b) MDD Void ratio, e=0.697

Figure 5.41: (a), (b) Snapshot of the MATLAB workspace showing the void ratio output

Figure 5.42 shows the variation of pore structure and void ratio with saturation of the specimen at 95% MDD. For the Burleson soil, the void ratio decreased from 0.79 at dry side to 0.59 at saturation. Figure 5.43 shows the snapshot of the MATLAB image processed output for Burleson soil.

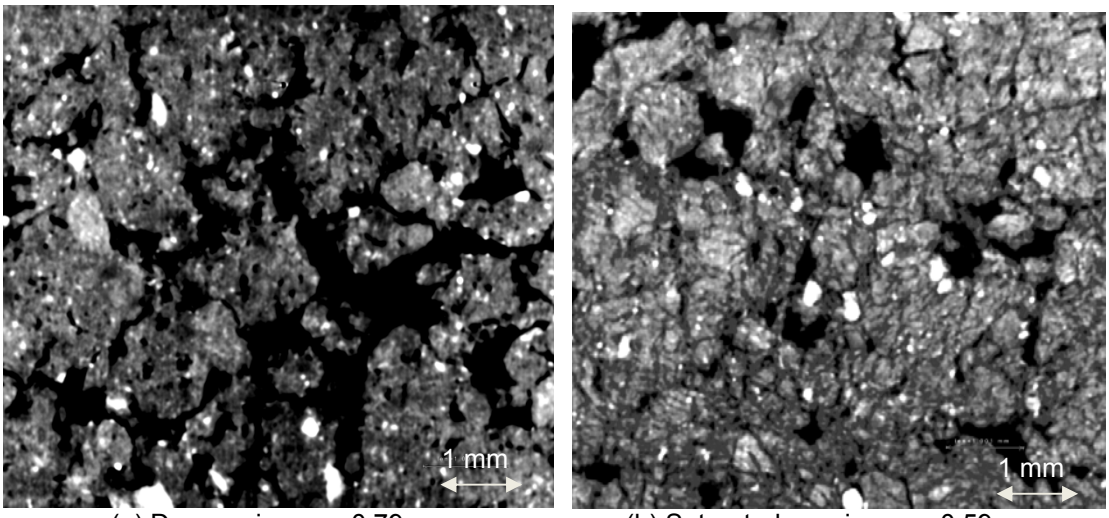

(a) Dry specimen e=0.79 (b) Saturated specimen e=0.59

Figure 5.42: XCT Scanned images on Burleson soil at 95% MDD; (a), (b) dry and saturated conditions

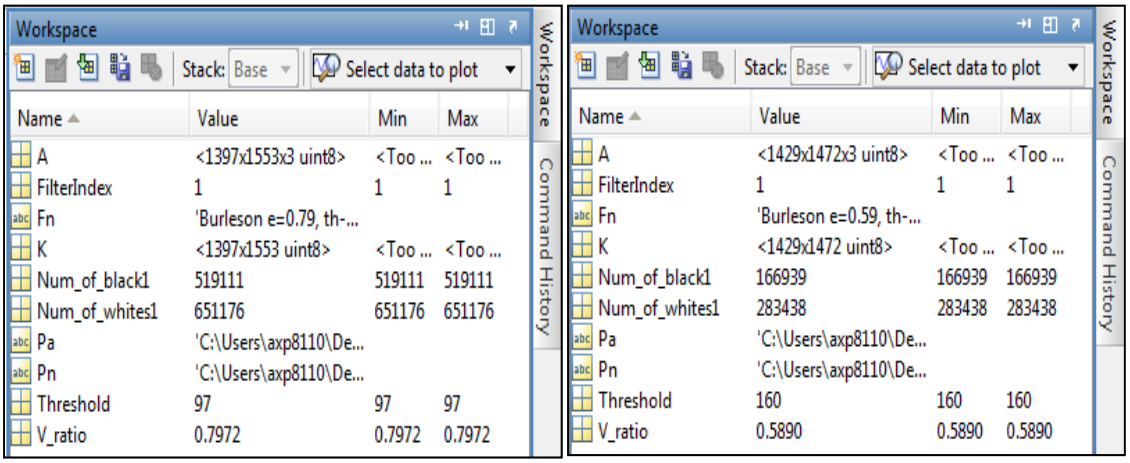

(a) Void ratio at dry e=0.797 (b) Void ratio at saturation e=0.589

Figure 5.43: (a), (b) Snapshot of the MATLAB workspace showing the void ratio output

5.4.3 Colorado soil CT scan

The reconstructed Colorado soil CT scan image at 95% MDD is presented in Figure 5.44. The 3-D image shows the packing and arrangement of particles of different sizes. The high density particles are represented by white color and low density particles with darker color.

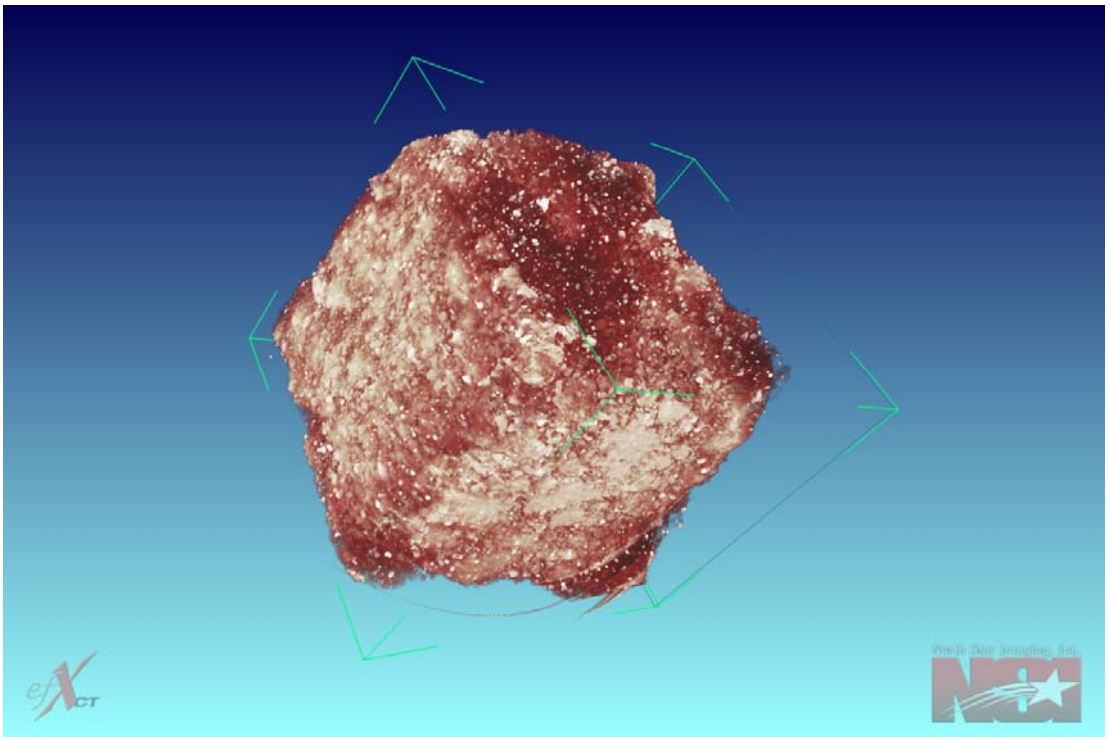

Figure 5.44: Reconstructed Colorado Soil specimen from XCT technique

Colorado soil specimen compacted at two density conditions, 95% MDD and MDD were used in the present study. The cut samples were oven dried for a period of 24 hours before scanning for X-ray tomography. Figure 5.45 shows the variation of particle arrangement in the soil mass with change in density from 95% MDD to MDD.

The void ratio of the mass is calculated using MATLAB image processing program as presented in the previous sections. For the Colorado soil the void ratio varied from 0.74 at 95% MDD to 0.67 at MDD condition. Figure 5.46 shows the snapshot of the MATLAB image processed output for Colorado soil.

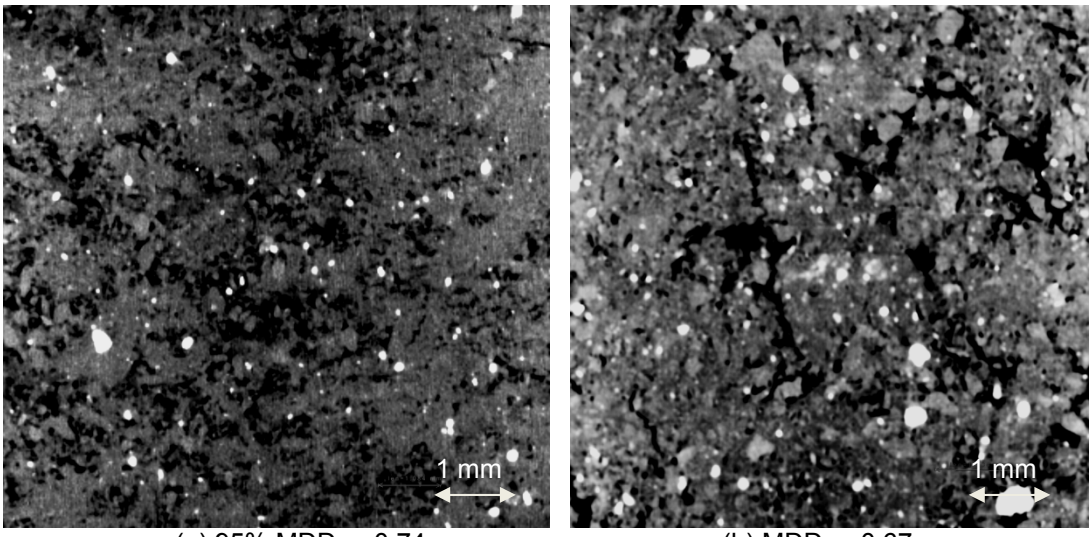

(a) 95% MDD e=0.74 (b) MDD e=0.67

Figure 5.45: (a), (b) XCT Scanned images on Colorado soil of different densities

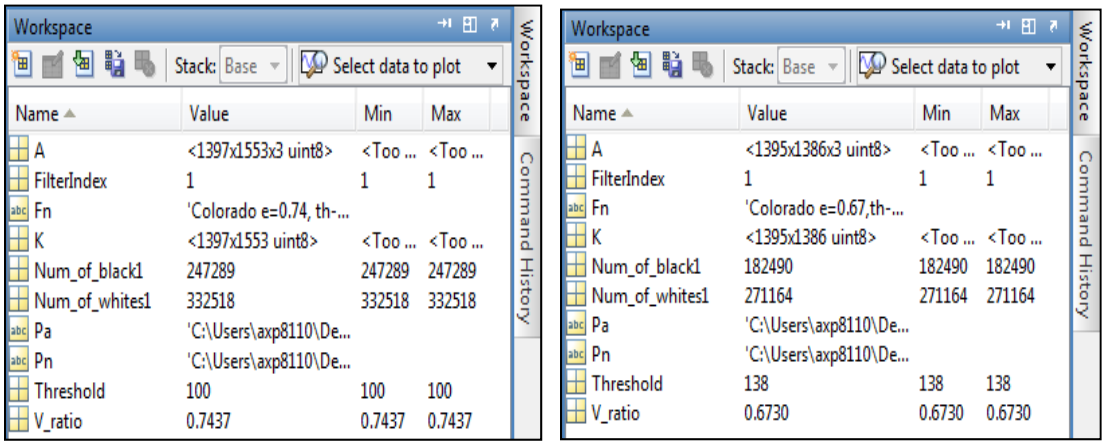

(a) 95% MDD Void ratio, e=0.743 (b) MDD Void ratio, e=0.673

Figure 5.46: (a), (b) Snapshot of the MATLAB workspace showing the void ratio output

Colorado soil specimen compacted at 95% MDD was used for monitoring the variation of void ratio with saturation. Figure 5.47 shows the variation of pore structure and void ratio with saturation of the specimen. For the Colorado soil, the void ratio decreased from 0.74 at dry side to 0.47 at saturation. Figure 5.48 shows the snapshot of the MATLAB image processed output for Colorado soil.

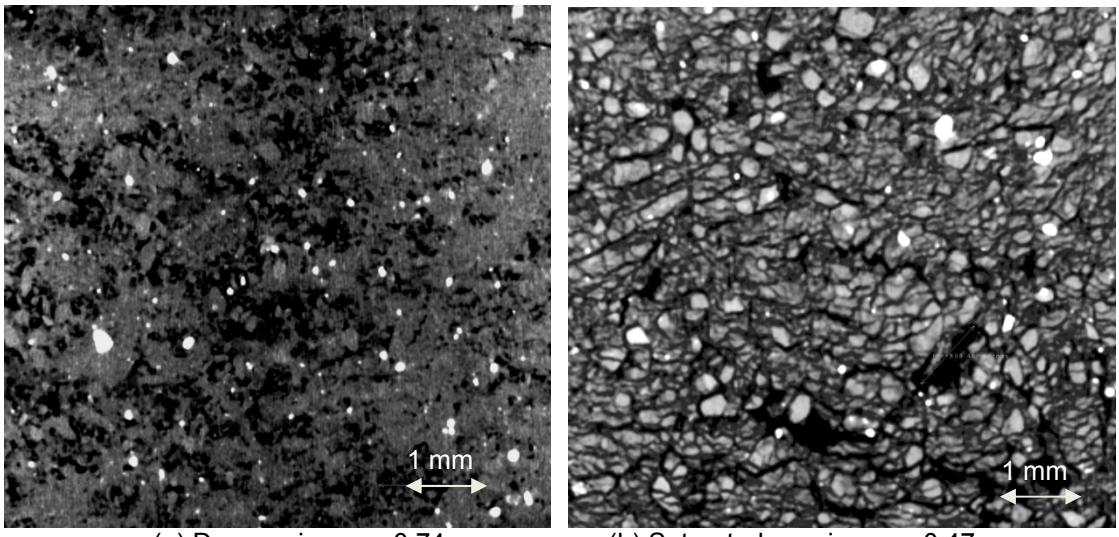

(a) Dry specimen e=0.74 (b) Saturated specimen e=0.47

Figure 5.47: XCT Scanned images on Colorado soil at 95% MDD; (a), (b) dry and saturated conditions

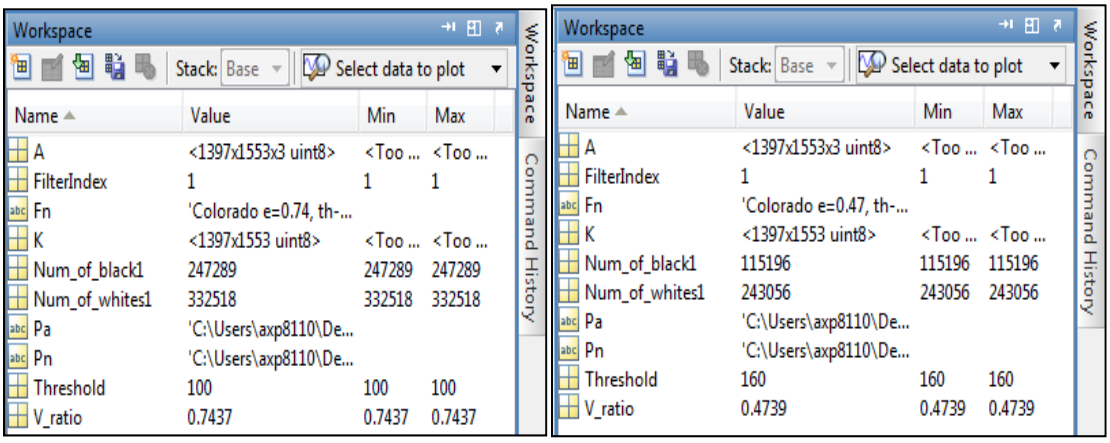

(a) Void ratio at dry e=0.743 (b) Void ratio at saturation e=0.473

Figure 5.48: (a), (b) Snapshot of the MATLAB workspace showing the void ratio output

5.4.4 Grayson soil CT scan

The reconstructed Grayson soil CT scan image at 95% MDD is presented in Figure 5.49. The 3-D image shows the packing and arrangement of particles of different sizes. The high density particles are represented by white color and low density particles with darker color.

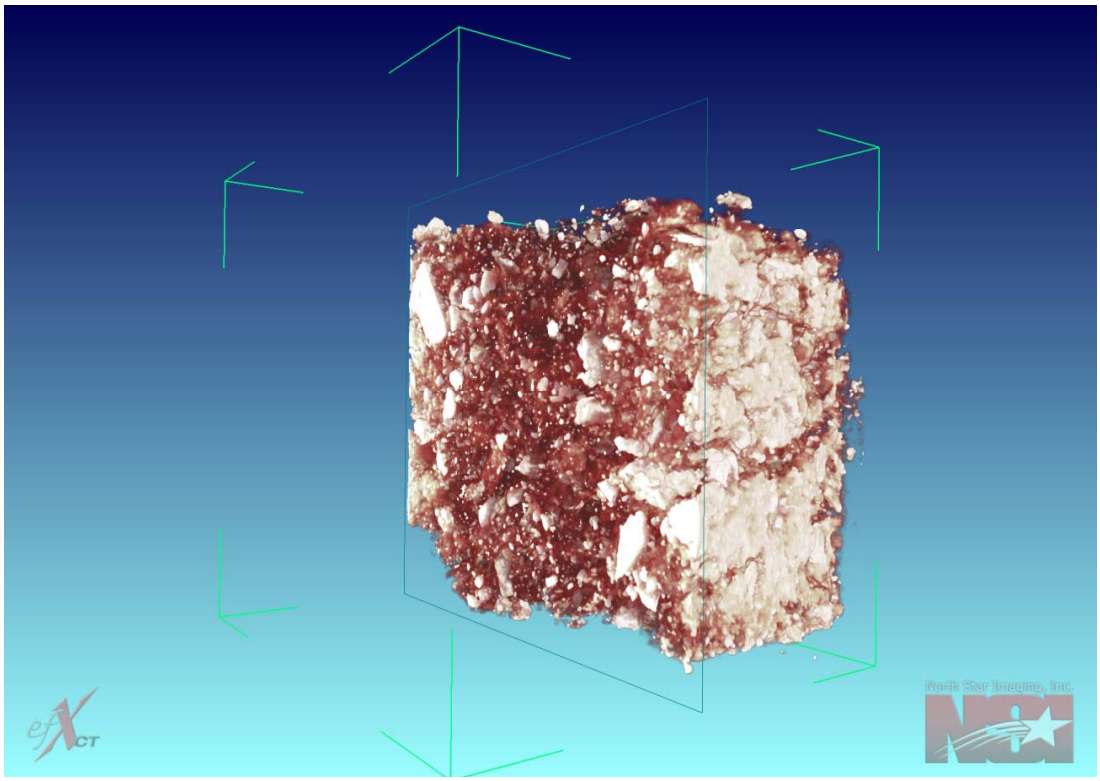

Figure 5.49: Reconstructed Grayson Soil specimen from XCT technique

Grayson soil specimens compacted at two density conditions, 95% MDD and MDD were used in the current study. The cut samples were oven dried for a period of 24 hours before scanning for X-ray tomography. Figure 5.50 shows the variation of particle arrangement in the soil mass with change in density from 95% MDD to MDD condition. The void ratio of the mass is calculated using MATLAB image processing program as presented in the previous sections. For the Grayson soil the void ratio varied from 01.04 at 95% MDD to 0.95 at MDD condition.

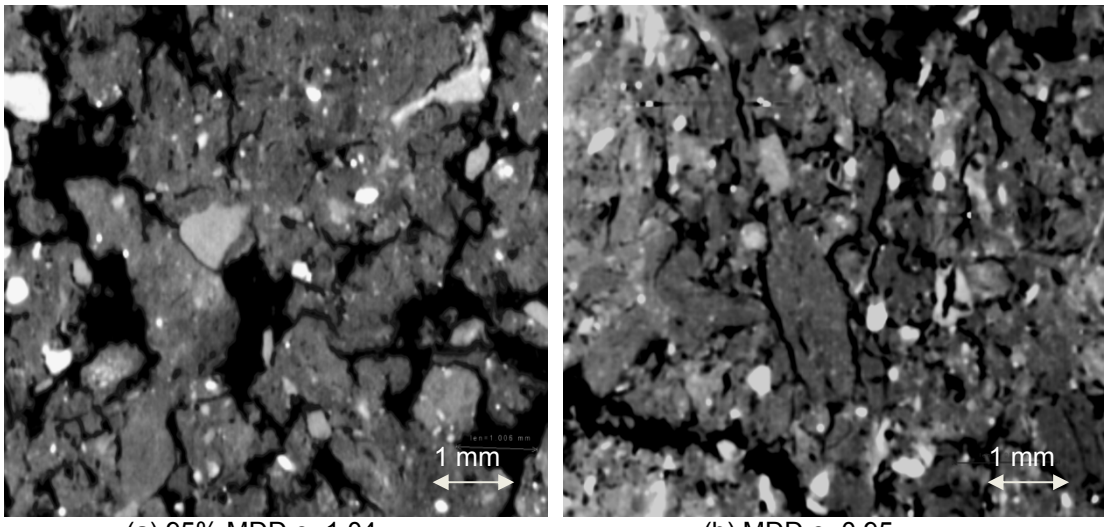

(a) 95% MDD e=1.04 (b) MDD e=0.95

Figure 5.50: (a), (b) XCT Scanned images on Grayson soil of different densities

Grayson soil specimen compacted at 95% MDD was used for monitoring the variation of void ratio with saturation. Figure 5.51 shows the variation of pore structure and void ratio with saturation of the specimen. For the Grayson soil, the void ratio decreased from 1.04 at dry side to 0.45 at saturation.

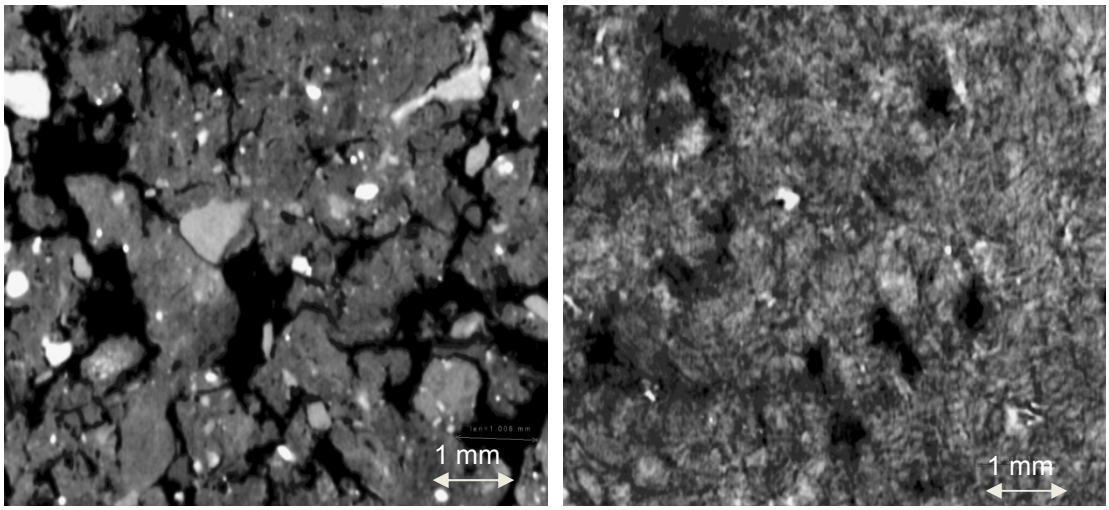

(a) Dry specimen e=1.04 (b) Saturated specimen e=0.45

Figure 5.51: XCT Scanned images on Grayson soil at 95% MDD; (a), (b) dry and saturated conditions

5.4.5 *Keller soil CT scan*

The reconstructed Keller soil CT scan image at 95% MDD is presented in Figure 5.52. The 3-D image shows the packing and arrangement of particles of different sizes. The high density particles are represented by white color and low density particles with darker color.

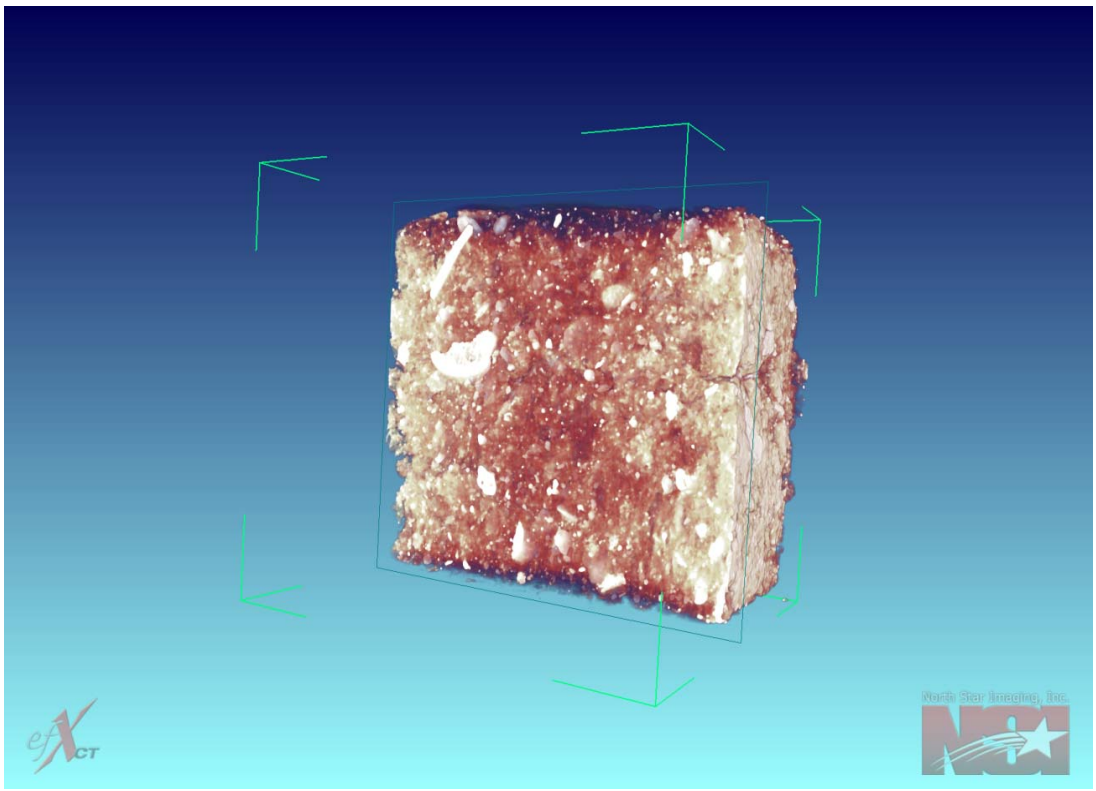

Figure 5.52: Reconstructed Keller Soil specimen from XCT technique

Keller soil specimens compacted at two density conditions, 95% MDD and MDD were used for the present study. The cut samples were oven dried for a period of 24 hours before scanning for X-ray tomography. Figure 5.53 shows the variation of particle arrangement in the soil mass with change in density from 95% MDD to MDD. The void ratio of the mass is calculated using MATLAB image processing program as presented in the previous sections. For the Keller soil the void ratio varied from 0.53 at 95% MDD to 0.47 at MDD condition.

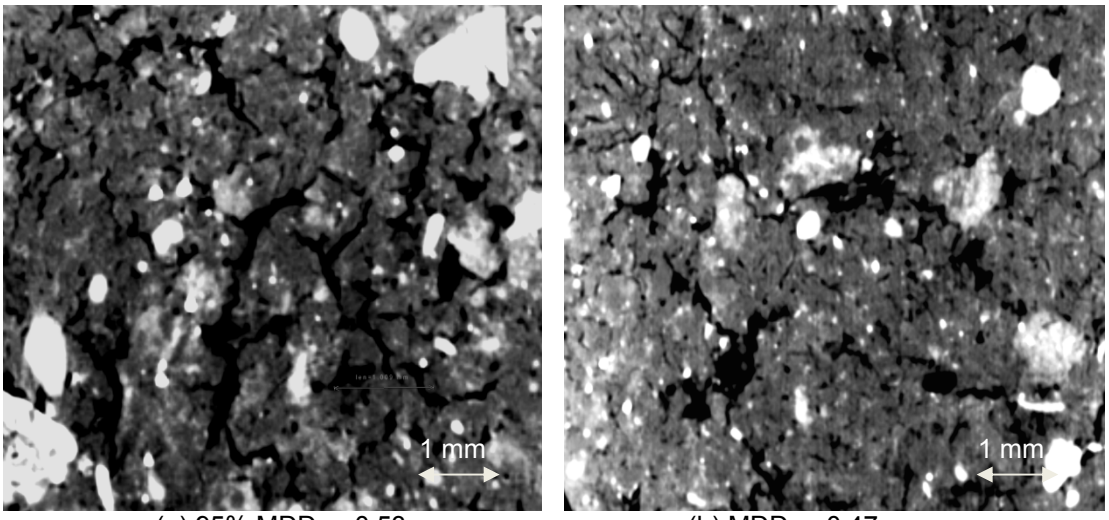

(a) 95% MDD e=0.53 (b) MDD e=0.47

Figure 5.53: (a), (b) XCT Scanned images on Keller soil of different densities

Keller soil specimen compacted at 95% MDD was used for monitoring the variation of void ratio with saturation. Figure 5.54 shows the variation of pore structure and void ratio with saturation of the specimen. For the Keller soil, the void ratio decreased from 0.53 at dry side to 0.3 at saturation.

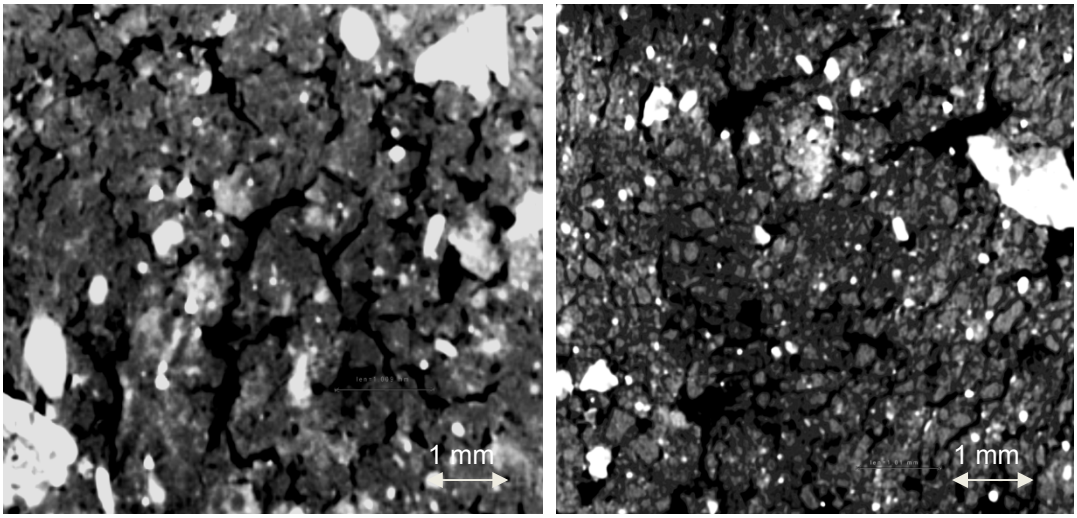

(a) Dry specimen e=0.53 (b) Saturated specimen e=0.3

Figure 5.54: XCT Scanned images on Keller soil at 95% MDD; (a), (b) dry and saturated conditions

5.4.6 Oklahoma soil CT scan

The reconstructed Oklahoma soil CT scan image at 95% MDD is presented in Figure 5.55. The 3-D image shows the packing and arrangement of particles of different sizes. The high density particles are represented by white color and low density particles with darker color.

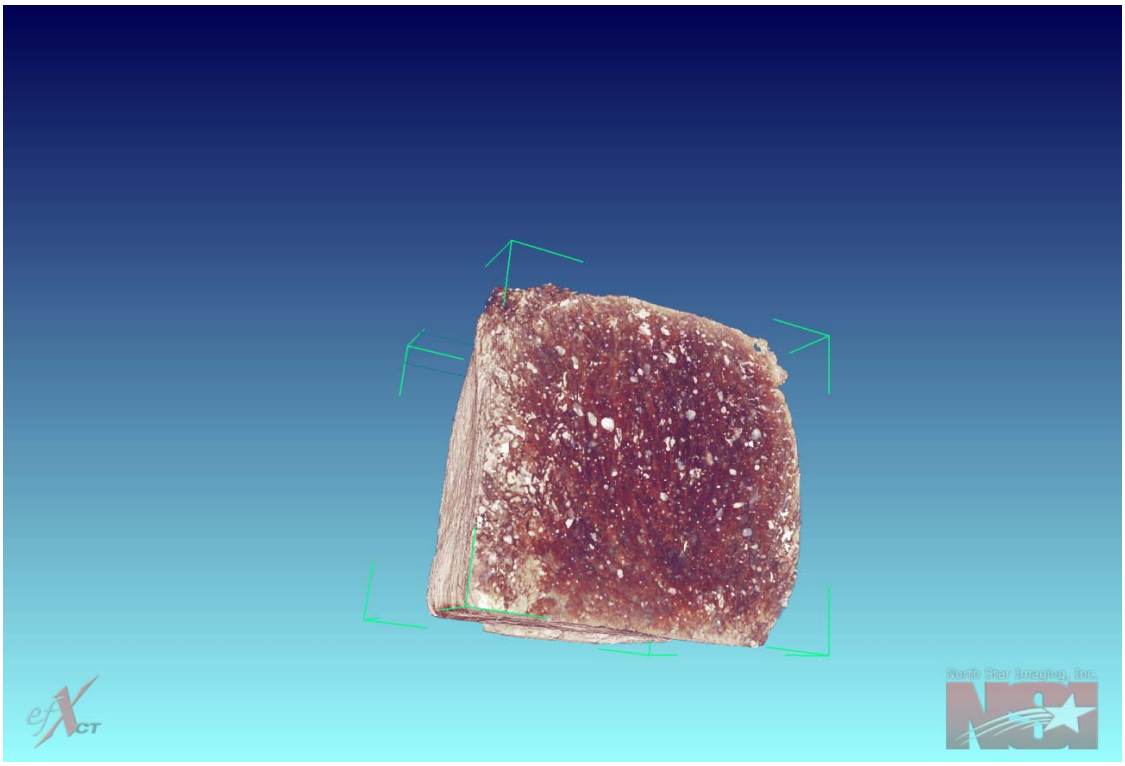

Figure 5.55: Reconstructed Oklahoma Soil specimen from XCT technique

Oklahoma soil specimens compacted at two density conditions, 95% MDD and MDD were used in the current study. The cut samples were oven dried for a period of 24 hours before scanning for X-ray tomography. Figure 5.56 shows the variation of particle arrangement in the soil mass with change in density from 95% MDD to MDD. The void ratio of the mass is calculated using MATLAB image processing program as presented in the previous sections. For the Oklahoma soil the void ratio varied from 0.96 at 95% MDD to 0.85 at MDD condition.

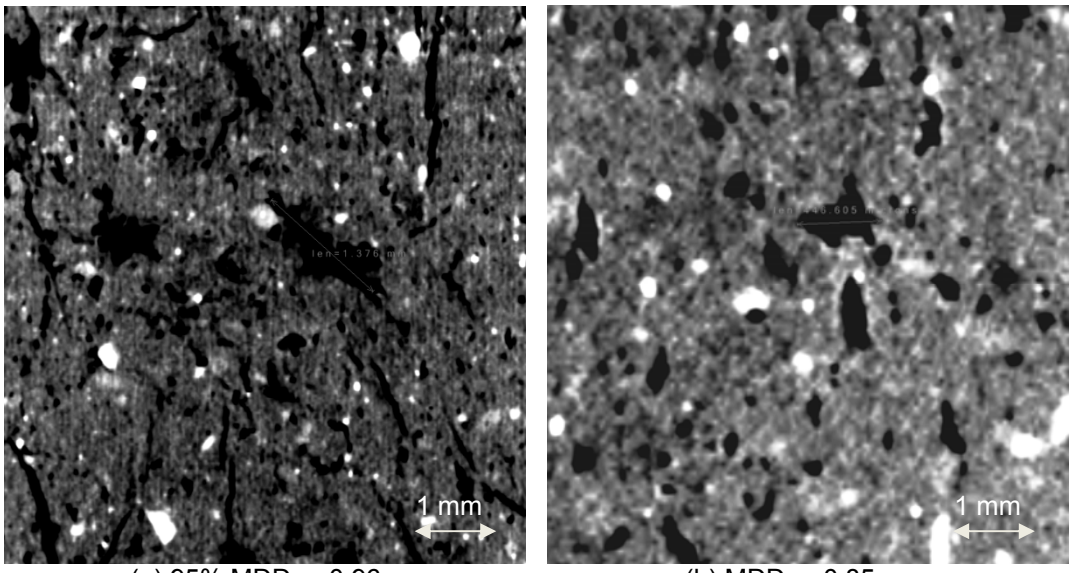

(a) 95% MDD e=0.96 (b) MDD e=0.85

Figure 5.56: (a), (b) XCT Scanned images on Oklahoma soil of different densities

Oklahoma soil specimen compacted at 95% MDD was used for monitoring the variation of void ratio with saturation. Figure 5.57 shows the variation of pore structure and void ratio with saturation of the specimen. For the Oklahoma soil, the void ratio decreased from 0.96 at dry side to 0.71 at saturation.

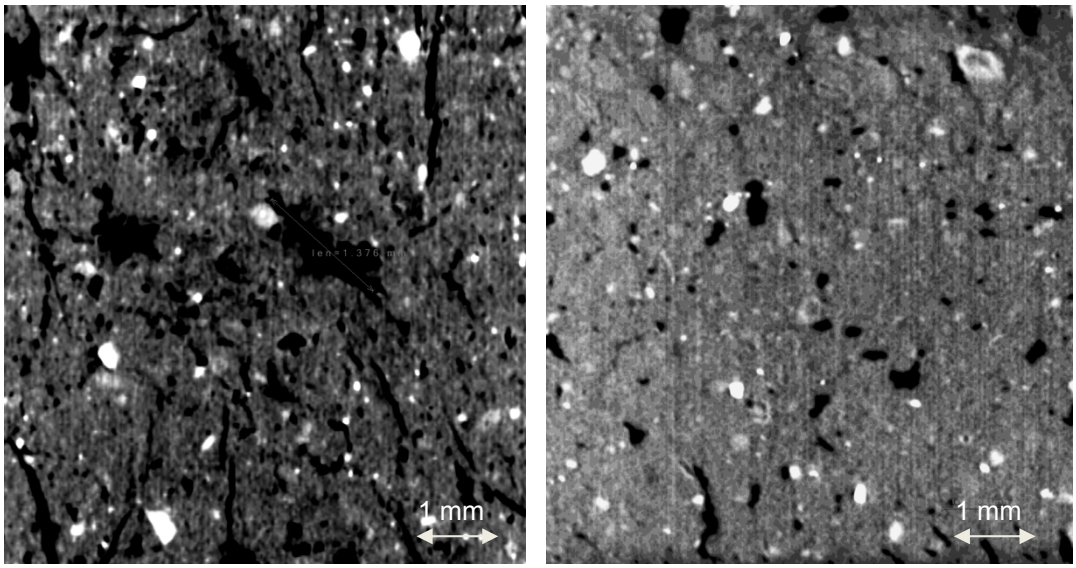

(a) Dry specimen e=0.96 (b) Saturated specimen e=0.71

Figure 5.57: XCT Scanned images on Oklahoma soil at 95% MDD; (a), (b) dry and saturated conditions

5.4.7 San Antonio soil CT scan

The reconstructed San Antonio soil CT scan image at 95% MDD is presented in Figure 5.58. The 3-D image shows the packing and arrangement of particles of different sizes. The high density particles are represented by white color and low density particles with darker color.

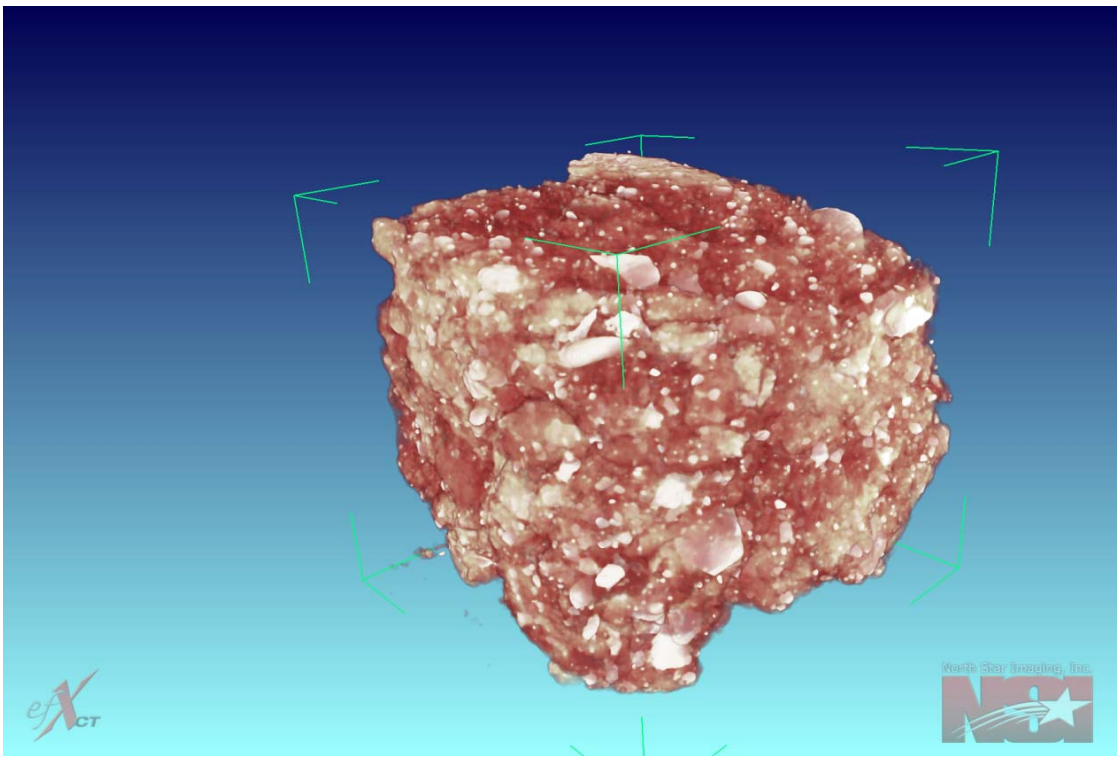

Figure 5.58: Reconstructed San Antonio Soil specimen from XCT technique

San Antonio soil specimens compacted at two density conditions, 95% MDD and MDD were used in the current study. The cut samples were oven dried for a period of 24 hours before scanning for X-ray tomography. Figure 5.35 shows the variation of particle arrangement in the soil mass with change in density from 95% MDD to MDD condition. The void ratio of the mass is calculated using MATLAB image processing program as presented in the previous sections. For the San Antonio soil the void ratio varied from 0.9 at 95% MDD to 0.84 at MDD condition.

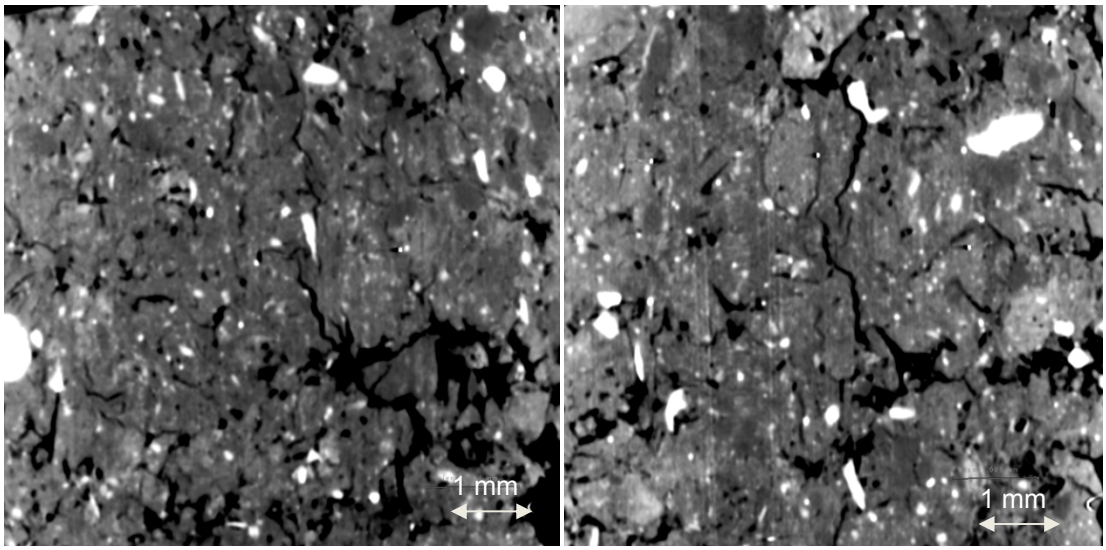

(a) 95% MDD e=0.9 (b) MDD e=0.84

Figure 5.59: (a), (b) XCT Scanned images on San Antonio soil of different densities

San Antonio soil specimen compacted at 95% MDD was used for monitoring the variation of void ratio with saturation. Figure 5.60 shows the variation of pore structure and void ratio with saturation of the specimen. For the San Antonio soil, the void ratio decreased from 0.9 at dry side to 0.54 at saturation.

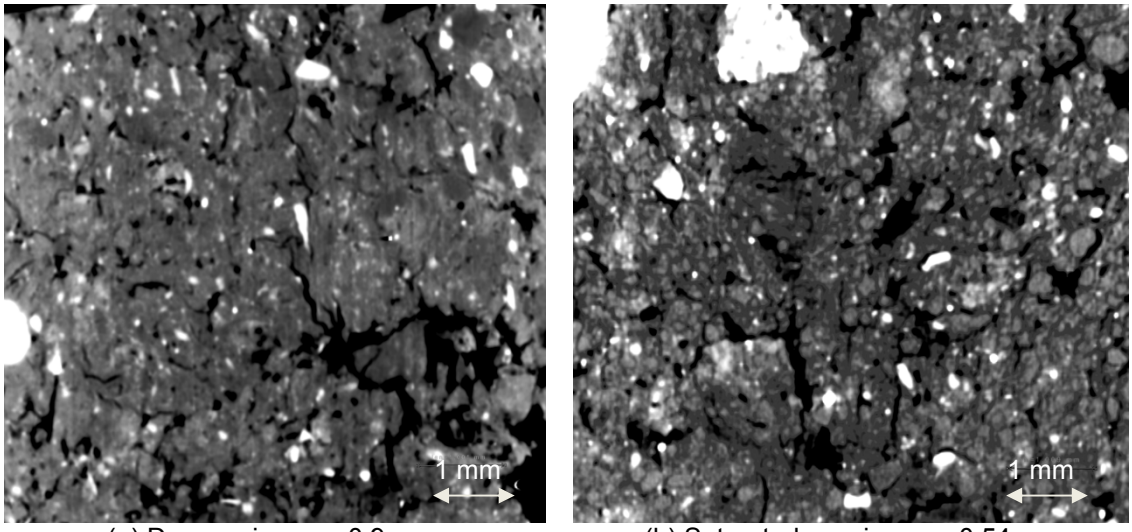

(a) Dry specimen e=0.9 (b) Saturated specimen e=0.54

Figure 5.60: XCT Scanned images on San Antonio soil at 95% MDD; (a), (b) dry and saturated conditions

5.4.8 San Diego soil CT scan

The reconstructed San Diego soil CT scan image at 95% MDD is presented in Figure 5.61. The 3-D image shows the packing and arrangement of particles of different sizes. The high density particles are represented by white color and low density particles with darker color.

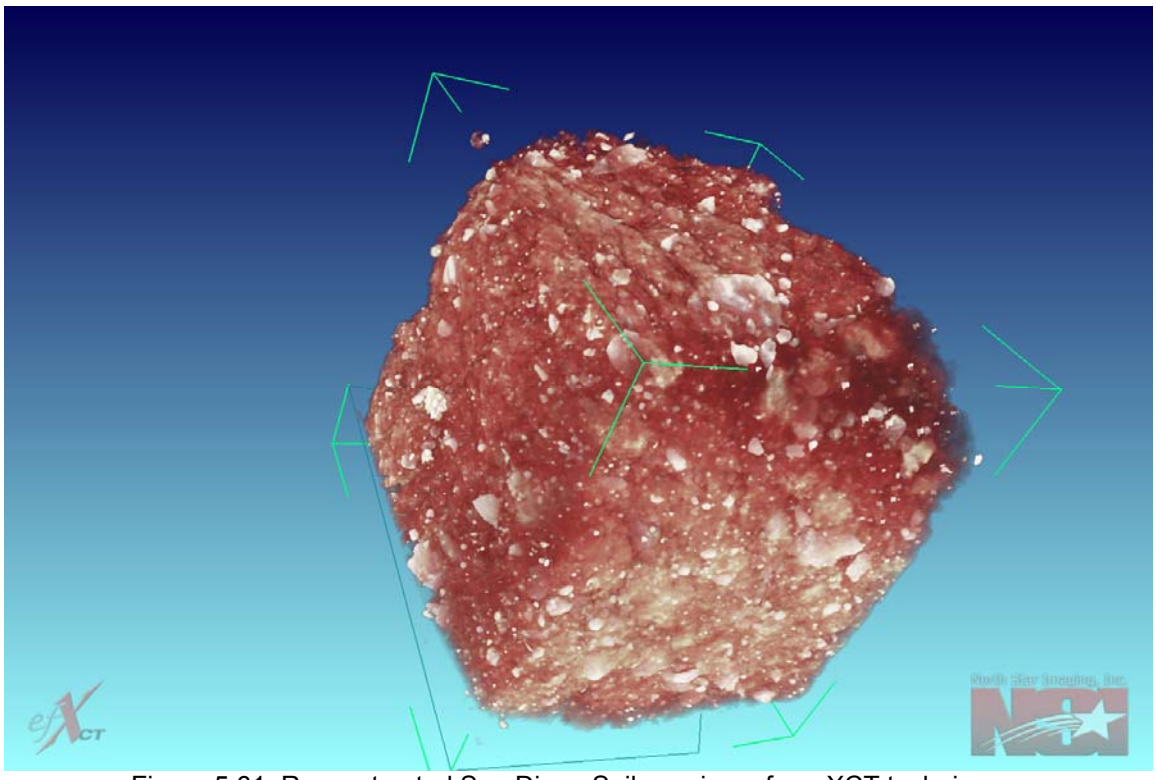

Figure 5.61: Reconstructed San Diego Soil specimen from XCT technique

San Diego soil specimens compacted at two density conditions, 95% MDD and MDD were used in the current study. The cut samples were oven dried for a period of 24 hours before scanning for X-ray tomography. Figure 5.62 shows the variation of particle arrangement in the soil mass with change in density from 95% MDD to MDD condition. The void ratio of the mass is calculated using MATLAB program as presented in the previous sections. For the San Diego soil the void ratio varied from 0.69 at 95% MDD to 0.6 at MDD condition.

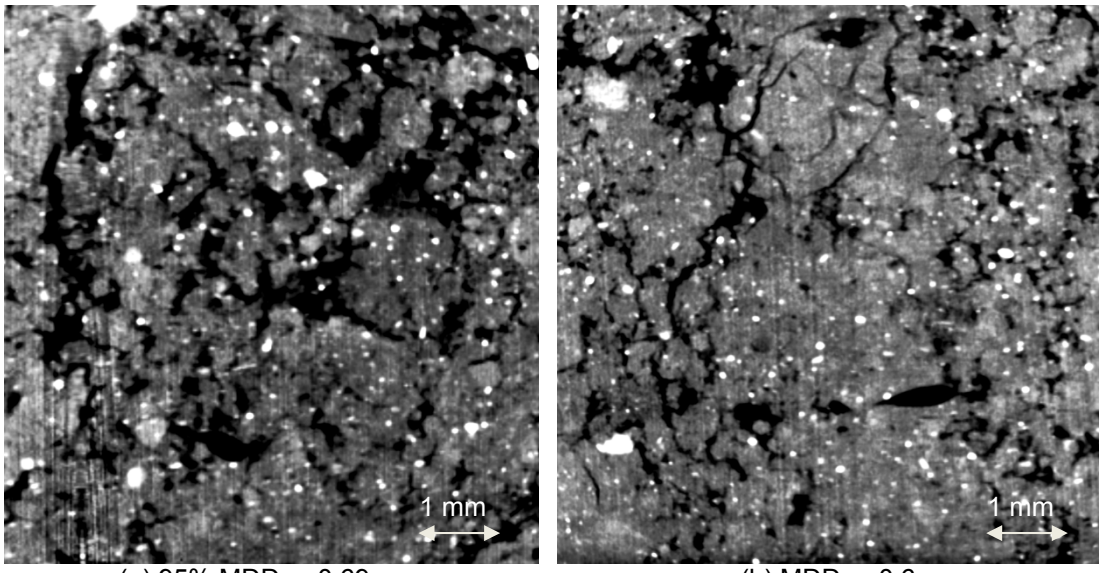

(a) 95% MDD e=0.69 (b) MDD e=0.6

Figure 5.62: (a), (b) XCT Scanned images on San Diego soil of different densities

San Diego soil specimen compacted at 95% MDD was used for monitoring the variation of void ratio with saturation. Figure 5.63 shows the variation of pore structure and void ratio with saturation of the specimen. For the San Diego soil, the void ratio decreased from 0.69 at dry side to 0.41 at saturation.

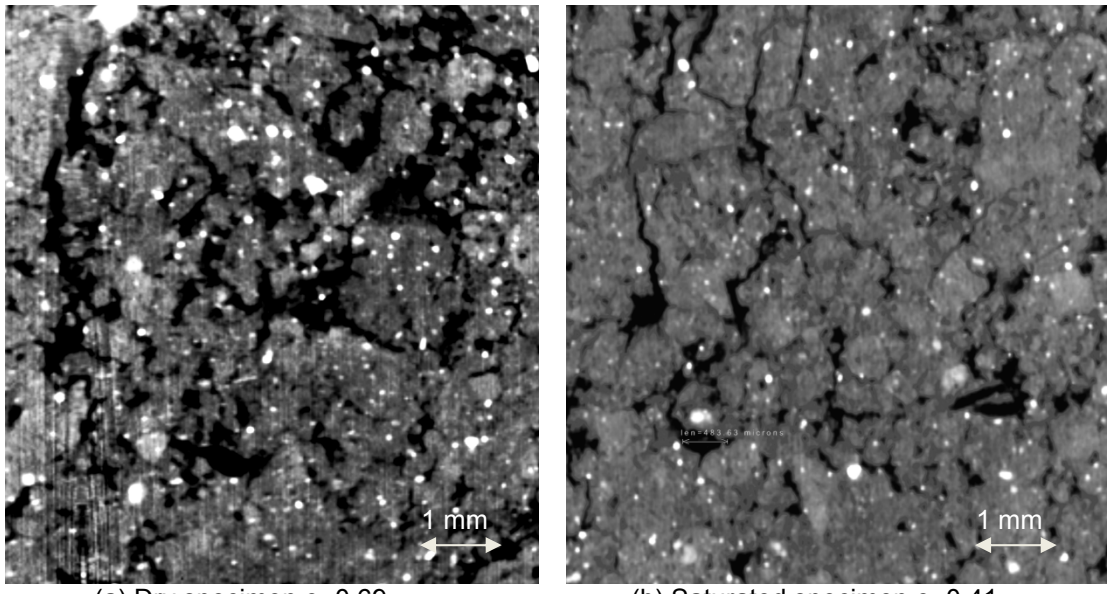

(a) Dry specimen e=0.69 (b) Saturated specimen e=0.41

Figure 5.63: XCT Scanned images on San Diego soil at 95% MDD; (a), (b) dry and saturated conditions

Table 5.5 presents the variation of void ratio calculated for all the eight natural soils at different density conditions using both XCT scans and from soil weight – volume relationships.

Table 5.5: Variation of computed void ratio at different density conditions

Soil	Void ratio for 95% MDD at dry state		Void ratio for MDD at dry state	
	From XCT scan (e_{X-T})	Estimated from weight/volume relationships (e_{W-V})	From XCT scan (e_{X-T})	Estimated from weight/volume relationships (e_{W-V})
Anthem	0.71	0.71	0.61	0.62
Burleson	0.79	0.78	0.69	0.71
Colorado	0.74	0.77	0.67	0.68
Grayson	1.04	1.03	0.95	0.95
Keller	0.53	0.53	0.47	0.47
Oklahoma	0.96	0.96	0.85	0.85
San Antonio	0.90	0.90	0.84	0.85
San Diego	0.69	0.69	0.60	0.60

It was found that there is a systematic difference of 0.06 to 0.10 between the two techniques in the void ratios determined at dry compaction conditions. Such systematic differences can be attributed to sampling technique induced soil disturbance to image analysis related errors. Nevertheless, the void ratio calculated from XCT technique has shown a good, if not perfect agreement with weight-volume relationships at both dry density conditions.

Figure 5.64 presents the void ratio results obtained from X-ray tomography technique and weight-volume relationships at 95% MDD dry condition.

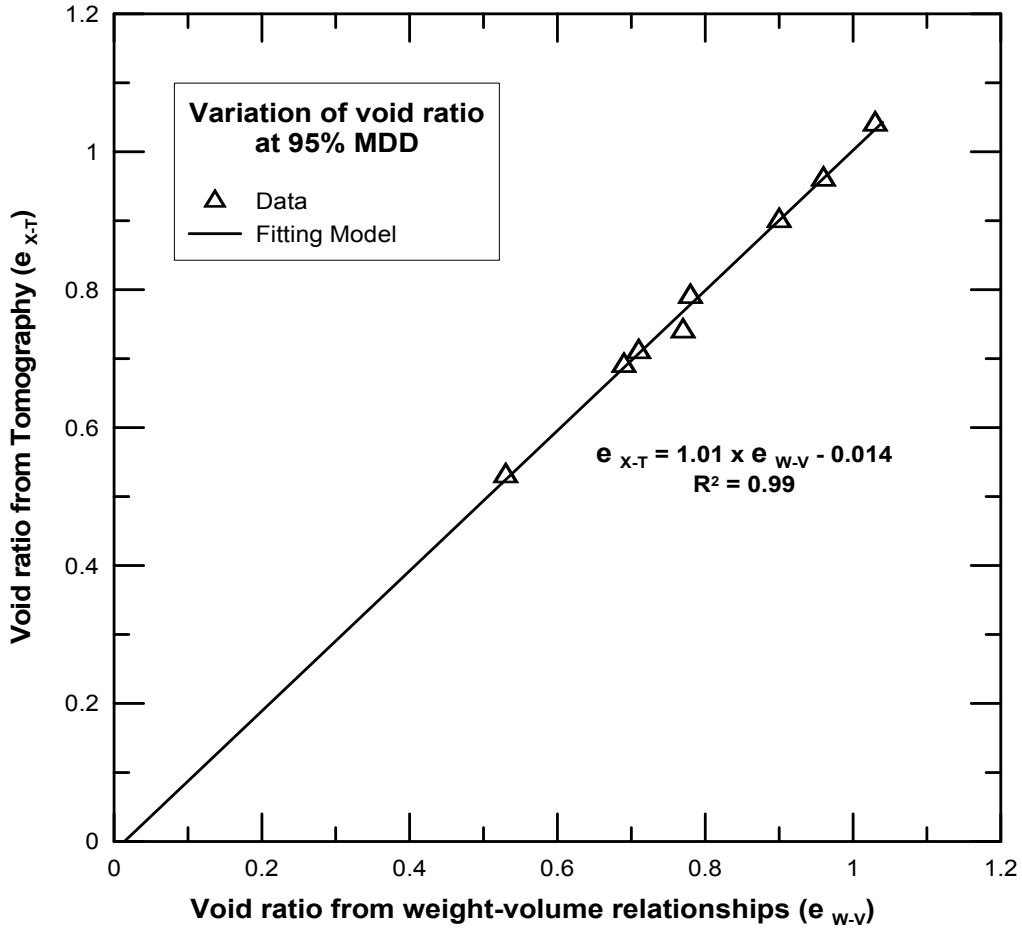

Figure 5.64: Void ratio's determined from the two techniques at 95% MDD dry condition

From the above figure, slight variations between the measured and predicted void ratios were noted. The results predicted from weight-volume relationships closely resemble the actual values measured from tomography test. The best fit equation for the current scenario was presented in the above figure. The coefficient of determination (R^2) value for the fitted model is equal to 0.99.

Similarly, Figure 5.65 presents the void ratio results obtained from tomography technique and weight-volume relationships at MDD condition.

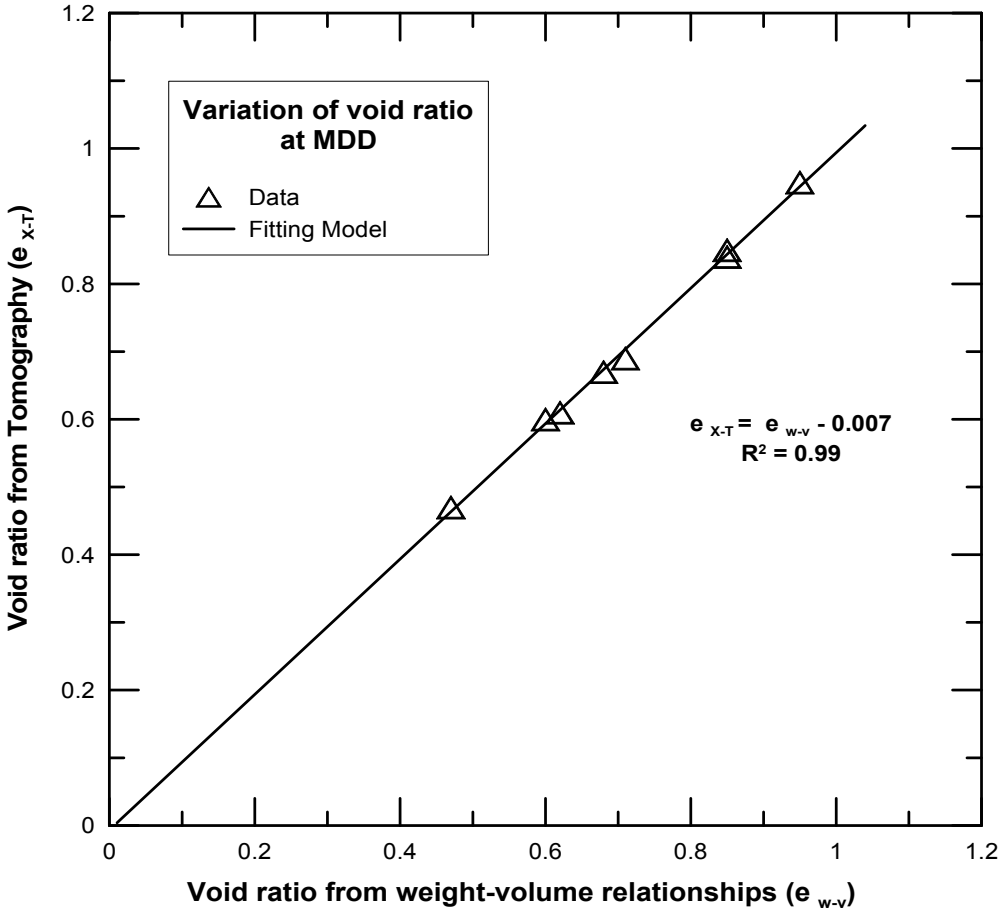

Figure 5.65: Void ratio's determined from the two techniques at MDD

The results predicted from weight-volume relationships closely resemble the actual values measured from tomography test. The best fit equation was presented in the above figure. The coefficient of determination (R^2) value for the fitted model is equal to 0.99.

Table 5.6 shown below presents the variation of void ratio calculated from XCT and respective weight/volume relationships. All the clays showed a decrease in void ratio when measured with X-ray computed tomography. Due to the fact that the free expansion of soil particles was neglected during the measurement of void ratio from weight/volume relationships, the predicted void ratio was high. The soil specimen underwent an internal crystalline expansion thereby decreasing the actual void space in the specimen. Hence, the XCT technique helps us in identifying the actual void space available after the soil specimen swells.

Table 5.6: Variation of computed void ratio at saturation for 95% MDD condition

Soil	Void ratio for 95% MDD at saturation	
	From XCT scan (e_{X-T})	Estimated from weight/volume relationships (e_{W-V})
Anthem	0.34	0.78
Burleson	0.59	0.93
Colorado	0.47	0.91
Grayson	0.45	1.23
Keller	0.30	0.57
Oklahoma	0.71	1.01
San Antonio	0.54	1.06
San Diego	0.41	0.71

Figure 5.66 presents the void ratio test results obtained from both tomography technique and weight-volume relationships at MDD condition. After swelling process, the actual void ratio of the soil specimen was determined using Tomography analysis.

A non-linear fitting model is included in the figure that closely resembles the actual variation of void ratio from the predicted ones. A low coefficient of determination (R^2) value was obtained for this model.

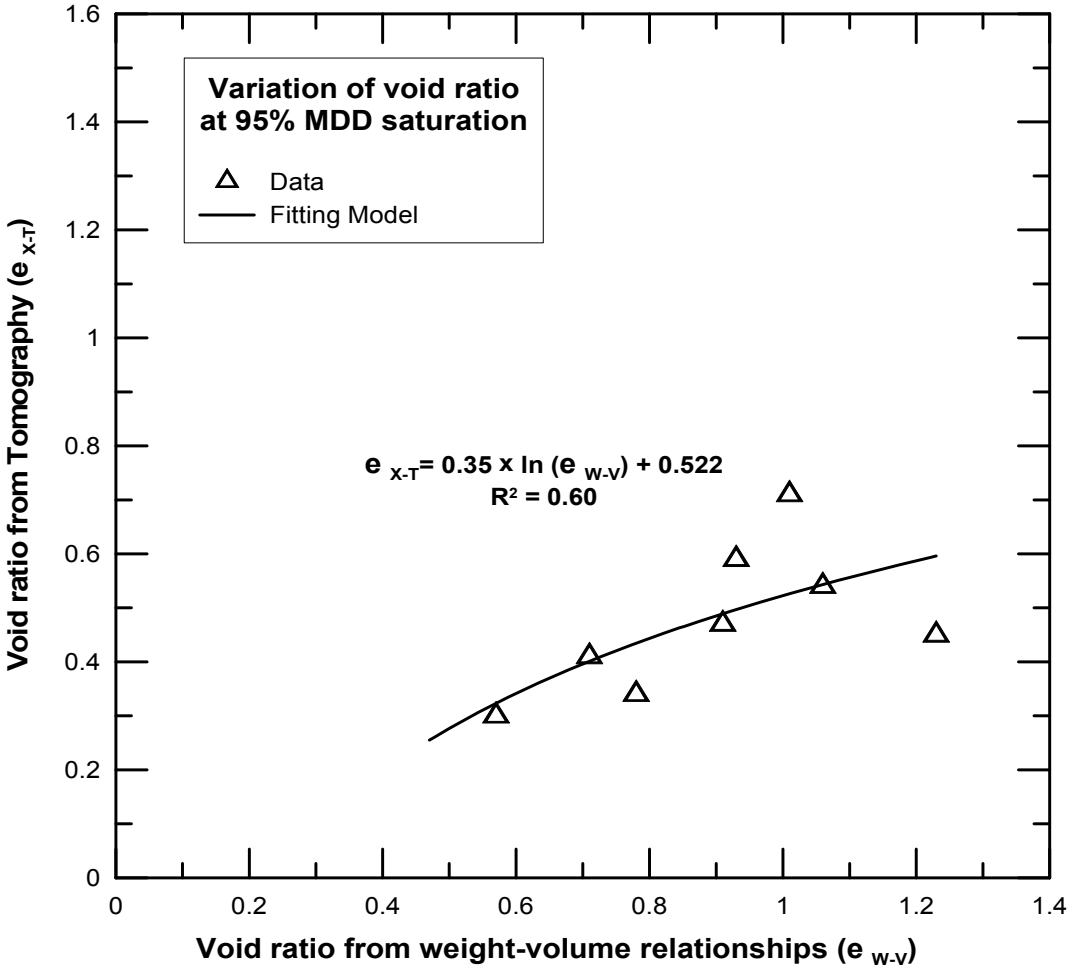

Figure 5.66: Void ratio calculated from tomography and weight-volume relationships at saturation

5.5 Summary

The present chapter deals with the study of different soil composition parameters on the eight soils collected. The mineralogical properties of these test soils are previously measured and presented in Chapter 3.

From mercury intrusion porosimetry testing, it was found that the high particle density at the MDD condition resulted in a lower volume of pore space. It was also found that Macro pores are abundant in specimens with low density (95% MDD), whereas micro and medium pores increase with high dense conditions (i.e. MDD).

The inter-connectivity of pores present in the soil specimen was closely observed with the help of X-ray tomography technique. The calculation of void ratio from the sliced sections was achieved using MATLAB image processing program and is based on pixel count.

From the tomography experiment, the variation of pore space and connectivity is clearly noticeable at different densities and moisture levels. The void ratio decreased from 95% MDD to MDD which is due to the more dense packing of particles. The void ratios determined from the XCT technique are in good agreement with those obtained from weight/volume relationships at dry conditions. The void ratio's generated during saturation condition are very low compared to those obtained from weight/volume relationships. The reason for this shift was that during the saturation process the clay minerals expand and occupy the pore spaces which in turn reduce the overall void ratio and hence were clearly noticed with the help of X-ray tomography. Both MIP and XCT techniques showed good repeatability of the test results. These tests provided pore size information of the present eight expansive soils. All these results are using the modeling analysis attempted in the next Chapter.

CHAPTER 6

ANALYSIS OF TEST RESULTS AND SWELL PREDICTION MODELS

6.1 Introduction

From the soil composition studies unique soil parameters which influence the swell behavior have been identified. Three swell prediction models have been introduced based on physical characteristics and pore distribution details of compacted soil as well as clay mineralogy data. Also, the validation of these models has been fully addressed in this chapter.

The first model is based solely on clay mineralogy information, which is the fundamental and basic contributing factor to swell behavior of expansive soils. The DDL theory in which the clay mineral surface charge attracts the moisture content in the soil medium thereby increasing the diffused double water layer thickness that ultimately contributes to soil heaving is considered for this model. Final diffused double layer induced swell thickness after soil expansion is determined for all the dominant clay minerals present in the soil mass. Later, the swell strains predicted are correlated with actual measured swell strains. A relationship between the predicted and measured swell strain is introduced and a correction factor for each initial condition is introduced that accounts for the variabiities in the model assumptions and the real behavior transpired during the soil swelling.

The second model targets the relationship of soil matric suction in unison with clay mineral content on the swell behavior of all the eight expansive soils. A new parameter called as the mechanical hydro chemical (MHC) parameter has been formulated for the working of this model. The term ‘Mechanical Hydro Chemical parameter’ (MHC) is derived from the following parameters. The variation of void ratio with soil matric suction is considered as the mechanical

contribution of swelling from the compacted soil. The initial matric suction which represents the moisture content condition of the soil is considered as hydro related parameter whereas the clay mineralogy of the soil is considered as the chemical parameter contributing to MHC modeling. All these parameters are interdependent and hence a product type term is introduced as a MHC parameter that accounts for these contributions to overall soil swelling. This parameter is correlated with the measured swell properties of the compacted soils.

Total surface area of a soil mass plays a vital role in governing the swell behavior. Hence, the third model developed here is based on the measured total surface area in the soil specimen in relation with pore surface area that is available to introduce moisture access to soil particles in a given soil specimen. A new parameter termed as 'Total Surface Area Ratio' (TSAR) which is formulated in this modeling was used in the swell behavior prediction. Further analysis performed on MIP test results provided lengths of different pore sizes and this information is utilized in this modeling.

6.2 Model 1: Diffused Double Layer (DDL) Swell Model

The diffused double layer (DDL) theory provides a strong basis for the understanding of swell behavior of a clay specimen (Mitchell and Soga, 2005). When clay comes in close contact with water, the negative charged clay particles tend to attract the water molecules. The water molecules distribute over the surface area of the clay particles thereby increasing the particle size.

The extent to which the clay particles have attraction forces on the water molecules can be termed as diffused double layer water. Likos (2004) specified that crystalline swelling or Type 1 swelling which is caused by interlayer absorption of water particles was followed by electrical double layer attraction forces which is also known as Type 2 swelling. These long range double layer attraction forces are the primary concern for the present research and are hence considered and used in the swell prediction model.

The diffused double layer for clay particles vary with minerals and the surface charge attraction forces. Figure 6.1 presents the diffused double layer thickness for a clay particle and the variation of ion concentration with distance from the clay particle.

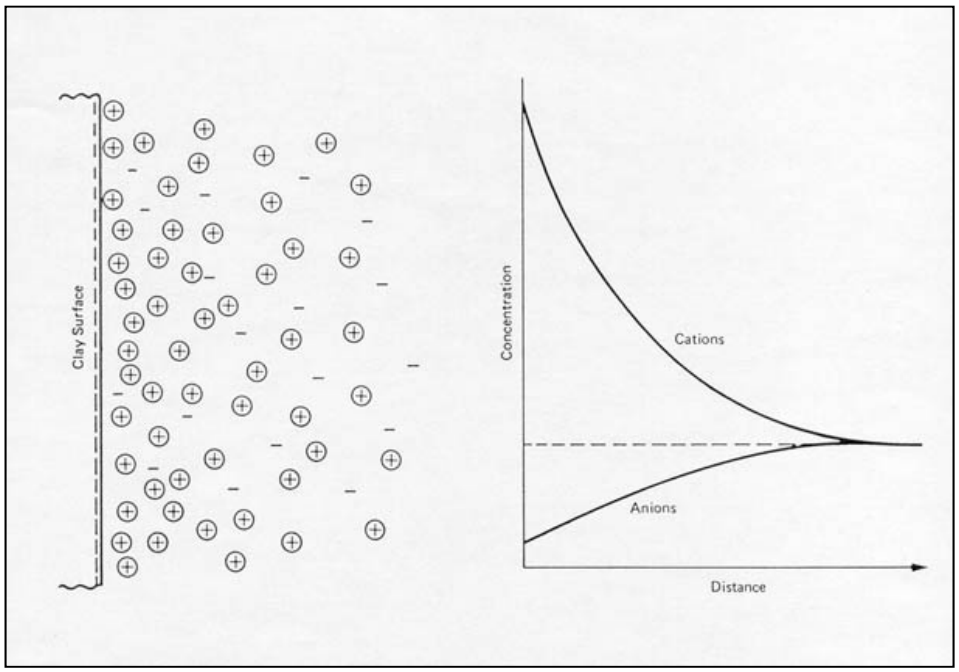

Figure 6.1: Showing the diffused double layer thickness of clay minerals and the variation of ion concentration with distance (Mitchell and Soga, 2005)

Figure 6.2 shown below presents the schematic of the double layer thickness between two clay particles. This thickness depends on the activity or surface charge density of the clay mineral particles.

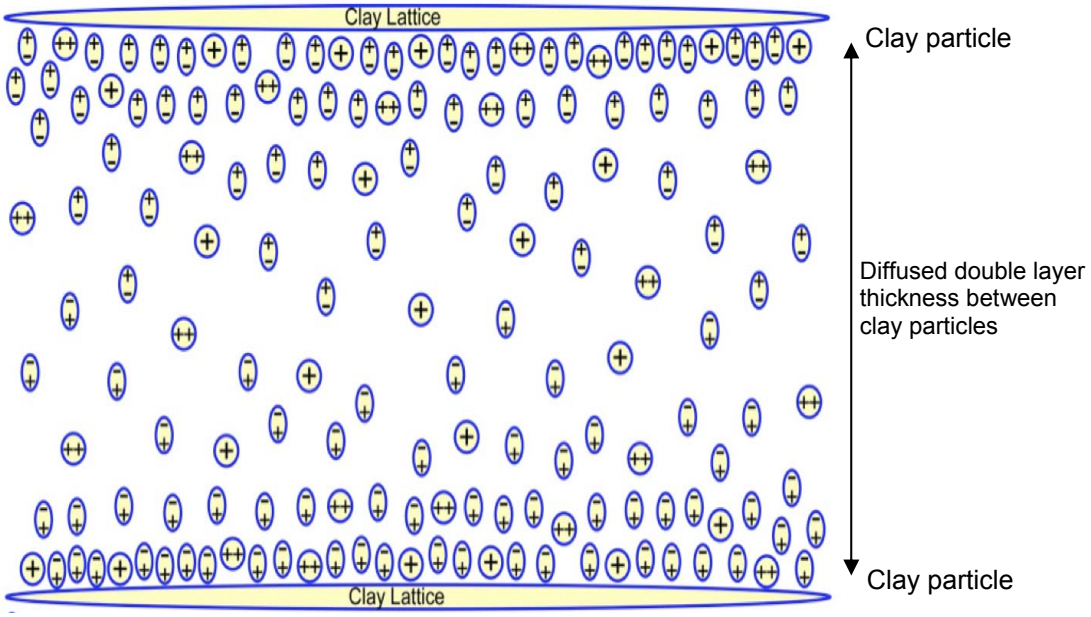

Figure 6.2: Schematic of the diffused double layer thickness between clay particles (Ref: www.agsssoilstabilization.com)

The assumptions used for the formulation of the Diffused Double Layer Swell Model (DDLSM) are discussed in the following:

6.2.1 Assumptions:

The following assumptions are made in order to study the effect of diffused double layer to swelling behavior of expansive clays:

1. All the particle plate like surfaces are aligned perpendicular to the direction of compaction. Figure 6.3 shows the particle arrangement perpendicular to the direction of static compaction force in a soil specimen.

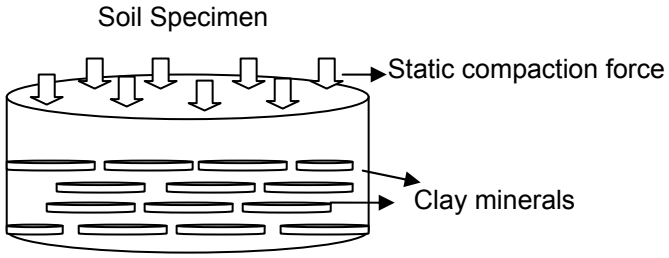

Figure 6.3: Assumed particle arrangement in the compacted soil specimen

2. All the particles in the soil mass are subjected to interact with water, no particle coagulation or overlapping of the surfaces is considered in the model. As shown in Figure 6.4 uniform stacking of all the clay particles is assumed in this model.

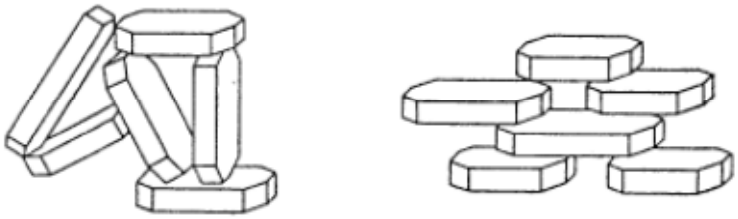

Figure 6.4: Coagulated and uniform arrangement of clay minerals (Ref: Lambe and Whitman, 1969)

3. Ions in double layer are point charges and are independent of self-interaction.
4. Surface charge of the individual particles is uniformly distributed over the area.
5. Swell behavior of the soil mass is independent of position of particles.
6. Only Montmorillonite, Illite and Kaolinite minerals' DDLs are considered in the analysis as this clay fraction is known as the dominant and stable phase in a soil that influence the clay behavior.

Diffused double layer for an individual particle could be calculated with the following Eq. 1 given by Mitchell and Soga (2005):

$$\frac{1}{K} = \left(\frac{\epsilon_0 \times D \times k \times T}{2 \times n_0 \times e^2 \times v^2}\right)^{\frac{1}{2}} \quad (1)$$

Where K is the diffused double layer induced swell thickness, ε_0 is the permittivity, D is dielectric constant, k is Boltzman constant, T is temperature, n_0 is electrolyte concentration (ions/m^3), e is electronic charge and v is cation valence. The average values for double layer thickness for the three clay minerals are calculated and presented in Table 6.1 along with their crystal thickness.

Table 6.1: Average crystal and diffused double layer thickness for clay minerals (Lambe and Whitman, 1969)

Clay mineral	Montmorillonite	Illite	Kaolinte
Average crystal thickness (Á)	10	30	1000
Average Diffused Double water layer thickness (Á)	400	75	700

From the above table it is evident that the Montmorillonite mineral having very small crystal size attracts or adsorbs higher amounts of water molecules, thereby affecting the total swell strains. Kaolinte mineral which had a very large crystal thickness attracts less amounts of water molecule density when compared to that of Montmorillonite. It is well known that the Montmorillonite mineral attracts more double layer water density than any other mineral due to larger surface area.

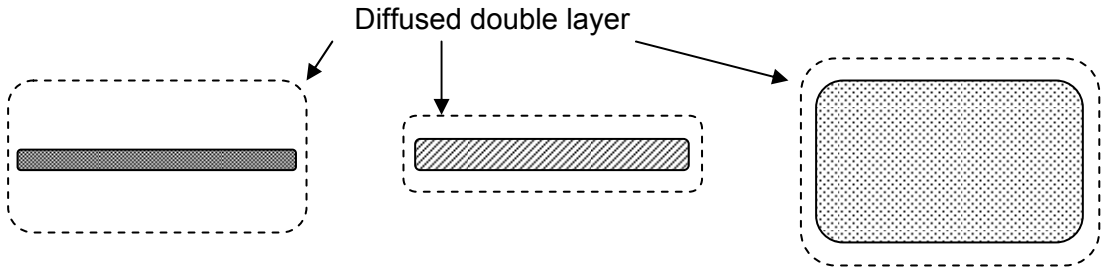

(a) Montmorillonite (b) Illite (c) Kaolinite

Figure 6.5: Comparison of diffused double layers of different clay mineral crystals

6.2.2 DDLS Model Formulation:

The model is based on the double layer water attraction capacity of individual clay minerals. As discussed above, upon contact with moisture, the clay minerals in soils undergo

expansion with increase in their double layer water thickness. Hence the clay minerals are assumed to be stacked in a uniform chain pattern.

The 1-D swell strains and swell pressures were performed on a conventional specimen having size of 2.54 cm (1 in) height and 6.3 cm (2.5 in) diameter. Hence the same specimen dimensions are used in the current model. The compacted soil specimen comprises of soil solids and voids. Among the soil solids the clay portions contribute to the swelling behavior. The determination of volume of clay minerals in a soil specimen was determined by dividing the clay portion as shown in Figure 6.6.

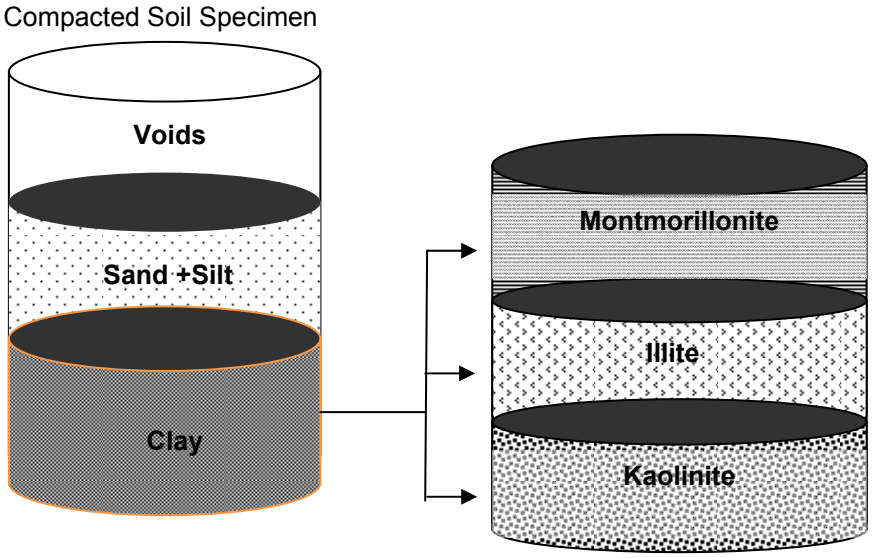

Figure 6.6: Identification of mineral volume in a compacted soil specimen

From mineralogy the fraction of minerals present in the clay portion of expansive clay have been determined and presented in Chapter 3. Determination of volume of clay fraction (V_c) can be achieved with the following Equations. 2, 3, 4 and 5.

$$V = \gamma_d \times w_s \tag{2}$$

$$V_s = \frac{V}{1+e} \tag{3}$$

$$V_s = V_{sand} + V_{silt} + V_{clay} \tag{4}$$

$$V_{clay} = CF * V_s \tag{5}$$

Where V is the total volume of soil solids, V_s is the volume occupied by solid particles, e is void ratio, V_{sand} is the volume of sand particles, V_{silt} is the volume of silt particles, V_{clay} is the volume of clay particles, CF is the clay fraction (obtained from gradation curve of soils). All the volumes are calculated based on a conventional consolidation specimen of 2.54 cm (1 in) height and 6.3 cm (2.5 in) diameter.

Table 6.2 below presents the determination of volume of clay fraction present in a compacted clay specimen.

Table 6.2: Volume of clay fraction at two dry density conditions

Soil	% Clay	95% MDD condition		MDD condition	
		Solids (g)	Vol. of clay, V_{clay} (m^3)	Solids (g)	Vol. of clay, V_{clay} (m^3)
Anthem	32	130	$2.51x10^{-5}$	137	$2.54x10^{-5}$
Burleson	52	124	$4.10x10^{-5}$	130	$4.13x10^{-5}$
Colorado	46	125	$3.65x10^{-5}$	132	$3.68x10^{-5}$
Grayson	55	110	$4.32x10^{-5}$	116	$4.37x10^{-5}$
Keller	34	143	$2.70x10^{-5}$	151	$2.71x10^{-5}$
Oklahoma	30	121	$2.36x10^{-5}$	127	$2.39x10^{-5}$
San Antonio	52	122	$4.12x10^{-5}$	129	$4.17x10^{-5}$
San Diego	23	131	$1.80x10^{-5}$	139	$1.83x10^{-5}$

Grayson soil contained the highest clay fraction volume at both density conditions, whereas San Diego soil has the lowest clay fraction volume.

The minerals present in the clay volume are pre-determined and the fractions occupied by each individual mineral are presented in Chapter 3. From the total volume of clay fraction present in the soil specimen, the volume of individual minerals can be calculated from the clay fractions. Since the surface area is constant in the swelling process (1 D swell and Swell pressure), the height is the variable parameter that vary and will influence the volume changes

of clay minerals. Figure 6.7 presents the volume occupied by individual clay minerals and their height of stacking arrangement within their volume.

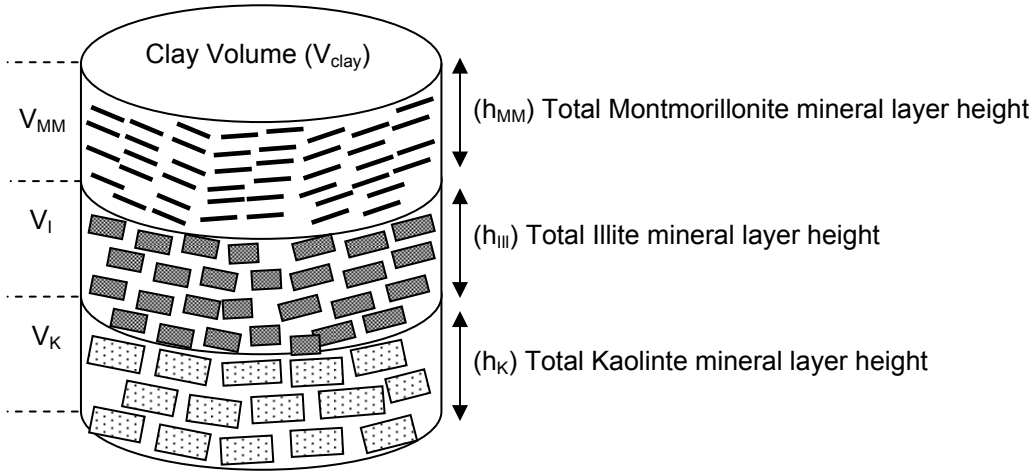

Figure 6.7: Stacking of individual clay minerals in their respective volumes

The individual heights of the clay mineral layers could be determined from Equations. 6 and 7:

$$V_{MM} = V_{clay} * MMF \tag{6}$$

$$h_{MM} = \frac{V_{MM}}{A} \tag{7}$$

Where V_{MM} is the volume of mineral Montmorillonite, MMF is the mineral Montmorillonite fraction in the clay fraction, h_{MM} is the total height of stacked mineral Montmorillonite layers within the soil specimen and A is the total cross-sectional area of the soil specimen (remains constant during the 1-D swell and swell pressure tests). Since Montmorillonite has the least crystal thickness, the particle density in the Montmorillonite clay fraction is very high when compared to Illite and Kaolinite fraction. All the mineral layers are stacked perpendicular to the direction of compaction and moisture induced soil swelling.

Table 6.3 below presents the height of individual mineral layers present in the compacted soil specimen.

Table 6.3: Calculated heights of individual crystal layers at different compaction dry densities

Soil	95% MDD condition			MDD condition		
	h_{MM} (m)	h_{ill} (m)	h_K (m)	h_{MM} (m)	h_{ill} (m)	h_K (m)
Anthem	$1.94x10^{-03}$	$1.88x10^{-03}$	$3.86x10^{-03}$	$2.04x10^{-03}$	$1.97x10^{-03}$	$4.05x10^{-03}$
Burleson	$4.21x10^{-03}$	$2.45x10^{-03}$	$5.82x10^{-03}$	$4.42x10^{-03}$	$2.57x10^{-03}$	$6.10x10^{-03}$
Colorado	$3.94x10^{-03}$	$3.86x10^{-03}$	$3.22x10^{-03}$	$4.16x10^{-03}$	$4.07x10^{-03}$	$3.41x10^{-03}$
Grayson	$5.67x10^{-03}$	$3.13x10^{-03}$	$4.39x10^{-03}$	$5.95x10^{-03}$	$3.28x10^{-03}$	$4.61x10^{-03}$
Keller	$1.80x10^{-03}$	$1.49x10^{-03}$	$4.87x10^{-03}$	$1.89x10^{-03}$	$1.57x10^{-03}$	$5.13x10^{-03}$
Oklahoma	$1.42x10^{-03}$	$5.04x10^{-03}$	$7.42x10^{-03}$	$1.49x10^{-03}$	$5.29x10^{-03}$	$7.79x10^{-03}$
San Antonio	$4.73x10^{-03}$	$3.86x10^{-03}$	$3.89x10^{-03}$	$5.00x10^{-03}$	$4.08x10^{-03}$	$4.12x10^{-03}$
San Diego	$1.48x10^{-03}$	$1.40x10^{-03}$	$2.64x10^{-03}$	$1.57x10^{-03}$	$1.47x10^{-03}$	$2.78x10^{-03}$

Where h_{MM} – total height of Montmorillonite layer, h_{ill} – total height of Illite layer and h_K – total height of Kaolinite layer

Grayson soil showed the highest Montmorillonite mineral layer thickness at both compaction dry density conditions. Large fractions of Illite and Kaolinte mineral layers were also observed in Oklahoma soil at both the density conditions. Once the layer height is calculated, the number of crystal stacks present in the layer height was calculated using the following Eq. 8.

$$N = \frac{h_i}{t_i} \tag{8}$$

Where N is the number of each mineral layers stacked in the total mineral volume, h_i is the total individual mineral layer height and t_i is the average mineral crystal thickness (Table 6.1). Once the number of mineral layer stacks for all three clay minerals are determined, the total diffused double layer thickness or expansion or swell displacement for a given expansive soil is given by Eq. 9

$$TDDLT = \sum_{i=1}^{n} N_i \times DDLT_i \tag{9}$$

Where TDDLT is the total diffused double layer induced swell thickness or displacement, n is the number of clay minerals (i.e. 3) in the soil, N_i is the number of crystal layers pertaining to individual mineral, $DDLT_i$ is the diffused double layer thickness of an individual mineral.

Figures 6.8 and 6.9 present the total double layer induced swell thickness determined for each individual mineral at 95%MDD and MDD conditions respectively.

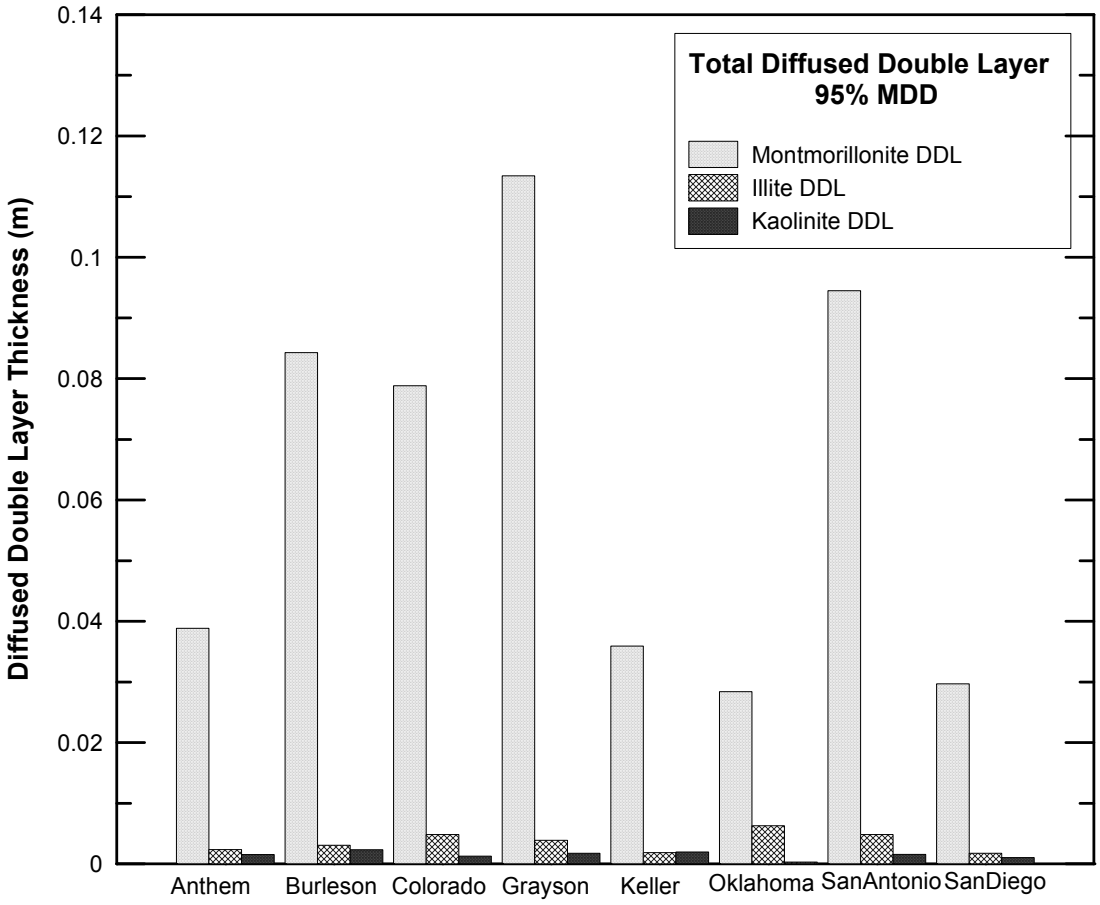

Figure 6.8: Showing the total diffused double layer thickness of individual minerals at 95% MDD

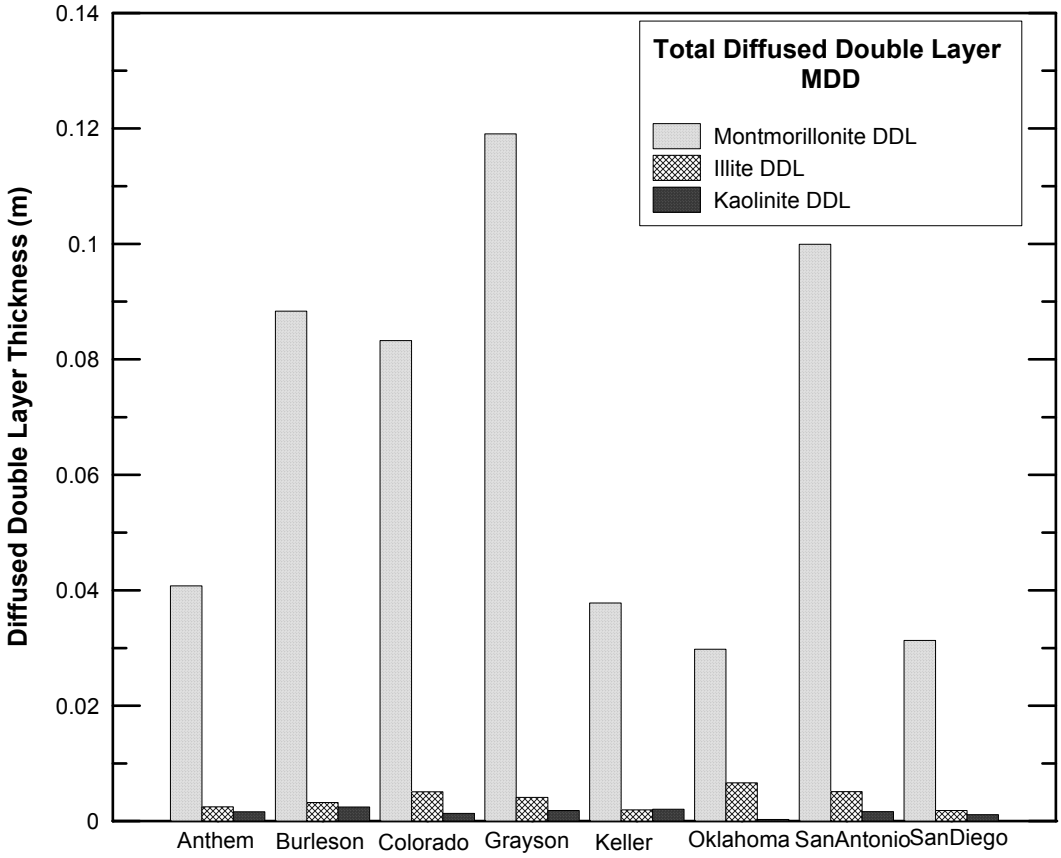

Figure 6.9: Showing the total diffused double layer thickness of individual minerals at MDD

Kaolinte mineral, due to the low surface charge and mineral density did not form or contribute to the total diffused double water layer. Hence, it was concluded that the major mineral contributing to the swelling behavior of expansive clay is Montmorillonite. Due to the high surface area and double layer water attraction, mineral Montmorillonite has the largest diffused double layer induced swell thickness compared to other clay minerals. Grayson soil, due to its high clay fraction and Montmorillonite content, exhibited the highest diffused double layer water thickness of 0.12 m at MDD condition. Double layer water thickness and related strains for the soil specimens are then determined using the following Eq. 10.

$$\in_{DDL} (\%) = \frac{TDDLT}{h} \times 100 \qquad (10)$$

Where ϵ_{DDL} is the strain caused by the formation of diffused double layer, TDDLT is the total diffused double layer induced swell displacement calculated for the specimen, h is the

initial specimen height. Table 6.4 shows the total double layer induced swell calculated for all the eight expansive clays at two different density conditions.

Table 6.4: Swell strain estimated from double layer induced swell displacement

Soil	95% MDD condition			MDD condition		
	h (m)	TDDLT (m)	ε_{DDL} (%)	h (m)	TDDLT (m)	ε_{DDL} (%)
Anthem	0.0254	0.0427	168.14	0.0254	0.0449	176.56
Burleson	0.0254	0.0896	352.91	0.0254	0.0940	369.99
Colorado	0.0254	0.0849	334.34	0.0254	0.0897	353.06
Grayson	0.0254	0.1190	468.76	0.0254	0.1250	492.10
Keller	0.0254	0.0397	156.34	0.0254	0.0418	164.62
Oklahoma	0.0254	0.0349	137.72	0.0254	0.0367	144.55
San Antonio	0.0254	0.1008	397.10	0.0254	0.1067	419.88
San Diego	0.0254	0.0324	127.83	0.0254	0.0343	134.85

Table shown above presents the total double layer water induced strain by each of the soil specimens. The compacted soil specimen has an initial height of 0.0254 m (1 in). During the saturation phase of the specimen, the minerals attract the moisture molecules and form a diffused Double water layer. The specimen strains are calculated based on the initial specimen height and the total double layer formed due to the mineral attraction forces between clay mineral and water molecules. It was evident that Grayson soil formed the largest double layer water thickness at both dry density conditions. Figures 6.10 and 6.11 present the variation of calculated diffused double layer swell strains with clay fraction and percent mineral Montmorillonite in the soils compacted at 95% MDD condition. Similarly, Figures 6.12 and 6.13 presents the variation of swell strains with clay fraction and mineral Montmorillonite fraction in the compacted soil at MDD condition.

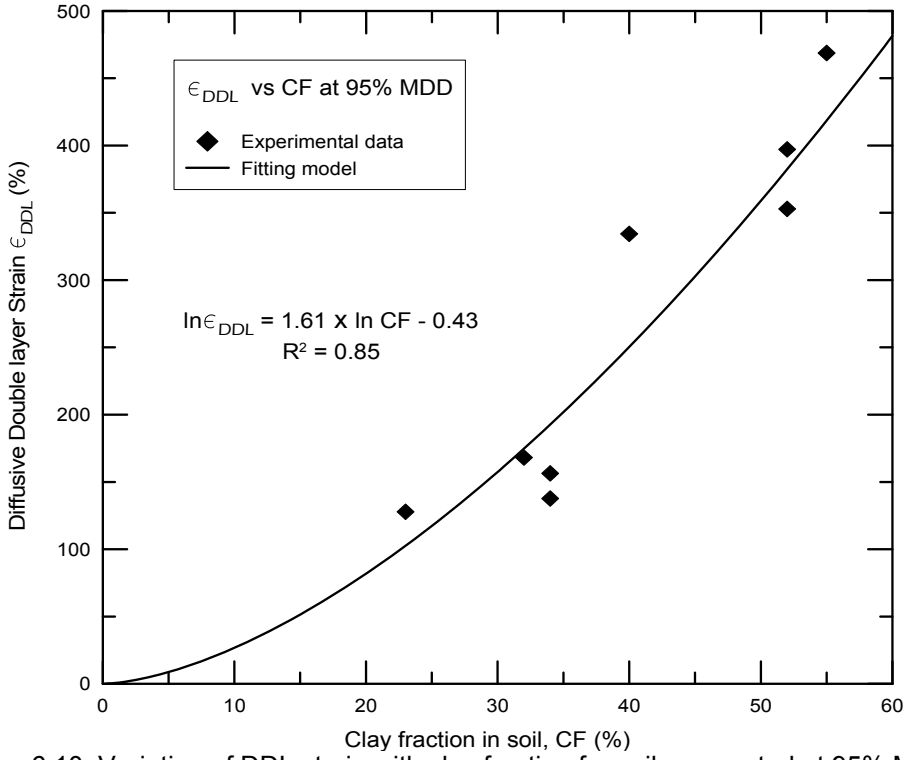

Figure 6.10: Variation of DDL strain with clay fraction for soil compacted at 95% MDD

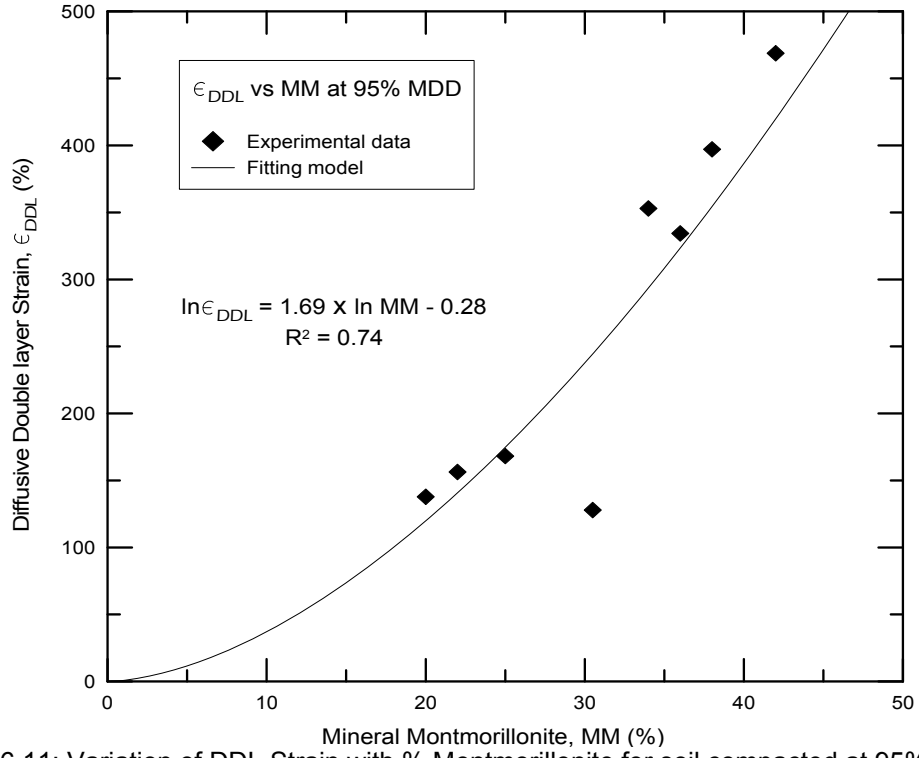

Figure 6.11: Variation of DDL Strain with % Montmorillonite for soil compacted at 95% MDD

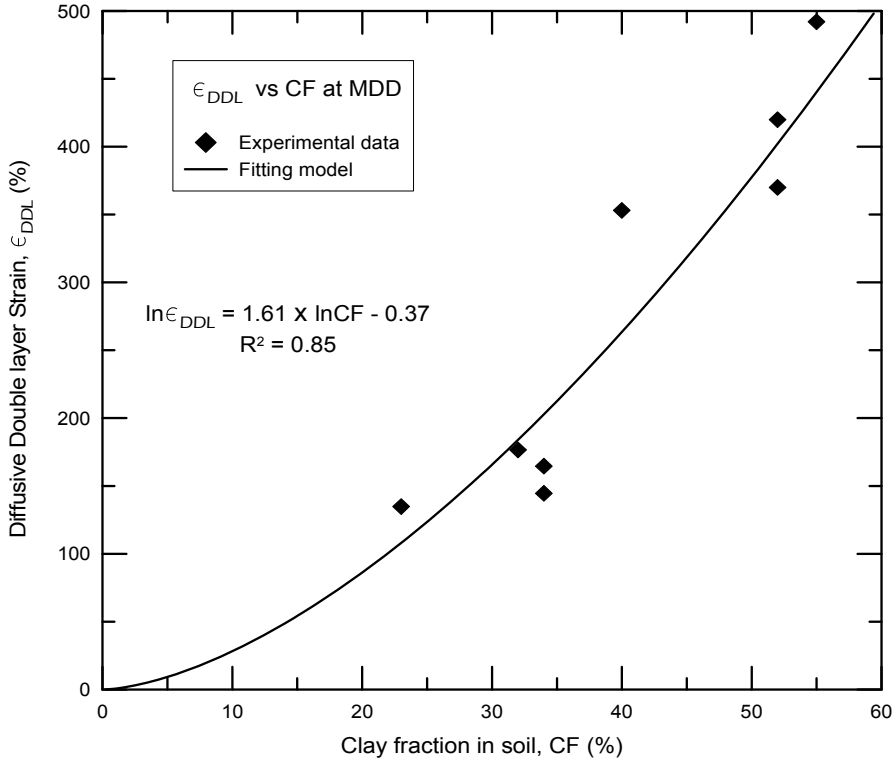

Figure 6.12: Variation of DDL strain with clay fraction for soil compacted at MDD

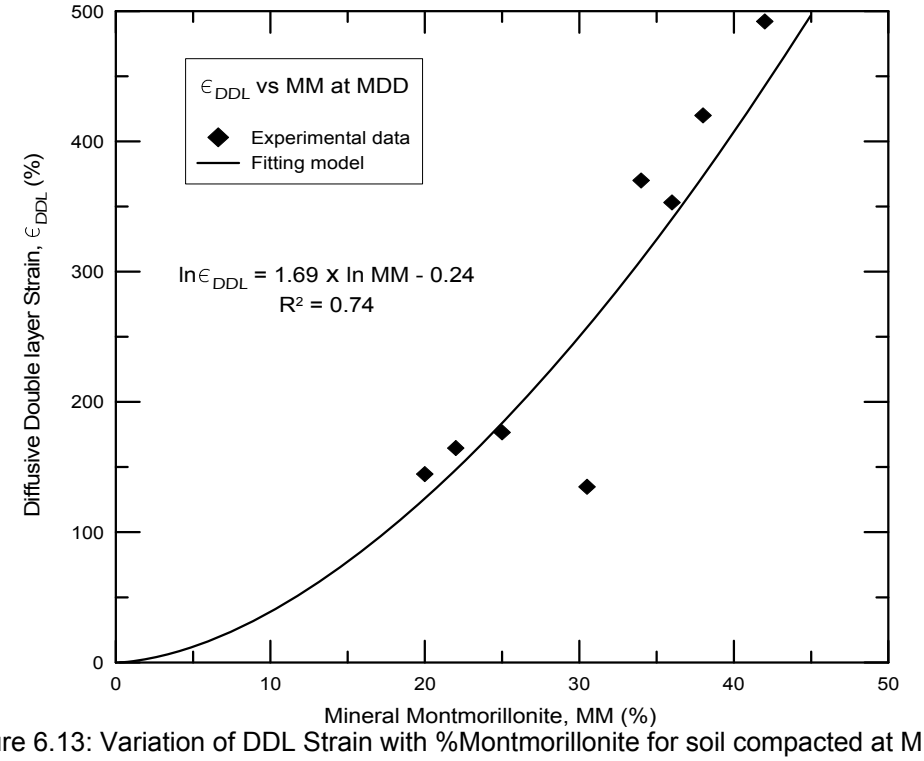

Figure 6.13: Variation of DDL Strain with %Montmorillonite for soil compacted at MDD

The best fit model equation for the experimental data and the coefficient of determination (R^2) values are presented in the above charts. From the above data and figures, it is well understood that the presence of large fraction of clay and in particular Montmorillonite mineral in a soil mass leads to large amount of soil swelling. Also, it can be concluded that strains from the diffused double layer are mainly influenced by the mineral Montmorillonite present in the clay fraction. Calculated strains from the DDLS model are plotted against the actual swell behavior for all eight soils and the relationships are studied in the following sections:

Table 6.5 presents the prediction models for the diffused double layer strain for expansive clay using clay fraction (CF) and Montmorillonite fraction (MM).

Table 6.5: Prediction models of $\in_{DDL}$ from Clay and Montmorillonite contents

Prediction of $\in_{DDL}$	95% MDD condition	MDD condition
Clay Fraction (CF)	$ln(\in_{DDL}) = 1.61 \times CF - 0.428$ $R^2 = 0.85$	$ln(\in_{DDL}) = 1.61 \times CF - 0.371$ $R^2 = 0.85$
Mineral Montmorillonite fraction (MM)	$ln(\in_{DDL}) = 1.69 \times MM - 0.277$ $R^2 = 0.74$	$ln(\in_{DDL}) = 1.61 \times MM - 0.238$ $R^2 = 0.74$

From the above prediction models and analysis, it can be concluded that the models based on clay fraction have a higher coefficient of determination than the ones based on Montmorillonite fraction. Similar pattern is detected at different compaction dry density condition.

6.2.3 DDLS Model - 1 D Swell strain

Figure 6.14 shown below presents the variation of diffused double layer strains with the measured swell strains at 95% MDD condition. The best fit model had a coefficient of determination (R^2) value of 0.79.

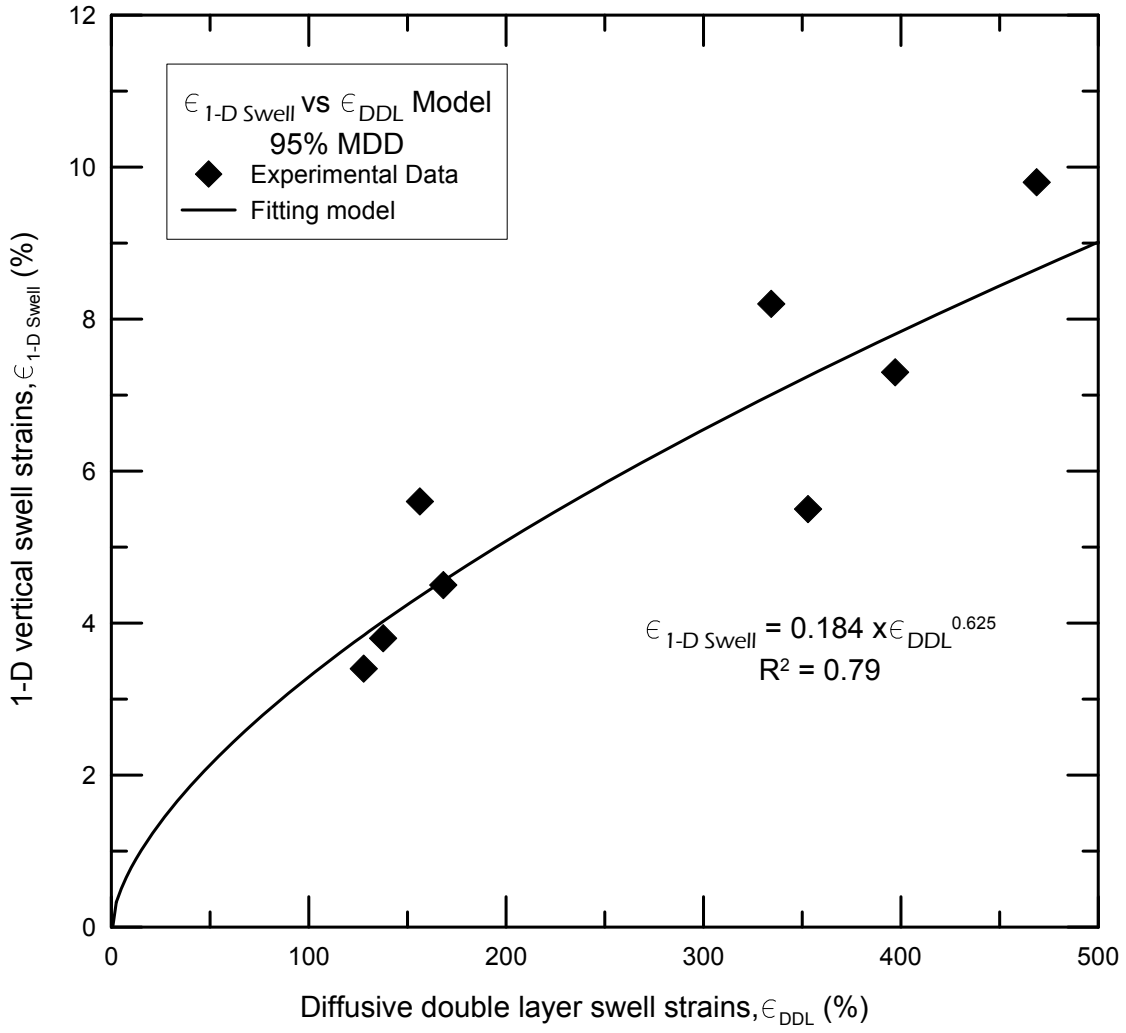

Figure 6.14: DDLS Model for 1 D Swell Strains at 95% MDD condition

Figure 6.15 also presents the variation of diffused double layer strains with the measured swell strains at MDD condition. The best fit model had a coefficient of determination (R^2) value of 0.84.

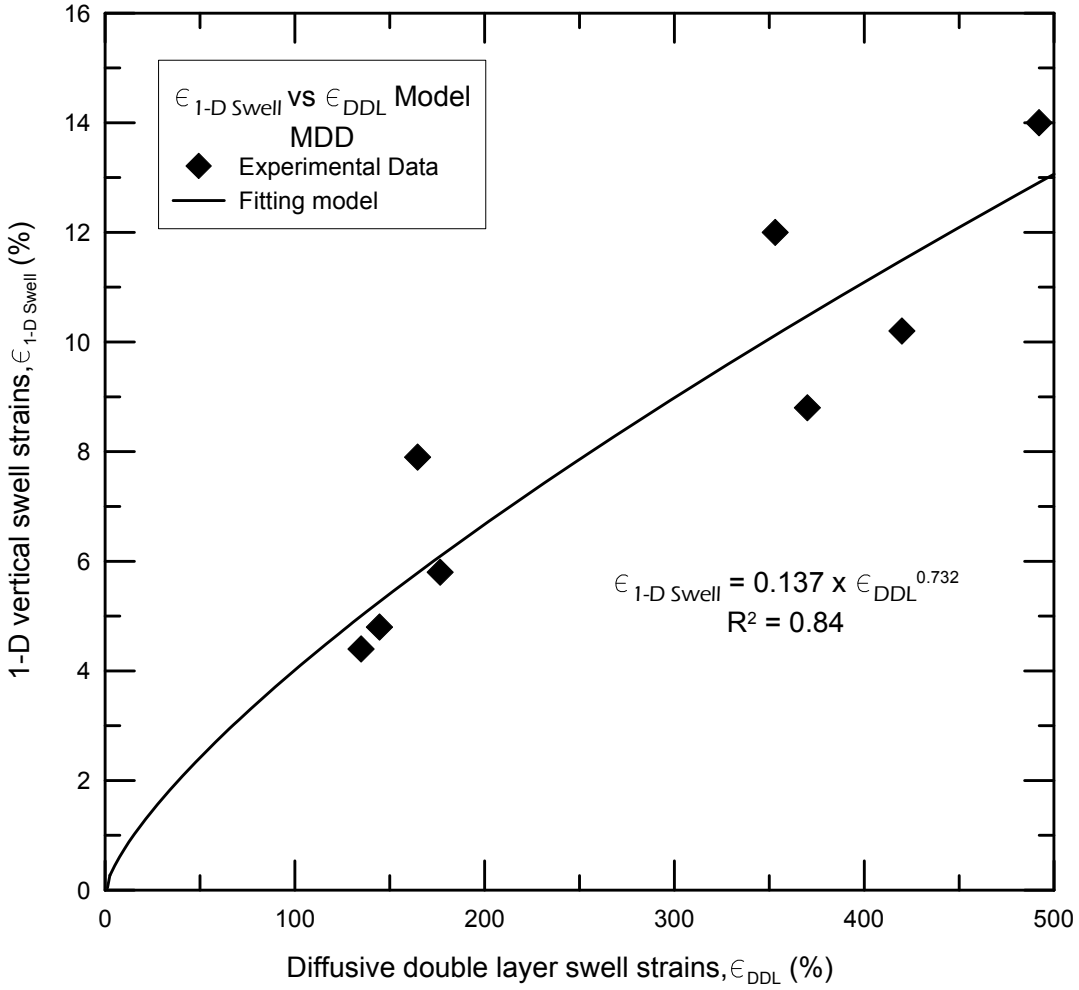

Figure 6.15: DDLS model for 1 D Swell Strains at MDD condition

6.2.4 DDLS Model - Swell Pressure

Figure 6.16 presents the variation of calculated diffused double layer swell strains from minerals with measured swell pressure at 95% MDD condition. The best fit model in this figure had a coefficient of determination (R^2) value of 0.82.

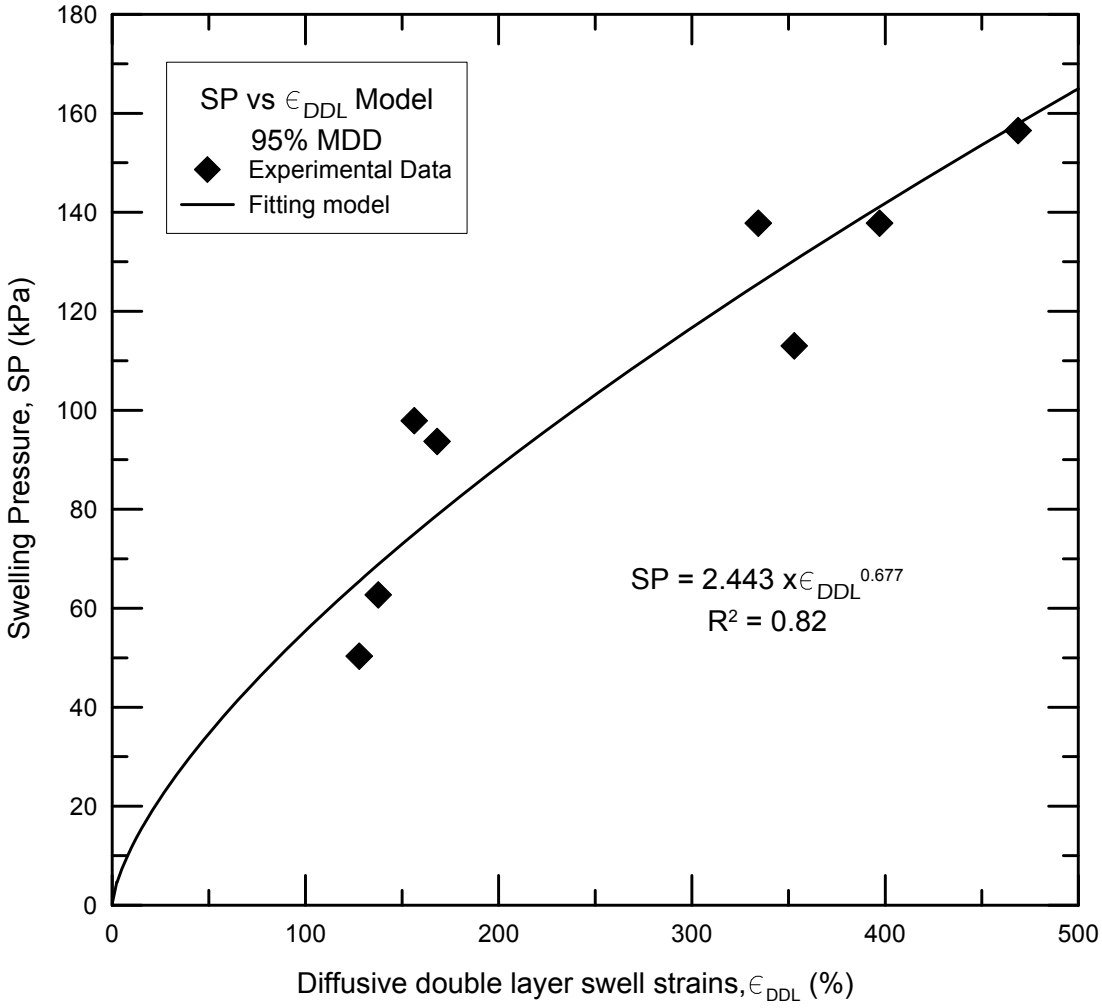

Figure 6.16: DDLS model Predictions and Correlations with Swell Pressure at 95% MDD condition

Figure 6.17 below presents the variation of calculated diffused double layer swell strains from minerals with measured swell pressure at 95% MDD condition. The best fit model had a coefficient of determination (R^2) value of 0.88.

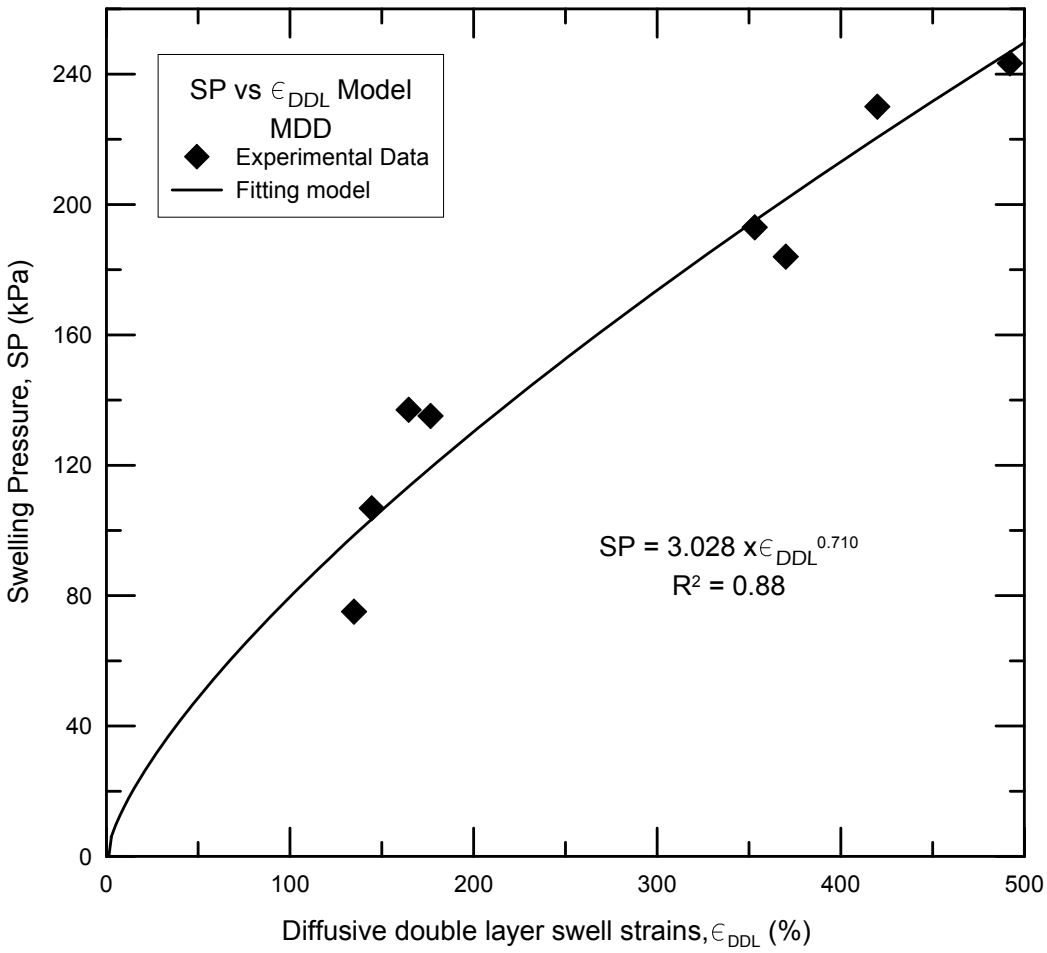

Figure 6.17: DDLS model for Swell Pressure at MDD condition

The coefficient of determination for the DDLS based models increased with an increase in compaction dry density of soil. This clearly states that an increase in dry density resulted in an optimum packing condition in the soil specimen where the minerals in such packing conditions are closely aligned as per the assumptions used in this modeling analysis. Overall, DDLS model predictions and comparisons with swell pressures should be treated as an indirect exercise to develop swell pressure predictions.

6.2.5 DDLS Model - Volumetric Swell Strain

Swell strains under confinements for all the eight soils were measured using a novel 3-D swell strain apparatus as discussed in Chapter 4. All the specimens were compacted at 95% MDD for this study. The dimensions of the specimens were 0.1 m (4 in) in height and 0.05 m (2 in) diameter. Hence soil volumes corresponding to these dimensions were utilized in measuring the double layer water thickness. Figure 6.18 shown below presents the variation of calculated diffused double layer swell strains from minerals with measured volumetric swell strain at 7 kPa confinement level.

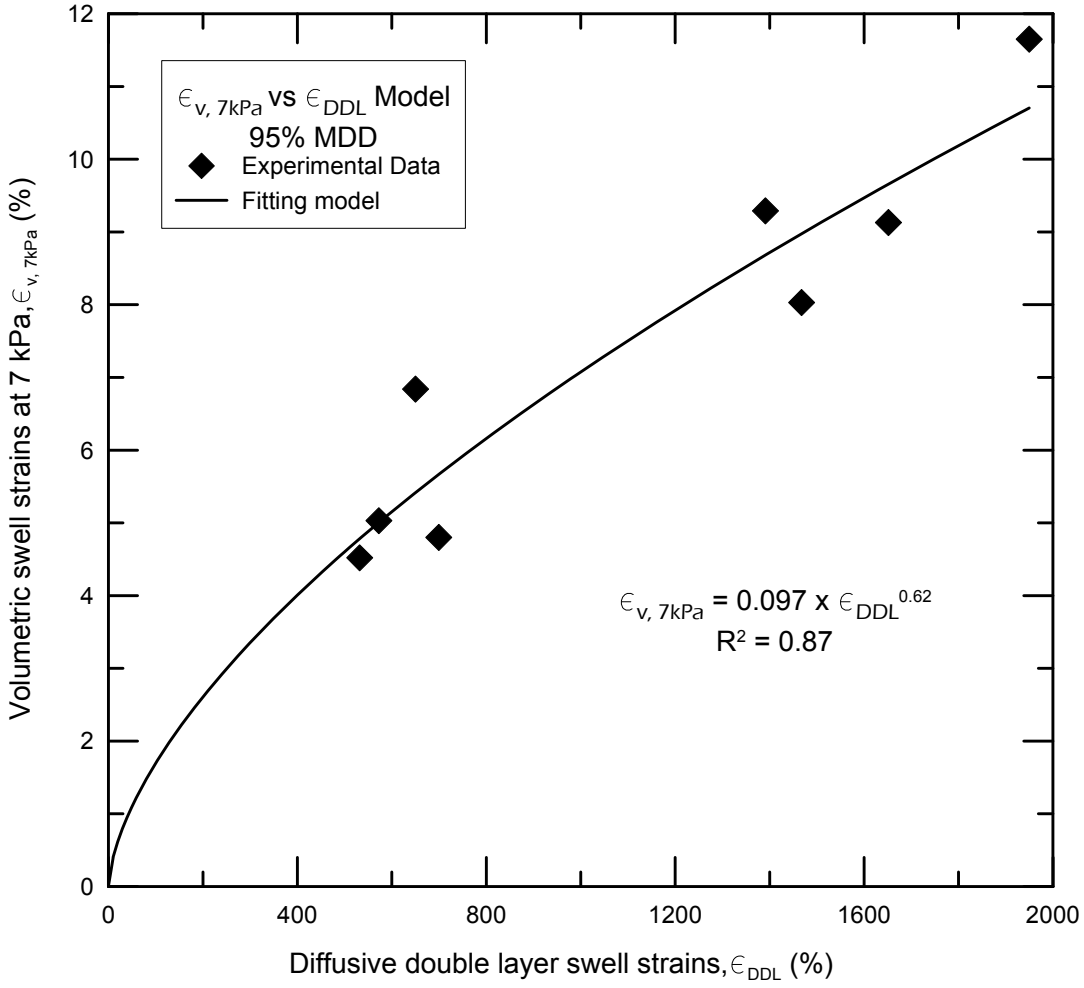

Figure 6.18: DDLS Model for the volumetric swell strains at 7kPa confinement

The swell strains measured from diffused double layer are very high when compared to conventional consolidation specimens. The reason for this was being the presence of more mineral crystals in the solids. The best fit model for 7 kPa confinement had a coefficient of determination (R^2) value of 0.87.

Figure 6.19 below presents the variation of calculated diffused double layer swell strains from minerals with measured volumetric swell strain at 50 kPa confinement level.

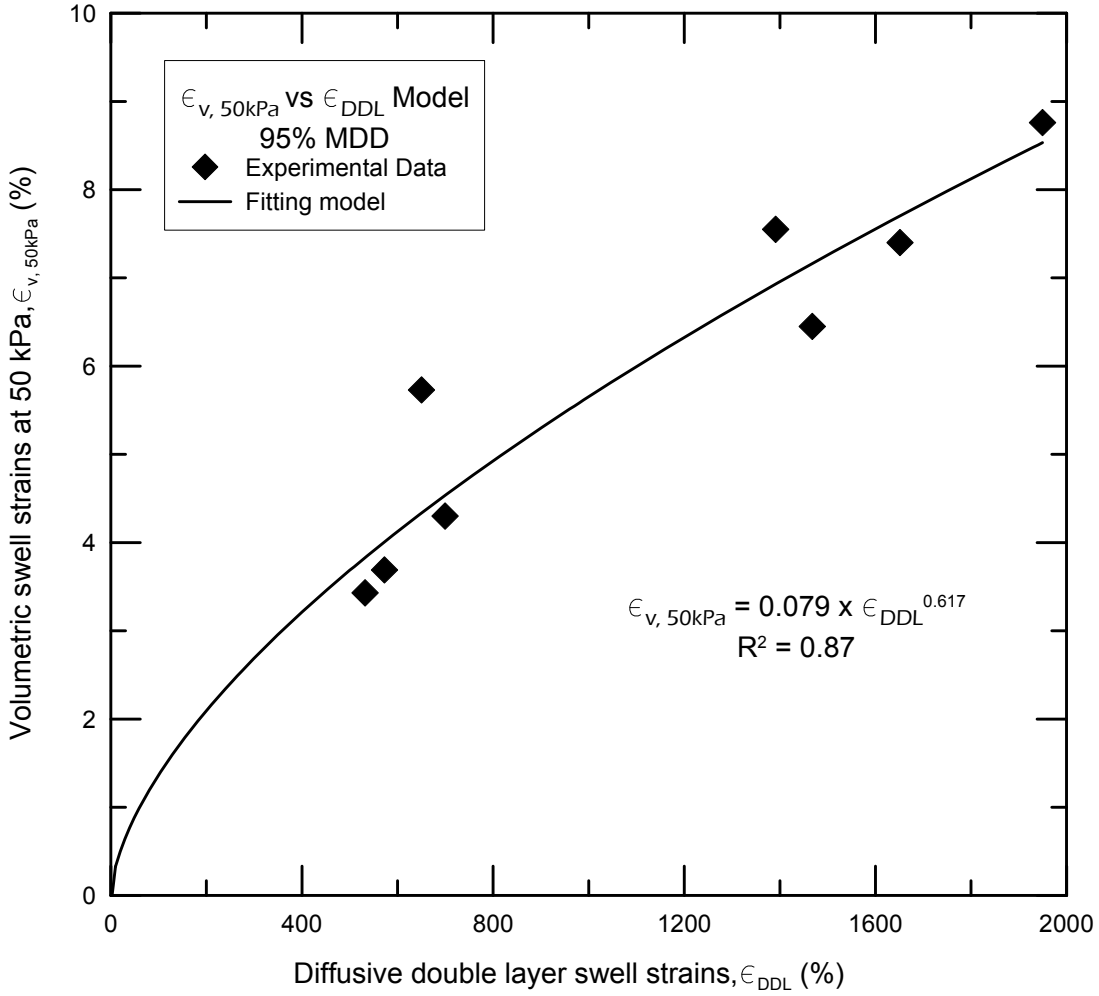

Figure 6.19: DDLS Model for the volumetric swell strains at 50kPa confinement

With increase in confinement levels, as expected, the swell strains decreased. The best fit model had a coefficient of determination (R^2) value of 0.87. Similarly, Figure 6.20 below

presents the variation of calculated diffused double layer swell strains from minerals with measured volumetric swell strain at 100 kPa confinement level.

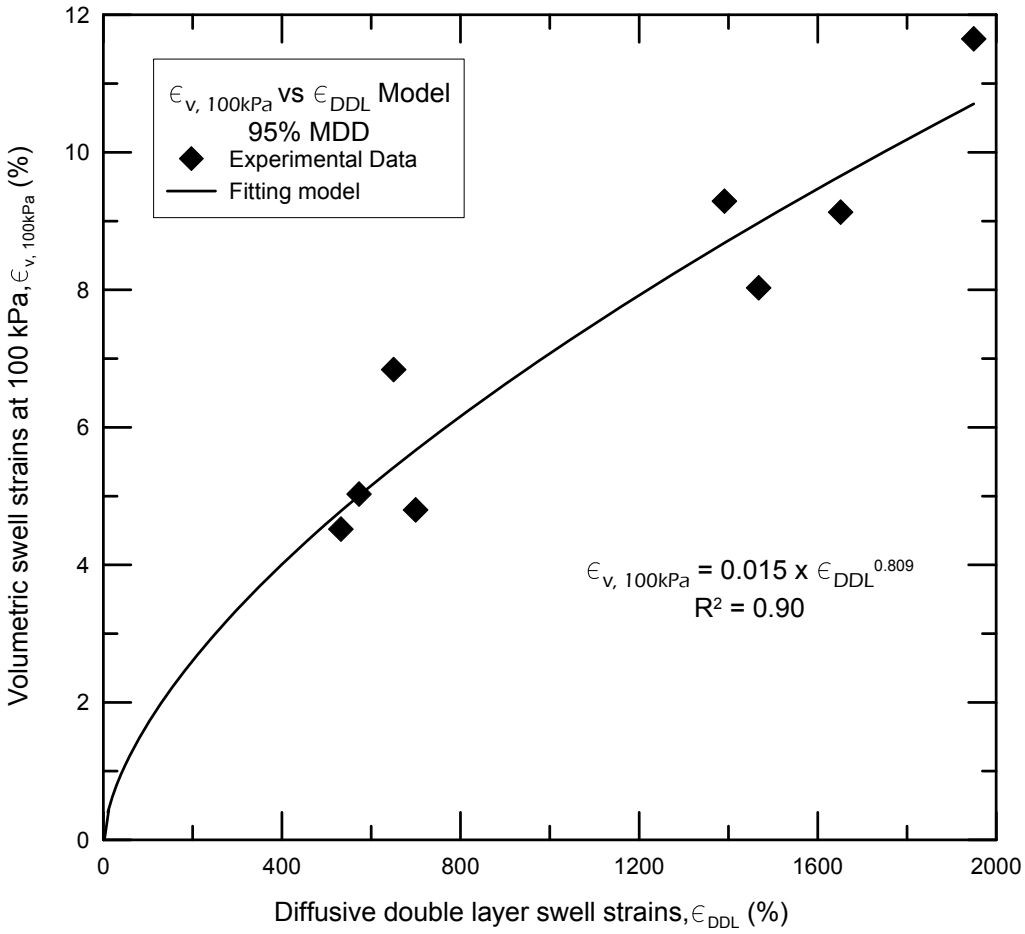

Figure 6.20: DDLS Model for the volumetric swell strains at 100kPa confinement

The best fit model had a coefficient of determination (R^2) value of 0.90.

All the specimens showed very large strains when compared to the measured swell strains. This could be due to the assumption that all the particles were aligned perpendicular to the direction of compaction and swelling. In the actual case, particle arrangements would be random and folcculated with considerable overlap. The swell strain, which is a function of mineral type and content, would be a direct measure for the actual swelling behavior.

6.2.6 Correction factors

The diffused double layers of a clay soil directly influence the true swelling behavior, but from the results presented here, it is observed that the true swelling behavior of a soil is low compared to diffused double layer induced swell strains. Main reason for this variation is attributed to the unrealistic yet analytically needed assumptions used in this modeling analysis. Hence, certain correction factors are needed to be introduced that will account for the following assumptions considered in this model.

1. Assumed mineral packing arrangement is an ideal case, most of the soils in the field have a flocculated and random arrangement of mineral particles.
2. The present model considers all the mineral crystals to come in full contact with water medium, the complete moisture access surrounding each clay mineral is not possible in real conditions where particle flocculation and pore distribution affects the moisture intake by the clay.

The following formulation was used to determine the correction factors, a and b and these are already depicted in the previous graphs:

$$\epsilon_i \ or \ SP = a \times {\epsilon_{DDL}}^b \tag{11}$$

Where ε_i is the swell strain measured at different initial compaction conditions, SP is the swell pressure of an expansive clay, ε_{DDL} is the diffused double layer induced swell strain and a, b are the correction factors.

Correction factors ‘a’ and ‘b’ are dependent on many independent soil and test parameters like particle arrangement during compaction, moisture access to the clay particles and direction of particle swelling. ‘a’ and ‘b’ are not unique and they are dependent on the swell property that is correlated with ε_{DDL}.

Table 6.6 Table 6.7 present the DDLS models with correction factors for 1-D swell strain and swell pressures and 3-D volumetric swell strains for soils compacted at 95% MDD and MDD conditions.

Table 6.6: Summary of correlations between ε_{DDL} and corresponding $\varepsilon_{1\text{-D swell}}$ and SP for soil specimens compacted at 95% MDD

DDLS Models	95% MDD	R^2	MDD	R^2
1-D Swell Strain (%)	$\epsilon_{1-\text{D Swell}} = 0.184\ \epsilon_{DDL}{}^{0.625}$ $\text{MSE} = 0.033$	0.79	$\epsilon_{1-\text{D Swell}} = 0.137\ \epsilon_{DDL}{}^{0.732}$ $\text{MSE} = 0.034$	0.84
Swell Pressure (kPa)	$\text{SP} = 2.443\ \epsilon_{DDL}{}^{0.677}$ $\text{MSE} = 34$	0.82	$\text{SP} = 3.028\ \epsilon_{DDL}{}^{0.71}$ $\text{MSE} = 22$	0.88

Where DDLSS is the diffused double layer swell, MSE = Mean Square Error

Table 6.7: Summary of correlations between ε_{DDL} and volumetric swell strain (ε_v) at different confinements for specimens compacted at 95% MDD

	Confinement pressure	DDLS Model	R^2
Volumetric swell strains, ε_v (%)	7 kPa	$\epsilon_{\text{v, 7kPa}} = 0.097\ \epsilon_{\text{DDL}}{}^{0.62}$ $\text{MSE} = 0.033$	0.87
	50 kPa	$\epsilon_{\text{v, 50kPa}} = 0.079\ \epsilon_{DDL}{}^{0.617}$ $\text{MSE} = 0.020$	0.87
	100 kPa	$\epsilon_{\text{v, 100kPa}} = 0.015\ \epsilon_{DDL}{}^{0.809}$ $\text{MSE} = 0.018$	0.90

Where DDLSS is the diffused double layer swell, MSE = Mean Square Error

The DDLS models showed good coefficient of determination values when fitted against the actual experimental swell test properties. From Table 6.6, ‘a’ and ‘b’ parameters represent a composite parameter that accounts for all tested soils. The model parameters show that both ‘a’ and ‘b’ correction parameters increased from 95% MDD to MDD for both 1 D swell strain and swell pressure models. Though exact variability with respect to compaction and moisture access are difficult to single out from these parameters; nevertheless these constants represent the variability due to the assumptions used in this modeling analysis. However, It is interesting

to mention that ‘a’ parameter is appear to be main controlling factor that affects the behavior of ε_{DDL} to ε_v or $\varepsilon_{1\text{-}D\ swell}$. In some cases ‘b’ parameter appears to have similar influence. Individual soil based analysis is not included here due to limited number of tests performed for each soil type.

6.3 Model 2: Mechanical Hydro Chemical (MHC) Model

Soil matric suction plays an important role in the swelling behavior of a soil. Fredlund and Morgenstern (1976) studied the volume change constitutive relationships for expansive soils from a semi-empirical model based on matric suction of the compacted clays. Many researchers including Alonso et al. (1999, 2005), Saiyouri et al. (2004), Yusuf and Erol (2007) and Agus et al. (2010) attempted to study the variation of soil matric suction parameters with soil swelling behavior patterns. However, the clay mineralogy of the soil is not often taken into consideration for these swell prediction models. Hence, a new model incorporating mechanical-hydro-chemical modeling with the inclusion of clay mineralogy content is attempted in this research.

The initial matric suction, air-entry suction, slope of soil suction-void ratio, mineral content and the percentage Montmorillonite are taken into consideration.

6.3.1 Assumptions:

For the ‘Mechanical Hydro Chemical’ Model (MHC) modeling formulation, the following assumptions are considered:

1. Montmorillonite mineral contributes to a major portion of the soil swelling behavior. Illite and Kaolinite minerals are assumed to be dormant or inactive with respect to soil swelling.
2. The variation of compaction moisture content to soil matric suction in the ‘e-s-w’ graph is assumed to be linear.

3. The SWCC of the expansive clay is assumed to be a major factor in governing the soil swelling behavior. Other parameters such as grain size distribution and pore size distributions are not explicitly considered in this modeling analysis. They are however accounted for implicitly in the analysis as void ratio changes during soil swelling are dependent on pore distribution.
4. The drying curve and the wetting curve of the SWCC are considered to be the same; hysteresis effects on the SWCC are neglected.
5. The current model considers only the matric suction of expansive clay; osmotic suction effects are not considered,

The individual variation of compaction void ratio with varying moisture contents during swell testing and soil matric suction with the same moisture contents are studied and based on the measured data, a cumulative plot is formulated. This plot is termed as void ratio-gravimetric moisture content-matric suction plot (e-w-log ψ plot). The e-w-log ψ plot is unique for a given soil type as swell governing factors like soil matric suction and void ratio are the basis for this particular plot. The e-w-log ψ plots for all the eight expansive clays studied in the present research are presented in the following. The variation of soil matric suction with compaction moisture content is assumed to be linear for the current modeling analysis.

6.3.2 Chemical factor (C) affecting swelling behavior:

Swelling behavior of compacted clay is often affected by the type and amount of clay mineral present in the clay fraction. In the current model a swell factor (SF) is introduced for each of the dominant three mineral types present in the clay fraction. Montmorillonite mineral being the dominant swelling clay mineral and has the highest diffused double layer capacity was allotted a swell factor of 90. Similarly, Illite and Kaolinite minerals are allotted swell factors (SF) of 9 and 1 respectively. The total contribution for swell from these three minerals is 100, and the SFs chosen are based on the moisture hydration phenomena of the minerals that are presented in the expansive clay.

In this model, the total chemical factor (C) which represents the chemical activity of a particular soil is given by the following Eq.12.

$$C = CF \times \sum_{i=1}^{n} SF * f_i \tag{12}$$

Where, C is the chemical factor for particular clay, CF is the clay fraction, SF is the swell factor, 'f_i' is the fraction of particular mineral in the clay.

6.3.3 Physico-Mechanical behavior of expansive soils:

In the current model, factors like grain size distribution, pore distribution are considered as the physical attributes governing swell behavior. These are represented by SWCC in the current model. Similarly, the mechanical attribute for clay is represented best by studying the variation of matric suction with void ratio during the swelling process. Hence, the cumulative variation of void ratio, matric suction and moisture content are considered as the physico-mechanical attributes on the swelling behavior of soil. Figure 6.21 shown below presents the variation of mechanical soil parameters with the soil experiencing swelling induced volume changes.

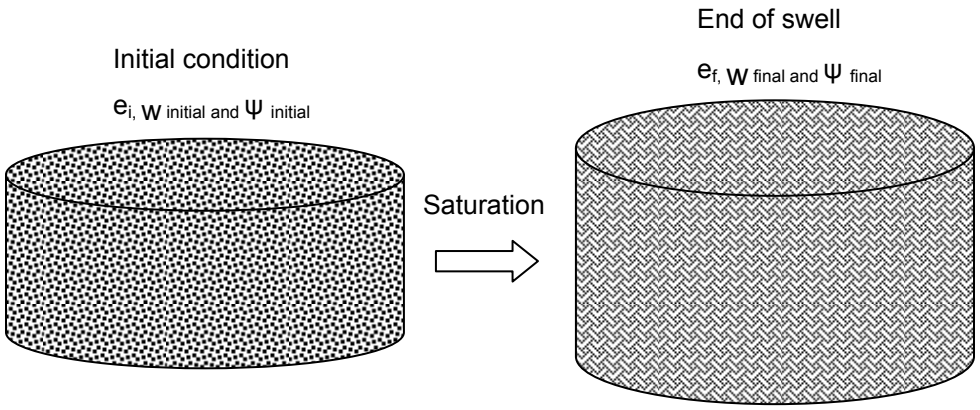

Figure 6.21: Variation of mechanical parameters of a soil specimen with swelling

Where e_i, $w_{initial}$ and $\psi_{initial}$ are the void ratio, moisture content and soil matric suction at initial compaction condition. Similarly, e_f, w_{final} and ψ_{final} are the void ratio, moisture content and

soil matric suction at saturation condition, i.e. at the end of swell testing. e-w-log ψ plots are presented for all the eight expansive soils studied in the present research.

The representation of hydro mechanical behavior of swelling clay can be better represented with a SWCC. The existence of drying and wetting paths in a SWCC details the behavior of expansive clay during shrinking and swelling process, respectively as shown in Figure 6.22. In the present research all the SWCC's are performed on drying paths.

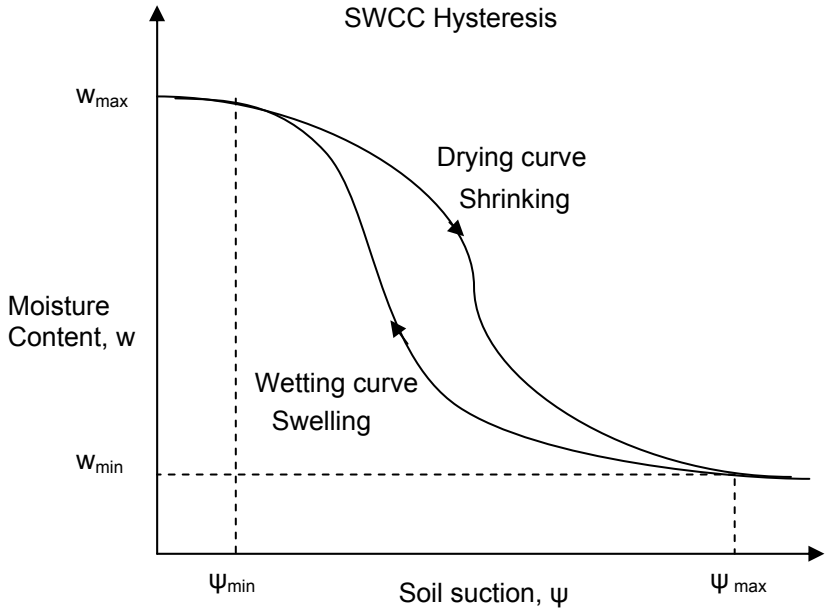

Figure 6.22: Showing the hysteresis effect and swelling behavior in a typical SWCC

The portion of wetting curve where the soil swelling occurs do not account for any change in air entry value of a soil. Since swell tests plotted in the void ratio - matric suction frame work, soil hysteresis effects are regarded as small and hence not considered in the analysis. Figure 6.23 presents the schematic for the determination of α from void ratio - matric suction plot along with an idealized and actual paths exhibited by soil specimen during hydration. From the SWCC, the moisture content matric suction relationship is correlated to void ratio and moisture contents, there by resulting in void ratio – log matric suction plot. The slope of soil matric suction (X-axis) and void ratio (Y-axis) plot (α) is considered as an important

parameter in mapping the variation of void ratio of the soil specimen with soil matric suction during swelling process.

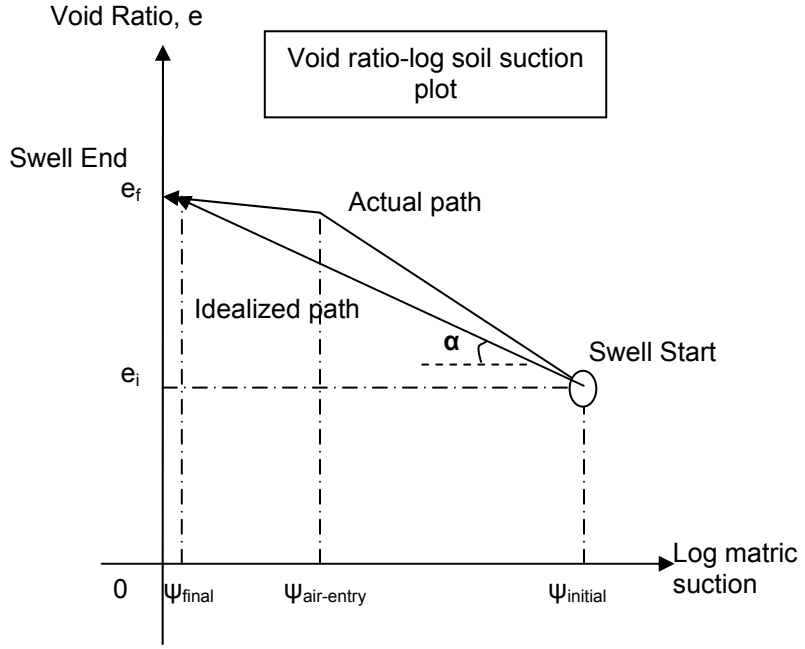

Figure 6.23: Schematic for the measurement of slope of void ratio and logarithmic of matric suction

The swelling behavior of a typical expansive clay on void ratio - matric suction plot is shown above. In the plot, the e_i is the initial void ratio, e_f is the void ratio at full saturation, $\psi_{initial}$ is the initial matric suction in the soil specimen before swell testing, $\psi_{air\text{-}entry}$ is the air entry value matric suction that will transpire during desaturation process, ψ_{final} is the final matric suction close to full saturation condition and α is the slope of idealized suction - void ratio path. Initially the soil specimen has a high matric suction ($\psi_{initial}$) and a low void ratio (e_i). During the swell testing process, the matric suction in the soil specimen decreases and the corresponding void ratio increases. In the current model, this variation of soil matric suction with void ratio is assumed to follow a linear trend. Hence, the slope of the idealized matric suction-void ratio path is given by the following Eq. 13.

$$\propto = \frac{(e_f - e_i)}{(\log(\psi_{final}) - \log(\psi_{initial}))} \tag{13}$$

The value of $\psi_{initial}$ was high when compared to ψ_{final} which leads to a negative slope value of α. The current 'Mechanical-Hydro' coupling effect is based only on the magnitude of α values and hence the negative magnitude of this slope is neglected. During the soil swelling process the moisture content in the soil specimen increases and this results in the reduction of soil matric suction. As the soil specimen attains a higher degree of soil saturation, the void ratio of the soil specimen will increase. This behavior is clearly noticed in the following e-w-log ψ plots of the eight expansive soils in the following sections.

6.3.3.1 Anthem e-w-log ψ plot:

Anthem soil which was compacted at 95% MDD and OMC condition was then tested for SWCC and swell behavior. The swell behavior exhibited by Anthem soil specimen on an e-w-log ψ plot is presented in Figure 6.24.

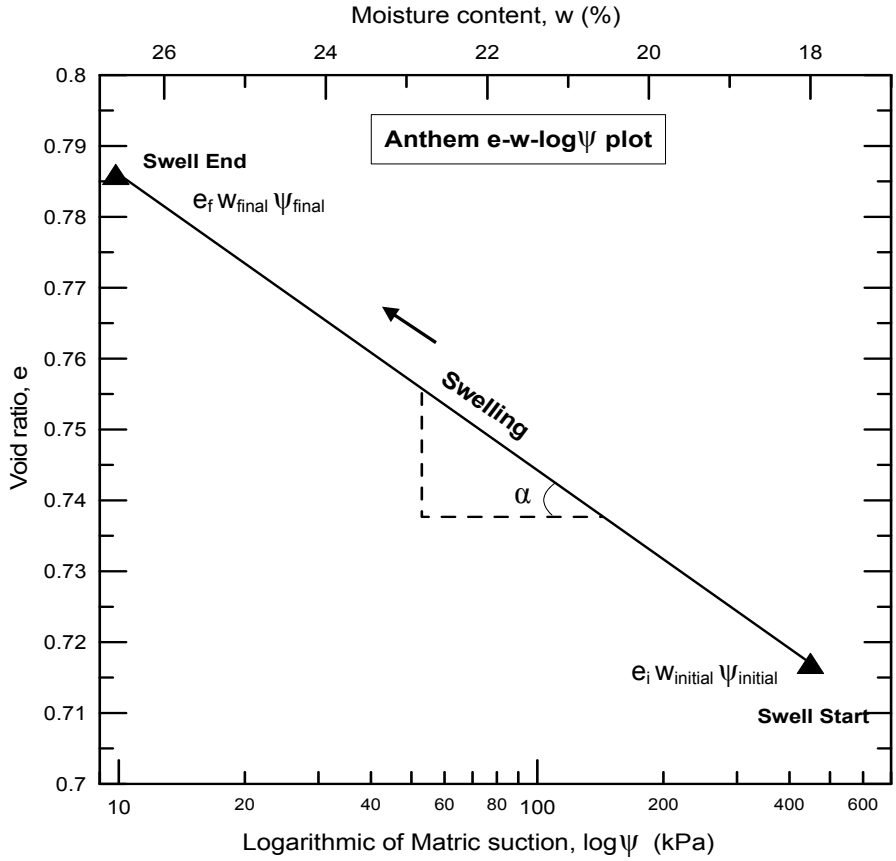

Figure 6.24: Behavior of Anthem soil specimen at 95% MDD on e-s-log ψ plot

During the swelling process, the Anthem soil specimen underwent a void ratio change from 0.716 to 0.786. Correspondingly, the gravimetric moisture content has increased from an initial 18% to a final value of 26.5%. From the SWCC studies, the soil matric suction values are determined by extracting from the corresponding moisture contents. It showed that the specimen had an initial matric suction of 450 kPa and it decreased to 10 kPa at saturation or end of swelling process.

6.3.3.2 Burleson e-w-log ψ plot

Burleson soil which was compacted at 95% MDD and OMC condition was then tested for SWCC and swell behavior. The swell behavior of Burleson soil on an e-w-log ψ plot is presented in Figure 6.25.

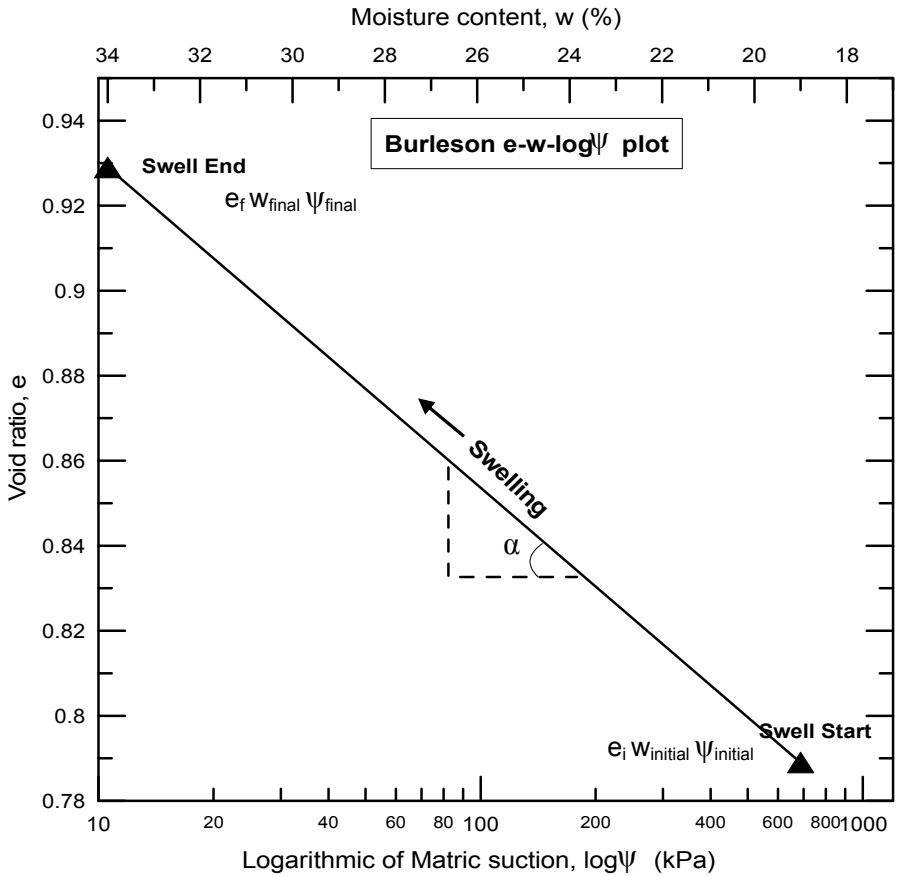

Figure 6.25: Behavior of Burleson soil specimen at 95% MDD on e-s-log ψ plot

During the swelling process, the Burleson soil specimen experienced a void ratio change from 0.79 to 0.93 during the soil swelling process. Correspondingly, the gravimetric moisture content increased form an initial 20% to 33.5%. From the SWCC the soil matric suction values are determined from the corresponding moisture contents. It was found that the soil specimen had an initial matric suction of 700 kPa and decreased to 10 kPa at saturation or the end of swelling process.

6.3.3.3 Colorado e-w-log ψ plot

Colorado soil which was compacted at 95% MDD and OMC condition was then tested for SWCC and swell behavior. The swell behavior of Colorado soil on an e-w-log ψ plot is presented in Figure 6.26.

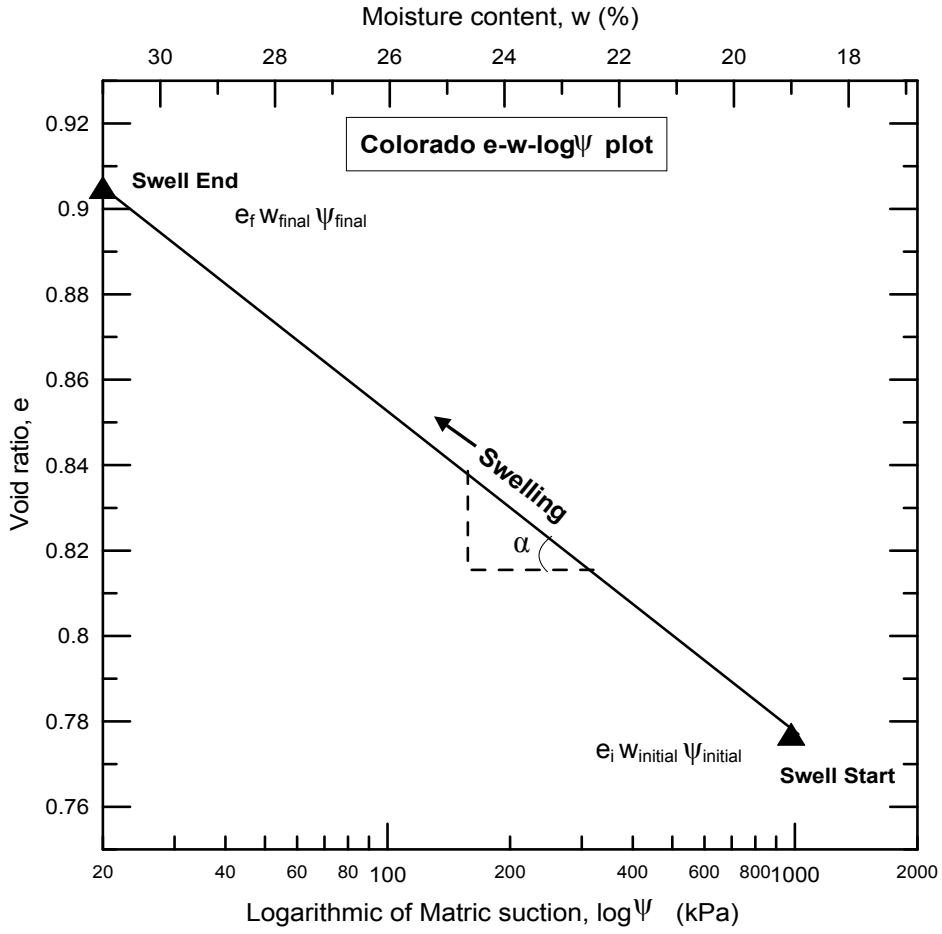

Figure 6.26: Behavior of Colorado soil specimen at 95% MDD on e-s-log ψ plot

During the swelling process, Colorado soil specimen experienced a void ratio change from 0.77 to 0.91. Correspondingly, the gravimetric moisture content increased form an initial 20.5% to 31.7%. From the SWCC data, the soil matric suction values are determined by correlating with the corresponding moisture contents. It showed that the specimen had an initial matric suction of 1050 kPa and decreased to 20 kPa at saturation or the end of swelling process. Colorado soil showed a high initial matric suction value when compared to other soils.

6.3.3.4 Grayson e-w-log ψ plot

Grayson soil which was compacted at 95% MDD and OMC condition was then tested for SWCC and swell characterization studies. The swell behavior of Grayson soil on an e-w-log ψ plot is presented in Figure 6.27.

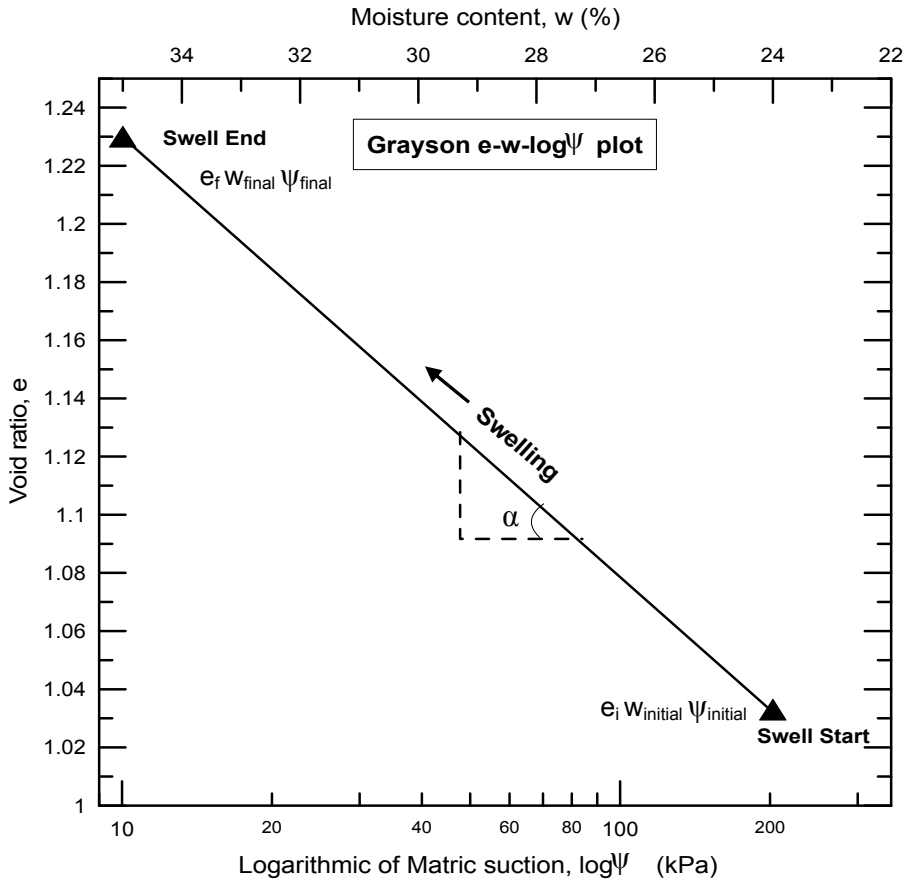

Figure 6.27: Behavior of Grayson soil specimen at 95% MDD on e-s-log ψ plot

Grayson soil specimen underwent a void ratio change from 1.03 to 1.23, during the swelling process. Correspondingly, the gravimetric moisture content increased form an initial 24% to 35.6%. From the SWCC the soil matric suction values are determined by correlating with the corresponding moisture contents. It showed that the specimen had an initial matric suction of 210 kPa and decreased to 20 kPa at saturation or end of swelling process. Grayson soil showed high moisture intake levels at saturation compared to other soils.

6.3.3.5 Keller e-w-log ψ plot

Keller soil which was compacted at 95% MDD and OMC condition was then tested for SWCC and swell patterns. The swell behavior of Keller soil on an e-w-log ψ plot is presented in Figure 6.28.

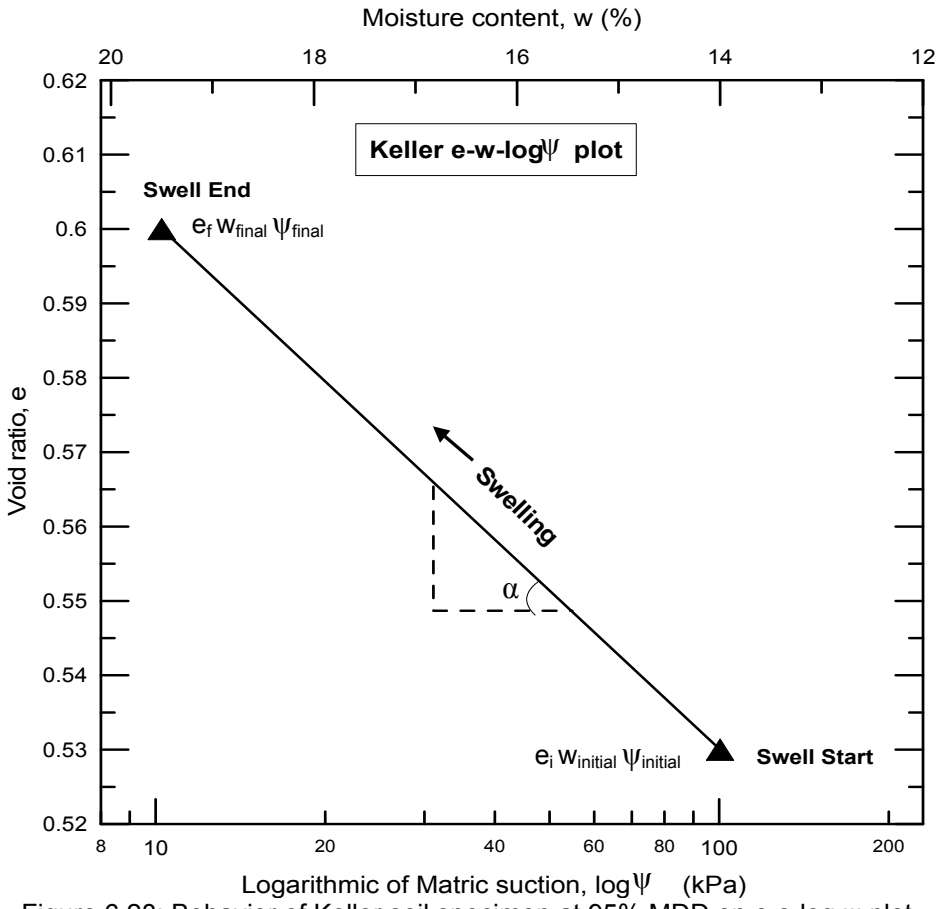

Figure 6.28: Behavior of Keller soil specimen at 95% MDD on e-s-log ψ plot

During the swelling process, Keller soil specimen underwent a void ratio change from 0.53 to 0.60. Correspondingly, the gravimetric moisture content increased form an initial 14% to 19.5%. From the SWCC the soil matric suction values are determined by correlating with the corresponding moisture contents. It showed that the specimen had an initial matric suction of 100 kPa and decreased to 10 kPa at saturation or end of swelling process.

6.3.3.6 Oklahoma e-w-log ψ plot

Oklahoma soil which was compacted at 95% MDD and OMC condition was then tested for SWCC and swell behavior. The swell behavior of Oklahoma soil on an e-w-log ψ plot is presented in Figure 6.29.

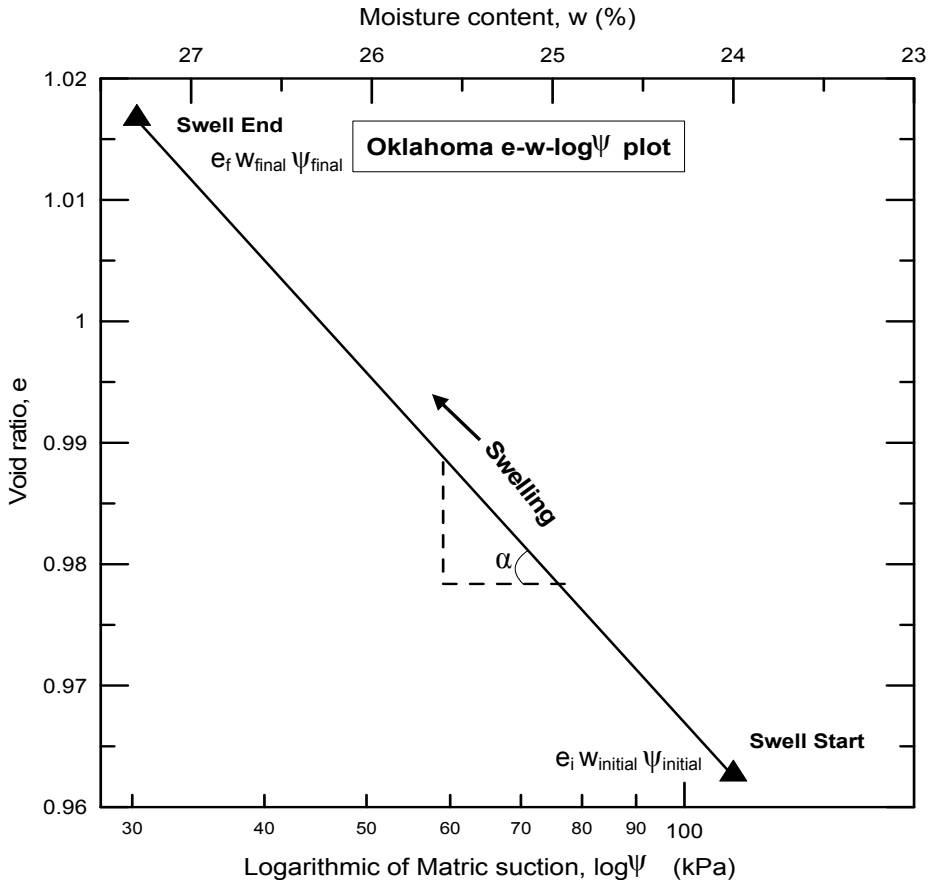

Figure 6.29: Behavior of Oklahoma soil specimen at 95% MDD on e-s-log ψ plot

Oklahoma soil specimen underwent a void ratio change from 0.96 to 1.02, during the swelling process. Correspondingly, the gravimetric moisture content increased form an initial

24% to 27.3%. From the SWCC the soil matric suction values are determined by correlating with the corresponding moisture contents. It showed that the specimen had an initial matric suction of 110 kPa and decreased to 25 kPa at saturation or end of swelling process.

6.3.3.7 San Antonio e-w-log ψ plot

San Antonio soil which was compacted at 95% MDD and OMC condition was then tested for SWCC and swell behavior. The swell behavior of San Antonio soil on an e-w-log ψ plot is presented in Figure 6.30.

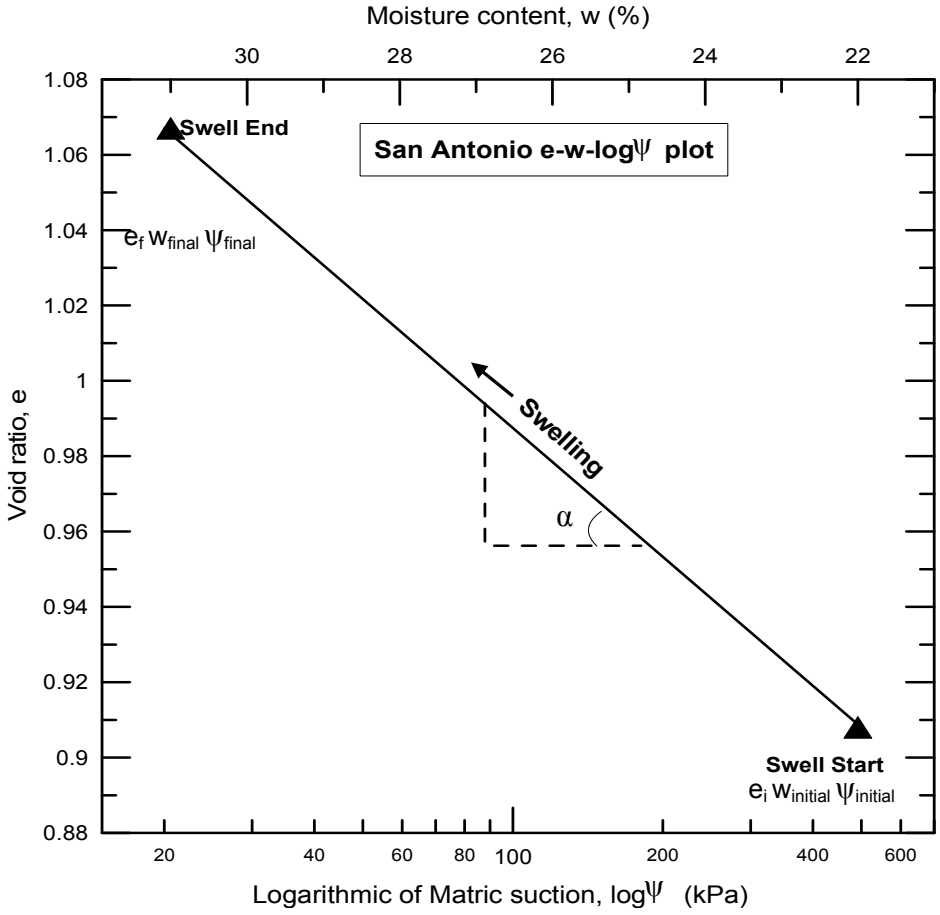

Figure 6.30: Behavior of San Antonio soil specimen at 95% MDD on e-s-log ψ plot

During the soil swelling process, San Antonio soil specimen experienced a void ratio change from 0.96 to 1.02. Correspondingly, the gravimetric moisture content increased form an initial 24% to 27.3%. From the SWCC the soil matric suction values are determined by

correlating with the corresponding moisture contents. It showed that the specimen had an initial matric suction of 110 kPa and decreased to 25 kPa at saturation or end of swelling process.

6.3.3.8 San e-w-log ψ plot

San Diego soil which was compacted at 95% MDD and OMC condition was then tested for SWCC and swell behavior. The swell behavior of San Diego soil on an e-w-log ψ plot is presented in Figure 6.31.

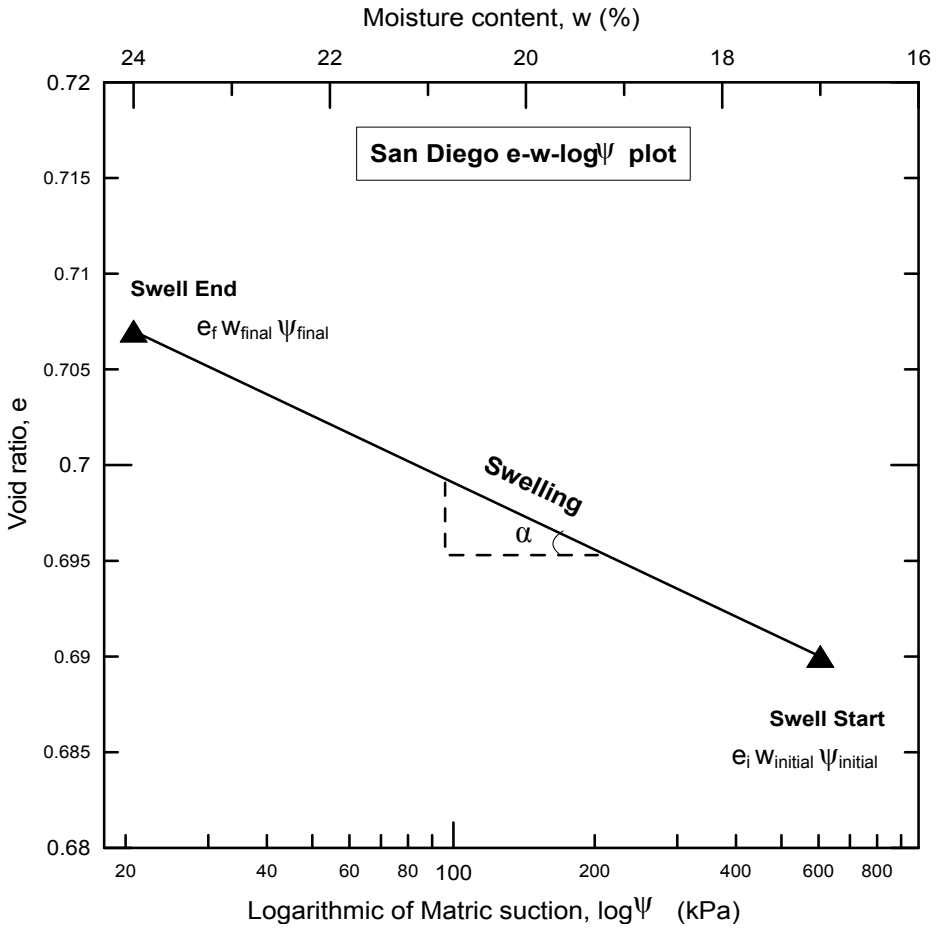

Figure 6.31: Behavior of San Diego soil specimen at 95% MDD on e-s-log ψ plot

During the swelling process, San Diego soil specimen underwent a void ratio change from 0.69 to 0.71. Correspondingly, the gravimetric moisture content increased form an initial 17% to 24%. From the SWCC the soil matric suction values are determined by correlating with

the corresponding moisture contents. It showed that the specimen had an initial matric suction of 650 kPa and decreased to 10 kPa at saturation or end of swelling process.

6.3.4 Mechanical Hydro Chemical parameter (MHCP)

A new parameter termed here as the Mechanical Hydro Chemical Parameter (MHCP) has been formulated based on the soil swell governing parameters like void ratio, initial soil matric suction, air entry suction, percentage clay fraction and percentage Montmorillonite mineral fraction in expansive clay.

Table 6.8 presents the slope of matric suction-void ratio plot of all the eight soils studied for soil matric suction behavior. The slope angle α determined on void ratio and matric suction plot was highest for Grayson clay and least for San Diego clay.

Table 6.8: Slope of matric suction-void ratio plot (α) for all the expansive clays

Soil	Slope of matric suction-void ratio plot (α)
Anthem	- 0.041
Burleson	- 0.078
Colorado	- 0.075
Grayson	- 0.151
Keller	- 0.070
Oklahoma	- 0.095
San Antonio	- 0.113
San Diego	- 0.011

The determination of Mechanical-hydro and chemical parameters has been discussed in the previous sections. The physical behavior of soil is often related to parameters like grain size distribution, pore distribution and soil matric suction. The chemical parameters like mineral contents and activity of clay minerals have a direct influence on the soil swelling behavior. In the

current model, the combined effect of physical mechanical and chemical parameters was considered as the sole governing parameter for swell behavior. Hence, a new parameter to address the combined effect of the total Mechanical Hydro Chemical Parameter (MHCP) was determined from the following Eq. 14.

$$MHCP = \pi(\alpha, C) \tag{14}$$

Where MHCP is the Mechanical Hydro Chemical Parameter, α is the mechanical hydro parameter, i.e. the slope of logarithmic value of matric suction - void ratio plot, C is the chemical parameter that accounts for soil swelling.

The negative effect on the slope is neglected in the determination of MHCP value. The MHCP parameters for all the eight expansive soils are determined using the soil matric suction - void ratio plots and soil water characteristic curves. Table 6.9 presents the determination of MHCP parameters from clay minerals (chemical), percent clays and soil matric suction and void ratio properties (Mechanical) of each soil.

Table 6.9: Calculation of MHCP from soil properties at 95% MDD condition

Soil	Mechanical Hydro parameter, α	Chemical parameter, C	MHCP
Anthem	0.041	8.51	0.349
Burleson	0.078	16.76	1.308
Colorado	0.075	16.48	1.236
Grayson	0.151	22.72	3.431
Keller	0.070	7.48	0.524
Oklahoma	0.095	7.36	0.700
San Antonio	0.113	19.52	2.206
San Diego	0.011	6.36	0.070

6.3.5 Mechanical Hydro Chemical (MHC) Model

The present model results are studied on soil specimens compacted at 95% MDD condition. MHC model is formulated on the basis of the unique MHCP value for each soil. The MHCP value is dependent on sensitive parameters like slope of void ratio and matric suction and clay mineral content. MHCP values measured for each soil are correlated against the measured swell strains and pressures.

Figure **6.32** shows the variation of measured swell to the unique soil Mechanical Hydro Chemical Parameter (MHCP).

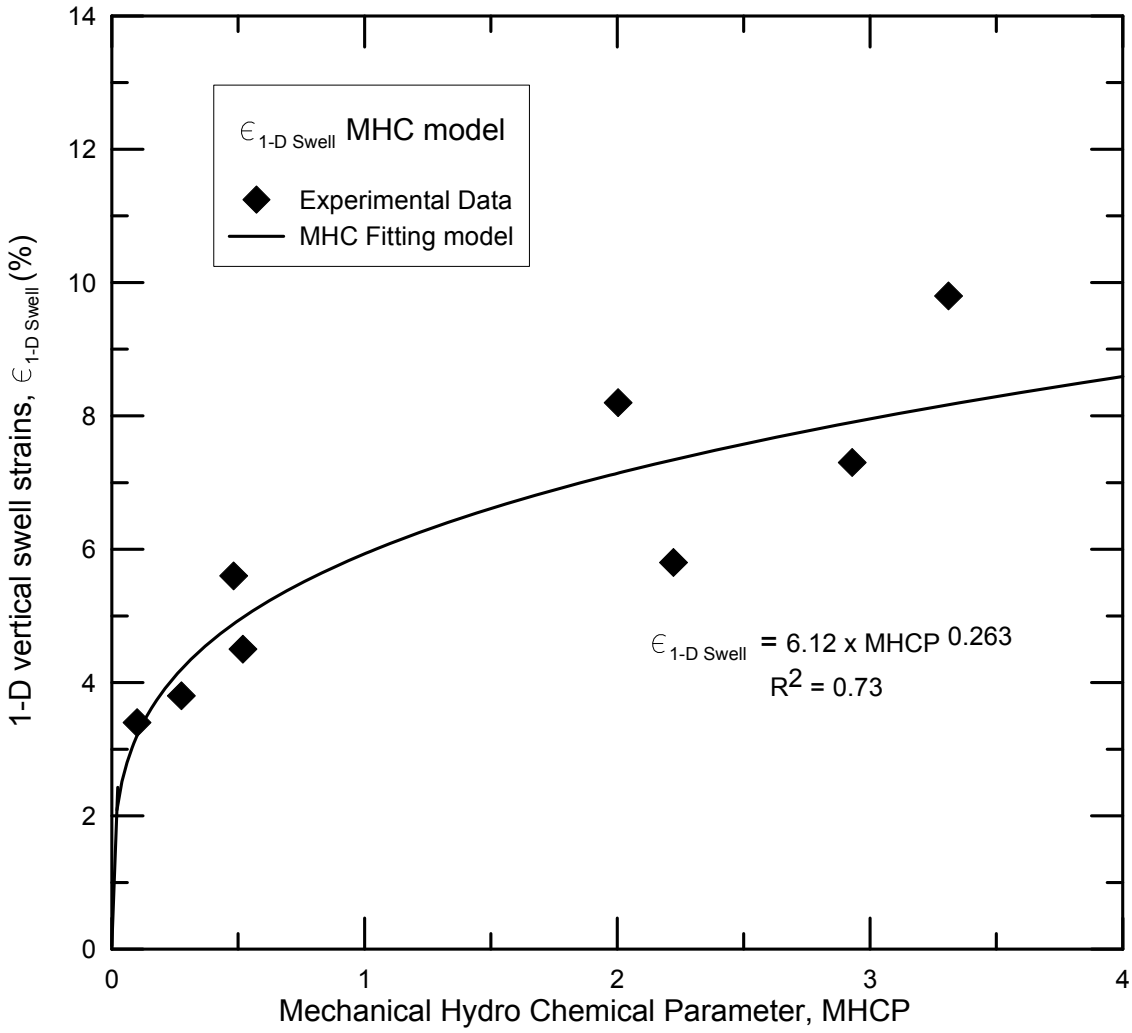

Figure 6.32: 1 D Swell Strain MHC Model at 95% MDD condition

An exponential variation between the measured swell strain and MHCP data was noticed. This variation is presented in the following Eq. 15.

$$\epsilon_{1-\text{D Swell}} = 6.12 * \text{MHCP}^{0.263} \quad (15)$$

The SSM model for 1-D swell strains showed a good fit with the measured experimental data. The coefficient of determination (R^2) for this model is found to be 0.73.

Similarly,

Figure 6.33 shows the variation of measured swell pressure to the unique soil Mechanical Hydro Chemical Parameter (MHCP).

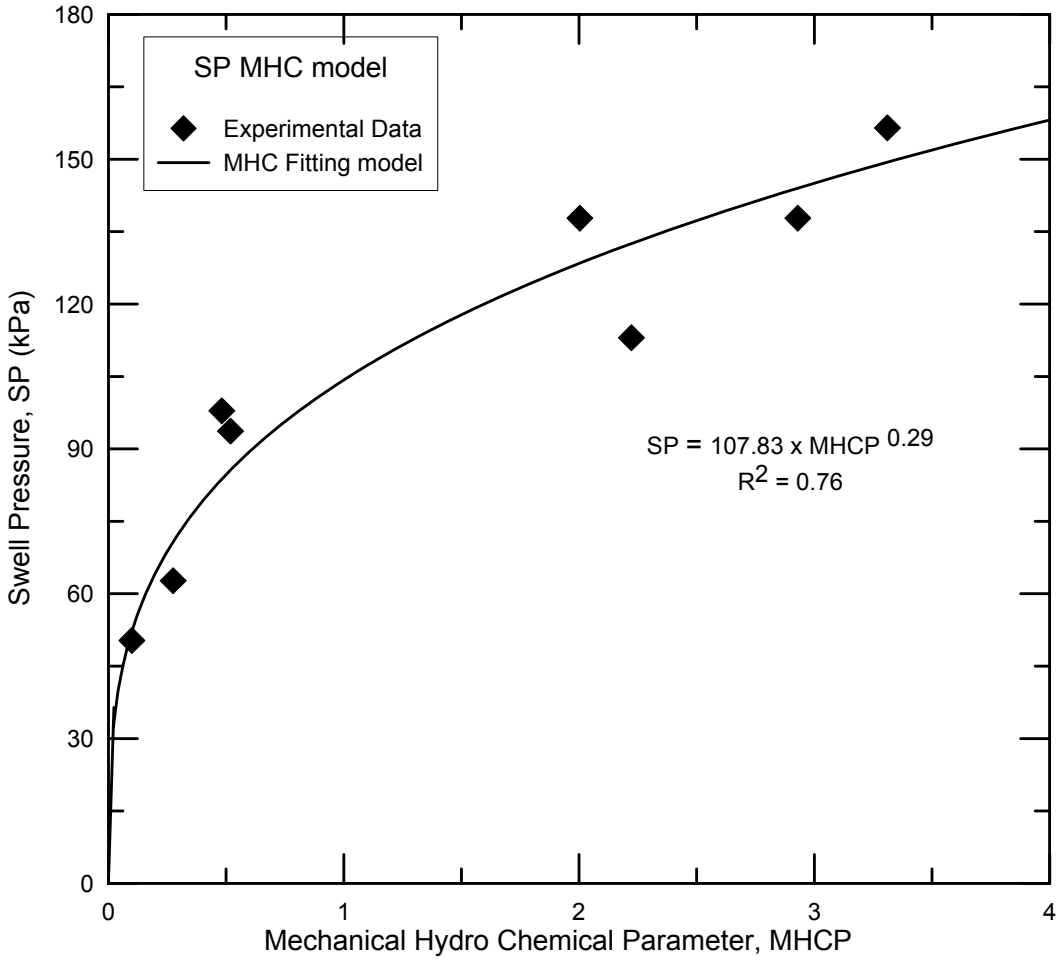

Figure 6.33: SSM Model for Swell Pressure at 95% MDD condition

Similar to the 1-D swell strains, exponential variation between the measured swell pressure and MHCP data was found and this is presented in the following Eq.16:

$$\mathrm{SP\ (kPa)} = 107.83 * \mathrm{MHCP}^{0.29} \tag{16}$$

The MHC model for swell pressure showed good fit with the measured experimental data. The coefficient of determination (R^2) for this model is found to be 0.76.

Figure 6.34 presents the variation of measured volumetric swell strain at 7 kPa confinement versus MHCP values.

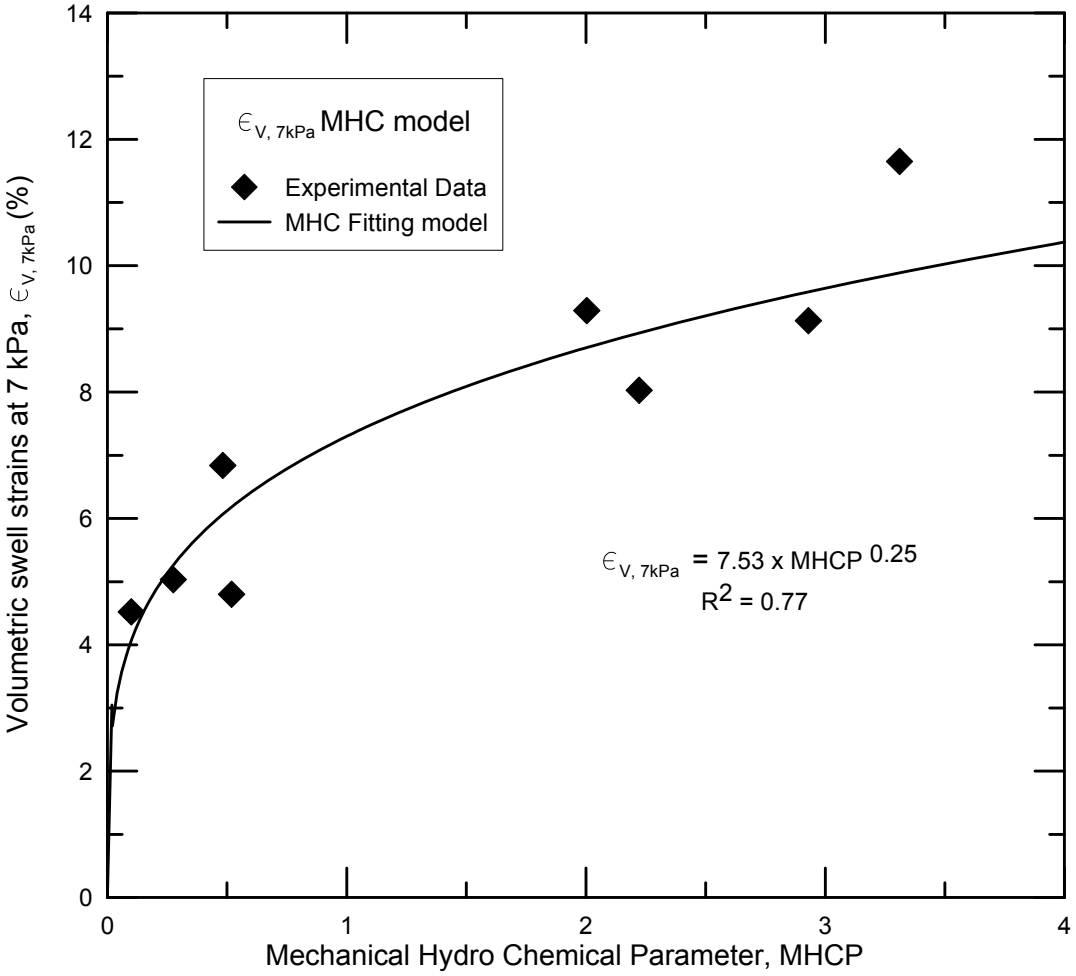

Figure 6.34: SSM model for volumetric swell at 7kPa for specimens compacted at 95% MDD condition

The volumetric swell predicted from the MHCP at 7 kPa confining pressure was given by the following Eq. 17.

$$\epsilon_{v,7kPa} = 7.53 * MHCP^{0.25} \quad (17)$$

The coefficient of determination (R^2) for this model is found to be 0.77. Figure 6.35 presents the variation of measured volumetric swell at 50 kPa confinement to the unique MHCP.

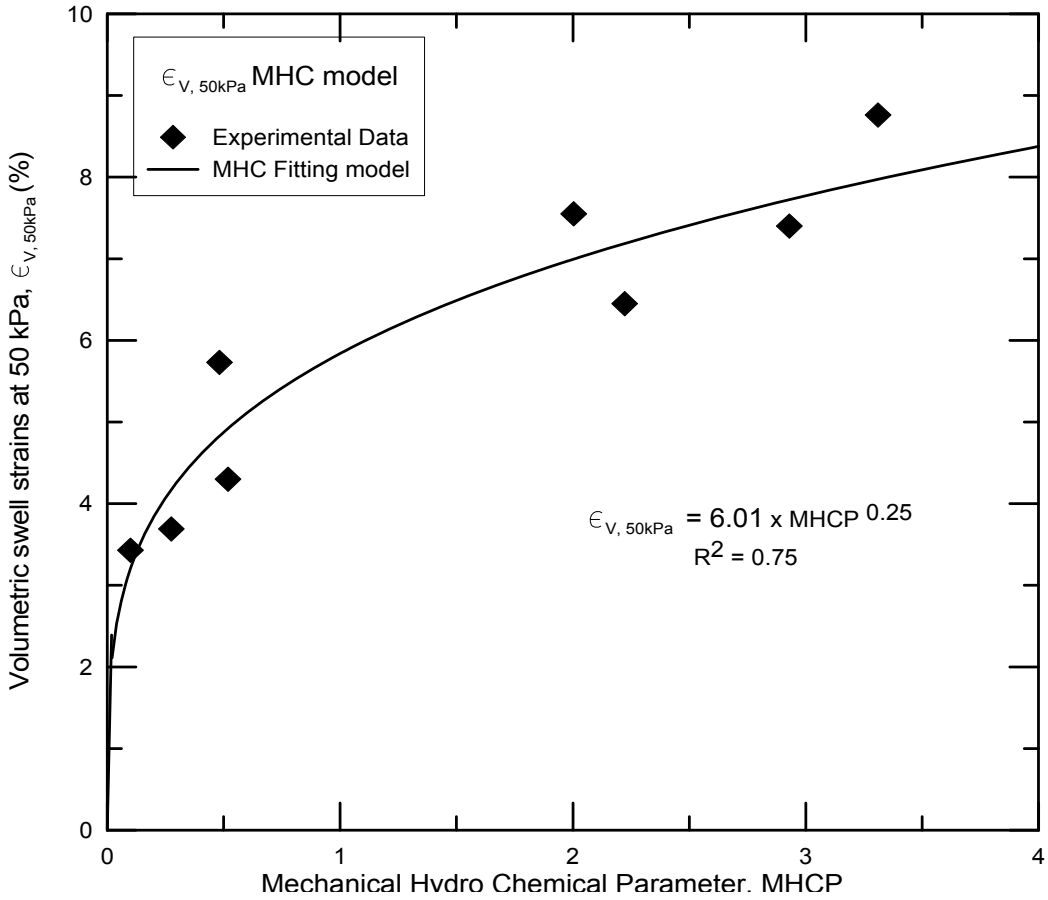

Figure 6.35: SSM model for volumetric strains at 50 kPa for specimens compacted at 95% MDD condition

The volumetric swell strain at 50 kPa confining pressure correlation with MHCP value is shown in Eq. 18.

$$\epsilon_{v,50kPa} = 6.01 * MHCP^{0.25} \quad (18)$$

The coefficient of determination (R^2) for this model is found to be 0.75. As the confinement level increased from 7 kPa to 50 kPa the multiplication parameter decreased from 7.53 to 6.01.

Figure **6.36** presents the variation of measured volumetric swell at 100 kPa confinement to the MHCP.

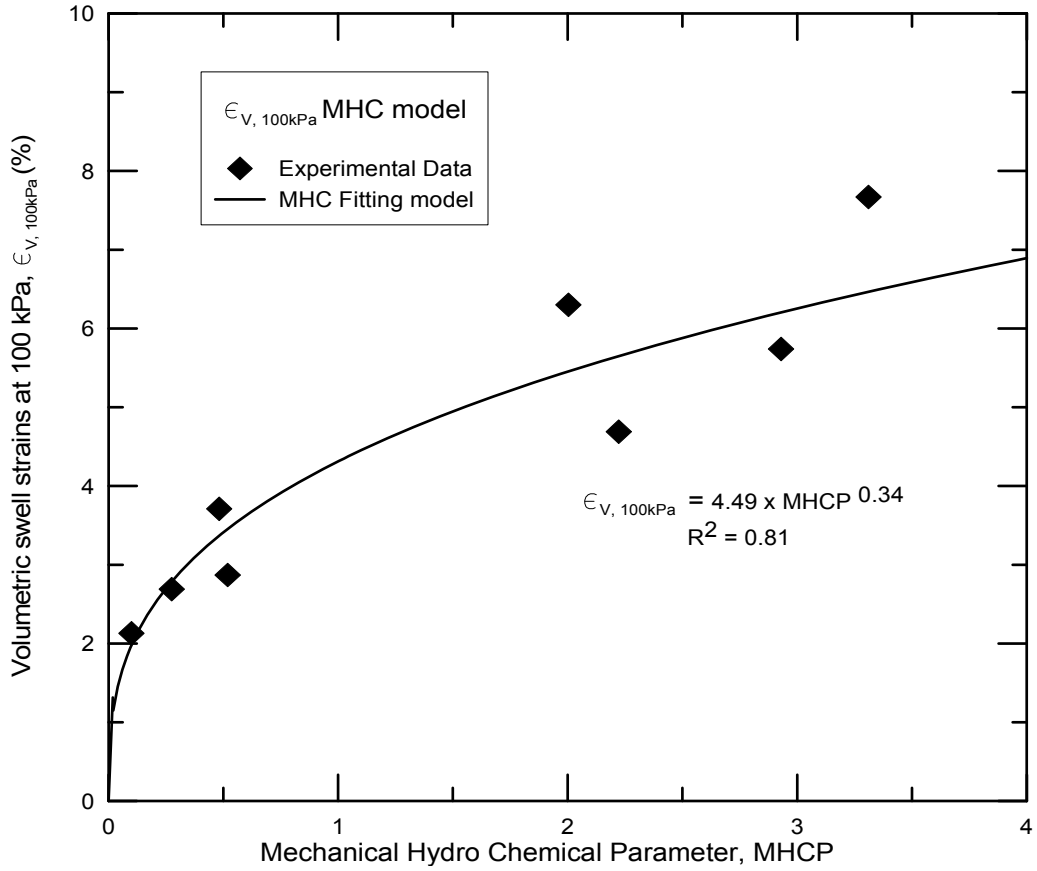

Figure 6.36: SSM model for volumetric strains at 100 kPa for specimens compacted at 95% MDD condition

The volumetric swell predicted from the MHCP model at 100 kPa confining pressure is presented here in the Eq. 19:

$$\epsilon_{v,100\text{kPa}} = 4.49 * \text{MHCP}^{0.34} \quad (19)$$

The MHC model for volumetric swell at 100 kPa showed a good fit with the measured experimental data. The coefficient of determination (R^2) for this model is found to be 0.81. As the confinement level increased from 50 kPa to 100 kPa, it was found that the multiplication parameter decreased from 6.01 to 4.49.

6.3.6 Summary of MHC model analysis

The present study was conducted on soil specimens compacted at 95% MDD. Table 6.10 presents the MHC models for 1-D swell strain and swell pressures for soils compacted at 95% MDD condition. MHC model for the prediction of swell pressures showed a moderate coefficient of determination values (R^2 = 0.76). The MHC models for prediction of swell strains and swell pressures provided reliable results for experimental data.

Table 6.10: Summary of SSM model for 1 D swell strain and swell pressure for specimens compacted at 95% MDD condition

Function	MHC Model	R^2
1-D Vertical swell strains (%)	$\epsilon_{1-\text{D swell}} = 6.12 \text{ x } \text{MHCP}^{0.26}$ MSE=0.045	0.73
Swell Pressure (kPa)	$\text{SP} = 107.23 \text{ x } \text{MHCP}^{0.29}$ MSE = 15.2	0.76

Where MSE = Mean Square Error

Similarly, Table 6.11 presents the MHC models for the prediction of volumetric swell strains at three different confinements for soils compacted at 95% MDD.

Table 6.11: Summary of MHC model for volumetric strains at different confinement levels for specimens compacted at 95% MDD condition

	Confinement Levels	MHC Model	R^2
Volumetric Strain (%)	7 kPa	$\epsilon_{\text{v,7kPa}} = 7.53 \text{ x } \text{MHCP}^{0.25}$ MSE=0.036	0.77
	50 kPa	$\epsilon_{\text{v,50kPa}} = 6.01 \text{ x } \text{MHCP}^{0.25}$ MSE=0.043	0.75
	100 kPa	$\epsilon_{\text{v,100kPa}} = 4.49 \text{ x } \text{MHCP}^{0.34}$ MSE=0.050	0.81

Where MSE = Mean Square Error

The consistent change in this multiplication parameter allows us to conclude that with an increase in confinement the multiplication parameter in the MHC model decreases, thereby reducing the volumetric swell strain of the expansive clay when exposed to larger overburden loading conditions.

6.4 Total Surface Area Ratio Model

Surface area of a clay specimen plays an important role in the swell behavior. Minerals like Montmorillonite have very high surface area when compared to other minerals like Kaolinite (Mitchell and Soga, 2005). Table 6.12 below presents the standard specific surface area values for different clay minerals.

Table 6.12: Standard SSA values for clay minerals (Mitchell and Soga, 2005)

	Clay Minerals	Specific Surface Area (SSA) (m^2/g)
1	Montmorillontie	70 – 800
2	Illite	65 – 100
3	Kaolinite	10 – 20

As shown above the specific surface area of Montmorillonite mineral is very high when compared to other minerals. Clay specimens having higher percentages of Montmorillonite mineral will tend to have more reactive surface area and hence attract large amounts of moisture. The present model attempts to map the variation of surface area parameter with the soil swelling behavior of expansive clay.

6.4.1 Assumptions

The following assumptions are made in the development of this model.

1. The total surface area of the clay particles in a soil specimen is the only factor contributing to the swell properties.
2. Chemical reactivity of the clay particles like cation exchange capacity and diffused double water layer characteristics are not explicitly considered in the present model, however surface area characteristics accounts for this.
3. All the pores are assumed to be cylindrical in shape and the cumulative volume at each pore diameter is considered in the calculation of pore lengths. Figure 6.37 shows the assumption of pore spaces as individual cylinders.

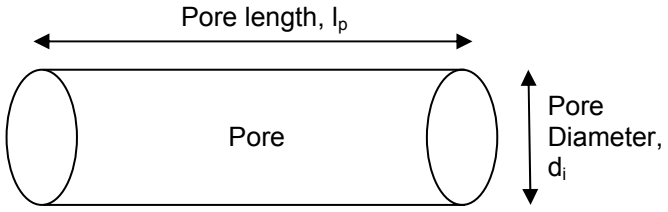

Figure 6.37: Assumption of cylindrical pores in the soil specimen

4. Surface area contributed from the silt and sand particles are neglected for swell behavior determination as those materials are inert.

6.4.2 Total surface area from clay mineralogy

The specific surface area for a clay soil was determined using standard procedure summarized in Chapter 3. Once the specific surface area of a soil specimen was measured the total surface area of the compacted specimen was measured by using weight of clay fraction in a given soil. The total surface area of a compacted soil specimen was determined from the weight of soil solids present in the clay fraction of the specimen as shown in Eq. 20.

$$W_c = W_S \times CF \tag{20}$$

Where W_c is the weight of clay fraction in a soil, W_s is the weight of solids and CF is the clay fraction of soil. Once the weight of clay solids are calculated the total surface area for the clay fraction of the soil specimen is given by the following Eq. 21.

$$TSA_{Clay\ minerals} = SSA \times W_c \tag{21}$$

Where $TSA_{clay\ minerals}$ is the total surface area calculated from clay minerals, SSA is the specific surface area for the soil, W_c is the weight of clay fraction in a soil.

The specific surface area of test soils previously determined are presented in Chapter 3, are used in the total surface area determination analysis. The total surface area determined from clay minerals is high for soils compacted at MDD condition than those at 95% MDD condition. The presence of more clay particle density at 100% MDD condition is responsible for the higher values in total surface area. Table 6.13 shown below presents the determination of total clay mineral surface area at two density conditions (95% MDD and MDD conditions).

Table 6.13: Total surface area calculated from clay minerals at two dry density conditions

Soil	Specific Surface Area (SSA) (m^2/g)	Weight of clay fraction for a vol. of 2 x $10^{-4}m^3$ (W_c) (g)		Total surface area from clay minerals (m^2/2 x $10^{-4}m^3$)	
		95% MDD	MDD	95% MDD	MDD
Anthem	118.5	41.72	43.84	4944.7	5195.0
Burleson	132.4	57.50	65.52	7613.0	8674.8
Colorado	185.0	53.36	57.96	9871.6	10432.8
Grayson	223.0	66.30	71.40	14784.9	15922.2
Keller	115.0	48.75	51.34	5606.9	5904.1
Oklahoma	76.3	36.30	38.10	2769.6	2907.1
San Antonio	192.4	63.44	67.08	12205.8	12906.1
San Diego	92.6	30.31	31.97	2807.0	2960.4

From the table the total surface area determined is highest for Grayson soil at both compaction dry density conditions. This could be due to the fact that Grayson soil has higher Montmorillonite mineral content and higher surface area density than other tested soils. San Diego clay exhibited the lowest amount of total surface area among the present expansive soils.

6.4.3 Total pore surface area from MIP data:

The determination of the total pore area contributing to soil swell is the primary objective of 'Total surface area ratio' (TSAR) model. For this the mercury intrusion data and results obtained for each soil type are utilized. The volume of mercury intruded into the soil specimen at different intrusion pressures is determined from MIP test. From Washburn's (1921) equation the intrusion pressure provides direct correlation to the pore diameter in the soil sample. Since all the pores are assumed to be cylindrical in shape, the volume occupied by the pores of the specimen at each diameter could be determined and these calculations are presented below.

Since the volume occupied by the pores at each diameter is known, the total length of each pore could be calculated by the following Eq. 22.

$$l_p = \frac{V_p}{A_p} \tag{22}$$

Where l_p is the length of individual pore, V_p is the volume of individual pore and A_p is the area of the pore. From the pore lengths calculated, the total pore surface area from individual pores is calculated using the following Eq. 23.

$$TPA_{MIP} = \pi\, d_1\, l_1 + \pi\, d_2\, l_2 + \pi\, d_3\, l_3 \ldots\ldots \pi\, d_n\, l_n = \sum_{i=1}^{n} \pi d_n l_p \tag{23}$$

Where TPA_{MIP} is the total pore area of a particular diameter pore from MIP test, d_i is the average diameter of the pore and l_p is the length of pore. The determination of total pore length corresponding to the particular pore diameter is determined and these results are used in Eq 19 to determine the total pore surface area for all the clays.

6.4.3.1 Anthem soil - pore length distribution

The distribution of pore lengths of Anthem soil specimen compacted at 95% MDD is presented in Figure 6.38. The distribution of pore lengths in macro, medium and macro region of the soil specimen are presented.

From the graph the soil specimen has a highest macro pore length of 30 mm at a diameter of 12 μm. Similarly, in the medium pores region a maximum length of $8x10^6$ mm is observed at 0.025 μm. The highest length of $2x10^8$ mm is observed at 0.003 and 0.005 μm in the micro pore region of the soil specimen. It was found that there is a discontinuous phase in the pore connectivity around pore diameters 0.006-0.008 μm. The total pore area determined for compacted Anthem soil at 95% MDD is 17,165 m^2.

Similarly, Figure 6.39 presents the pore length distribution of Anthem soil specimen compacted at MDD condition. From the graph the soil specimen had a highest macro pore length of 28 mm at a diameter of 12 μm. Similarly, in the medium pores region, a maximum length of $8.5x10^6$ mm is observed at 0.025 μm. The highest length of $1.5x10^8$ mm is observed at 0.0035μm in the micro pore region of the soil specimen.

When compared to the specimen at 95% MDD, the MDD specimen comprised more volume of micro pores than macro pore lengths. The total pore area determined for compacted Anthem soil at MDD is 17,964 m^2.

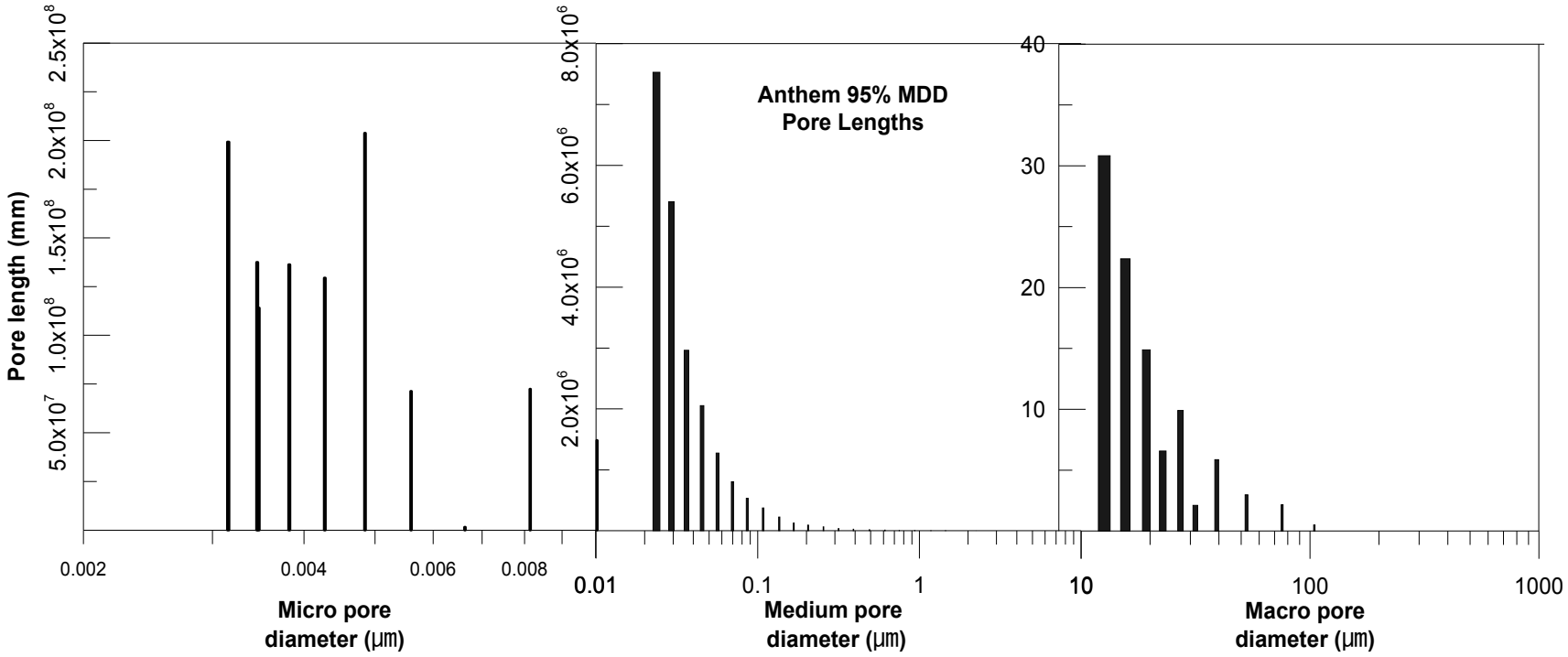

Figure 6.38: Pore length distribution chart for Anthem soil compacted at 95% MDD condition

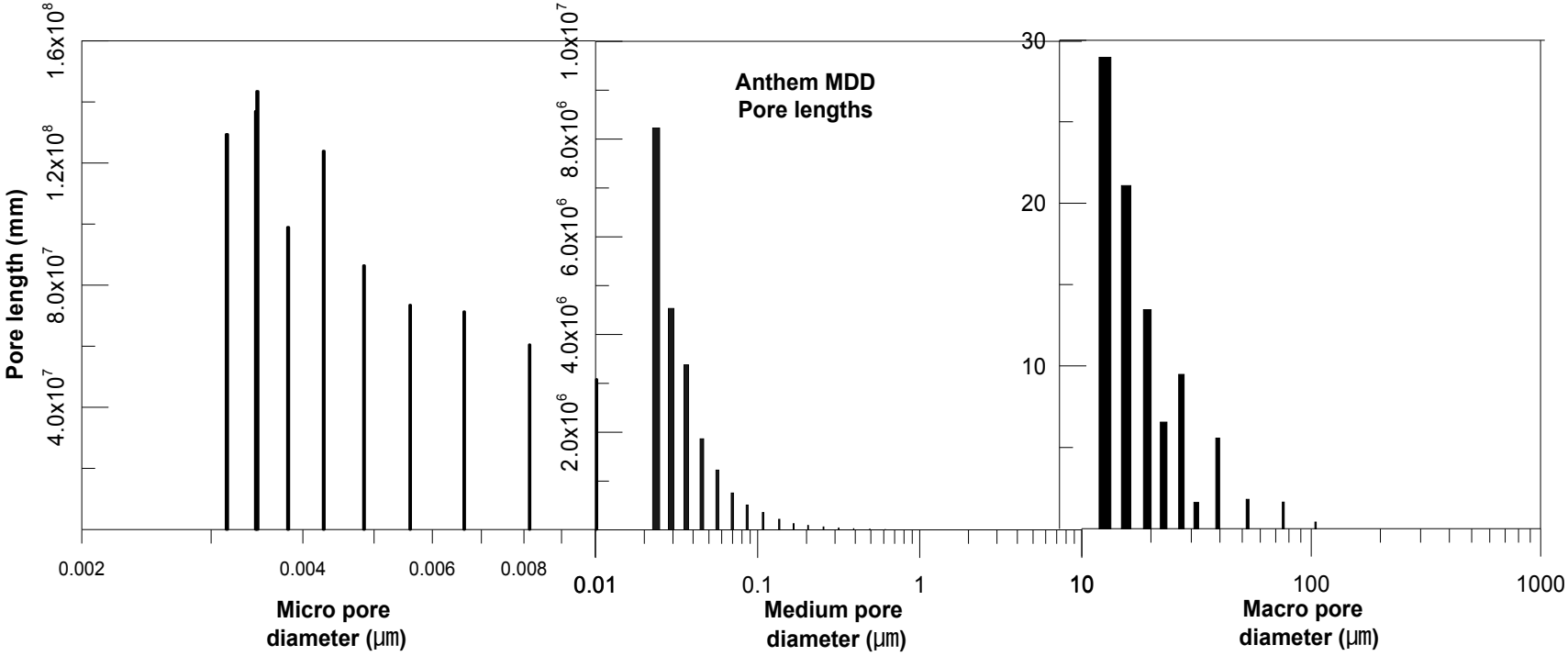

Figure 6.39: Pore length distribution chart for Anthem soil compacted at MDD condition

6.4.3.2 Burleson soil - pore length distribution

The distribution of pore lengths of Burleson soil specimen compacted at 95% MDD condition is presented in Figure 6.40. The distribution of pore lengths in macro, medium and macro region of the soil specimen are presented. From the graph the soil specimen had a highest macro pore length of 40 mm at a diameter of 12 μm. Similarly, in the medium pores region a maximum length of $9.2x10^6$ mm is observed at 0.025 μm. The highest length of $1.8x10^8$ mm is observed at 0.0035 μm in the micro pore region of the soil specimen. The total pore area determined for compacted Burleson soil at 95% MDD is 15,295 m^2.

Similarly, Figure 6.41 presents the pore length distribution of Burleson soil specimen compacted at MDD condition. From the graph the soil specimen had a highest macro pore length of 25 mm at a diameter of 12 μm. Similarly, in the medium pores region a maximum length of $9.2x10^6$ mm is observed at 0.025 μm. The highest length of $2.5x10^8$ mm is observed at 0.0035μm in the micro pore region of the soil specimen.

When compared to the specimen at 95% MDD, the MDD specimen comprised more volume of micro pores than macro pore lengths. The total pore area determined for compacted Burleson soil at MDD is 15,560 m^2.

The total pore area from MDD condition is higher than at 95% MDD due to larger pore length volume in the micro region.

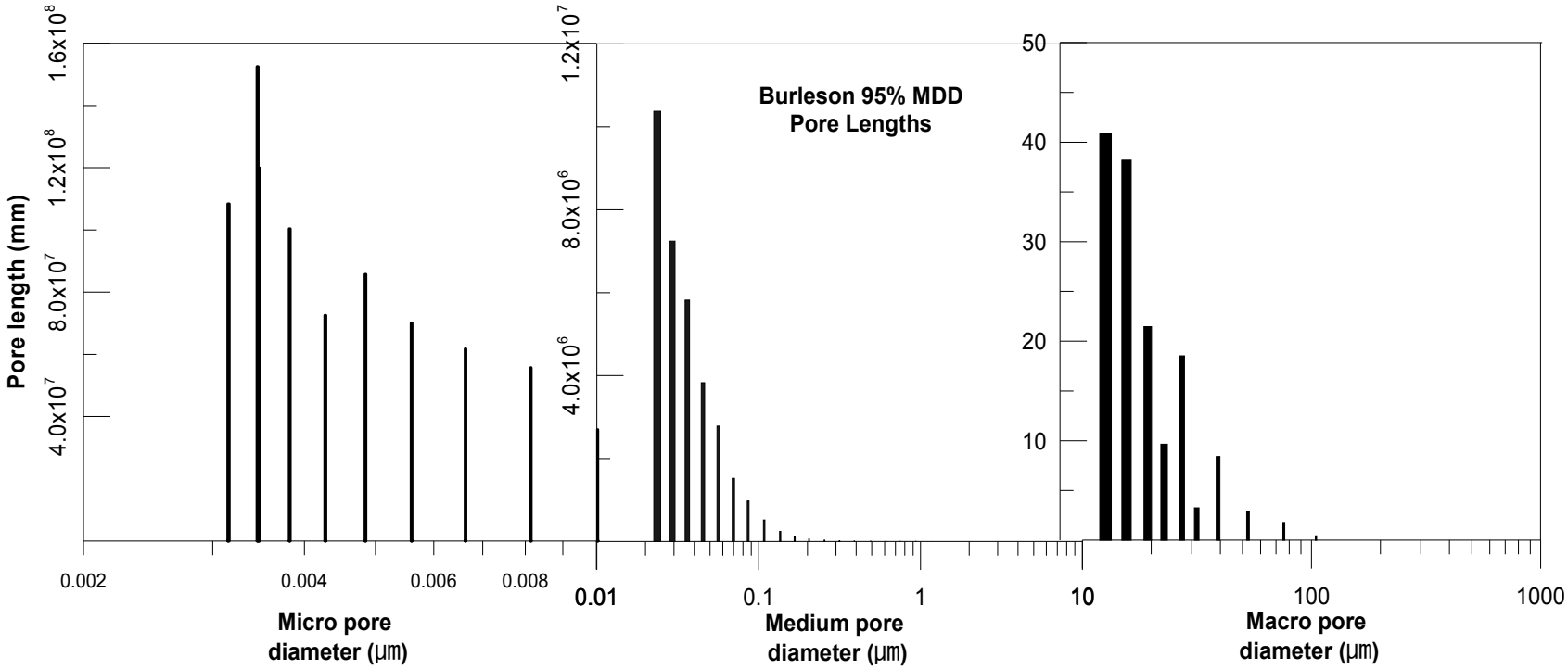

Figure 6.40: Pore length distribution chart for Burleson soil compacted at 95% MDD condition

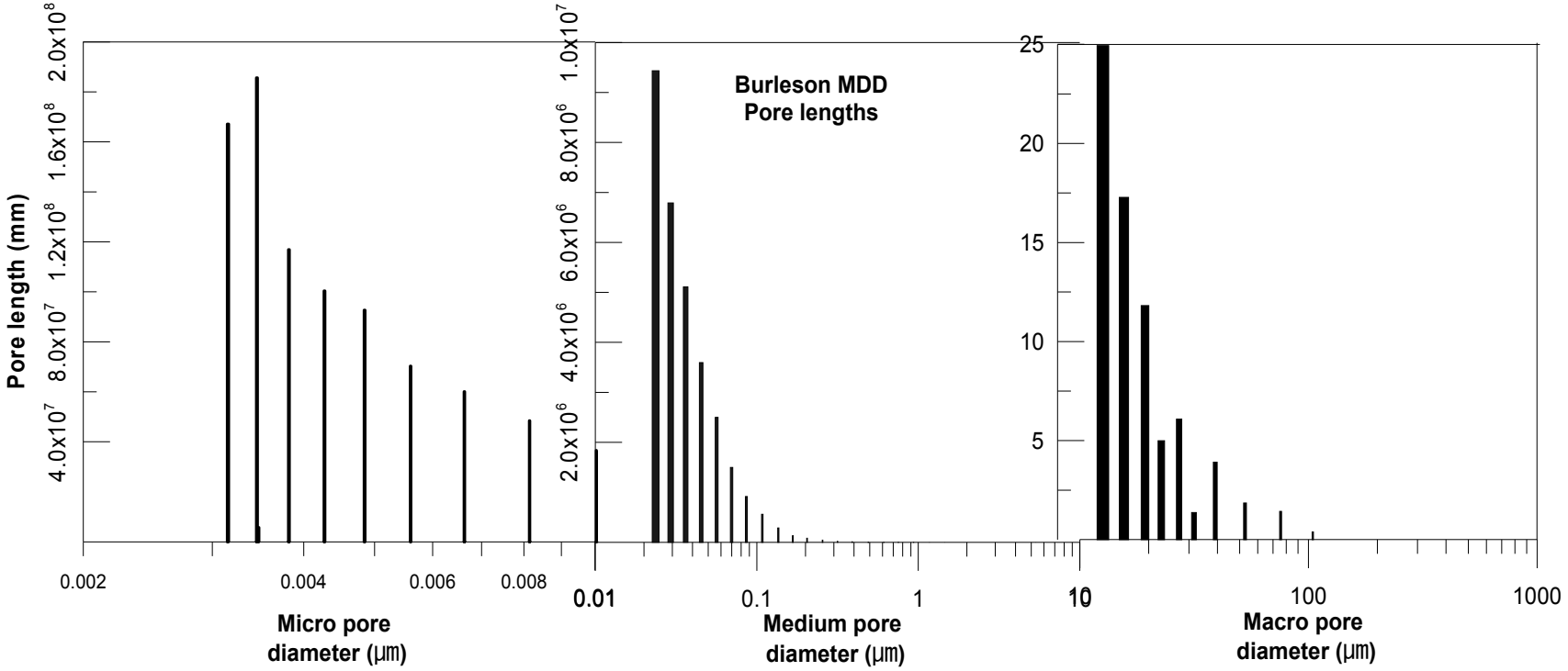

Figure 6.41: Pore length distribution chart for Burleson soil compacted at MDD condition

6.4.3.3 Colorado soil - pore length distribution

The distribution of pore lengths of Colorado soil specimen compacted at 95% MDD is presented in Figure 6.42. In this figure the distribution of pore lengths in macro, medium and macro region of the soil specimen are presented. From the graph the soil specimen had a highest macro pore length of 41 mm at a diameter of 12 μm. Similarly, in the medium pores region a maximum length of $8.2x10^6$ mm is observed at 0.025 μm. The highest length of $2x10^8$ mm is observed at 0.0038 μm in the micro pore region of the soil specimen.

The total pore area from pores determined for compacted Colorado soil at 95% MDD is 13,873 m^2.

Similarly, Figure 6.43 presents the pore length distribution of Colorado soil specimen compacted at MDD condition.

From the graph the soil specimen had a highest macro pore length of 35 mm at a diameter of 12 μm. Similarly, in the medium pores region a maximum length of $9.7x10^6$ mm is observed at 0.025 μm. The highest length of $2.7x10^8$ mm is observed at 0.0031μm in the micro pore region of the soil specimen. The total pore area determined for compacted Colorado soil at MDD is 13,930 m^2.

When compared to the specimen at 95% MDD, the MDD specimen comprised more volume of micro pores than macro pore lengths. The total pore area from MDD condition is higher than at 95% MDD due to larger pore length volume in the micro and medium pore regions.

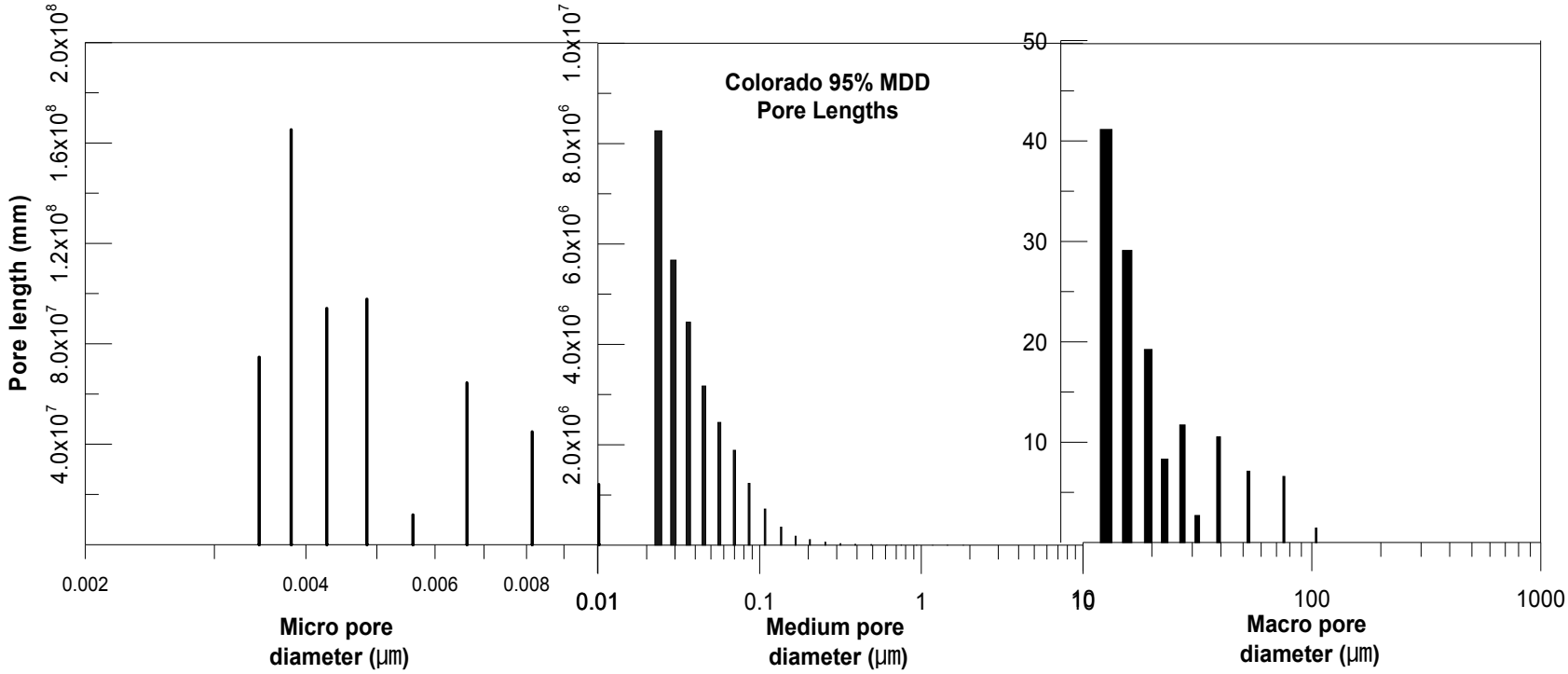

Figure 6.42: Pore length distribution chart for Colorado soil compacted at 95% MDD condition

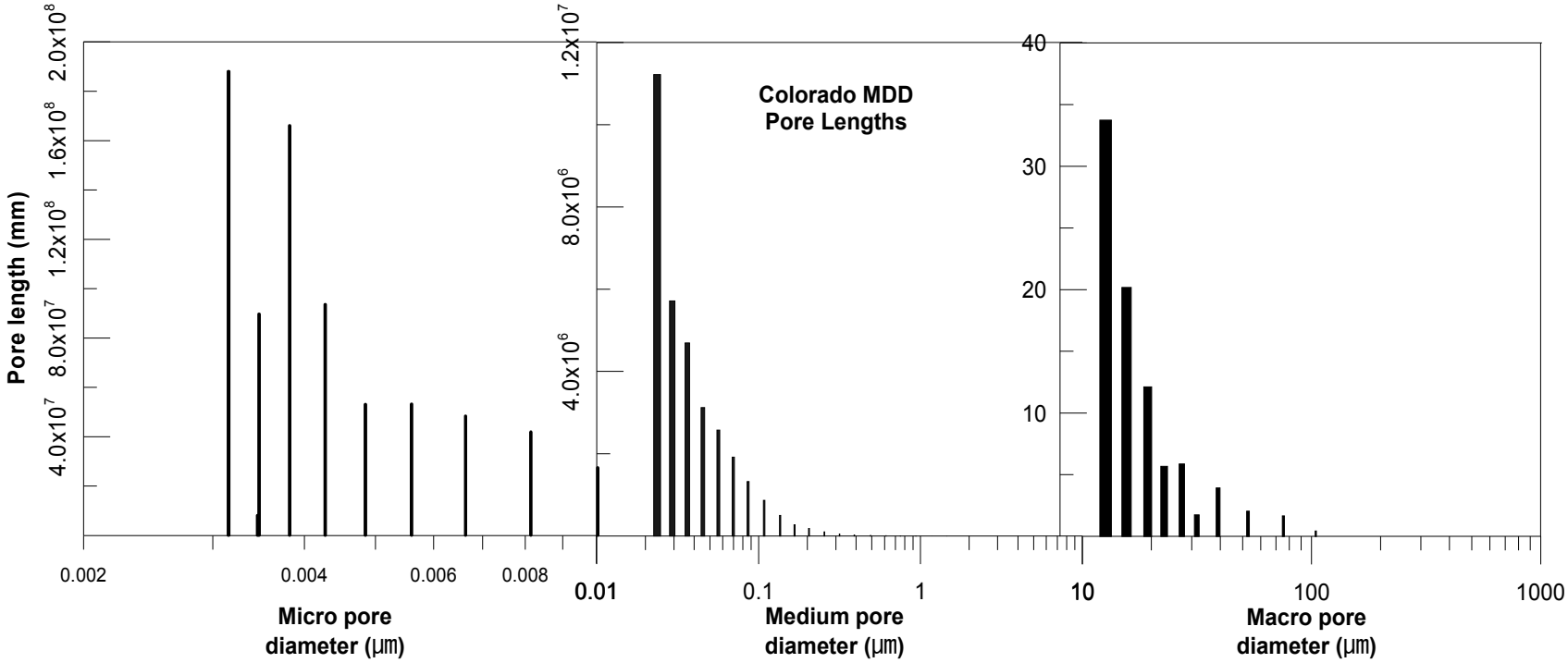

Figure 6.43: Pore length distribution chart for Colorado soil compacted at MDD condition

6.4.3.4 Grayson soil - pore length distribution

The distribution of pore lengths of Grayson soil specimen compacted at 95% MDD is presented in Figure 6.44. In this figure the distribution of pore lengths in macro, medium and macro region of the soil specimen are presented. From the graph the soil specimen had a highest macro pore length of 26 mm at a diameter of 12 μm. Similarly, in the medium pores region a maximum length of $1.3x10^6$ mm is observed at 0.025 μm. The highest length of $2.1x10^8$ mm is observed at 0.0042 μm in the micro pore region of the soil specimen. The total pore area determined for compacted Grayson soil at 95% MDD is 22,130 m^2.

Similarly, Figure 6.45 presents the pore length distribution of Grayson soil specimen compacted at MDD condition.

From the graph the soil specimen has a highest macro pore length of 28 mm at a diameter of 12 μm. Similarly, in the medium pores region a maximum length of $1.5x10^7$ mm is observed at 0.025 μm. The highest length of $3.5x10^8$ mm is observed at 0.0031μm in the micro pore region of the soil specimen.

The total pore area determined for compacted Grayson soil at MDD is 23,711 m^2. When compared to the specimen at 95% MDD, the MDD specimen comprised more volume of micro pores than macro pore lengths. The Grayson soil specimen has the largest pore length in the micro pore region among other expansive clays. This might be due to the large portion of mineral Montmorillonite in the soil's clay fraction.

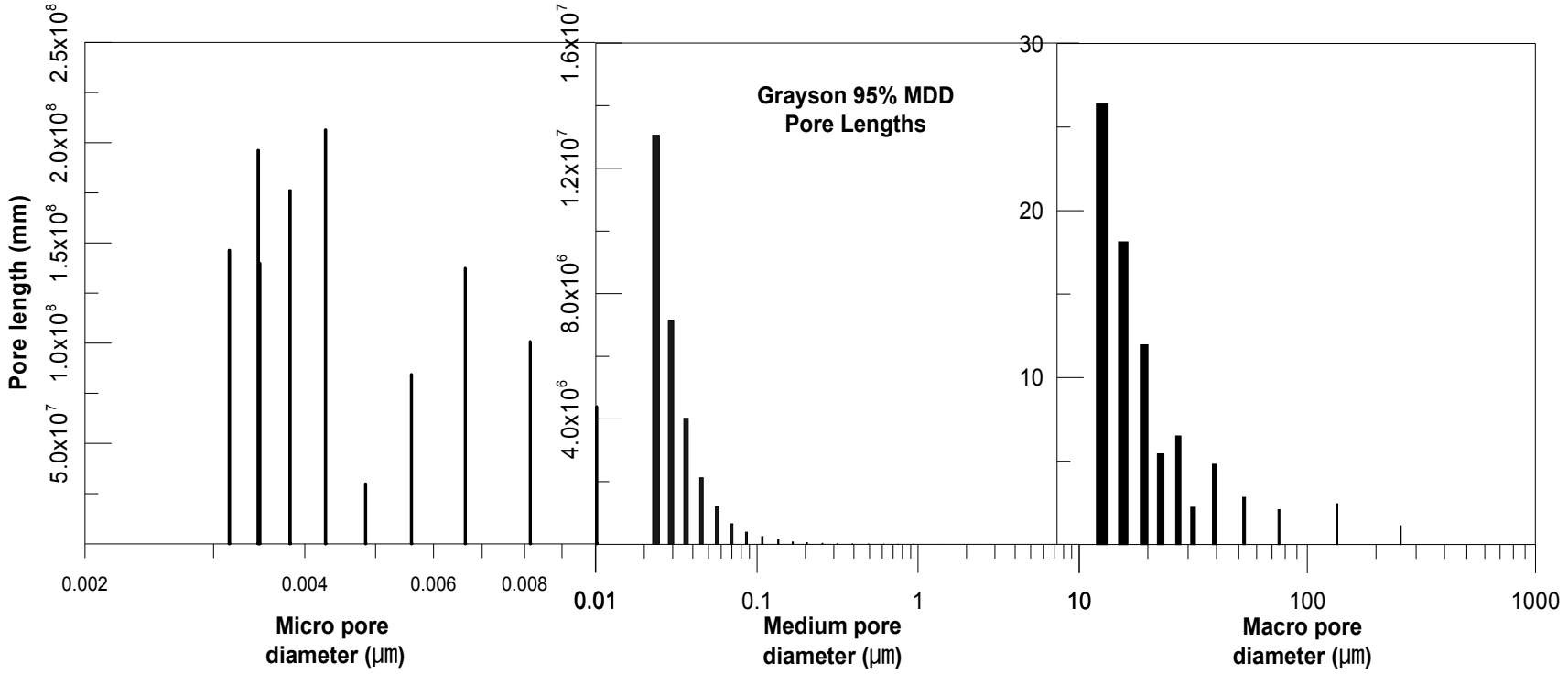

Figure 6.44: Pore length distribution chart for Grayson soil compacted at 95% MDD condition

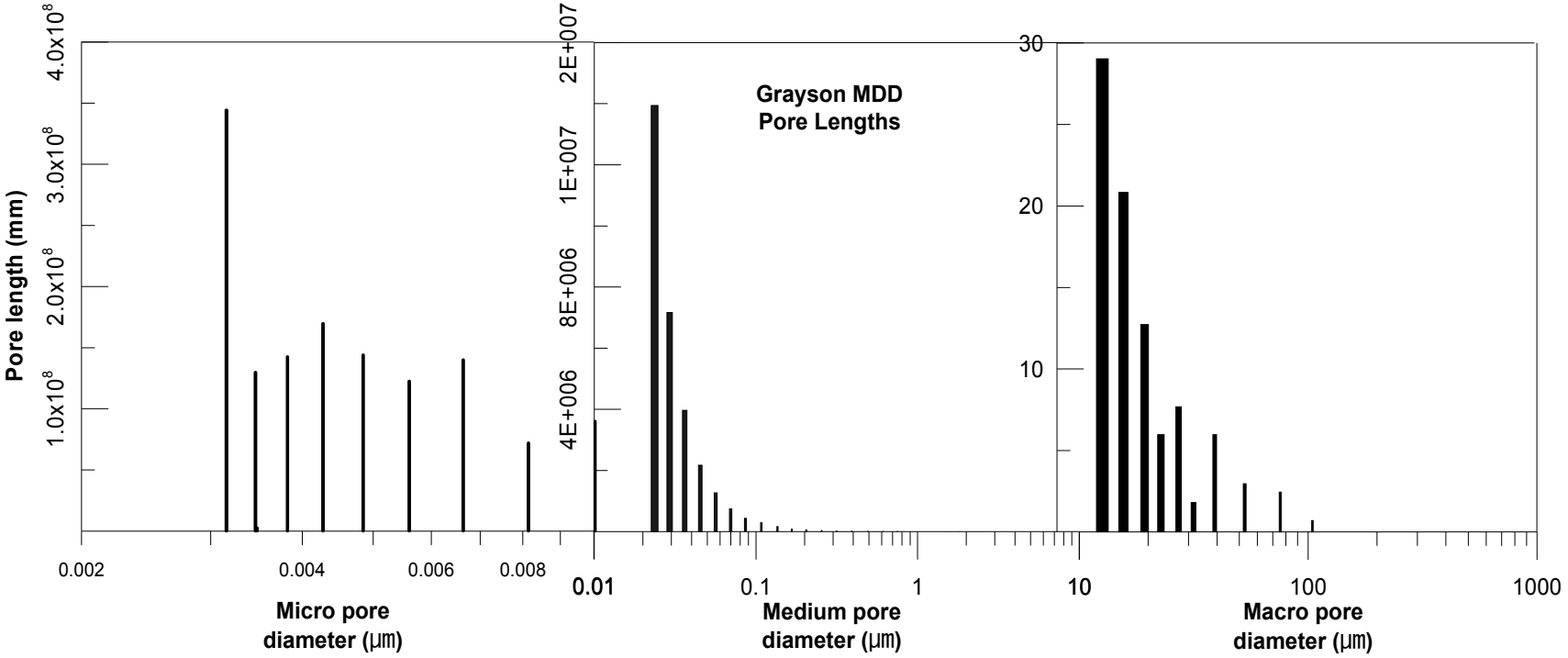

Figure 6.45: Pore length distribution chart for Grayson soil compacted at MDD condition

6.4.3.5 Keller soil - pore length distribution

The distribution of pore lengths of Keller soil specimen compacted at 95% MDD is presented in Figure 6.46. In this figure the distribution of pore lengths in macro, medium and macro region of the soil specimen are presented. From the graph the soil specimen had a highest macro pore length of 31 mm at a diameter of 12 μm. Similarly, in the medium pores region a maximum length of 6 $x10^6$ mm is observed at 0.025 μm. The highest length of $2.5x10^8$ mm is observed at 0.0035 μm in the micro pore region of the soil specimen. The total pore area determined for compacted Keller soil at 95% MDD is 15,519 m^2.

Similarly, Figure 6.47 presents the pore length distribution of Keller soil specimen compacted at MDD condition. From the graph the soil specimen had a highest macro pore length of 19.5 mm at a diameter of 12 μm. Similarly a maximum macro pore length of $6.8x10^6$ mm is observed at 0.025 μm. The highest length of $2.5x10^8$ mm is observed at 0.0035 μm in the micro pore region of the soil specimen.

When compared to the specimen at 95% MDD, the MDD specimen comprised more volume of micro pores than macro pore lengths. The total pore area determined for compacted Keller soil at MDD is 16,416 m^2. There exists a large variation in the total pore area calculated from MDD and 95% MDD.

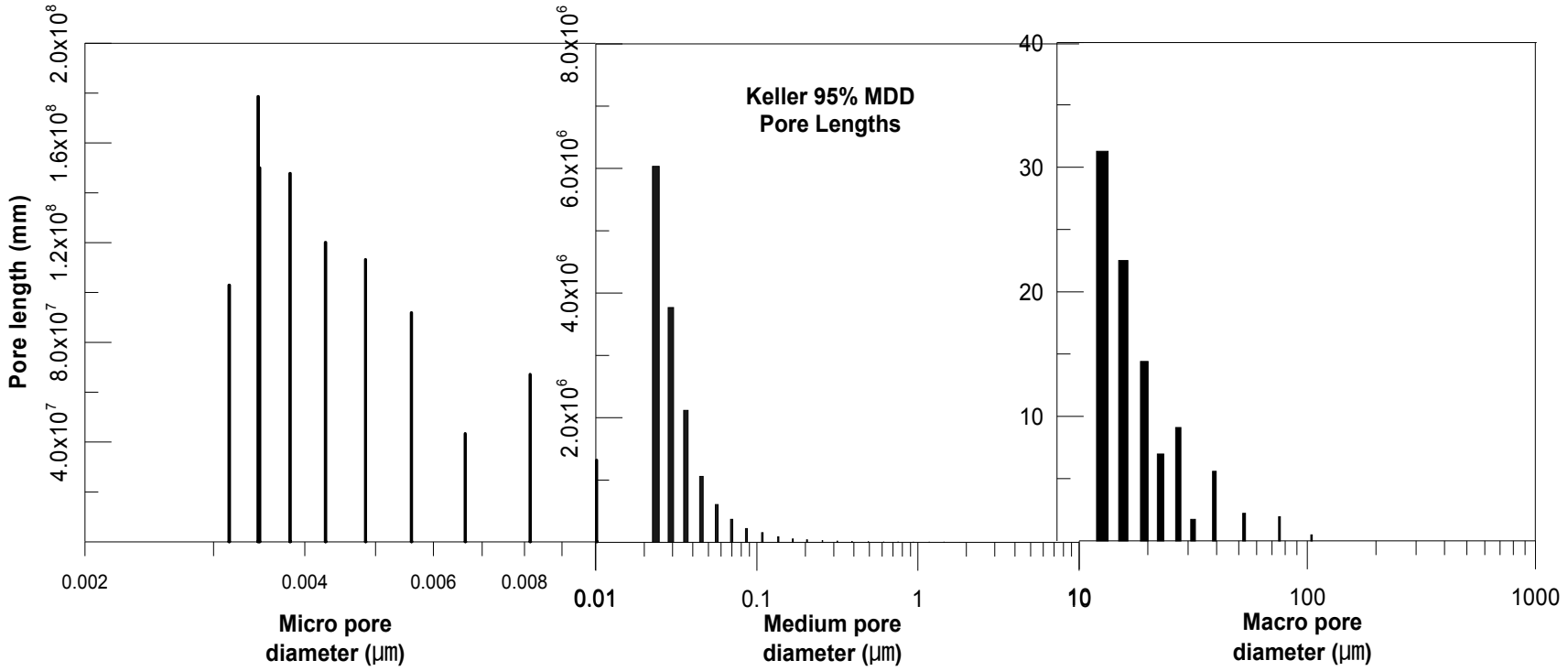

Figure 6.46: Pore length distribution chart for Keller soil compacted at 95% MDD condition

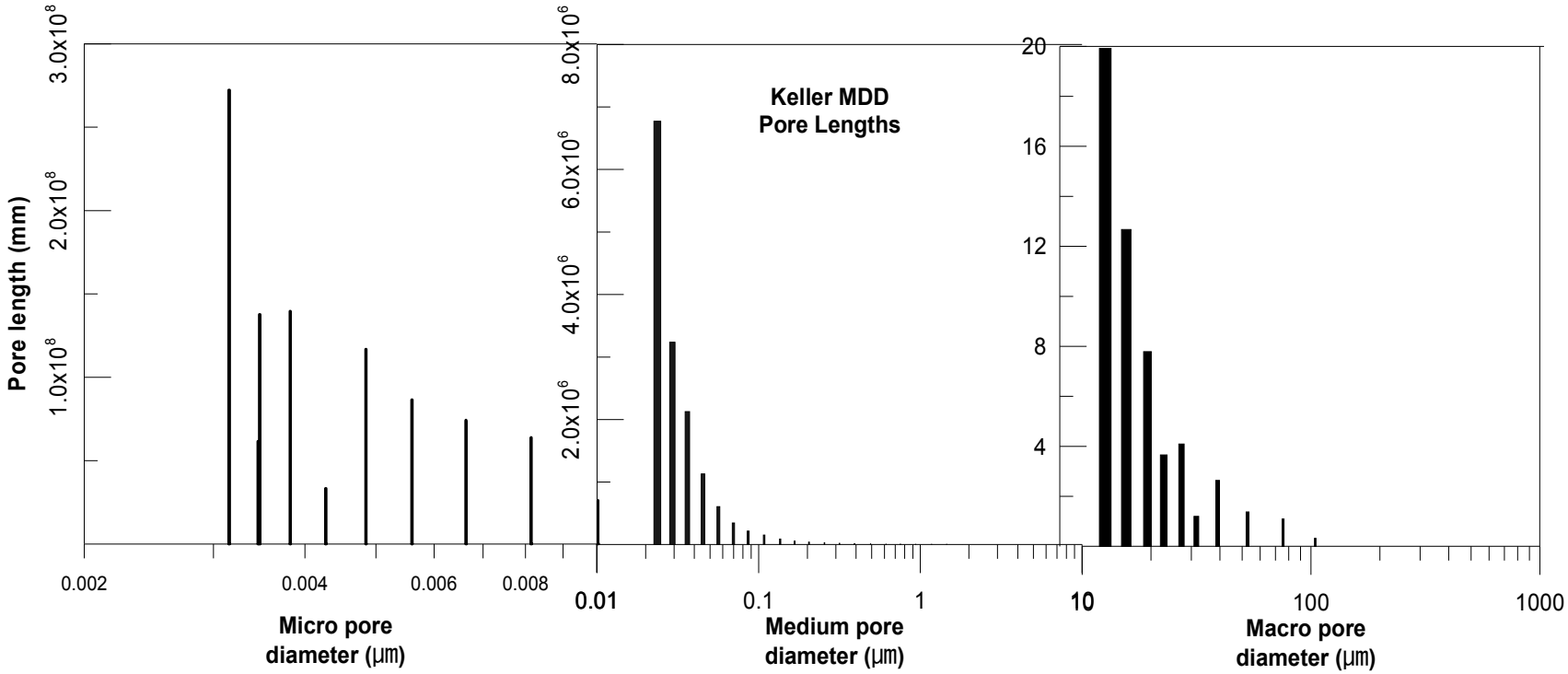

Figure 6.47: Pore length distribution chart for Keller soil compacted at MDD condition

6.4.3.6 Oklahoma soil - pore length distribution

The distribution of pore lengths of Oklahoma soil specimen compacted at 95% MDD is presented in Figure 6.48. In this figure the distribution of pore lengths in macro, medium and macro region of the soil specimen are presented.

From the graph the soil specimen has a highest macro pore length of 20 mm at a diameter of 12 μm. Similarly, in the medium pores region a maximum length of 3 $x10^7$ mm is observed at 0.025 μm. The highest length of $2.5x10^8$ mm is observed at 0.0035 μm in the micro pore region of the soil specimen. The total pore area determined for compacted Oklahoma soil at 95% MDD is 24,998 m^2.

Similarly, Figure 6.49 presents the pore length distribution of Oklahoma soil specimen compacted at MDD condition. From the graph the soil specimen has a highest macro pore length of 9 mm at a diameter of 12 μm. Similarly, in the medium pores region a maximum length of $3x10^7$ mm is observed at 0.025 μm. The highest length of $2.5x10^8$ mm is observed at 0.0031 μm in the micro pore region of the soil specimen.

When compared to the specimen at 95% MDD, the MDD specimen comprised more volume of micro pores than macro pore lengths. The total pore area determined for compacted Oklahoma soil at MDD is 27,222 m^2. There exists a large variation in the total pore area calculated from MDD and 95% MDD.

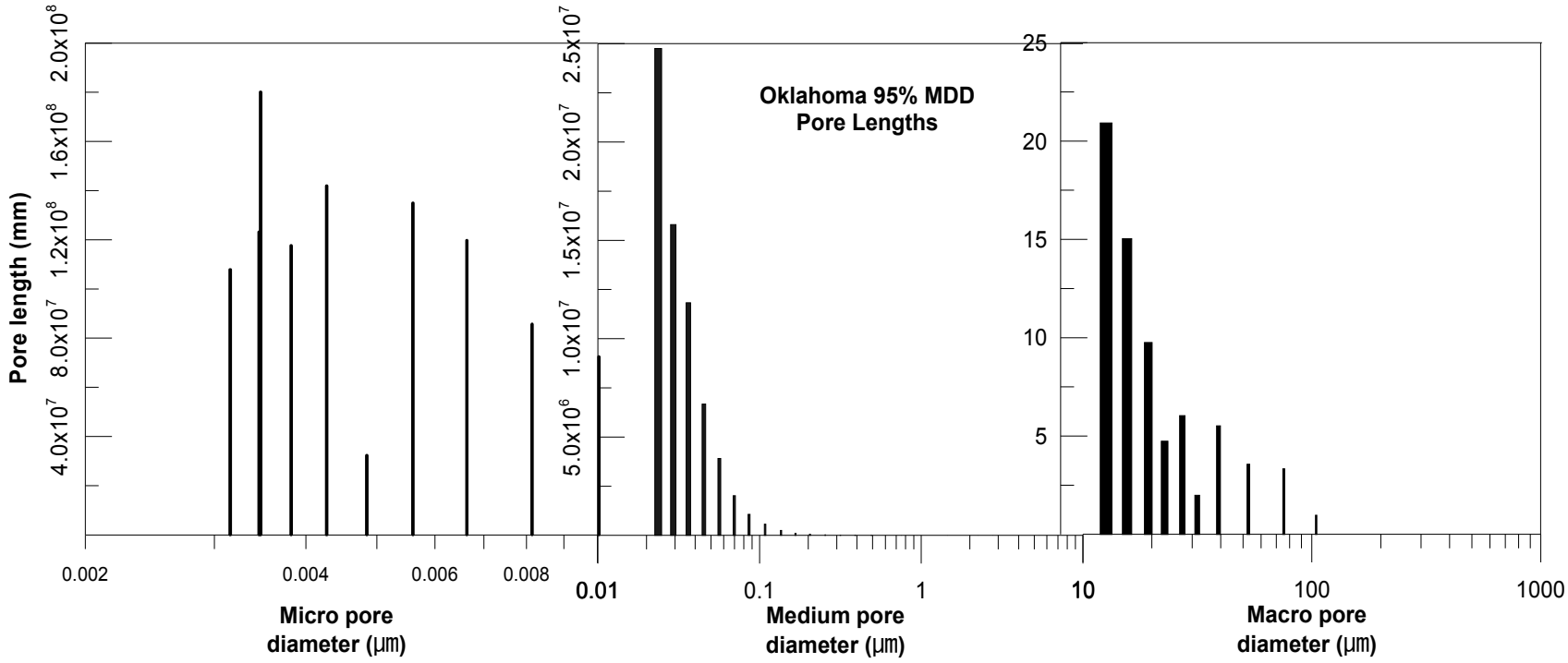

Figure 6.48: Pore length distribution chart for Oklahoma soil compacted at 95% MDD condition

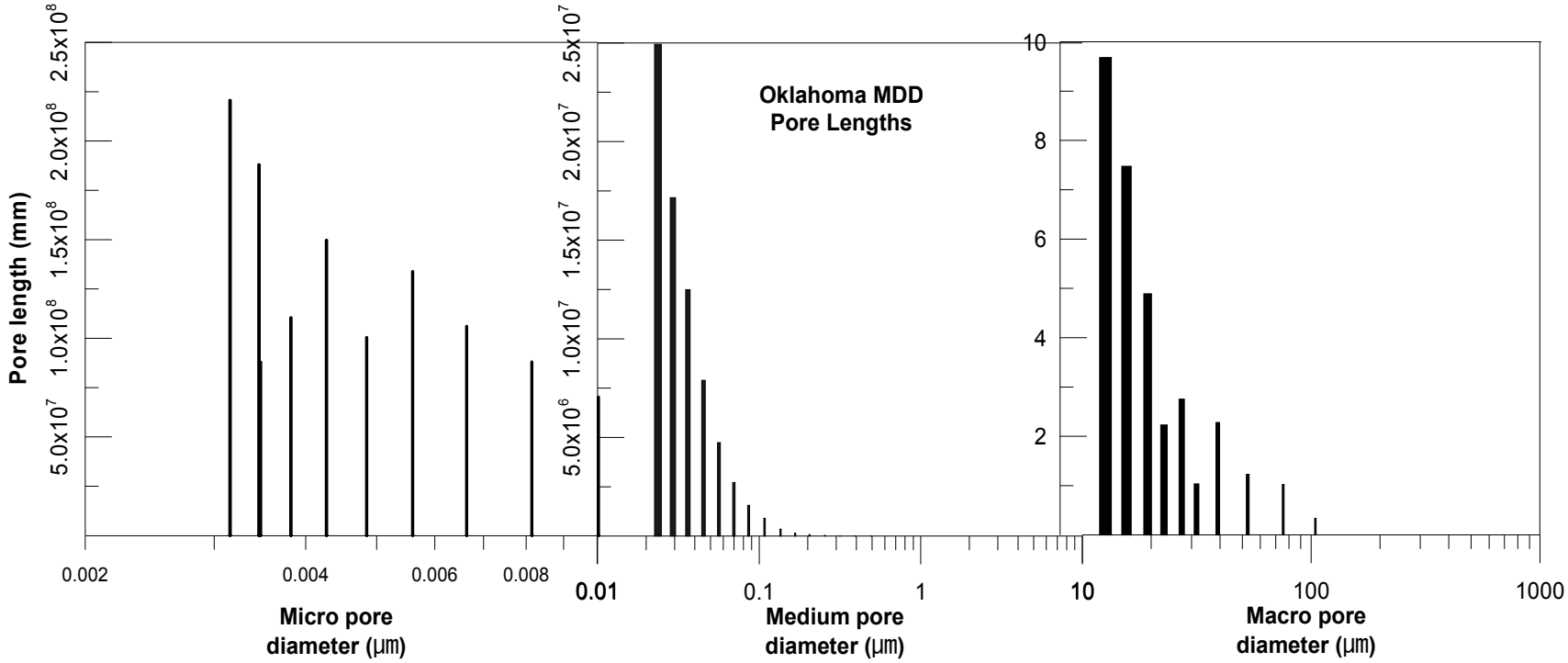

Figure 6.49: Pore length distribution chart for Oklahoma soil compacted at MDD condition

6.4.3.7 San Antonio soil - pore length distribution

The distribution of pore lengths of San Antonio soil specimen compacted at 95% MDD is presented in Figure 6.50. In this figure the distribution of pore lengths in macro, medium and macro region of the soil specimen are presented.

From the graph the soil specimen has a highest macro pore length of 23 mm at a diameter of 12 μm. Similarly, in the medium pores region a maximum length of 1.3 $x10^7$ mm is observed at 0.025 μm. The highest length of $2.5x10^8$ mm is observed at 0.0035 μm in the micro pore region of the soil specimen. The total pore area determined for compacted San Antonio soil at 95% MDD is 19,000 m^2.

Similarly, Figure 6.51 presents the pore length distribution of San Antonio soil specimen compacted at MDD condition. From the graph the soil specimen has a largest macro pore length of 25 mm at a diameter of 12 μm. Similarly, in the medium pores region a maximum length of $1.5x10^7$ mm is observed at 0.025 μm. The largest length of $2.8x10^8$ mm is observed at 0.0035 μm in the micro pore region of the soil specimen.

The total pore area determined for compacted San Antonio soil at MDD is 19,198 m^2. When compared to the specimen at 95% MDD, the MDD specimen comprised more volume of micro pores than macro pore lengths.

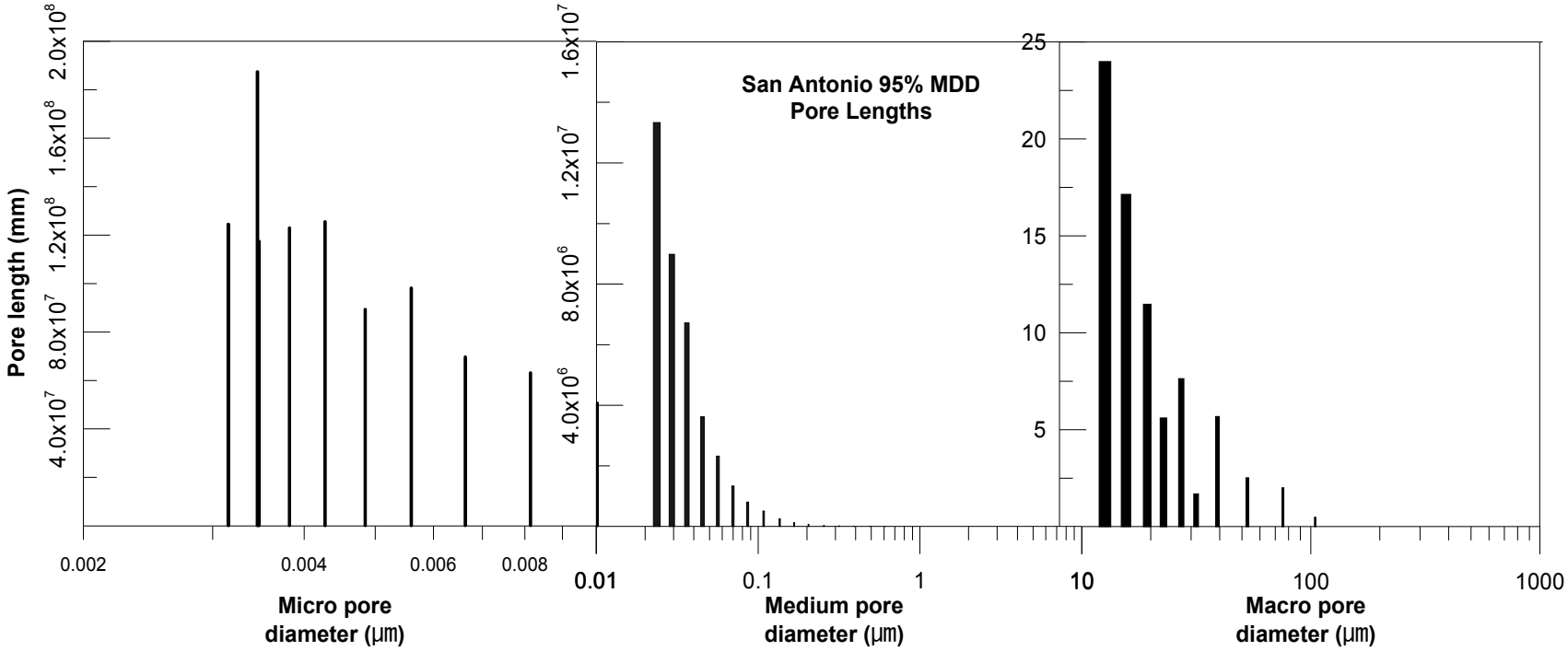

Figure 6.50: Pore length distribution chart for San Antonio soil compacted at 95% MDD condition

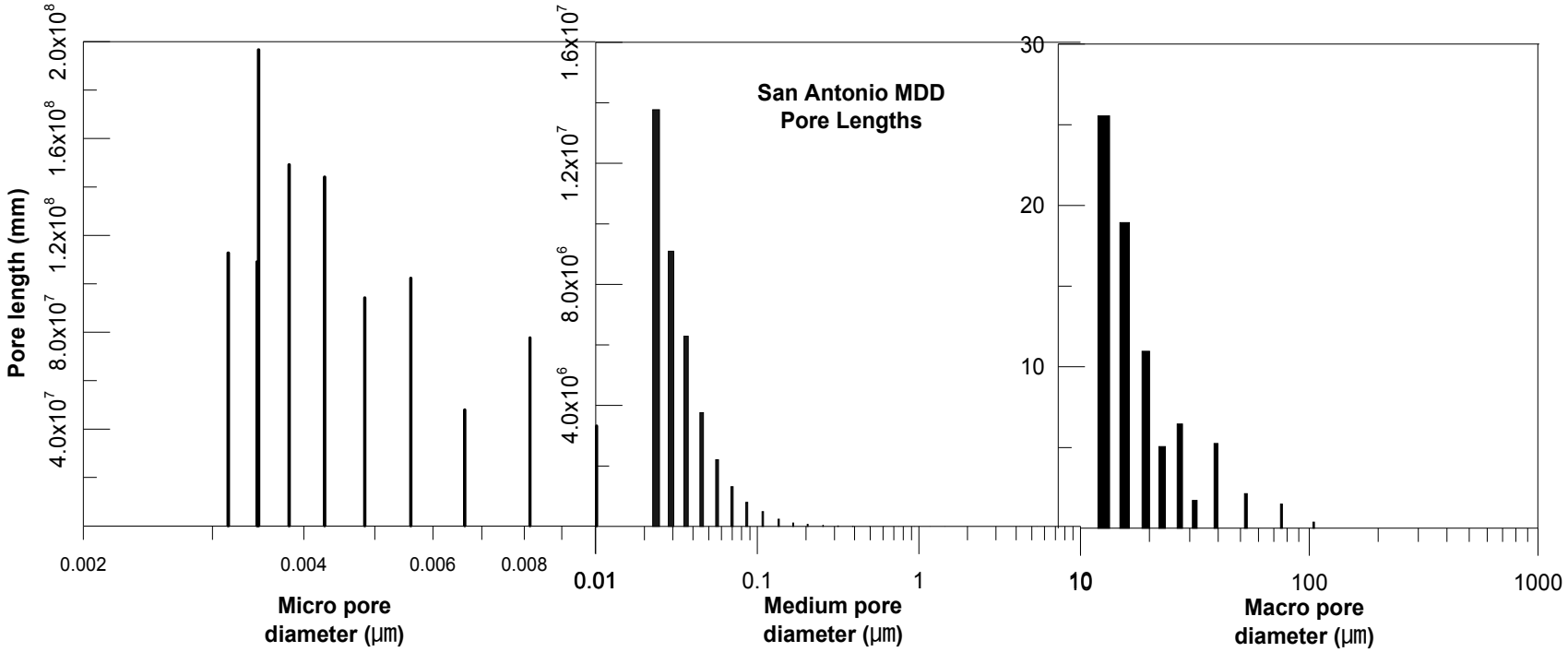

Figure 6.51: Pore length distribution chart for San Antonio soil compacted at MDD condition

6.4.3.8 San Diego soil - pore length distribution

The distribution of pore lengths of San Diego soil specimen compacted at 95% MDD is presented in Figure 6.50. In this figure the distribution of pore lengths in macro, medium and macro region of the soil specimen are presented.

From the graph the soil specimen has a highest macro pore length of 63 mm at a diameter of 12 μm. Similarly, in the medium pores region a maximum length of 5 $x10^6$ mm is observed at 0.025 μm. The highest length of $3x10^7$ mm is observed at 0.0035 μm in the micro pore region of the soil specimen. The total pore area determined for compacted San Diego soil at 95% MDD is 15,880 m^2.

Similarly, Figure 6.53 presents the pore length distribution of San Diego soil specimen compacted at MDD condition. From the graph the soil specimen has a largest macro pore length of 64 mm at a diameter of 12 μm. Similarly, in the medium pores region a maximum length of $5x10^6$ mm is observed at 0.025 μm. The largest length of $7x10^7$ mm is observed at 0.0038 μm in the micro pore region of the soil specimen.

The total pore area from pores determined for compacted San Diego soil specimen at MDD condition is 17,480 m^2. There exists a large variation in the total pore area calculated from MDD and 95% MDD. When compared to the specimen at 95% MDD, the MDD specimen comprised more volume of micro pores than macro pore lengths.

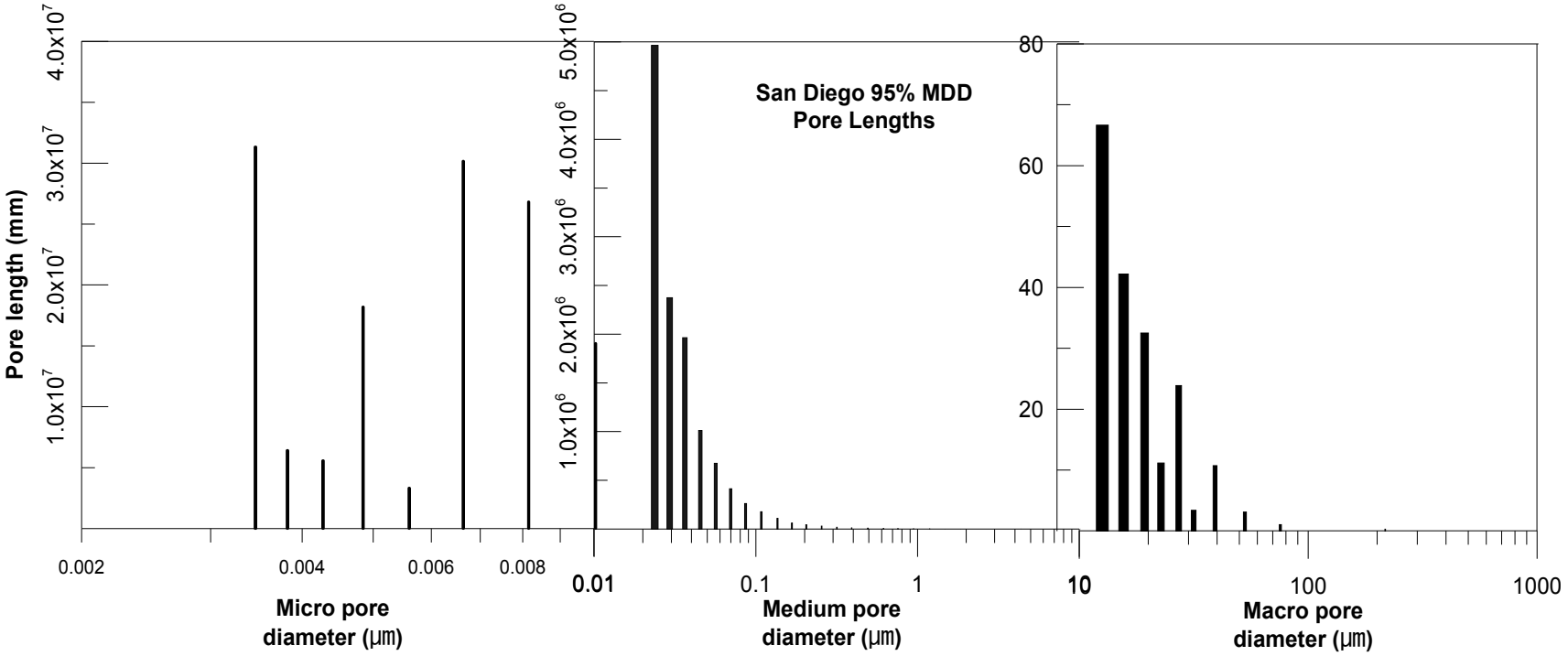

Figure 6.52: Pore length distribution chart for San Diego soil compacted at 95% MDD condition

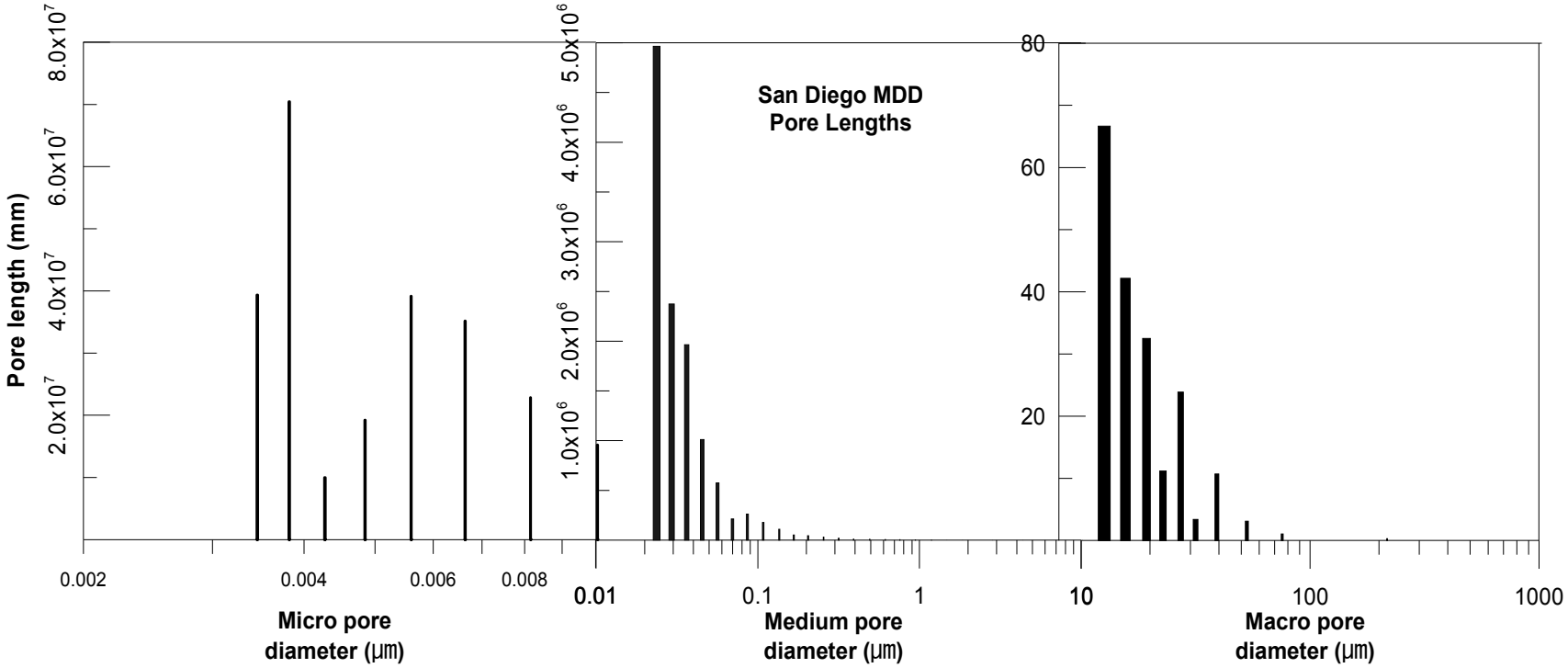

Figure 6.53: Pore length distribution chart for San Diego soil compacted at MDD condition

6.4.4 Total surface area ratio (TSAR):

Surface area of the clay minerals plays an important role on the swelling behavior of expansive clays. The surface area contributed from the total clay minerals represents the amount of moisture absorption capability for a particular clay. This moisture absorption capability is affected severely by the pore distribution and the pore area available within the soil specimen for moisture access to individual clay mineral particles. Hence, the total pore surface area obtained from mercury intrusion porosimetry (MIP) tests are utilized to estimate the pore surface area. A new hypothetical parameter termed as the Total Surface Area Ratio (TSAR) which governs the effects of surface area from clay mineralogy and pore area in a compacted soil specimen is hence formulated in this modeling.

Total Surface Area Ratio (TSAR) is defined as the ratio of total surface area calculated from the clay mineralogy in a soil specimen to the total pore surface area calculated from MIP tests of the same soil specimen. TSAR value for a soil specimen is determined from Eq. 24 shown below.

$$TSAR = \frac{TSA_{CM}}{TPA_{MIP}} \tag{24}$$

Where TSAR is the total surface area ratio, TSA_{CM} is total surface area from clay minerals and TPA_{MIP} is total pore area form mercury intrusion porosimetry studies. The details for the determination of total surface area from both the tests are presented in the previous sections.

Table 6.14 presents the total surface area from clay mineralogy and MIP test which are based on the compacted specimen having a volume of $8.02 \times 10^{-5} m^3$.

Table 6.14: TSAR for expansive clays compacted at 95% MDD condition

Soil	Total surface area from clay mineralogy ($m^2/8.02 \times 10^{-5} m^3$)	Total pore area surface from MIP test ($m^2/8.02 \times 10^{-5} m^3$)	TSAR at 95% MDD
Anthem	4944.7	17165.6	0.288
Burleson	7613.0	15295.2	0.498
Colorado	9871.6	13873.6	0.712
Grayson	14784.9	22130.4	0.668
Keller	5606.9	15519.2	0.361
Oklahoma	2769.6	24998.4	0.111
San Antonio	12205.8	19003.2	0.642
San Diego	2807.0	15880.0	0.177

For soil specimens compacted at 95% MDD condition, the TSAR value is highest for Colorado soil specimen. The lowest TSAR value is observed for Oklahoma clay. The surface area values calculated from the mineralogy were low when compared to the MIP test. The reason could be the non-consideration of surface area from sand and silt particles in the total surface area calculations. Also, the pore surface area calculation assumes that all the pores are cylindrical in shape which is an ideal case.

Table **6.15** presents the total surface area from clay mineralogy and MIP test which are based on the compacted specimen having a volume of $8.02 \times 10^{-5} m^3$.

Table 6.15: TSAR for expansive clays compacted at MDD condition

Soil	Total surface area from clay mineralogy ($m^2/8.02 \times 10^{-5} m^3$)	Total pore area from MIP test ($m^2/8.02 \times 10^{-5} m^3$)	TSAR at MDD
Anthem	5195.0	17964.8	0.289
Burleson	8674.8	15599.2	0.556
Colorado	10432.8	13929.6	0.749
Grayson	15922.2	23711.2	0.672
Keller	5904.1	16416.0	0.360
Oklahoma	2907.1	27222.4	0.107
San Antonio	12906.1	19198.4	0.672
San Diego	2960.4	17480.0	0.169

Similar analysis was attempted for soils compacted at 95% MDD condition, Colorado soil specimen has the highest TSAR value at MDD condition while Oklahoma soil exhibited the lowest value among all soils tested.

The total surface area calculated form clay mineralogy is higher for MDD soil specimen than at 95% MDD condition. The high particle density contributing to more surface area is the major factor governing the surface area. Similarly, high pore area is found in specimens compacted at MDD than at 95% MDD condition due to the presence of large volume of micro pores. The TSAR value for the soil specimens at MDD condition showed a slight increase in values when compared to 95% MDD condition.

6.4.5 TSAR Modeling for 1-D Swell strains:

Once the TSAR ratio values are determined for each compacted soil specimen, these results are compared with the vertical swell strain values of the same soils. The best fit 1-D vertical swell TSAR model for the specimens compacted at 95% MDD is given in Figure 6.54.

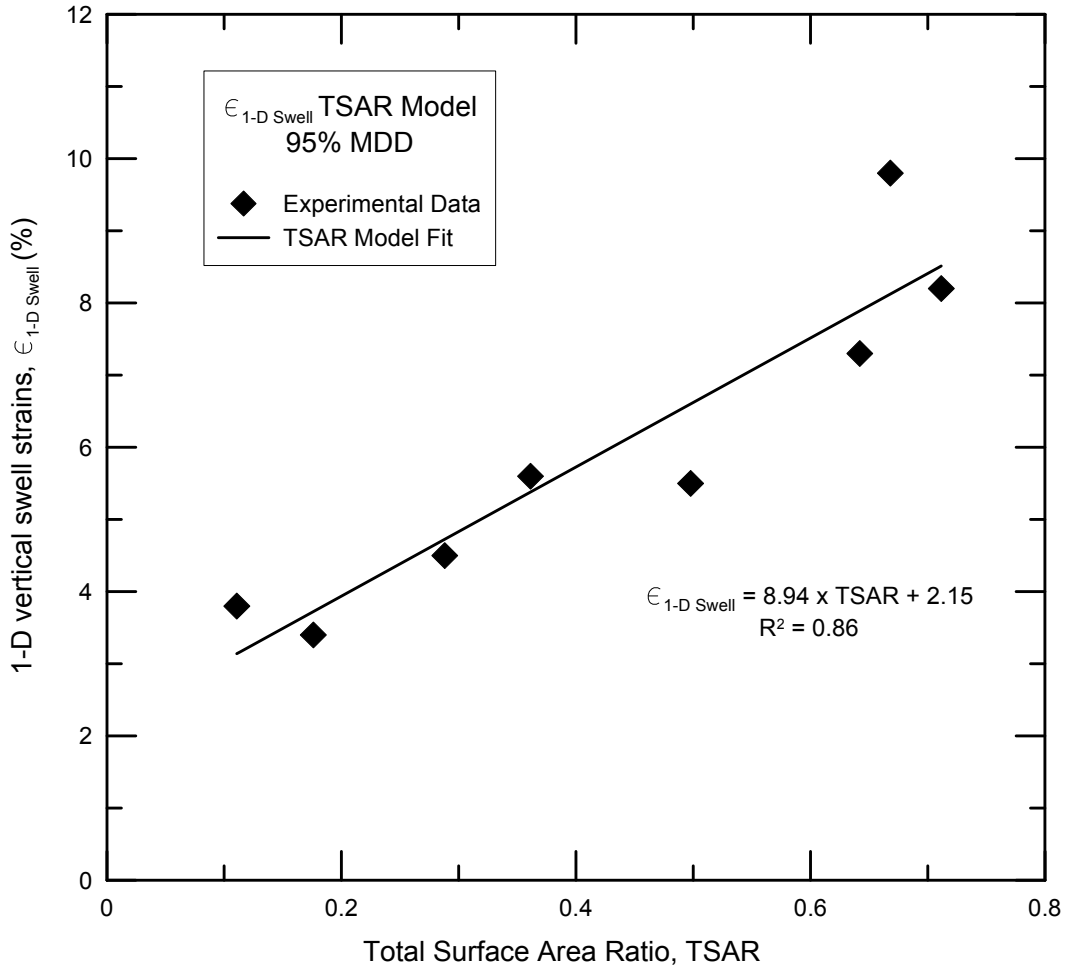

Figure 6.54: 1- D vertical strains TSAR Model for specimens compacted at 95% MDD

The linear curve model that fits best with the experimental data has yielded a coefficient of determination (R^2) value of 0.86. The prediction model is in good agreement with the measured experimental data. Similarly, the best fit 1-D vertical swell strain and TSAR model for the specimens compacted at MDD is given in Figure 6.55.

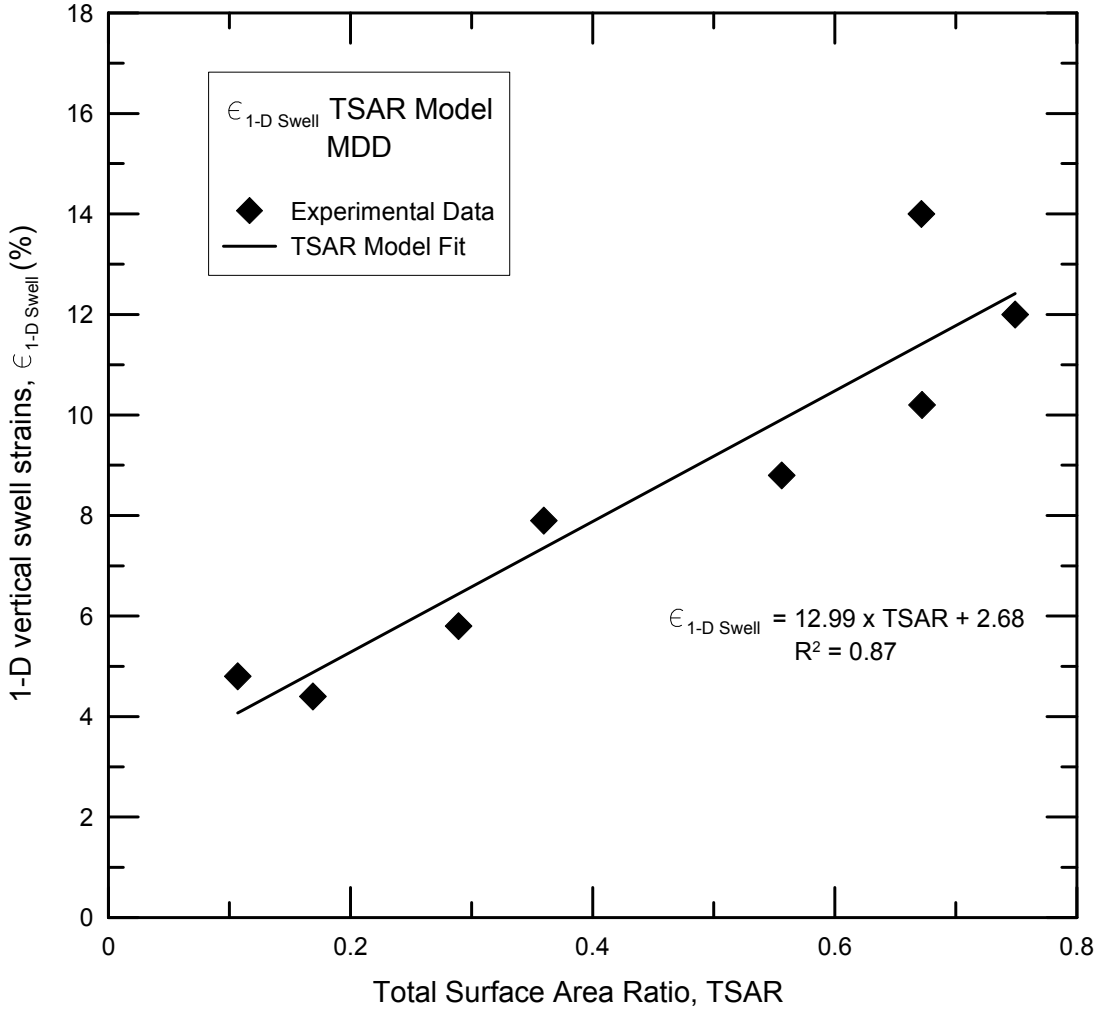

Figure 6.55: 1- D vertical strains TSAR Model for specimens compacted at MDD

6.4.6 TSAR Model for Swell pressure:

Similarly, the TSAR ratio values are compared with the corresponding swell pressure values of the same soils. The best fit swell pressure TSAR model for the specimens compacted at 95% MDD is given in Figure 6.56.

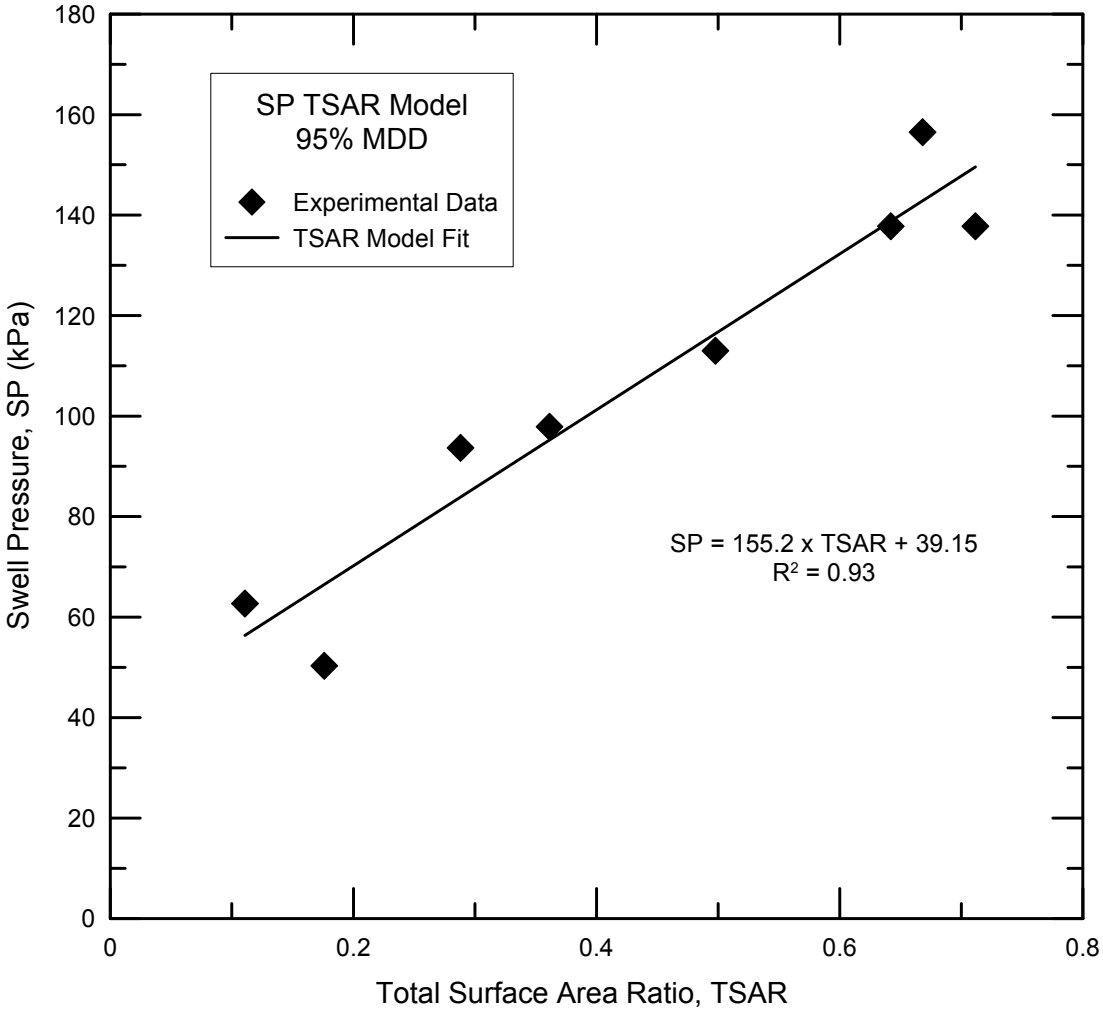

Figure 6.56: Swell Pressure TSAR Model for specimens compacted at 95% MDD

Figure 6.57 presents the same results for MDD condition.

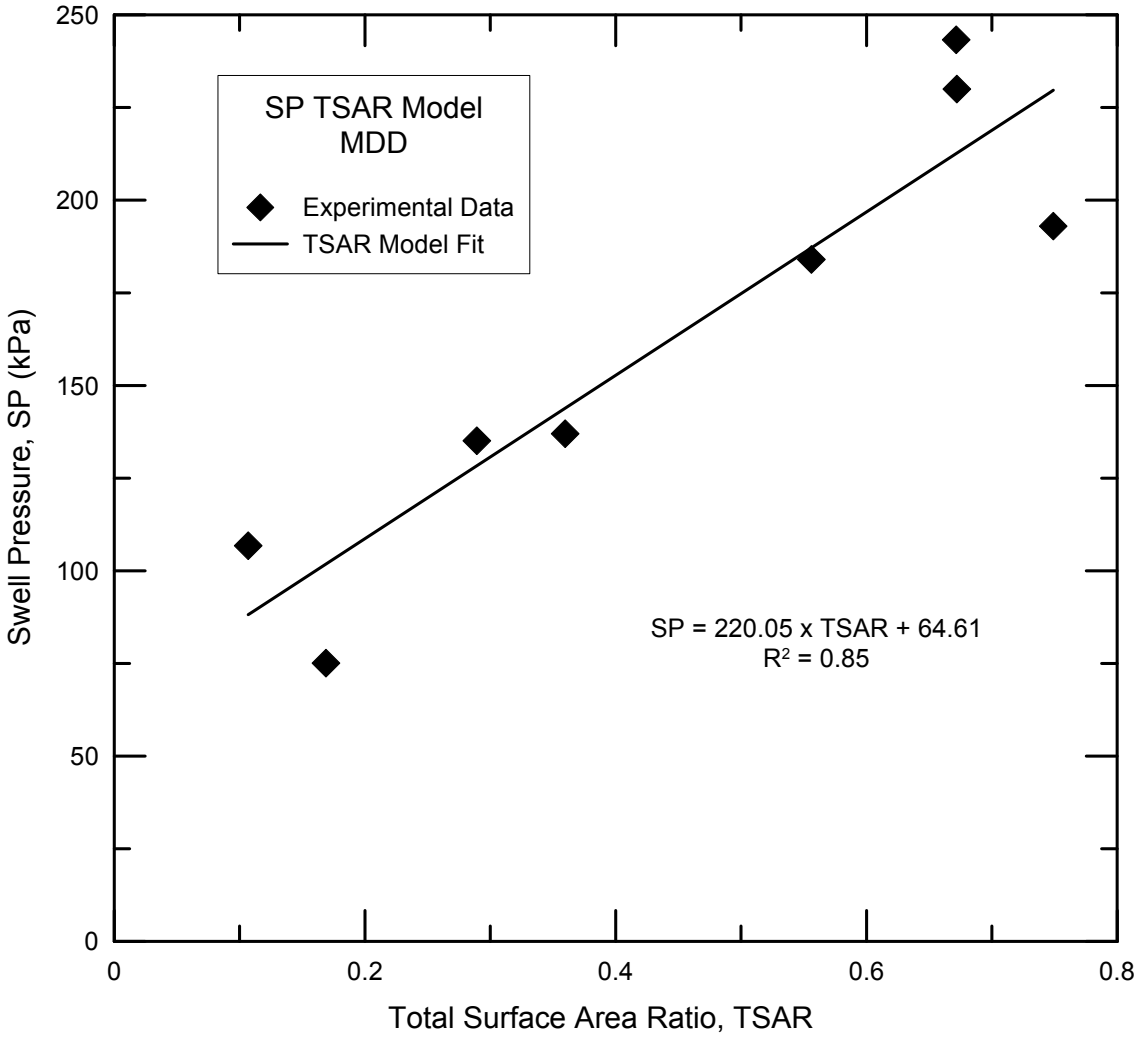

Figure 6.57: Swell Pressure TSAR Model for specimens compacted at MDD

6.4.7 TSAR Model for Volumetric swell strains:

The determination of total surface area from both the tests is presented before. The dimensions of the specimens used for volumetric swell strains were 0.1 m (4 in.) in height and 0.05 m (2 in.) diameter. Table 6.16 presents the total surface area from clay mineralogy and MIP test which are based on the compacted specimen having a volume of 2 x $10^{-4}m^3$. The calculated TSA ratio is also presented in detail.

Table 6.16: TSAR values for expansive clays compacted at 95% MDD

Soil	Total surface area from clay minerals ($m^2/2 \times 10^{-4} m^3$)	Total pore area from MIP test ($m^2/2 \times 10^{-4} m^3$)	TSAR for 95% MDD
Anthem	12754.7	43943.9	0.743
Burleson	21153.5	39155.7	1.383
Colorado	27450.7	35516.4	1.979
Grayson	38133.0	56653.8	1.723
Keller	14453.7	39729.2	0.931
Oklahoma	7134.8	63995.9	0.285
San Antonio	31474.1	48648.2	1.656
San Diego	7233.9	40652.8	0.456

For soil specimens compacted at 95% MDD, the TSAR value was highest for Colorado soil. The lowest TSAR value was observed for Oklahoma clay. The results obtained at MDD were similar to the results obtained for 95% MDD specimens compacted for a volume of 8.02 x 10^{-5} m^3. The values calculated from the mineralogy were low compared to the MIP test. The reason could be the assumption that neglects the surface area occupied by sand and silt particles. Also the MIP test assumes that all the pores are cylindrical in shape which is an ideal case.

The measured swell properties of these soils are compared with their respective TSAR ratio. The volumetric strain of the soil specimens at different confining pressures are presented along with their respective TSA ratio.

The best fit volumetric strain at 7 kPa confinement TSAR model for the specimens compacted at 95% MDD is given in Figure 6.58.

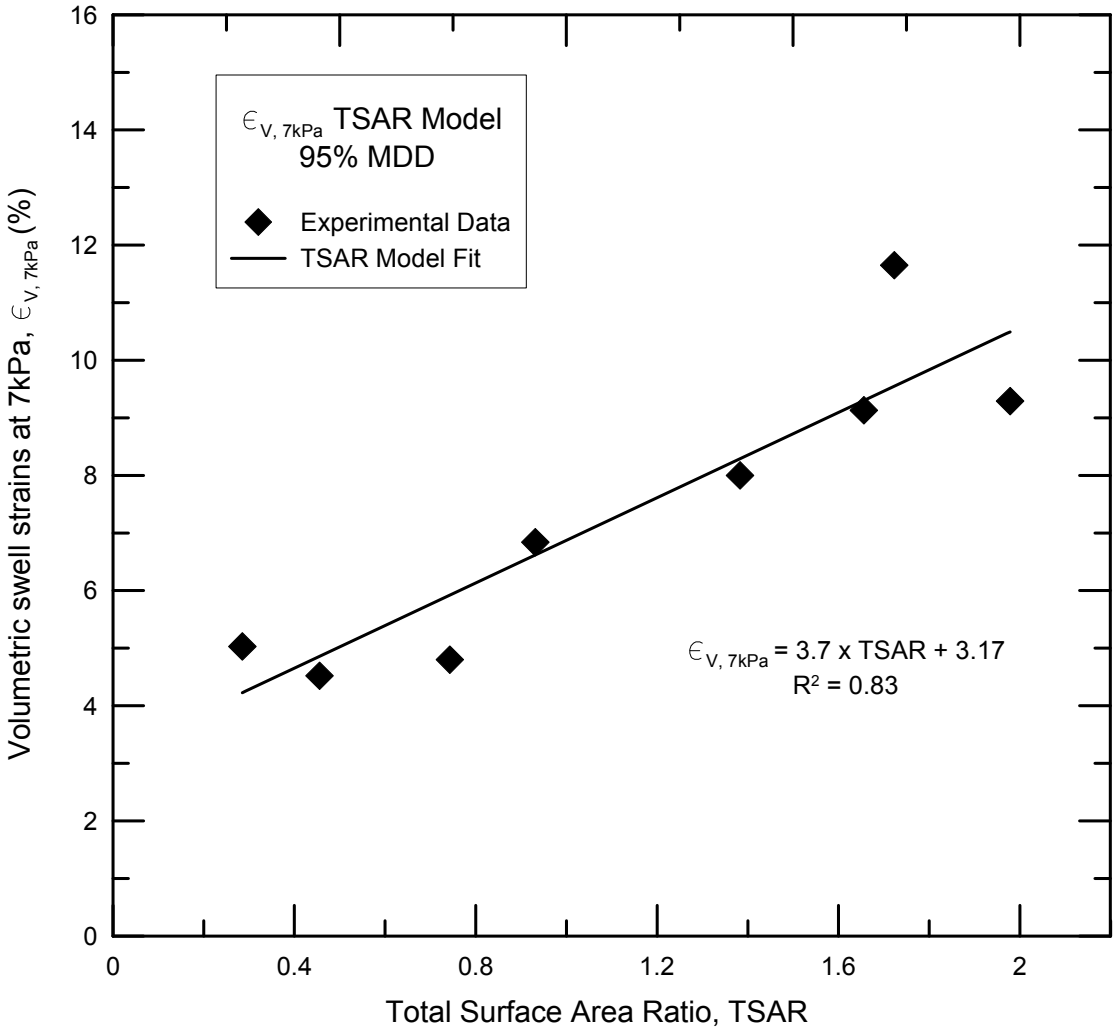

Figure 6.58: Volumetric strain at 7 kPa TSAR Model for specimens compacted at 95% MDD

The fitting model has a coefficient of determination (R^2) value of 0.83. Similarly, the best fit volumetric strain at 50 kPa confinement TSAR model for the specimens compacted at 95% MDD is presented in Figure 6.59.

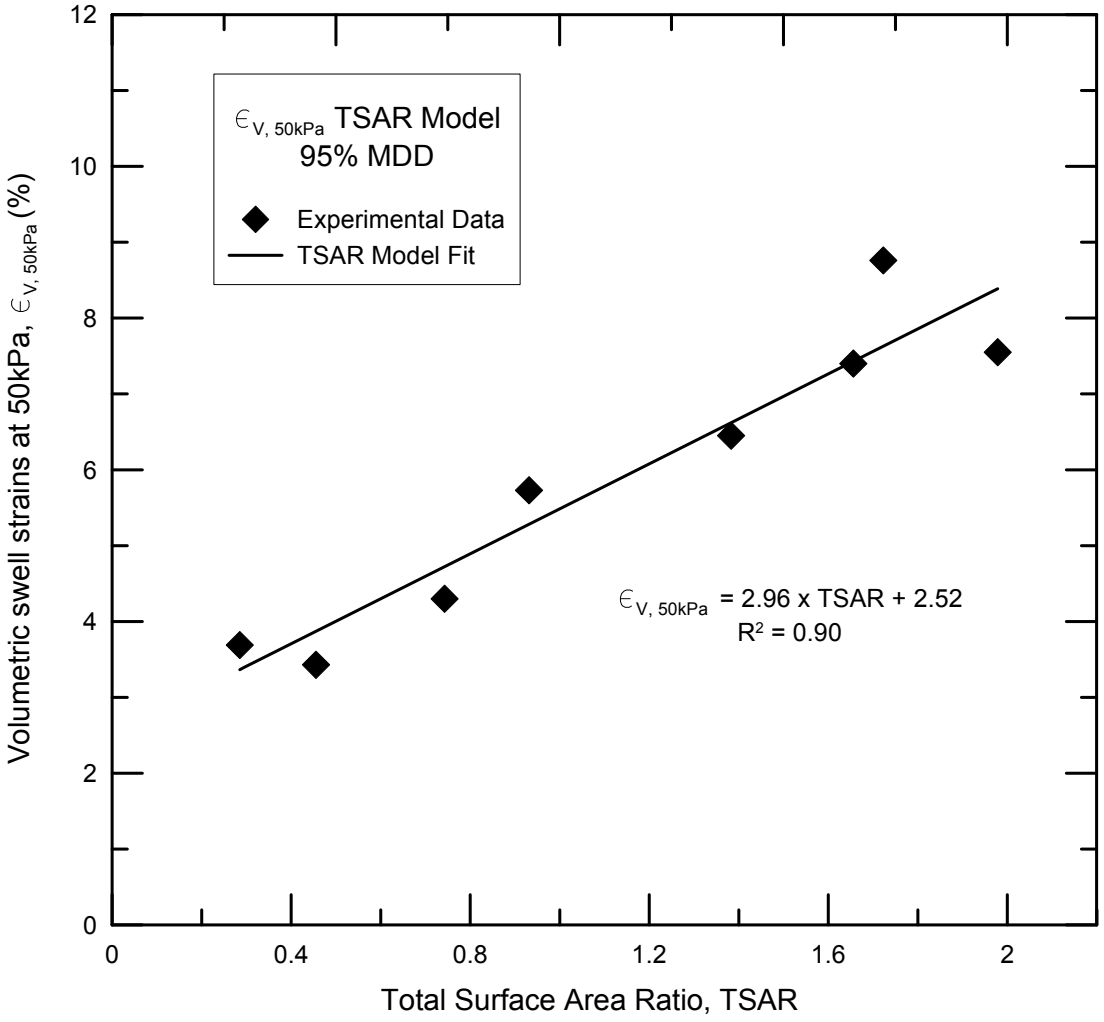

Figure 6.59: Volumetric swell strain at 50 kPa TSAR Model for specimens compacted at 95% MDD

The best fit model has a coefficient of determination (R^2) value of 0.90. The prediction model is in good agreement with the measured experimental data.

Similarly, the best fit volumetric strain at 100 kPa confinement TSAR model for the specimens compacted at 95% MDD is presented in Figure 6.60.

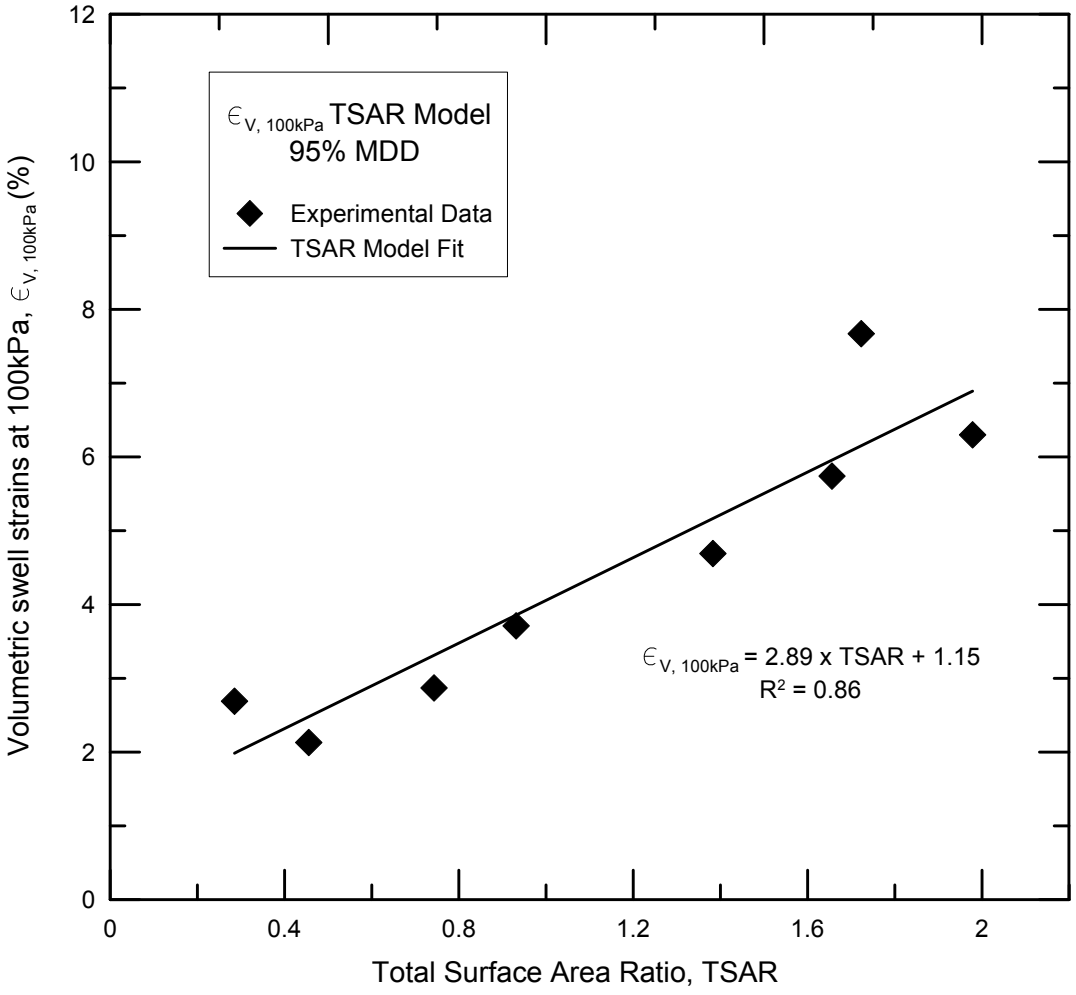

Figure 6.60: Volumetric strain at 100 kPa TSAR Model for specimens compacted at 95% MDD

6.4.8 TSAR model Summary:

The TSAR models for prediction of swell strains and swell pressures provided reliable fitting models for experimental data. It is important to study the TSAR further as several assumptions using MIP data and scaling can result in errors in the estimation of pore surface area. Nevertheless the approach appears to provide reliable results when compared with swell behavior trends. Table 6.17 presents the TSAR models for 1-D swell strain and swell pressures for soils compacted at 95% MDD and MDD conditions.

Table 6.17: Summary of TSAR models for 1 D vertical swell and swell pressures

Model	95% MDD	MDD
1 D Vertical Swell strain ,	$\in_{1-D\ swell}= 8.94\ (TSAR) + 2.15$ R^2 = 0.86, MSE = 0.85	$\in_{1-D\ swell}= 12.99\ (TSAR) + 2.68$ R^2 = 0.87, MSE = 1.84
Swell Pressure, SP (kPa)	$SP = 155.2\ (TSAR) + 39.15$ R^2 = 0.93, MSE = 12	$\in_{1-D\ swell}= 220\ (TSAR) + 64.61$ R^2 = 0.85, MSE = 14

Where TSAR-Total surface area ratio, MSE = Mean Square Error

Similarly, Table 6.18 presents the TSAR models for prediction of volumetric swell strains for soils compacted at 95% MDD and MDD.

Table 6.18: Summary of TSAR models for volumetric swell strains at different confinements

	Confinement levels	TSAR Model	R^2
Volumetric swell ε_v (%)	7 kPa	$\in_{v,7kPa}= 3.7\ (TSAR) + 3.17$ MSE = 1.34	0.83
	50 kPa	$\in_{v,50kPa}= 2.96\ (TSAR) + 2.52$ MSE = 1.45	0.90
	100 kPa	$\in_{v,100kPa}= 2.89\ (TSAR) + 1.15$ MSE = 0.63	0.86

Where TSAR-Total surface area ratio, MSE = Mean Square Error

The models for volumetric swell strain prediction show good fit with the measured swell strains. The multiplication factor and addition factors of the models decreased consistently with increase in confinement pressures.

6.5 Summary

The present chapter details the formulation of three swell prediction models based on soil composition and unsaturated soil properties. The first model termed as the DDLS model was based on the diffused double layer theory. These model predictions are in good agreement with the actual measured swell potential for the eight expansive clays. Two correction factors which govern the DDL model are introduced within the current study. These factors are based on independent parameters like the compaction type, hydration of clay particles and initial specimen conditions.

The second model named MHC was based on two swell governing parameters which are Mechanical hydro variation and chemical behavior. These two parameters are coupled to a unified Mechanical Hydro Chemical Parameter (MHCP), which constitutes the effect of soil matric suction, void ratio change and clay mineralogy. The model showed reliable predictions which matched with with the measured swell properties. The present model study was conducted on soil specimens compacted at 95% MDD condition. Similar predictions are expected for soil specimens compacted at MDD condition.

The final model called the TSAR model was based on the ratio of total surface area estimated from clay mineralogy data and mercury intrusion porosimetry results. The model showed good validation results with prediction matching with measured swell test results. It should be noted that the present model provides good results when TSAR values lie between 0.2 and 2. Experimental studies on more clay types are required to map the overall variation of swell behavior with a wider range of TSAR values.

The next chapter details the summary and conclusions of the swelling behavior of expansive soils and the prediction models formulated in this chapter.

CHAPTER 7

SUMMARY OF FINDINGS AND FUTURE RECOMMENDATIONS

7.1 Introduction

Swell behavior of expansive soils has been studied by many researchers and different correlations have been formulated over the past few years. Understanding the unique characteristics of expansive soils and studying their dependency on the basic soil composition properties is the main focus of the present research.

A total of eight natural expansive soils collected from, central southern and south western parts of the United States are studied for this research. Once the basic soil classification is conducted, swell behavior of these expansive clays under different compaction conditions are performed. The soils are studied under different initial conditions like compaction dry density, confining pressures and type of testing. A novel three dimensional swell strain measurement apparatus is introduced in the current research to determine swell strains at different confining pressure values.

Unique soil composition parameters that govern the swell behavior of expansive clay have been identified and studied using techniques like clay mineralogy, soil-water characteristic, mercury intrusion porosimetry and X-ray Tomography. Three swell prediction models have been introduced in the current research based on soil composition parameters like mineralogy, total surface area and matric suction properties.

The first model is based on the diffused double layer water induced soil swell theory which emphasizes on the attraction of water molecules adhering to the surface of the clay minerals thus resulting in the swelling of soil mass. The second model is based on the

Mechanical, Hydro, and Chemical properties governing the swell behavior of soil. Clay mineralogy and soil water characteristic related soil parameters are the governing parameters in this model. The third model is based on the total surface area present in the soil specimen. The total surface area measured from clay minerals and the total pore area measured from mercury intrusion porosimetry studies are the governing parameters in this model.

7.2 Summary of Findings

From the above swell and soil composition studies conducted, findings are presented in the following sections. The following lists the major findings obtained from the present research.

7.2.1 Findings from Soil composition, swell behavior and pore distribution studies

1. Basic soil classification studies on all the eight expansive clays were performed and results from the plasticity indices show that Grayson soil exhibited a high PI value while Keller soil attained the least value. Grain size distribution analysis on these soils revealed that Grayson soil has the highest amount of clay fraction while San Diego soil has the least amount.

2. The mineral contents of the expansive clays are determined using standard chemical analyses methods. From the results, Grayson soil exhibited the highest Montmorillontie mineral content in its clay fraction. Similarly, Oklahoma soil had the highest Illite mineral content and Keller soil has the highest Kaolinite content in the respective clay fraction.

3. From the swell test results, it was found out that the soil exhibiting the maximum swell strains was Grayson soil and the one exhibiting the least swell strains was San Diego soil. The soils exhibiting maximum swell strains (Grayson) also showed a higher swell pressure due to the presence of high Montmorillonite content. Soils compacted at maximum dry density (MDD) condition showed higher swell strains and swell pressures due to the presence of more soil particles and mineral content than than the soil samples compacted at 95% MDD condition.

4. 3-D swell strain tests conducted with a novel test apparatus produced results that are comparable with the 1-D vertical swell strain test results. The measured radial strains are low when compared to the measured vertical strains of the same soil specimen. This reduction in

radial swell strains is attributed due to the large height/diameter ratio of the specimen and also the direction of compaction of the soil specimen. Grayson soil showed the highest volumetric swell strains and San Diego soil exhibited the lowest swell strains at all confining pressures. As the confining pressure applied to the soil specimen has decreased swell strains in soils. Also, it was observed that with an increase in Montmorillonite mineral content, the soils exhibited higher volumetric swell strains.

5. Soil water characteristic curves obtained for all the soils using standard laboratory techniques. Burleson and Colorado soils exhibited large air entry suction value among other soils whereas Keller soil exhibited low air entry values.

6. SWCC's determined for all the eight expansive soils are analyzed using commonly used Van Genuchten and Fredlund & Xing models. Anthem soil has the highest 'a' parameter from Van Genuchten model whereas Colorado soil has the lowest 'a' value. Similarly, parameters 'n' and 'm' from Van Genuchten model are highest for Keller soil. For the Fredlund and Xing fitting model, 'a_1' parameter was highest for Burleson and Colorado soils. Similarly, 'n_1' parameter was highest for Colorado soil and least for Anthem and San Diego soils. The 'm_1' parameter was the highest for Burleson and Grayson soils. Parameters n, m, n_1, and m_1 from both Van Genuchten and Fredlund and Xing models did not exhibit any variation with changes in clay fraction or percent mineral Montmorillonite. This could be due to the dependency of SWCC on grain size distribution, rather than the degree of expansion of a soil or the presence of a clay mineral.

7. Mercury intrusion porosimetry studies revealed the internal pore size distribution in a soil specimen. It was found that the variation of dry density and moisture content of soils had a major influence on the pore distribution of the soil specimen. The volume of micro pores is found to be more in specimens compacted at MDD than specimens compacted at 95% MDD. Similarly, macro pore volume is found to be higher in the case of 95% MDD compaction condition than at MDD condition. The high compaction level at MDD condition packs the soil

particles together thereby increasing the micro pore volume and decreasing the macro pore volume when compared to 95% MDD condition.

8. All the soil specimens compacted at various dry density conditions were studied using X-ray Tomography test. The output images from tomography are analyzed using pixel count code in MATLAB software. The void ratio calculated from XCT technique is in good agreement with weight-volume relationships at both dry density conditions. At the saturation level, all the soils showed a decrease in void ratio when measured with X-ray computed tomography test. This is due the fact that the free expansion of soil particles was neglected during the measurement of void ratio from weight/volume relationships; the predicted void ratio was high. The XCT technique assisted researchers in identifying the actual void space available after the swelling of the soil specimen.

7.2.2 Findings on analytical models based on soil composition parameters

1. Summary of Diffused Double Layer model (DDL):

Diffused double layer theory provides a strong foundation for the swell prediction model and shows a good fit of measured swell data for all the eight soils studied in the present research. Two correction factors ‘a’ and ‘b’ are introduced in this model which governs the behavior of the model.

i. The correction factors available from this model are dependent on many independent parameters like particle arrangement during compaction, moisture access to the clay particles and direction of particle swelling
ii. The ‘a’ and ‘b’ correction parameters in the equations increased from 95% MDD to MDD condition for both 1 D swell strain and swell pressure models.
iii. The 3-D swell strain model showed a decreasing trend for both ‘a’ and ‘b’ parameters with an increase in confinement levels.

2. Summary of Mechanical Hydro Chemical model (MHC):

The MHC models for the prediction of swell strains and swell pressures provided reliable results. A new parameter which couples the combined effects of mechanical, hydro, and chemical related properties of an expansive soil has been introduced and this parameter was termed as 'MHCP'.

i. The MHCP parameter is highest for Grayson soil and least for San Diego soil.
ii. The present MHCP values were obtained for soil specimens compacted at 95% MDD. Similar, variation of the model results are assumed for specimens compacted at MDD condition.

3. Summary of Total Surface Area Ratio model (TSAR):

The TSAR models for prediction of swell strains and swell pressures provided reliable fitting of the experimental data. However, further study on the TSAR is required as several assumptions using MIP data and scaling can result in errors in the estimation of pore surface area. Nevertheless the approach appears to provide reliable results when compared with swell behavior trends.

i. Large pore area is available within the soil specimens compacted at MDD condition than at 95% MDD condition due to the presence of more micro pore volume. The TSAR value for the soil specimens at MDD condition showed a slight increase when compared to the same at 95% MDD condition.
ii. The surface area values calculated from the mineralogy were low compared to the MIP test. The reason could be the non-inclusion of surface area from sand and silt particles in the total surface area calculation.
iii. At both dry density conditions, the TSAR value is highest for Colorado soil. The lowest TSAR value is observed for Oklahoma clay.
iv. The present model is valid between TSAR values of 0.2 to 2. Studies on more clay types are required to map the overall variation of swell behavior with TSAR values.

7.3 Future Recommendations

Three swell prediction models have been formulated and discussed in the present research study. All the three models showed a good validity with the measured swell data. But each model has their own limitations based on their assumed boundary conditions. Hence in order to comprehensively map any expansive clay's swelling behavior the following future recommendations are suggested.

1. The consideration of wetting curve from the SWCC will provide better insights into the swell prediction model analysis.

2. X-ray Tomography studies are to be conducted on specimens at different levels of moisture contents in order to map the variation of void ratio with moisture content for different types of clays.

3. Correction factors 'a' and 'b' from DDL model are to be standardized by comprehensively studying them at different compaction levels and moisture access theories.

4. Slope of logarithmic matric suction to void ratio plot plays an important role in the swelling behavior. Usage of tomography studies to measure the actual void ratio in a soil specimen would result in more accurate swell behavior predictions.

5. TSAR model is valid only from 0.2 to 2. Hence, studies on wide ranges of clay types are required to map the overall variation of swell behavior with TSAR.

6. Focus on a unified model based on the above three models might result in a more accurate prediction of swell behavior from soil composition studies.

REFERENCES

1. Abduljauwad. (1993). "*Study on the performance of calcareous expansive clay.*" Bulletin of the association of engineering geologists, vol. 30(4), pp. 481-498.
2. Agus, S.S., Leong, E.C., and Rahardjo H. (2001). "*Soil-water characteristic curves of Singapore residual soils.*" Geotechnical and Geological Engineering, vol. 19, pp. 285-309.
3. Alonso, E.E., and Gens J.V. (1999). "*Modelling the mechanical behaviour of expansive clays.*" Engineering Geology, vol. 54, pp. 173-183.
4. Alonso, E.E., Gens, A., and Josa A. (1990). "*A constitutive model for partially saturated soils.* " Géotechnique, vol. 40, pp. 405-430.
5. Alonso, E.E., Romero, E., Hoffmann, C., and Garcia-Escudero, E. (2005). "*Expansive bentonite–sand mixtures in cyclic controlled-suction drying and wetting*", Engineering Geology, vol. 81, pp. 213-226.
6. Alramahi, B.A., and Alshibli, K.A. (2006). "*Applications of Computed Tomography (CT) to Characterize the Internal Structure of Geomaterials : Limitations and Challenges*, Site and Geomaterial Characterization, (GSP 149)- ASCE, pp. 88-95.
7. Alshibli, K.A., Batiste, S.N., Swanson, R.A., Sture, S., Costes, N.C., and Lankton, M.R. (2000). "*Quantifying Void Ratio in Sand Using Computed Tomography.*" Geotechnical Measurements – Lab and Field, ASCE Geotechnical Special Publication 106, pp. 30-43.
8. Anon. (1979). *"Classification of rocks and soils for engineering geological mapping."* Part 1: Rock and soil materials. (IAEG Commission of engineering geological mapping). Bull. IAEG.,vol.19, pp. 364–371.

9. Avsar, E., Ulusay, R., Sonmez, H. (2009). "*Assessments of swelling anisotropy of Ankara clay*." Engineering Geology, vol. 105, pp. 24–31.

10. Bailey, S. W. (1980). "*Summary of recommendations of AIPEA nomenclature committee on clay minerals*." American Mineralogist, vol. 65, pp. 1-7.

11. Bernier, F., Volckaert, G., Alonso, E., and Villar, M. (1997). "*Suction-controlled experiments on Boom clay*." Engineering Geology, vol. 47, pp. 325-338.

12. Borchardt, G. (1989), "*Smectites*", In J.B. Dixon and S.B. Weed, eds., Minerals in Soil Environments, 2nd ed., Madison, WI: Soil Science Society of America

13. Brooks, R.H., and Corey, A.T. (1964). "*Hydraulic properties of porous media."* Hydrol.pap. Colorado State University, Fort Collins.

14. Budge, W.D., Sampson, E. Jr., and Schuster, R.L. (1966). "*A Method of Determining Swell Potential of an Expansive Clay*." Highway Research Record.

15. Chen, F.H (1988). "*Foundations on expansive soils 2nd Ed.*" Elsevier Science Publications, New York.

16. Chen, F.H. (1965). "*The use of piers to prevent the uplifting of lightly loaded structures founded on expansive soils.*" Engineering Effects of Moisture Change in soils, Proceedings of the International research and Engineering Conference on Expansive Clay soils, Texas A&M University, pp. 152-171.

17. Chittoori, B. C. S, and Puppala, A. J. (2011). "*Quantitative estimation of clay mineralogy in fine-grained soils." Journal of Geotechnical and Geoenvironmental Engineering*, vol. 137(11), pp. 997-1008.

18. Chittoori, B.C.S. (2008). "*Clay Mineralogy Effects On Long-Term Performance Of Chemically Treated Expansive Clays*." Dissertation submitted to the Department of Civil Engineering at University of Texas at Arlington.

19. Cho, S., and Lee, S. (2002). "*Evaluation of Surficial Stability for Homogeneous Slopes Considering Rainfall Characteristics*." Journal of Geotechnical Geoenvironment Engineering, vol. 128(9), pp. 756-763.

20. Cui, Z.D, Tang, Y. (2011). "*Microstructures of different soil layers caused by the high-rise building group in Shanghai*." Environmental Earth Science, vol. 63, pp. 109–119.

21. Dedier, G. (1973). "*Prediction of Potential and Swelling Pressure of Soils.*" Proceeding of 8th International Society for Soil Mechanics and Foundation Engineering, vol. 22, pp. 1-20.

22. Delage, P., Howat, M.D., Cui, Y.J. (1998). "*The relationship between suction and swelling properties in a heavily compacted unsaturated clay*." Engineering Geology, vol. 50, pp. 31–48.

23. Delage, P. (2010). "*A microstructure approach to the sensitivity and compressibility of some Eastern Canada sensitive clays"* Geotechnique, V 60, No. 5, pp 353–368

24. Desrues, J., Chambon, R., Mokni, M., and Mazerolle, F. (1996). "*Void ratio evolution inside shear bands in triaxial sand specimens studied by computed tomography*." *Geotechnique*, vol. 46(3), pp. 529–546.

25. El-Ramli, A.H. (1965). "*Swelling Characteristics of Some Egyptian Soils.*" Journal of the Egyptian Society of Engineering, vol. 4(1),pp. 25-35.

26. Ferber, V., Jean-Claude Auriol , Yu-Jun Cui , Jean-Pierre Magnan. (2009). "*On the swelling potential of compacted high plasticity clays*", Engineering Geology, vol. 104, pp. 200–210.

27. Fredlund, D. G., and Rahardjo, H. (1993). "*Soil Mechanics for Unsaturated Soils.*" Wiley, New York.

28. Fredlund, D.G, and Morgenstern, N.R, (1976). "*Constitutive relations for volume change in unsaturated soils*", Canadian Geotechnical Journal, vol. 13, pp. 261 -276.

29. Fredlund, D.G. (1989). "*Soil suction monitoring for roads and airfields.*" Symposium on the State-of-the Art of Pavement Response Monitoring Systems for Road and Airfields.

30. Fredlund, D.G. (2006). "*The Terzaghi Lecture: Unsaturated soil mechanics in engineering practice.*" Journal of Geotechnical and Geoenvironmental Engineering, vol. 132(3), pp. 286–321.

31. Fredlund, D.G. and Xing, A. (1994). "*Equations for the soil water characteristic curve*." Canadian Geotechnical Journal, vol. 31, pp. 521-532.

32. Fredlund, D.G., and Houston, A.L. (2009). "*Protocol for the assement of unsaturated soil properties in geotechnical engineering practice*." Canadian Geotechnical Journal, vol. 46, pp. 694-707.

33. Fredlund, D.G., and Morgenstern, N.R. (1996). "*Constitutive relations for volume change in unsaturated soils.*" Canadian Geotechnical Journal, Vol.13, pp. 261-276.

34. Fredulund, D.G.(1969). "*Consolidometer test procedural factors affecting swell properties.*" Proceedings of 2nd International Conference on Expansive Clay Soils, Texas A&M University, College Station, pp. 435-456.

35. Grim, R. E. (1953). "*Clay Mineralogy*." Mc Graw Hill Book Company, New York.

36. Grim, R.E. (1962). "*Applied Clay Mineralogy*", McGraw Hill, New York.

37. Habib, S.A., and Karube, D. (2011). "*Swelling Pressure Behavior Under Controlled Suction*." Geotechnical testing Journal, pp. 271 - 275.

38. Hilf, J.W. (1956). "*An Investigation of Pore-Water Pressure in Compacted Cohesive Soils.*" Tech. Memo. 654, U.S. Department of the Interior, Bureau of Reclamation Design and Construction Div, Denver, Colorado.

39. Holtz, W.G., and Gibbs, H.J. (1956)."*Engineering properties of expansive clays*." Transactions of the American Society of Civil Engineers, vol. 121, pp. 641–663.

40. Hui, Z., Ying-guang, F., Ren-guo, G., and Cheng, Z. (2011)."*Microscopic analysis of saturated soft clay in Pearl River Delta.*" Journal of Cent. South University Technology, vol. 18, pp. 504−510.

41. Hussein E.A. (2001). "*Viscoplastic Finite Element Model for Expansive Soils.*" EJGE, paper 2001-0122.

42. Johnson, L.D., Stroman, W.R.(1976). "*Analysis of Behavior of Expansive Soil Foundations.*" U.S. Army Engineer Waterways Experiment Station Technical Report S-76-8.

43. Jones, D. E., and Holtz, W. J. (1973). "*Expansive soils: The hidden disaster*." Civil Engineering, New York, vol. 430(8), pp. 49-51.

44. Kassif, G., Komornik, A., Wiseman, G. and Zeitlen, J. G. (1965). "Studies and design criteria for structures on expansive clays." Proceeding of 1st Res. Conf. on Exp. Soils, Texas.

45. Kormonik, A., and David, D. (1969). "*Prediction of swell pressure of clays.*" Journal of Soil Mechanics and Foundation Division ASCE, vol. 95 (SM1), pp. 209-225.

46. Lambe, T.W., and Whitman, R.V. (1969). " Soil mechanics - series in soil engineering" John Wiley and Sons.

47. Leong, E-C., Tripathy, S., Rahardjo, H. (2003). "*Total suction measurement of unsaturated soils with a device using the chilled-mirror dew-point technique.*" Géotechnique, vol. 53(2), pp. 173–182.

48. Lins, Y., and Schanz, T. (2004). "Determination of hydro-mechanical properties of sand." International Conference on Experimental Evidence towards Numerical Modeling of Unsaturated Soils, T. Schanz, ed., Lecture Notes in Applied Mechanics, Springer, New York, pp. 11–29.

49. Lu, N., and Likos, W. J. (2004). "*Unsaturated Soil Mechanics.*" John Wiley & Sons, New York.

50. Luiz, F.P, Fabio A.M.Ca´ssaro , Klaus, R., Osny, O.S., Bacchi, (2008). "*Soil porous system changes quantified by analyzing soil water retention curve modifications*." Soil & Tillage Research, vol. 100, pp. 72–77.

51. Luo, L., Lin, H., Li, S. (2010). "*Quantification of 3-D soil macropore networks in different soil types and land uses using computed tomography*." *Journal of Hydrology*, vol. 393(1-2), pp. 53-64.

52. Luo, L., Lin, H., and Halleck, P. (2008). "*Quantifying soil structure and preferential flow in Intact soil using X-ray computed tomography*." SSAJ, vol. 72(4).

53. Marinho, F.A.M., and Oliveira O.M. (2006). "*The Filter Paper Method Revisited*", Geotechnical Testing Journal, Vol. 29(3).

54. Matsuhima, T., Katagiri, J., Uesugi, K., Nakano, T., and Tsuchiyama, A. (2006). "*Micro X-ray CT at spring-8 for granular mechanics*." Soil stress-strain behavior: Measurement, Modeling and Analysis, A collection of papers of the Geotechnical Symposium in Rome, pp. 16–17.

55. McCleskey, L.K., Puppala, A.J., Dronamraju, S.V., and Perrin, L. (2008). "*Remedial Measures Planned to Prevent Surficial Failures*", GeoEdmonton, Canadian Geotechnical Society.

56. McKeen, R. G. (1980). "*Field studies of airport pavements on expansive clay.*" Proceeding of 4th International Conference on Expansive Soils, Denver, vol. 1, pp. 242–261.

57. Mitchell, J.K., and Soga, K. (2005). "*Fundamentals of Soil Behavior*." 3rd Edition, John Wiley and Sons Inc., Hoboken, New Jersey.

58. Mokwa, R.L., and Nielsen, B. (2006). " *Nondestructive Measurements of Soil Geotechnical Properties Using X-Ray Computed Tomography*." GeoCongress - ASCE.

59. Mollins, L.H., Stewart, D.I., and Cousens, T.W. (1996). "*Predicting the properties of bentonite-sand mixtures.*" Clay Minerology, vol. 31, pp. 243-252.

60. Mowafy, Y.M. and Bauer, G.E. (1985a). "*Prediction of Swelling Pressure and Factors Affecting the Swell Behavior of an Expansive Soil*." Transportation Research Record, vol. 1032, pp.23-33.

61. Mowafy, Y.M. and Bauer, G.E. (1985a). "*Prediction of Swelling Pressure and Factors Affecting the Swell Behavior of an Expansive Soil.*" Transportation Research Record 1032. pp. 23-33.

62. Nagaraj, T.S., and Murthy, B.R.S. (1985). "*Prediction of the Preconsolidation Pressure and Recompression Index of Soils*." Geotechnical Testing Journal, vol.8(4).

63. Nagaraj, T.S., and Srinivasa Murthy, B.R. (1985). "*Rational Approach to Predict Swelling Soil Behavior*." Transportation Research Record 1032, pp.1-7.

64. Nelson, D., and Miller, D. J. (1992), "*Expansive Soils Problems and practice in Foundation and Pavement Engineering.*" John Wiley & Sons, New York, pp. 40-80.

65. Ofer, Z., and Komornik, A. (1983). "*Lateral swelling pressure of compacted clay.*" 7th Asian Regional conference on Soil Mechanics and Foundation Engineering, vol. 1, pp. 56-63.

66. Ohri, M.L. (2003). "*Swelling behavior of clays and its control*." Proceeding of International Conference on Problematic soils, Nottingham, U.K, pp. 427-433.

67. Olsen, R.E., Langfelder, L.I. (1965). "*Pore water pressures in unsaturated soils.*" Journal of Soil Mechanics and Foundation Division, ASCE 91, pp. 127– 150.

68. O'Neill, M.W. and Poormoayed, N. (1980). "*Methodology for foundations on expansive soils*" Journal of Geotech Eng. Div., ASCE 106 (GT12, December): 1345-1367.

69. Otani, J., Mukunoki, T., and Obara, Y. (2000). "*Application of X-ray CT method for characterization of failure in soils.*" *Soils Found.*, vol. 40(2), pp. 111–118.

70. Petry, T.M., and Jiang, C. (2007). "*Round-Robin Testing of a Dewpoint Potentiameter Versus Filter Paper to Determine Total Suction.*" Geo-Denver Advances in Measurement and Modeling of Soil Behavior.

71. Punthutaecha, K., Puppala, A.J., Vanapalli, S.K., and Inyang, H. (2006). "*Volume change behaviors of expansive soils stabilized with recycled ashes and fibers*." Journal of Materials in Civil Engineering, vol. 18(2), pp. 295-306.

72. Puppala, A.J., Thammanoon, M., Soheil, N., and Hoyos, L.R. (2011). "*Threshold moisture content and matric suction potentials in expansive clays prior to initiation of cracking in pavements.*" Canadian Geotechnical Journal, v 48, n 4, p 519-531.

73. Puppala, A.J., Griffin, J.A., Hoyos, L.R., and Chomtid, S. (2004). "*Studies on Sulfate-Resistant Cement Stabilization Methods to Address Sulfate-Induced Soil Heave.*" *Journal of Geotechnical and Geoenvironmental Engineering.*

74. Rabba, S. (1975). "*Factors Affecting Engineering Properties of Expansive Soils.*" M.S. Thesis, Al-Azhar University, Cairo, Egypt.

75. Rahardjo, H., and Leong, E.C. (2006). "*Suction Measurements*." Proceedings of the 4th International Conference on Unsaturated Soils, Carefree, Arizona, pp. 81-104.

76. Rahardjo, H., Li, X.W., Toll, D. G., and Leong, E.C. (2001). "*The effect of antecedent rainfall on slope stability*." Geotechnical and Geological Engineering, vol.19(3-4), pp. 371-399.

77. Rawas, A.A., Hago, A.W., and Al-Sarmi, H. (2005). "*Effect of lime, cement and Sarooj (artificial pozzolan) on the swelling potential of an expansive soil from Oman*" Journal of Building and Environment**,** vol. 40(5), pp. 681–687.

78. Rezanezhad, F., and Quinton, W.L., Price, J.S., Elliot, T.R., Elrick, D., and Shook, K.R. (2010). "*Influence of pore size and geometry on peat unsaturated hydraulic conductivity computed from 3D computed tomography image analysis*." Hydrological Processes, vol. 24, pp. 2983–2994.

79. Saiyouri, N., Tessier, D., and Hicher, P.Y. (2004). "*Experimental study of swelling in unsaturated compacted clays*." Clay Minerals, vol. 39, pp. 469–479.

80. Sander, T., Gerke, H.H., Rogasik, H. (2008). "*Assessment of Chinese paddy-soil structure using X-ray computed tomography*." Geoderma, vol. 145, pp. 303-314.

81. Seed, H.B., Woodward, R.J., and Lundgren, R. (1962). "*Prediction of swelling potential for compacted clays*." Journal of Soil Mechanics and Foundation Division ASCE, Vol. 88 (SM3), pp. 53-87.

82. Simms, P.H, and Yanful, E.K. (2004). " *Estimation of Soil–Water Characteristic Curve of Clayey Till Using Measured Pore-Size Distributions*." Journal of Environmental Engineering, pp. 847-854.

83. Snethen, D.R. (1979b). "*An Evaluation of methodology for prediction and minimization of volume change of expansive soils in highway subgrades.*" Research Report No. FHWA-RD-79-49., U. S. Army Eng. Waterway Exp. Sta., Vicksburg, MS.

84. Snethen, D.R., and Johnson, L.D. (1980). "*Evaluation of soil suction from filter paper*." Geotech. Lab., U.S. Army Eng. Waterway Exp. Sta., Vicksburg, Mississippi, Misc. Paper No. 6L-80-4.

85. Soto, M.A., and Vilar, O.M. (2006). "*Evaluation of a Pore Fractal Model for the Prediction of Soil Water Retention Curve*", Unsaturated Soils - ASCE, pp. 2441-2452.

86. Sudhakar, M.R, Revanasiddappa, K. (2005). "*Role of microfabric in matrix suction of residual soils*." Engineering Geology, vol. 80, pp. 60 – 70.

87. Teresa, L.L., Hernández, J.B., Zaragosa, Cajun C. López. (2004). "*Mineralogical characterization of stabilized soils.*" Electronic journal of Geotechnical engineering, vol. 9F.

88. Thakur, V.K.S., and Singh, D.N. (2005). "*Swelling and suction in clay minerals. Advanced Experimental Unsaturated Soil Mechanics. In: Tarantino A, Romero E, Cui YJ (eds).''* Proc Int Symp (Experus 2005), Trento, Italy. A.A. Balkema, Rotterdam, pp. 27–31.

89. Thakur, V.K.S., Sreedeep, S., and Singh, D.N. (2006). "*Laboratory investigations on extremely high suction measurements for finegrained soils*." Journal of Geotechnical and Geological Engineering, Springer, vol. 24(3), pp. 565-578.

90. Thompson, M. L., and Ukrainczyk, L. (2002). "*Micas*" Edited by Dixon, J.B., and Schulze, D.G. Soil mineralogy with environmental applications, SSSA, Madison, WI, pp. 431-466.

91. Tippko¨tter, R., Thilo Eickhorst , Heidi Taubner , Beke Gredner, and Guido Rademaker (2009). "*Detection of soil water in macropores of undisturbed soil using microfocus X-ray tube computerized tomography (mCT)*." Soil & Tillage Research, vol. 105, pp. 12–20.

92. Torrance,J.K., Elliot, T., Martin, R., and Heck, R.J. (2008). "*X-ray computed tomography of frozen soil*." Cold regions Science and Technology, vol. 53, pp. 75-82.

93. Van Der Merwe, D.H. (1964). "*The prediction of heave from the plasticity index and percentage clay fraction of soil.*" Trans. S. Afr. Instr.Civ. Engrs., vol. 6, pp. 103–107.

94. Van Genuchten, M.T. (1980).*"A closed-form equation for predicting the hydraulic conductivity of unsaturated soils."* Soil Science Society American Journal, vol. 44, pp. 892–898.

95. Vanapalli, S.K., Fredlund, D.G., and Pufahl, D.E. (1999). "*The influence of soil structure and stress history on the soil-water characteristic of a compacted till.*" Geotechnique, vol.49(2),pp.143-159.

96. Vergés, E., Tost, D., Ayala, D., Ramos E., and Grau, S. (2011). "*3D pore analysis of sedimentary rocks*." Sedimentary Geology, vol. 234, pp. 109–115.

97. Washburn, E.W., (1921). "Note on a method of determining the distribution of pore sizes in a porous material", Proceedings of the National Academy of Sciences 4, pp. 115– 116.

98. Wattanasanticharoen, E. (2004). **"***Experimental studies to address volume change behaviors of chemically treated sulfate bearing soils.***"** Dissertation submitted to the Department of Civil Engineering at University of Texas at Arlington.

99. Williams, H.F.L. (2003). "*Urbanization pressure increases potential for soils-related hazards Denton County, Texas.*" *Environmental Geology*, vol. 44(8), pp. 933-938.

100. Yusuf, E., and Erol O. (2007). "*Swell pressure prediction by suction methods*." Engineering Geology, vol. 92, pp. 133–145.

101. Zeitlin, J.G., and Komornik, A. (1961). "*Deformations and moisture movements in expansive clays."* Proceedings of the 5th International Conference on Soil Mechanics and Foundation Engineering, vol. 1, pp. 873-879.

102. Zhan, L., Chen, P., and NG C.W.W. (2007). "*Effect of suction change on water content and total volume, of an expansive clay*." Journal of Zhejiang University Science A, vol. 8(5), pp. 699-706.

BIOGRAPHICAL INFORMATION

Aravind Pedarla was born in Vijayawada, India on 27th December, 1985. He graduated from GMR Institute of Technology, India, with a Bachelor's Degree in Civil Engineering in 2007. After working as a project engineer in GMR group of industries, he joined University of Texas at Arlington (UTA) to pursue his Masters degree in Civil Engineering under the guidance of Prof. Anand J. Puppala. The topic of his thesis during Masters Program was 'DURABILITY STUDIES ON STABILIZATION EFFECTIVENESS OF SOILS CONTAINING DIFFERENT FRACTIONS OF MONTMORILLONITE' which he defended successfully in Decmber 2009.

In 2010, he pursued doctoral program in the Department of Civil Engineering at the University of Texas at Arlington (UTA), Arlington, Texas with Geotechnical Engineering as the major area of research. At UTA, he performed research studies on expansive soils behaviors and soil composition properties under the guidance of Prof. Anand J. Puppala and successfully defended his dissertation in April 2013. During the course of his study, he worked in various research areas related to field instrumentation, ground improvement, soil-suction testing, expansive soils behaviors and advanced internal structure of solid study techniques like Mercury Intrusion Porosimetry and X-ray Computed Tomography.